A Multi-Fidelity Approach for Aerodynamics and Aeroacoustics of Vertical Axis Wind Turbines

Shubham

MSc Aerospace Engineering, BTech Mechanical Engineering

A thesis submitted in partial fulfilment of the requirements of Nottingham Trent University for the degree of Doctor of Philosophy

May 2024

Summary

This thesis performs an in-depth exploration of Vertical Axis Wind Turbines (VAWTs), motivated by the urgent need to address global climate change through sustainable energy solutions. The research predominantly focuses on the aerodynamics and aeroacoustics of VAWTs using computational simulations. This thesis aims to contribute to the body of knowledge and state-of-the-art surrounding VAWTs, a less explored yet promising design of wind turbines, especially suitable for urban and floating offshore applications.

This thesis employs a multi-fidelity computational approach, leveraging both mid-fidelity and high-fidelity methods. The mid-fidelity Lifting Line Free Vortex Wake (LLFVW) method offers a balance between computational cost and accuracy. The high-fidelity Lattice Boltzmann/Very Large Eddy Simulation (LB-VLES) method provides detailed insights into the complex aerodynamics and aeroacoustics of VAWTs. These methodologies are implemented using the open-source software QBlade and the commercial software Dassault Systèmes SIMULIA PowerFLOW, respectively. The thesis examines VAWTs over a range of both design and operational parameters, including different number of blades, supporting structures (struts and central towers), tip speed ratio, and non-uniform inflow such as skewed inflow and VAWT clusters in parallel and tandem configurations.

The study highlights how the above-mentioned operational and design parameters significantly influence the force-field and flow-field of VAWTs and how the force-field mutually affects the flow-field. Additionally, the focus is on understanding how the VAWT force-field affects the pressure perturbations in the far-field and therefore, the noise generated. The study shows the potential of VAWT designs which can exhibit high power performance and low aerodynamic noise. Notably, the research underscores the increased power density achievable in VAWT clusters compared to standalone VAWTs.

A comparative analysis between mid-fidelity and high-fidelity methods demonstrates that while mid-fidelity methods accurately predict general performance trends, high-fidelity methods are essential for capturing the complex fluid dynamic interactions in the VAWT force-field and flow-field. This is found to be true when any combination of the design or operational parameters is used. The thesis concludes that VAWTs hold significant potential for urban and offshore applications, debunking common misconceptions about their inefficiency.

The thesis outlines numerous areas for future research, including exploring different VAWT blade shapes, assessing the impact of flow control devices, and understanding the influence of variable pitch on performance and aeroacoustics. Further investigations into the clustering of VAWTs and the use of different vortex methods for performance prediction are also recommended.

Acknowledgements

My journey at Nottingham Trent University (NTU) has been a remarkable blend of technical, professional, and personal growth. These years have shaped me in more ways than I could have ever imagined.

First and foremost, I extend my heartfelt gratitude to Prof Anton Ianakiev and Prof Nigel Wright. Without your belief in me and the opportunity to pursue this PhD, I wouldn't have had this incredible chance. Heartfelt thanks to Prof Anton for navigating me through all the bureaucratic hurdles, taking care of the small things, and making me feel at home at NTU.

My journey has been rich with learning, both technical and professional. Delving into the study of sustainability and wind turbines has broadened my perspective on the future of the world's energy needs. Living in the urban environment of Nottingham in a bustling city life has provided me with valuable insights into how urban areas can and should evolve sustainably in the future. My professional development has been significantly enhanced by organizing workshops, conferences, and meetings, where I had the privilege of interacting with people from both industry and academia. This helped me plan my future career goals by getting a much broader perspective.

A major highlight of my journey has been collaborating with colleagues as part of the Horizon 2020 Zephyr project. A special appreciation to Prof Francesco Avallone. Working with you on research papers has not only been a high point of my academic career but also an incredible learning experience. I owe a debt of gratitude to all my colleagues and partner universities from the Zephyr project for providing me the opportunity to develop professionally and collaborate on an international level. On a personal note, I have also grown immensely, forming amazing friendships while working on my thesis.

I am grateful to my Nottingham friends Kevin, Payal, Sharmila, Arijit, and Sherna. Our numerous coffee breaks, life-sharing experiences, hiking tours, and visits to street food places have made this PhD journey enjoyable and easier to navigate. Joining the PhD program during the lockdown was challenging, but my personal life became much more vibrant when I started meeting you all in the Maudslay building. You made Nottingham feel like home for me.

Special thanks to my mom and dad for your unwavering support throughout this PhD process. It wouldn't have been possible without you. And finally, no words can express my gratitude to my wife, Sushmita, who has supported me throughout this journey and understood me at every step. From meeting as strangers in the Future Factory office to becoming colleagues, friends, partners, and eventually husband and wife, our personal journey is no less than a PhD thesis on its own. Together, we explored the UK, India, and Europe, and in the midst of all of this even planned an Indian wedding — a feat requiring no less effort than a PhD thesis, if not more! It is said that if a relationship can survive a PhD thesis, it can withstand anything in life. And we both endured two of our PhD theses. I eagerly look forward to exploring our world together.

Thank you!

Shubham
Nottingham, May 2024

Contents

Summary 3

Acknowledgements 5

List of Figures 11

List of Tables 19

List of Abbreviations 21

List of Symbols 23

1 Introduction 1
- 1.1 Perspectives on Wind Energy . . . 2
- 1.2 Vertical Axis Wind Turbine . . . 3
- 1.3 Thesis Objectives and Research Questions . . . 5
- 1.4 Thesis structure . . . 8

2 Computational Methodology 13
- 2.1 Introduction . . . 14
- 2.2 The Lattice-Boltzmann Method . . . 15
  - 2.2.1 The Boltzmann's Kinetic Theory . . . 15
  - 2.2.2 Domain discretisation and macroscopic flow quantities . . . 16
  - 2.2.3 LBM procedure . . . 17
  - 2.2.4 Velocity-Space Discretisation and the BGK Collision Operator . . . 19
  - 2.2.5 Boundary Conditions . . . 22
  - 2.2.6 Rotating Geometries . . . 22
  - 2.2.7 LBM-VLES Turbulence Modelling . . . 23
  - 2.2.8 LBM Acoustic Properties . . . 24
- 2.3 Computational Aeroacoustics . . . 25
  - 2.3.1 Direct Noise Computation . . . 25
  - 2.3.2 Hybrid CAA Methods . . . 25
  - 2.3.3 Ffowcs Williams & Hawkings Acoustic Analogy . . . 27
- 2.4 Lifting Line Free Vortex Wake Method . . . 33
  - 2.4.1 The LLFVW Algorithm . . . 33
  - 2.4.2 Wake Lattice and Connectivity . . . 34
  - 2.4.3 Vortex Core Desingularisation . . . 35
  - 2.4.4 Unsteady Aerodynamics and Dynamic Stall . . . 35
  - 2.4.5 Tower Influence . . . 39
  - 2.4.6 Wake Truncation . . . 39
  - 2.4.7 Wake Coarsening . . . 40
- 2.5 Double Multiple Streamtube (DMS) method . . . 41

3 Vertical axis wind turbine **43**
3.1 Historical perspective . . . 44
3.2 Aerodynamic performance . . . 45
3.2.1 Horizontal axis wind turbine vs Propeller . . . 45
3.2.2 Vertical axis wind turbine . . . 46
3.3 State-of-the-art: Aerodynamics . . . 47
3.3.1 Experimental benchmark studies . . . 48
3.3.2 Airfoil profile . . . 48
3.3.3 Blade pitch . . . 49
3.3.4 Rotor solidity . . . 50
3.3.5 Aspect ratio . . . 51
3.3.6 Blade shape . . . 52
3.3.7 External structures . . . 53
3.4 VAWT noise . . . 53
3.5 State-of-the-art: Aeroacoustics . . . 55
3.6 Research gap and the current study . . . 56

4 Stand-alone VAWT I: grid convergence study and tip speed ratio **59**
4.1 Introduction . . . 60
4.1.1 Grid convergence study and Richardson extrapolation . . . 60
4.1.2 Variation in TSR: aerodynamic and aeroacoustic behaviour . . . 61
4.1.3 Research objectives . . . 62
4.2 Computational setup . . . 62
4.2.1 Geometry . . . 62
4.2.2 Numerical setup . . . 64
4.2.3 Flow conditions and grid settings . . . 65
4.2.4 Richardson Extrapolation . . . 68
4.3 Results . . . 70
4.3.1 Grid convergence study and Richardson extrapolation . . . 70
4.3.2 Validation . . . 75
4.3.3 Force and flow field analysis . . . 77
4.4 Conclusions and Discussions . . . 87

5 Stand-alone VAWT II: number of blades **89**
5.1 Introduction . . . 90
5.1.1 Literature Review . . . 90
5.1.2 Research objectives . . . 92
5.2 Computational setup . . . 93
5.2.1 Geometry . . . 93
5.2.2 Numerical setup . . . 94
5.2.3 Flow conditions and grid settings . . . 95
5.3 Results . . . 97
5.3.1 Temporal and grid convergence study . . . 97
5.3.2 Numerical validation . . . 101
5.3.3 Effect of number of blades . . . 101
5.4 Conclusions and Discussions . . . 114

6 Stand-alone VAWT III: supporting struts and central tower 117
6.1 Introduction . . . 118
6.1.1 Literature Review . . . 118
6.1.2 Research objectives . . . 120
6.2 Computational setup . . . 121
6.2.1 Geometry . . . 121
6.2.2 Numerical setup . . . 123
6.2.3 Flow conditions and grid settings . . . 124
6.3 Results . . . 126
6.3.1 Temporal and grid convergence study . . . 126
6.3.2 Numerical validation . . . 130
6.3.3 Effect of struts and a central tower . . . 131
6.4 Conclusions and Discussions . . . 143

7 Stand-alone VAWT IV: skewed inflow 147
7.1 Introduction . . . 148
7.1.1 Literature Review . . . 148
7.1.2 Research objectives . . . 151
7.2 Computational setup . . . 152
7.2.1 Geometry . . . 152
7.2.2 Numerical setup . . . 153
7.2.3 Flow conditions and grid settings . . . 153
7.3 Results . . . 154
7.3.1 Temporal and grid convergence study . . . 154
7.3.2 Effect of skewed inflow . . . 156
7.4 Conclusions and Discussions . . . 172

8 VAWT cluster 175
8.1 Introduction . . . 176
8.1.1 Literature Review . . . 176
8.1.2 Research Objectives . . . 180
8.2 Computational setup . . . 180
8.2.1 Geometry . . . 181
8.2.2 Numerical setup . . . 181
8.2.3 Flow conditions and grid settings . . . 183
8.3 Results . . . 184
8.3.1 Temporal and grid convergence study . . . 184
8.3.2 Parallel VAWT cluster: effect of VAWT separation . . . 185
8.3.3 Parallel VAWT cluster: co-rotating vs contra-rotating . . . 192
8.3.4 Tandem VAWT cluster: effect of VAWT separation . . . 197
8.4 Conclusions and Discussions . . . 203

9 Conclusions and Discussions 207
9.1 Major findings in this study . . . 208
9.1.1 On temporal and grid convergence (Chapter 4) . . . 208
9.1.2 On tip speed ratio (Chapter 4) . . . 209
9.1.3 On number of blades (Chapter 5) . . . 210
9.1.4 On supporting struts and central tower (Chapter 6) . . . 210
9.1.5 On skewed inflow (Chapter 7) . . . 211
9.1.6 On VAWT clusters (Chapter 8) . . . 211

9.1.7 Implications for designers . . . 212
9.2 Contributions to knowledge . . . 213
9.3 Recommendations for future studies . . . 213
9.4 Final comments . . . 216

A List of publications **217**
A.1 First author journal papers . . . 217
A.2 First author conference papers . . . 218
A.3 Co-author journal papers . . . 218
A.4 Co-author conference papers . . . 218

B Curriculum Vitae **219**

Bibliography **223**

List of Figures

1.1 Examples for big-onshore and small-urban wind turbines . . . 3
1.2 Different types of VAWT design: lift-based Darrieus vs drag-based Savonius . . . 5
1.3 Visualisation of results for the thesis objectives and research questions. The mid-fidelity and high-fidelity results are compared, the force field is visualised along the blade span in a single rotation and the flow field is visualised in the downstream wake. The first four figures are for a 2-bladed Darrieus VAWT . . . 7

2.1 Illustration of the LBM algorithm. Within the lattice, individual fluid particles are denoted by dots, and their discrete velocity vectors are depicted using arrows. To represent the advection of the velocity vectors emanating from the central four voxels of the lattice, arrows of varied colours are utilised. (adapted from Teruna [333]) . . . 18
2.2 Discretisation of the simulation domain in the LBM framework showing volume mesh (voxels) and surface mesh (surfels). The part of surface voxels which are penetrating inside the solid surface will be removed to form an overall smooth layer of surfels on the solid surface. (adapted from Teruna [333]) . . . 19
2.3 A schematic of two different LBM stencil examples: D2Q9 with 9-velocity vectors in 2D and D3Q19 with 19-velocity vectors in 3D (adapted from Teruna [333]) . . . 21
2.4 A schematic of the two wall boundary conditions: bounce-back condition for no-slip wall and specular reflection for free-slip wall. The thick black region represents the lattice-aligned surfel (adapted from Teruna [333]) . . . 22
2.5 Problem formulation of the FW-H acoustic analogy (adapted from Casalino [60] and Romani [281]) . . . 28
2.6 Flowchart for aerodynamic calculations for a single timestep as implemented in QBlade for a VAWT (adapted from Marten [215]) . . . 34
2.7 Dynamic stall hysteresis loop; adapted from Marten [215]; (1) Delay in Boundary Layer separation (2) Formation of Leading Edge vortex (3) Convection of vortex over airfoil (4) Leading Edge vortex leaves trailing edge (5) Delay in Boundary Layer reattachment 37
2.8 Tower shadow model illustration; tip speed ratio is 4 and streamwise velocity contour is visualised . . . 39
2.9 Three different wake truncation lengths for a 2-bladed VAWT at TSR = 4, depicting downstream vortex lifting lines . . . 40

3.1 Darrieus 1931 US patent drawings of vertical axis wind turbine [212] . . . 44
3.2 Common types of VAWT design historically [340] . . . 44
3.3 Velocities experienced by blades of horizontal axis wind turbine and propeller; in each case, length of ωR and V_∞ arrows represent their relative values . . . 45
3.4 Darrieus VAWT aerodynamics . . . 46
3.5 Darrieus VAWT performance obtained using the DMS method . . . 47
3.6 Some examples of airfoil used for VAWT blades . . . 48
3.7 Preset blade pitch on a VAWT blade. The configuration shown here is that of a negative pitch (toe-out) with angle β. . . . 49
3.8 Power coefficient variation with TSR and three different pitch angles obtained using the DMS method . . . 50

3.9 Variation in number of blades for VAWT, showing the extent of blockage to the flow . . 50
3.10 Power coefficient variation with TSR and different number of blades and chord lengths obtained using the DMS method 51
3.11 Power coefficient variation with TSR and three different blade heights causing a change in blade and rotor aspect ratio obtained using the DMS method 52
3.12 Some examples of VAWT blade designs, all having the same swept area of 1.54 m^2 . . . 53
3.13 Power coefficient variation with TSR and two different blade shapes obtained using the DMS method 53
3.14 Fourier transform from sampled pressure signal (left) to noise spectra (right) 54
3.15 An example of a VAWT noise spectra by Pearson [261], at TSR = 3, BPF = 12 Hz and V_∞ = 6.4 m/s 55
3.16 Results by Weber [356], at N = 800 RPM and V_∞ = 21.28 m/s 56

4.1 VAWT geometries used in this chapter (figures are not to scale) 63
4.2 Computational setup used in this chapter 64
4.3 Cross-sectional view of the finest mesh around the blade for setup 1 67
4.4 Cross-sectional view of the mesh for the high-fidelity LBM simulation 68
4.5 Statistical temporal convergence for all 3 setups; u denotes uncertainty in integral values after 8th rotation with LBM and after 30th rotation with LLFVW 71
4.6 Grid convergence study for VAWT thrust coefficient C_T and cross-streamwise force coefficient C_{Fz} for a single blade, for setup 1 72
4.7 Grid convergence study for VAWT torque coefficient C_Q for a single blade, for setup 1 73
4.8 Grid convergence study for VAWT thrust coefficient C_T and torque coefficient C_Q using the high-fidelity LBM for setup 2; values are reported for a single blade for TSR = 3.3 74
4.9 Grid convergence study for VAWT thrust coefficient C_T and torque coefficient C_{Fz} using the mid-fidelity LLFVW method for setup 3; values are reported for a single blade . 75
4.10 Grid convergence study of noise spectra at point [(X,Y,Z) = (0,0,7D)] for the overall VAWT, using high-fidelity LBM 76
4.11 Grid convergence study for OSPL at point [(X,Y,Z) = (0,0,7D)] for [20-2000] Hz range for the overall VAWT, using high-fidelity LBM 77
4.12 Comparison of C_P values for a 1-bladed VAWT having the same blade design as setup 3, with the results reported by Balduzzi et al. [22]; both the high-fidelity LBM and mid-fidelity LLFVW have been reported from the present study 77
4.13 Instantaneous 3D flowfield using iso-surfaces of the λ_2 criterion (λ_2 = -5000 1/sec^2) for vortices visualisation for setup 1; velocity magnitude is non-dimensionalised with V_∞ 78
4.14 Comparison of average values for a single rotation with the upwind and downwind halves separately, for setup 1; s denotes the ratio of contribution from upwind and downwind halves and values are reported for a single blade 79
4.15 Variation of thrust coefficient C_T and torque coefficient C_Q for the overall rotor (blades and the central tower) over a complete rotation at different tip speeds ratios 80
4.16 Instantaneous turbulent kinetic energy contour, non-dimensionalised with V_∞^2, in the YZ plane showing the evolution of wake in the VAWT flowfield 81
4.17 Instantaneous vorticity magnitude contour in the YZ plane, located at the blade mid-span, showing the evolution of wake in the VAWT flowfield 82
4.18 Instantaneous vorticity magnitude contour in the YZ plane, located at the blade tip, showing the evolution of wake in the VAWT flowfield 82
4.19 Instantaneous streamwise (Y-axis) velocity contour, non-dimensionalised with V_∞, in the YZ plane showing the evolution of wake in the VAWT flowfield for setup 1 83

4.20 Instantaneous streamwise (Y-axis) velocity contour, non-dimensionalised with V_∞, in the XY plane showing the evolution of wake in the VAWT flowfield for setup 1 84
4.21 Streamwise (Y-axis) velocities, averaged over a rotation, plotted along the Z-axis (lateral direction) in YZ plane, comparing the extent of the wake for TSR 1.12, 2.23 and 2.97 85
4.22 Raw unsteady pressure data for the overall VAWT comparing 3 different TSRs 85
4.23 Noise spectra for the overall VAWT comparing 4 different TSRs, for setup 1 86
4.24 Directivity plot of overall sound pressure level (OSPL) comparing 4 different TSRs, along a circular array of 36 points situated at a distance of 7D from the origin of VAWT ([0,0,0]) for setup 1 87

5.1 VAWT configuration used in this chapter (Balduzzi [22]) 94
5.2 Computational setup used in this chapter 95
5.3 Cross-sectional view of the finest mesh around the blade 97
5.4 Cross-sectional view of the mesh for the high-fidelity LBM simulation 98
5.5 Statistical temporal convergence study for VAWT thrust coefficient C_T and torque coefficient C_Q using the high-fidelity LBM and mid-fidelity LLFVW; the values are representative of the overall rotor 99
5.6 Statistical temporal convergence study for unsteady pressure data at TSR = 3.3 at location (X,Y,Z)=(0,0,7**D**), using the high-fidelity LBM for the finest Grid 4 100
5.7 Grid convergence study for VAWT thrust coefficient C_T and torque coefficient C_Q using the high-fidelity LBM 100
5.8 C_P values for a 1-bladed VAWT obtained using mid-fidelity LLFVW and high-fidelity LBM compared with the results reported by Balduzzi et al. [22] 101
5.9 Power and thrust curve obtained for different number of blades using the mid-fidelity LLFVW and high-fidelity LBM; line plot is for mid-fidelity LLFVW and single dot at TSR = 3.3 is for high-fidelity LBM 102
5.10 Variation of thrust coefficient C_T and torque coefficient C_Q for the overall rotor over a complete rotation, using the high-fidelity LBM and mid-fidelity LLFVW at TSR = 3.3 . 103
5.11 Variation of thrust coefficient C_T and torque coefficient C_Q for a single blade over a complete rotation, using the high-fidelity LBM and mid-fidelity LLFVW at TSR = 3.3 . 104
5.12 Normal force contour for a single blade over azimuthal and spanwise directions, using the high-fidelity LBM and mid-fidelity LLFVW, at TSR = 3.3 105
5.13 Instantaneous 3D flowfield using iso-surfaces of the λ_2 criterion (λ_2 = -500 1/sec^2) for vortices visualisation, using high-fidelity LBM, at TSR = 3.3 107
5.14 Visualization of vortex lines shed from the VAWT blades and instantaneous 3D flowfield using iso-surfaces of the Q-criterion (Q = 6 1/sec^2) for vortices visualisation, using mid-fidelity LLFVW at TSR of 3.3 108
5.15 Visualization of vortex lines shed from the VAWT blades and instantaneous 3D flowfield using iso-surfaces of the Q criterion (Q = 6 1/sec^2) for vortices visualisation, using mid-fidelity LLFVW method for 2-bladed VAWT 109
5.16 Instantaneous streamwise velocity contours in the VAWT wake on a 2D plane located at the blade mid-span location, using both LBM and LLFVW methods, at TSR = 3.3 . . 110
5.17 Comparison of streamwise velocities, averaged over a rotation, in the downstream VAWT flowfield using high-fidelity LBM and mid-fidelity LLFVW at two different locations, at TSR = 3.3 111
5.18 Comparison of instantaneous velocities experienced by a VAWT blade at the most upstream (90°) and the most downstream location (270°) for the 1-bladed and 3-bladed configurations, using the high-fidelity LBM, at TSR = 3.3 112

5.19 Raw unsteady pressure data for different VAWT configurations using the high-fidelity LBM at TSR = 3.3 . . . 112
5.20 Power Spectral Density (PSD) spectra using the high-fidelity LBM at two different locations, at TSR = 3.3 . . . 113
5.21 Directivity plot of overall sound pressure level (OSPL) comparing VAWTs with different number of blades at TSR = 3.3, along a circular array of 36 points situated at a distance of 7D from the origin of VAWT ([0,0,0]) . . . 114

6.1 VAWT configurations used in this chapter; O represents origin of the coordinate system 122
6.2 Cross-sectional view of the finest mesh around the blade . . . 125
6.3 Cross-sectional view of the mesh for the high-fidelity LBM simulation . . . 126
6.4 Statistical temporal convergence study for VAWT thrust coefficient C_T and torque coefficient C_Q using the high-fidelity LBM and mid-fidelity LLFVW for the finest Grid 3; the values are representative of the overall rotor . . . 127
6.5 Statistical temporal convergence study for unsteady pressure data for the first configuration without struts and tower at TSR = 4, at two different locations using the high-fidelity LBM for the finest Grid 3 . . . 128
6.6 Grid convergence study for VAWT normal force coefficient C_{Fn} of a single blade, using the high-fidelity LBM for TSR = 4 . . . 129
6.7 Grid convergence study for VAWT thrust coefficient C_T and torque coefficient C_Q for the first configuration without struts and tower, using the high-fidelity LBM at TSR = 4 129
6.8 Normal force coefficient C_{Fn} of a single blade using high-fidelity LBM and mid-fidelity LLFVW in the current study, compared with experimental and reference high-fidelity LBM results, at TSR = 4; [ref] - reference . . . 130
6.9 Instantaneous streamwise velocities experienced by a VAWT blade at different azimuth locations for the VAWT configuration without struts and tower, using the high-fidelity LBM at TSR = 4 . . . 131
6.10 Instantaneous streamwise velocities experienced by a VAWT blade at different azimuth locations as obtained by Brandetti et al. [47]; u: streamwise velocity, U_∞: freestream velocity (reprinted after written permission) . . . 132
6.11 Power and thrust curve obtained for the three VAWT configurations using the mid-fidelity LLFVW and high-fidelity LBM; line represents mid-fidelity and dot represents high-fidelity results . . . 132
6.12 Variation of thrust coefficient C_T and torque coefficient C_Q for the overall rotor over a complete rotation, using the high-fidelity LBM and mid-fidelity LLFVW at TSR = 4 . . 134
6.13 Variation of thrust coefficient C_T and torque coefficient C_Q for a single blade over a complete rotation, using the high-fidelity LBM and mid-fidelity LLFVW at TSR = 4 . . 135
6.14 Normal force contour for a single blade over azimuthal and spanwise directions, using the high-fidelity LBM and mid-fidelity LLFVW, at TSR = 4 . . . 136
6.15 Instantaneous 3D flowfield using iso-surfaces of the λ_2 criterion (λ_2 = -500 1/sec^2) for vortices visualisation, using high-fidelity LBM at TSR = 4 . . . 137
6.16 Visualization of vortex lines shed from the VAWT blades and instantaneous 3D flowfield using iso-surfaces of the Q-criterion (Q = 6 1/sec^2) for vortices visualisation, using mid-fidelity LLFVW at TSR = 4 . . . 138
6.17 Instantaneous streamwise velocity contours in the VAWT wake on a 2D plane located at the blade mid-span location, using both LBM and LLFVW methods, at TSR = 4 . . . 139
6.18 Comparison of streamwise velocities, averaged over a rotation, in the downstream VAWT flowfield using high-fidelity LBM and mid-fidelity LLFVW at two different downstream locations, at TSR = 4 . . . 140

6.19 Comparison of instantaneous velocities experienced by a VAWT blade at the most upstream (90°) and the most downstream location (270°) for all three configurations, using the high-fidelity LBM at TSR = 4 . . . 141
6.20 Raw unsteady pressure data using the high-fidelity LBM at two different locations, at TSR = 4 . . . 142
6.21 Power Spectral Density (PSD) spectra using the high-fidelity LBM at two different locations, at TSR = 4 . . . 142
6.22 Directivity plot of overall sound pressure level (OSPL) comparing different VAWT configurations at TSR = 4, along a circular array of 36 points situated at a distance of $7D$ from the origin of VAWT ([0,0,0]) . . . 143

7.1 Reference used for skewed inflow condition; positive angle β is referred to as positive vertical direction for the airflow . . . 148
7.2 VAWT configuration used in this chapter; 'O' denotes the coordinate origin . . . 152
7.3 Statistical temporal convergence study for VAWT thrust coefficient C_T and torque coefficient C_Q using the high-fidelity LBM and mid-fidelity LLFVW; the values are representative of the overall rotor . . . 155
7.4 Power and thrust curve obtained for different skew angles using the mid-fidelity LLFVW and high-fidelity LBM . . . 156
7.5 Variation of thrust coefficient C_T and torque coefficient C_Q for the overall rotor over a complete rotation, using the high-fidelity LBM and mid-fidelity LLFVW at TSR = 4 . . . 158
7.6 Variation of thrust coefficient C_T and torque coefficient C_Q for a single blade over a complete rotation, using the high-fidelity LBM and mid-fidelity LLFVW at TSR = 4 . . . 159
7.7 Normal force contour for a single blade over azimuthal and spanwise directions, using the high-fidelity LBM and mid-fidelity LLFVW, at TSR = 4 . . . 160
7.8 Instantaneous 3D flowfield using iso-surfaces of the λ_2 criterion (λ_2 = -1500 1/sec^2) for vortices visualisation, using high-fidelity LBM at TSR = 4 . . . 161
7.9 Visualization of vortex lines shed from the VAWT blades in the downstream wake, using mid-fidelity LLFVW method at TSR of 4 . . . 162
7.10 Instantaneous 3D flowfield using iso-surfaces of the Q-criterion (Q = 6 1/sec^2) for vortices visualisation, using mid-fidelity LLFVW at TSR of 4 . . . 163
7.11 Visualization of vortex lines shed from the VAWT blades in the downstream wake, using mid-fidelity LLFVW method at TSRs 3 and 5 . . . 164
7.12 Instantaneous 3D flowfield using iso-surfaces of the Q-criterion (Q = 6 1/sec^2) for vortices visualisation, using mid-fidelity LLFVW at TSRs 3 and 5 . . . 165
7.13 Instantaneous streamwise velocity contours in the VAWT wake on a 2D plane located along the VAWT rotational axis, using both LBM and LLFVW methods, at TSR = 4 . . . 166
7.14 Instantaneous streamwise velocity contours in the VAWT wake on a 2D plane located at the blade mid-span location, using both LBM and LLFVW methods, at TSR = 4 . . . 167
7.15 Comparison of streamwise velocities, averaged over a rotation, in the downstream VAWT flowfield using high-fidelity LBM and mid-fidelity LLFVW at two different locations, at TSR = 4 . . . 168
7.16 Comparison of streamwise velocities, averaged over a rotation, in the downstream VAWT flowfield using high-fidelity LBM and mid-fidelity LLFVW at two different locations, at TSR = 4 . . . 169
7.17 Comparison of instantaneous velocities experienced by a VAWT blade at the most upstream (90°) and the most downstream location (270°) for the three skewed inflow conditions, using the high-fidelity LBM, at TSR = 4 . . . 170
7.18 Raw unsteady pressure data using the high-fidelity LBM at two different locations, at TSR = 4 . . . 170

7.19 Power Spectral Density (PSD) spectra using the high-fidelity LBM at two different locations, at TSR = 4 . . . 171
7.20 Directivity plot of overall sound pressure level (OSPL) comparing different VAWT configurations at TSR = 4, along a circular array of 36 points situated at a distance of 7D from the origin of VAWT ([0,0,0]) . . . 171

8.1 Schematic of the VAWT configurations used in this chapter, where VAWT1 and VAWT2 are on the right- and left-hand side, respectively; Case 2 is with additional contra-rotating down configuration . . . 182
8.2 Cross-sectional view of the finest mesh around the blade . . . 183
8.3 Cross-sectional view of the mesh for the high-fidelity LBM simulation . . . 184
8.4 Statistical temporal convergence study for thrust coefficient C_T and torque coefficient C_Q for Case 1 VAWT clusters; the values are representative of one of the rotors VAWT1 185
8.5 Effect of VAWT separation on thrust coefficient C_T and torque coefficient C_Q for Case 1 VAWT clusters . . . 186
8.6 Effect of VAWT separation on thrust coefficient C_T and torque coefficient C_Q of each VAWT in the VAWT cluster: VAWT1 (leeward side) and VAWT2 (windward side), and compared to a standalone VAWT . . . 187
8.7 Variation of thrust coefficient C_T and torque coefficient C_Q for a single blade of VAWT1 over a complete rotation . . . 187
8.8 Instantaneous 3D flowfield using iso-surfaces of the λ_2 criterion (λ_2 = -2000 1/sec^2) for vortices visualisation of two different VAWT clusters and comparison with the standalone VAWT . . . 188
8.9 Instantaneous streamwise velocity contours in the downstream wake on a 2D plane located at the blade mid-span location . . . 189
8.10 Comparison of streamwise velocities, averaged over a rotation, in the downstream VAWT flowfield of the cluster and compared with the standalone VAWT . . . 190
8.11 Raw unsteady pressure data for two different VAWT separations for Case 1 VAWT clusters 190
8.12 Power Spectral Density (PSD) spectra for two different VAWT separations for Case 1 VAWT clusters . . . 191
8.13 Directivity plot of overall sound pressure level (OSPL) comparing two different VAWT separations for Case 1 VAWT clusters, along a circular array of 36 points situated at a distance of 7D from the origin of VAWT cluster ([0,0,0]) . . . 192
8.14 Effect of rotation direction on thrust coefficient C_T and torque coefficient C_Q for Case 2 VAWT clusters; C2 - co-rotating, CC2 - contra-rotating down . . . 193
8.15 Variation of thrust coefficient C_T and torque coefficient C_Q for a single blade of VAWT1 over a complete rotation and comparison with the standalone VAWT . . . 193
8.16 Instantaneous 3D flowfield using iso-surfaces of the λ_2 criterion (λ_2 = -2000 1/sec^2) for vortices visualisation of two different VAWT clusters of Case 2 . . . 194
8.17 Instantaneous streamwise velocity contours in the downstream wake on a 2D plane located at the blade mid-span location, for Case 2 VAWT clusters . . . 195
8.18 Comparison of streamwise velocities, averaged over a rotation, in the downstream VAWT flowfield of the cluster C2 and CC2 of Case 2 and compared with the standalone VAWT . . . 195
8.19 Raw unsteady pressure data for co-rotating and contra-rotating configuration of Case 2 VAWT clusters . . . 196
8.20 Power Spectral Density (PSD) spectra using the high-fidelity LBM at two different locations . . . 196

8.21 Directivity plot of overall sound pressure level (OSPL) comparing two different VAWT configurations for Case 2 VAWT clusters, along a circular array of 36 points situated at a distance of 7D from the origin of VAWT cluster ([0,0,0]) 197
8.22 Effect of VAWT separation on thrust coefficient C_T and torque coefficient C_Q for Case 3 tandem VAWT clusters; numbering represents VAWT separation in metres 198
8.23 Variation of thrust coefficient C_T and torque coefficient C_Q over a complete rotation, for a single blade of VAWT1 and VAWT2 of Case 3 tandem cluster configurations and comparison with the standalone VAWT 199
8.24 Isometric view of the instantaneous 3D flowfield using iso-surfaces of the λ_2 criterion (λ_2 = -2000 1/sec^2) for vortices visualisation of two different VAWT clusters of Case 3 . 199
8.25 Side view of the instantaneous 3D flowfield using iso-surfaces of the λ_2 criterion (λ_2 = -2000 1/sec^2) for vortices visualisation of two different VAWT clusters of Case 3 200
8.26 Instantaneous streamwise velocity contours in the downstream wake on a 2D plane located at the blade mid-span location, for Case 3 VAWT clusters 200
8.27 Comparison of streamwise velocities, averaged over a rotation, in the downstream VAWT flowfield of the Case 3 VAWT clusters and compared with the standalone VAWT 201
8.28 Raw unsteady pressure data using the high-fidelity LBM at two different locations . . 202
8.29 Power Spectral Density (PSD) spectra using the high-fidelity LBM at two different locations 202
8.30 Directivity plot of overall sound pressure level (OSPL) comparing three different VAWT separations for Case 3 VAWT clusters, along a circular array of 36 points situated at a distance of 7D from the origin of VAWT cluster ([0,0,0]) 203

List of Tables

4.1 VAWT geometry and operational settings . . . 63
4.2 Simulation parameters used for the LLFVW method for Setup 3 . . . 65
4.3 VAWT operational settings for setup 1 . . . 66
4.4 VAWT operational settings for setup 2 and 3; setup 2 is simulated only for TSR 3.3 and setup 3 is simulated for all TSRs . . . 66
4.5 VAWT grid settings for both the benchmark VAWT geometries, using high-fidelity LBM 66
4.6 VAWT grid settings for the four different grid sizes for setup 1 . . . 67
4.7 VAWT blade spanwise panel settings for setup 3, using mid-fidelity LLFVW method . . 67
4.8 Grid convergence parameters and discretisation error using Richardson Extrapolation method for TSR = 2.23 for setup 1; C_T, C_{Fz} and C_Q are for a single blade while OSPL is for overall VAWT . . . 72
4.9 Grid convergence parameters and discretisation error using Richardson Extrapolation method for TSR = 2.23 for setup 1; C_T, C_{Fz} and C_Q are for single blade while OSPL is for overall VAWT . . . 76

5.1 VAWT geometry and operational settings . . . 93
5.2 Simulation parameters used for the LLFVW method . . . 96
5.3 VAWT operational settings for the high-fidelity method (LBM) . . . 96
5.4 VAWT grid settings for the VAWT benchmark using high-fidelity LBM . . . 97

6.1 VAWT geometrical parameters for all three configurations . . . 123
6.2 VAWT geometrical parameters for the second and third configurations with struts and central towers A and B, respectively . . . 123
6.3 Simulation parameters used for the LLFVW method . . . 124
6.4 VAWT operational settings for the mid-fidelity (LLFVW) and high-fidelity method (LBM) 124
6.5 VAWT grid settings for the high-fidelity LBM simulation . . . 125

7.1 VAWT geometrical parameters for all three configurations . . . 152
7.2 Simulation parameters used for the LLFVW method . . . 153
7.3 VAWT operational settings for the mid-fidelity (LLFVW) and high-fidelity method (LBM) for all the inflow conditions studied in this chapter . . . 154

8.1 A single VAWT geometry and operational settings . . . 181
8.2 Different VAWT cluster configurations and their naming convention used in this chapter; each cluster involved two VAWTs . . . 181
8.3 VAWT operational settings for each VAWT in a cluster . . . 183
8.4 Variation of power density with different VAWT separation and comparison with the standalone VAWT; Area is calculated for a square with diameter D as one side . . . 186
8.5 Variation of power density with different direction of rotation for the Case 2 VAWT cluster and comparison with the standalone VAWT; Area is calculated for a square with diameter D as one side . . . 192
8.6 Variation of power density with different VAWT separation and comparison with the standalone VAWT for Case 3 tandem VAWT clusters; Area is calculated for a square with diameter D as one side . . . 198

List of Abbreviations

AoA	Angle of Attack
AR	Aspect Ratio
BC	Boundary Condition
BEMT	Blade Element Momentum Theory
BPF	Blade Passage Frequency
CAA	Computational Aeroacoustics
CAD	Computer Aided Design
CFD	Computational Fluid Dynamics
FFT	Fast-Fourier Transform
FWH	Ffowcs-Williams and Hawkings
LBM	Lattice Boltzmann Methods
MATLAB	MATrix LABoratory
OSPL	OverAll Sound Pressure Level
Re	Reynolds number
RPM	Rotations Per Minute
rps	rotations per second
SPL	Sound Pressure Level
UK	United Kingdom
TSR	Tip Speed Ratio
VLES	Very Large Eddy Simulation
VLM	Vortex Lattice Method
VLP	Vortex Panel Method
VLP	Vortex Particle Method
VR	Variable Resolution region

List of Symbols

Latin lower case

Symbol	Unit	Description
c	m	Blade chord
e_a	[-]	Relative error
e_{ext}	[-]	Extrapolated relative error
f	Hz	Frequency
f_i	[-]	Physical quantity at particular grid spacing
f_{exact}	[-]	Continuum value at zero grid spacing
h	m	Grid spacing
n	Hz	Rotations per second
p	[-]	Order of Richardson extrapolation function
p'	Pa	Pressure perturbations
r	m	VAWT radius
t	sec	Time
U_s	[-]	Uncertainty
v	m/sec	Velocity vector
w	[-]	Particle collision weights
y	m	Distance from the wall
y^+	[-]	Dimensionless wall distance

Latin upper case

Symbol	Unit	Description
A	m^2	VAWT swept area
C_P	[-]	Power coefficient
C_Q	[-]	Torque coefficient
C_T	[-]	Thrust coefficient
C_{Fz}	[-]	Cross-streamwise force coefficient
D	m	VAWT diameter
F_z	N	VAWT cross-streamwise force
M	[-]	Freestream Mach number
M_r	[-]	Relative Mach number

N	[-]	Total number of voxels in a particular VR region
P	Pa	RMS of pressure perturbations
P_{in}	Watt	Input power
P_{ref}	Pa	Reference pressure level
Q	Nm	VAWT Torque
R	m	VAWT radius
T	N	VAWT Thrust
T_{ij}	N/m^2	Lighthill's stress tensor
T_p	sec	VAWT rotation period
V_∞	m/sec	Freestream velocity
V_{eff}	m/sec	Resultant velocity
V_{tip}	m/sec	Blade tip velocity

Greek symbols

Symbol	**Unit**	**Description**
ρ	kg/m^3	Air density
ρ'	kg/m^3	Density perturbations
ω	rad/sec	VAWT rotational speed
λ	[-]	Tip speed ratio
λ_2	1/sec^2	Isosurface criterion
α	^{o}	Angle of Attack
σ	[-]	VAWT solidity
Γ	m^2/sec	Circulation around a vortex

1

Introduction

Summary

The importance of renewable energy, especially wind energy, in the context of climate change and the increase in greenhouse gas emissions, is discussed. Wind energy can complement the solar energy sector to achieve sustainable energy and net-zero carbon emission goals. Floating offshore and urban wind turbines can increase wind energy adoption significantly and vertical axis wind turbines are best suited for such applications and present the bigger motivation for this study. The chapter discusses the broader foresight of the research to be carried out, thesis objectives and research questions. Finally, the structure of the thesis and methods used are discussed.

1.1. Perspectives on Wind Energy

The increasing significance of wind energy derives from its pivotal role in addressing pressing global concerns, particularly the profound impact of climate change on present and future generations. The alarming trajectory of global warming, evidenced by swift increases in global temperatures [3], the rapid warming of oceans, dwindling ice sheets, diminishing Arctic sea ice, retreating glaciers and decreasing snow cover, rising sea levels, extreme weather events or the acidification of the ocean underscores the urgency of concerted action [247]. This perilous trend is primarily driven by the accumulation of greenhouse gases, notably carbon dioxide (CO2), methane (CH4), nitrous oxide (N2O), and fluorinated gases, which intensify Earth's natural greenhouse effect, trapping heat within the atmosphere. The genesis of these gases traces back to the Industrial Revolution, marking a pivotal point in human history when industrial activities surged, ushering in a spike in greenhouse gas emissions.

Greenhouse gases such as Carbon Dioxide (CO_2), Methane (CH_4), and Nitrous Oxide (N_2O) play a pivotal role in regulating the Earth's temperature through the greenhouse effect. These gases effectively trap heat within the Earth's atmosphere by allowing sunlight to enter and warm the planet's surface. However, they also hinder the escape of this heat back into space, leading to a gradual increase in the overall temperature of the Earth [68]. Human activities have significantly increased the atmospheric concentration of these gases, particularly CO_2, which has surged by 48% since the onset of the Industrial Revolution and by 27% in just the last half-century [249]. This augmentation is primarily attributed to activities such as deforestation, alterations in land use, and the combustion of fossil fuels. The cumulative effect of these actions has considerably amplified the greenhouse effect, contributing substantially to the accelerated pace of global warming observed in recent times.

The magnitude of this environmental challenge prompted a collective response, culminating in the historic Paris Agreement of 2015 [342], where 195 nations pledged unified efforts to mitigate the impact of greenhouse gases on the planet's climate system. At the heart of this agreement lies a commitment to curtail global temperature rise well below 2 degrees Celsius above pre-industrial levels, and preferably limit the increase to 1.5 degrees Celsius [342]. An important milestone of this accord involves nations submitting comprehensive plans detailing their intended contributions to reducing carbon emissions, reflecting a diverse array of strategies and targets tailored to individual country contexts. A nation's pledges to curb emissions must address the energy challenge, given that approximately 30% of global greenhouse gas emissions stem from electricity generation and heating sources worldwide [151].

Climate Change and Sustainable Future

"Climate change is the single greatest threat to a sustainable future but, at the same time, addressing the climate challenge presents a golden opportunity to promote prosperity, security and a brighter future for all."

- Ban Ki-Moon, Former Secretary-General of UN [85]

The United Kingdom has implemented several policies and agreements to boost the use of renewable energy, particularly wind energy, reflecting its commitment to reducing carbon emissions and promoting sustainable energy sources. Introduced in 2002, the Renewables Obligation (RO) was one of the UK's first major policies to encourage renewable energy [257]. It required electricity suppliers to source a certain percentage of their electricity from renewable sources, with a significant focus on wind energy. The Climate Change Act, originally passed in 2008 and amended in 2019, sets legally binding carbon budgets which act as stepping stones towards the 2050 net-zero target [103]. Wind energy, both onshore and offshore, plays a crucial role in meeting these budgets. The UK gov-

ernment has legally committed to achieving net zero greenhouse gas emissions by 2050 [258]. This commitment, enshrined in law in 2019, includes significant contributions from renewable energy sources, especially wind power. As part of the UK's Industrial Strategy, the Offshore Wind Sector Deal, announced in 2019, aims to generate one-third of the UK's electricity from offshore wind by 2030 [96].

Numerous nations are increasingly focusing on wind energy as a primary energy source for the forthcoming decades [108]. The significance of wind power, when compared to other renewable energy technologies, is attributed to its widespread resource availability and technological maturity [113]. Globally, the capacity of installed wind energy, encompassing both onshore and offshore facilities, has reached an impressive 906 GW. Remarkably, this figure has quadrupled over the past ten years and total installed wind capacity has grown at a 9% rate in 2022 compared to 2021 [84]. Looking ahead, the wind energy sector expects offshore installations to take a leading role, projecting an annual growth rate of 17% over the next decade [115]. Similarly, the growth of urban wind turbines is also expected to increase significantly. To sustain and enhance these trends into the future, it is crucial to further reduce the costs associated with wind energy. Achieving cost-effectiveness is essential for renewable energy to competitively match the market prices of other electricity sources. This goal is attainable through continued technological innovation.

(a) Onshore horizontal axis wind turbine [133] (b) Urban helical-bladed QR6 wind turbine [265]

Figure 1.1: Examples for big-onshore and small-urban wind turbines

1.2. Vertical Axis Wind Turbine

In the past decades, various types of wind turbines have emerged, Horizontal Axis Wind Turbines (HAWTs) being the most prevalent, especially in onshore locations. However, to broaden the scope of wind energy adoption and exploit the wind energy potential to its fullest, it is essential to consider both urban and offshore areas. The adaptation of horizontal axis wind turbines (HAWTs), which have achieved technological maturity for onshore rural applications and currently lead the market, to urban areas and floating offshore settings presents significant challenges and is not straightforward.

While big-scale HAWTs are well-established on land, their translation to floating platforms is difficult due to their top-heavy nature [27]. This characteristic necessitates the use of substantial and heavy floating structures, which in turn substantially increases the costs associated with offshore wind turbine installations. Moreover, the motion of the floating platforms introduces operational complexities that differ markedly from those encountered with bottom-fixed turbines [229]. These factors complicate the economic feasibility of deploying conventional HAWTs in offshore environments, particularly in deep-sea conditions [92]. Similarly, the use of HAWTs for urban applications is not ideal. The performance of HAWT deteriorates significantly in turbulent wind conditions and when the wind direction is yawed to the rotational axis, both of which are common factors in urban areas [31, 172]. Furthermore, HAWTs are associated with high maintenance costs, noise generation and mechanical complexities due to the yawing mechanism and therefore may not be the most efficient or economical choice for urban settings.

In this context, Vertical Axis Wind Turbines (VAWTs) have emerged as a promising alternative for use in urban environments [2, 149] and deep offshore areas [88, 177]. VAWTs offer a broad design space, enabling the creation of cylindrical actuation surfaces [92, 121]. These surfaces generate a dynamic and complex 3D force field that varies both spatially and temporally. The design of VAWTs can be highly versatile, with variations in diameter along the height, as shown by the troposkien or helical-shaped rotor, and the surface may comprise a combination of intersecting actuation surfaces, such as those formed by blades and struts. This intricate 3D force field not only facilitates efficient energy extraction but also influences wake development and energy mixing on a wind farm scale. VAWTs have demonstrated potential for achieving higher power densities (watts per square meter) than HAWTs [87]. This advantage is attributed to their ability to encompass a large swept area with a minimal footprint and high aspect ratio, coupled with their capacity for faster wake recovery [87, 253, 334].

VAWTs are particularly advantageous in urban settings due to their suitability for areas with low wind speeds, high turbulence and omni-directional behaviour. Previous studies have shown that VAWTs can perform more effectively in these conditions compared to HAWTs, leading to higher power generation efficiency in urban landscapes [160, 165]. For offshore applications, especially in deep-water settings where floating wind turbines are considered, VAWTs offer several operational benefits. They have a lower centre of gravity compared to HAWTs, enhancing their stability, particularly in floating applications [183, 295]. Their insensitivity to wind direction obviates the need for a yaw system, simplifying their design and their lower noise signature helps for a higher public acceptance [172]. Additionally, VAWTs exhibit scalable properties, making them adaptable to various sizes and applications. Additionally, the ability to harness wind from any direction in a VAWT without the need for orientation mechanisms simplifies their offshore deployment [260]. The integration of VAWTs in both urban and offshore settings represents a strategic approach to diversifying and expanding wind energy generation. This not only helps in evenly distributing wind energy production across different terrains but also ensures a more resilient and adaptable renewable energy infrastructure. However, it is important to acknowledge that VAWTs face challenges, notably in terms of unsteady loads and fatigue issues [81].

VAWT has two primary designs: the drag-based Savonius [223, 290] and the lift-based Darrieus [156, 340]. Both VAWT designs are shown in Figure 1.2. In terms of power generation, the Savonius turbine relies on differential drag force acting upon its flat blades, while the Darrieus turbine generates power through lift forces on its airfoil-shaped blades. The mechanism of force generation on an airfoil is inherently more efficient than that on a flat plate, rendering the Darrieus design more effective than the Savonius design in extracting energy per unit of swept area and in terms of Annual Energy Output (AEO) [35]. The Darrieus design allows for an increase in energy production without breaching city noise limits, making it a more suitable option for urban renewable energy projects.

Darrieus VAWTs have a rich history, yet the complexities of their operation and the complex na-

ture of their flow fields remain not fully understood. This gap in understanding within the wind energy community has fostered a misconception that VAWTs are inherently less efficient than HAWTs and lack commercial viability [92]. However, this view overlooks the potential of VAWTs, especially in specific applications such as urban wind turbines and floating far-offshore wind farms. Therefore, to advance our understanding and modelling of their force-field and flow-field, this study endeavours to contribute to the knowledge of VAWT aerodynamics and aeroacoustics, addressing some of the challenges encountered in designing a VAWT.

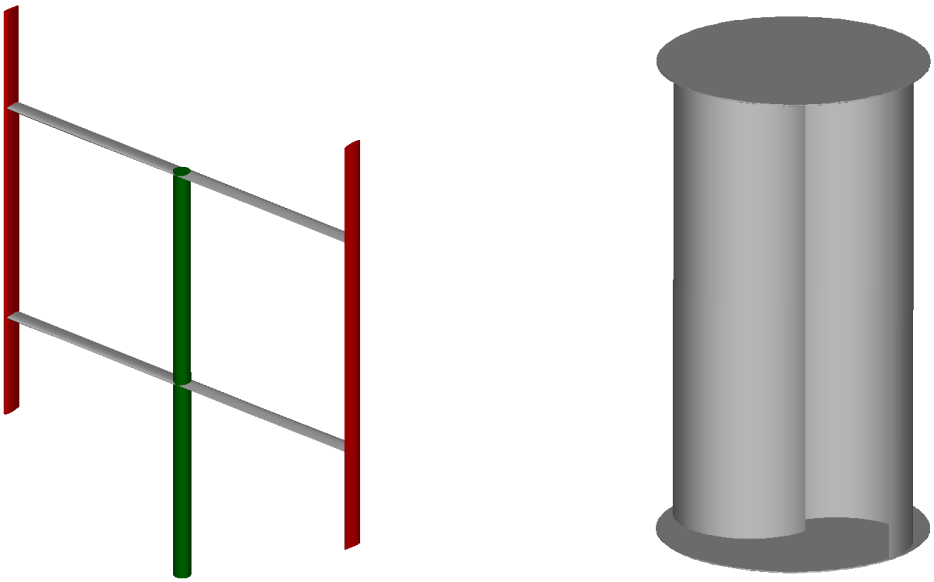

(a) Darrieus 2-bladed VAWT (b) Savonius 2-bladed VAWT

Figure 1.2: Different types of VAWT design: lift-based Darrieus vs drag-based Savonius

1.3. Thesis Objectives and Research Questions

VAWTs generate a 3D force and flow field through their airfoil-shaped blades. These turbines interact with the fluid medium by exerting a force field that alters the flow, thereby exchanging momentum and energy. The actuation surface, which is the area over which these forces act, differs fundamentally between horizontal-axis and vertical-axis wind turbines. While horizontal-axis wind turbines utilise a disc-shaped actuation surface, VAWTs employ a cylindrical surface. This cylindrical configuration grants VAWTs greater flexibility to create a complex and dynamic 3D force field that varies both spatially and temporally.

In the realm of aerodynamic and aeroacoustic modelling of VAWTs, various methods can be employed, each with differing levels of fidelity. *Low-fidelity* methods offer basic, simplified models that require less computational power but may lack detailed accuracy. *Mid-fidelity* methods strike a balance, offering more detail than low-fidelity models while still being less resource-intensive than high-fidelity methods. *High-fidelity* methods, on the other hand, provide the most detailed and accurate simulations, capturing intricate aerodynamic and aeroacoustic phenomena at the cost of higher computational demands.

This study primarily focuses on mid and high-fidelity methods to explore the 3D design space of VAWTs. These methods are employed to examine the force field characteristics of VAWTs in both time and space, particularly how these forces are distributed between the upwind and downwind halves of the rotor rotation. Streamwise vortices are generated as a result of the blade forces, which

mutually influence the wake development and overall force field of the VAWT, thereby impacting its performance.

The thesis aims to evaluate how effectively each computational method captures the interaction of the force field with the flow and affects the downstream wake development. It also investigates how variations in operational and design parameters alter the force and flow fields, and how these changes affect the performance predictions made by each method. The high-fidelity method is also used to investigate how the unsteady blade forces cause aerodynamic noise generation in the far-field at a range of frequencies. This comprehensive analysis is crucial for advancing our understanding of VAWT aerodynamics and aeroacoustics and for optimizing their design and operational strategies.

VAWT's operational condition is designated using *tip speed ratio (TSR)* which is defined as the ratio of the blade rotational speed and the freestream velocity, i.e. $\omega r/V_\infty$, where ω denotes the rotational speed in radians per second, r signifies the wind turbine radius and V_∞ represents the *freestream velocity*. The VAWT is composed of a particular *number of blades* which along with rotor diameter decides the rotor solidity. The more the solidity, the more blockage is provided to the oncoming flow. A VAWT is supported by *supporting struts and a central tower* which affects the fluid dynamic interactions in the flow field and the VAWT performance. VAWTs can also experience non-uniform inflow conditions such as *skewed inflow* on rooftop locations in urban areas and floating offshore platforms during tilting motion. This causes a part of the freestream velocity skewed towards the rotational axis.

All the above parameters although an inherent part of VAWT design, are often overlooked or understudied when optimizing a VAWT design for higher power performance and lower noise, and this thesis will aim to investigate such parameters in detail. The thesis will also highlight the potential advantages/disadvantages of *VAWT clusters*, particularly compared to standalone VAWT in urban built environment contexts where traditional HAWTs may not be as effective or feasible. This research could play a pivotal role in redefining the perceived limitations of VAWTs, in the context of both computational modelling and practical applications and establishing them as a viable option in the broader spectrum of wind energy solutions.

Some examples of the results obtained in this thesis are shown in Figure 1.3. The overall objective of the thesis is to increase the aerodynamic and aeroacoustic state-of-the-art in the field of VAWT and is formalised below:

Thesis Objectives

- Understand and compare the capabilities of the mid-fidelity and high-fidelity methods in predicting the 3D force-field, flow-field and overall performance of a VAWT
- Investigate the effect of different operational and design parameters on how the unsteady blade loading influences the downstream wake development and energy extraction from the flow
- Develop a first-hand understanding of the VAWT aeroacoustic behaviour and the effect of different operational and design parameters
- Investigate the aerodynamic and aeroacoustic performance of a VAWT cluster and how the force-field and flow-field of VAWTs interact with each other in close proximity

Based on these objectives, the following research questions have been formulated which form the basis for the whole thesis:

- What is the difference in predictions made by mid-fidelity and high-fidelity methods?

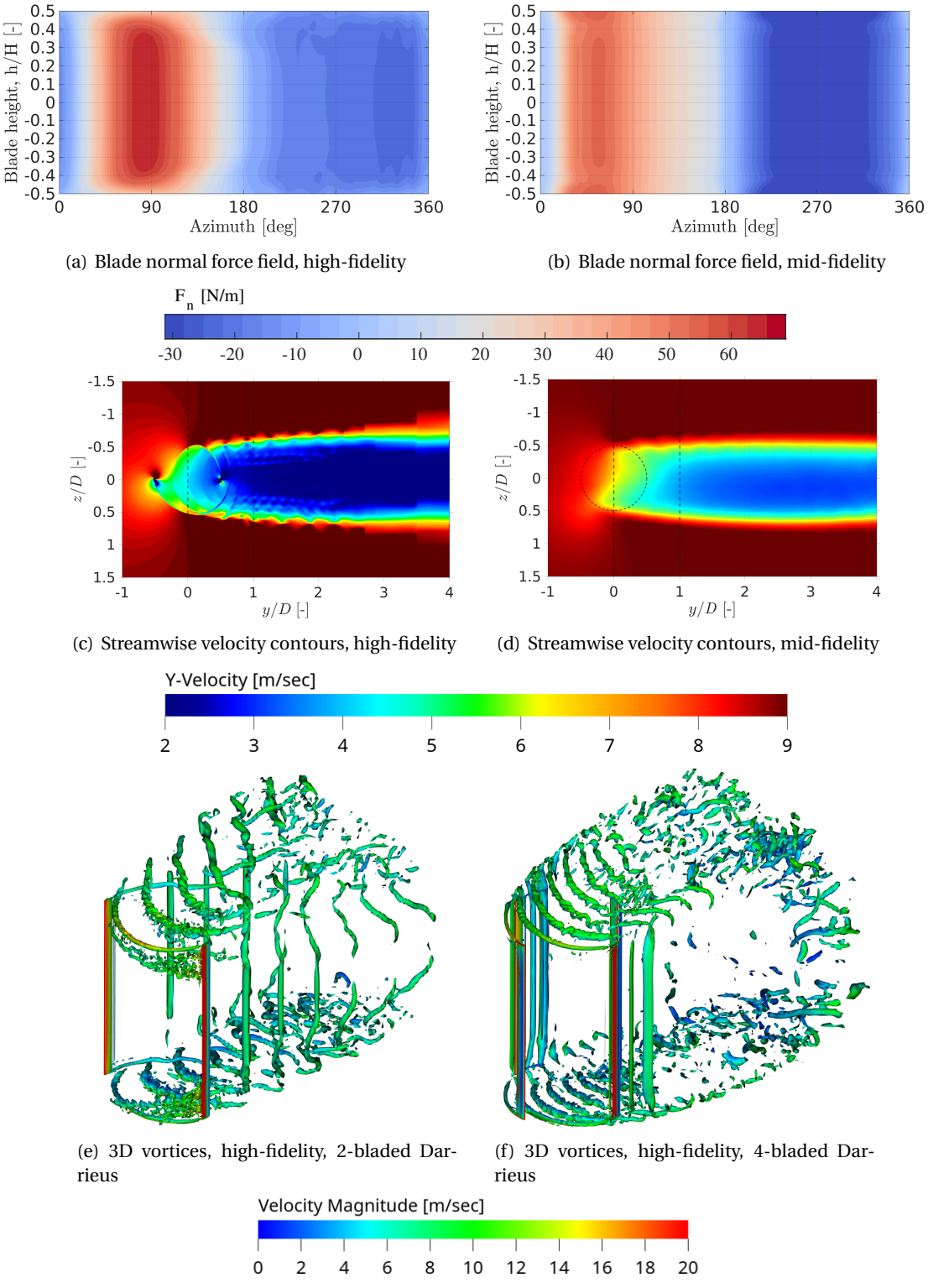

(a) Blade normal force field, high-fidelity

(b) Blade normal force field, mid-fidelity

(c) Streamwise velocity contours, high-fidelity

(d) Streamwise velocity contours, mid-fidelity

(e) 3D vortices, high-fidelity, 2-bladed Darrieus

(f) 3D vortices, high-fidelity, 4-bladed Darrieus

Figure 1.3: Visualisation of results for the thesis objectives and research questions. The mid-fidelity and high-fidelity results are compared, the force field is visualised along the blade span in a single rotation and the flow field is visualised in the downstream wake. The first four figures are for a 2-bladed Darrieus VAWT

– Can both methods capture the azimuthal and spanwise variation in blade loading in a VAWT accurately, including the tip vortex effect?

  - What is the effect of variation in design and operational parameters on the predictions made by both methods?
  - How does the modelling of blade forces and streamwise vortices influence the predictions made by both methods and the differences observed between them?
  - Can the mid-fidelity method be proposed as a direct replacement for the high-fidelity in VAWT design and performance analysis?

- What is the effect of different operational and design parameters on the force field and flow field development of a VAWT?
  - How does any operational or design parameter affect the development of 2D and 3D force fields in a single rotation of a VAWT?
  - How does the force field affect the flow and downstream wake development?
  - How does any operational or design parameter affect the blade-wake/blade-vortex interaction in the flow field?

- What is the effect of different operational and design parameters on the aeroacoustic behaviour of a VAWT?
  - What are the different noise sources in a VAWT and how are they affected when any operational or design parameter is varied?
  - How do the force field development and blade-wake/blade-vortex interaction in a VAWT influence the unsteady pressure field and noise generation?

- What is the difference in performance of a VAWT cluster as compared to a standalone VAWT?
  - How do the VAWTs interact with each other in a cluster and how does it affect the force field of a VAWT as compared to a standalone VAWT?
  - How does the force field in a VAWT cluster affect the flow field and wake aerodynamics?
  - What is the difference in noise generation of a VAWT cluster as compared to a standalone VAWT?

For this thesis, Dassault Systèmes SIMULIA PowerFLOW ® 6-2020 has been utilised which uses the Lattice-Boltzmann Very Large Eddy Simulation (LB-VLES) method for the high-fidelity aerodynamic simulations. For aeroacoustic post-processing of far-field noise, the Ffowcs Williams and Hawkings (FW-H) analogy is used. The post-processing is based on the pressure fluctuations sampled using the high-fidelity Lattice-Boltzmann Method (LBM) simulations. LBM is preferred over traditional Navier-Stokes solver due to its computational efficiency and effectiveness in solving unsteady problems since it has low dispersion and dissipation properties [52] [213]. Finally, for mid-fidelity aerodynamic simulations, the Lifting Line Free Vortex Wake (LLFVW) method is utilised using the open-source software QBlade 2.0. The computational methodologies behind each method are discussed in detail in Chapter 2.

1.4. Thesis structure

The report has been divided further into 5 parts consisting of a total of 9 chapters. Each chapter portrays a part of the story which when combined forms the overall storyline of the thesis. All studies help to investigate the mutual interaction between the force field and flow field of a VAWT with varying operational and design parameters, using both mid-fidelity and high-fidelity methods. This research also addresses some of the aerodynamic and aeroacoustic design challenges for VAWTs for

practical applications in urban and floating off-shore environments. Each chapter also investigates VAWT aeroacoustics using the results of high-fidelity aerodynamic simulations. The thesis structure is outlined below with a simplified one-line research question after each chapter's description.

- **Part I: Introduction and Methodology**

  This part gives an introduction to the thesis including a broader perspective on wind energy, thesis objectives and research questions, fundamentals of VAWT aerodynamics and aeroacoustics, state-of-the-art in mid-fidelity and high-fidelity simulations and computational methodologies utilised in the whole thesis.

  – **Chapter 1 - Introduction**: The current chapter sets the foundation for the research to be carried out in the thesis by outlining its motivation and significance. It delves into the critical role of wind energy as a sustainable solution in combating climate change, emphasizing the potential contributions of VAWTs in urban and offshore settings. The chapter then defines the research objectives and poses relevant research questions. Additionally, it provides a structured outline of the study, guiding the reader through the subsequent sections and their thematic focus.

    - What is the significance of Vertical Axis Wind Turbine in the current study?

  – **Chapter 2 - Computational methodology**: The methodology employed in the Lattice-Boltzmann Very Large Eddy Simulation (LB-VLES) method is described in detail as implemented in the commercial software PowerFLOW. The Ffowcs Williams and Hawkings (FW-H) analogy for the post-processing of the far-field unsteady pressure data is discussed then. Finally, the chapter describes the Lifting Line Free Vortex Wake (LLFVW) and Double Multiple Streamtube (DMS) methods as implemented in the open-source software QBlade.

    What are the different methodologies used in this thesis and why?

  – **Chapter 3 - Vertical axis wind turbine**: This chapter gives a brief history of VAWT along with its fundamental aerodynamic and aeroacoustic performance. Then it summarises the latest research going on in VAWT aerodynamics and aeroacoustics and discusses the areas that are essential to investigate to push the state-of-the-art in this field and how they fit into the storyline of the thesis.

    How does a Vertical Axis Wind Turbine work and the current state-of-the-art?

- **Part II: Standalone VAWT**

  This part discusses the effect of four different parameters on the aerodynamic and aeroacoustic characteristics of standalone VAWTs. The design parameters are the number of blades, supporting struts and central tower and operational parameters are tip speed ratio and skewed inflow. The objective is to understand how these parameters affect the blade-wake/blade-vortex interaction which influences the non-uniform blade loading in the spanwise and azimuthal directions, the unsteady flow field and noise generation.

- **Chapter 4 - Standalone VAWT I: grid convergence study and tip speed ratio**: This chapter presents the application of the Richardson extrapolation method to the grid convergence study using the high-fidelity aerodynamic and aeroacoustic data. After selecting an appropriate grid resolution, the effect of TSR on the force field and flow field development of a VAWT and noise generation is investigated.

  > What is the optimal tip speed ratio of a VAWT for both high performance and low noise?

- **Chapter 5 - Standalone VAWT II: number of blades**: This chapter investigates the effect of the number of blades on the aerodynamic and aeroacoustic characteristics of a VAWT. A comparison is made between the results of mid-fidelity and high-fidelity simulations for both unsteady force field and flow field and the differences observed are analysed.

  > What is the optimal number of blades in a VAWT for both high performance and low noise?

- **Chapter 6 - Standalone VAWT III: supporting struts and central tower**: This chapter investigates the effect of the supporting struts and central tower on the aerodynamic and aeroacoustic characteristics of a VAWT. A comparison is made between the results of mid-fidelity and high-fidelity simulations for both with and without the struts and tower and the differences observed are analysed.

  > How does the addition of struts and a central tower affect VAWT aerodynamics and aeroacoustics?

- **Chapter 7 - Standalone VAWT IV: skewed inflow**: This chapter investigates the effect of a non-uniform inflow such as skewed inflow on the aerodynamic and aeroacoustic characteristics of a VAWT. A comparison is made between the results of mid-fidelity and high-fidelity simulations for both unsteady force field and flow field and the differences observed are analysed.

  > What is the effect of skewed inflow on VAWT aerodynamics and aeroacoustics?

• Part III: VAWT cluster

This part discusses the aerodynamic and aeroacoustic characteristics of VAWT clusters and compares them to standalone VAWTs. VAWT clusters are relevant both for urban and deep-offshore areas where using multiple VAWTs together will be essential to efficiently utilise the available space.

- **Chapter 8 - VAWT cluster**: This chapter investigates the force field and flow field of a VAWT cluster using high-fidelity aerodynamic simulations. For a cluster containing two VAWTs, the separation between them and the direction of rotor rotation is varied, for both parallel and tandem configuration. A comparison is made with the results of a

standalone VAWT to analyse the cluster performance for both aerodynamics and aeroacoustics.

> Can a VAWT cluster perform better than a standalone VAWT in both aerodynamic performance and noise generation?

- **Part IV: Conclusions**:

  This part discusses the overall knowledge gained as part of the research conducted in this thesis, answering the thesis objectives and research questions.

  - **Chapter 9 - Conclusions and Discussions**: This chapter presents the conclusions of the thesis based on the results obtained and the overall storyline. It also discusses recommendations for future investigations based on the broader wind energy outlook.

    > What conclusions can be derived from this thesis for VAWT design and analysis?

- **Part V: Miscellaneous**:

  This part covers supplementary information for the reader to complete the whole thesis.

  - **List of publications**: This chapter presents various journal and conference articles that have been published and articles that are in the peer-review process, as part of this thesis.
  - **Curriculum Vitae**: This chapter presents a concise summary of the professional and personal milestones of the author, highlighting how these achievements have contributed to the overall success and depth of the current research.
  - **Bibliography**: This chapter lists all the literature which are referenced in this thesis.

2

Computational Methodology

Summary

A detailed description of the computational methodology used in the current study is provided. For high-fidelity aerodynamic simulations, the Lattice Boltzmann Method (LBM) is employed. For aeroacoustic post-processing of far-field noise, the Ffowcs Williams and Hawkings (FW-H) analogy is used. The post-processing is based on the pressure fluctuations sampled using the high-fidelity LBM simulations. For mid-fidelity aerodynamic simulations, the Lifting Line Free Vortex Wake (LLFVW) method is used and for low-fidelity aerodynamic simulations, the Double Multiple Streamtube (DMS) method is employed. The theoretical frameworks for all these methods are discussed. The advantages and disadvantages of each method and the reasoning behind the choice of each, in the context of numerically representing VAWT flow physics, are discussed.

2.1. Introduction

With the advancement of computational capabilities, various methodologies have been developed, spanning from empirical models to intricate computational fluid dynamics (CFD) simulations, to capture the complex flow structures and acoustic signatures of different classes of rotor systems such as VAWTs. This section provides an overview of these computational methods in brief, focussing on the flow physics investigation and the underlying principles that govern them. The computational methods are generally classified as low-fidelity, mid-fidelity and high-fidelity methods, in the increasing order of computational expenses.

Low-fidelity methods are pivotal in the early stages of analysis, optimisation, and design of systems, providing rapid and computationally efficient evaluation of performance. The foundation for low-fidelity methods has been served by potential flow methods. These methods simplify the full Navier-Stokes equations, based on the assumptions of incompressible and inviscid flow, to form Laplace's equation. A direct application of potential flow theory is the Panel (or Boundary Element) method. The surface of the body (e.g., VAWT blade) is discretised into panels, with each panel representing either a source or vortex or sometimes both. They can provide the basic aerodynamic loads on the blades and becomes an essential analytical tool for understanding many flow features and offering computational efficiency. However, the primary limitation remains in accounting for viscous effects, which are especially important in phenomena like dynamic stall and unsteady downstream wake, and predicting performance metrics like lift and drag of VAWT blades with high accuracy, especially in post-stall regimes. For VAWTs, various types of low-fidelity methods based on potential flow theory have been developed including the Actuator Disk Theory, Multiple Streamtube Model such as the Double Multiple Streamtube (DMS) method, Blade Element Momentum Theory (BEMT), Actuator Cylinder (AC) model, etc.

Mid-fidelity methods serve as a bridge between low-fidelity analytical or empirical models and high-fidelity, resource-intensive CFD simulations. They aim to strike a balance between computational expense and accuracy, making them suitable for detailed design stages, optimisation, and performance assessments. Mid-fidelity methods generally consist of vortex methods, which are a class of computational techniques focused on simulating inviscid, incompressible fluid flows using vorticity as the primary variable. The core philosophy behind vortex methods is to represent the vorticity of a fluid flow discretely, allowing for a highly accurate representation of the flow's essential characteristics. Vortex methods naturally capture the rotational characteristics of the flow, making them adept at representing tip vortices, dynamic stall vortices, and the intricate wake structures behind VAWT blades. Although being an inviscid method, vortex methods don't inherently capture boundary layers or viscous dissipation. They generally require coupling with boundary layer models for a more comprehensive representation. Moreover, resolving the near-blade region can be challenging due to high vorticity and velocity gradients. Some common mid-fidelity methods include Lifting Line method (both fixed and free wake), Vortex Panel Method (VPM), Vortex Lattice Method (VLM) and Vortex Particle Method (VPM).

High-fidelity methods represent the most detailed and accurate computational approaches available. They aim to capture the complete range of scales and intricacies of the flow phenomena, allowing for in-depth investigations and predictions. The computational demand for these methods is typically high, making them more suited for final design validations, detailed studies, or when the utmost accuracy is essential. High-fidelity methods using Navier-Stokes equations in decreasing order of computational effort are Direct Numerical Simulation (DNS), Large Eddy Simulation (LES), Detached Eddy Simulation (DES), and Reynolds Averaged Navier-Stokes (RANS). In recent years, the Lattice-Boltzmann method (LBM) has emerged as a viable alternative to the conventional Navier-Stokes solvers for CFD simulations. LBM models microscopic processes through the interactions of discrete fictitious particles on a lattice structure. These pseudo-particles move over the lattice and collide, and it is through these discrete actions that macroscopic fluid dynamics emerge.

In the current study, the Lattice-Boltzmann Method (LBM) method is chosen for high-fidelity 3D aerodynamic simulations, using the commercially available software SIMULIA PowerFLOW ® 6-2020. Additionally, for mid-fidelity and low-fidelity aerodynamic simulations, the Lifting Line Free Vortex Wake (LLFVW) and Double Multiple Streamtube (DMS) models are chosen, using the open-source software QBlade 2.0. The DMS model is only used in Chapter 3, the LLFVW model is used in Chapters 5, 6 and 7, while the LBM method is used in all chapters (4-8). The next sections explain these methods in detail and how they are implemented in their respective framework. A detailed description of the same is also presented by Romani [281], Teruna [333] and Marten [215].

2.2. The Lattice-Boltzmann Method

The fluid dynamics phenomena can be understood through three distinct layers of description: macroscopic, mesoscopic, and microscopic [171, 281]. At the macroscopic level, the behaviour of the fluid is portrayed using broad continuum concepts, including variables such as density, velocity, and temperature. This realm is predominantly governed by the compressible Navier-Stokes equations, especially for flows with viscosity. Diverging from this, the microscopic description delves into the intricacies at the molecular scale, providing insight by monitoring individual molecular trajectories which align with Newtonian motion principles. Positioned between the macroscopic and microscopic description of fluid dynamics lies the mesoscopic approach. Instead of focusing on individual molecular behaviour, this methodology focuses on the behaviour of groups or clusters of molecules, using the principles of kinetic theory [171]. The Lattice Boltzmann method (LBM) operates within this mesoscopic framework, using particle density distribution functions as its core. The macroscopic flow properties are captured as aggregated measures of these particle distribution functions [71–73].

Recently, the Lattice-Boltzmann Method (LBM) has emerged as a noteworthy alternative amongst various CFD methodologies for the numerical modelling of transient turbulent flows. LBM has several distinct features relative to the methods based on Navier-Stokes equations. Specifically, its inherent structure supports efficient parallel computation, facilitates the modelling of a diverse array of fluid types, and offers a simplified approach for navigating complex geometries and boundary conditions [72–74]. Given its characteristics such as low dissipation, compressibility, and provision for transient solutions, LBM is particularly suited for aeroacoustic simulations. Such characteristics position LBM as a leading CFD tool for complex, large-scale industrial challenges, encompassing component-specific [61, 62] and overall investigations of fixed-wing aircraft [117, 162], jet-induced noise [345], turbofan aeroacoustics [63, 130], propeller noise [302] and .

The next few sections briefly describe the LBM as implemented in the commercial software SIMULIA PowerFLOW ®. For a more detailed and exhaustive description of LBM and the underlying theory, the interested reader may refer to the publications by Krüger et al. [171], Succi [321] and Shan et al. [299].

2.2.1. The Boltzmann's Kinetic Theory

The Lattice-Boltzmann Method (LBM) is based on Boltzmann's kinetic theory. This theory portrays a fluid as a collection of particles, perpetually progressing towards a state of thermodynamic equilibrium. Such macroscopic properties of the fluid, encompassing momentum, pressure, and temperature, emerge from the underlying microscopic particle motions and their respective momentum exchanges. However, rather than continuously monitoring each particle's behaviour, the kinetic theory by Boltzmann employs a statistical methodology. This approach is particularly suited for a range of aerodynamic challenges wherein the fluid can be treated as a continuum. The condition of continuum states that at standard atmospheric conditions, 1 mm^3 of air consists of approximately 26.9 quadrillion (10^{15}) molecules [333]. The instantaneous state of the fluid is characterised using

a probability density function $F(\boldsymbol{x}, t, \boldsymbol{V})$, denoting the probability of finding a particle at a specific spatial point $\boldsymbol{x}$ and temporal moment t with velocity $\boldsymbol{V}$. Neglecting the impact of body forces (for instance, gravity), the Boltzmann Transport Equation (BTE) can be represented by the equation 2.1.

$$\frac{\partial F}{\partial t} + \boldsymbol{V} \cdot \nabla F = \kappa \ . \tag{2.1}$$

On the left side of the equation, the advection of the fluid particle is represented. On the equation's right side, the collision operator is introduced, denoted as κ. This collision operator describes the variation in particle velocity distribution due to momentum exchanges among the particles and helps in directing the state of fluid particles toward thermodynamic equilibrium. Within Boltzmann's classical framework, the collision operator presumes the fluid as "a dilute gas of point-like, structure-less molecules interacting via a short-range two-body potential" [321]. Such a conceptualisation infers that particle interactions happen predominantly through elastic collisions, ensuring the conservation of energy pre- and post-collision. LBM algorithms frequently adopt a simplified version of the collision operator that mirrors the integral depiction of κ, as mentioned above. Notably, the Bhatnagar-Gross-Krook (BGK) model [34] stands out as a widely recognised approach, though subsequent advancements and variations have emerged [77].

2.2.2. Domain discretisation and macroscopic flow quantities

In the LBM methodology, the BTE is discretised into discrete components on a Cartesian grid, often referred to as a lattice. Within this framework, fluid particles are anchored at the grid nodes, and their velocity vectors are fixed to a defined set of directions. The mathematical representation for the discretised lattice-Boltzmann equation can be represented as follows:

$$F_{\mathrm{q}}\left(\boldsymbol{x} + \boldsymbol{V}_{\mathrm{q}}\Delta t, t + \Delta t\right) - F_{\mathrm{q}}(\boldsymbol{x}, t) = \kappa_{\mathrm{q}}(\boldsymbol{x}, t) \ , \tag{2.2}$$

where, F_q represents the particle distribution function along the q^{th} direction of the lattice, while $\boldsymbol{V}_q$ signifies the discrete particle velocity vector. Here, q spans values from 0 to Q, with Q indicating the total count of discrete velocity vectors. The left-hand side of the discretised lattice-Boltzmann equation 2.2 denotes a time-explicit advection, characterised by spatial increments of $\Delta\boldsymbol{x} = \boldsymbol{V}_q\Delta t$ and a temporal increment of Δt. The equation's right-hand side shows the collision operator, denoted as κ_q. The macroscopic flow characteristics of density ρ, velocity $\boldsymbol{u}$, and total energy E can be determined by calculating the moments of the distribution function F_q, as follows:

$$\rho(\boldsymbol{x}, t) = \sum_{\mathrm{q}} F_{\mathrm{q}}(\boldsymbol{x}, t) \ , \tag{2.3}$$

$$\rho\boldsymbol{u}(\boldsymbol{x}, t) = \sum_{\mathrm{q}} \boldsymbol{V}_{\mathrm{q}} F_{\mathrm{q}}(\boldsymbol{x}, t) \ , \tag{2.4}$$

$$\rho E(\boldsymbol{x}, t) = \sum_{\mathrm{q}} \frac{1}{2}\boldsymbol{V}_{\mathrm{q}}^2 F_{\mathrm{q}}(\boldsymbol{x}, t) \ . \tag{2.5}$$

Consequently, one can interpret macroscopic flow parameters as a weighted mean derived from their microscopic counterparts. The total energy, denoted as E, is a composition of internal energy E_o and the associated kinetic energy, as outlined in the equation below:

$$E(\boldsymbol{x}, t) = E_o(\boldsymbol{x}, t) + \frac{1}{2}|\boldsymbol{u}(\boldsymbol{x}, t)|^2 \ . \tag{2.6}$$

The total kinetic energy of the gas particles, which correlates with their entropy and temperature status, is represented by the internal energy of the gas. It is imperative to differentiate this from the macroscopic kinetic energy, inherently associated with the flow velocity $\boldsymbol{u}$, as shown below:

$$\rho E_o(\boldsymbol{x},t) = \sum_{\mathrm{q}} \frac{\left|\boldsymbol{V}_{\mathrm{q}} - \boldsymbol{u}\right|^2}{2} F_{\mathrm{q}}(\boldsymbol{x},t) \ . \tag{2.7}$$

As a result, the temperature of the gas can be calculated from its internal energy as follows:

$$T(\boldsymbol{x},t) = \frac{E_o(\boldsymbol{x},t)}{c_v} \ , \tag{2.8}$$

where, the specific heat capacity at constant volume is denoted as $c_v = \frac{RD}{2}$ for monoatomic gases, wherein R stands for the specific gas constant and D represents the number of spatial dimensions. Drawing upon the ideal gas equation, one can subsequently determine the static pressure as:

$$p(\boldsymbol{x},t) = \rho(\boldsymbol{x},t) R T(\boldsymbol{x},t) \ . \tag{2.9}$$

One can demonstrate that the macroscopic conservation laws, consisting of the Navier-Stokes equations, can be recovered from the BTE by calculating the zeroth, first, and the trace of the second order moments from equation 2.2. This derivation, however, results in a closure problem [4]. Noteworthy solutions to this mathematical problem have been presented by Hilbert [144] and Chapman and Cowling [69]. This solution methodology, termed the Chapman-Enskog (C-E) expansion, is a result of expanding the distribution function in terms of the Knudsen number Kn.

$$F = F^{(0)} + \mathrm{Kn} F^{(1)} + \mathrm{Kn}^2 F^{(2)} + \cdots = \sum_{m=1}^{\infty} \mathrm{Kn}^m F^{(m)} \ . \tag{2.10}$$

The Knudsen number is defined as the ratio of the mean free path of a particle to the characteristic length scale within the flow [333]. In equation 2.10, the parameter m denotes the order of expansion. Chen [71] showed that the Navier-Stokes (N-S) equations can be derived from the Boltzmann equation by implementing a first-order truncation of the Chapman-Enskog (C-E) expansion. Typically, this approach holds true for small Knudsen numbers (i.e., $\mathrm{Kn} < 10^{-2}$), under which conditions the fluid can be treated as a continuum, consistent with the conditions set by the N-S equations.

2.2.3. LBM procedure

There are four steps involved in the LBM simulation: initialisation, advection, collision, and the application of the boundary conditions. All these steps are shown in Figure 2.1 and explained in detail below:

Initialisation

The computational domain undergoes discretisation, followed by the imposition of an initial condition. One may opt for, let's say, a rest state, meaning a zero-velocity condition across the entire lattice or even a fixed-velocity condition. Another common approach is to use the results from a prior simulation to set the initial condition, a technique commonly termed "seeding". The following few chapters will highlight the advantage of seeding in terms of statistical time convergence of VAWT thrust and torque.

Advection

In this phase, the particle distribution function in each lattice element is advected towards its adjacent elements, aligning with the discrete velocity directions formulated in equation 2.11. Although this procedure bears similarity to the advection found in conventional N-S Finite Volume Method (FVM) solvers, the LBM approach removes the requirement for numerical schemes, such as interpolation. As a result, there is no numerical dissipation introduced in the solution. Subsequent to the advection stage, macroscopic flow parameters are calculated at every nodal point.

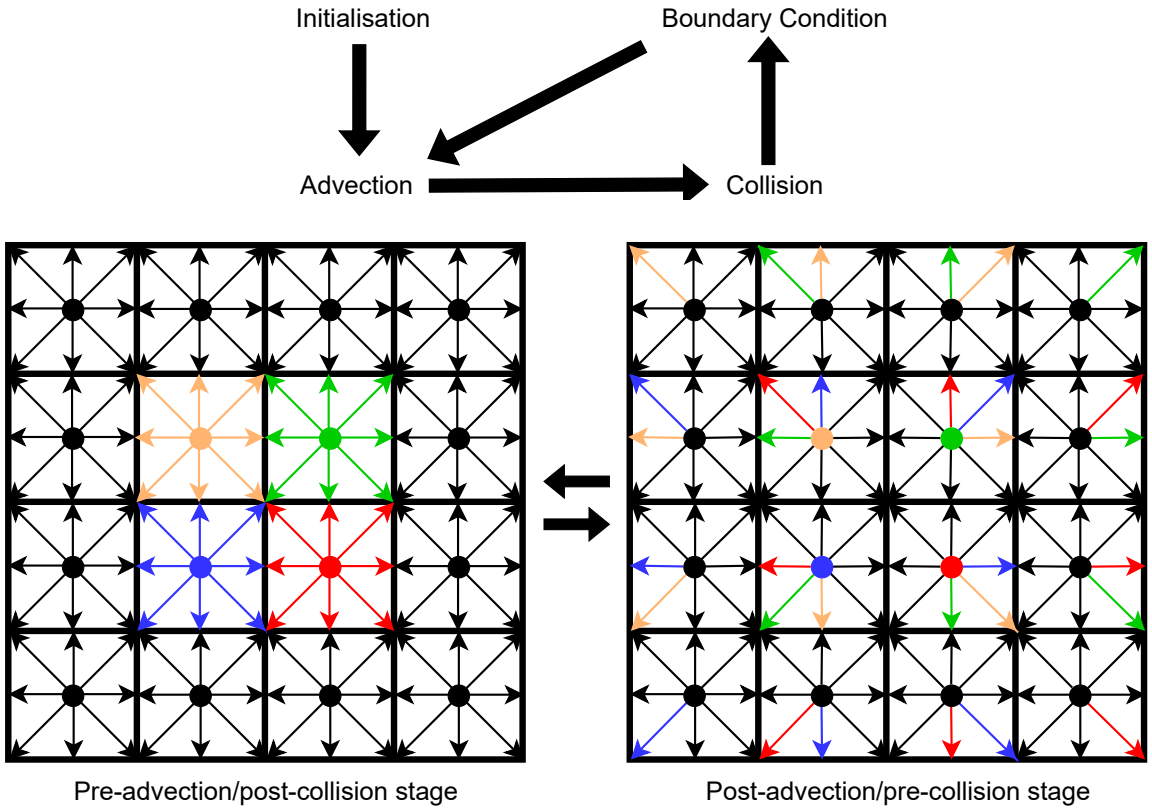

Figure 2.1: Illustration of the LBM algorithm. Within the lattice, individual fluid particles are denoted by dots, and their discrete velocity vectors are depicted using arrows. To represent the advection of the velocity vectors emanating from the central four voxels of the lattice, arrows of varied colours are utilised. (adapted from Teruna [333])

$$F_{\mathrm{q}}\left(\boldsymbol{x}+\boldsymbol{V}_{\mathrm{q}}\Delta t, t+\Delta t\right)=F_{\mathrm{q}}(\boldsymbol{x}, t)\ . \tag{2.11}$$

Is it important to note that numerical dissipation in the LBM framework might still arise from the discretisation of particle velocity and the collision operator [333].

Collision

In the collision stage, macroscopic flow parameters are used for determining the local equilibrium distribution function. Subsequently, the collision term is computed, as presented in equation 2.2. Post this computation, local distribution functions, represented as F_q^*, are updated to account for the result of the collision process, consistent with the equation 2.12. The collision procedure is executed locally at each nodal point, rendering the computation at each node independent from the rest. This structural independence facilitates a highly optimised parallelisation in the LBM computational framework, much better than traditional N-S solvers.

$$F_{\mathrm{q}}^{*}\left(\boldsymbol{x}+\boldsymbol{V}_{\mathrm{q}}\Delta t, t+\Delta t\right)=F_{\mathrm{q}}\left(\boldsymbol{x}+\boldsymbol{V}_{\mathrm{q}}\Delta t, t+\Delta t\right)+\kappa_{\mathrm{q}}\ . \tag{2.12}$$

Boundary Conditions

Lattice elements adjoining the simulation domain boundary require critical handling. This is due to the advection in distribution functions: some may exit the domain, while others may enter. The same considerations are applicable to a wall's surface. The modification of the distribution function will be dependent on the specific boundary condition, be it a fluid inlet, or no-slip wall, among

others. A more comprehensive exploration of these boundary conditions will follow later in this chapter.

Within the LBM framework, the simulation space is structured into cubic units termed voxels, or volume elements [72]. This space or domain can be divided into areas of varying voxel density or grid size, where the ratio in resolution levels between neighbouring sections is 2 [75]. The finest voxel scale (or the highest resolution) is represented by counting the number of voxels spanning a characteristic reference length (e.g., the chord of an airfoil). Correspondingly, a timestep is determined so that the Courant–Friedrichs–Lewy (CFL) number remains unity. Each voxel distribution function is calculated and updated at intervals based on the voxel resolution level. For the highest resolution, this action occurs at every time step. Given the highest resolution level as M, voxels of a resolution level that are reduced by N (i.e. the resolution becomes $M - N$) are updated every 2^N timestep intervals. To ensure the conservation of mass, momentum, and energy across regions of various resolutions, a voxel-centered lattice scheme is adopted [75].

In the context of solid boundaries, they are depicted using flat interfaces that align tangentially to the inherent surface curvature. Hence, a curved surface is illustrated through a multifaceted geometric shape (polygon), depicted in Figure 2.2. These planar interfaces are termed surfels, another word for surface elements.

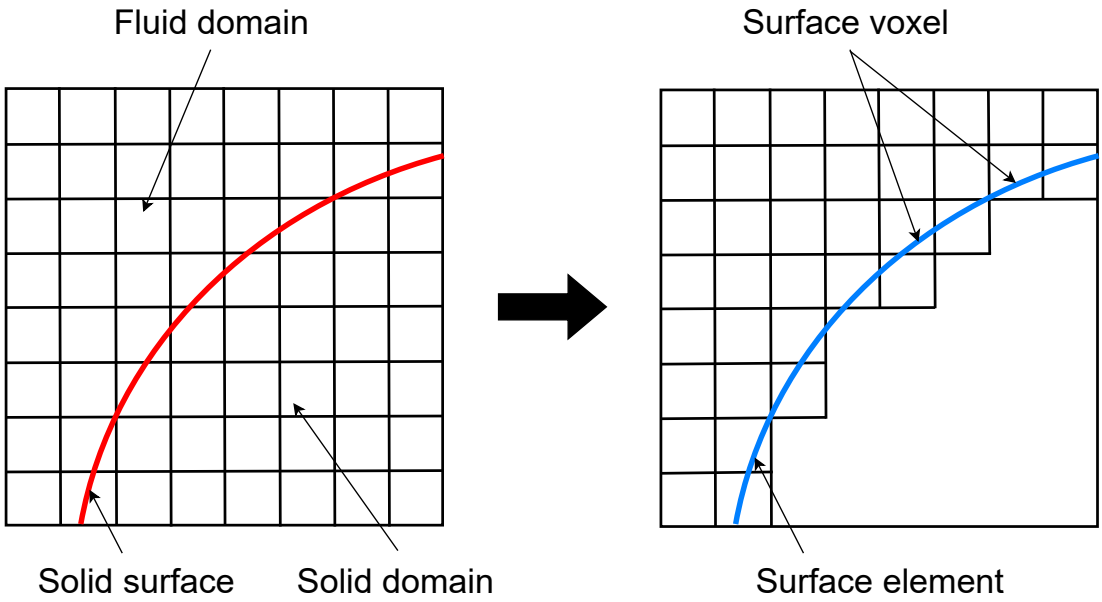

Figure 2.2: Discretisation of the simulation domain in the LBM framework showing volume mesh (voxels) and surface mesh (surfels). The part of surface voxels which are penetrating inside the solid surface will be removed to form an overall smooth layer of surfels on the solid surface. (adapted from Teruna [333])

2.2.4. Velocity-Space Discretisation and the BGK Collision Operator

The most common collision operator is Bhatnagar-Gross-Krook (BGK) model, which can be mathematically expressed as follows:

$$\kappa = -\frac{1}{\tau}\left[F_{\mathrm{q}}(\boldsymbol{x}, t) - F_{\mathrm{q}}^{\mathrm{eq}}(\boldsymbol{x}, t)\right] . \tag{2.13}$$

The BGK model offers a simplified version of the discrete LB equation. Instead of relying on a complex integral function present in the traditional collision operator, it utilises a single relaxation time, denoted as τ [321]. The core premise of the BGK model suggests that the local distribution function, F, tends towards its equilibrium state, F^{eq}, within a time scale defined by τ. Although τ

typically depends on F, the BGK model makes a generalizing assumption that all relaxation processes happen at a uniform rate. This assumption is particularly apt for Newtonian flows, wherein the shear stress and shear rate share a direct proportionality via viscosity, especially when the fluid's deviation from equilibrium remains minimal. It's pertinent to note that the equilibrium distribution function, $F_{\mathrm{q}}^{\mathrm{eq}}$, might be represented using the conventional Maxwell-Boltzmann distribution as follows:

$$F_{\mathrm{q}}^{\mathrm{eq}} = \frac{\rho}{(2\pi \mathrm{R}T)^{\mathrm{D}/2}} e^{\left(-\frac{|V_{\mathrm{q}}-\boldsymbol{u}|^2}{2\mathrm{R}T}\right)} . \tag{2.14}$$

The Boltzmann equation undergoes discretisation in spatial, temporal, and notably, in the velocity domain (represented as V_q). An effective strategy for this velocity discretisation utilises the Gauss-Hermite quadrature. This technique stemmed from Grad's proposition of representing the distribution function via Hermite polynomial expansion [132]. A more comprehensive formulation of this discretisation process was later detailed by Shan et al. [299]. Grad postulated that the Boltzmann-BGK equation can be projected onto a Hermite orthogonal framework, leading to a transformation from equation 2.1 to equation 2.15:

$$\frac{\partial F_{\mathrm{q}}}{\partial t} + \boldsymbol{V}_{\mathrm{q}} \cdot \nabla F_{\mathrm{q}} = \frac{F_{\mathrm{q}}^{\mathrm{eq}} - F_{\mathrm{q}}}{\tau} . \tag{2.15}$$

Here, F_q is expressed through a Hermite expansion corresponding to specific discrete velocities V_q (where q ranges from 0 to Q). The choice for the number Q of discrete velocities is influenced by the truncation level of the Hermite expansion. If n symbolises the truncation order for F_q, then:

$$F_{\mathrm{q}} = \mathrm{w}_{\mathrm{q}} \sum_{\mathrm{n}=0}^{\infty} \frac{1}{\mathrm{n}!} \mathrm{a}^{(\mathrm{n})} H^{(\mathrm{n})}\left(\boldsymbol{V}_{\mathrm{q}}\right), \text{ where } , \tag{2.16}$$

$$\mathrm{a}^{(\mathrm{n})} = \sum_{\mathrm{q}=1}^{\mathrm{Q}} F_{\mathrm{q}} H^{(\mathrm{n})}\left(\boldsymbol{V}_{\mathrm{q}}\right) , \tag{2.17}$$

and $\mathrm{a}^{(\mathrm{n})}$ is identified as the Hermite expansion coefficient, w_q serves as a weighting function, and $H^{(\mathrm{n})}\left(\boldsymbol{V}_{\mathrm{q}}\right)$ is the n^{th}-order Hermite polynomial. As might be anticipated, the truncation order inherently governs the accuracy of equation 2.16 when approximating equation 2.15. Previous studies have indicated that to fully recover the Navier-Stokes (N-S) equations, while following the principles of momentum and energy conservation, a fourth-order truncation (n=4) is required. When truncated using n=3, energy conservation is not preserved, yet it is still possible to derive the N-S equations under isothermal conditions devoid of errors. However, truncating at the second order introduces extra errors, particularly within the viscous stress tensor description, which has a M_∞^3 dependence. This is related to the LBM method's weakly compressible limit [140].

In this study, while the primary emphasis is on flows with low Mach numbers, a third-order expansion has been adopted to represent F_q [71, 76], given as:

$$F_{\mathrm{q}} \approx \rho \mathrm{w}_{\mathrm{q}} \left[1 + \frac{\boldsymbol{V}_{\mathrm{q}} \cdot \boldsymbol{u}}{\Theta} + \frac{\left(\boldsymbol{V}_{\mathrm{q}} \cdot \boldsymbol{u}\right)^2}{2\Theta^2} - \frac{\boldsymbol{u}^2}{2\Theta} + \frac{\left(\boldsymbol{V}_{\mathrm{q}} \cdot \boldsymbol{u}\right)^3}{6\Theta^3} - \frac{\left(\boldsymbol{V}_{\mathrm{q}} \cdot \boldsymbol{u}\right)\boldsymbol{u}^2}{2\Theta^2} \right] . \tag{2.18}$$

The weighing functions, denoted as w_q, are dependent upon the magnitude of V_q and the count of discrete velocity vectors. Their selection ensures the conservation of both mass and momentum alongside the isotropy of the subsequent moments. Specifically, the Lattice Boltzmann Method (LBM) solver employed here is designed for low-Mach-number flows and is based on a 3D lattice structure encompassing 19 discrete velocity vectors. This model is often termed the D3Q19 configuration (as depicted in Figure 2.3). For such a structure, the non-dimensional lattice temperature

stands at $\Theta = 1/3$, with $w_q = 1/3$ for stationary velocity (when q=0), $1/18$ for main axes, and $1/36$ for diagonal directions. Broadly, these weighing functions must adhere to the following conditions:

$$\sum_{q} w_q \underbrace{\boldsymbol{V}_q \dots \boldsymbol{V}_q}_{q} \begin{cases} \Theta^{q/2}\Delta^q, & q = 2,4,\dots,2q \\ 0, & q = 1,3,\dots,2q-1 \end{cases}, \tag{2.19}$$

where Δ^q is the q^{th} order Kronecker delta function tensor.

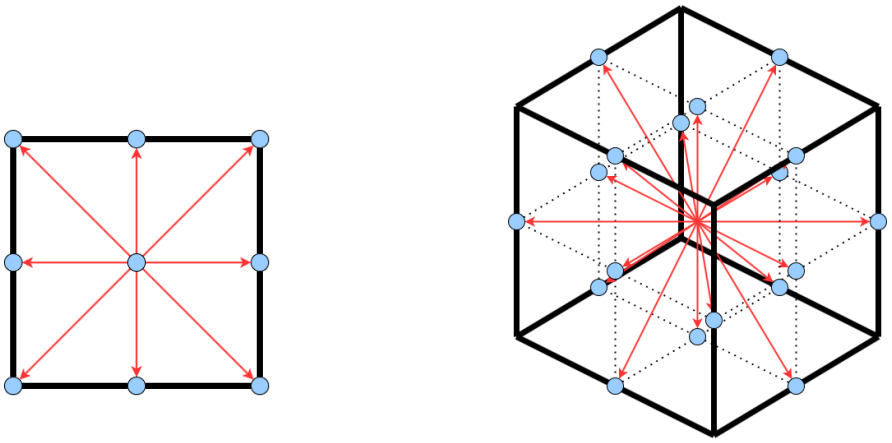

(a) D2Q9 (b) D3Q19

Figure 2.3: A schematic of two different LBM stencil examples: D2Q9 with 9-velocity vectors in 2D and D3Q19 with 19-velocity vectors in 3D (adapted from Teruna [333])

It's pertinent to note that the relaxation time, τ, within the BGK model, is analogously representative of the kinematic viscosity, ν. For scenarios with high Reynolds numbers, where viscous forces are of less significance, a smaller ν value is anticipated. This translates to a reduced τ value, indicating a quicker return of fluid particles to their local equilibrium state. Given a lattice with grid spacing Δx and a timestep Δt, it can be shown that ν and τ are inter-related, via a Chapman-Enskog expansion [140], expressed in equation 2.20.

$$\nu = \frac{1}{3}\left(\frac{\Delta x}{\Delta t}\right)^2 \left(\tau - \frac{\Delta t}{2}\right). \tag{2.20}$$

While the BGK model is frequently selected due to its simplistic formulation, it comes with its own limitations [365]. It employs a single relaxation time suggesting an inability within the BGK model to differentiate between the relaxation rates associated with momentum transfer via viscosity and energy transfer via thermal conduction. Additionally, the BGK model operates under the presumption of a unitary Prandtl number [77], a value that doesn't consistently align with observed values across various fluid types. Proposed enhancements to the BGK framework aim to address these challenges [231], one of which is the multiple-relaxation-time (MRT) method introduced by d'Humières [99]. This approach defines the collision operator based on the velocity moments of the particle distribution function rather than the function itself, as is the case in the BGK model. This inevitably renders the MRT model more complex in its implementation than its BGK counterpart. Furthermore, introducing varying relaxation rates within the same reference frame could potentially breach the principles of Galilean invariance. ("Galilean invariance implies that the laws of motion are identical in all inertial frames of reference. Thus, all inertial frames share the same universal time." [333]) In contrast, the BGK model inherently respects Galilean invariance. Seeking alternatives, Chen et al. [77] introduced a two-relaxation-time (TRT) methodology, allocating

distinct relaxation times for both dynamic viscosity and thermal conductivity. Also, Galilean invariance can be reestablished by defining the collision operator within a relative reference frame, wherein discrete velocity vectors are portrayed relative to the macroscopic flow velocity.

2.2.5. Boundary Conditions

Boundary conditions play a pivotal role in defining the distribution functions at the edges of a computational domain subsequent to the advection process. Within the context of this study, the employed boundary conditions are as follows:

- Periodic Boundary Condition:
  Such boundaries are designed to mimic an infinite domain characterised by repetitive geometric and flow attributes. Their application is straightforward, with distribution functions from one domain edge being advected seamlessly to its opposite edge.

- Inlet and Outlet Boundary Conditions:
  For these boundaries, it is postulated that F_q is equal to F_q^{eq} at the boundary. This approach facilitates the treatment of specific macroscopic parameters, such as density, velocity, and pressure, at both the domain inlet and outlet points.

- Wall Boundary Condition:
  This boundary condition is illustrated in Figure 2.4 [72]. To establish a no-slip wall, a 'bounce-back' methodology is deployed. Here, particles approaching a wall are instantaneously reflected along their original trajectory, maintaining their prior velocities; this is denoted as $\boldsymbol{V}_{\mathrm{q}*} = -\boldsymbol{V}_\mathrm{q}$, where $\boldsymbol{V}_{\mathrm{q}*}$ symbolises the particle velocity after the bounce-back process has occurred. Conversely, a free-slip wall is conceptualised using a specular reflection mechanism, which ensures the conservation of tangential velocity components of the incoming particles, while the normal velocity component is inverted. Mathematically, this is written as $V_{\mathrm{q}'} \cdot \boldsymbol{n} = -\boldsymbol{V}_\mathrm{q} \cdot \boldsymbol{n}$ for the velocity component perpendicular to the wall and $\boldsymbol{V}_{\mathrm{q}'} - \left(\boldsymbol{V}_{\mathrm{q}'} \cdot \boldsymbol{n}\right)\boldsymbol{n} = \boldsymbol{V}_\mathrm{q} - \left(\boldsymbol{V}_\mathrm{q} \cdot \boldsymbol{n}\right)\boldsymbol{n}$ for the velocity component parallel to the wall, where n represents a local unit wall-normal vector.

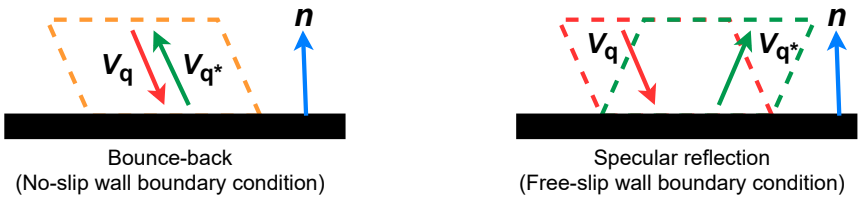

Figure 2.4: A schematic of the two wall boundary conditions: bounce-back condition for no-slip wall and specular reflection for free-slip wall. The thick black region represents the lattice-aligned surfel (adapted from Teruna [333])

2.2.6. Rotating Geometries

In simulations exhibiting a rotating geometry about a stationary axis, the computational domain is bifurcated into an outer "stationary" or "ground-fixed" frame of reference and an inner "body-fixed" Local Reference Frame (LRF). The LRF is distinguished by an axisymmetric mesh that synchronously rotates with the rotating geometry, ensuring there is no relative movement between the LRF mesh and the enclosed geometry. Outside this LRF, the fluid dynamics is computed using the lattice-Boltzmann equation with the BGK collision operator but omitting the body-force term [281]. Conversely, within the LRF, the same equation is used with the external body-force acceleration term, denoted by b, which is the inertial force attributed to the non-inertial rotating LRF [373]:

$$\boldsymbol{b}(\mathbf{x},t) = -\boldsymbol{\Omega}(t)\times(\boldsymbol{\Omega}(t)\times\boldsymbol{r}(\mathbf{x},t)) - 2\boldsymbol{\Omega}(t)\times\boldsymbol{u}^{*}(\mathbf{x},t) - \frac{\mathrm{d}\boldsymbol{\Omega}(t)}{\mathrm{d}t}\times\boldsymbol{r}(\mathbf{x},t)\ , \tag{2.21}$$

where $\boldsymbol{\Omega}(t)$ signifies the LRF angular velocity, $\boldsymbol{r}$ represents the radial vector stemming from the rotation centre to a given local voxel, and $\boldsymbol{u}^{*}$ is the pre-collide fluid velocity $\boldsymbol{u}$ adjusted by $\Delta t\boldsymbol{b}/2$, which translates to $\boldsymbol{u}^{*} = \boldsymbol{u} + \Delta t\boldsymbol{b}/2$. To bridge the transition between the boundaries of the inner and outer reference frames, a surface treatment approach is employed, ensuring the conservation principles remain intact across the LRF interface [373].

2.2.7. LBM-VLES Turbulence Modelling

The solution of the lattice-Boltzmann equation is analogous to conducting a Direct Numerical Simulation (DNS) of the Navier-Stokes equations, within the limits of the dynamic range (specifically, the Mach number) accurately covered by lattice velocities and the grid resolution necessary for resolving the smallest turbulent scales [281]. Yet, in the context of high Reynolds number flows, the computational expenses for LBM-DNS simulations become exorbitantly high, necessitating the adoption of turbulence modelling. The LBM can be easily coupled with various turbulence modelling methodologies, including one- or two-equation turbulence models, LES sub-grid scale models and hybrid approaches. These methods aid in determining a turbulent relaxation time (τ_{turb}) which is added to the viscous/laminar time (τ). It is important to note that for LBM-DNS or LBM-ILES (Implicit Large Eddy Simulation [42]) simulations, such a turbulent relaxation time is 0.

Within PowerFLOW ®, turbulence modelling has been integrated into the LBM framework [73]. This is achieved by employing a modified two-equation $k-\epsilon$ model, based on the Re-Normalization Group (RNG) theory [366, 367], on the unresolved scales [330] which are chosen based on a method related to the local flow swirl [9]. This method is termed LBM-Very Large Eddy Simulation (LBM-VLES). It bears a conceptual resemblance to non-zonal hybrid strategies like RANS/LES, DES, or Scale Adaptive Simulations [233]. Notably, the two-equation RNG $k-\epsilon$ model, refined to include a swirl modification and solved using a second-order time-explicit finite-difference approach on the same LBM grid, is employed to derive a turbulent relaxation time. This time is then combined with the viscous relaxation time, leading to τ evolving to τ_{eff}:

$$\tau_{\mathrm{eff}} = \tau + \tau_{\mathrm{turb}} = \tau + C_{\mu}\frac{k^{2}/\epsilon}{T\left(1+\tilde{\eta}^{2}\right)^{1/2}}\ , \tag{2.22}$$

where, C_{μ} stands at 0.09, with k representing turbulent kinetic energy and ϵ indicating turbulent dissipation. The parameter η is a function of a local strain metric $\eta_{s} = k\left|S_{ij}\right|/\epsilon$, a local vorticity measure $\eta_{\omega} = k\left|\Omega_{ij}\right|/\epsilon$, and a local helicity parameter. The swirl modification integrated within the modified RNG $k-\epsilon$ model is intended to mitigate the effects of the modelled eddy viscosity in high vorticity zones. This enables a local resolution of big anisotropic vortex structures when the computational grid is sufficiently small [170]. Notably, this methodology isn't analogous to the application of an RNG $k-\epsilon$ model in a RANS context. Within the current methodology, there is no direct alteration of eddy viscosity in the manner that the modellled Reynolds stresses are directly included within the governing equations, characteristic of the RANS method. Instead, the RNG $k-\epsilon$ model is employed to adjust the evolution of the particle system towards thermodynamic equilibrium (via changes in the relaxation time). This is harmonised with the turbulent flow intrinsic time scales, leading to Reynolds stresses emerging from LBM calculations rather than semi-empirical modelling [64, 74].

Wall Modelling

The Lattice-Boltzmann Method (LBM) utilises a Cartesian grid, meaning that varying cell sizes in the spatial dimensions or the grid stretching solely in the direction perpendicular to the wall is unfeasible [281]. This poses challenges in adequately resolving boundary layers adjacent to the no-slip

wall, especially when the wall-normal distance in viscous units (represented as y^+) should be less than 1 [353]. This resolution becomes notably costly for high Reynolds number scenarios. Hence, in PowerFLOW ®, a wall function strategy models boundary layers on solid boundaries. This model builds upon the fundamental law-of-the-wall concept and extends it [178], integrating both positive (favourable) and negative (adverse) pressure gradient effects [330].

$$u^+ = \begin{cases} y^+ & \text{if } y^+ \leq 5 \\ \frac{1}{\kappa}\ln\left(\frac{y^+}{A}\right) + B & \text{otherwise} \end{cases}, \tag{2.23}$$

where $u^+ = u_s/u_\tau$ and $y^+ = yu_\tau/\nu$ (with $u_\tau = \sqrt{\tau_w/\rho}$ and $\tau_w = \frac{1}{2}\rho C_f u_s^2$ representing the friction velocity and the wall shear-stress) denote the frictionless velocity and wall-distance direction, respectively. κ and B hold values of 0.41 and 5 and are empirically determined in the logarithmic region, respectively, for the range $30 \leq y^+ \leq 300$. In the buffer zone (spanning $5 < y^+ < 30$), these constants adjust to ensure continuity between the viscous sub-layer and the logarithmic regions. The model accounts for the deceleration and expansion of the velocity profile due to negative pressure gradients through a function denoted as A. The scaling function A is expressed as:

$$A = \begin{cases} 1 + \ell\left|\frac{\mathrm{d}p}{\mathrm{d}\tilde{s}}\right|/\tau_w & \text{if } \hat{\boldsymbol{u}}_{\boldsymbol{s}} \cdot \frac{\mathrm{d}p}{\mathrm{d}\tilde{s}} > 0 \\ 1 & \text{otherwise} \end{cases}, \tag{2.24}$$

where $\mathrm{d}p/\mathrm{d}\tilde{s}$, $\hat{\boldsymbol{u}}_{\boldsymbol{s}}$ and l represent the pressure gradient along the flow direction, the local slip velocity u_s unitary vector, and a length-scale mirroring the same order of the unresolved near-wall area region, respectively. Equations given by 2.23 and $\tau_w = \rho u_\tau^2 = \frac{1}{2}\rho C_f u_s^2$ form a set of two equations with C_f and u_τ as the unknowns. By solving these, one can determine a wall-shear stress for the wall boundary condition in the LBM, aligning with the law-of-the-wall methodology [111]. This wall model also establishes the boundary conditions for the modified RNG $k-\epsilon$ turbulence model, where $k = u_\tau^2/\sqrt{C_\mu}$ and $\epsilon = u_\tau^3/(ky)$. Here, y represents the "slip" surface's distance from the wall in the wall-normal direction [330].

2.2.8. LBM Acoustic Properties

The Lattice-Boltzmann Method (LBM), as previously discussed, has inherent unsteady and compressible qualities. This permits direct noise extraction from CFD simulations. Brès et al. [52] explored the acoustic characteristics of the LBM within PowerFLOW ® by studying the temporal decay of a standing planar wave in a periodic fluid domain and the spatial decay of a propagating planar Gaussian acoustic pulse, all on a uniform computational grid. When measured against theoretical predictions, the results highlighted the minimal dispersive and dissipative errors of the LBM method. ("An error introduced by a numerical scheme on the amplitude of a propagating wave is called dissipation error, whereas the dispersion error is related to acoustic waves of different wavelengths propagating at different speeds." [281]) This underscores the method's potential for simulating time-domain acoustic propagation.

Furthermore, both LBM-DNS and LBM-VLES simulations were executed by Brès et al. [52]. They emphasised that while turbulence modelling doesn't infuse any additional dispersion to the LBM approach, it increases the numerical dissipation in inverse proportion to the grid resolution or the number of points for every acoustic wavelength (N_{ppw}). Additionally, they evaluated the decibel loss per wavelength and per cell of propagation to offer clarity on resolution requirements for practical and industrial applications. It was observed that the former scales roughly with $1/N_{\text{ppw}}$, while the latter displayed a $1/N_{\text{ppw}}^2$ relationship. They approximated a loss of around 0.068 dB for each wavelength at N_{ppw} values ranging from 12 to 16, and for N_{ppw} equal to 14, a loss of 0.0046 dB was observed per cell of propagation, both resulting in an attenuation of under 1 dB at 5kHz and a distance of 1 m from the sound origin.

For industrially significant scenarios, integrating the Lattice-Boltzmann Method (LBM) with the Ffowcs Williams & Hawkings' acoustic analogy is often essential. This integration helps ease the constraints on far-field grid resolution and facilitates noise computation in the acoustic far-field at a manageable computational expense. Thus, even though the LBM offers a theoretical framework for direct noise computation, a combined LBM/FW-H strategy is predominantly favoured. In this study, all far-field noise calculations follow this hybrid approach. Here, the LBM is employed to accurately calculate the unsteady and compressible flow within the near-field, while the FW-H acoustic analogy helps in calculating the subsequent far-field noise. The next section offers a brief derivation and explanation of the FW-H acoustic analogy.

2.3. Computational Aeroacoustics

Computational aeroacoustics (CAA) exhibits all the numerical techniques that are used to predict the generation and propagation of sound produced by aerodynamic phenomena. Subsequently, a concise summary of various CAA methodologies will be provided. For readers looking for a further in-depth understanding, these references can be studied [188, 328]

2.3.1. Direct Noise Computation

Direct noise computation (DNC) denotes a numerical method wherein acoustic data, such as the time history of acoustic pressure, are extracted directly from the simulation domain as part of the computational solution. While this method seems inherently logical and simple, DNC typically demands significant computational resources for various reasons [327, 328]. In a way, it can be considered analogous to Direct Numerical Simulation (DNS) for CFD simulations.

Within the human hearing range, acoustic waves span a vast spectrum of frequencies, having wavelengths that oscillate between approximately 10^1 m and 10^{-3} m. Consequently, to correctly capture the acoustic waveform, the spatial resolution within the simulation domain needs to be appropriately fine, often requiring more than six grid points for every wavelength, especially at higher frequencies [327]. Additionally, to sample accurate spectral data, particularly for lower frequencies, the simulation data collection duration must be long enough, especially in terms of sound wave period.

Given that numerous aeroacoustic challenges primarily focus on noise levels in the acoustic far-field (where the observer's distance from the noise origin surpasses several sound wavelengths), a DNC mandates a vast simulation domain that contains the observer's position and simultaneously maintains a considerable spatial resolution. When combined, these conditions result in substantial computational effort. Direct noise computation (DNC) requires a numerical method that minimises dispersion and dissipation, ensuring that acoustic data isn't artificially distorted or dampened as it moves to the far-field. Thus, solvers suitable for DNC often demand high-order numerical methods, typically with an order of accuracy of three or greater. ("A numerical method is of order n if the solution error ϵ is proportional to the grid size to the power of n, i.e.,$\epsilon \propto (\Delta x)^n$." [333, 355]) While the lattice-Boltzmann method (LBM) has been demonstrated to be effective for DNC [213], hybrid computational aeroacoustics (CAA) techniques tend to be more cost-efficient and are usually favoured [188].

2.3.2. Hybrid CAA Methods

In contrast to DNC, hybrid CAA techniques divide the noise computation process into distinct phases:

1. Noise sources, which include turbulence and other flow-field non-linearities, are computed utilizing CFD approaches, examples being LBM-VLES or LES. This step is confined to a comparatively small domain, focusing on the area where the noise originates.

2. For areas extending beyond the noise source, noise propagation is addressed using methods based on the linear acoustic theory [127].

Numerous hybrid CAA methodologies exist [202], including the linearised Euler equations (LEE) [17], acoustic perturbation equations (APE) [95], and acoustic analogies. Lighthill [195] originally introduced the concept of the acoustic analogy by leveraging continuity and momentum conservation equations, excluding scenarios of mass introduction and external forces.

$$\begin{aligned} \frac{\partial \rho}{\partial t} + \frac{\partial (\rho u_i)}{\partial x_i} &= 0 \ , \\ \frac{\partial (\rho u_i)}{\partial t} + \frac{\partial (\rho u_i u_j)}{\partial x_i} &= -\frac{\partial p}{\partial x_i} + \frac{\partial \varsigma_{ij}}{\partial x_i} \ , \end{aligned} \tag{2.25}$$

where ς_{ij} represent the stress tensor. By differentiating the continuity equation with respect to time and subtracting the divergence of the momentum equation, the Lighthill's equation is derived.

$$\begin{aligned} \frac{\partial}{\partial t}\left[\frac{\partial \rho}{\partial t} + \frac{\partial (\rho u_i)}{\partial x_i}\right] - \frac{\partial}{\partial x_i}\left[\frac{\partial (\rho u_i)}{\partial t} + \frac{\partial (\rho u_i u_j)}{\partial x_i} + \frac{\partial p}{\partial x_i} - \frac{\partial \varsigma_{ij}}{\partial x_i}\right] &= 0 \ , \\ \frac{\partial^2 \rho}{\partial t^2} - c_0^2 \frac{\partial^2 \rho}{\partial x_i^2} = \frac{\partial^2 \mathrm{T}_{ij}}{\partial x_i \partial x_j} \ . \end{aligned} \tag{2.26}$$

The constant c_0 is equal to the speed of sound, represented as $c_0 = a_\infty = \sqrt{\partial p \partial \rho|_s} = \sqrt{\gamma R T_\infty}$, under the presumption of isentropic sound wave propagation within a uniform temperature distribution in a region. Furthermore, by employing the Reynolds decomposition $\rho' = \rho - \rho_\infty$ and the isentropic relation $\rho' = p'/a_\infty^2$, we can express the aforementioned equation 2.26 in terms of pressure perturbations.

$$\begin{aligned} \frac{1}{a_\infty^2}\frac{\partial^2 p'}{\partial t^2} - \frac{\partial^2 p'}{\partial x_i^2} &= \frac{\partial^2 \mathrm{T}_{ij}}{\partial x_i \partial x_j} \ , \\ \mathrm{T}_{ij} = \rho u_i u_j - \zeta_{ij} + \left(p' - a_\infty^2 \rho'\right)\delta_{ij} \ . \end{aligned} \tag{2.27}$$

The Lighthill stress tensor T_{ij} comprises three distinct elements: the Reynolds stress ($\rho u_i u_j$), the viscous stress (ζ_{ij}), and an entropy component ($p' - a_\infty^2 \rho'$). Here, δ_{ij} is denoted as the Kronecker delta. For high Reynolds numbers, typically observed in aerospace contexts, the viscous stress element is anticipated to be smaller compared to the inertial component, or the Reynolds stress. Given the absence of significant density inhomogeneities within the flow domain, the entropy component tends to be negligible. The existence of the second-order spatial derivative alongside Lighthill's stress tensor suggests its description as a distribution of quadrupole sources. Moreover, while Lighthill's equation is mathematically exact, it lacks an analytical solution due to the presence of 11 unknowns (3 in u_i, 6 in $u_i u_j$, p' and ρ') but only a single equation. Nonetheless, if the value of T_{ij} is established and the source region is within an infinite domain, then equation 2.27 can be addressed using the free-field Green's function.

$$p'(\boldsymbol{x}_o, t) = \frac{1}{4\pi}\iiint_{\mathbb{V}} \frac{\partial^2 \mathrm{T}_{ij}\left(\boldsymbol{x}_s, t - \frac{|\boldsymbol{x}_s - \boldsymbol{x}_o|}{a_\infty}\right)}{\partial x_i x_j} \frac{1}{|\boldsymbol{x}_s - \boldsymbol{x}_o|} \mathrm{d}\mathbb{V} \ , \tag{2.28}$$

where x_s and x_s represent the positions of the source and observer, respectively. $\mathbb{V}$ denotes a control volume enclosing the quadrupole sources. It's crucial to note that the acoustic pressure at the observer time t is determined from prior data, specifically when the sound was originally emitted from the source [127]. This time difference corresponds to the duration required for a sound wave for its journey from its source to an observer, a concept known as the retarded time principle. Another method, based on the advanced time concept, has been introduced by Casalino [60] and will be detailed further in this section. While Lighthill's analogy offers significant physical understanding, it presents several challenges that hinder its practical application. Specifically, Equation

2.28 necessitates knowledge of Lighthill's stress at all points within the sound source domain (i.e., the volume $\mathbb{V}$). Storing data across this 3D space would demand considerable memory resources.

Curle [86] extended Lighthill's concept by factoring in a nearby solid boundary to the turbulence. This refined formulation is commonly known as Curle's analogy. When non-isentropic effects are disregarded, the formula emerges as depicted in equation 2.29.

$$\rho'(\boldsymbol{x}_o, t) = \frac{1}{4\pi a_\infty^2}\left[\frac{\partial^2}{\partial x_i x_j}\iiint_{\mathbb{V}}\frac{\rho u_i u_j}{|\boldsymbol{x}_s - \boldsymbol{x}_o|^2}\,\mathrm{d}\mathbb{V} - \frac{\partial}{\partial x_i}\iint_{\mathbb{S}}\frac{p'\cdot\boldsymbol{n}}{|\boldsymbol{x}_s - \boldsymbol{x}_o|^2}\,\mathrm{d}\mathbb{S}\right]. \tag{2.29}$$

The volume-integral component in this above equation mirrors Lighthill's analogy, signifying noise originating from the Reynolds shear stresses in turbulence. The subsequent term encompasses a surface integral of pressure fluctuations p' on the solid surface. This additional noise contribution is attributed to a distribution of dipole sources on the surface of the body. Through dimensional analysis, Curle assessed the acoustic efficiency of each source term. He discovered that the sound intensity from the surface integral (dipole) aligned with $U_\infty^3 M_\infty^3$, while the volume integral (quadrupole) followed a dependency of $U_\infty^3 M_\infty^5$. Thus, in low Mach number flows, the interaction between turbulence and a solid boundary emerges as a more efficient noise producer than the turbulence in isolation. This analogy by Curle was further refined by Ffowcs Williams and Hawkings [361] to consider a moving boundary, a modification that remains as the foundation in many recent aeroacoustic research.

2.3.3. Ffowcs Williams & Hawkings Acoustic Analogy

In this section, the acoustic analogy applied throughout this study to determine aerodynamically generated noise from moving surfaces is elaborated. This analogy utilises flow data sampled on the surface, derived from transient and compressible LBM evaluations. The approach builds up on the source-time dominant solution [60] introduced by Farassat [116], which serves as a solution to the Ffowcs Williams & Hawkings (FW-H) equation [34]. This study employs the FW-H solver which is integrated into the post-processing tool, SIMULIA PowerACOUSTICS ® in PowerFLOW ®. Firstly, this section offers an overview of the FW-H equation. Subsequently, the specifics of Farassat's formulation 1A concerning the FW-H equation are discussed. Then, the retarded (observer-time) and advanced (source-time) time solutions of the FW-H equation are discussed, focusing on the distinctions between solid and permeable formulations.

Ffowcs Williams & Hawkings Equation

The Ffowcs Williams & Hawkings' equation [50, 361] serves as an extension of Lighthill's acoustic analogy [195], from a generic turbulence region enclosed by an undisturbed boundless fluid to flows restricted by arbitrary motion of surfaces. Essentially, the FW-H equation restructures the exact Navier-Stokes equations into an inhomogeneous wave equation that accounts for the influence of moving surfaces on its right-hand side. Central to an acoustic analogy is the division of the flow into two areas: one where equivalent non-zero noise sources exist and another, an undisturbed fluid region of acoustic propagation where these sources are absent [281]. A fundamental premise of this analogy is that no interaction occurs between the flow and the acoustic field i.e. the acoustic field does not affect the noise source.

The FW-H acoustic analogy begins by establishing a control surface, denoted as S, defined by the equation $f(\mathbf{x}, t) = 0$. Here, x represents the observer's position, and t stands for the reception time. The function f holds values less than zero within the flow enclosed by the surface and values greater than zero outside this flow, as illustrated in Figure 2.5. In this figure, $\hat{\mathbf{n}}$ represents a unit vector normal to the surface S and directed outward, such that the gradient of f equals $\hat{\mathbf{n}}$ ($\Delta f = \hat{\mathbf{n}}$). Moreover, u and v signify the flow and integration surface velocity vectors, respectively, with y indicating the source position. An observer in this setup moves at a speed denoted by v_0. The assumption is made that the interior volume of the control surface is filled with a stationary fluid, characterised by its

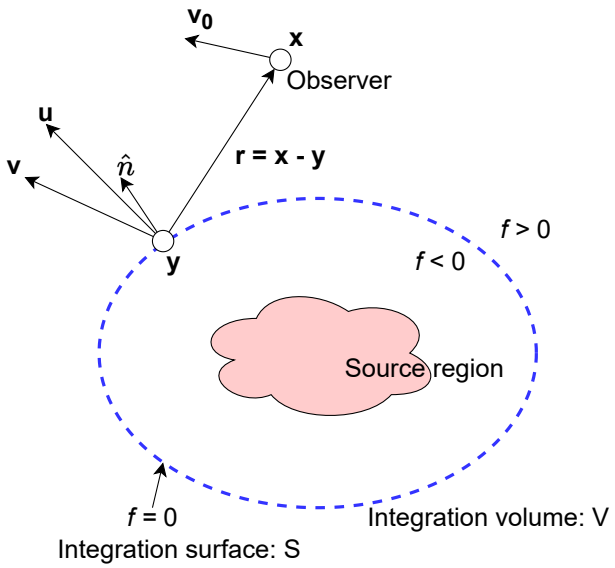

Figure 2.5: Problem formulation of the FW-H acoustic analogy (adapted from Casalino [60] and Romani [281])

density ρ_0, pressure p_0, and velocity $u_i = 0$. In order to maintain the conservation nature of the field, a distribution of mass and momentum sources is introduced on the control surface. This distribution can be expressed using the generalised continuity and momentum equations, incorporating the Dirac $\delta(f)$ and Heaviside $H(f)$ functions as follows:

$$\bar{\partial}\frac{\bar{\partial}}{\partial t}\left[\left(\rho-\rho_0\right)H(f)\right]+\frac{\bar{\partial}}{\partial x_i}\left[\rho u_i H(f)\right]=Q\delta(f) \quad \text{with} \ , \tag{2.30}$$

$$Q=\rho_0 U_i \hat{n}_i \quad \text{and} \quad U_i=\left(1-\frac{\rho}{\rho_0}\right)v_i+\frac{\rho u_i}{\rho_0} \ , \tag{2.31}$$

and

$$\frac{\bar{\partial}}{\partial t}\left[\rho u_i H(f)\right]+\frac{\bar{\partial}}{\partial x_j}\left[\left(\rho u_i u_j+P_{ij}\right)H(f)\right]=L_i\delta(f) \quad \text{with} \ , \tag{2.32}$$

$$L_i=P_{ij}\hat{n}_j+\rho u_i\left(u_n-v_n\right) \quad \text{and} \quad P_{ij}=\left(p-p_0\right)\delta_{ij}-\tau_{ij} \ , \tag{2.33}$$

where

$$\frac{\bar{\partial}H(f)}{\partial t}=\delta(f)\frac{\partial f}{\partial t}=-\delta(f)v_n \quad \text{and} \quad \frac{\bar{\partial}H(f)}{\partial x_i}=\delta(f)\frac{\partial f}{\partial x_i}=\delta(f)\hat{\mathbf{n}} \ , \tag{2.34}$$

are generalised derivatives, whereas the right-hand side terms of Eq. 2.30 and 2.32 depict the mass and momentum source distributions on the integration surface S, respectively. Within Eq. 2.33, P_{ij} and τ_{ij} are identified as compressive and viscous stress tensors, respectively. Additionally, δ_{ij} refers to the widely recognised Kronecker's delta. It's vital to note the presence of the Heaviside function $H(f)$ in the left-hand side terms of Eq. 2.30 and 2.32, which reestablishes quiescent conditions within the integration surface, with $H(f) = 0$ inside S and $H(f) = 1$ outside it. By modifying Eq. 2.30 and 2.32, an inhomogeneous wave equation can be obtained, which accounts for the influence of arbitrarily moving surfaces, positioned as source terms on its right side. This is achieved by subtracting the divergence of Eq. 2.32 from the time derivative of Eq. 2.30, as follows:

$$\bar{\Box}^2\left\{p'H(f)\right\} = \frac{\bar{\partial}}{\partial t}\{Q\delta(f)\} - \frac{\bar{\partial}}{\partial x_i}\left\{L_i\delta(f)\right\} + \frac{\bar{\partial}^2}{\partial x_i \partial x_j}\left\{T_{ij}H(f)\right\} \ . \tag{2.35}$$

The above equation represents the differential form of the FW-H equation for acoustic pressure p', where $\bar{\Box}^2$ stands for the wave or D'Alembertian operator in a 3D space with generalised differential operators. Here, $T_{ij} = \rho u_i u_j + (p' - c_0^2\rho')\delta_{ij} - \tau_{ij}$ denotes the perturbed version of Lighthill's stress tensor. Based on Eq. 2.35, it can be deduced that the pressure fluctuations outside of S are equal to those linked with an equivalent quiescent acoustic medium, forced by three source terms. The first two terms on Eq. 2.35 right-hand side, which appear as monopole and dipole terms [127, 281], respectively, symbolise surface source term distributions, indicated by the Dirac function $\delta(f)$. Conversely, the third term, the quadrupole source, portrays a volume distribution, evident from the Heaviside function $H(f)$.

When the control surface S aligns with a solid or impenetrable surface, all three source terms can be explained using a physical interpretation. Specifically, the monopole term demonstrates fluid displacement effects due to body motion. In contrast, the dipole term recognises the unsteady loading the surface applies on the adjacent fluid. Lastly, the quadrupole term captures all the physical sources and non-linear phenomena, such as shocks, turbulence, vorticity, non-linear propagation, etc., outside the integration surface $S(f > 0)$.

Farassat's Formulation 1A of the FW-H Equation

The FW-H equation can be represented in integral form by convoluting Eq. 2.35 with the free-space Green's function, defined as $G = \delta(g)/(4\pi r)$, where $g = t - \tau - r/c_0$, $r = |\mathbf{x} - \mathbf{y}|$ and τ represents the source (emission) time and by utilizing the properties of the Heaviside and Dirac functions:

$$\begin{aligned} 4\pi p'(\mathbf{x},t) = &\frac{\partial^2}{\partial x_i \partial x_j}\int_{-\infty}^{t}\int_{f>0}\frac{\delta\left(t-\tau-r/c_0\right)}{r}T_{ij}\,\mathrm{d}V(\mathbf{y})\mathrm{d}\tau \\ &- \frac{\partial}{\partial x_i}\int_{-\infty}^{t}\int_{f=0}\frac{\delta\left(t-\tau-r/c_0\right)}{r}L_i\,\mathrm{d}S(\mathbf{y})\mathrm{d}\tau \\ &+ \frac{\partial}{\partial t}\int_{-\infty}^{t}\int_{f=0}\frac{\delta\left(t-\tau-r/c_0\right)}{r}Q\,\mathrm{d}S(\mathbf{y})\mathrm{d}\tau \ . \end{aligned} \tag{2.36}$$

In the aforementioned Eq. 2.36, the integration variable can be adjusted by taking into account that [60]:

$$\int_{-\infty}^{t}\mathscr{F}(\tau)\delta(g(\tau))\mathrm{d}\tau = \sum_{n=1}^{N}\frac{\mathscr{F}}{|\partial g/\partial\tau|}\left(\tau_n^*\right) \quad \text{and} \quad \frac{\partial g}{\partial\tau} = -1 + M_r \ , \tag{2.37}$$

where the summation is over the zeros τ_n^* of the retarded time equation, $g = t - \tau - r/c_0 = 0$ and $M_r = M_i\hat{r}_i$ indicates the projected source Mach number vector $\mathbf{M} = \mathbf{U}/c_0$ (with $\mathbf{U} = \{U_i\}$) in the observer's direction, represented by the unit vector $\hat{r}_i = (x_i - y_i)/r$. The absolute magnitude of the source-time derivative of the retarded time equation, $|1 - M_r|$, acts as the Jacobian for the transformation from τ to g in Eq. 2.37. This represents the Doppler effects, or the expansion/contraction of the observer time scale relative to the source time scale, in the case when the source moves towards/away from the listener. For a surface moving at subsonic speeds, Eq. 2.36 can be rewritten as:

$$
\begin{aligned}
4\pi p'(\mathbf{x},t) = & \frac{\partial^2}{\partial x_i \partial x_j}\int_{f>0}\left[\frac{T_{ij}}{r\,(1-M_r)}\right]_{\text{ret}} \mathrm{d}V(\mathbf{y}) \\
& - \frac{\partial}{\partial x_i}\int_{f=0}\left[\frac{L_i}{r\,(1-M_r)}\right]_{\text{ret}} \mathrm{d}S(\mathbf{y}) \\
& + \frac{\partial}{\partial t}\int_{f=0}\left[\frac{Q}{r\,(1-M_r)}\right]_{\text{ret}} \mathrm{d}S(\mathbf{y})\ ,
\end{aligned}
\tag{2.38}
$$

where the term ret implies integral calculations at the retarded time $\tau = t - |\mathbf{x}(t) - \mathbf{y}(\tau)|/c_0$. By changing space derivatives to time derivatives, shifting them inside the integrals (for a comprehensive analysis, the interested reader can consult references [50, 60, 116]), and disregarding the quadrupole term $p'_Q(\mathbf{x},t)$, meaning all linear sources outside the integration surface are excluded, the equation becomes $p'(\mathbf{x},t) = p'_T(\mathbf{x},t) + p'_L(\mathbf{x},t)$, where:

$$
\begin{aligned}
4\pi p'_T(\mathbf{x},t) = & \int_{f=0}\left[\frac{\rho_0\left(\dot{U}_n + U_{\dot{n}}\right)}{r\,(1-M_r)^2}\right]_{\text{ret}} \mathrm{d}S(\mathbf{y}) \\
& + \int_{f=0}\left[\frac{\rho_0 U_n\left(r\dot{M}_r + c_0\left(M_r - M^2\right)\right)}{r^2\,(1-M_r)^3}\right]_{\text{ret}} \mathrm{d}S(\mathbf{y})\ , \\
4\pi p'_L(\mathbf{x},t) = & \frac{1}{c_0}\int_{f=0}\left[\frac{\dot{L}_r}{r\,(1-M_r)^2}\right]_{\text{ret}} \mathrm{d}S(\mathbf{y}) + \int_{f=0}\left[\frac{L_r - L_M}{r^2\,(1-M_r)^2}\right]_{\text{ret}} \mathrm{d}S(\mathbf{y}) \\
& + \frac{1}{c_0}\int_{f=0}\left[\frac{L_r\left(r\dot{M}_r + c_0\left(M_r - M^2\right)\right)}{r^2\,(1-M_r)^3}\right]_{\text{ret}} \mathrm{d}S(\mathbf{y})\ .
\end{aligned}
\tag{2.39}
$$

The above equation 2.39 is indicative of Farassat's Formulation 1A, a primary focus of the current study. When analyzing an impermeable surface ($u_n = v_n$), these equations physically interpret thickness and loading noise, in the order mentioned above. In these equations, time derivatives concerning source time τ (distinct from observer time t) are indicated by dots, observed in the frame of reference fixed with the quiescent medium. The subscripts r and n represent projections along radiation and surface normal directions, respectively, where $U_{\dot{n}} = U_i \hat{n}_i$ and $L_M = L_i M_i$.

Retarded and Advanced Time Solutions

To find the integral solution of the FW-H equation as represented in Eq. 2.39, two methods can be used, namely, the retarded-time approach or the advanced-time approach [60, 281]. In the retarded-time formulation, the computation revolves around the observer, utilizing the reception time t. To compute the acoustic signal the observer perceives at time t, the acoustic disturbances which are generated at various retarded times τ must be taken into account. The corresponding distances covered by these acoustic disturbances are determined by $|\mathbf{x}(t) - \mathbf{y}(\tau)|/c_0$, which hinge on individual sources on the integration surface. This necessitates calculating the roots, denoted as τ of the retarded-time equation of the equation $t - \tau - |\mathbf{x}(t) - \mathbf{y}(\tau)|/c = 0$. Furthermore, one must interpolate the initial discrete data of the unsteady flow at time τ for each element of the integration surface. While simple source translations allow for an analytical derivation to find the roots of the retarded-time equation, more complex source movements often demand an iterative procedure.

Contrastingly, the advanced-time method focuses on the source time, symbolised as τ. Here, the calculation of both the acoustic disturbance and the time it takes to reach the observer, given as $t = \tau + |\mathbf{x}(t) - \mathbf{y}(\tau)|/c_0$, is vital for each element of the integration surface. Given that Doppler effects result in a non-uniform spacing of t for all source elements, a necessary step before integrating all contributions from various surface elements is the interpolation of the acoustic disturbance time histories on a reception time vector with equal intervals. An observer when stationary or when moving at a constant velocity enables the explicit determination of observer time t [60].

In this study, the utilised FW-H solver operates on the advanced-time solution of the FW-H equation. This choice is informed by a variety of benefits that the advanced-time approach offers over its retarded-time counterpart. Firstly, the former promises greater computational efficiency, necessitating fewer floating-point operations, an advantage especially pronounced when handling a substantial quantity of elements on the integration surface, numerous timesteps in the observer time history, and/or a high number of computations of requisite coordinate transformations [51].

Secondly, the advanced-time algorithm facilitates the computation of integrands in Eq. 2.39 utilizing time points already present in the flow data solution, circumventing the requirement for time interpolation of the original discrete transient flow data at the retarded time. Consequently, it only mandates access to integration surface data one source time step at a time. This contrasts sharply with the continuous access to extensive data concerning the integration surface, a requirement in retarded-time algorithms given that an individual observer acoustic signal is the summation of contributions from different surface elements generated at varying source times [129]. This feature distinctly enhances the memory efficiency of the advanced-time algorithm. Lastly, it provides the flexibility to conduct aeroacoustic calculations concurrently with CFD simulations, removing the necessity to reserve substantial volumes of aerodynamic data [60]. This adaptability not only streamlines the computational process but also substantially reduces the data storage demands, illustrating the pragmatic advantages of adopting the advanced-time approach.

Solid and Permeable FW-H Formulation

In the development of the FW-H equation, represented as Eq. 2.35, a generally applicable permeable (or porous) integration surface S was assumed, which might not always align with the physical boundary of a body. When this integration surface matches the body surface, the flow velocity at any point on the surface matches the surface velocity, denoted as $u_i = v_i$. Here, the FW-H methodology is termed as solid or non-permeable, leading Eq. 2.35 to simplify terms Q and L_i from:

$$Q = \rho_0 U_n \quad \text{and} \quad L_i = \big(p - p_0\big)\delta_{ij}\hat{n}_j - \tau_{ij}\hat{n}_j + \rho u_i \left(u_n - v_n\right) \tag{2.40}$$

to:

$$Q = \rho_0 v_n \quad \text{and} \quad L_i = \big(p - p_0\big)\delta_{ij}\hat{n}_j - \tau_{ij}\hat{n}_j \ . \tag{2.41}$$

This helps to reinstate the original interpretations of thickness and loading noise as discussed earlier.

Various solutions to the FW-H equation, including the Farassat formulation 1A adopted in the current study, omit the quadrupole element $p'_Q(\mathbf{x}, t)$. This omission occurs since calculating this component is not always easy and demands time-intensive volume integration. It is imperative to note that this quadrupole term considers the entirety of noise sources situated in volume V beyond the integration surface, encompassing phenomena like shocks, turbulence, and non-linear propagation. Consequently, the absence of the volume term in a solid FW-H strategy might introduce inaccuracies in scenarios where quadrupole effects are significant, for instance in jet flows or transonic blade-tip Mach numbers for rotors. One solution to this limitation is in the implementation of a permeable FW-H formulation, which is based on the concept of inclusion of significant quadrupole sources (contributing non-negligibly to the acoustic signature) within a porous integration surface [49, 50, 100].

In a study by di Francescantonio concerning a stationary and hovering helicopter rotor [100], it was shown that positioning the integration surface distant from the physical body surface facilitates the capture of quadrupole noise source through the surface source terms included in Eq. 2.39. However, it also carries a risk of capturing spurious noise signals if essential quadrupole sources are not wholly included within the integration surface [335]. In such scenarios, the assumption of encompassing all quadrupole sources within the integration surface loses its validity, casting doubts

on the methodology behind excluding volume integral. It should be noted that the FW-H equation is an exact rearrangement of continuity and momentum equations, therefore it computes both the hydrodynamic and acoustic phenomena. This integral solution operates based on the free-space Green's function, implicating that vortex structures penetrating the porous integration surface could potentially emit non-physical sounds [200]. This spurious noise can essentially be negated through the contribution of the quadrupole sources present external to the integration surface. Therefore, this spurious noise emerges due to the selective accounting for quadrupole sources situated solely within the integration surface, disregarding those existing outside it [200].

In utilizing a permeable FW-H method, it is important to strategically position the integration surface within a high-resolution area of the CFD grid. This ensures that the simulation adequately represents turbulence-related phenomena (when relevant) and the acoustic propagation up to the integration surface. Typically, the optimum location corresponds to the region close to the body's volume (near-field). While bringing the FW-H surface nearer to the body reduces computational demands, it can be problematic due to the potential emergence of non-physical (spurious) noise, a phenomenon discussed earlier. Despite this, there are several strategies to minimise this unwanted noise creation within a permeable FW-H acoustic analogy, some of which hold substantial importance in industrial settings and are outlined briefly below.

One straightforward method is to adopt an open integration surface, consequently excluding areas of the surface influenced by hydrodynamic structures during noise calculation [200]. This strategy, however, has a downside, as it also removes the genuine physical acoustic contributions originating from the removed surface section, potentially inducing inaccuracies in noise directivity, particularly at observer angles orthogonal to the removed surface. An alternative strategy includes establishing a departure region wherein the porous integration surface extends sufficiently away from the body coupled with a systematic reduction in the CFD grid resolution. This methodology is based on the idea of allowing the simulation to wholly or partly diminish small-scale turbulence before reaching the permeable integration surface, either through numerical dissipation or subgrid-scale modelling [315]. This method, however, is not straightforward to implement, as initiating it too near the solid body might alter the aerodynamic solution associated with the solid body itself. Furthermore, it allows an artificial (non-physical) reduction of turbulent formations and structures, potentially leading to the calculation of noise related to non-physical quadrupole sources.

A frequently utilised and fruitful methodology is the application of several porous surfaces characterised by varying downstream end-caps, whereby the noise extracted from each surface is averaged either in the time or frequency domain to remove unwanted hydrodynamic spurious fluctuations from the acoustic signature [221]. This concept, known as cap-averaging, operates on the idea that the acoustic signature calculated using the FW-H equation aggregates contributions from surface sources progressing toward the observer at sonic speed (speed of sound). Consequently, the unwanted spurious noise created by a large eddy at a specific end-cap, through the FW-H equation's surface integrals, and which propagates at convective flow velocity, is significantly diminished through the averaging procedure implemented with other end-caps not capturing the identical vortex structures, thereby not producing similar spurious acoustic waves [315]. In addition to the above, there exist advanced methodologies based on the approximate corrections on the assumption of static (frozen) turbulence convecting through the end-caps, as put forward by numerous researchers [150, 198, 269]. Despite witnessing a degree of success in preceding attempts in recent years, employing these strategies presents a considerable challenge, rendering them unsuitable for industrially relevant scenarios.

2.4. Lifting Line Free Vortex Wake Method

The implementation of the Lifting Line Free Vortex Wake (LLFVW) method in QBlade is detailed in this section. A number of analytical models are also implemented within the LLFVW framework to account for dynamic stall, tower influence, blade crossflow effects, and ground effects. Furthermore, free wake formulation is optimised to reduce computational expense. The current discussion is meant to give a brief introduction; for a more detailed description, the reader is referred to Marten [215].

2.4.1. The LLFVW Algorithm

The LLFVW algorithm used in QBlade largely follows the methodology established by van Garrel [346] during the development of ECN's AWSM code. This algorithm has been encoded into the QBlade utilizing the object-oriented C++ programming language that operates with the assistance of the cross platform Qt framework [41]. In this system, the rotor is represented as a lifting line strategically positioned at the quarter chord points on the mid chord of the 2D airfoil sections [215]. Each blade panel is represented through a ring vortex, which is formed using four straight vortex filaments. The circulation of these bound vortex lines is determined through the relative inflow speed, coupled with lift and drag coefficients derived from the tabulated airfoil data. The Kutta-Joukowski theorem is used to calculate the circulation as follows:

$$\partial C_L(\alpha) = \rho V_{rel} \times \partial\Gamma \ . \tag{2.42}$$

To calculate the relative speed, denoted as V_{rel}, vector addition is performed for the free stream velocity (V_∞), the blade motion (V_{mot}), and the induced velocity (V_{ind}). This latter velocity, V_{ind}, is calculated by considering the contribution of all vortex elements within the specified domain via the Biot-Savart law:

$$V_{\text{ind}} = -\frac{1}{4\pi}\int \Gamma \frac{\vec{r} \times d\vec{l}}{r^3} \ . \tag{2.43}$$

As each time step commences, iterations are performed by the algorithm to calculate a circulation distribution for the bound vortices on the lifting line, which matches with the lift and drag coefficients obtained through the self-induced angle of attack. Throughout this iterative cycle, only the distribution of bound vorticity undergoes modification, with the induction of wake elements on the blade being a single-event evaluation. After the convergence criterion is reached, the rotor rotation is progressed for a single time step.

Subsequent to this, the individual free wake vortex elements convect aligned with the local inflow and the locally induced velocity. This phase is succeeded by the generation of fresh vortex elements in between each blade panel's trailing edge and the last row of wake vortices which have convected away from the trailing edge. In the last phase, computation and allocation of circulation to the newly shed vortex lines are done following the Kutta condition:

$$\begin{aligned} \Gamma_{\text{trail}} &= \frac{\partial \Gamma_{\text{bound}}}{\partial x}\Delta x \ , \\ \Gamma_{\text{shed}} &= \frac{\partial \Gamma_{\text{bound}}}{\partial t}\Delta t \ . \end{aligned} \tag{2.44}$$

In the wake convection step, three distinct integration schemes are operational. Firstly, the first-order Euler forward (EF) integration scheme has been utilised:

$$\vec{x}_{t+1,EF} = \vec{x}_t + (V_\infty + V_{\text{ind}}\ (\vec{x}_t))\,\Delta t \ . \tag{2.45}$$

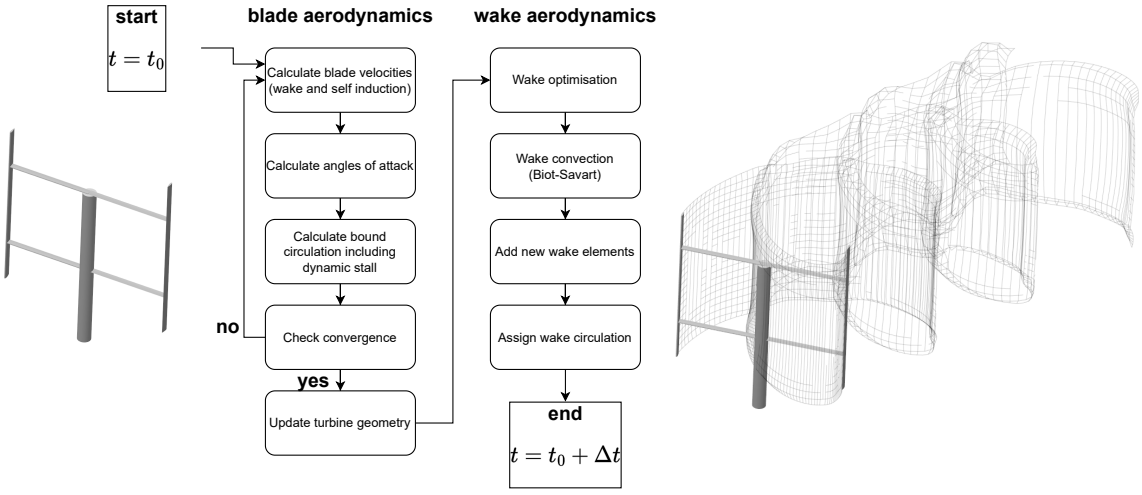

Figure 2.6: Flowchart for aerodynamic calculations for a single timestep as implemented in QBlade for a VAWT (adapted from Marten [215])

Secondly, a predictor-corrector (PC) method, which performs a reevaluation of the induced velocity based on the calculated position (in Eq. 2.45), has been incorporated as a second-order integration methodology:

$$\vec{t}_{x+1,PC} = \vec{x}_t + \left(2V_\infty + V_{\text{ind}}\left(\vec{x}_t\right) + V_{\text{ind}}\left(\vec{x}_{t+1,EF}\right)\right)\frac{\Delta t}{2}\,. \tag{2.46}$$

Finally, a second-order predictor-corrector method, proposed by Bhagwat and Leishman [32] has also been incorporated:

$$\vec{t}_{x+1,PC2B} = \vec{x}_t + \left(3\vec{x}_{t+1,PC} - \vec{x}_t - 3\vec{x}_{t-1} + \vec{x}_{t-2}\right)\frac{1}{4}\,. \tag{2.47}$$

While the second-order methodologies incorporate an increased degree of accuracy, they decrease computational efficiency since the velocity field evaluations (which in itself is expensive to perform) must be carried out two times for each single timestep. This effectively doubles the duration that is required to compute and evaluate the wake convection phase. Contrastingly, even though the first-order method facilitates a relatively lower computational expense, it imposes a restriction on the time step size allowed affecting the level of accuracy. This prompted the choice of second-order methods as mentioned above. The chronological sequence of the aerodynamic computations during a single time step is shown in Figure 2.6.

2.4.2. Wake Lattice and Connectivity

Within the structure of the wake lattice, shed and trailing vortices are inter-linked through common vortex nodes. Throughout the free wake convection phase, the development of the wake is assessed by advancing the vortex nodes' locations over time. Each vortex filament is affixed to two vortex nodes situated at its endpoints. Assuming an infinitely extended vortex lattice, every vortex node would connect with four vortex elements, implying that the total count of vortex nodes is approximately half that of the vortex filaments. As a result, the Biot-Savart equation must undergo approximately:

$$N_{nodes} * N_{vortices} \approx \frac{N_{vortices}^2}{2} , \tag{2.48}$$

evaluations for a fully-populated infinite wake lattice (in the case when it can be assumed that no vortex elements have been removed [215]). This architectural design contrasts markedly with a vortex particle discretisation strategy where no inter-connectivity is present, having a computational cost benefit characterised by a factor of 2 ($f_{opt} \approx 2$), attributed to the wake lattice's interconnected nature. To implement approaches that decrease the count of free vortices in the wake, a method has been introduced allowing for the removal of distinct vortices from the wake grid through the detachment of the vortex filament from its respective nodes. Throughout each step of the simulation, a verification process is undertaken to remove isolated vortex nodes not linked to any vortex filament. It should be noted that as the vortex removal from the wake lattice increases, the aforementioned advantage derived from the interconnections proportionately diminishes.

2.4.3. Vortex Core Desingularisation

In the context of Eq. 2.43, the Biot-Savart equation, a singularity is observed at the core where $\vec{r} = 0$ [215]. To maintain the simulation's numerical stability and more accurately represent the viscous core of both bound and free vortices, it is important to incorporate a suitable model for a viscous vortex core. Various models are available to represent the tangential velocity distribution surrounding the core, including but not limited to the Rankine, Lamb-Oseen, or Ramasay and Leishman models [147]. The QBlade utilises a cut-off radius, incorporated into the denominator of Eq. 2.43 as r_c^2, facilitating a gentle approach of the induced velocity to zero as it nears the core. This strategy is notable for its computational efficiency since it embeds the viscous core modelling directly into the induced velocity calculation.

Contrastingly, alternative vortex models necessitate the determination of a viscous parameter derived from the relative positions of the vortex in conjunction with the Biot-Savart equation, imposing a significant negative effect on the efficiency of the simulation. This is due to the repeated evaluation of the viscous parameter, occurring $N_{vortices}^2/2$ times every time step. Getting shed from the blade trailing edge, a vortex emerges with a predefined initial core size denoted as r_c (generally taking this value as 10% of the local chord is recommended [215]). This core size is updated at each time step based on:

$$r_c = r_0 + \sqrt{\frac{4a\delta_v \nu \Delta t}{1+\epsilon}} , \tag{2.49}$$

where a is kept constant at 1.25643, δ_v is the turbulent viscosity coefficient (which is dependent on the rotor size [287]), ν is the kinematic viscosity, and Δt represents the time step size. The strain rate of the vortex filament is calculated as:

$$\epsilon = \frac{\Delta l}{l} . \tag{2.50}$$

The desingularised Biot-Savart equation can then be written as:

$$V_{ind} = -\frac{1}{4\pi} \int \Gamma \frac{\vec{r} \times \partial \vec{l}}{r^3 + r_c^2} . \tag{2.51}$$

2.4.4. Unsteady Aerodynamics and Dynamic Stall

In order to incorporate the phenomenon of dynamic stall into the QBlade framework, the LLFVW method has been integrated with the ATEFlap [30] model which involves the assessment of unsteady aerodynamic characteristics associated with 2D airfoil dynamics [359]. This dynamic stall model

essentially includes two components. Firstly, it consists of an attached or potential flow model inspired by the work of Bergami and Gaunaa [30]. Secondly, it integrates the Beddoes-Leishman dynamic stall model, additionally including a tailored formulation for vortex lift, as shown by Hansen and Gaunaa [136]. Furthermore, this ATEFlap model includes the calculation of the unsteady lift effects generated by trailing edge flaps.

Polar Decomposition

The unsteady aerodynamics model is implemented on the principle of decomposition of the static, 2D lift (denoted as Cl_st) into distinct constituents: one being the fully attached (Cl_att) segment and the other being the fully separated (Cl_sep) segment. The different contributions from these segments are described through a separation function "f":

$$Cl_{st} = f * Cl_{att} + (1-f) * Cl_{sep} \ . \tag{2.52}$$

Within the QBlade's airfoil data pre-processor, a module has been integrated to facilitate this polar data decomposition. The user is required to input specific parameters including the angles of attack for both the positive and negative stall points, alongside the attached lift slope of the static polar. An example graph of static polar data decomposition is shown by Marten [215].

Attached Flow Contribution

Within this framework, the potential flow model takes into account two different aspects [215]: the non-circulatory or the added mass effects, and the circulatory lift which includes the wake memory effects, a phenomenon that notably plays a role before the stall starts. The term representing added mass models the force dynamics induced by both the fluid response to the airfoil movements and the movement of its trailing edge flap:

$$Cl^{nc} = \pi \frac{b_{hc}}{V_\infty} \dot{\alpha}^{str} + \frac{F_{dydxLE}}{\pi} \frac{b_{hc}}{V_\infty} \dot{\beta} \ . \tag{2.53}$$

The above equation includes several variables including the half-chord length of the airfoil (expressed as b_{hc}), the freestream velocity (V_∞), and the pitch rate because of torsional deformations (denoted as $\dot{\alpha}^{str}$). Furthermore, it includes the deflection shape integral (F_{dydxLE}), a geometric attribute dependent on the airfoil shape and the fluctuation rate of the flap (denoted as $\dot{\beta}$). In addition, a quasi-steady lift component is calculated, characterised as the steady lift generated by the airfoil under the influence of the current angle of attack (α_{qs}) and the current flap deflection (β_{qs}) computed from the relative movements between the airfoil and freestream velocity. This is performed without the effects of shed wake vortex activity:

$$Cl^{qs} = Cl^{att}(\alpha_{qs}, \beta_{qs}) \ . \tag{2.54}$$

Significantly, wake memory effects take into account the impact of span-wise or shed vortex in the wake on the quasi-steady angle of attack. The ATEFlap model, designed to be compatible with BEM codes, employs an effective angle of attack calculated using step responses which are described through exponential indicial response functions, to represent the downwash of the wake. In the context of QBlade formulation, this effective angle of attack is derived directly, given that the induction from the free vortex wake formation is inherently integrated into the assessment of on-blade velocities:

$$Cl^{circ} = Cl^{att}(\alpha eff) \ . \tag{2.55}$$

However, within the free vortex wake formulation utilised by QBlade, there exists an unknown quasi-steady angle of attack, an angle omitting wake vorticity effects. This angle, denoted as α_{qs}, is required for subsequent analyses pertaining to induced drag contributions. Consequently, it is

separately calculated through an isolated assessment of the wake vorticity effect on the angle of attack, hereby referred to as α_{shed}. The determination of α_{shed} involves evaluating the induction of the total shed vorticity in close proximity to the blade, extending up to a distance of eight chord lengths from the trailing edge. Given the dynamic stall model formulation is for a standalone 2D airfoil, it is imperative to confine the vortices involved in the α_{shed} evaluation to the immediate surroundings of the blade. This strategy effectively removes the substantial effects exerted by the total shed vorticity from all prior time steps on the global flow field. Subsequently, α_{shed} is utilised in computing the quasi-steady angle of attack from the effective angle of attack:

$$\alpha_{qs} = \alpha_{eff} - \alpha_{shed} \ . \tag{2.56}$$

The incorporation of this additional process stems from the structure of common unsteady aerodynamics models tailored for BEM codes. These traditionally employ indicial functions, a feature replaced by the free vortex wake model in the current adaptation, thereby necessitating this supplementary procedural step.

Separated Flow Contribution

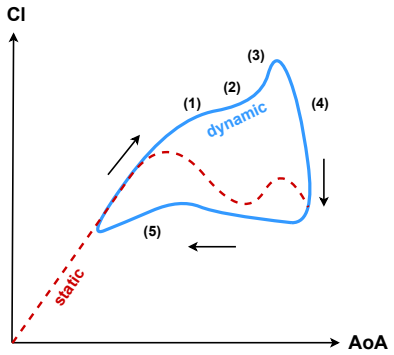

Figure 2.7: Dynamic stall hysteresis loop; adapted from Marten [215]; (1) Delay in Boundary Layer separation (2) Formation of Leading Edge vortex (3) Convection of vortex over airfoil (4) Leading Edge vortex leaves trailing edge (5) Delay in Boundary Layer reattachment

The incorporation of the Beddoes-Leishman dynamic stall model is performed as proposed by Bergami [30]. This models the dynamic stall phenomenon through three different contributions. The primary contribution in this model structure is the lagged potential lift, also known as the leading edge pressure temporal lag, which is calculated utilizing a low-pass filter with a pressure time lag constant denominated as τ_p:

$$\dot{Cl}^{lag} = -\frac{V_\infty}{b_{hc}}\frac{1}{\tau_p} Cl^{lag} + \frac{V_\infty}{b_{hc}}\frac{1}{\tau_p} Cl^{pot} \ . \tag{2.57}$$

Utilizing this lagged potential lift, denoted as Cl^{lag}, a dynamic separation function, f^{dyn}, is computed. This is achieved by passing the separation function f, acquired from the polar decomposition, through a low-pass filter characterised by a boundary layer lag constant τ_f:

$$\begin{aligned} f^{dyn} &= -\tfrac{V_\infty}{b_{hc}}\tfrac{1}{\tau_f} f^{dyn} + \tfrac{V_\infty}{b_{hc}}\tfrac{1}{\tau_f} f(\alpha^*) \ , \\ \alpha^* &= \tfrac{Cl^{lag}}{\frac{\partial Cl}{\partial \alpha}} + \alpha_0 \ . \end{aligned} \tag{2.58}$$

Subsequent to this, the dynamic circulatory lift, termed $Cl_{circ,dyn}$, is calculated from the multiplication of the dynamic separation function f_{dyn} with the fully attached Cl_{att} and the fully separated Cl_{sep} lift contributions, sourced from polar decomposition:

$$Cl^{circ,dyn} = Cl^{att}\left(\alpha_{eff},\beta_{eff}\right) f^{dyn} + Cl^{sep}\left(\alpha_{eff},\beta_{eff}\right)\left(1 - f^{dyn}\right) . \tag{2.59}$$

In the framework of ATEFlap designated for analyzing separated flow, a term to represent the vortex lift exists:

$$C_v = Cl^{\text{circ},dyn}\left(1 - \frac{\left(1+\sqrt{f^{dyn}}\right)^2}{4}\right) . \tag{2.60}$$

Nonetheless, in practical VAWT simulations experiencing sizable variations in the angle of attack, this term exhibited a tendency for substantial oscillations, leading to disproportionately large readings for the total dynamic lift coefficient. Consequently, to sustain system robustness, this facet was omitted from the total lift computation. The total lift calculation, encompassing both the attached and separated flow terms, while excluding the vortex lift, hereby becomes:

$$Cl^{dyn} = Cl^{circ,dyn} + Cl^{nc} . \tag{2.61}$$

The dynamic drag is calculated using three different contributions [215]. The steady drag at the effective angle of attack is written as:

$$Cd^{eff} = Cd\left(\alpha_{eff},\beta_{eff}\right) . \tag{2.62}$$

Utilizing the quasi-steady angle of attack, the drag induced from the shed wake vorticity is calculated as:

$$Cd_{ind} = Cl^{circ,dyn}\left(\alpha_{qs} - \alpha_{eff}\right) . \tag{2.63}$$

The induced drag term due to the flap deflection is calculated according to:

$$Cd^{\beta}_{ind} = Cl^{circ,dyn}\frac{\frac{\partial Cl}{\partial \beta}}{\frac{\partial Cl}{\partial \alpha}}\left(\beta^{st} - \beta^{eff}\right) f^{dyn} . \tag{2.64}$$

Finally, the drag variation because of the separation delay is calculated as:

$$Cd^{f}_{ind} = \left(Cd^{eff} - Cd\left(\alpha_0\right)\right)\left[\frac{\left(1-\sqrt{f^{dyn}}\right)^2}{4} - \frac{\left(1+\sqrt{f^{st}}\right)^2}{4}\right] . \tag{2.65}$$

The total drag can then be calculated as the summation of all these terms:

$$Cd = Cd^{eff} + Cd_{ind} + Cd^{\beta}_{ind} + Cd^{f}_{ind} . \tag{2.66}$$

A comprehensive elaboration on the formulation and validation of this unsteady aerodynamics model is accessible in work published by Wendler [359]. For validation, some graphs extracted from this document are shown by Marten [215], accurately illustrating the responsiveness and sensitivity of the dynamic stall hysteresis loop to variations in reduced frequency and amplitude.

2.4.5. Tower Influence

In QBlade, a tower shadow model has been implemented, as an extension of the work conducted by Bak [242]. The implementation of this model follows a superposition of an analytical solution describing the potential flow around a cylinder and a solution for the wake in the downwind direction of a cylinder, based on the tower drag coefficient. This results in a velocity deficit behind the tower, as shown in Figure 2.8, where rotor diameter and tower diameter are 1.5m and 0.12m, respectively, and the tip speed ratio is 4. A noteworthy characteristic of this model is that it solely affects the velocities in the direction perpendicular to the axis of the tower, while the z-component — aligned parallel to the tower's longitudinal axis — remains unchanged. The operative scope of the tower shadow model is distinctly defined; it is utilised only when the z-component of the location is either equal to or below the given tower height. A practical application of the tower model with validation with data derived from CFD simulations and experiments, one can refer to work by Klein [168].

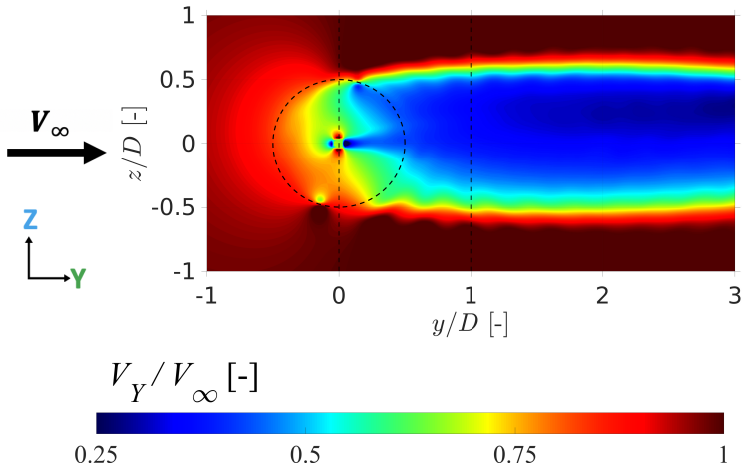

Figure 2.8: Tower shadow model illustration; tip speed ratio is 4 and streamwise velocity contour is visualised

Some other models have also been implemented in QBlade such as the Stall Delay (Himmelskamp) effect [314], Turbulent wind input [215] and Ground effect [187].

2.4.6. Wake Truncation

If N is the number of free vortex wake elements, then computational cost scales as N^2 in the LLFVW framework [215]. To control the indefinite increase of the number N, a necessary step involves the termination of the wake at a determined downstream location, as depicted in Figure 2.9. This removes all wake vortex elements once they attain a specified maturity or age. In the current setup, vortex age is expressed in terms relative to the number of rotor revolutions that occurred since the shedding of the vortex elements from the rotor surfaces. The tip speed ratio (TSR) affects the state of the wind turbine wake and dictates the minimal vortex age requisite for an accurate depiction of the wake induction within the swept volume of the VAWT rotor blades. A detailed illustration of the effects of wake truncation on power and thrust coefficients for a standard 3-bladed wind turbine is shown by Marten [215]. It was shown that the error margins, attributable to wake truncation, increased in correspondence with an increase in TSR. Additionally, the impact of wake truncation was more significant on the power coefficient than on the thrust coefficient.

Therefore, the selection of an appropriate wake truncation parameter is influenced by the operational TSR of the wind turbine. For example, it is recommended that at design TSR, a wake length of 12 rotor revolutions should be maintained since it ensures the error is within a marginal bracket of 1% for the power coefficient.

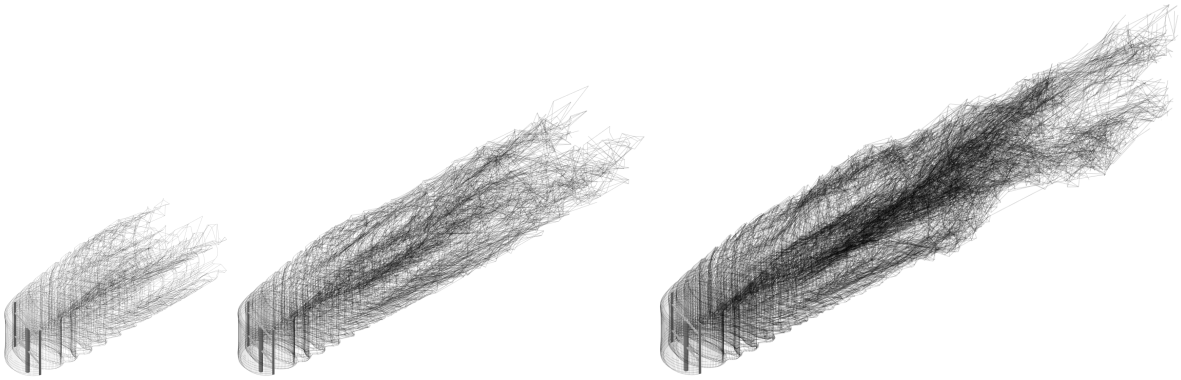

(a) 6 revolutions (b) 12 revolutions (c) 18 revolutions

Figure 2.9: Three different wake truncation lengths for a 2-bladed VAWT at TSR = 4, depicting downstream vortex lifting lines

2.4.7. Wake Coarsening

The current LLFVW framework also includes a wake coarsening method for decreasing computational expenses. This approach decreases the number of free wake elements through a systematic reduction of the spatial resolution of the wake lattice in the streamwise direction across four designated zones. This reduction process is denoted by four distinct lengths, demarcated as vortex ages (l_1, l_2, l_3, and l_4), accompanied by three distinct integer coarsening factors (f_1, f_2, and f_3) [215].

Upon attaining the vortex age of l_1, the wake lattice undergoes a modification in its chordwise resolution, decreased by the factor f_1. This involves the fusion of f_1 attached trailing vortex elements to form a single new trailing vortex. In the course of this combination, a mean vorticity is derived from all merged vortices based on the respective lengths of the initial vortex filaments of the contributing vortices. While for the shed vorticity, all vortex elements barring the f_1^{th} shed vortices are eliminated from the lattice structure. To conserve the total shed vorticity within the wake, the vorticity belonging to the eliminated vortex elements is distributed amongst the adjacent shed vortex elements, weighted according to their relative distances.

This method is repeated as the vortex progresses in age, utilizing the factors f_2 and f_3 when the vortex ages reach l_2 and l_3 respectively. Following the realisation of the vortex age l_4, the wake is truncated. Consequently, the total factor, denoted as f_{opt} describes the extent to which the computational expenses can be reduced, and is computed as follows:

$$f_{opt} = \left(\frac{l_1 + l_2 + l_3 + l_4}{l_1 + \frac{l_2}{f_1} + \frac{l_3}{f_1 + f_2} + \frac{l_4}{f_1 + f_2 + f_3}} \right)^2 . \tag{2.67}$$

Figure 2.9 illustrates a practical example of the reduction in wake resolution implemented for a 2-bladed VAWT at TSR of 4, across different wake zones with a time step size of 3 degrees. Specifically, Figure 2.9 (b) depicts the total length of the wake of 12 revolutions, where the near wake constitutes 2 revolutions. Subsequently, the first, second and third zones consist of 2, 6 and 2 revolutions, respectively. The reduction factor between every individual wake zone is kept at 2, resulting in a total reduction factor f_{opt} of 6.16.

Other strategies such as adaptive wake reduction techniques are also implemented to reduce the number of free wake vortex elements, where particular vortices are eliminated with low circulation. The reasoning behind this originates from the fact that these vortices have negligible impact on the total induced VAWT wake velocity field [215]. Furthermore, parallelisation techniques are implemented in the QBlade framework for faster computations. The parallelisation is implemented

within the OpenCL framework [316].

2.5. Double Multiple Streamtube (DMS) method

This method is based on the model developed by Paraschivoiu [255] in 1988 and is derived from a combination of the actuator disk and the blade element theory [216, 256], both of which are extensively used for a wind turbine or propeller low-fidelity aerodynamic analysis. The momentum conservation (from actuator disk theory) and forces on the blades (from blade element theory) are balanced until the system has reached convergence. In QBlade, an improved version of the model is used, called the Double Multiple Streamtubes Approach With Variable Interference Factors, originally proposed by Paraschivoiu [256].

The operation of a VAWT forms a bigger streamtube flowing through it, which is split into several smaller streamtubes, both in the cross-streamwise (lateral) and axial directions. VAWT blades, during its 360° circular path, pass through those streamtubes and extract energy from the flow, similar to the working of a horizontal axis wind turbine. Therefore, standard actuator disk theory can be applied to every small streamtubes mentioned above. In a single rotation, the blades pass through the streamtubes twice. To accommodate this, a single streamtube is divided into two parts: upstream and downstream halves, each having its own actuator disk. They act as two actuator disks working in tandem and mutually affect the fluid flowing through each of them [256]. The smaller streamtubes in the axial direction represents different blade sections at respective height, where they interact with the fluid flow. Each blade section is a 2D airfoil and is considered independent from other sections. The sections produce lift and drag forces based on the local angle of attack (α) which is calculated from the velocities experienced by each section. The resultant total forces on the blade are found by integrating over the whole blade length.

The interference factor indicates the amount of energy extracted by a single actuator disk and is calculated as a ratio of velocities downstream and upstream of the actuator disk. The two tandem actuator disks in the DMS method, therefore, have an upwind and a downwind interference factor. The iterative procedure is followed for the calculation of the interference factors at every blade height position for all upwind azimuthal angles (every small streamtube) until the user-defined convergence criteria are achieved. The convergence can be achieved separately for every azimuthal angle (when the interference factor is kept variable) or for the whole upwind rotor half (when the interference factor is kept constant).

Glauert's correction has been implemented with the most recent improvements based on experimental data [59], along with Lanchester-Prandtl model [58] for finite aspect ratio blades. Several dynamic stall models have been used (Berg, Strickland, and Paraschivoiu [256]) in addition to streamtube expansion models as mentioned by Paraschivoiu [256], to increase the accuracy of the aerodynamic calculations. The validation and prediction capabilities of the code used in this study have been reported by Balduzzi [22].

3

Vertical axis wind turbine

Summary

The chapter gives a detailed introduction to the fundamentals of vertical axis wind turbines (VAWT). It starts with a brief history of VAWT, its development in the last 6-7 decades and its current relevance in the 21st century. The next section describes the underlying aerodynamics of a VAWT and how airfoil-shaped blades help achieve optimal power generation. Following this, the current state-of-the-art is presented which highlights the latest work in VAWT aerodynamic design. The next section gives an introduction to the basics of aeroacoustics, followed by a section on the latest work in understanding noise generation from VAWT and the effect of geometrical and operational parameters on the same. The chapter ends by outlining the overall goal of the current work with specific objectives about VAWT and urban wind resources.

3.1. Historical perspective

Vertical axis wind turbines have two fundamental designs - Savonius and Darrieus [230]. Owing to the simplicity of drag-based Savonius design, its origins date back to the 12th century when it was used for grinding mills, lifting water, or any such high-torque operation. Darrieus, on the other hand, is a much newer design first proposed in 1925 by a French engineer having the same name. Both the curved and straight-bladed designs were presented in his 1931 US patent drawings [212] as shown in Figure 3.1. In due course, the Darrieus design evolved over several decades, a detailed chronological sequence of which is shown by Tjiu [340].

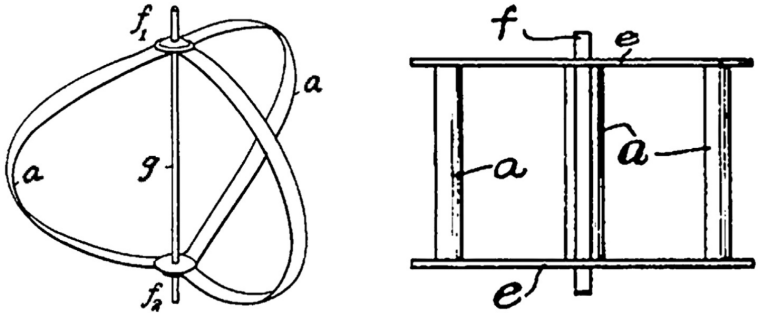

Figure 3.1: Darrieus 1931 US patent drawings of vertical axis wind turbine [212]

Both for curved and straight-bladed designs, initially large-scale rotors were experimented with in the second half of the 20th century. In case of the curved blade, the Guy-wired phi (ϕ) rotor was experimented with from 1968-early 1990s. The wind turbines' capacity ranged from 30-500 kW, even going towards 2.5-4 MW (largest VAWT in the world by NRC Canada) from 1988-93. Following the lessons learnt from these designs and some failures happening in 1978-81, the design evolved towards Fixed on tower/Cantilevered phi (ϕ) rotor from 2000s-present. In case of the straight blade, the variable-geometry (Musgrove) and the variable-pitch (Giromill) rotors were experimented with during 1970s-80s. Due to high cost of operation and less competitive nature in the open market as compared to HAWTs, the design evolved towards simple straight-blade design after 1988 and fixed-pitch design (H-rotor) after 2000s, partly due to efforts by Musgrove [245] [246].

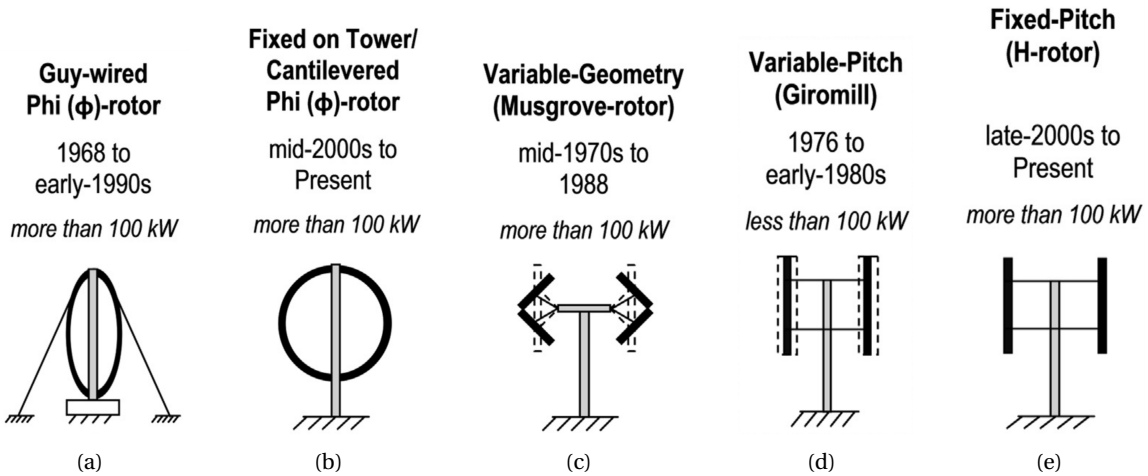

Figure 3.2: Common types of VAWT design historically [340]

The current study focusses on small-scale VAWTs, the development of which accelerated only after 2000s, specifically 2010s, due to increasing focus on sustainability in urban areas. The small scale

allowed the researchers to easily experiment with different design parameters at a relatively low cost, and variations such as articulating, tilted and helical H-rotor emerged. Since the knowledge of high-Re rotor aerodynamics (common in HAWTs) cannot be directly applied to such designs, a separate field for low-Re aerodynamic design and optimisation became more common amongst researchers working on VAWTs (also aided partly by advances in low-Re aircraft propellers). Currently, research on VAWTs focusses on urban rooftop installations (either grid-connected or standalone) [172], VAWT wind farms for semi-urban areas [87, 90] and floating offshore wind turbines [92].

3.2. Aerodynamic performance

Before discussing about VAWT, it is imperative to briefly introduce the functioning of HAWT and aircraft propellers, since their technology has matured much more over the past few decades as compared to VAWT which is still in a developing phase. Besides, the way torque and thrust are produced in HAWT and VAWT are significantly different and a comparison between them will help in a better understanding of each.

3.2.1. Horizontal axis wind turbine vs Propeller

Both the HAWT and propeller consist of airfoil blades with varying chord sizes and twist angles, rotating about a horizontal axis parallel to the wind direction. A wind turbine converts the kinetic energy of air to mechanical torque (and subsequently, electrical power) while a propeller does the exact opposite by converting the input mechanical torque to the kinetic energy of air (translated to aerodynamic thrust). Both use airfoil-shaped blades to achieve this task, although in a fairly opposite manner. Figure 3.3 compares velocities experienced by both wind turbine and propeller blades, and the resulting AoA. *Wind turbine*: incoming airflow generates lift and drag forces on the blade, which gives rise to thrust (in the streamwise direction) and torque (in the direction of rotation). *Propeller*: torque is provided to the blades which then rotates and generates lift and drag forces on the blade, and gives rise to thrust (in the streamwise direction).

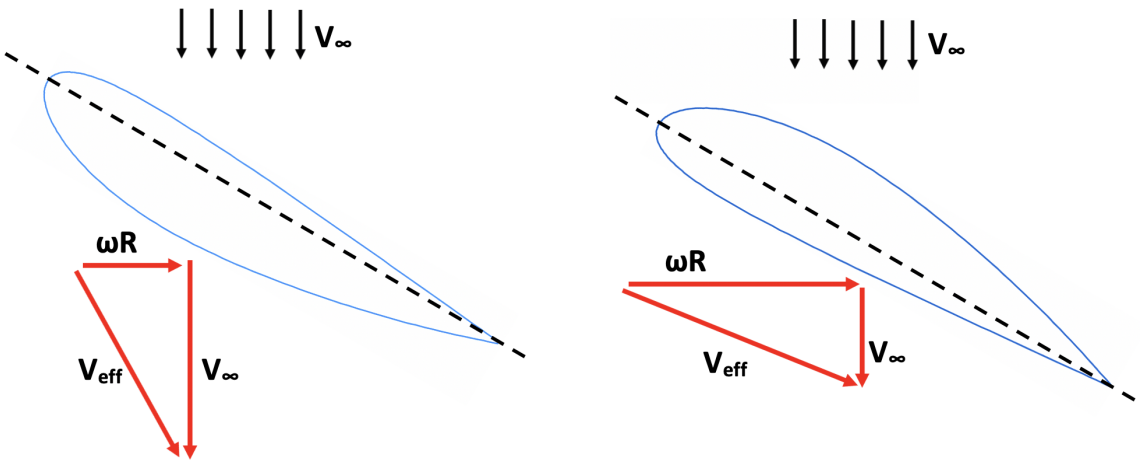

(a) HAWT (b) Propeller

Figure 3.3: Velocities experienced by blades of horizontal axis wind turbine and propeller; in each case, length of ωR and V_∞ arrows represent their relative values

For the same freestream velocity, the rotational velocity of a propeller is more than a wind turbine. This can be concluded from the figure 3.3 which shows the opposite direction of the incoming resultant velocity (V_{eff}) and AoA with respect to the chord line. Rotating a wind turbine at a higher tip speed ratio (TSR = $\omega r / V_\infty$) eventually converts it to a propeller mode (although an inefficient

propeller due to negative camber).

3.2.2. Vertical axis wind turbine

Darrieus-type vertical axis wind turbine consists of airfoil-shaped blades rotating about a vertical axis perpendicular to the wind direction, as opposed to a horizontal axis in the case of HAWT. Torque and thrust production from a VAWT is highly dependent on the aerodynamic characteristics of such blades, which in turn is dependent on parameters such as airfoil, aspect ratio, pitch angle, blade design, etc. Aerodynamic, aeroacoustic and structural requirements put heavy constraints on VAWT design and therefore, it is important to understand its basic aerodynamics before investigating further the detailed flow physics.

Figure 3.4 (a) depicts the position of VAWT blades in a single rotation, in addition to the azimuth reference system and velocities experienced by the blade. 90° azimuth is the most upstream position and 270° azimuth is the most downstream position; while 0°-180° azimuth is called upwind and 180°-360° (0°) azimuth is called downwind half of the rotation. The Y-axis and Z-axis are the streamwise and cross-streamwise directions, while the X-axis is the axis of rotation. This nomenclature is kept constant throughout this study. At every TSR, blades experience varying angle of attack (AoA) and effective velocity (V_{eff}) as shown in figure 3.4 (b) and (c), respectively. The values shown are geometric values and are different from the real values induced at the blades due to the blockage effect [261]. The resulting lift and drag forces on rotating blades produce a typical power and thrust curve for VAWT shown in figure 3.5 (a) and (b), respectively.

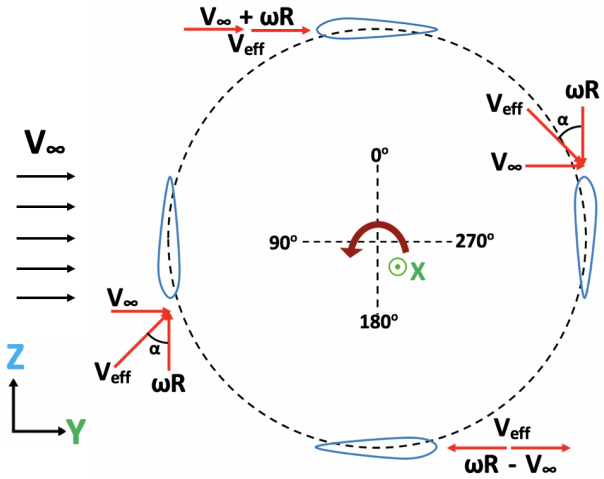

(a) Position of Darrieus VAWT blades over a single rotation

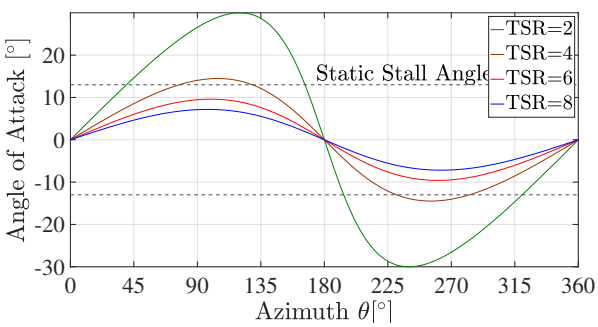

(b) Geometric angle of attack variation for V_∞=9 m/sec and D=1.03m

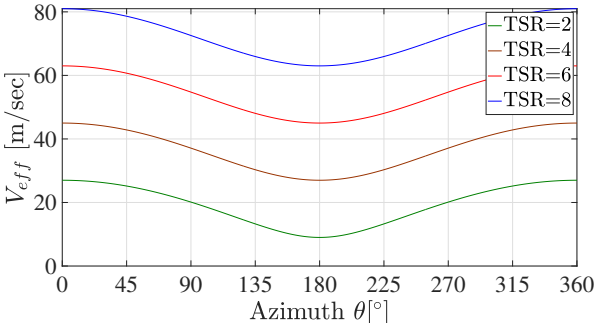

(c) Effective velocity (V_{eff}) perceived by the blade (without induction) for V_∞=9 m/sec and D=1.03m

Figure 3.4: Darrieus VAWT aerodynamics

At low TSRs, AoA variation is high and it crosses static stall angle for a major part of the rotation. The consistent variation in AoA gives rise to dynamic stall in both the upwind and downwind part of the rotation. In such conditions, flow over an airfoil is characterised by leading-edge separation, formation of 'dynamic stall vortex', extra lift generation due to the vortex and a state of full flow separation before becoming attached again [219, 261]. This phenomenon can result in a significantly different lift and drag behaviour relative to a static aerofoil, sometimes exceeding the static values by 100% [187]. The 'Dynamic stall' regime is depicted in figure 3.5 (a) and (b) which shows its adverse effect on VAWT power and thrust values. A further decrease in TSR will push the VAWT into a 'Deep stall' regime where power production is almost negligible.

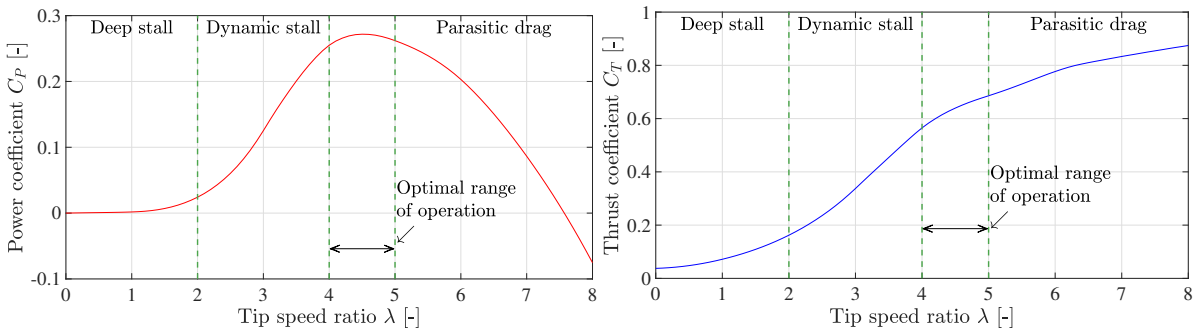

(a) Power coefficient (b) Thrust coefficient

Figure 3.5: Darrieus VAWT performance obtained using the DMS method

As TSR increases, the extent of dynamic stall decreases, and power and thrust production increase due to an increase in lift-to-drag ratio. Further increase in TSR gives rise to high parasitic drag on airfoil which reduces the amount of power generated (in the 'Parasitic drag' regime). Another phenomenon significant at high TSRs is blade-vortex interaction (BVI). Blades in the upwind half of rotation shed vortices, which convect downstream, interact with blades in the downwind half and distort the flow over the airfoil. This increases unsteady loading on the blade surface and is detrimental to the performance of such wind turbines. This effect is made worse by the presence of tip vortices from upstream blades which convect towards the mid-span of downstream blades [292, 312] and is especially prominent in smaller aspect ratio blades. Thrust keeps increasing with TSR but the rate of increase is less in the 'Parasitic drag' regime, due to a decline in performance of the downstream blades. This also shows that VAWT at very high TSR will behave like an aircraft propeller, producing thrust and consuming power (negative C_P values).

3.3. State-of-the-art: Aerodynamics

Darrieus VAWT has a huge 3D design space comprising various geometrical parameters such as number of blades, aspect ratio, airfoil shape, blade design, etc. and operational parameters such as tip speed ratio, turbulent inflow, skewed inflow, etc. Given such flexibility in design, it is important to understand the effect of each parameter on the torque and thrust production of VAWT, before proceeding with a detailed flow analysis and designing an optimum wind turbine. In the next few pages, the latest developments about each parameter have been discussed. Most of the work is focussed on increasing the power production of the Darrieus turbine by increasing the lift on blades and decreasing the drag forces [156, 323, 358], and to develop low order tools to accurately predict VAWT performance. The discussion starts with experimental benchmarks available in the literature, which are important for validating numerical simulations. Then it proceeds to 2D design parameters such as airfoil shape and preset pitch, and then to 3D design parameters such as aspect ratio, blade design, solidity, etc. The section also presents results obtained using the low-fidelity Double

Multiple Streamtube (DMS) method to study these design parameters and a detailed study on the same has been already published by Shubham et al. [305].

What are the 3D effects?

- Non-uniform blade loading
- Trailing vortices and especially, tip vortices

3.3.1. Experimental benchmark studies

Kaushik [161] provides a review of experiments conducted on various designs of Darrieus VAWT. Blackwell [40] presents detailed wind tunnel performance data for the Darrieus wind turbine with NACA 0012 blades for different wind velocities, rotational speed, solidities and Reynolds number. Battisti [29] examines both H-shaped and troposkien Darrieus VAWT using experimental methods, compares their aerodynamic performance and provides a benchmark for validation of computational tools. Previously, Battisti [28] performed wind tunnel measurements on an H-rotor and examines the effect of blockage and full 3D flow features including the tip vortices effect. Howell [148] tested a small-scale H-rotor for different wind velocities, TSR, solidities (2-bladed and 3-bladed rotor) and rotor blade surface finish while making comparisons with 2D and 3D CFD results. Li [194] investigated the effects of ice and snow attached to the rotor blades, on Darrieus rotor power performance. This assumes special significance in the northern UK and north-western Europe, where there is significant snowfall in cold climates. Fiedler [123] investigated a high-solidity 3-bladed Darrieus H-rotor to study the effects of blade pitch, both positive and negative values, and blade mount-point offset on VAWT performance. LeBlanc [180, 182] presented an experimental benchmark to validate studies on using active variable pitch on individual rotor blades.

3.3.2. Airfoil profile

Flow over airfoil-shaped blades produces lift and drag forces which are responsible for VAWT torque and thrust output. Since the AoA varies over both positive and negative values, symmetrical airfoils are commonly used such as the NACA 00XX series, as shown in figure 3.6 (a). Mohamed [234] simulated 20 different airfoil shapes using URANS simulation. In the case of the symmetrical NACA series, a maximum C_P of 0.2964 was obtained by NACA 0018. Lower thickness airfoil produces more power at higher TSR values while higher thickness airfoil produces more power at lower TSR values. The same conclusion was obtained by Roh [280] and Healy [142]. This means the higher thickness airfoil is better for self-starting a VAWT since it concerns low TSR values. On the other hand, non-symmetrical airfoils (such as shown in figure 3.6 (b)) were also simulated by Mohamed [234] and it was shown that symmetrical airfoils both performed better and have higher operating range than the former. The main reason is symmetrical airfoils delay stall, thus reducing the adverse effects on blade loads. The highest C_P value amongst all 20 airfoils was obtained for the S-1046 airfoil.

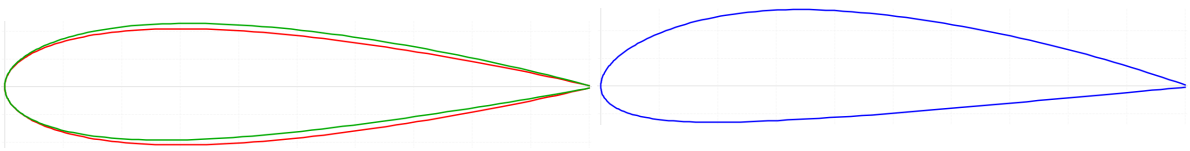

(a) NACA 0021 (red) and virtually cambered airfoil (green) (b) Highly cambered NACA 4420 airfoil

Figure 3.6: Some examples of airfoil used for VAWT blades

Rainbird [270] showed the importance of the virtual camber effect [232] for low-to-mid fidelity aerodynamic models, which is due to the curved path taken by the airfoil blade. The bigger the

chord-to-radius ratio, the stronger the effect [37]. This is especially significant since the choice of airfoil polars (symmetrical vs cambered airfoil) plays a significant role in the final output. An example of a virtually cambered airfoil for NACA 0021 at TSR = 4 and $c/R = 0.1$ is shown in figure 3.6 (a). A number of authors use a zig-zag trip, both on the suction and pressure side of the airfoil blade, to force boundary-layer transition at a specific chord location [261]. This has the potential to reduce flow separation which in turn increases power performance and reduces laminar boundary layer noise [259].

3.3.3. Blade pitch

A possible solution to avoid dynamic stall is to constantly vary blade pitch so as to achieve the optimal angle of attack (and optimal loading) at every azimuth. Initial efforts were made by Mauri [218] to design an active control pitch system for use in both external conditions and wind tunnels. A few researchers have focussed on passive pitching control [164, 165], although they are not as efficient as their active counterparts. Recently, LeBlanc [180, 182] tested an active pitching system on an H-rotor Darrieus VAWT and validated the results using the 2D Actuator Cylinder model [204]. The method of active pitching can also be used to control the direction of rotor wake for wind farm control and structural fatigue reasons [179].

Active blade pitch control is challenging to implement due to the extra mechanical and electronic systems required. To avoid such complexities, a number of researchers opt for fixed preset blade pitch, as described in figure 3.7. With reference to figure 3.4 (b), a negative pitch angle (also called toe-out configuration) will shift the whole curve down by the same amount. This will decrease AoA values in the upwind half, reduce flow separation and dynamic stall, and increase torque production. In the case of the downwind half, AoA values increase, dynamic stall becomes more severe and torque production decreases. The opposite story happens for the positive pitch angle (toe-in configuration). Armstrong [11], using a 3-bladed H-rotor with NACA 0015 profile, showed that C_P value increased by 15% if the preset pitch was changed from 0° to -6°. A similar increase in C_P values was obtained by Klimas [169] and Coton [83] for a preset pitch of -2°. In general, it has been found that C_P increases up to a value of negative pitch angle (toe-out angle) and then decreases, the initial increase being favoured by an increase in performance of the upwind half which already has a favourable performance than the downwind half, at 0° preset pitch.

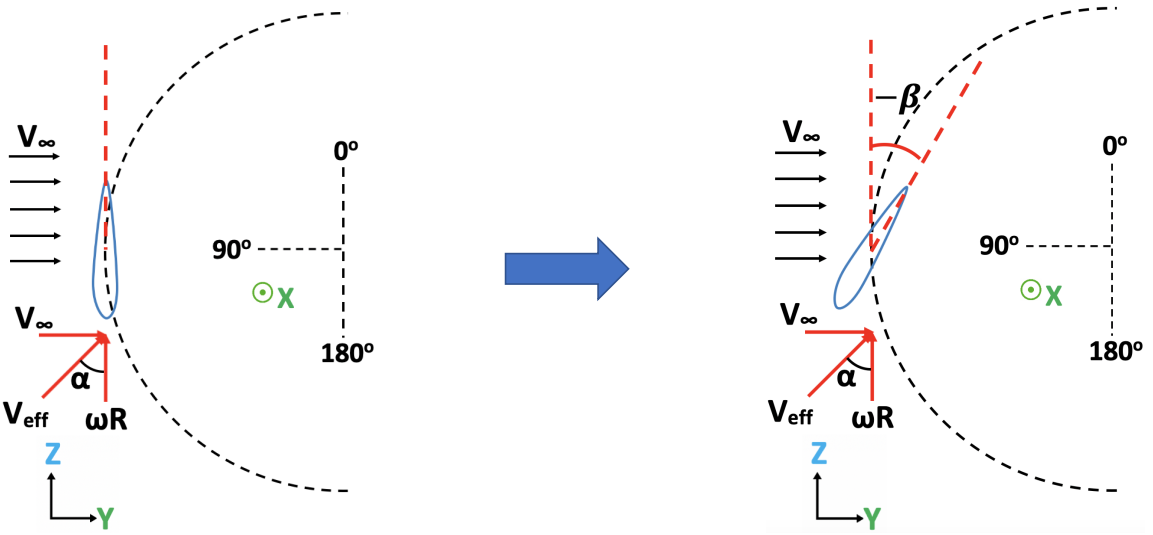

Figure 3.7: Preset blade pitch on a VAWT blade. The configuration shown here is that of a negative pitch (toe-out) with angle β.

Figure 3.8 shows the advantage of having a toe-out (negative pitch angle) configuration obtained

using the low-fidelity DMS method. There is a negligible difference in power at low TSRs, while power increases at the optimal TSR and higher TSRs. C_P vs TSR gradient for the toe-out configuration is more than the toe-in configuration. The higher the blade loading, the higher the increase in induction factor for the overall rotor as TSR increases. At high TSRs, the rate of decrease in induced velocity and tangential loading for the blades is, therefore, higher.

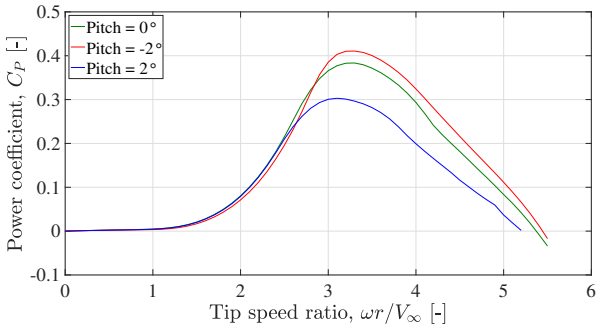

Figure 3.8: Power coefficient variation with TSR and three different pitch angles obtained using the DMS method

3.3.4. Rotor solidity

Solidity is a measure of the blockage provided by VAWT blades to the incoming flow and is defined as $\sigma = Bc/R$, where B is the number of blades, c is chord size and R is rotor radius. Therefore, the higher the number of blades or chord size, the higher the blockage to the flow. This can be understood from figure 3.9, where variation in the number of blades has been shown (a 10-bladed rotor is shown only for comparison and is not a practical design due to extremely high BVI). This has an impact on the velocities and AoA induced at the blades, and in turn the blade loading. Mohamed [234] simulated S-1046 airfoil for solidities ranging from 0.1-0.25. Larger C_P was produced by a higher solidity turbine at lower TSR values and a lower solidity turbine at higher TSR values, which is also shown by Howell [148] and the results obtained using the DMS method for both the variation in number of blades and chord length, in Figure 3.10. When blockage to the flow increases, freestream velocity induced in the upwind half of rotation reduces which decreases AoA values. This decreases dynamic stall severity for lower TSR and increases torque production. Besides that, when solidity increases, a stronger wake is produced which leads to more BVI in the downwind half of rotation. BVI is especially significant at higher TSR values, which leads to lower torque production. Figure 3.10 portrays a similar story by obtaining the results using the low-fidelity DMS method. Results are shown for variation in both the number of blades and chord lengths.

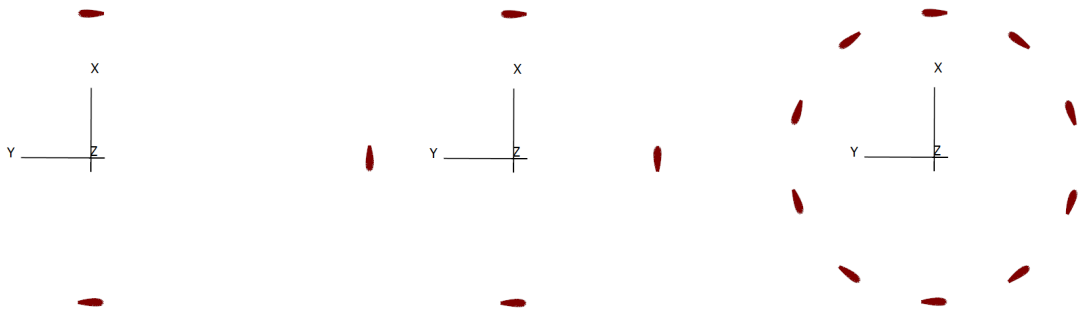

(a) 2-bladed (b) 4-bladed (c) 10-bladed

Figure 3.9: Variation in number of blades for VAWT, showing the extent of blockage to the flow

An individual blade will be the most efficient in a 1-bladed VAWT since it has minimum BVI.

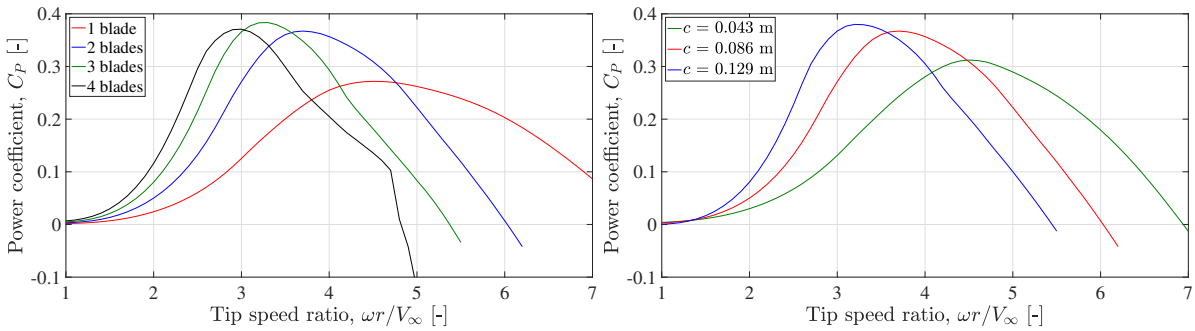

(a) Number of blades (b) Chord length

Figure 3.10: Power coefficient variation with TSR and different number of blades and chord lengths obtained using the DMS method

Unfortunately, this is not good for performance at low TSR values which has a direct impact on the self-starting capability. Good work on self-starting capability is done by Baker [18], Dominy [102] and Hill [145]. To improve self-starting, rotor solidity needs to be high, which will compromise the performance at higher TSR where the wind turbine may operate for the majority of its service life. On the contrary, lower rotor solidity provides a higher operating range for any Darrieus VAWT which makes it more suitable for urban environments where wind velocities vary significantly. The power curve is smoother around the optimum TSR point (highest C_P), so easier for the control system to operate around that point [166]. The design of Darrieus VAWT is therefore a compromise between self-starting characteristics (low TSR) and a higher operating range (mid to high TSR). Several manufacturers these days focus on the latter since they have found ways to self-start the turbine by providing initial input power.

3.3.5. Aspect ratio

Aspect ratio (AR) can be categorised in two ways: rotor aspect ratio and blade aspect ratio. They seem to be used interchangeably in the literature, but both of them are defined differently. The rotor aspect ratio is the ratio of rotor height to rotor diameter whereas the blade aspect ratio is the ratio of blade span to chord size. The rotor aspect ratio of most VAWTs these days ranges from 0.6 to 2, whereas the blade aspect ratio can range anywhere from 4 to 25.

Ghonim [125] showed that an optimum value of rotor AR is required to get the maximum C_P value; for V_∞ = 10 m/sec the value of AR is 1.3 for a 3-bladed Darrieus H-rotor. The reason is that a higher AR rotor will be a more efficient power producer since it reduces the adverse effect of tip vortices on blade loading. Although, higher AR requires more supporting struts to support the rotor structurally as can be seen for the WindSpire turbine [283]. This increases the parasitic drag force on the struts and also the turbulence content in the rotor wake. Due to increased interaction between the downstream blades and higher turbulent wake, there is a potential decrease in torque. An optimum value of AR is also required for a good self-starting capability. This is shown by the opposite conclusions of Ghonim [125] who proposed to decrease rotor AR and Du [105] who proposed to increase rotor AR, for increasing the self-starting capability of the rotor at lower wind velocities. Brusca [56] highlighted similar results to the former by showing that a lower AR rotor produces higher power coefficients due to a higher blade Reynolds number (by increasing the rotor diameter). This can help in self-starting the rotor and also provide higher structural stability.

The above discussion shows that there are three ways to change rotor AR, which will be fundamentally different from the blade aerodynamics point of view. A fairly simple way is to change blade height while keeping rotor diameter the same (this will also change blade AR). In this case, the difference in performance will come due to a change in the swept area of the rotor and tip vortices effect

on individual blade loading. The second method is to keep the blade height the same and change the rotor diameter (this will keep the blade AR the same). The third method is to change both blade height and rotor diameter by keeping the same swept area. This will be a fairer comparison to study the effect of changes in AR. In the second and third methods, two differences occur: changes in chord Reynolds number (Re_c) and blade-vortex interaction (due to change in solidity), with an additional change in the swept area for the former. The final difference in VAWT performance will be a combination of all these factors.

As an example of the third method of changing AR, Figure 3.11 shows the effect of having different blade heights and also varying the rotor diameter (to keep the same swept area), obtained using the low-fidelity DMS method. At lower TSRs, VAWT with the longest blade (and smallest diameter) produces the maximum C_P, while at higher TSRs, the trend reverses and VAWT with the shortest blade (and largest diameter) produces the maximum C_P. This behaviour is similar to when rotor solidity is varied since a smaller diameter has higher solidity and vice-versa.

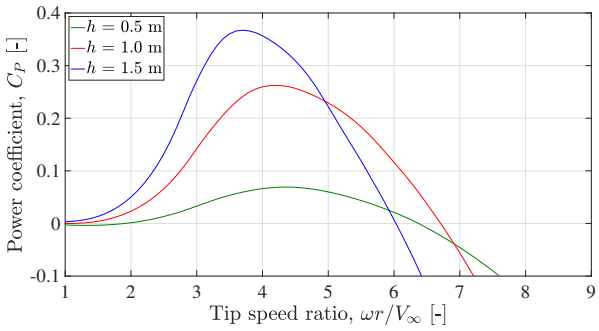

Figure 3.11: Power coefficient variation with TSR and three different blade heights causing a change in blade and rotor aspect ratio obtained using the DMS method

3.3.6. Blade shape

In the first patent by Darrieus in 1931[212], he proposed two blade shapes - straight-bladed and curved-bladed or troposkien shape as shown previously in figure 3.1. In the next few decades, numerous blade designs have been materialised, each providing a host of benefits over the original design. Figure 3.12 shows a comparison of three common blade shapes, all having the same swept area of 1.54 m^2. Straight-bladed VAWT (H-rotor) is the most common amongst them, as they are easier and less costly to manufacture and maintain. Helical-bladed design, as in the case of Quiet Revolution [268], provides multiple benefits such as slightly higher effective chord, smoother blade loads or driving torque in a single rotation which can help to reduce mechanical vibrations and aerodynamic noise produced. It also improves aesthetics which is important for public acceptance. A similar design was experimented with by Bussel [344] in 2004, named TURBY, which is designed specifically for the built environment.

As powerful computational tools become available and manufacturing technology improves (since helical blades are more expensive to manufacture than straight blades [172]), several manufacturers are starting to opt for the helical design. Another commonly experimented blade design is the 3D troposkien shape [29] which gives a higher C_P than a straight-bladed rotor at higher TSR values. This is shown in Figure 3.13 in which the results are obtained for straight and troposkein shapes by keeping the same swept area and using the low-fidelity DMS method. Troposkien shape helps mitigate the adverse effects of tip vortices and therefore performs better at higher TSRs. However, blades having straight shapes tend to have a better self-starting capability at low TSRs and higher maximum C_P at optimal TSR.

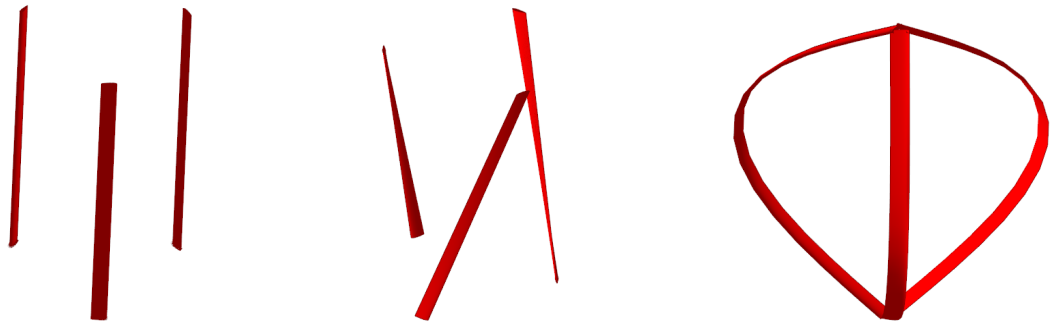

(a) Straight-bladed (b) Helical-bladed (c) Troposkien shape

Figure 3.12: Some examples of VAWT blade designs, all having the same swept area of 1.54 m^2

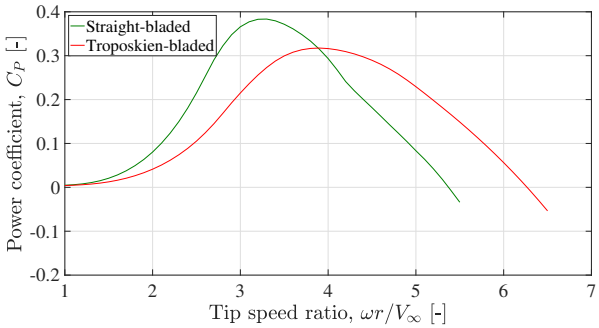

Figure 3.13: Power coefficient variation with TSR and two different blade shapes obtained using the DMS method

3.3.7. External structures

A few authors experimented with additional structures placed around the Darrieus VAWT to increase its power performance. The concept is similar to ducted HAWT or propeller in which the rotor is shrouded by a diffuser to direct the incoming flow direction. Kim [163] placed a flat plate deflector in front of a pair of counter-rotating Darrieus VAWTs, which increased the flow velocity on each rotor by 10-30% more than the freestream velocity. Longer and narrower deflectors produced higher C_P values (2-3 times) than shorter and wider deflectors. In addition, the closer the rotors were to the deflector (in the streamwise direction), the higher the values of C_P were. A major drawback of using such structures is that it makes the turbine more directional, which can be disadvantageous in an urban setting.

3.4. VAWT noise

Since the current study focuses on VAWTs in urban environments, attenuation of noise generated is a key factor for public acceptance, adhering to local city noise regulations and fast expansion of VAWT markets [19, 167]. A majority of the discussion in the upcoming chapters pertains to aerodynamic noise generated by different VAWT design configurations and in different operational conditions and therefore, it is essential to discuss the fundamentals of noise generation. Noise can be measured by sampling the pressure perturbations in the medium for which the fundamental unit used is Pascal (Pa). For humans, 2×10^{-5} Pa is the threshold of hearing and 200 Pa is the threshold of pain. The most common physical quantity to measure noise is Sound Pressure Level (SPL) which is defined as

$$\text{SPL} = 10 \cdot log \frac{P^2}{P_{\text{ref}}^2}, \tag{3.1}$$

where, P is root mean square of pressure perturbations measured, P_{ref} is the reference pressure level and is usually defined as 2×10^{-5} Pa (threshold of hearing). The unit is decibel (dB).Generally, a sampled pressure signal consists of various frequencies and it is important to separate the contributions of different frequencies. This is done using the Fourier transform, which uses the Fourier series to separate a signal into various cosine and sine terms. Each of these terms is associated with a particular frequency and the amplitude of these terms gives the contributions to the overall noise. A common algorithm for Fourier transform is the Fast Fourier Transform (FFT) which has been employed in the present study using MATLAB and Welch's power spectral density estimate.

A common method to represent contributions of different frequencies is by plotting noise spectra, as shown in Figure 3.14 using the units dB/Hz. Log scale is used to accommodate a large range of frequencies of interest which vary over several orders of magnitude. Thus by analyzing a noise spectrum, the energy contained in each frequency can be obtained. Another quantity commonly used is Overall SPL (OSPL) which includes the sum of contributions over a range of frequencies. This is obtained by integrating the energy contained in a spectrum over the specified range of frequency.

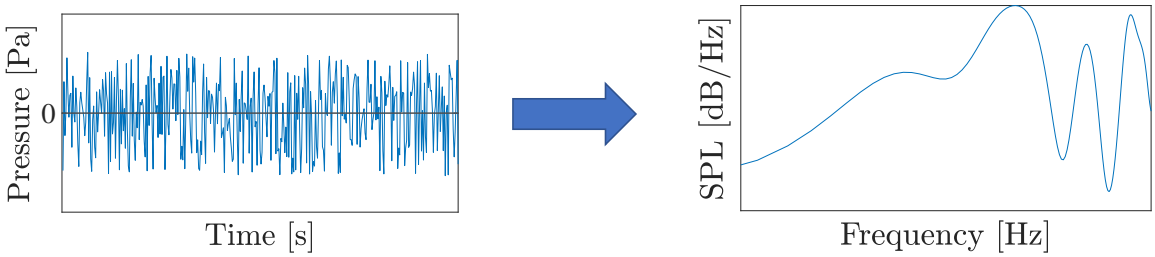

Figure 3.14: Fourier transform from sampled pressure signal (left) to noise spectra (right)

In the past, noise sources have been extensively investigated for large-scale HAWTs and no significant work exists for small-scale VAWTs. Noise sources in the former are different than in the latter, due to differences in operating Reynolds number and blade aerodynamics as a result of it. In addition, VAWT aerodynamics is highly unsteady as compared to that of a HAWT, due to the dominant phenomenon of dynamic stall and BVI in the former. Therefore, the knowledge gained in the past decades for the latter cannot be applied to the former and a whole new campaign for the calculation of VAWT noise generated, understanding of noise sources and their mitigation techniques is required.

An example of a VAWT noise spectrum by Pearson [261] is shown in figure 3.15. VAWT noise is generated due to different noise sources [46]. At the low-frequency range (10-100 Hz), maximum noise contribution comes from blade passage frequency (BPF) and its multiples. In the mid-frequency range (100-600 Hz), multiple peaks are observed and this is expected to be the contribution from Laminar Boundary Layer - Vortex Shedding (LBL-VS) noise (Brooks [53]) which occurs at low Reynolds number ($\text{Re} < 5 \times 10^5$). LBL-VS noise causes vortex shedding which has a distinctive tonal nature through a feedback loop. This noise can be reduced by using a boundary layer zig-zag trip on the blade surface to force laminar-to-turbulent transition [261]. Another contribution comes from Turbulent Boundary Layer - Trailing Edge (TBL-TE) noise which occurs at higher Reynolds number ($\text{Re} > 5 \times 10^5$). This happens due to the interaction of turbulent flow over the blade surface with the surface discontinuity at the trailing edge, where pressure fluctuations are scattered as noise. However, TBL-TE noise is expected to be less since VAWT blades generally operate at Reynolds numbers ranging from 1×10^4 to 1.5×10^5. In the high-frequency range (600-1000 Hz and more), the major contribution comes from Blade-Vortex Interaction (BVI) noise, due to the

interaction of VAWT wake vortices with the blades in the downwind half of rotation, which causes high-frequency unsteady loading fluctuations on the blade surface. This means BVI noise will be higher at higher TSR due to higher intensity of BVI [261].

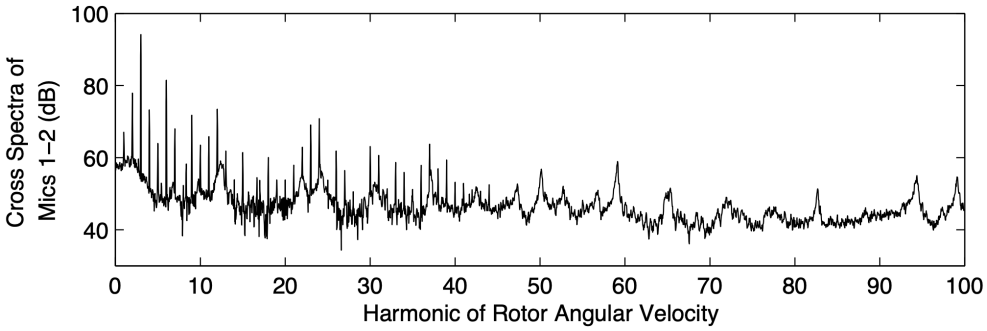

Figure 3.15: An example of a VAWT noise spectra by Pearson [261], at TSR = 3, BPF = 12 Hz and V_∞ = 6.4 m/s

3.5. State-of-the-art: Aeroacoustics

Studies by Möllerström [239, 240] and Dumitrescu [107] have reported VAWTs to produce less noise than HAWTs of similar size and power which makes them ideal for urban applications. In the case of Dumitrescu, VAWT noise is 47 dB and HAWT noise is 56 dB, both for C_P=0.4. Pearson [261] investigated a 3-bladed H-rotor and found that higher harmonic (tonal) content dominates lower TSRs and broadband (stochastic) content dominates higher TSRs. The former is due to dynamic stall, which is dominant in the low-to-mid frequency range at blade loading harmonics, and the latter is due to BVI which is dominant in the mid-to-high frequency range. Increasing solidity (number of blades) decreases harmonic content. This happens due to a decrease in AoA on VAWT blades in the upwind half of rotation and therefore, dynamic stall reduces. An increase in turbulence inflow also decreases harmonic content (and increases stochastic content) due to an increase in BVI and the periodic nature of dynamic stall being disrupted by the impingement of turbulent eddies on Darrieus blades. A general trend was found that noise decreases with an increase in TSR due to an increase in induction factor. This rate of increase or decrease is higher for high-solidity rotors due to their higher induction factors. This means that the off-design penalty for noise will be more for high-solidity rotors, which is similar to the penalties in aerodynamic performance. This makes turbine control significant for such rotors, especially in regions of rapidly varying wind speeds.

Mohamed [236] investigated a 3-bladed H-rotor and reported that increasing TSR and solidity resulted in increased overall noise, the results of which are opposite to Pearson [261]. This discrepancy is possible because the former used higher solidity VAWT (σ = 0.25) and 2D CFD simulation while the latter used lower solidity VAWT (σ = 0.12) and wind tunnel experiments. Weber [356] tested a 3-bladed Darrieus VAWT and showed that, in a flowfield, some major noise sources are present around vortices generated in the wake, flow separation over blades and Karman vortices behind the wind turbine tower. Noise spectra and acoustic source terms are shown in figure 3.16. Variation in lift and drag forces on a blade in a single rotation is also a source of loading noise and contributes to the harmonic content. Goccmen [128] optimised 6 different airfoils, such as FX 63-137, S822, S834, etc. both for noise and power performance. Generally speaking, reducing airfoil thickness and increasing camber helps to reduce noise and increase the ratio of lift over drag over a range of AoA. Mohamed [236] simulated a 3-bladed H-rotor with different airfoils, with S-1046 producing the lowest noise. Increasing TSR and solidity both contributed to increased overall noise, due to higher BVI and unsteady loading on the blades. The finding related to the increase in TSR values is again opposite to what is mentioned by Pearson [261]. This shows that there can be an optimum value of

TSR where the noise will be maximum or minimum.

Multiple studies have reported VAWTs to produce less noise than HAWTs of similar size and power [107, 239, 240] which makes them ideal for urban applications.

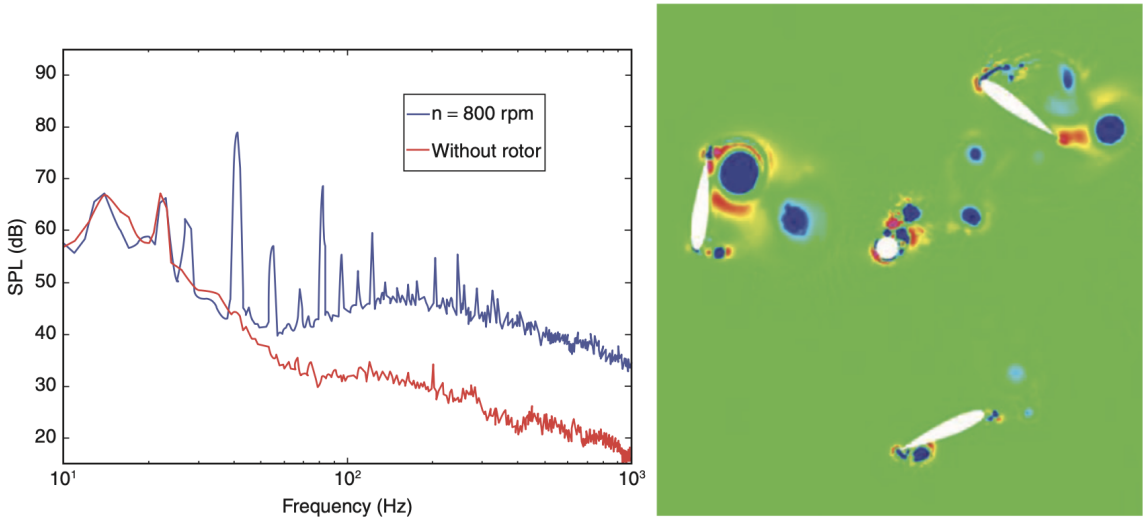

(a) Noise spectra comparing with and without rotor conditions (b) Acoustic source terms at 80° azimuth

Figure 3.16: Results by Weber [356], at N = 800 RPM and V_∞ = 21.28 m/s

Higher AR can also lead to an increase in noise generated due to increased blade-wake interaction [261]. Availability of vertical space and wind resources in an urban locality will play a significant role in the same [122]. Venkatraman [349] simulated noise generated due to flow non-uniformity experienced by a Darrieus VAWT on an urban rooftop. The directivity of overall sound increases in the direction of the velocity gradient with a slight increase in higher frequency harmonic noise and broadband noise.

3.6. Research gap and the current study

Current research in VAWTs primarily falls into two distinct areas: the development and refinement of low-fidelity to mid-fidelity tools for the accurate prediction of power and noise performance, and the application of available multi-fidelity tools for in-depth analysis of VAWT flow physics. This study is concentrated on the latter. Substantial progress has been made in understanding the aerodynamic performance of straight-bladed Darrieus VAWTs, particularly regarding the effects of various geometric and operational parameters.

To advance the design and optimisation of the Darrieus VAWTs, it is crucial to conduct a detailed investigation into specific aspects of VAWT flow physics. These include examining the loading on upwind and downwind blades, the influence of Blade Vortex Interaction (BVI) on mean and unsteady blade loading, the effect of blade loading on the development of near and far wake of the VAWT, the effects of tip vortices, and the 3D flow structures within the wake. Additionally, exploring the interaction between blade aerodynamics and overall structural dynamics, assessing the influence of atmospheric turbulence on VAWT performance, and analyzing the acoustic footprint of VAWTs under various operational conditions are imperative for a holistic understanding and improvement of VAWT designs.

Previous research has also indicated the potential benefits of innovative blade designs like helical and troposkien in VAWTs over traditional straight-blade configurations. However, there remains a gap in understanding the intricate fluid dynamics and blade-wake interactions within their flow

fields which can help in improving the design even further and reducing noise generation. Specifically, the performance of these novel blade designs under non-ideal flow conditions, such as those involving turbulence and vertical skew, has not been adequately explored. Furthermore, there exists a notable discrepancy in the literature regarding the terminology related to aspect ratios. The terms 'blade aspect ratio' and 'rotor aspect ratio' are distinct yet have often been used interchangeably without proper differentiation, leading to potential confusion in the interpretation of study results.

Regarding the aeroacoustic characteristics of VAWTs, limited studies exist that thoroughly examine their noise signatures. Various researchers have explored the aeroacoustics of VAWTs using differing configurations and sizes, leading to some contradictory findings in the field. Consequently, it is imperative to systematically compare these various configurations for a cohesive analysis and compare against a standardised benchmark VAWT model.

Moreover, there is a notable gap in aeroacoustic research concerning specific VAWT designs such as helical and troposkein VAWTs, VAWT clusters, ducted/shrouded VAWTs, and aeroacoustic performance analysis under a wide range of operational conditions and non-ideal inflow conditions like turbulence and vertical skew. Additionally, assessing the impact of different blade surface features and modifications on noise reduction, along with the exploration of active and passive flow control methods, will be crucial for developing quieter VAWT systems suitable for varied environments.

In the subsequent chapters, some of these topics will be revisited and investigated in depth, with the establishment of *objectives* and *sub-objectives* in each chapter to guide the investigation. The simulations and analyses in each chapter are designed to achieve these objectives, thereby advancing the understanding of the complex and highly unsteady fluid dynamics and acoustics associated with VAWTs. This detailed exploration will encompass two different methodologies: the mid-fidelity Lifting Line Free Vortex Wake (LLFVW) method and the high-fidelity Lattice Boltzmann Method (LBM). The ultimate objective is to enhance the fundamental understanding of VAWT aerodynamic and aeroacoustic behaviour for different design configurations and under various operational conditions, thereby contributing significantly to the field of wind energy research.

4

Stand-alone VAWT I: grid convergence study and tip speed ratio

Summary

The aerodynamics and aeroacoustics of small-scale Darrieus VAWTs are investigated at chord-based Reynolds number below 1.5×10^5. A 2-bladed H-Darrieus VAWT is used, featuring a 0.6m diameter, a 0.4m height, a solidity of 0.33 and a blade cross-section of the symmetrical NACA 0022. A grid convergence study is carried out and Richardson Extrapolation is used to estimate the continuum value of each performance parameter and calculate the grid convergence index (GCI). A range of tip speed ratios (TSRs) is investigated keeping a constant freestream incoming velocity. These values resemble an experimental and a numerical campaign corresponding to the two VAWT geometries used in this study. Results show that thrust, cross-streamwise (lateral) force and Overall Sound Pressure Level (OSPL) have better grid convergence (GCI is 0.015%, 2.2% and 0%, respectively) than torque (GCI is 9.02%). Furthermore, grid convergence varies with TSR depending on different VAWT flow regimes. These observations are also found using the mid-fidelity vortex method LLFVW. Blades in the downwind half of rotation are found to always produce less thrust and torque than in the upwind half, due to the effect of VAWT wake on the former. The ratio of thrust values between the upwind and downwind halves increased with increasing TSR due to the wake getting stronger at higher TSR; the ratio went from 1.3 for TSR = 0.37 to as high as 17.6 for TSR = 2.97. In terms of noise, higher TSR produces more noise than the lower TSR configuration, across the whole frequency spectrum, due to an increase in unsteady blade loading and blade-wake interaction with increasing TSR. Regarding OSPL directivity on a circular array of points, noise is highest at the most upstream azimuth location (90°) corresponding to the location where blade loading is highest in a single rotation.

4.1. Introduction

High-fidelity aerodynamic modelling and simulation of VAWTs have commonly involved 2D or quasi-2D (2.5D) computational setups. Although advantageous with lower computational resources, such setups cannot capture fundamental fluid dynamic interactions about the 3D effects of blade loading on the flow field. Previous studies have shown that 3D effects such as tip and trailing vortices are major contributors to power performance losses [92]. They are also expected to affect the grid convergence behaviour at different tip speed ratios (TSRs) and rotor aspect ratios. This lack of understanding also undermines the development of lower-order analytical models, which require empirical corrections for accurate performance prediction.

4.1.1. Grid convergence study and Richardson extrapolation

Some common sources of numerical uncertainty in a computational fluid dynamics (CFD) solution are numerical grid, time-stepping and numerical or analytical methods used in the study. This is based both on acquired experience and previous studies. In that respect, a grid and temporal (time-step) convergence study is conducted to check the dependency of a numerical simulation on the size of the grid used and the time elapsed, respectively. Furthermore, proper verification and validation of numerical results are performed along with setup checks before proceeding with a physical analysis of VAWT.

Past studies have shown three major approaches to check the validity of a CFD solution of VAWT. The first approach consists of refining the numerical grid until the solution is no longer modified and becomes 'grid-independent'. Bhargav et al. [33], Li et al. [190] and Bianchini et al. [39] use only two different grids, while Chen et al. [78] and Meng et al. [224] use three different grids for their VAWT simulations. Other authors have used five [21, 209], seven [157, 197] or even eight different grids [354] and sometimes also varying time step sizes. The second approach consists of comparing the numerical results with experiments and considering the discretisation approach valid if both the results resemble each other. While Lam et al. [174], Yang et al. [368] and Lee et al. [184] validated only with experiments, Abdalrahman et al. [1] validated results with both experiments and CFD benchmarks to study the effect of blade pitch angle on VAWT power output. Finally, the third approach consists of combining verification by grid convergence study along with validation by experimental results. Subramanian et al. [320] and Wekesa et al. [358] used two different grids and experimental validation for their studies. Lei et al. [186] used three different grids and selected the grid with medium refinement since it resembled the experimental results better. Qamar et al. [266] and Tian et al. [338] also used three different grids for their CFD simulations while Réthoré et al. [273] validated an actuator disk model using four different grids, in addition to validating with experiments.

In this respect, grid convergence behaviour based on the Richardson Extrapolation (RE) method has been used in previous studies for various fluid dynamics problems [67, 211, 279, 332]. Rezaeiha et al. [274] and Rezaeiha et al. [275] studied the effect of central tower on VAWT power performance using the RE method after validating with experiments. Fernández et al. [220] used the RE method for a range of TSR values for a 2D CFD simulation of a VAWT while other authors have used the RE method only on the nominal working point of a VAWT [10, 339, 369]. Moreover, Lockard et al. [199] and Vassberg et al. [348] found that inconsistencies and disappointing convergence properties are sometimes common in using a CFD code.

The available literature lacks an elaborate grid convergence study of a full range of operational, performance and design parameters, which can help to understand the numerical modelling of VAWTs. Most grid convergence studies focus only on aerodynamic parameters such as thrust or torque. Due to the operation of VAWTs in the urban environment, aeroacoustic parameters are as important. Secondly, as shown by Fernández et al. [220], grid convergence behaviour varies with TSR which is not covered in most of the literature. VAWT flow and force field are highly unsteady

and it is necessary to also include effects due to 3D flow (which cannot be captured by 2D or quasi-2D simulations found in most studies) and changes in VAWT blade geometry (such as aspect ratio or blade shape). Similarly, detailed grid convergence studies are also missing for mid-fidelity vortex mesh-based simulations [26, 70, 217, 295].

4.1.2. Variation in TSR: aerodynamic and aeroacoustic behaviour

The second part of this chapter focuses on studying the unsteady force and flow field, and far-field noise of a VAWT for a range of TSRs. In that respect, multiple studies have been conducted using multi-fidelity CFD simulations and aeroacoustic post-processing. Tavernier [92] simulated straight-bladed VAWTs using different aerodynamic models such as 2D and 3D actuator cylinder model [91, 205], free and fixed wake vortex models [244] and actuator line model [15]. VAWT aerodynamics is found to be inherently 3D due to the presence of finite blade length, trailing and especially tip vortices and spanwise variation of operation conditions and blade loading, the effects of which are not included in any 2D aerodynamic models. Furthermore, VAWT wake dynamics and 3D power losses vary significantly depending on the ratio of upwind and downwind loading, which in turn depends on the tip speed ratio and VAWT design parameters (aspect ratio, solidity, etc.).

Bangga et al. [24] simulated three straight-bladed VAWTs having different rotor solidities (0.23, 0.53 and 1.325) using Double-Multiple-Streamtube (DMS), Improved-DMS (IDMS), Unsteady Blade Element Momentum (UBEM), Vortex Model and fully resolved computational fluid dynamics (CFD) methods. There is a noticeable deviation in power prediction by different CFD approaches, although thrust results are accurate. This is strongly influenced by the inaccurate prediction of drag force on the blades for which grid topology and density, and resolution of downstream wake play an important role. In contrast, all other analytical models deliver consistent power prediction in light-loaded cases (low TSR) but have noticeable discrepancies in heavy-loaded cases (high TSR). The latter observation is attributed to downstream wake expansion, unsteady and decambering effects.

In respect of the aerodynamic noise, Pearson [261] investigated a 3-bladed H-rotor and found that higher harmonic (tonal) content dominates lower tip speed ratios (TSR) due to the dynamic stall being dominant at such speeds and at blade loading harmonics. At higher TSR, blade vortex interaction (BVI) becomes dominant which increases the broadband or stochastic content in the noise spectra. Increasing solidity or turbulence inflow also increases the stochastic content due to the periodic nature of dynamic stall being disrupted by impingement of turbulent eddies on Darrieus blades. Goccmen [128] reported that reducing airfoil thickness and increasing camber helps to reduce noise and increase the ratio of lift/drag. Mohamed [236] investigated a 3-bladed H-rotor and reported that increasing TSR and solidity resulted in increased overall noise, the results of which are opposite to Pearson [261]. This discrepancy is possible because the former used higher solidity VAWT (σ = 0.25) and 2D CFD simulation while the latter used lower solidity VAWT (σ = 0.12) and wind tunnel experiments.

The available literature lacks a full investigation into the scale-resolved wake and blade aerodynamics of VAWT. Due to the highly unsteady, 3D and turbulent nature of fluid dynamic interactions between the blade and wake, it is necessary to include aspects such as dynamic stall, blade-vortex interaction, non-uniform blade loading, and flow separation on the blade surface for an accurate power prediction. Concerning aeroacoustics, previous studies also miss detailed investigations into VAWT noise sources and far-field noise spectra for the full range of TSRs and 3D design space. High-fidelity CFD simulations can resolve complex flow fields of a VAWT at a much finer level, especially the flow around the blade and in the near and far wake, without the requirement of any empirical approximation (commonly used in low and mid-fidelity models). This can provide consistent drag values for the blades, which is an underlying challenge in unsteady low-Reynolds number rotor aerodynamics. Similarly, better resolution of the unsteady force and flow field improves the prediction of VAWT aeroacoustics as well. The knowledge gained from these exercises will also help

increase the accuracy of analytical aerodynamic models [24, 263, 289] such as the vortex model used in this study.

4.1.3. Research objectives

Based on this motivation, an investigation is performed to provide the first step towards creating a standard methodology for the grid and temporal convergence study of a VAWT or any applications exhibiting unsteady rotor aerodynamics and aeroacoustics. High-fidelity 3D aerodynamic simulations based on the Lattice-Boltzmann method are performed for straight-bladed VAWTs. Aeroacoustic post-processing is done using Ffowcs Williams and Hawkings (FW-H) methodology to calculate the far-field noise. In addition, mid-fidelity aerodynamic simulations are performed using Lifting Line Free Vortex Wake (LLFVW) model. One important conclusion of this exercise will be comparing the significance of grid convergence study between the mid-fidelity and high-fidelity aerodynamic methods. The high-fidelity simulation campaign accurately resolves the flow around the VAWT blades and in the wake. This allows for studying 3D effects on the force and flow field, such as non-uniform blade loading and non-uniform wake, dynamic stall, blade-vortex interaction and wake recovery. The following research questions are formulated for this chapter:

Research Questions

- How does the grid resolution affect VAWT performance parameters such as thrust, power, and far-field noise?
- How sensitive are the results of the grid convergence study to variations in TSR and aspect ratio?
- How do the results of the grid convergence study obtained using the mid-fidelity and high-fidelity methods compare?
- How do 3D effects of blade loading on thrust and power values, trailing and shed vortices, and wake dynamics vary at different tip speed ratios?
- What are the key noise sources contributing to the aeroacoustic performance of VAWTs at different tip speed ratios?

The chapter is structured as follows. Section 4.2 presents the computational setup of both mid-fidelity LLFVW and high-fidelity LBM, including VAWT geometrical properties, flow and grid settings and basics of the Richardson extrapolation method. Section 4.3 reports the results obtained for the grid convergence study, comparing the three setups and the two methods used. The section further presents a detailed force and flow field analysis of the VAWT for a range of TSRs. The last section 4.4 presents important conclusions of the study and a discussion on the understanding of the highly unsteady and turbulent VAWT fluid dynamic interactions.

4.2. Computational setup

To establish the reliability and accuracy of the numerical simulation and enable the reader to evaluate the validity of the subsequent results, a thorough explanation of the numerical and geometrical aspects of the simulation has been included, along with a description of the flow conditions and the generation of the computational grids.

4.2.1. Geometry

Two benchmark VAWTs with different geometric characteristics are considered in this study. Both are 2-bladed VAWTs with straight blades and are taken from experimental and computational ref-

erences by Howell et al. [148] and Balduzzi et al. [22], respectively. They are named Setup 1 and Setup 2, respectively. Figure 4.1 illustrates their geometric models and Table 4.1 compares their geometric values and operational conditions. The former VAWT has a higher solidity (0.33) and lower aspect ratio (0.67) compared to the latter VAWT, which has a lower solidity (0.17) and higher aspect ratio (1.46). This results in stronger 3D effects and increased blade-vortex interaction in the former VAWT compared to the latter VAWT. These differences in solidity and aspect ratio are expected to produce variations in the unsteadiness of VAWT blade loading and, subsequently, in grid convergence behaviour. The former also includes a central tower of 5 mm radius and 400 mm length, which was included to mimic the experimental geometry closely. However, the tower was found to have a negligible effect on the grid convergence behaviour and performance analysis of the VAWTs.

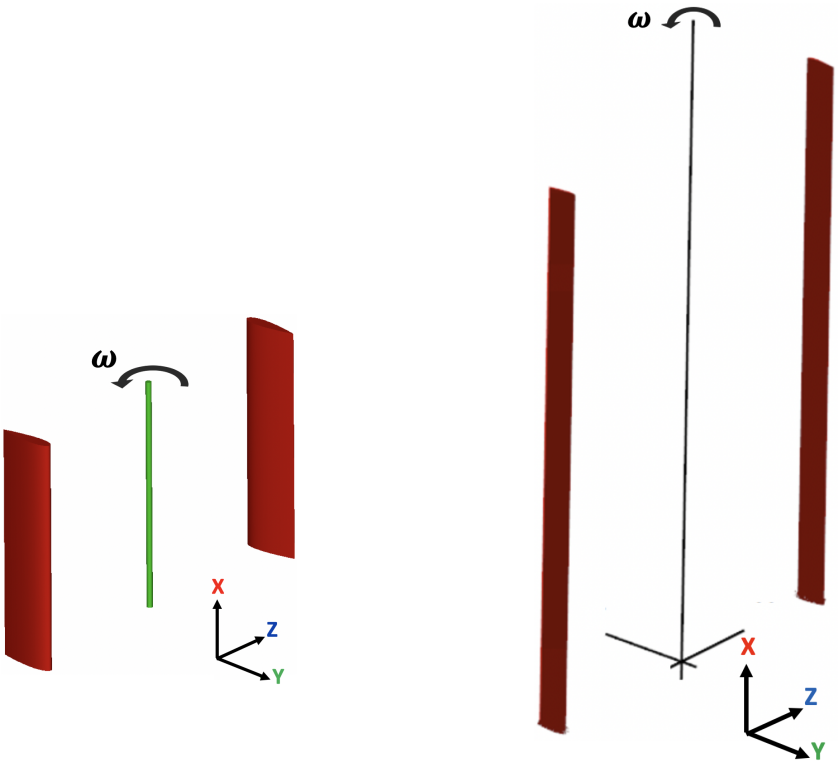

(a) Setup 1 by Howell [148] (b) Setup 2 by Balduzzi [22]

Figure 4.1: VAWT geometries used in this chapter (figures are not to scale)

Table 4.1: VAWT geometry and operational settings

	Blade length (L)	**Rotor diameter (D)**	**Chord length (c)**	**Freestream velocity (V_∞)**	**Airfoil**
Setup 1 [148]	0.4 m	0.6 m	0.1 m	5.07 m/s	NACA 0022
Setup 2 and 3 [22]	1.5 m	1.03 m	0.086 m	9 m/s	NACA 0021

Both VAWT setups are simulated using the high-fidelity Lattice Boltzmann Method (LBM). The latter VAWT by Balduzzi [22] is also simulated using the mid-fidelity Lifting Line Free Vortex Wake (LLFVW) method at a range of tip speed ratios (TSRs) and will be called Setup 3. The aerodynamic results from the LLFVW method are also subjected to a grid convergence investigation. Accurate and high-quality airfoil data is essential for obtaining accurate results using low and mid-fidelity methods. In that respect, a virtual geometry is obtained from the NACA 0021 profile to account for

the virtual camber effect [270] using the conformal transformation technique based on the chord-to-radius ratio, as described by Bianchini et al. [37]. The transformed airfoil is shown in Figure 4.2 (c). Lift and drag polars were obtained for Reynolds numbers between 1×10^5 and 1×10^6 using XFoil [104] with an *NCrit* value of nine and forced transition at the leading edge of both the pressure and suction side. The airfoil static polar data is extrapolated to 360° angle of attack (AoA) using the Montgomerie method [241] to ensure a smooth extrapolation in the post-stall regime. An example of 360° extrapolated polars is shown by Balduzzi et al. [22].

4.2.2. Numerical setup

For the high-fidelity setup (Setup 1 and 2), a simulation volume consisting of a cube of $100D$ on each side is used, with the Darrieus geometry located at its centre. The boundary conditions for the domain are depicted in Figure 4.2 (a). At the velocity inlet, the velocity is set to the freestream velocity V_∞ in the direction of the Y-axis (as shown in the figure) while an ambient pressure of 101.325 kPa is applied at the pressure outlet. A no-slip boundary condition is applied to the blade and central strut surface. PowerFLOW discretises the domain using a structured Cartesian grid with different variable resolution (VR) regions. This study utilises 17 VR regions, with the highest resolutions applied near the blade surface with an offset and coarser regions located farther from the blade and rotor. Figure 4.2 (b) shows this grid refinement when approaching the centre of the domain where the VAWT is located. The resolution decreases by a factor of 2 from a finer to a coarser VR region. This optimisation of computational expense is achieved by increasing discretisation efforts only in regions of interest and where high flow gradients are expected.

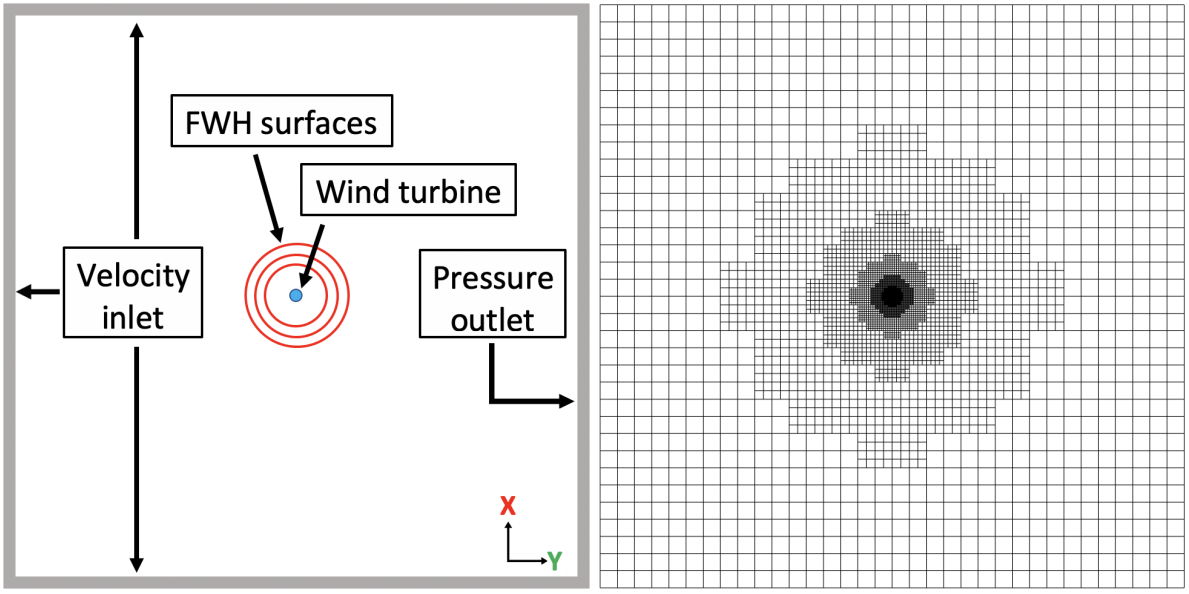

(a) Schematic representation of the high-fidelity domain (b) Cross-sectional view of the mesh for the whole domain

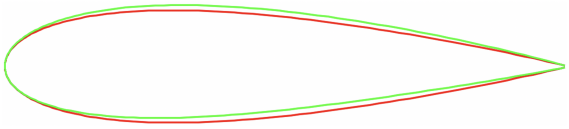

(c) Virtual camber airfoil (green) and original airfoil (red) for low-fidelity simulation

Figure 4.2: Computational setup used in this chapter

Figure 4.2 (a) shows three spherical surfaces (in red) surrounding the rotor flow field, which is

used as FW-H permeable surfaces. These surfaces are implemented to eliminate spurious noise sources resulting from hydrodynamic fluctuations in the VAWT wake vortices that pass through them. This is achieved by averaging the sampled pressure data on all the permeable surfaces which cancels out the fluctuating components associated with the hydrodynamic sources. Acoustic sources, on the other hand, are less affected by this averaging process since their wavelengths are smaller than the former (in other words, frequency is higher). The hydrodynamic fluctuations are often localized to specific regions, such as boundary layers or wake regions. By placing permeable surfaces that encompass these regions and averaging the data, the aim is to reduce the impact of these spurious fluctuations.

The blade and central tower surfaces of the VAWT are designated as FW-H solid surfaces. In this study, only the FW-H solid formulation is used for aeroacoustic investigation because it has been found to be challenging to remove spurious noise sources from FW-H permeable data using only three spherical surfaces. VAWT wake is highly unsteady and wake vortices are stronger than compared to the wake of HAWTs or propellers of similar size, which is the reason for its ineffectiveness. In the future, a separate study will be conducted to examine the use of the FW-H permeable formulation for VAWT aeroacoustics in an effective manner which is outside the scope of this thesis.

To accurately capture an acoustic wave, a criterion of a minimum of 15 points per wavelength is chosen [282]. Previous studies have indicated that analyzing the noise spectra up to 4000 Hz is sufficient for our purposes. Therefore, in accordance with the Nyquist criterion, pressure data are sampled at a frequency of 8000 Hz. Once statistical steady state is achieved, noise spectra are plotted and compared across different sampling durations, ranging from one rotor rotation to over ten rotations. The analysis revealed that minimal changes in the noise spectra occur after eight rotor rotations across the entire frequency range. Consequently, this duration (8 rotor rotations) is adopted as the standard throughout the thesis for calculating noise spectra. Noise spectra are calculated using a Hanning window with 50% overlap and a frequency resolution (Δf) of 10 Hz, using the *pwelch* function in MATLAB.

For the LLFVW simulation, Table 4.2 lists all the simulation parameters used for Setup 3.

Table 4.2: Simulation parameters used for the LLFVW method for Setup 3

	LLFVW
Freestream velocity V_∞	9 m/s
Density	1.225 kg/m^3
Kinematic viscosity	1.65 e-5 m^2/s
Blade discretisation	21 (cosine)
Azimuthal discretisation	3 deg
Full wake length	12
Vortex time offset	1 e-4 sec
Turbulent vortex viscosity	100

4.2.3. Flow conditions and grid settings

For the current study, Tables 4.3 and 4.4 show the VAWT operational settings for all three VAWT setups investigated using the RE method. Tip speed ratio (TSR) is defined as the ratio of blade rotational speed and freestream velocity, i.e. $\omega r/V_\infty$, where ω is the rotational speed in rad/s, r is the wind turbine radius and V_∞ is the freestream velocity. There are three potential ways to change the TSR of a VAWT: by altering ω, V_∞, or both. A good overview is given by Pearson [261], who opts for the third option to keep a constant value of relative wind velocity and, subsequently, Re_c. In this study, V_∞ is kept constant to match the reference values [22, 148], and ω is varied to change the TSR value. This exercise keeps the investigation close to a practical case, where the control system varies

rotational speed based on instantaneous wind speed measured to keep the TSR close to the optimal point. It is important to point out that Re_c remains below 4×10^5 considering all cases in this study. The freestream turbulence intensity (I_t) and turbulence length scale (L_t) are set to 0.1% and 1 mm, respectively. Still, based on previous studies [63], these two parameters are not expected to have a significant impact on the development of the unsteady flowfield.

Table 4.3: VAWT operational settings for setup 1

Parameter	**Value**			
Tip speed ratio (TSR)	0.37	1.12	2.23	2.97
Rotations per minute (RPM)	60	180	360	480
Chord-based Reynolds number (Re_c)	3.43×10^4	3.82×10^4	7.64×10^4	1.02×10^5

Table 4.4: VAWT operational settings for setup 2 and 3; setup 2 is simulated only for TSR 3.3 and setup 3 is simulated for all TSRs

Parameter	**Value**		
Tip speed ratio (TSR)	2	3.3	5
Rotations per minute (RPM)	333.76	550.71	834.41
Chord-based Reynolds number (Re_c)	1.05×10^5	1.73×10^5	3.15×10^5

For the grid convergence study, four grid resolutions are simulated for each TSR. The finest VR region around the blade surface has varying numbers of voxels per chord for the Grid 1, Grid 2, Grid 3, and Grid 4 resolutions, with the lowest resolution being for Grid 1 and the highest for Grid 4. Table 4.5 presents y^+ values and voxels per chord for the first two VAWT setups (which are simulated using high-fidelity LBM) for all grids. y^+ value represents the distance between the wall of the computational domain and the first grid point in the wall-normal direction, and voxels per chord represent the number of grid cells along the chord of the blade. It can be observed that the same voxels per chord are targeted for each corresponding grid in the two configurations.

Table 4.5: VAWT grid settings for both the benchmark VAWT geometries, using high-fidelity LBM

		Grid 1	**Grid 2**	**Grid 3**	**Grid 4**
Setup 1	y^+	50	31.3	25	16.7
	Voxels per chord	8.62×10^1	1.38×10^2	1.72×10^2	2.58×10^2
		Grid 1	**Grid 2**	**Grid 3**	**Grid 4**
Setup 2	y^+	100	62.5	50	33.3
	Voxels per chord	8.9×10^1	1.42×10^2	1.78×10^2	2.67×10^2

The grid of setup 1 is further detailed to depict the mesh framework in PowerFLOW. Figure 4.3 shows the finest mesh around the blade with 4 different VRs for the setup with Grid 4 of setup 1. Figure 4.4 shows the cross-sectional view of the mesh in the domain for Grid 4, both near the VAWT blades and further away from it. For setup 1, the total number of voxels and fine equivalent voxels are listed in Table 4.6. These fine equivalent voxels are determined by weighting the number of voxels by the time stepping rate, which is directly proportional to the mesh resolution level. It is noteworthy that a solution with a voxel size twice as coarse is updated using a time step that is twice as large, resulting in a computational cost that is two times cheaper. The fine-equivalent voxels are consistent for different TSRs simulated in this study. For the TSR of 0.37 of setup 1, the CPU hours required for simulating 12 rotor rotations (12 secs) using Mesh 1 and Mesh 4 for the 2-bladed VAWT are 1613 and 24720, respectively, using a Linux workstation equipped with an AMD Ryzen Threadripper 3990X Gen3 64 Core 128GB DDR4 3GHz platform. The required CPU hours decrease

as the TSR increases. Furthermore, the physical time step for all the grids is listed in Table 4.6, which corresponds to a Courant-Friedrichs-Lewy (CFL) number of 1 in the finest VR level.

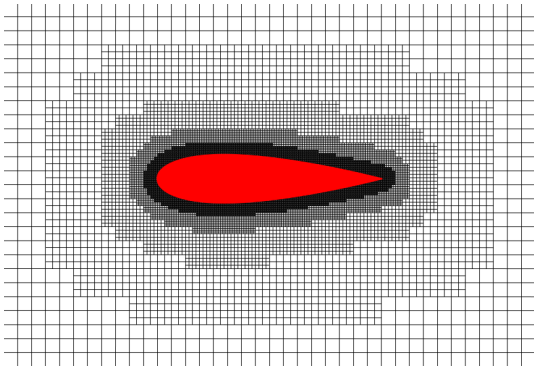

Figure 4.3: Cross-sectional view of the finest mesh around the blade for setup 1

Table 4.6: VAWT grid settings for the four different grid sizes for setup 1

	Grid 1	**Grid 2**	**Grid 3**	**Grid 4**
Total number of voxels (million)	18.5	26.9	33.8	55.8
Fine equivalent voxels (million)	3.4	7.4	10.8	22.6
Voxels per chord (finest VR)	8.62×10^{1}	1.38×10^{2}	1.72×10^{2}	2.58×10^{2}
Physical time step (secs)	1.29×10^{-5}	8.06×10^{-6}	6.44×10^{-6}	4.29×10^{-6}

Table 4.7 reports the four different spanwise panel settings for Setup 3 which uses the mid-fidelity LLFVW method, all having cosine distribution along the blade span. These are equivalent to grid settings in high-fidelity LBM and are denoted in a similar way. dx_{sp} is an equivalent representation of the length of each panel and is obtained by dividing the blade span by the number of panels. Similar grid convergence studies can be performed on other mid-fidelity numerical parameters such as length of wake, azimuthal discretisation, etc. In this study, only the spanwise panel settings are investigated and other settings are borrowed from Balduzzi et al. [22].

Table 4.7: VAWT blade spanwise panel settings for setup 3, using mid-fidelity LLFVW method

		Grid 1	**Grid 2**	**Grid 3**	**Grid 4**
Setup 3	Number of spanwise panels	12	15	18	21
	Panel spacing, dx_{sp} (m)	0.125	0.1	0.083	0.071

The integral and time-varying behaviour of the VAWT thrust coefficient (C_T), cross-streamwise force coefficient (C_{Fz}) and torque coefficient (C_Q) are reported and grid convergence parameters are analysed for all the above-mentioned cases. These coefficients are defined as:

$$C_T = \frac{T}{\rho n^2 D^4}\,, \tag{4.1}$$

$$C_{Fz} = \frac{F_z}{\rho n^2 D^4}\,, \tag{4.2}$$

$$C_Q = \frac{Q}{\rho n^2 D^5}\,, \tag{4.3}$$

where, T, F_z and Q are VAWT thrust, cross-streamwise force and torque respectively, ρ is air density, n is rotations per second and D is VAWT diameter. Using high-fidelity LBM, Power Spectral

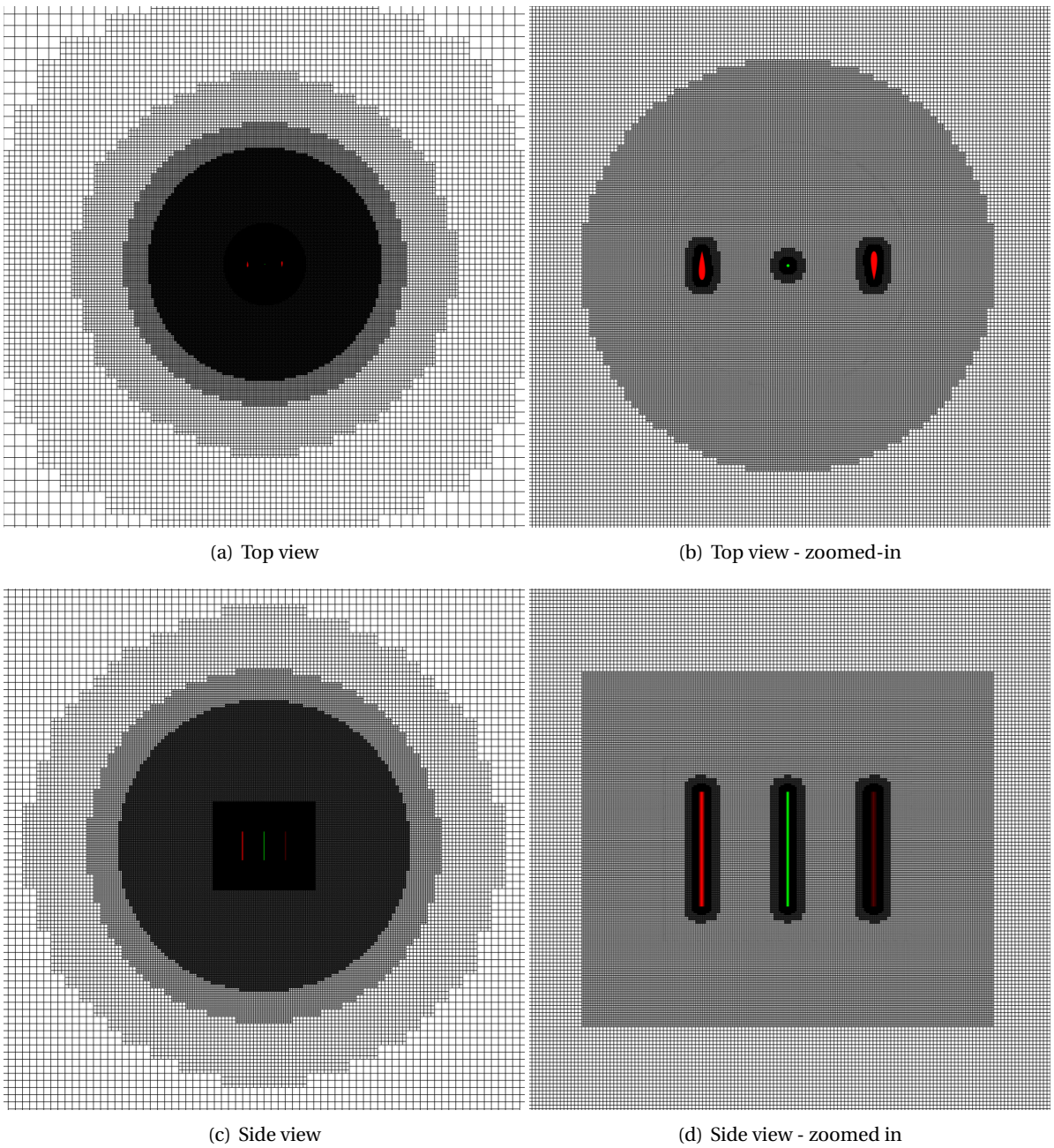

(a) Top view

(b) Top view - zoomed-in

(c) Side view

(d) Side view - zoomed in

Figure 4.4: Cross-sectional view of the mesh for the high-fidelity LBM simulation

Density (PSD) spectra and Overall Sound Pressure Level (OSPL) are also reported and analysed. The noise spectrum is calculated by taking 10 times the logarithm base 10 of the ratio of the power spectral density (PSD) of the raw acoustic signal to the square of p_{ref} ($2 \times 10^{-}5$ Pa). To calculate the OSPL across a frequency range, the integral of the PSD over the frequency band of interest is obtained and converted to decibels through the same logarithmic transformation.

4.2.4. Richardson Extrapolation

The concept of Richardson extrapolation, also referred to as "h^2 extrapolation," "the deferred approach to the limit," or "iterated extrapolation" [277], is utilised in the present grid convergence study. The aim of this method is to derive a higher-order estimate of the zero grid spacing value (i.e.

the continuum value) from a series of lower-order discrete values. Equations introduced by Roache et al. [278] in 1997 and Fern'andez et al. [220] in 2019 were utilised for this purpose. A numerical simulation that yields a quantity f can be expressed as:

$$f = f_{\text{exact}} + g_1 h + g_2 h^2 + g_3 h^3 + \dots \,, \tag{4.4}$$

where h represents the grid spacing, f_{exact} is the continuum value at zero grid spacing, and g_i are functions defined for the continuum and therefore independent of grid spacing. The grid refinement ratio is defined as:

$$r_g = \frac{h_{\text{coarse}}}{h_{\text{fine}}} \,. \tag{4.5}$$

The generalised equation for a pth order method to calculate f_{exact} (as presented by Roache et al. [279]) is defined as:

$$f_{\text{exact}} \simeq f_1 + \frac{f_1 - f_2}{r_g^p - 1} \,, \tag{4.6}$$

where f_1 and f_2 are the results from two different grids with spacing h_1 (fine) and h_2 (coarse), respectively. To determine the value of h, the cell size of the finest VR region is used for each grid resolution in this study. However, this choice is not unique; if the value of h were to be taken from another VR region, the value of r_g (i.e. $h_{\text{coarse}} / h_{\text{fine}}$) would remain the same, as the cell size increases by a factor of 2 in successive VR regions for each grid resolution case. The guidelines for applying this method in practice have been proposed by ASME [66]. As shown by Fern'andez [220], the order of the method p is determined through an iterative process. To do so, three data points (f_1, f_2, and f_3) are required, which are taken from the three finest grid resolutions: Grid 4, Grid 3, and Grid 2, respectively. After the exact value of p is known, Eq. 4.6 is used to calculate the extrapolated solution at zero grid spacing (an estimator of the exact solution) as:

$$f_{\text{exact}}^{21} = \frac{r_{g21}^p f_1 - f_2}{r_{g21}^p - 1} \,. \tag{4.7}$$

The error estimates for the relative error (e_a), extrapolated relative error (e_{ext}) and grid convergence index (GCI) are calculated as:

$$e_a^{21} = \left| \frac{f_1 - f_2}{f_1} \right| \,, \tag{4.8}$$

$$e_{\text{ext}}^{21} = \left| \frac{f_{\text{exact}}^{21} - f_1}{f_{\text{exact}}^{21}} \right| \,, \tag{4.9}$$

$$\text{GCI}^{21} = \frac{F_S \quad e_a^{21}}{r_{g21}^p - 1} \,, \tag{4.10}$$

where F_S is a security factor and can be set as 1.25 when using three different grid resolutions [279].

Since Richardson extrapolation method is a polynomial method being applied to the physics of VAWT, there are some limitations in its application and this should be understood before interpreting the results obtained in this chapter in a physical sense. Nevertheless, this extrapolation method provides a good idea of the level of grid convergence obtained for different design and operational parameters.

- **Sufficient Resolution**: The grids used must be sufficiently fine to ensure that the physics of VAWT flow-field and force-field are sufficiently captured. If the grids are too coarse, the extrapolation can estimate an inaccurate continuum value which may not be physical. This is made sure in the current study, with low y^+ values.

- **Smoothness of the Solution**: The method assumes that the solution is smooth and well-behaved. If the solution has discontinuities, singularities, or sharp gradients, the extrapolation may not be reliable. Problems with discontinuities include shock waves in compressible flow or phase changes.

- **Numerical Stability**: The method can be sensitive to numerical instability. If the numerical solutions are not stable or if there are significant round-off errors, the extrapolated solution may be inaccurate.

- **Highly Nonlinear Problems**: In highly nonlinear problems where the error behavior is complex and cannot be captured by a simple polynomial series, the extrapolation may fail to provide accurate estimates.

4.3. Results

4.3.1. Grid convergence study and Richardson extrapolation

Figure 4.5 shows the temporal convergence behaviour (evolution of values with time/rotations) of thrust and torque coefficient for three test cases: setup 1 at TSR = 2.97 using high-fidelity LBM, setup 2 at TSR = 3.3 using high-fidelity LBM and setup 3 at TSR = 3.3 using mid-fidelity LLFVW, where the finest grid (Grid 4) is used for each case. Results for setup 1 represent the values extracted from the blades and central tower while setup 2 represents values extracted only from the blades (since there is no central tower).

Statistical temporal convergence for LBM values is achieved after the initial 4 rotations for both setups 1 and 2. For setup 3 with LLFVW values, the convergence is achieved after the initial 30 rotations. This is shown by very low uncertainty values u (< 1%), which are calculated as a % of the standard deviation of integral values averaged over a rotation. In this study, if the value of u is < 1%, it is considered temporally converged. Following best practice, uncertainty is calculated after the 8th rotation for LBM and the 30th rotation for LLFVW. The current finding deviates from what is reported by Rezaeiha [274] in which over 20 rotations are needed to obtain time convergence. In this study, LBM simulations for the finer grid are seeded by the results from the coarser grid, which means the simulations for the former are initiated using results of the last timestep of the latter. This is the reason for a decreased transient period of the former. On the other hand, no seeding option was available in setup 3 using LLFVW; therefore, the temporal convergence was delayed till 30 rotations compared to only 4 rotations for LBM.

Higher blade-vortex interaction (BVI) in a VAWT flowfield leads to increased unsteadiness in blade loading fluctuations in a single rotation [261]. This translates to increased uncertainty values in temporal convergence and can be seen when comparing the results of setups 1 and 2 (u is 0.29% for the former and 0.035% for the latter, for C_T), where the former has more BVI than the latter due to higher rotor solidity. Apart from solidity, higher TSR also exhibits more BVI than lower TSR [220]. This means, that if convergence is achieved after n-th rotation for a higher TSR condition, then convergence is also achieved for lower TSR values after n rotations. This was found in the results of all simulation campaigns conducted in this thesis. Therefore, temporal convergence using LBM for setup 1 and LLFVW for setup 3 is reported for the highest TSR used in the present study (reported in Table 4.3 and 4.4). Using LBM for setup 2, values for TSR = 3.3 are reported which is the only TSR used for the high-fidelity setup.

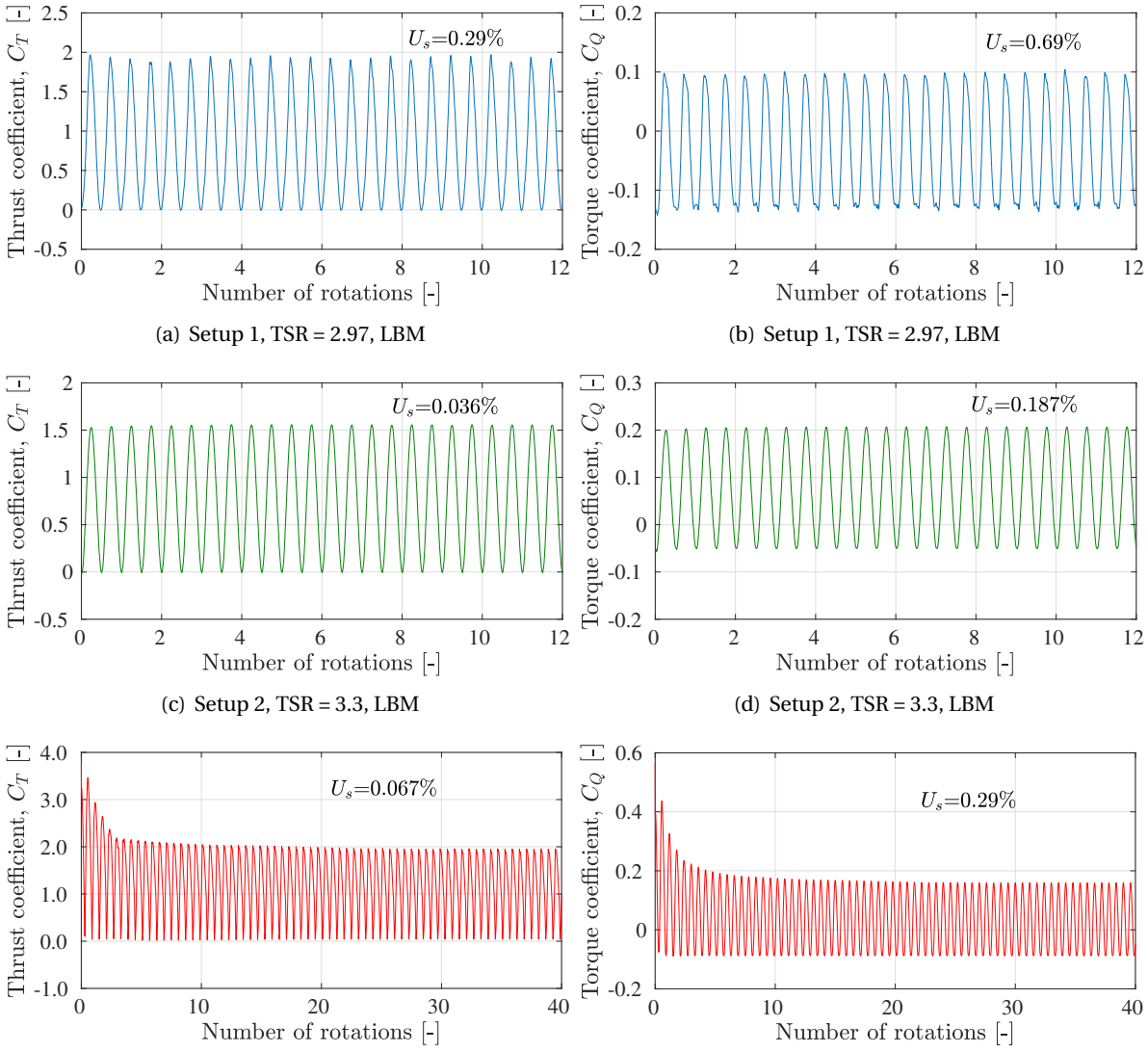

(a) Setup 1, TSR = 2.97, LBM

(b) Setup 1, TSR = 2.97, LBM

(c) Setup 2, TSR = 3.3, LBM

(d) Setup 2, TSR = 3.3, LBM

(e) Setup 3, TSR = 5, LLFVW

(f) Setup 3, TSR = 5, LLFVW

Figure 4.5: Statistical temporal convergence for all 3 setups; u denotes uncertainty in integral values after 8th rotation with LBM and after 30th rotation with LLFVW

Fig. 4.6 and 4.7 show the results obtained for the grid convergence study of C_T, C_{Fz} and C_Q for setup 1, where the values are reported for a single blade. Resolution for each case is represented by the grid spacing h introduced earlier, non-dimensionalised with blade chord c. This figure also shows the values obtained when $h/c \rightarrow 0$, by using the Richardson extrapolation method. Physically, this means approaching the continuum value or using an infinite number of cells in the Cartesian grid. Negative values of C_{Fz} indicate the direction of loading with reference to the axis shown in Fig. 4.1. Power values are not shown because the grid convergence behaviour of power is the same as that of torque (since power = torque $\times$ ω). As an example for different grid convergence parameters for C_T, C_{Fz} and C_Q, Table 4.8 lists the values for TSR = 2.23.

A few trends can be observed from the grid convergence study. Generally speaking, C_T values show the best grid convergence, followed by C_{Fz} and then C_Q. Grid convergence index (GCI_{34}) for C_T and C_{Fz} goes as low as 0.015% and 2.2%, respectively, for TSR = 2.23. For C_Q, lowest value of GCI_{34} is 9.02% for TSR = 2.23. Similar observations are made for extrapolated relative error (e^{34}_{ext}) which is 0.012% for C_T, 1.79% for C_{Fz} and 7.78% for C_Q for TSR = 2.23 shown in Table 4.8. Numerically, this

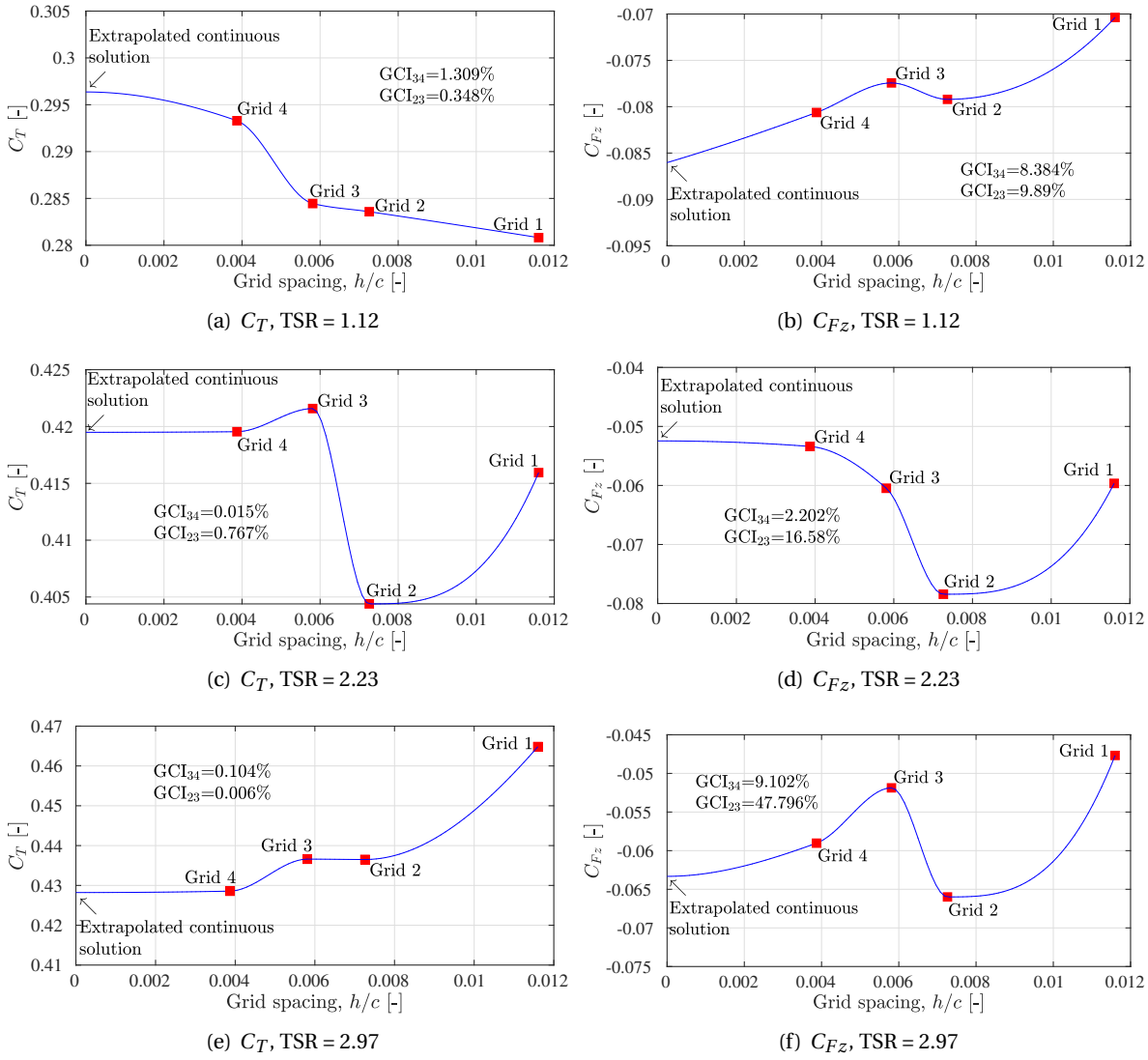

(a) C_T, TSR = 1.12 (b) C_{Fz}, TSR = 1.12

(c) C_T, TSR = 2.23 (d) C_{Fz}, TSR = 2.23

(e) C_T, TSR = 2.97 (f) C_{Fz}, TSR = 2.97

Figure 4.6: Grid convergence study for VAWT thrust coefficient C_T and cross-streamwise force coefficient C_{Fz} for a single blade, for setup 1

Table 4.8: Grid convergence parameters and discretisation error using Richardson Extrapolation method for TSR = 2.23 for setup 1; C_T, C_{Fz} and C_Q are for a single blade while OSPL is for overall VAWT

Parameter	C_T	C_{Fz}	C_Q	OSPL
f_1	0.4195	-0.0534	0.0165	58.416
f_2	0.4216	-0.0605	0.0207	58.4098
f_3	0.4044	-0.0784	0.0276	57.2228
p	9.1270	5.2745	3.7127	23.6071
f^{34}_{exact}	0.4195	-0.0525	0.0153	58.416
e^{34}_a	0.486%	13.259%	25.401%	0.011%
e^{34}_{ext}	0.012%	1.793%	7.777%	7e-7%
GCI^{34}	0.015%	2.202%	9.019%	9e-7%

means that a coarser grid is enough to capture converged blade loading values in the streamwise or lateral direction, albeit, a finer grid is required to capture converged blade torque (or power) values. The former depends mostly on the lift obtained from the blade while the latter depends on both

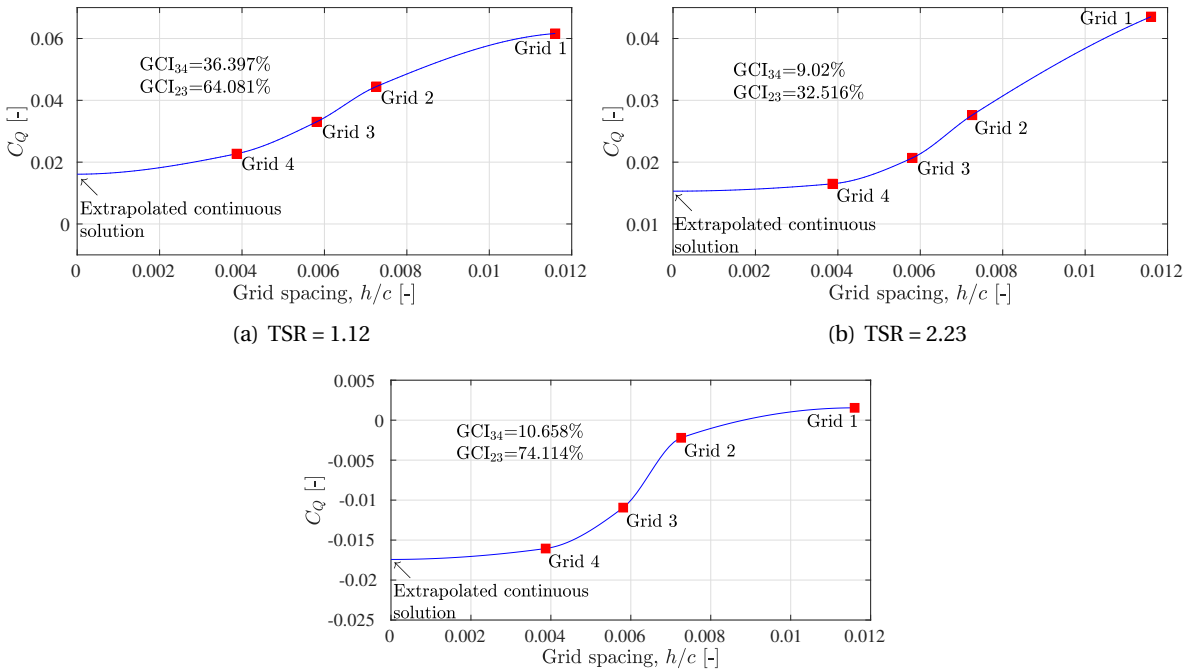

(a) TSR = 1.12

(b) TSR = 2.23

(c) TSR = 2.97

Figure 4.7: Grid convergence study for VAWT torque coefficient C_Q for a single blade, for setup 1

the lift and drag values. The variation in y^+ values (due to variation in the finest grid size) causes a significant change in the predicted values of wall shear stress and skin friction, which affects the drag and torque values much more than lift and thrust values. Accurate drag prediction on airfoils for both low and high Reynolds number flows is an ongoing area of research [347] and will be looked at in more detail in VAWT in future studies.

Another trend found is based on the variation with TSR. The best grid convergence for all three performance parameters is shown by TSR = 2.23 compared to higher or lower TSR values (GCI_{34} is 0.015% compared to 0.104% and 1.309%). This shows that different grid refinement is required to reach a better convergence level for VAWTs operating in different flow regimes, such as parasitic drag (high TSR) or dynamic stall (low TSR). Different flow regimes are schematically shown by McIntosh [219]. Higher rotational speed results in a thinner attached boundary layer on the blade surface, which requires finer levels of the grid for correctly modelling the flow behaviour. Another challenge arises due to higher levels of BVI in the case of higher TSR which gives rise to higher unsteady loading fluctuations on the blades. In the case of the dynamic stall phenomenon, flow separation and stall occur over a range of azimuth angles which also require fine grid refinement. This is consistent with the results of Fernández [220] who reported varying convergence levels for different TSR values. It is interesting to note that, when the grid is refined, the variation in values is not always found to be monotonic. Furthermore, as opposed to what is normally expected, GCI_{34} is not always lower than GCI_{23}. These inconsistencies are also observed in different numerical fluid dynamic problems [199] [348].

Fig. 4.8 shows the grid convergence behaviour of C_T and C_Q for setup 2 at TSR = 3.3, using the high-fidelity LBM. Values are reported for a single blade from the 2-bladed VAWT. Results for only TSR = 3.3 is shown since it is close to the optimal TSR value [22], the same way as TSR = 2.23 is for setup 1. The comparison between the two aforementioned cases will help in understanding the effect of changes in VAWT geometry (aspect ratio and solidity) on the grid convergence behaviour. Setup 2 shows lower GCI_{34} and GCI_{23} for both C_T and C_Q, when compared with the corresponding

values of TSR = 2.23 for setup 1. GCI_{34} reaches as low as 0.014% for C_T and 0.86% for C_Q. Setup 2 has a lower solidity and higher aspect ratio, which leads to lower BVI and unsteady blade loading fluctuations. This is beneficial from a grid convergence point of view and shows that lower mesh resolution is required for VAWTs with similar geometrical properties. Similar to setup 1, C_T has better convergence than C_Q (GCI_{34} is 0.014% and 0.859%, respectively), cementing the fact that predicting lift and thrust values requires less grid resolution and poses less numerical challenge than drag and torque values.

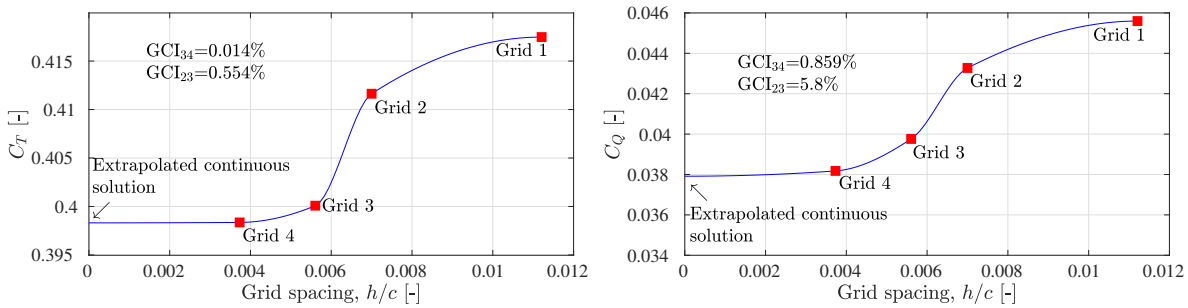

Figure 4.8: Grid convergence study for VAWT thrust coefficient C_T and torque coefficient C_Q using the high-fidelity LBM for setup 2; values are reported for a single blade for TSR = 3.3

Fig. 4.9 shows the grid convergence behaviour of setup 3 using the mid-fidelity LLFVW method. Values are reported for TSR = 3.3 and TSR = 5 for a single blade. For TSR = 2, the variation between C_T and C_Q values for different spanwise panel settings is negligible and achieves $GCI_{12} \sim 0\%$ (between Grid 1 and Grid 2) and therefore, hasn't been reported here. Based on TSR = 3.3 and TSR = 5, the trends in GCI values found are similar to what is found with the high-fidelity LBM. The former TSR shows better convergence than the latter TSR, in both the parameters reported. For each TSR, blade loading values (C_T) show better convergence than blade torque values (C_Q) (GCI_{34} is 0.986% and 2.59%, respectively, for TSR = 3.3). Observations related to the non-monotonicity of values with the variation in panel refinement and GCI_{23} sometimes being lower than GCI_{34} are also found. These observations show that the mid-fidelity vortex method can significantly capture the effect of the grid size (or panel density) on the performance characteristics of a VAWT, similar to the high-fidelity method. These performance parameters (C_T, C_{Fz} and C_Q) are only a reflection of the highly unsteady and turbulent fluid dynamic interactions in a VAWT flowfield. The capability of the mid-fidelity method to capture such interactions at a significantly lower computational cost will be explored in detail in the following chapters.

Figure 4.10 shows the results obtained for noise spectra for the three finest grids plotted with a frequency resolution of 10 Hz. PSD values are reported for both setups 1 and 2 for the point [(X,Y,Z) = (0,0,7D)] with reference to the axis shown in Fig. 4.1, where D is the wind turbine diameter corresponding to each setup. The value of 7D is chosen to emulate the average distance of humans from a small detached house rooftop-based standalone VAWT. Results depict a good agreement between Grid 3 and Grid 4. For all the cases shown, high-frequency PSD values show more variation between different grids than the values at lower frequencies. This shows that the effect of grid size is significantly more on Turbulent Boundary Layer Trailing Edge (TBL-TE) noise which is the main contributor to high-frequency noise [47, 261]. The effect of grid size on tonal noise at blade passage frequency (BPF) and Turbulence-Interaction (TI) noise is less which contributes to low-frequency noise.

To check the convergence of noise levels for a range of frequencies, overall sound pressure level (OSPL) values are calculated at [(X,Y,Z) = (0,0,7D)] for [20-2000] Hz range and analysed using the RE method, for both the setups 1 and 2. This is shown in Fig. 4.11. As an example of grid convergence

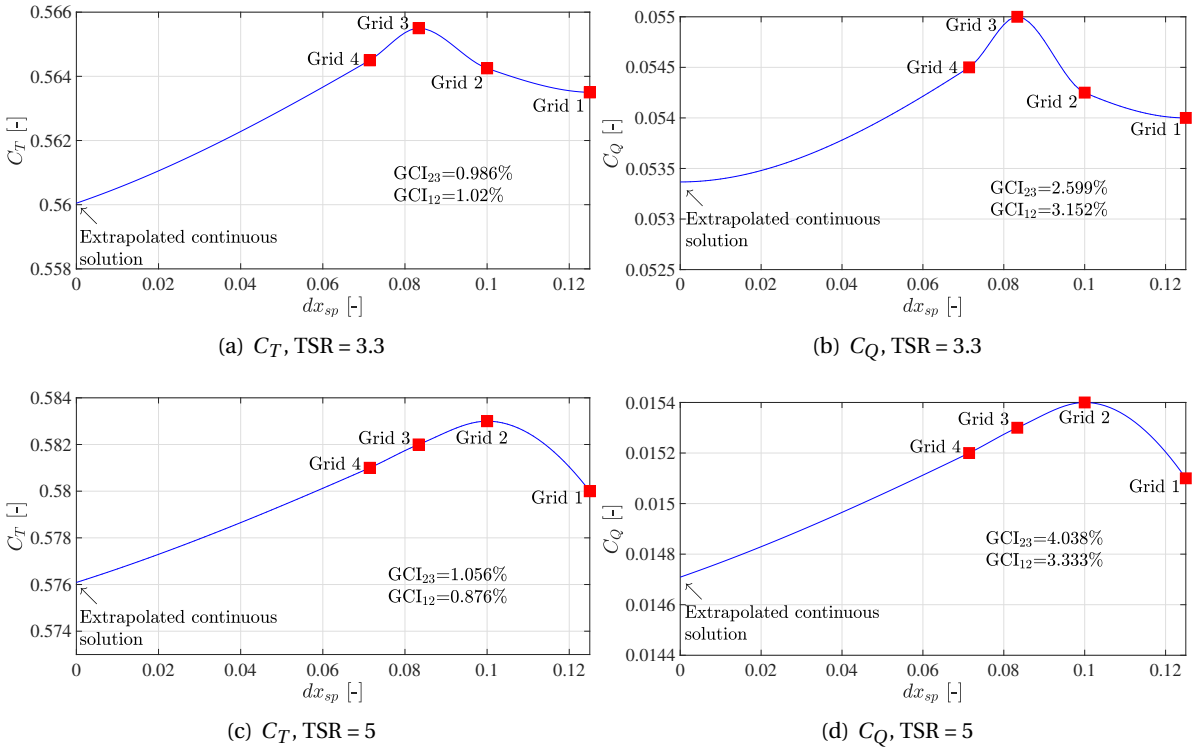

(a) C_T, TSR = 3.3

(b) C_Q, TSR = 3.3

(c) C_T, TSR = 5

(d) C_Q, TSR = 5

Figure 4.9: Grid convergence study for VAWT thrust coefficient C_T and torque coefficient C_{Fz} using the mid-fidelity LLFVW method for setup 3; values are reported for a single blade

parameters for OSPL, table 4.8 lists the values for TSR = 2.23 for setup 1. Similar to thrust, OSPL values show a very good convergence level (GCI_{34} = 1.61% for TSR = 1.12, even going down to GCI_{34} = 0% for TSR = 2.23). Convergence at TSR = 2.23 is better than at the other two TSRs for setup 1, similar to what was reported earlier for aerodynamic parameters. This shows that a coarser grid will be enough to accurately predict VAWT far-field noise. The GCI values for OSPL are comparable to the GCI values reported earlier for the C_T, as compared to C_Q or C_{Fz}. This coincides well with the fact that at low Mach-number operating conditions (M = 0.044 for setup 1 and M = 0.087 for setup 2), VAWT noise contribution is majorly from unsteady blade loading, as compared to blade loading or quadrupole noise [127]. These observations are also true for setup 2, whose GCI values for OSPL are also similar to the GCI values reported earlier for its C_T values, as compared to C_Q or C_{Fz}.

After observing grid convergence behaviour for all test cases, Grid 4 is accepted to be converged for both aerodynamics and aeroacoustics. It is chosen for all future numerical simulations and is considered enough to provide an accurate physical analysis of VAWT fluid dynamic interactions. In case only aeroacoustic analysis is required, then Grid 3 for LBM can also be chosen to reduce computational expenses.

4.3.2. Validation

Both setups 1 and 2 are compared with published experimental and numerical results, with the values being taken for Grid 4. Table 4.9 compares the experimental torque of setup 1 [148] with the value obtained with Grid 4 (f_1) and the extrapolated continuous solution (f^{34}_{exact}). No experimental thrust results are reported to compare with. There is some difference between the numerical and experimental results, with the former being 12.8% lower than the latter. The possibility of over/under-prediction of skin friction values and wall shear stress over the blade surface can be a reason for the observed difference. This is the same reason expected for the lower levels of grid convergence for

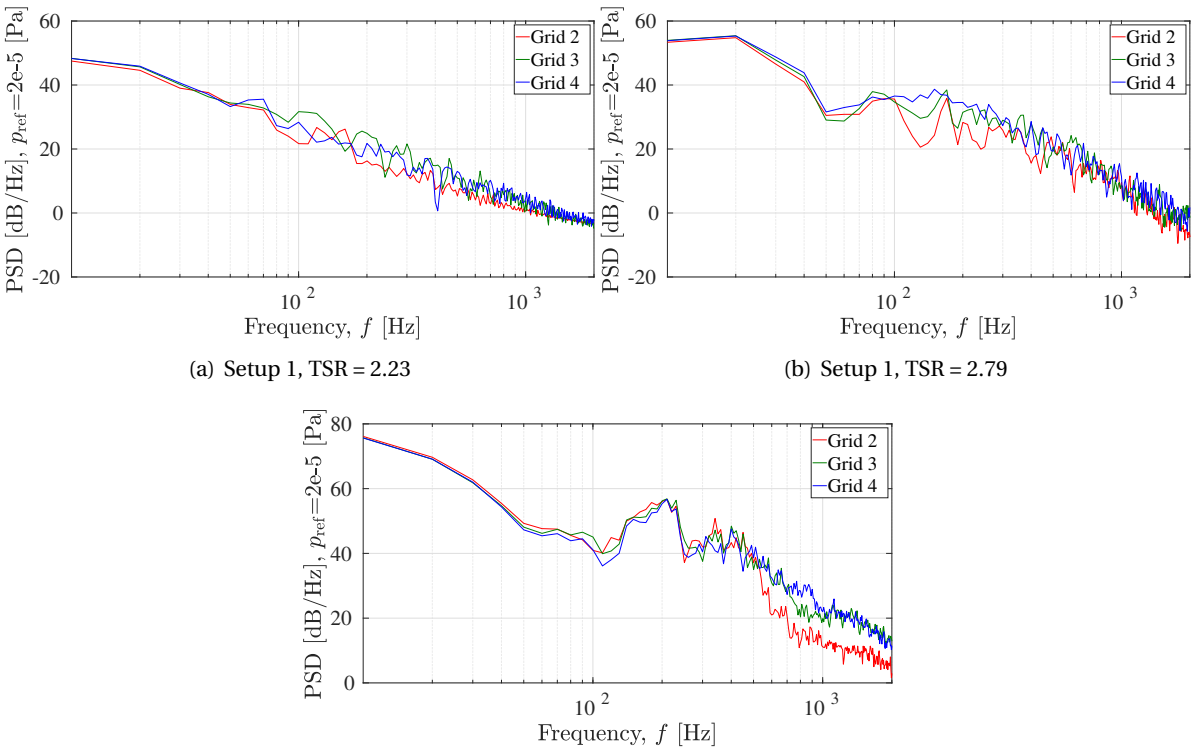

(a) Setup 1, TSR = 2.23

(b) Setup 1, TSR = 2.79

(c) Setup 2, TSR = 3.3

Figure 4.10: Grid convergence study of noise spectra at point [(X,Y,Z) = (0,0,7D)] for the overall VAWT, using high-fidelity LBM

torque reported earlier.

Table 4.9: Grid convergence parameters and discretisation error using Richardson Extrapolation method for TSR = 2.23 for setup 1; C_T, C_{Fz} and C_Q are for single blade while OSPL is for overall VAWT

Parameter	**C_T**	**C_{Fz}**	**C_Q**	**OSPL**
f_1	0.4195	-0.0534	0.0165	58.416
f^{34}_{exact}	0.4195	-0.0525	0.0153	58.416
Experiment [148]	-	-	0.0189	-

A comparison between extrapolated (f^{34}_{exact}) and experimental torque value reveals that both show values of a similar order of magnitude. The difference can also be attributed to other aspects, either numerical or physical, which are not captured by PowerFLOW as compared to the experiment. From acquired experience, these discrepancies in experimental validation are common for a VAWT and depend on the geometrical properties, and will be subject to future investigations. Since torque and thrust values show a similar trend when TSR is varied, as compared to previous authors [29, 148, 280], this suggests that relative comparison between different TSR cases in the present study will still provide significant insights on the fluid dynamic interactions.

Fig. 4.12 compares C_P values for a 1-bladed VAWT (since reference numerical results are only available for a 1-bladed VAWT and not for more number of blades), using the same blade geometry of setup 2 or 3, obtained using both mid-fidelity LLFVW and high-fidelity LBM with the results reported by Balduzzi et al. [22]. Results are reported using Grid 4 for both methods. The reference dataset also consists of the mid-fidelity LLFVW method and high-fidelity CFD using the RANS method (only for TSR = 3.3). On the whole, the LLFVW method used in this study predicts the typical

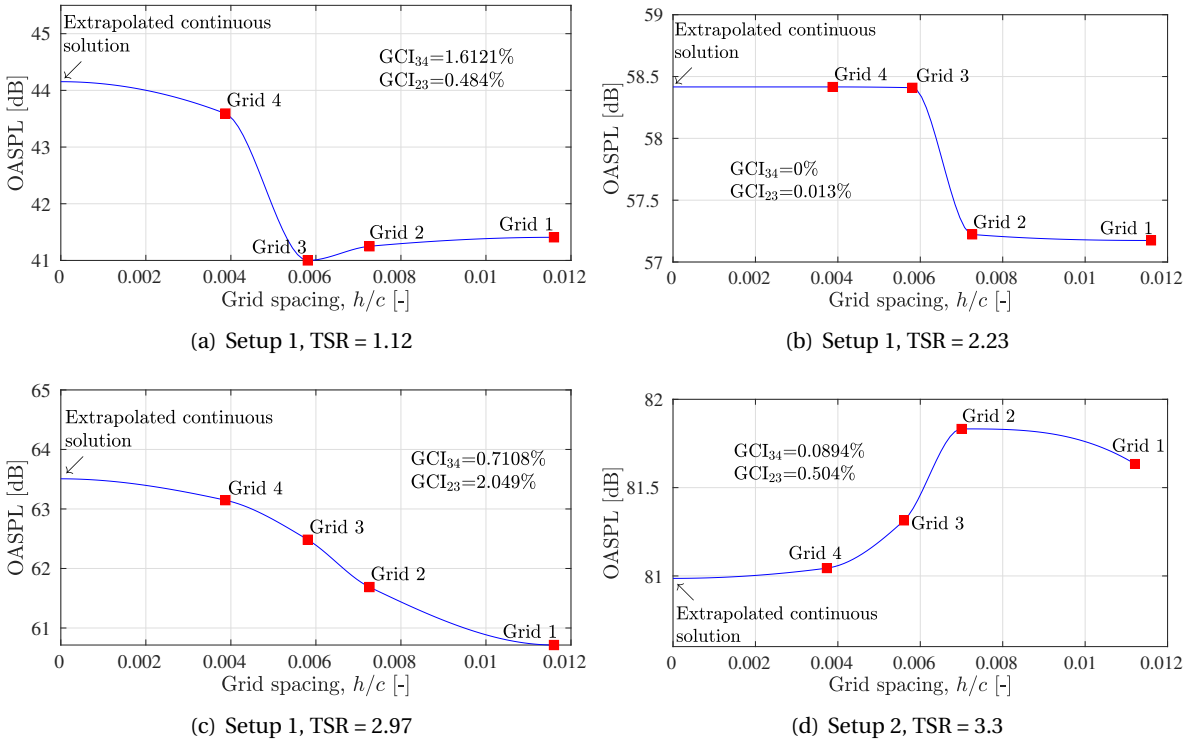

(a) Setup 1, TSR = 1.12

(b) Setup 1, TSR = 2.23

(c) Setup 1, TSR = 2.97

(d) Setup 2, TSR = 3.3

Figure 4.11: Grid convergence study for OSPL at point [(X,Y,Z) = (0,0,7D)] for [20-2000] Hz range for the overall VAWT, using high-fidelity LBM

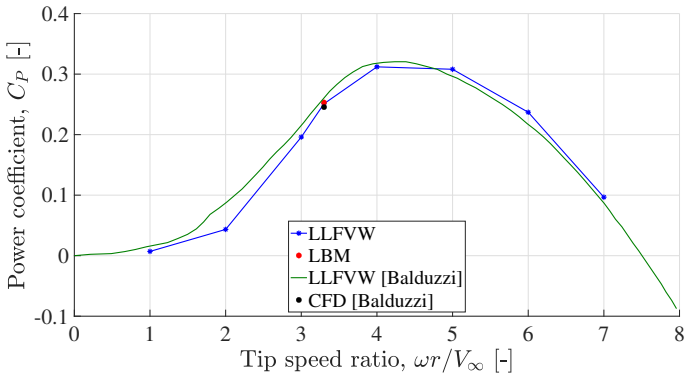

Figure 4.12: Comparison of C_P values for a 1-bladed VAWT having the same blade design as setup 3, with the results reported by Balduzzi et al. [22]; both the high-fidelity LBM and mid-fidelity LLFVW have been reported from the present study

shape of the VAWT power curve [256, 261] in a satisfactory way. LLFVW results match very well with the reference results, over the whole range of TSR, except for a slight mismatch around TSR = 2. LBM results have a very good match with both the LLFVW results and with the CFD result, at TSR = 3.3. Further investigation into setups 2 and 3 (using LBM and LLFVW) for aerodynamic and aeroacoustic analyses is conducted in the following chapters. For the next section, the results of only setup 1 are reported using high-fidelity LBM.

4.3.3. Force and flow field analysis

Figure 4.13 shows instantaneous 3D flowfield using iso-surfaces of the λ_2 criterion (λ_2 = -5000 1/sec^2), comparing TSR = 0.37 and TSR = 2.97 at θ=0° azimuth location (azimuth reference system

is shown in Fig. 4.1 (a)). Higher TSR shows the presence of large coherent structures which are shed from the blade tip, and travel downstream, forming a distinct "vortex ring" spiral pattern around the turbine's axis. This convective motion of the large vortex structures is accompanied by wake expansion, eventually fragments into smaller structures due to flow instabilities and spatial modulation, which then disperse and merge with the surrounding fluid [12, 196]. In the case of lower TSR, these structures are weak and mostly absent. Smaller scale vortices are also generated in the wake and are present in higher number in case of higher TSR. This increases the intensity of BVI between these vortical structures in the near wake and blades in the downwind half of rotation, leading to higher unsteady loading fluctuations on the blades in case of higher TSR than in lower TSR.

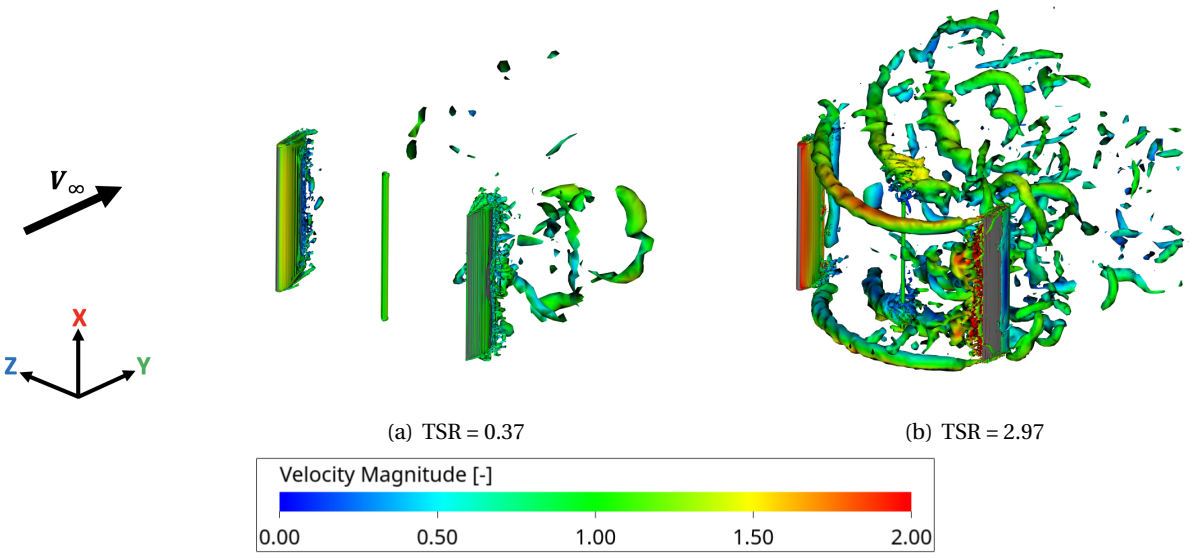

Figure 4.13: Instantaneous 3D flowfield using iso-surfaces of the λ_2 criterion (λ_2 = -5000 1/sec^2) for vortices visualisation for setup 1; velocity magnitude is non-dimensionalised with V_∞

Figure 4.14 describes the relationship between the TSR and the performance coefficients of a VAWT — namely, C_T, C_{Fz}, C_Q and C_P. It evaluates the mean values for a single blade throughout an entire rotation, distinguishing the relative contributions from the upwind and downwind halves of rotation. The parameter s signifies the proportional contribution from the upwind versus downwind halves. Observations show that the downwind half invariably generates lower thrust and torque across all TSRs, with the difference between the two halves becoming more pronounced as TSR increases. The underlying mechanism for this phenomenon is the interaction of the blades in the downwind half with the wake shed by the upwind blades, as shown in Figure 4.13. As TSR increases, corresponding to a rise in blade rotational speed at a constant freestream velocity, the strength of the wake intensifies. Blades traversing the downwind half experience a velocity deficit and reduced effective angle of attack (AoA), reducing their thrust and torque generation in comparison to the upwind half. Furthermore, the wake-induced turbulence, which is significantly more at higher TSRs, exacerbates the difference in aerodynamic loading between the two halves.

A monotonic increasing trend is observed for C_T with respect to TSR. Particularly in the upwind section, C_T exhibits a consistent rise, while the downwind portion initially sees an increase followed by a subsequent decline. Consequently, the overall C_T increases monotonically as the TSR increases, given the increasing difference in the thrust contribution between the upwind and downwind halves, signified by the increasing value of s (from 1.3 at TSR = 0.37 to 17.6 at TSR = 2.97). For C_{Fz}, negative values shown are with reference to the axis in Fig. 4.1. The behaviour of C_{Fz} is distinct, showing a peak at an intermediate TSR of 1.12, while the difference between the two rotation

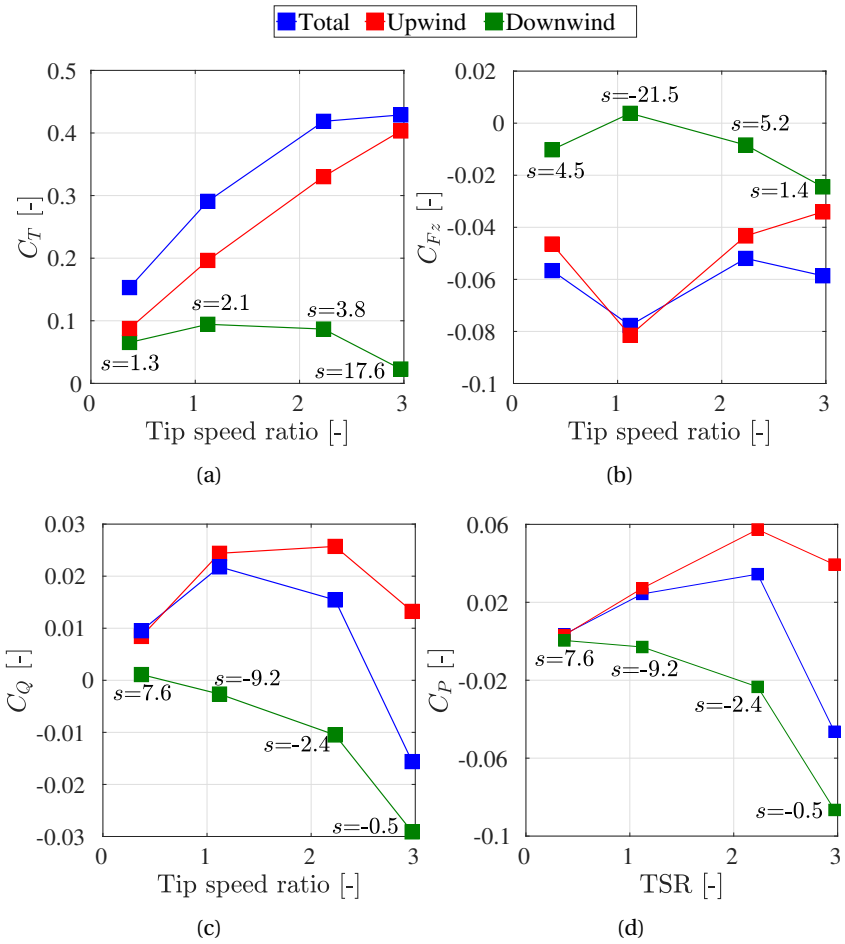

Figure 4.14: Comparison of average values for a single rotation with the upwind and downwind halves separately, for setup 1; s denotes the ratio of contribution from upwind and downwind halves and values are reported for a single blade

halves also peaks at the same TSR (with s = -21.5). The total C_{Fz} value (and the value of s) declines at the extremities of the TSR spectrum, which could imply a reduction in the bending moments exerted on the turbine tower in the lateral direction. This pattern suggests that there is an optimal TSR range wherein the lateral forces exerted by the blade rotation are balanced, potentially minimizing structural stresses on the turbine.

Upwind C_T monotonically increases with TSR whereas downwind C_T initially increases and then decreases. Since the value of s keeps increasing with TSR, the contribution from the downwind half reduces as TSR increases and this results in a monotonic increase of overall C_T. This result is similar to a HAWT or an aeronautical propeller, where thrust increases with RPM. For C_{Fz}, negative values shown are with reference to the axis in Fig. 4.1. The behaviour is slightly different than C_T and all three curves have a peak at TSR = 1.12. At lower and higher TSR values, total C_{Fz} decreases which will reduce the bending moment in the cross-streamwise direction on the wind turbine tower.

The variation in overall C_Q and C_P with TSR is similar to what is reported by Paraschivoiu [256], where it follows a typical bell curve. Upwind C_Q and C_P initially increase with TSR due to a decrease in the dynamic stall and then decrease at higher TSR due to a decrease in blade AoA and an increase in parasitic drag. Downwind C_Q and C_P directly start decreasing with an increase in TSR due to the damaging effect of VAWT wake on the downwind blades. Notably, VAWT solidity (σ = 0.33) in the current study is higher as compared to lower solidity values used by previous authors (σ = 0.12

[261] and $\sigma = 0.25$ [236]). In the case of the former, when TSR increases, the contribution from the downwind half decreases faster due to the stronger effect of blade-vortex interaction (BVI) on VAWT performance, as compared to the latter. Combining the upwind and downwind parts, the difference in contribution between them (represented by s) increases at low TSRs and then decreases at high TSRs.

Understanding this C_P behaviour from an alternative perspective, the typical C_P-λ curve for VAWTs [256, 261, 301, 305], suggests that the effective TSR for the downwind half of rotation increases due to the reduced incoming velocity within the wake region, leading to a decrease in downwind C_P. As the overall TSR of the VAWT increases, the effective TSR for the downwind half increases disproportionately, causing the disparity between the two halves of the rotation to widen. At very high TSRs, the overall C_Q and C_P turn negative, indicating a state where the turbine consumes rather than generates power, functionally analogous to a propeller generating thrust.

Figure 4.15 shows the unsteady variation in C_T and C_Q across a single rotational cycle for three distinct TSRs: 1.12, 2.23, and 2.97. The depicted values integrate the contributions from both the blades and the central supporting tower and resonate with the data presented in Figure 4.14. Mean values over the full 360° azimuth angle are also plotted as horizontal lines.

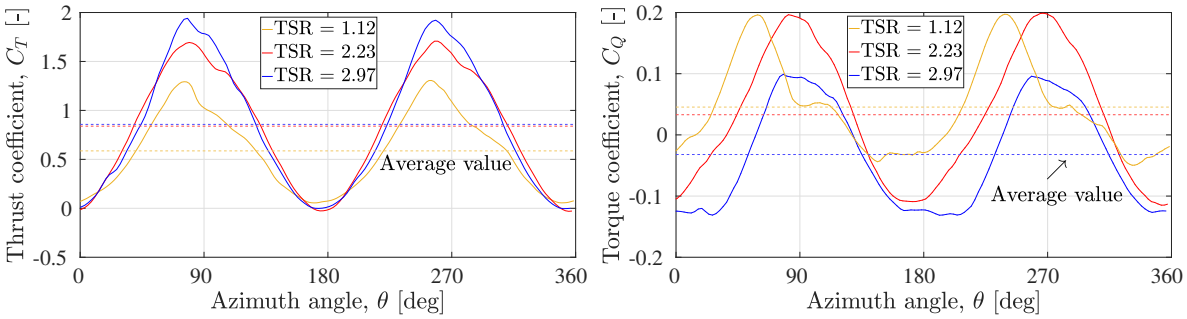

(a) Thrust coefficient, C_T (b) Torque coefficient, C_Q

Figure 4.15: Variation of thrust coefficient C_T and torque coefficient C_Q for the overall rotor (blades and the central tower) over a complete rotation at different tip speeds ratios

As TSR increases, a corresponding increase in C_T is observed, which is more evident at the peak values of C_T at approximately 90° and 270° azimuthal angles. This is reflective of the increased aerodynamic forces exerted on the blades as they move at higher rotational velocities and exert more flow blockage. In contrast, C_Q exhibits a higher value at the lower TSR of 1.12, which shows a decline with increasing TSRs. The peak C_Q values for TSRs of 1.12 and 2.23 are similar and differences are mainly visible on the windward and leeward part of rotor rotation. Notably, at TSR 2.97, C_Q predominantly exhibits negative values throughout the rotation cycle. This indicates that, at this higher rotational speed, the tangential forces acting upon the blades frequently oppose the direction of rotation. This phenomenon could be ascribed to lower blade AoA and adverse BVI/BWI in the downstream wake as shown in Figure 4.13. This is a region of operation inefficiency where the rotor may absorb energy to maintain its motion rather than generate usable torque.

Figure 4.16 presents the 2D contours of turbulent kinetic energy (TKE) distribution within the instantaneous VAWT flowfield, visualised in the YZ plane at mid-span blade location and non-dimensionalised with V_∞^2. TKE quantifies the energy contained within the turbulent eddies and is mathematically represented as half of the sum of the variances of the velocity fluctuations in all three spatial dimensions (TKE = $\frac{1}{2}(\overline{u'^2} + \overline{v'^2} + \overline{w'^2})$). These velocity fluctuations are the deviations from the mean flow velocity, indicative of the chaotic and stochastic nature of turbulence.

At higher TSRs, such as 2.97, TKE contours reveal regions of higher energy, corresponding to stronger and more coherent vortical formations, as opposed to the relatively weaker structures

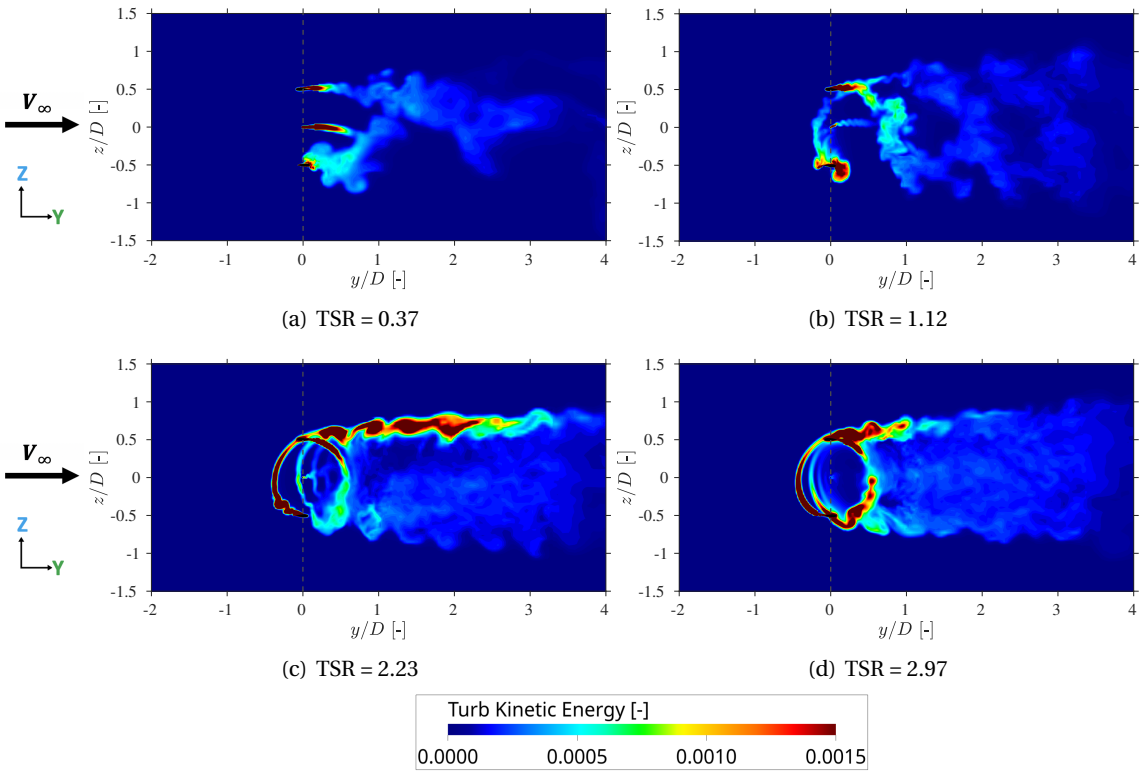

Figure 4.16: Instantaneous turbulent kinetic energy contour, non-dimensionalised with V_∞^2, in the YZ plane showing the evolution of wake in the VAWT flowfield

present at lower TSRs, such as 0.37. This suggests that an increase in TSR amplifies the turbulence intensity within the wake, exhibiting a multitude of smaller-scale vortices, as shown in Figure 4.13. The intensified turbulent wake and vortex structures, especially at higher TSRs, lead to more pronounced BVI/BWI contributing to significant unsteady aerodynamic loads on the blades, particularly in the downwind half of the rotation. Such unsteady loading is manifested as fluctuations in C_T and C_Q (Figure 4.15), affecting the VAWT performance. At lower TSRs, blades exhibit reduced unsteady loads and possibly a more stable performance, albeit at the expense of lower overall energy extraction (C_P).

The above discussion can also be visualised using the 2D vorticity magnitude contours within the YZ plane located at the blade mid-span location, shown in Figure 4.17. Vorticity magnitude is a scalar measure that quantifies the intensity of rotation at a point in a fluid flow and is mathematically defined as the curl of the velocity field, represented by $|\omega| = \sqrt{\left(\frac{\partial w}{\partial y} - \frac{\partial v}{\partial z}\right)^2 + \left(\frac{\partial u}{\partial z} - \frac{\partial w}{\partial x}\right)^2 + \left(\frac{\partial v}{\partial x} - \frac{\partial u}{\partial y}\right)^2}$, where u, v, and w are the velocity components in the x, y, and z directions, respectively. The contours exhibit the evolution of rotational flow structures (vortices) in the wake of the VAWT blades.

The results are congruent with the TKE contour in Figure 4.16. At the lower TSR of 0.37, vorticity magnitudes are moderate, reflecting the presence of relatively weak vortices. As TSR increases, vorticity intensifies indicative of stronger and more coherent vortices getting shed from the blades and the central tower. Consequently, this increases the TKE within the downstream flow field resulting in a highly vigorous and turbulent wake.

Similarly, Figure 4.18 shows vorticity magnitude contours within the YZ plane situated at the blade tip location, instead of the blade mid-span location. For lower TSRs of 0.37 and 1.12, vortex strength decreases at the blade tip location, as compared to at the blade mid-span location. At the latter location, deep stall and dynamic stall are significant due to high blade AoA which increases

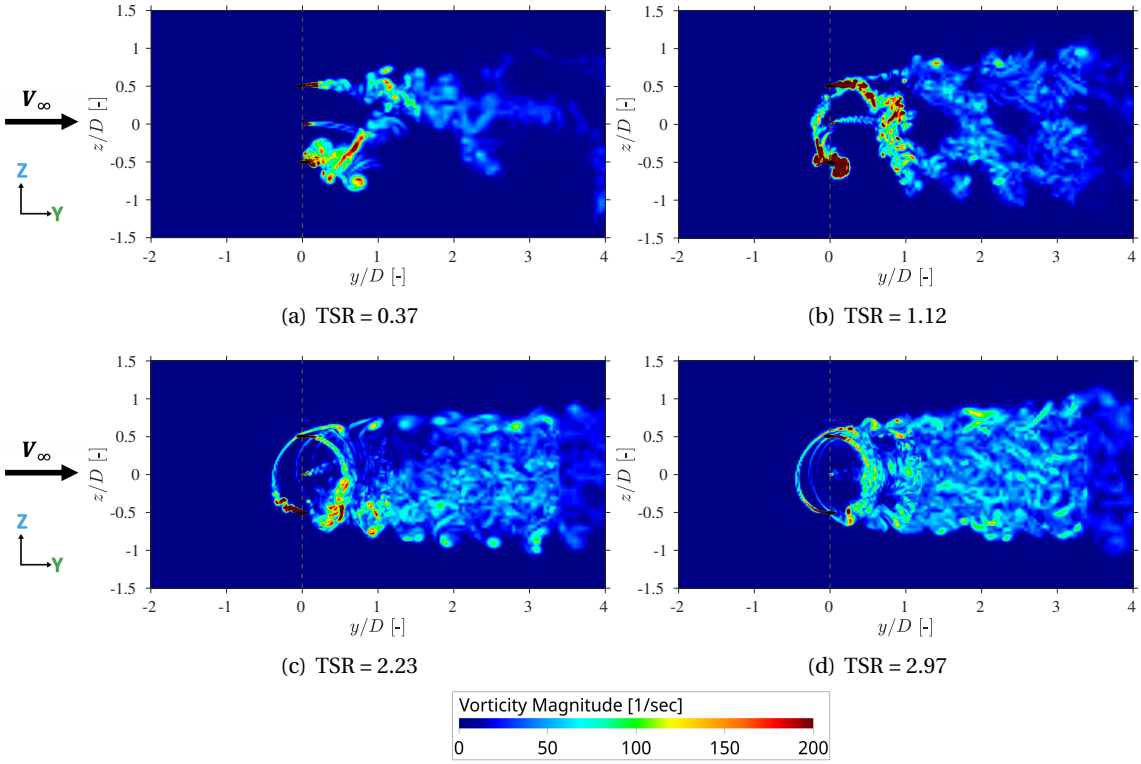

(a) TSR = 0.37 (b) TSR = 1.12

(c) TSR = 2.23 (d) TSR = 2.97

Figure 4.17: Instantaneous vorticity magnitude contour in the YZ plane, located at the blade mid-span, showing the evolution of wake in the VAWT flowfield

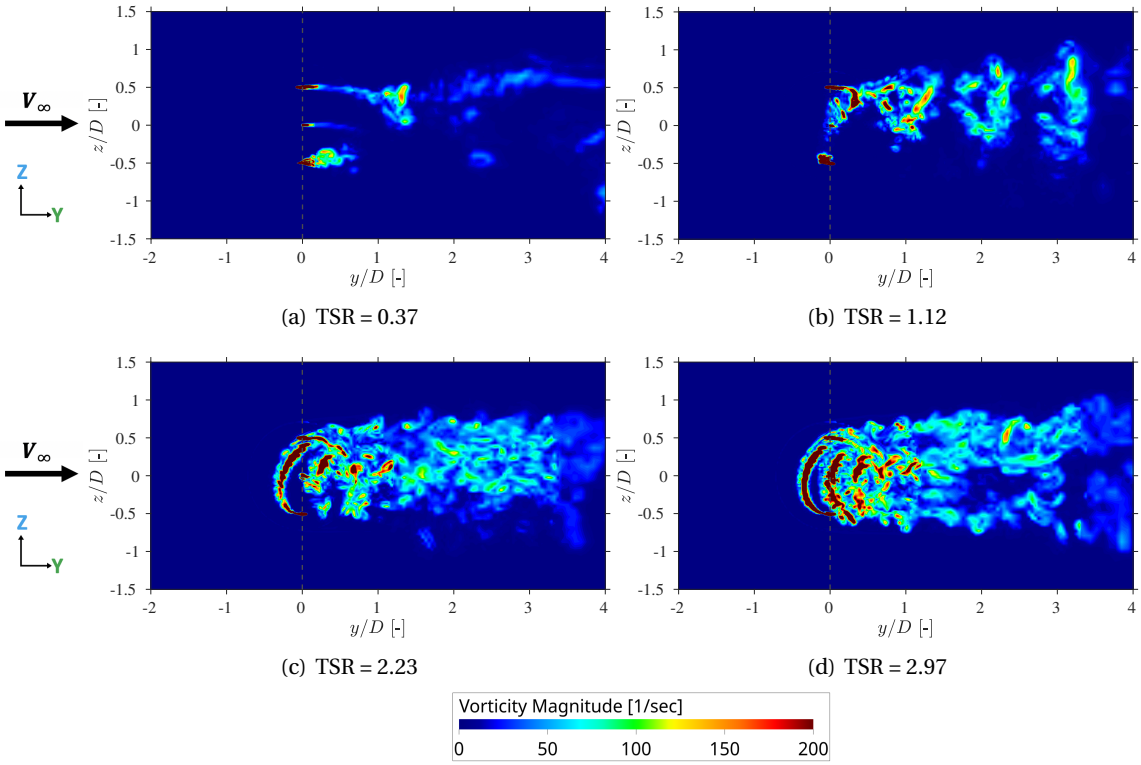

(a) TSR = 0.37 (b) TSR = 1.12

(c) TSR = 2.23 (d) TSR = 2.97

Figure 4.18: Instantaneous vorticity magnitude contour in the YZ plane, located at the blade tip, showing the evolution of wake in the VAWT flowfield

the intensity of vortices in the near wake. For the former, due to the tip vortex effect, the deep stall and dynamic stall effect are reduced reducing the intensity of downstream vortices. On the other hand, for higher TSRs of 2.23 and 2.97, vorticity strength increases at the blade tip location than at the blade mid-span location. Due to a higher blade rotational speed, the effect of the tip vortex is more significant. This is also visible as coherent 3D vortex structures shed from the blade tip, in Figure 4.13. In addition, stall reduces at higher TSR due to low blade AoA, which reduces the vortices produced as a result of flow separation of the blades, over the major part of blade length.

Figures 4.19 and 4.20 depict the streamwise velocity contours, non-dimensionalised with V_∞, within the YZ and XY planes, respectively, at two different TSRs of 0.37 and 2.97. At lower TSR, such as 0.37, the wake behind the VAWT blades exhibits less blockage and higher streamwise velocities, indicating a milder interaction with the oncoming airflow. As TSR increases, a significant reduction in streamwise velocity immediately behind the rotor in the near wake is observed and a significantly stronger wake extends farther downstream.

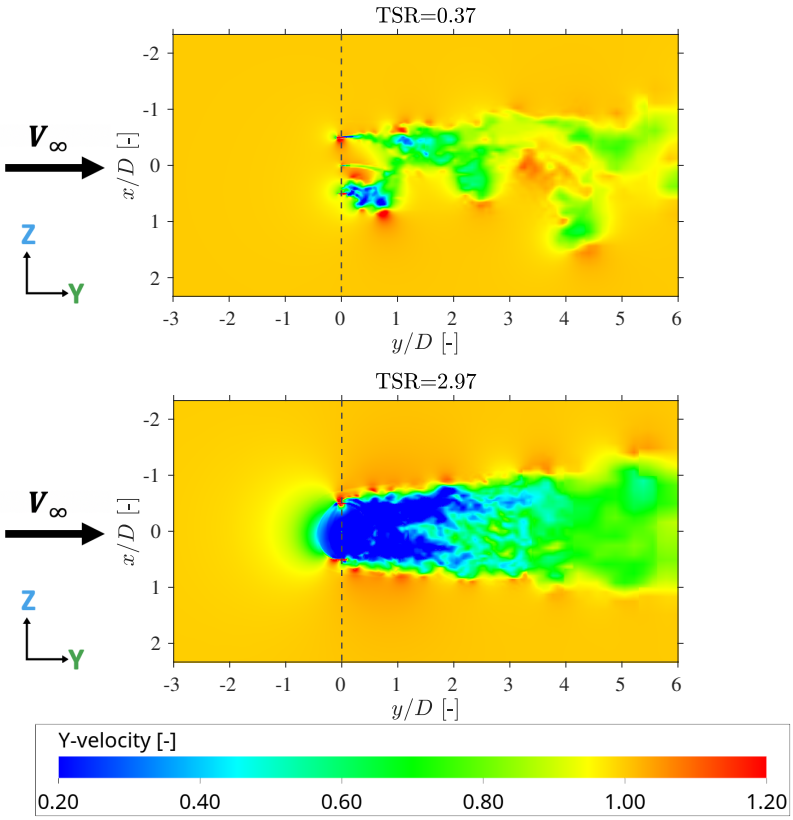

Figure 4.19: Instantaneous streamwise (Y-axis) velocity contour, non-dimensionalised with V_∞, in the YZ plane showing the evolution of wake in the VAWT flowfield for setup 1

The TSR-induced variations in streamwise velocity have direct implications for VAWT performance. The lower velocity regions correlate to reduced effective angles of attack (AoA) on the downwind blades, reducing the thrust and torque generated, evidenced in the trends observed in Figure 4.14. As TSR increases, an initial increase in downwind C_T is reported which can be attributed to an increased blockage effect by the blades. However, this trend is reversed at higher TSRs due to a significant reduction in downstream wake velocity. When combined with the behaviour of upwind C_T, increasing TSR results in an overall increase in VAWT thrust. For the highest C_P, flow blockage needs to be at an optimal level, which happens at TSR = 2.23 in the present study. At higher TSRs, the intense blockage in the streamwise flow also implies higher energy in the turbulent structures as seen in Figures 4.16 and 4.17. These structures exert unsteady loading on the blades, leading to

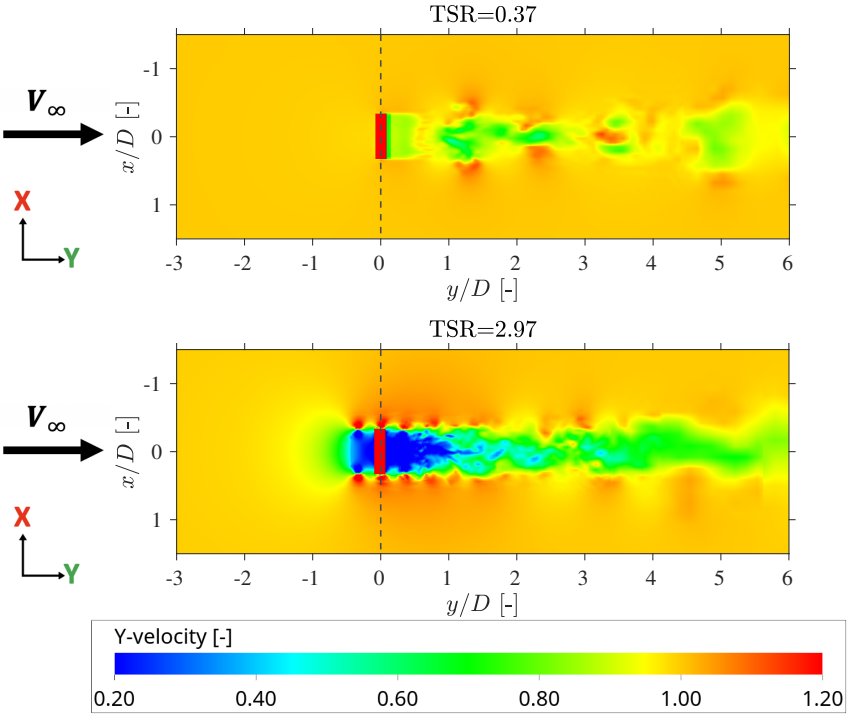

Figure 4.20: Instantaneous streamwise (Y-axis) velocity contour, non-dimensionalised with V_∞, in the XY plane showing the evolution of wake in the VAWT flowfield for setup 1

variations in C_T and C_P values as the blades rotate through the wake.

An increase in TSR is followed by an increase in the value of s for VAWT blade loading, which means the loading dominates on the upwind side of the rotor rotation. The above figures show that there is an expansion of the wake in the YZ plane while a contraction in the XY plane at high TSRs. In fact, at lower TSRs, the wake dissipates and disintegrates after a distance of approximately 3 to 4D downstream. This is similar to results reported by Tavernier [92] using an Actuator Cylinder Model. Such behaviour has implications for the spatial configuration of VAWT clusters, suggesting that the placement of downstream VAWTs can be optimised closer to their upstream counterparts by shifting them along the axial direction (X-axis) by operating the latter at higher TSRs with a high s value.

The peak operational efficiency of a VAWT cluster may not always be realised at the optimal TSR of individual VAWTs. Instead, the optimal cluster efficiency, potentially suboptimal on a per-VAWT basis, may result from the balance between the performance characteristics of adjacent VAWTs and their spatial arrangement. Consequently, a denser configuration of VAWTs, made feasible by exploiting high-TSR wake behaviour, could be particularly beneficial for installations with spatial constraints, such as urban rooftops, conserving space within the unsteady and confined flow environments characteristic of built environments.

Figure 4.21 provides a quantitative depiction of the streamwise velocity distribution along the Z-axis (lateral direction) within the YZ plane, for TSRs of 1.12, 2.23, and 2.97. As TSR increases, there is a visible decrease in streamwise velocity within the wake region, which aligns with the aerodynamic blockage effects presented in previous figures. At TSR 2.97, the lateral extent of the wake on the YZ plane is notably broader compared to TSR 1.12, which corroborates with the wake expansion observed in the streamwise velocity contours in Figure 4.19.

The effect of stronger coherent vortices is visible as pronounced drops in velocity, with a higher drop at higher TSR, at approximately -0.5 and 0.5 z/D (i.e. on both the leeward and windward sides of the turbine, respectively). This agrees with the vortices visualisation in Figures 4.13, 4.16 and 4.17.

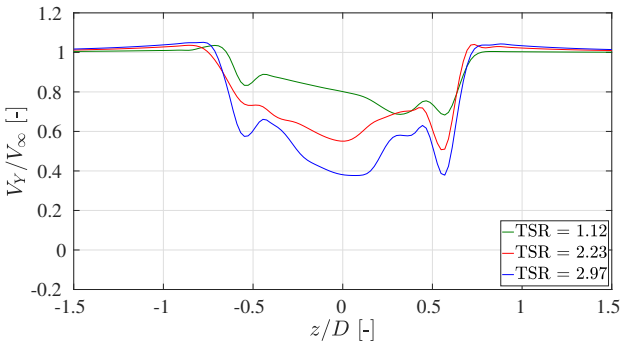

(a) Located at 0.5D from the VAWT axis

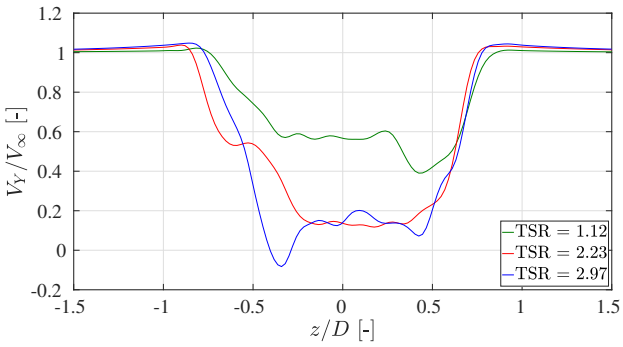

(b) Located at 1D from the VAWT axis

Figure 4.21: Streamwise (Y-axis) velocities, averaged over a rotation, plotted along the Z-axis (lateral direction) in YZ plane, comparing the extent of the wake for TSR 1.12, 2.23 and 2.97

The asymmetry of the VAWT wake can be seen (also visible in the velocity contours in Figure 4.19), around the $z/D = 0$ line, which is an inherent characteristic of the VAWT flow field [256].

Figure 4.22 presents the temporal behaviour of unsteady pressure data sampled over a single rotor rotation at two distinct spatial locations: one coincident with the rotor plane at (0,0,7D) and the other away from the plane at (4D,0,7D). The recorded data integrate the contributions of both the rotating blades and the central tower. The location situated away from the rotor plane experiences both a reduced amplitude in pressure fluctuations and reduced high-frequency pressure fluctuations when compared with the location on the rotor plane.

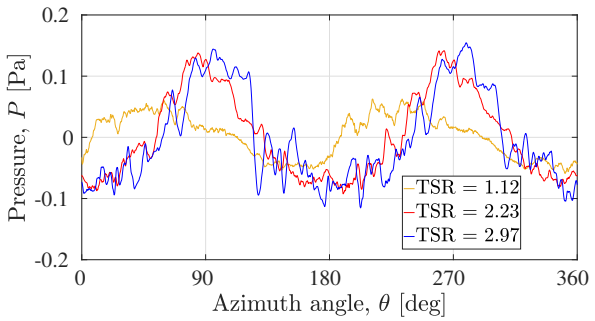

(a) Point A (X,Y,Z) = (0,0,7D)

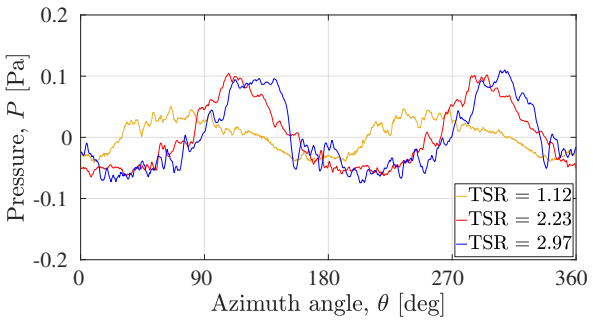

(b) Point B (X,Y,Z) = (4D,0,7D)

Figure 4.22: Raw unsteady pressure data for the overall VAWT comparing 3 different TSRs

Further analysis as the TSR is increased shows two trends. Firstly, there is a notable increase in the magnitude of the pressure fluctuations during a single rotation at both points of interest.

Secondly, particularly at the TSR of 2.97, the high-frequency pressure fluctuations are significantly higher than the lower TSRs. Such observations indicate that higher TSRs exhibit increased BVI/BWI, consequentially increasing unsteady loads and pressure perturbations on the blade surfaces.

For a thorough analysis of the effect of TSR on noise generation, noise spectra are depicted in Figure 4.23 at the two locations (0,0,7D) and (4D,0,7D), comparing four different TSRs, plotted with a frequency resolution (Δf) of 10 Hz. The noise spectra are not plotted below the human hearing range (20 Hz) where some blade passage frequency (BPF) peaks are observed. An overall look at the spectral data shows a clear trend: an increase in TSR correlates with an increase in PSD values over the whole frequency range of interest. This correlation is consistent with the increased aerodynamic loading on the blades (C_T), since under the low Reynolds number (Re) conditions ($< 5 \times 10^5$) typical for VAWT operations, the noise generation is predominantly attributable to blade loading noise, as compared to blade thickness or quadrupole noise [127]. The increase in blade loading directly translates to amplified pressure fluctuations at any location in the VAWT far-field, a phenomenon shown by the unsteady pressure profiles observed in Figure 4.22.

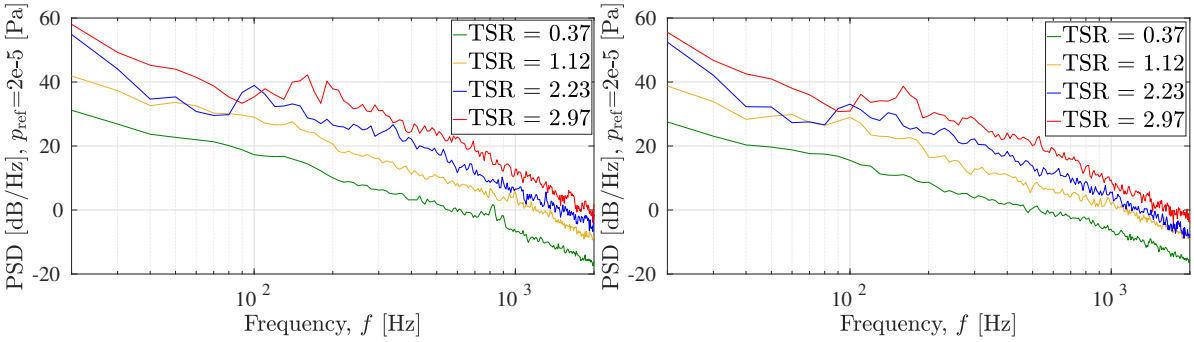

(a) Point A (X,Y,Z) = (0,0,7D) (b) Point B (X,Y,Z) = (4D,0,7D)

Figure 4.23: Noise spectra for the overall VAWT comparing 4 different TSRs, for setup 1

To gain a deeper understanding of noise generation in VAWTs, it is crucial to examine the various noise-generating mechanisms involved [47, 261]. The spectral distribution of noise ranges across various frequency domains, each dominated by distinct aerodynamic phenomena. Within the lower frequency spectrum (20-100 Hz), the predominant acoustic contributions come from the blade passage frequency (BPF) and its harmonics. This frequency range is intrinsically linked to the cyclic motion of the blades as they produce thrust and torque. In the mid-frequency spectrum (100-600 Hz), a series of peaks are observed which is related to the Laminar Boundary Layer - Vortex Shedding (LBL-VS) noise [53], particularly prominent at reduced Reynolds numbers ($Re < 5 \times 10^5$). The characteristic tonal noise results from the vortex shedding phenomenon, sustained by a feedback mechanism. Mitigation of this noise can be achieved through the usage of a boundary layer zig-zag trip on the blade surfaces to force an earlier transition from laminar to turbulent flow [261].

At higher Reynolds numbers ($Re > 5 \times 10^5$), Turbulent Boundary Layer - Trailing Edge (TBL-TE) noise is a major source of noise. This arises as the turbulent flow over the blade surface encounters the surface discontinuity at the trailing edge, scattering pressure variations as noise. However, under the low-Re operating conditions prevalent in the current study, as reported in Table 4.3, the TBL-TE noise is expected to be significantly less. Further into the high-frequency spectrum (600-1000 Hz and above), the principal source of noise is attributed to Blade-Vortex Interaction (BVI) noise. This is a direct consequence of the vortices, inherent to the VAWT wake, interacting with the blades during their downwind half of rotation, causing substantial high-frequency aerodynamic loads on the blade surfaces. Therefore, increasing TSRs increase the BVI noise, which is consistent with the increased intensity of BVI inferred from the preceding analyses on wake aerodynamics.

Figure 4.24 shows the Overall Sound Pressure Level (OSPL) directivity in both the YZ and XY planes for the VAWT operating at the four distinct TSRs. The pressure values are sampled along a circular arc consisting of 36 equidistant points, each point residing $7D$ away from the VAWT centre ([0,0,0]).

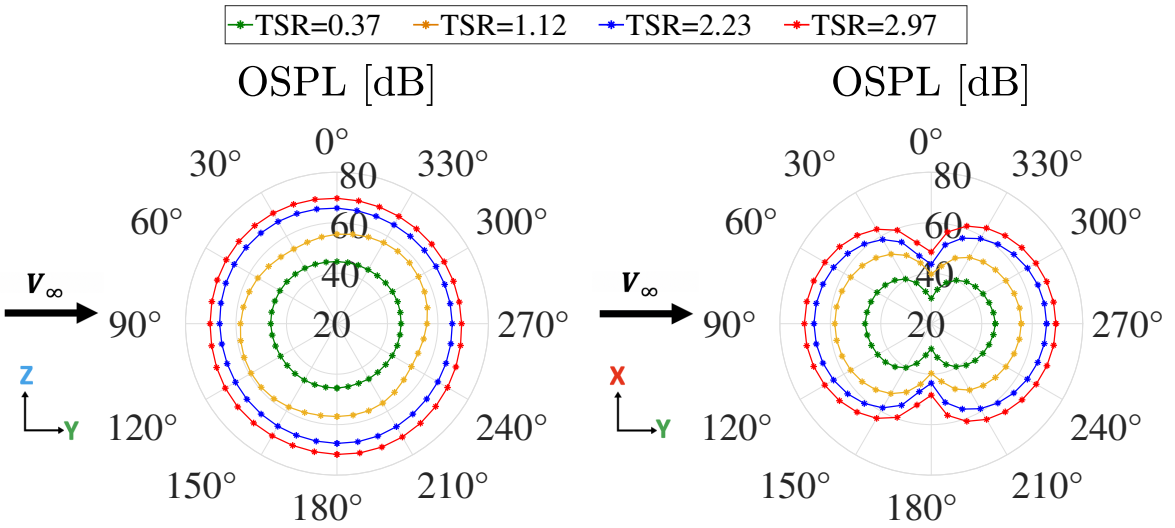

(a) YZ plane at blade mid-span location

(b) XY plane, coinciding with VAWT rotational axis

Figure 4.24: Directivity plot of overall sound pressure level (OSPL) comparing 4 different TSRs, along a circular array of 36 points situated at a distance of $7D$ from the origin of VAWT ([0,0,0]) for setup 1

Being consistent with the prior observations on noise spectra and C_T values, a trend can be observed: an increase in TSR invariably leads to an increase in noise at every sampled location. Specifically, within the YZ plane, a peak in noise levels is observed between azimuth angles of 90° and 120°. This is indicative of the high blade loading prevalent at the most upstream point of the rotor rotation (seen in Figure 4.15), a pattern that remains consistent across the TSR spectrum, albeit more pronounced at lower TSRs. For the XY plane, the maximum noise levels are observed also at the most upstream blade position, at the mid-span of the blade. This trend persists across all TSRs evaluated, underscoring a similar directivity pattern irrespective of the TSR.

4.4. Conclusions and Discussions

This study presents the results of a grid convergence study obtained using the Richardson Extrapolation (RE) method and flow physics study over a range of TSRs. The aim is to, firstly, increase the knowledge of grid convergence behaviour of a full 3D CFD simulation and study the inconsistencies and variation in convergence properties for the full operational range of Darrieus VAWT. The second aim is to have a better understanding of the physical phenomenon by studying detailed fluid dynamic interactions and noise sources in a VAWT flowfield. Two benchmark geometries are used, both having two straight airfoil-shaped blades. The first geometry has a higher solidity and lower aspect ratio than the second geometry. For both benchmarks, commercial software 3DS Simulia PowerFLOW 6-2020 is used which uses the Lattice Boltzmann/Very Large Eddy Simulation (LB-VLES) method for high-fidelity CFD calculations and the Ffowcs Williams and Hawkings (FW-H) acoustic analogy for calculation of far-field noise. This results in two setups: Setup 1 and 2 for the first and second geometry, respectively. Setup 3 also uses the second geometry but utilises the mid-fidelity Lifting Line Free Vortex Wake method (LLFVW). A range of TSRs is investigated for the grid convergence study. Re_c for all TSRs are below 1.5×10^5.

Thrust, cross-streamwise force coefficients and overall sound pressure level (OSPL) show much better grid convergence than torque coefficients. This means a coarser grid is enough to model blade loading and noise values, but a finer grid is required to model torque (or power) values. This is found to be true for both setups 1 and 2, although, setup 2 showed better convergence than setup 1 in each performance parameter. For setup 1, TSR = 2.23 reports better grid convergence than both TSR = 1.12 and 2.97, which means that VAWTs operating in different flow physics regimes (such as dynamic stall or parasitic drag) require different levels of grid refinement for accurate modelling of fluid dynamic interactions physics. Setup 3 with LLFVW results also shows these same observations on the grid convergence level, which shows that the mid-fidelity method can capture significant VAWT fluid dynamic interactions, as compared to the high-fidelity method. Grid convergence for noise spectra shows that variation in mid-to-high-frequency noise with different grids is higher than that of low-frequency noise, although the contribution to overall noise comes majorly from the low-frequency part.

Comparison of C_T, C_{Fz}, C_Q and C_P values in upwind and downwind halves of rotation show that the downwind half always performed worse than the upwind half, in all these performance parameters. For C_T, the difference between upwind and downwind halves increases as TSR increases. This is due to both blade-vortex interaction (BVI) and blade-wake interaction (BWI) for the blades in the downwind half, which gets stronger at higher TSRs. This is shown by both 2D flow contours of turbulent kinetic energy, vorticity magnitude and streamwise velocity, and 3D flow visualisation of coherent and incoherent vortex structures. In the case of C_Q, this difference initially increases and then decreases since at higher TSRs, upwind C_Q also starts decreasing due to a decrease in AoA and an increase in parasitic drag. Higher TSR also contributes to more noise due to an increase in unsteady blade loading values. This increase happens due to an increase in overall C_T values, contributing towards low-to-mid frequency noise, and due to an increase in BVI, contributing towards high-frequency noise. On a circular arc around the VAWT, noise is found to be highest at the most upstream location due to blade loading being largest around the same location.

Since VAWTs have a large 3D design space, further investigations are required into investigating the effect of geometrical parameters such as the number of blades, aspect ratio, blade design, etc. and flow parameters such as non-uniform inflow for both aerodynamic performance and noise generation. These parameters will be investigated in the next chapters.

5

Stand-alone VAWT II: number of blades

Summary

The aerodynamics and aeroacoustics of small-scale Darrieus VAWTs are investigated at chord-based Reynolds number below 4×10^5. A statistical temporal and grid convergence study is carried out for thrust and torque coefficients. Four different VAWTs are investigated having a different number of blades: 1, 2, 3 and 4, using the high-fidelity Lattice Boltzmann Method (LBM) and mid-fidelity Lifting Line Free Vortex Wake (LLFVW) method. Results show that the statistical temporal convergence was achieved much earlier for the 1-bladed rotor than for the 3-bladed rotor, using both methods. Power performance analysis showed that having more blades in VAWT generates more power at lower TSRs, while the opposite trend is observed at higher TSRs. The aerodynamic efficiency of each blade decreases as the number of blades increases, which also leads to a decreased amplitude of rotor loading variation in a single rotation. Both the mid-fidelity LLFVW and high-fidelity LBM capture these physical trends well. However, LLFVW is found to predict lower peak C_T and C_Q values in a single rotation and higher streamwise velocities in the wake, as compared to LBM. Additionally, the former predicts higher average power output than the latter and the discrepancy increases as the number of blades increases. In terms of noise, low-frequency BPF noise was found to be higher in VAWTs with fewer blades, while high-frequency noise was found to be higher in VAWTs with more blades. Overall Sound Pressure Level values revealed that overall noise increased with an increase in the number of blades except for the 4-bladed VAWT for which the noise decreased.

5.1. Introduction

In this chapter, we delve deeply into a critical, yet often underappreciated, aspect of vertical axis wind turbine (VAWT) design - the number of blades. Despite being a trivial parameter, it significantly influences the aerodynamic and aeroacoustic characteristics of VAWTs. Due to an increase in rotor solidity with number of blades, accurately capturing the complex 3D fluid dynamic interactions with a higher number of blades remains a challenge, especially when solely relying on low or medium-fidelity aerodynamic models. As such, an in-depth investigation of the effect of the number of blades on VAWT performance is essential for the development of efficient and low-noise VAWT designs and for optimising the design based on specific application requirements and local wind speeds experienced by a VAWT.

5.1.1. Literature Review

Some numerical and experimental studies have been conducted on the effect of blade number on the aerodynamic performance of VAWTs. The starting torque of the turbine is enhanced with an increase in the number of blades, leading to improved performance at low wind speeds. However, increasing the number of blades also results in a decrease in the overall aerodynamic efficiency due to the presence of blade-to-blade interactions and increased drag [280]. A study conducted by Maeda et al. [206] investigates the energy performance and aerodynamic forces at different numbers of blades through wind tunnel experiments using a NACA 0021 blade. They found that the power absorbed by the turbine depends on the upstream region of the azimuth angle and that the power coefficient decreases with an increase in the number of blades. They also found that two blades have a higher annual generating capacity in high wind velocity areas, while five blades are better in low wind velocity areas.

In another series of wind tunnel experiments measuring flow field characteristics using Laser Doppler Velocimetry (LDV), Li et al. [191] found that the relationship between wind turbine power coefficient (C_P) and tip speed ratio varies with blade pitch angle and the blade pitch angle that yields the maximum C_P differ with blade number. Furthermore, an increase in blade number resulted in a decrease in the maximum value of C_P and an increase in the maximum value of torque coefficient C_Q. The flow field around the rotor showed asymmetry in the streamwise velocity vector in the VAWT wake, and the presence of a backflow region downstream was confirmed for 4- and 5-bladed wind turbines. Additionally, the width of the velocity deficit zone increases with an increase in blade number. The author suggested further detailed investigation to better understand the complex flow phenomena around the rotor. Similar conclusions were made by the same author [207] when studying the effect of variation in solidity by varying the number of blades.

Qu et al. [267] investigated the effect of blade number on the self-starting performance of a VAWT with self-adapting wind speed (VAWT-SWS). A prototype with 2, 3, and 4 blades was compared to a Darrieus straight-bladed wind turbine. The wind tunnel experiment showed that VAWT-SWS had better self-starting performance than the Darrieus turbine, and increasing the blade number improved the static self-starting performance but degraded the dynamic self-starting performance. Sunyoto et al. [325] conducted an experimental study of an H-Darrieus wind turbine model in a wind tunnel and concluded that the number of blades affects the rotor rotation, with more blades making it easier for the turbine to rotate at low wind speeds and also resulting in shorter performance and higher torque. Additionally, a three-bladed rotor was found to have a more stable performance compared to a two- or four-bladed rotor. Similar conclusions are made by Howell et al. [148] who also conducted wind tunnel experiments for a 2- and 3-bladed VAWT.

Delafin et al. [94] used a vortex model to predict the power coefficient and forces on five different vertical axis wind turbines with two, three, and four blades. Results showed that increasing the number of blades while keeping the same solidity had similar power curves, and increasing the number of blades from two to three significantly reduced torque, thrust, and lateral force ripples

at all tip speed ratios. Adding a third or fourth blade further reduced these ripples but increased the frequency of maximum loads. Mohamed [234] performed numerical simulations to validate against experimental measurements, and the unsteady flow around the VAWT was quantitatively and qualitatively analysed using the realizable k-ϵ turbulence model. The study investigated over 20 different symmetric and non-symmetric airfoil shapes to obtain the best possible performance, as measured by the power coefficient C_P. The S-1046 airfoil is found to be the best one since it increases C_P by 26.83% and efficiency by 10.87% compared to the conventional design using NACA airfoils. This performance gain for the new design is found to be true for the full operating range of the VAWT. Using S-1046, a low solidity design is recommended for the H-rotor Darrieus turbine to obtain a wider operating range since increasing solidity (by increasing the number of blades) from 0.1 to 0.25 decreased the TSR operating range from 10 to 6.

Sun et al. [324] used a numerical method to investigate the effects of fixed offsetting pitching angles and changing blade numbers in vertical axis wind turbines (VAWTs). The results showed that at high wind speeds, a turbine with 3-blades had a larger mean power coefficient. The self-starting time was not significantly affected by the offsetting pitching angle or blade number at low wind speeds, but at high wind speeds, a turbine with more blades and an offsetting pitching angle of -4 degrees had a smaller self-starting period. A turbine with 5-blades and an offsetting pitching angle of -4 degrees suppressed or delayed vortex formation around the blade surface, resulting in a higher mean power coefficient and acceleration.

Rezaeiha et al. [276] employed high-fidelity CFD simulations to investigate the impact of rotor solidity (by varying blade chord length) and the number of blades on VAWT performance. The findings reveal that augmenting both parameters causes the optimal tip speed ratio (TSR) to shift towards lower values and increases the maximum attainable power. The power augmentation is attributed to Reynolds number effects, as the increment in power is absent when solidity is elevated at a constant Reynolds number (Re_c). Furthermore, enhancing solidity leads to an asymptotic rise in the rotor thrust coefficient, an upsurge in the turbine upstream induction field, an increase in velocity deficit in the wake, an expansion of the wake, and a reduction in turbine wake length. Additionally, an analytical correlation was established between optimal TSR and solidity based on vast amounts of numerical and experimental data.

Castelli et al. [65] found that an increase in blade number led to a lower peak power coefficient (in contrast to Rezaeiha et al. [276] who predicted an increase in peak power coefficient) and a shift to lower tip speed ratios, indicating reduced efficiency. However, larger numbers of blades allowed the maximum power coefficient to be reached at lower angular velocities. The aerodynamic effect of increasing the blade number was similar to that of inclining a three-dimensional blade, and further investigation of this analogy is suggested. The study also found that increasing the blade number led to a decrease in the radial component of the aerodynamic forces, which is desirable from a structural perspective. Further analysis is suggested to investigate the combined effect of aerodynamic radial force and centrifugal force on the structural behaviour of the blade. Similar studies have been conducted by previous researchers regarding the impact of the number of blades [110, 139, 176, 192, 208, 235, 284, 320, 329, 364].

The aeroacoustic performance of VAWTs is also affected by the number of blades (or solidity). Higher blade numbers can potentially result in a higher noise level due to increased blade loading [236], which is a significant concern for their use in urban areas. A definitive correlation has been established between exposure to turbine noise and the resultant perception of annoyance [98, 362]. Understanding the effect of blade number on the acoustic signature of VAWTs is therefore essential for developing low-noise designs.

Mohamed [236] investigated the aerodynamic noise sources associated with VAWTs by performing CFD simulations in ANSYS Fluent and post-processing the pressure data using Ffowcs Williams and Hawkings (FW-H) methodology. The results indicate that reducing solidity from 0.25 to 0.1 can

reduce noise emissions by 7.6 dB. In addition, the S-1046 airfoil has been identified as the most optimal due to its minimal aerodynamic noise emissions. Another study by Mohamed [238] evaluated the J-shaped airfoil for a VAWT in the normal operating range of TSR = 2 to 6. Fifteen airfoil configurations were tested, including three standard airfoils and twelve J-shaped designs with different cut ratios. The results show that overall the J-shaped design did not contribute to any performance improvement but it reduced the torque and power output coefficients for all solidities and increased the noise emissions at low frequencies (less than 2500 Hz), as compared to standard airfoils. Increasing solidity increased the noise generated at all frequencies due to an increase in blade drag and pressure fluctuations due to the J-shaped design.

Rasekh et al. [272] shows that increasing solidity increases the interference of blades with the wake region, reducing the effective angle of attack and increasing steady loading noise at blade passage frequency (BPF). However, averaged Overall Sound Pressure Level (OSPL) values (calculated by averaging the value of OSPL at different azimuthal positions) increase as solidity decreases. The study also highlights the importance of using precise numerical methods for aeroacoustic performance investigation. Various other authors have worked on characterising the VAWT noise generated using numerical and experimental methods [45, 97, 124, 237, 319].

Despite the existing body of literature on the influence of the number of blades on the performance of VAWTs, there is still a lack of detailed flow physics studies utilizing full 3D high-fidelity numerical simulations studying unsteady blade loads and downstream turbulent near-wake. Additionally, the capability of mid-fidelity analytical aerodynamic methods in capturing the effects of blade number on VAWT force and flow field remains poorly understood. In the field of aeroacoustics, a significant research gap exists in determining the impact of the number of blades (or solidity) on VAWT aeroacoustic performance, as well as identifying the various noise sources that affect the overall noise signature. Hence, this chapter aims to address these gaps in fundamental knowledge and contribute to the development of low-noise and high-performance VAWT designs.

5.1.2. Research objectives

Given the above-mentioned motivation, the current investigation's objective is to take the first step towards creating a multi-fidelity simulation framework for studying the effects of blade number on the aerodynamic and aeroacoustic performance of VAWTs. To achieve this, high-fidelity 3D aerodynamic simulations based on the Lattice Boltzmann Method (LBM) are conducted for straight-bladed VAWTs. Subsequently, aeroacoustic post-processing is performed using the Ffowcs Williams and Hawkings (FW-H) methodology to calculate the far-field noise. Additionally, mid-fidelity aerodynamic simulations are carried out using the Lifting Line Free Vortex Wake (LLFVW) model.

The study will draw important conclusions regarding the significance of different fluid dynamic interactions for different blade numbers, that can be captured by mid-fidelity and high-fidelity aerodynamic methods. The high-fidelity simulation campaign enables accurate resolution of the flow around the VAWT blades and in the wake, thus enabling the study of 3D effects on the force and flow field for different blade numbers. These effects include non-uniform blade loading and non-uniform wake, dynamic stall, blade-vortex interaction, and wake recovery. On the other hand, the mid-fidelity simulation offers simplified modelling of the flow field using vortex lifting lines and will help in the fundamental understanding of the 3D effects for different blade numbers.

A comparative analysis between the two methods will help in comprehending the possibility of the mid-fidelity method as a potential substitute for the high-fidelity method, thereby conserving significant time and computational resources. This assessment of the reliability and accuracy of the mid-fidelity solver is imperative for certain applications that do not necessitate a comprehensive examination of the VAWT flow and force field. This research also aims to bridge the gap in the literature regarding the optimal blade number for VAWTs in terms of both aerodynamic and aeroacoustic performance. The following research questions are formulated for this chapter:

Research Questions

- How does the number of blades affect VAWT performance parameters such as thrust, power, and far-field noise?
- How do the results for different number of blades obtained using the mid-fidelity and high-fidelity methods compare? What are the fluid dynamic interactions responsible for any differences observed?
- How do 3D effects of blade loading on thrust and power values, trailing and shed vortices, and wake dynamics vary for different number of blades?
- What are the key noise sources contributing to the aeroacoustic performance of VAWTs for different number of blades?

The chapter is structured as follows. Section 5.2 presents the computational setup of both mid-fidelity LLFVW and high-fidelity LBM, including VAWT geometrical properties, flow and grid settings. Section 5.3 reports the results obtained for the grid convergence study, detailed force and flow field analysis and aeroacoustic performance of the VAWT for the different number of blades. The last section 5.4 presents important conclusions of the study and a discussion on the understanding of the highly unsteady and turbulent VAWT fluid dynamic interactions.

5.2. Computational setup

A detailed account of the numerical and geometrical aspects of the simulation, including the description of the flow conditions and the generation of the computational grids is provided. This will help in establishing the reliability and accuracy of the numerical simulation, and it enables the reader to assess the validity of the results presented in the subsequent sections.

5.2.1. Geometry

This chapter employs a straight-bladed vertical axis wind turbine (VAWT) design with geometrical parameters that have been replicated from the study by Balduzzi et al. [22]. The results obtained by Balduzzi et al. have been utilised for the validation of a single-bladed rotor. Four configurations have been simulated to investigate the flow physics, with varying numbers of blades - 1, 2, 3 and 4. As an example, Figure 5.1 depicts the geometric model for the 2-bladed and 4-bladed rotors, while Table 5.1 presents the geometric values and operational conditions for all configurations. The VAWT solidity is set at 0.08 for the single-bladed rotor and increases proportionally to the number of blades. The rotor aspect ratio for all configurations is 1.46. The inclusion of additional blades (i.e., higher solidity) gives rise to stronger three-dimensional (3D) effects and increased blade-vortex interaction. The variations in these fluid dynamic interactions are expected to result in differences in the unsteadiness of VAWT blade loading, which, in turn, affects wake dynamics and aeroacoustic behaviour.

Table 5.1: VAWT geometry and operational settings

	Blade length (L)	**Rotor diameter (D)**	**Chord length (c)**	**Freestream velocity (V_∞)**	**Airfoil**
VAWT benchmark [22]	1.5 m	1.03 m	0.086 m	9 m/s	NACA 0021

The current chapter involves the high-fidelity Lattice Boltzmann Method (LBM) to simulate all the VAWT configurations. Each configuration is also simulated using the mid-fidelity Lifting Line

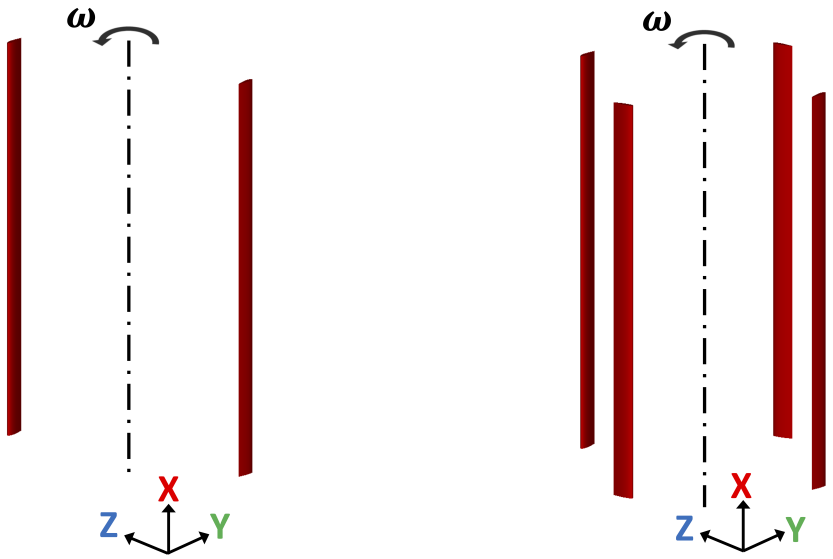

(a) 2-bladed (b) 4-bladed

Figure 5.1: VAWT configuration used in this chapter (Balduzzi [22])

Free Vortex Wake (LLFVW) method. Obtaining accurate and high-quality airfoil data is vital to produce precise results through low and mid-fidelity methods. To achieve this objective, a virtual geometry is derived from the NACA 0021 profile to account for the virtual camber effect [270]. This process is accomplished through the conformal transformation technique based on the chord-to-radius ratio, as described by Bianchini et al. [37]. The transformed airfoil is presented in Figure 5.2 (c). Lift and drag polars are obtained for Reynolds numbers ranging between 1×10^5 and 1×10^6 using XFoil [104]. This process employs an *NCrit* value of nine and forced transition at the leading edge of both the pressure and suction side. The airfoil static polar data is extrapolated to 360° angle of attack (AoA) using the Montgomerie method [241] to ensure a smooth extrapolation in the post-stall regime. An example of the 360° extrapolated polars is presented by Balduzzi et al. [22].

5.2.2. Numerical setup

A simulation volume is implemented, which comprises a cube with dimensions of $100D$ on each side. The Darrieus geometry is situated at the centre of this volume. The boundary conditions for the domain are shown in Figure 5.2 (a). At the velocity inlet, the velocity is set to the freestream velocity V_∞ in the direction of the Y-axis. An ambient pressure of 101.325 kPa is imposed at the pressure outlet. A no-slip boundary condition is applied to the blade surface. PowerFLOW generates a Cartesian volume grid around the individual solid components in the domain, beginning with the minimum hexahedral cell (voxel) size and a specified number of variable resolution (VR) levels. The VR levels range from fine to coarse, with a voxel size change factor of 2 between adjacent VRs which generated distinct VR regions. Figure 5.2 (b) shows this grid refinement when approaching the centre of the domain where the VAWT is located. The software employs an automatic algorithm to intersect the Cartesian mesh with the solid parts and produce a collection of polygons, or surfels, that represent the true surface of the body. To optimise computational efficiency, the present study employs 17 VR regions, with the highest resolutions near the blade surface with an offset, and coarser regions located farther from the blade and rotor. This approach enables computational effort to be allocated primarily to regions of interest and where high flow gradients are expected.

Figure 5.2 (a) displays three red spherical surfaces surrounding the rotor flow field, which act as FW-H permeable surfaces to eliminate hydrodynamic fluctuations in the VAWT wake vortices.

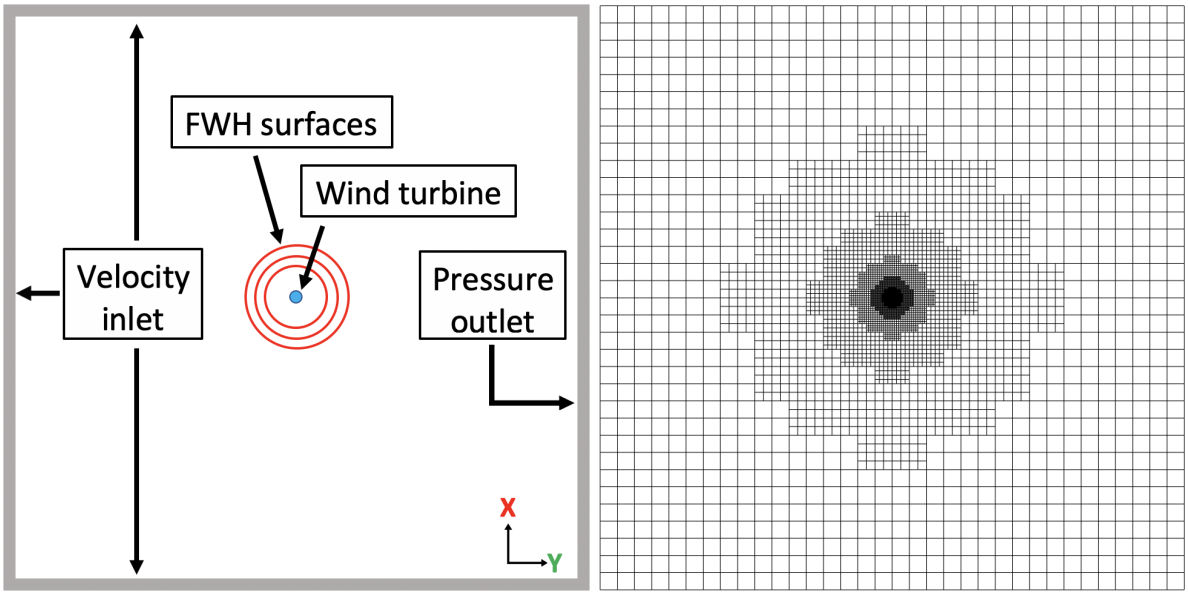

(a) Schematic representation of the high-fidelity domain (b) Cross-sectional view of the mesh for the whole domain

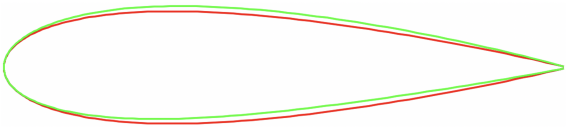

(c) Virtual camber airfoil (green) and original airfoil (red) for low-fidelity simulation

Figure 5.2: Computational setup used in this chapter

Averaging the sampled pressure data on all the permeable surfaces helps mitigate spurious noise sources by cancelling out the fluctuating components associated with the hydrodynamic sources. The blade surfaces of the VAWT are classified as FW-H solid surfaces. Acoustic sources, on the other hand, are less affected by this averaging process since their wavelengths are smaller than the former (or, frequency is higher). Although the use of the FW-H permeable formulation is a possible alternative, it has not been employed in this study since it is challenging to eliminate spurious noise sources from FW-H permeable data using only three spherical surfaces, for a VAWT. VAWT wake is highly unsteady and wake vortices are stronger than compared to the wake of HAWTs or propellers of similar size, which is the reason for its ineffectiveness. In future, a separate investigation will examine the application of the FW-H permeable formulation for VAWT aeroacoustics more effectively which is outside the scope of this thesis.

As explained in Chapter 4, analyzing the noise spectra up to 4000 Hz is sufficient for VAWT aeroacoustics while using a sampling time of 8 steady rotor rotations. Therefore, pressure data are sampled at a frequency of 8000 Hz, in accordance with the Nyquist criterion. To ensure accurate acoustic wave capture, a criterion of a minimum of 15 points per wavelength is selected [282]. Subsequently, noise spectra are calculated utilizing a Hanning window with 50% overlap and a frequency resolution (Δf) of 15 Hz, using the *pwelch* function in MATLAB.

For the LLFVW simulation, Table 5.2 outlines the values of the simulation parameters utilised.

5.2.3. Flow conditions and grid settings

For the present investigation, Table 5.3 illustrates the operational settings of the VAWT for the high-fidelity method (LBM). Tip speed ratio (TSR), defined as the ratio of the blade rotational speed and

Table 5.2: Simulation parameters used for the LLFVW method

	LLFVW
Freestream velocity V_∞	9 m/s
Density	1.225 kg/m^3
Kinematic viscosity	1.65 e-5 m^2/s
Blade discretisation	31 (cosine)
Azimuthal discretisation	3 deg
Full wake length	12
Vortex time offset	1 e-4 sec
Turbulent vortex viscosity	100

the freestream velocity, i.e. $\omega r/V_\infty$, where ω denotes the rotational speed in radians per second, r signifies the wind turbine radius and V_∞ represents the freestream velocity, is used as a measure of the system's operational condition. To change the TSR, V_∞ is maintained at a constant value of 9 m/s to match the reference value [22], while ω is varied to adjust the TSR value. This methodology aligns the investigation with practical scenarios, where the rotational speed is adjusted based on instantaneous wind speed measurements to ensure that the TSR remains close to the optimal point. The freestream velocity corresponds to the freestream Mach number of 0.026 and chord-based Reynolds number of 1.73×10^5. The high-fidelity method (LBM) is exclusively employed for the simulation of TSR = 3.3, while the mid-fidelity method (LLFVW) is utilised to simulate a spectrum of TSR ranging from 1 to 7. It should be noted that Re_c remains below 4×10^5 for all operational conditions considered in this study. The freestream turbulence intensity (I_t) and turbulence length scale (L_t) are assigned values of 0.1% and 1 mm, respectively. However, based on a prior study [63], it is anticipated that these two parameters will not have a substantial impact on the evolution of the unsteady flow field.

Table 5.3: VAWT operational settings for the high-fidelity method (LBM)

Parameter	**Value**
Tip speed ratio (TSR)	3.3
Rotations per minute (RPM)	550.71
Chord-based Reynolds number (Re_c)	1.73×10^5

In the context of the grid convergence study, each VAWT undergoes simulation at four different grid resolutions using high-fidelity LBM at the TSR of 3.3. Specifically, the variable resolution (VR) regions in proximity to the blade surface are characterised by varying voxel densities per chord for Grid 1, Grid 2, Grid 3, and Grid 4 resolutions, with the minimum and maximum voxel densities correspondingly allocated to Grid 1 and Grid 4. The resolutions of other VR regions are changed proportionally. The y^+ values and voxels per chord pertaining to all the grid resolutions are presented in Table 5.4. The y^+ value is a dimensionless parameter that indicates the distance of the first cell centre from the computational domain's wall in the wall-normal direction, while the voxels per chord specify the number of grid cells along the blade chord direction. Figure 5.3 shows the finest mesh around the blade with 4 different VRs for the setup with Grid 4.

Figure 5.4 shows the cross-sectional view of the mesh in the domain for Grid 4, both near the VAWT blades and further away from it. The minimum voxel sizes of Grid 1 and Grid 4 are 0.964 mm and 0.321 mm, respectively. For the 2-bladed VAWT, the number of fine equivalent voxels in the computational domain is 5.3 million and 45.4 million for Grid 1 and Grid 4, respectively. These fine equivalent voxels are determined by weighting the number of voxels by the time stepping rate, which is directly proportional to the mesh resolution level. It is noteworthy that a solution with a

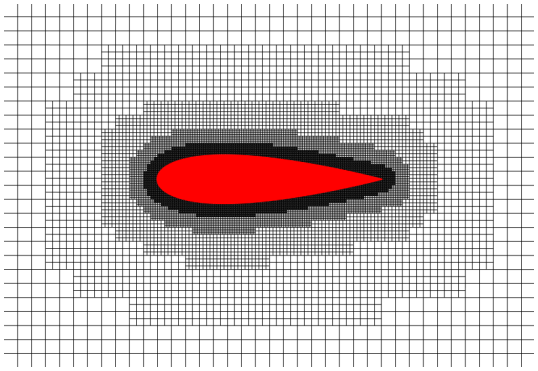

Figure 5.3: Cross-sectional view of the finest mesh around the blade

voxel size twice as coarse is updated using a time step that is twice as large, resulting in a computational cost that is two times cheaper.

Table 5.4: VAWT grid settings for the VAWT benchmark using high-fidelity LBM

		Grid 1	**Grid 2**	**Grid 3**	**Grid 4**
VAWT benchmark [22]	y^+	100	62.5	50	33.3
	Voxels per chord	8.9×10^1	1.42×10^2	1.78×10^2	2.67×10^2

The CPU hours required for simulating 12 rotor rotations (1.31 s) using Grid 1 and Grid 4 for the 2-bladed VAWT are 2613 and 44720, respectively, using a Linux workstation equipped with an AMD Ryzen Threadripper 3990X Gen3 64 Core 128GB DDR4 3GHz platform. Both the fine equivalent voxels and CPU hours vary proportionally with the number of blades for different VAWT configurations. Furthermore, the physical time step for Grid 1 and Grid 4 corresponds to a Courant-Friedrichs-Lewy (CFL) number of 1 in the finest VR level and is 4.53×10^{-6} s and 1.51×10^{-6} s, respectively. The integral and time-varying behaviour of the VAWT thrust coefficient (C_T) and torque coefficient (C_Q) are reported and grid convergence parameters are analysed for all the above-mentioned cases. These coefficients are defined as:

$$C_T = \frac{T}{0.5\rho A V^2}\,, \tag{5.1}$$

$$C_Q = \frac{Q}{0.5\rho A V^2 R}\,, \tag{5.2}$$

where, T and Q are VAWT thrust and torque respectively, ρ is the air density, A is swept area ($D \times L$) where is D is rotor diameter and L is blade length, R is rotor radius and V is freestream velocity. Using high-fidelity LBM, Power Spectral Density (PSD) spectra and Overall Sound Pressure Level (OSPL) values are also reported and analysed.

5.3. Results

5.3.1. Temporal and grid convergence study

Figure 5.5 reports a subset of the results to depict the temporal convergence characteristics of thrust coefficient (C_T) and torque coefficient (C_Q) for two distinct VAWT configurations, namely the 1-bladed and 3-bladed rotor, as obtained using high-fidelity LBM and mid-fidelity LLFVW method. The values reported in these figures are representative of the overall rotor, comprising all blades in a rotor.

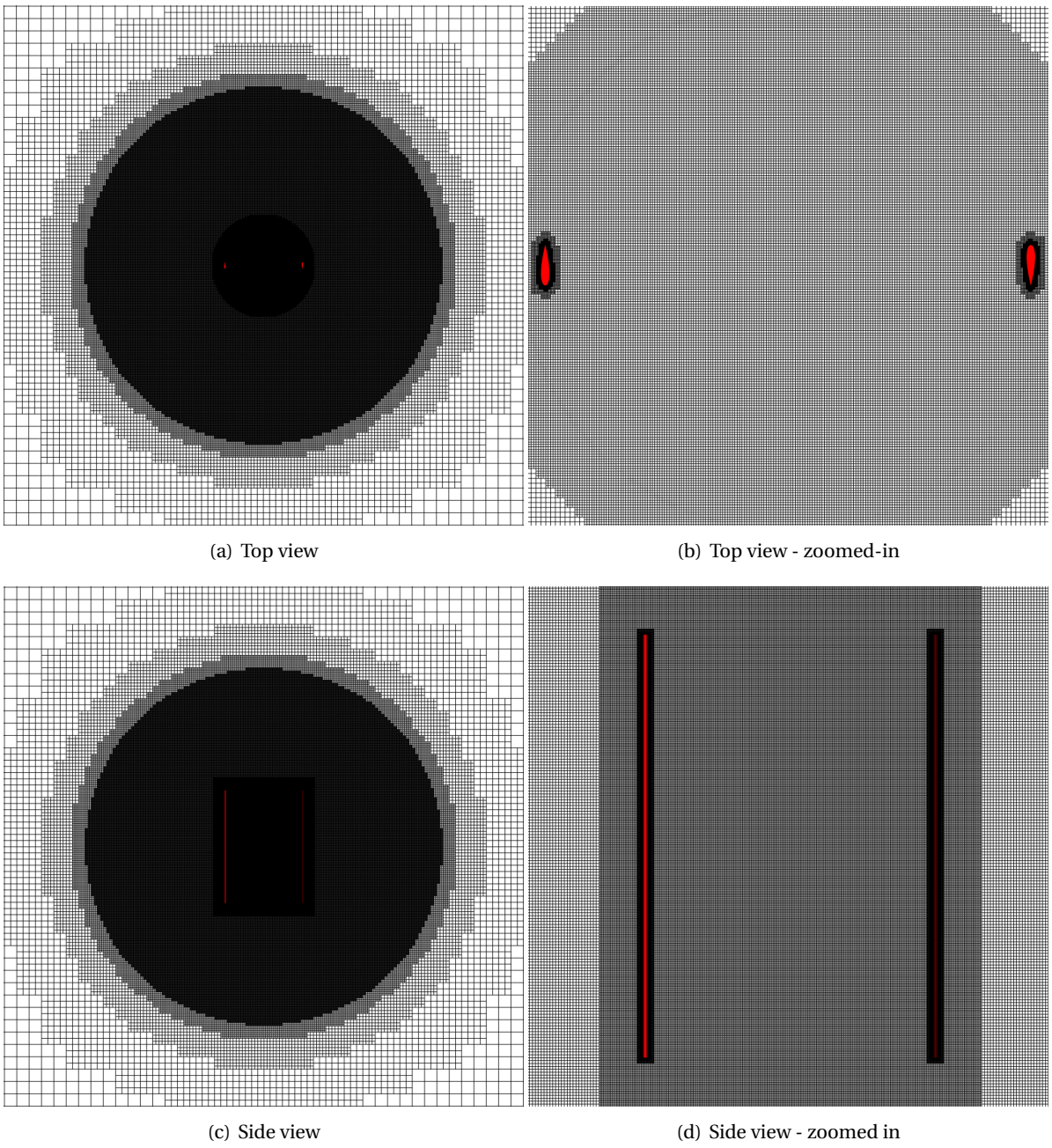

(a) Top view

(b) Top view - zoomed-in

(c) Side view

(d) Side view - zoomed in

Figure 5.4: Cross-sectional view of the mesh for the high-fidelity LBM simulation

The uncertainty values (u) presented in each figure are calculated as a percentage of the standard deviation of thrust and torque values averaged over a complete rotation. These uncertainty values represent the level of uncertainty or variability in the calculated thrust and torque coefficients over time due to the inherent unsteadiness and randomness in the fluid dynamic interactions. Lower values of u indicate a higher level of confidence in the simulation results, suggesting that the simulation has achieved temporal convergence. All u values shown are calculated after the 10th rotor rotation for LBM and the 20th rotor rotation for LLFVW.

The figures indicate that the statistical temporal convergence for the 1-bladed rotor is achieved much earlier than that for the 3-bladed rotor, as observed for both the LBM and LLFVW methods. Specifically, convergence is achieved after approximately 4 rotations for LBM and 6 rotations for

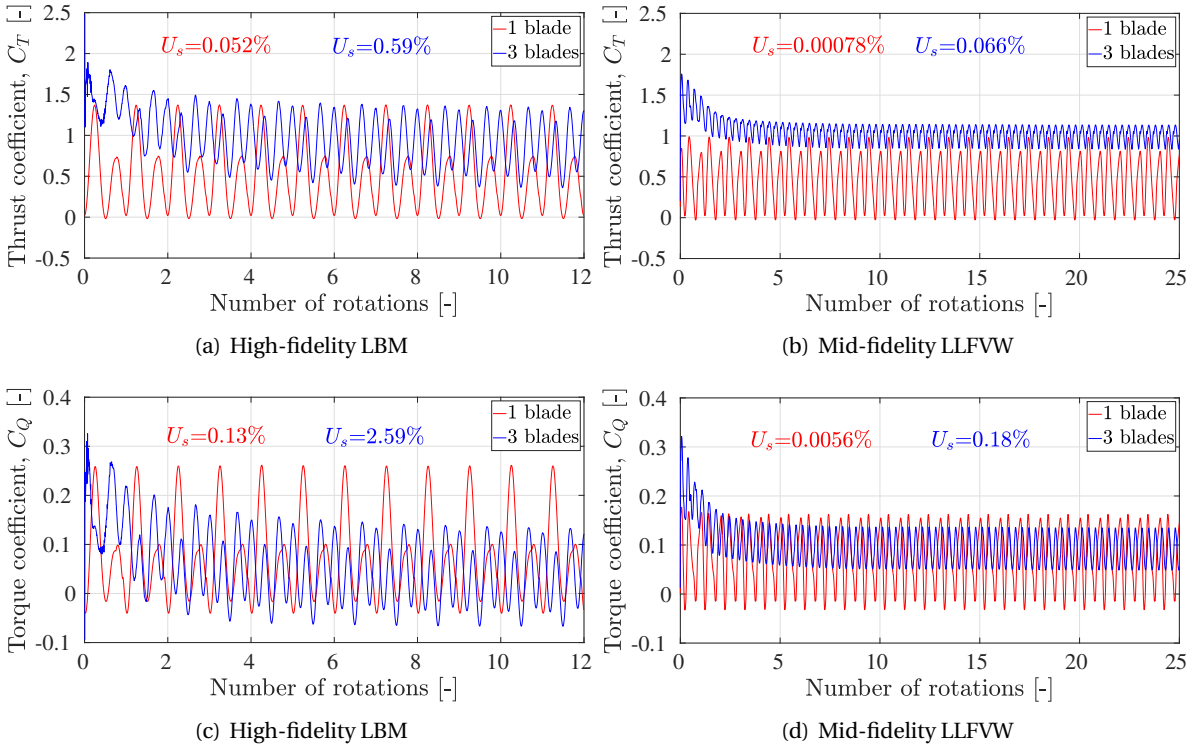

(a) High-fidelity LBM (b) Mid-fidelity LLFVW

(c) High-fidelity LBM (d) Mid-fidelity LLFVW

Figure 5.5: Statistical temporal convergence study for VAWT thrust coefficient C_T and torque coefficient C_Q using the high-fidelity LBM and mid-fidelity LLFVW; the values are representative of the overall rotor

LLFVW in the case of the 1-bladed rotor, while it takes around 8 rotations for LBM and 10 rotations for LLFVW for the 3-bladed rotor. The low uncertainty values (u) for both configurations confirm the temporal convergence. Notably, the mid-fidelity LLFVW method accurately captures this unsteady phenomenon in a VAWT force field, as demonstrated by the convergence results. Interestingly, these findings are in contrast to the outcomes reported by Rezaeiha [274], wherein over 20 rotations were required to achieve temporal convergence in a high-fidelity CFD simulation. It is worth mentioning that in this study, the LBM simulations for the finer grid are seeded using the results from the coarser grid, which might have contributed to the decreased transient period. This seeding approach aligns with the current best practice for simulations of this nature, where a coarser resolution is first simulated for a minimum of 10 rotor rotations. The final frame of this simulation is then utilised to seed a finer resolution simulation, which is executed with an initial settling time of a few blade-passage periods [63].

Similarly, Figure 5.6 illustrates the temporal convergence of unsteady pressure data acquired using the high-fidelity LBM for the finest Grid 4. The data is collected at a specific location in the blade mid-span plane of rotation, situated at a distance of $7D$ from the VAWT centre, in the lateral direction. To conserve computational resources, the pressure data is recorded starting from the 6th rotation. It can be observed that temporal convergence is achieved after the 6th rotation for both 2-bladed and 4-bladed rotors. In this study, all subsequent results are reported on data obtained after the 10th rotation for the high-fidelity LBM and the 20th rotation for the mid-fidelity LLFVW.

Two VAWT configurations, 1-bladed and 2-bladed rotor, are simulated by employing the four different grids. Figure 5.7 presents the outcomes of the grid convergence study conducted for C_T and C_Q of the overall rotor. Such studies help to check that the results are independent of the numerical grid used. The resolution is represented by the grid spacing h, which is normalised with respect to the blade chord c; h corresponds to the smallest grid (voxel) size in the numerical domain. Addition-

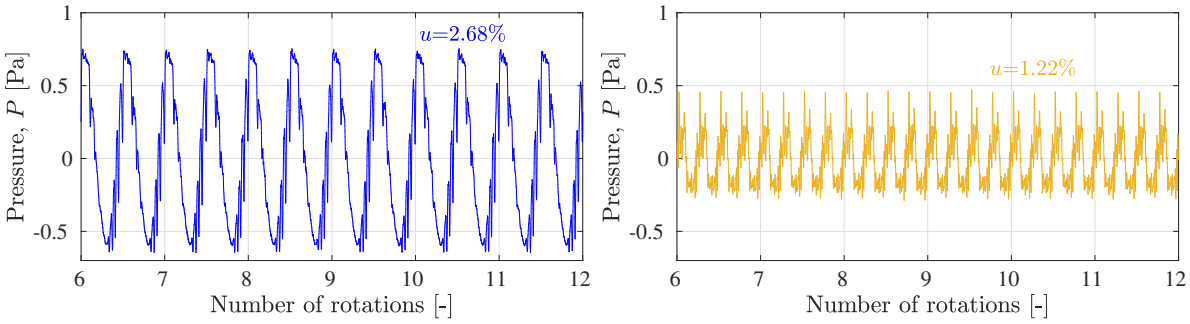

(a) 2-bladed (b) 4-bladed

Figure 5.6: Statistical temporal convergence study for unsteady pressure data at TSR = 3.3 at location (X,Y,Z)=(0,0,7**D**), using the high-fidelity LBM for the finest Grid 4

ally, the figure presents the values obtained by utilizing the Richardson extrapolation method [304], which enables the calculation of C_T and C_Q when $h/c \rightarrow 0$. Physically, this indicates the approach towards the continuum limit or using an infinite number of cells in the Cartesian grid. Grid convergence index (GCI) is also shown in each figure and is calculated based on the difference between two adjacent grid resolutions and provides an estimate of the error in the solution [220, 304].

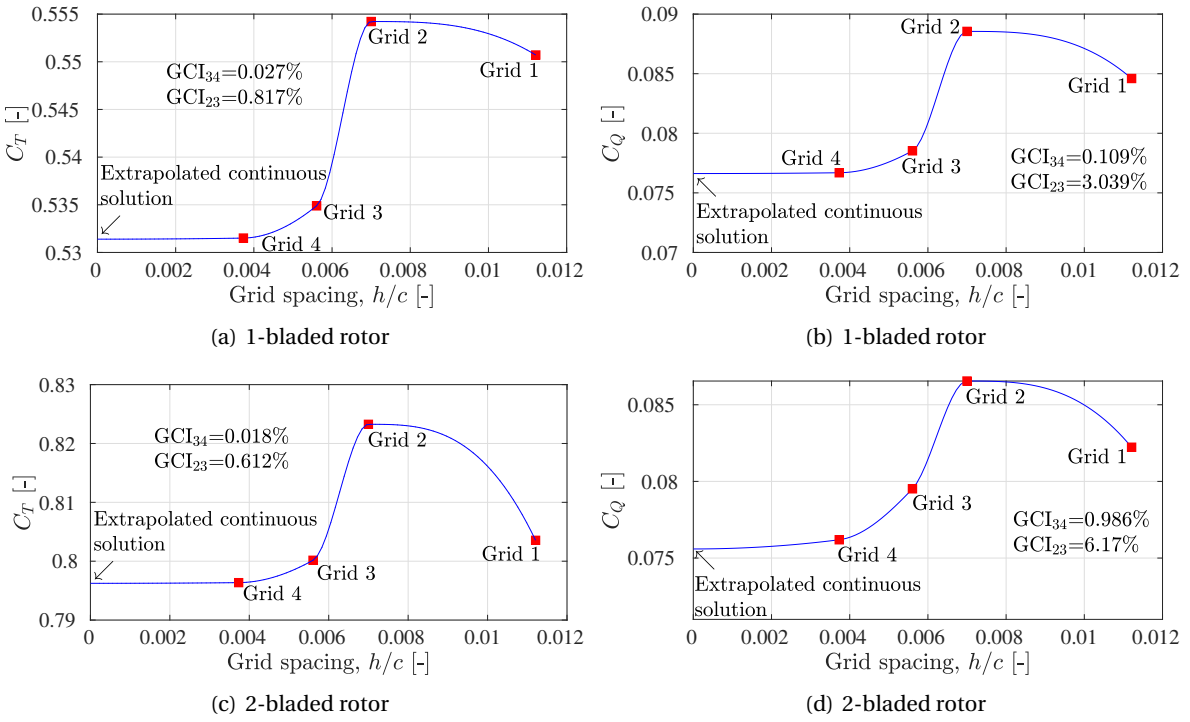

(a) 1-bladed rotor (b) 1-bladed rotor

(c) 2-bladed rotor (d) 2-bladed rotor

Figure 5.7: Grid convergence study for VAWT thrust coefficient C_T and torque coefficient C_Q using the high-fidelity LBM

The grid convergence analysis reveals that for both VAWT configurations, the thrust values exhibit better grid convergence than the torque values. The 2-bladed rotor exhibits the lowest GCI for thrust values between Grid 3 and Grid 4. Overall, this indicates that a coarser grid is sufficient to capture converged blade loading values, while a finer grid is required to capture converged blade torque (or power) values. This is due to the significant dependence of skin friction and drag values on the variation in y^+ values. Accurate prediction of airfoil drag for both low and high Reynolds number flows is still an area of active research [347]. GCI_{34} is consistently lower than GCI_{23} for all

cases, indicating that increasing the grid resolution can lead to more accurate and reliable results for the present VAWT setup since the difference related to the numerical grid reduces as the grid resolution increases. However, it should be noted that this is not always the case with VAWT simulations, and the relative GCI values can vary depending on the simulated tip speed ratio and rotor scale [304]. Furthermore, the previous chapter 4 revealed that the grid convergence of Overall Sound Pressure Level (OSPL) was found to be comparable to that of thrust values and better than torque values [304].

Based on the grid convergence analysis, Grid 4 is deemed to be converged for both aerodynamics and aeroacoustics and is chosen for all future numerical simulations. It is considered sufficient to provide an accurate physical analysis of VAWT fluid dynamic interactions.

5.3.2. Numerical validation

Figure 5.8 presents a comparison of the power coefficient (C_P) values for the 1-bladed VAWT obtained using the mid-fidelity LLFVW and high-fidelity LBM methods, with reference results reported by Balduzzi et al. [22]. The reference dataset consists of the mid-fidelity LLFVW method for a range of TSR and high-fidelity 3D CFD method using the compressible formulation of the Reynolds-averaged Navier-Stokes (RANS) equations only for a TSR of 3.3. This will help validate the current setup (using both mid and high-fidelity methods) with the standard method commonly used in high-fidelity rotor aerodynamics, RANS. The results obtained using the current LLFVW method exhibit a close agreement with the reference data, predicting the typical VAWT power curve shape [256, 261] over the entire range of TSR. The C_P value at TSR = 3.3, obtained using the high-fidelity LBM corresponding to Grid 4, closely matches all three other results. The validation of both the current numerical setups is deemed to be very good, not only with the published results but also among each other. Consequently, they can be used to further investigate VAWT fluid dynamic interactions and wake dynamics. The forthcoming sections will compare the results obtained using mid-fidelity and high-fidelity methods for varying numbers of blades, highlighting the effects of differences in numerical modelling as the VAWT geometry changes.

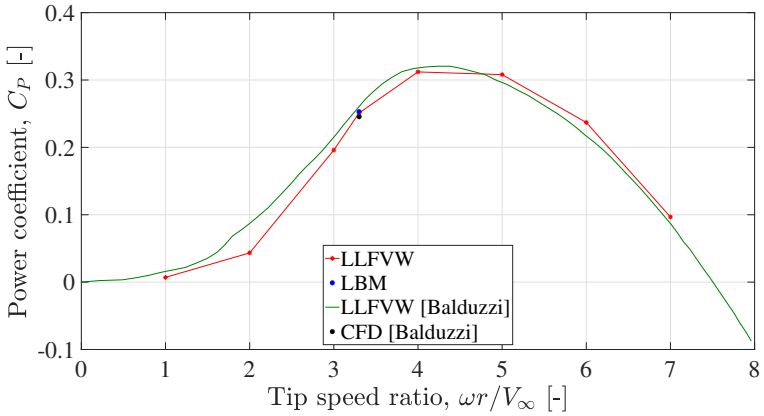

Figure 5.8: C_P values for a 1-bladed VAWT obtained using mid-fidelity LLFVW and high-fidelity LBM compared with the results reported by Balduzzi et al. [22]

5.3.3. Effect of number of blades

Fig. 5.9 shows the values obtained for power coefficient (C_P) and thrust coefficient (C_T) for the four different VAWT configurations with different number of blades - 1, 2, 3 and 4. While mid-fidelity LLFVW is simulated for the full range of TSR, high-fidelity LBM is simulated only for TSR of 3.3. It is expected that high-fidelity simulations at TSR = 3.3 combined with mid-fidelity simulations at all TSRs will be enough to provide insights into fluid dynamic interactions of a VAWT when the number

of blades is varied.

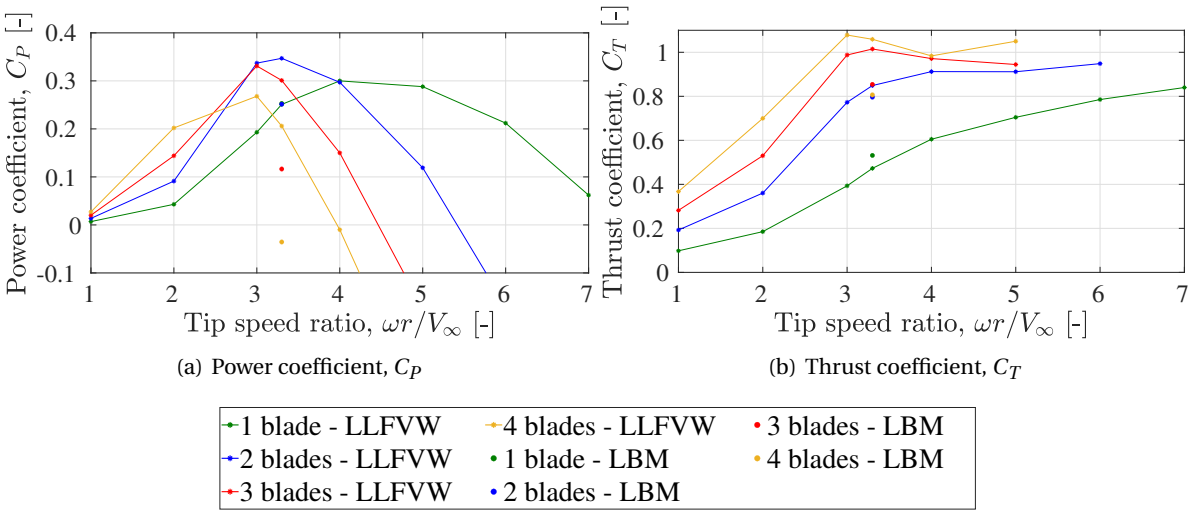

(a) Power coefficient, C_P (b) Thrust coefficient, C_T

Figure 5.9: Power and thrust curve obtained for different number of blades using the mid-fidelity LLFVW and high-fidelity LBM; line plot is for mid-fidelity LLFVW and single dot at TSR = 3.3 is for high-fidelity LBM

The mid-fidelity results show a few trends. At lower TSRs, having more blades generate more power while the opposite trend is shown at higher TSRs. Blades act more independently at low TSR and increasing solidity negligibly increases blade-wake/blade-vortex interaction; this helps increase total blade tangential loading and power produced. As TSR increases, induction factor and blade-wake/blade-vortex interaction also increase and increasing solidity worsens the tangential loading on each blade and the overall rotor power. Consequently, higher solidity leads to a sharper gradient in C_P values than lower solidity cases, over the whole range of TSR. These observations also show that VAWT design optimisation with an objective to increase its self-starting capability (C_P at very low TSR) will therefore lean towards higher solidity designs. For the same reasons, C_P values show that optimal TSR decreases as the number of blades increases. These characteristics are an established norm for a VAWT [172] and are modelled fairly well by the mid-fidelity method. The thrust coefficient (C_T) shows an increasing trend both with an increase in TSR and the number of blades, except for the 4-bladed rotor where it starts showing an asymptotic or decreasing trend.

At TSR = 3.3, LBM shows a small 0.63% decrease of C_P when the number of blades increases from 1 to 2, and then 53.7% and 130.5% decrease when it further increases to 3 and 4, respectively. The power generation goes negative for the 4-bladed rotor, signified by a >100% decrease for the 4-bladed VAWT. LBM shows a monotonic decrease of C_P as the number of blades increases, whereas, LLFVW shows an initial increase for the 2-bladed VAWT and then decreases for 3-bladed and 4-bladed VAWTs. Looking at the trends of C_P vs TSR, this means that LBM results will predict the peak C_P to reach at a lower TSR than the LLFVW results. Furthermore, at TSR = 3.3, the difference between C_P values of LBM and LLFVW increases with an increasing number of blades, where the former always predicts lower values than the latter (except for the 1-bladed rotor where the match is very good). While the difference in C_P is only 0.0021 (0.79%) for the 1-bladed rotor, LBM predicts lower values by 0.11 (27.5%), 0.15 (61.32%) and 0.25 (117.23%) for the 2, 3 and 4-bladed rotor, respectively.

For C_T at TSR = 3.3, LBM shows an increase of 49.84% when the number of blades increases from 1 to 2, and then an increase of 7.25% and a decrease of 5.6% when it further increases to 3 and 4, respectively. Comparing LBM and LLFVW results, the difference in C_T values shows a similar trend as C_P; the difference increases as the number of blades increases, except for the 2-bladed VAWT. The difference is 11.1%, 6.6%, 15.8% and 23.9% in the order of increasing number of blades. Furthermore, LBM predicts lower values than LLFVW, except for the 1-bladed VAWT.

The observed trends indicate that the LLFVW method does not capture the complex 3D effects in a VAWT flow and force field as strongly as LBM, especially when the number of blades increases. This is especially true in the near-wake region where blade-wake and blade-vortex interactions (BWI/BVI) are significant. This discrepancy is not unexpected, given the inherent differences in fluid modelling between the two methods. C_T values using the LLFVW method start showing an asymptotic or decreasing trend at higher TSRs and for the higher number of blades (the conditions in which BWI/BVI becomes significant). Even at a low TSR value of 3.3, LBM results show a similar trend where the 4-bladed rotor thrust is lower than the 3-bladed rotor. This again reiterates the point that LBM captures the effect of BWI/BVI more strongly than LLFVW. An investigation with an even higher number of blades is recommended for future studies, which can provide much clearer insights into the effect of the number of blades on C_T variation.

Figure 5.10 illustrates the variation in C_T and C_Q plotted for the overall rotor for a complete 360° azimuth, using high-fidelity LBM and mid-fidelity LLFVW at TSR = 3.3. The figure also shows the average value over the rotation corresponding to the values shown in Figure 5.9. The analysis reveals that as the number of blades increases, the amplitude of variation in thrust and torque values decreases, resulting in smoother overall rotor loading variation. This is attributed to the distribution of rotor loading over more blades as the number of blades increases. Specifically, at any given instant, the peak loading of one blade in the upwind part of the rotation is balanced by a reduced loading of another blade in the downwind part of the rotation.

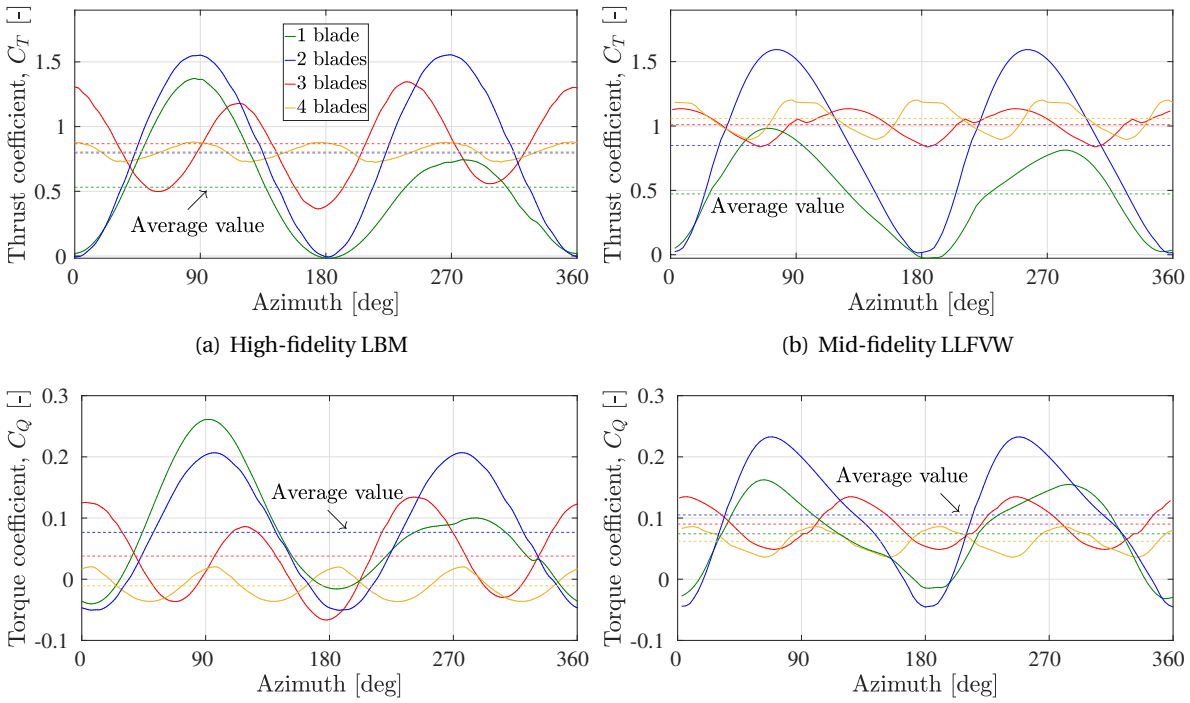

(a) High-fidelity LBM

(b) Mid-fidelity LLFVW

(c) High-fidelity LBM

(d) Mid-fidelity LLFVW

Figure 5.10: Variation of thrust coefficient C_T and torque coefficient C_Q for the overall rotor over a complete rotation, using the high-fidelity LBM and mid-fidelity LLFVW at TSR = 3.3

The mid-fidelity LLFVW and high-fidelity LBM both model this physical behaviour well. However, when comparing the peak C_T and C_Q values in the upwind and downwind parts of rotation, LLFVW predicts lower values as compared to LBM, except for the 2-bladed rotor where there is a good match. This behaviour can also be seen in statistical time convergence results in Figure 5.5. This is attributed to the XFOIL polar values (C_l and C_d vs angle of attack α) taken in the analytical formulation of LLFVW, which affect the blade angle of attack and induced velocity. These results

suggest that the polars need to be modified accordingly by introducing empirical corrections in future investigations. Another option is to use the airfoil polar values for 360° AoA obtained using wind tunnel experiments [300].

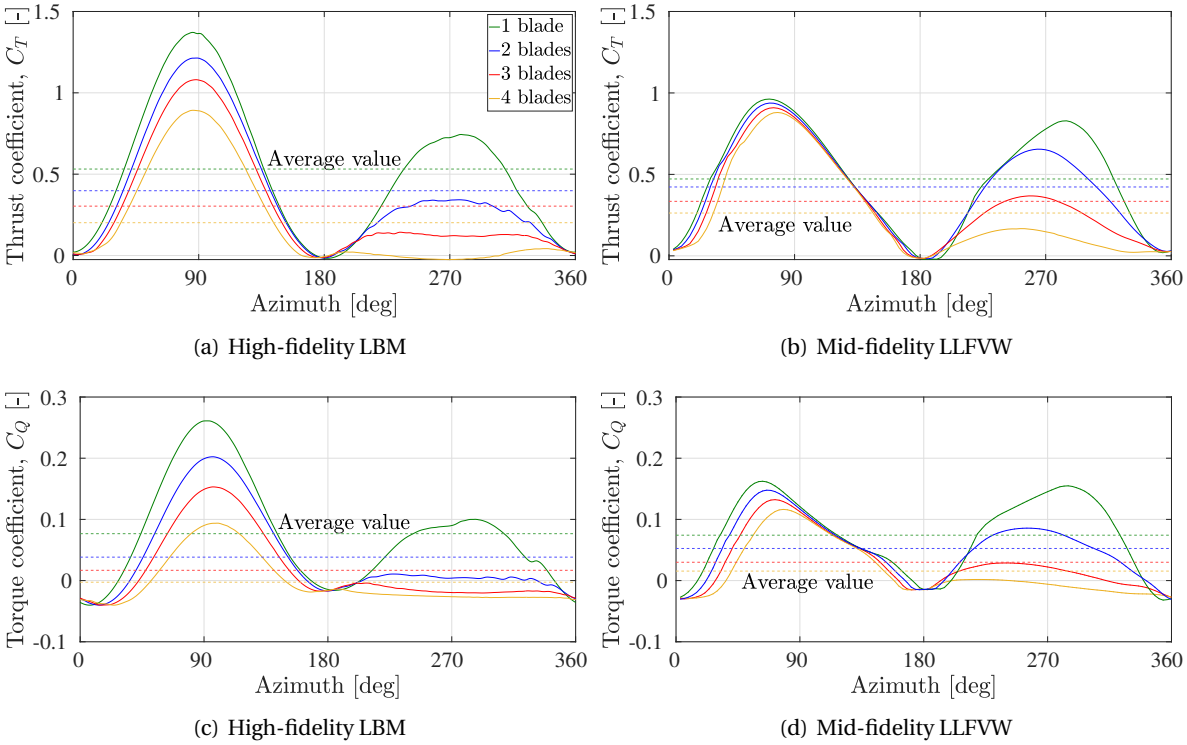

(a) High-fidelity LBM

(b) Mid-fidelity LLFVW

(c) High-fidelity LBM

(d) Mid-fidelity LLFVW

Figure 5.11: Variation of thrust coefficient C_T and torque coefficient C_Q for a single blade over a complete rotation, using the high-fidelity LBM and mid-fidelity LLFVW at TSR = 3.3

Figure 5.11 illustrates the variation in C_T and C_Q plotted for a single blade for a complete 360° azimuth, using high-fidelity LBM and mid-fidelity LLFVW at TSR = 3.3. The figure also shows the average value over the rotation. Both C_T and C_Q values decrease monotonically with an increase in the number of blades for both upwind and downwind parts of the rotation. This is attributed to increased blade-wake and blade-vortex interactions, leading to degraded individual blade aerodynamic efficiency. Furthermore, downstream blades produce lower thrust and torque values than the upstream blades, with the contribution from the latter, as part of the overall rotor, increasing as the number of blades increases. The results also indicate negative torque production for a significant part of the downwind rotation in the case of the 4-bladed rotor, indicating the extent of blade-wake interaction in high-blade-number VAWTs. Both the mid-fidelity LLFVW and high-fidelity LBM model these physical characteristics well. However, when comparing C_T and C_Q values, a mismatch between LBM and LLFVW peak values is observed, with LLFVW predicting lower values, and this mismatch is slightly improved with an increase in the number of blades. Furthermore, the investigation reveals that LBM shows a more pronounced degradation in blade performance with an increase in the number of blades, than LLFVW, and this highlights a potential drawback of vortex-based methods in modelling unsteady aerodynamic interactions and wake dynamics.

The above-mentioned unsteady force field characteristics can also be visualised from Figure 5.12 which presents the variation in blade normal forces (F_n) for a single blade over the equivalent 3D cylindrical surface traced by the VAWT blades at TSR = 3.3. The variation in values over both azimuthal and spanwise directions are compared for all four VAWT configurations between LBM and LLFVW.

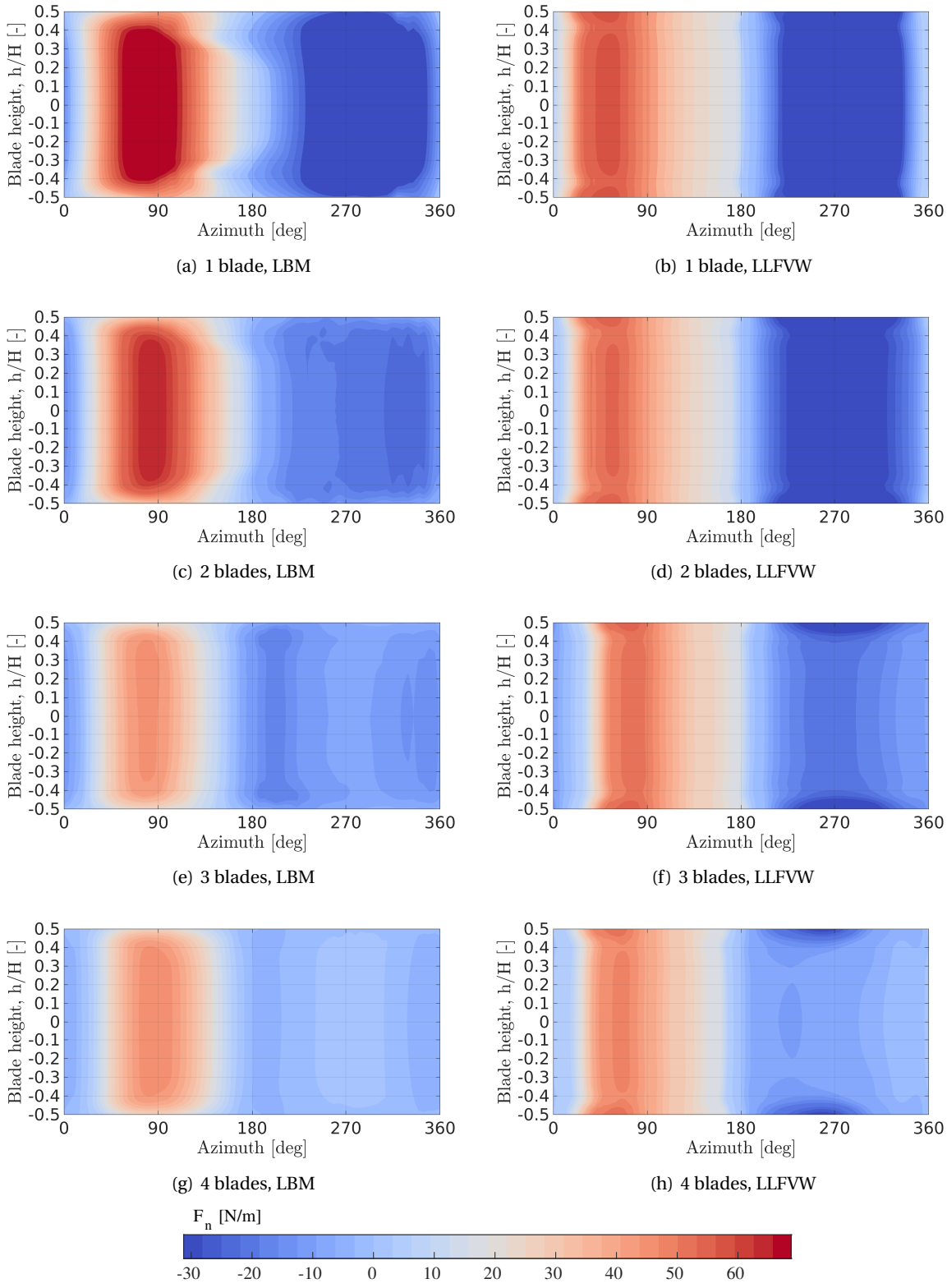

(a) 1 blade, LBM

(b) 1 blade, LLFVW

(c) 2 blades, LBM

(d) 2 blades, LLFVW

(e) 3 blades, LBM

(f) 3 blades, LLFVW

(g) 4 blades, LBM

(h) 4 blades, LLFVW

Figure 5.12: Normal force contour for a single blade over azimuthal and spanwise directions, using the high-fidelity LBM and mid-fidelity LLFVW, at TSR = 3.3

The analysis reveals that normal blade forces degrade in the downwind part of rotation as compared to the upwind part, which is well captured by both methods for all VAWT configurations.

Moreover, the decrease in peak normal forces and the increase in the contribution of the upwind part, as compared to the downwind part, with an increase in the number of blades can also be observed. However, the two methods differ in two aspects. Firstly, LLFVW predicts lower peak values of normal blade forces both in the upwind and downwind parts of rotation, as compared to LBM. This discrepancy is reflected in the thrust and torque values of a single blade and overall rotor seen earlier in Figure 5.11 and 5.10, respectively. Secondly, the 3D effects of tip vortices on the force field are more pronounced with LBM than with LLFVW, as can be seen around h/H of -0.5 and 0.5 in Figure 5.12. This observation further supports the conclusion that mid-fidelity vortex methods may not accurately model 3D fluid dynamic interactions, although the trends are consistent with those of the high-fidelity LBM method.

To better understand the blade-wake and blade-vortex interactions and their effect on the overall rotor performance, visualizing the 3D VAWT flowfield is crucial. Figure 5.13 provides insight into instantaneous vortices in the downstream part of the VAWT flowfield using iso-surfaces of the λ_2 criterion (λ_2 = -500 1/sec^2). The visualisation is done for the TSR of 3.3. As the number of blades increases, the large vortex structures, consisting of the coherent shed and trailing (tip) vortices, and smaller incoherent vortex structures increase proportionately in the flowfield. The flow field becomes highly turbulent due to the dense and complex vortex structures. The shed vortices originate at 0° and 180° azimuth and are due to the change in the direction of the airflow around the blade as it moves from the downwind to the upwind part of the rotation and vice versa. The coherent tip vortices shed from the tip of each blade are particularly significant and its effect is seen in Figure 5.12 around h/H of -0.5 and 0.5. The tip vortices convect downstream and create a spiral flow pattern, also known as "vortex ring", that wraps around the axis of the turbine. The density of these vortices in the vortex ring increases as the number of blades increases.

As the large vortex structures convect downstream, they experience wake expansion and gradually break down into smaller-scale structures due to flow instabilities and spatial modulation, which eventually dissipate and are mixed into the surrounding fluid [12, 196]. As the number of blades increases, the increase in blade vortex interaction leads to a disturbance in the ideal pressure and loading distribution along the chordwise and spanwise directions, resulting in the lower aerodynamic performance of the downstream blades as compared to the upstream blades (seen previously in Figure 5.10 and 5.11) which experience clean freestream flow.

Figure 5.14 presents a set of visualizations for the wake structures of VAWTs with different numbers of blades (1, 2, 3, and 4), simulated using the mid-fidelity LLFVW method at a TSR of 3.3. The left column depicts the vortex lines shed from the VAWT blades, while the right column illustrates the instantaneous 3D flow field using iso-surfaces of the Q-criterion (Q = 6 1/sec^2). The figures show the increase in vortex density and wake strength as the number of blades increases, similar to the high-fidelity results. At a lower number of blades, the wake structure is relatively simple, characterized by coherent and well-defined vortex lines and vortex structures with minimal secondary vortex formation. As the number of blades increases, the wake becomes complex with increased BWI/BVI and more convoluted iso-surfaces, resulting in denser structures and the breakup of primary vortices into secondary vortices.

The comparison between the mid-fidelity LLFVW and high-fidelity LBM results (in Figure 5.13) reveals several key differences in the modelling and visualization of vortices. The high-fidelity method provides higher resolution and captures finer details of the vortex structures compared to the mid-fidelity method. This allows for a more accurate representation of small-scale vortices and intricate flow features. The mid-fidelity method, while capturing the overall wake structure and major vortex interactions, lacks the resolution to depict smaller vortices and detailed flow dynamics. Nevertheless, both methods show increased wake complexity with a higher number of blades, indicating more intense vortex interactions and turbulence. The high-fidelity results depict a more nuanced picture of vortex breakup and fragmentation.

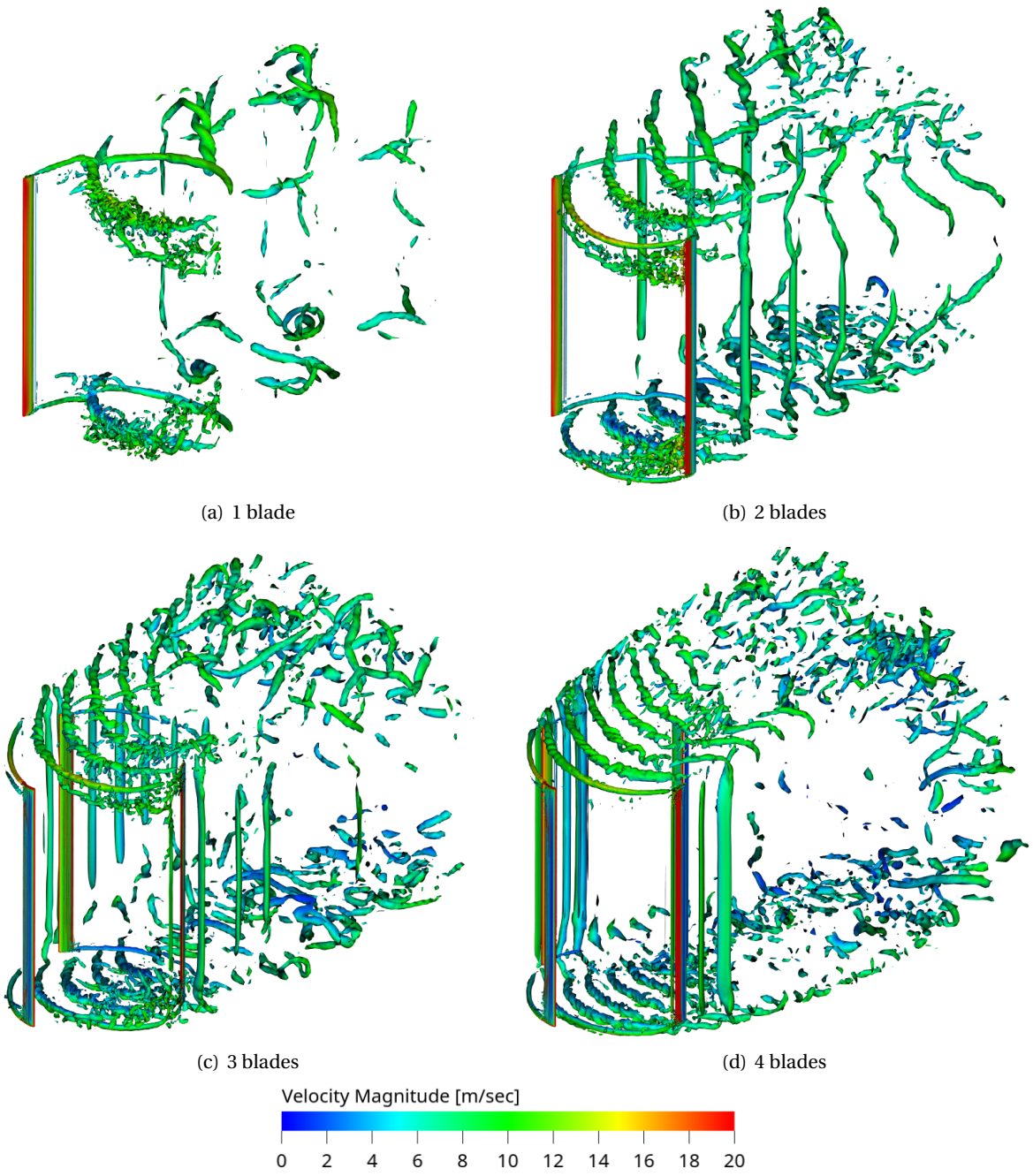

(a) 1 blade (b) 2 blades

(c) 3 blades (d) 4 blades

Figure 5.13: Instantaneous 3D flowfield using iso-surfaces of the λ_2 criterion (λ_2 = -500 1/sec^2) for vortices visualisation, using high-fidelity LBM, at TSR = 3.3

Figure 5.15 depicts the variation in the VAWT flowfield as TSR is varied, using the mid-fidelity LLFVW method for the 2-bladed VAWT. The results are similar to the effect of the number of blades since flow blockage and BWI/BVI are affected both by the number of blades and TSR. As TSR increases, the wake becomes more complex and dense with vortex structures, which is also seen in the results of Chapter 4. This has a degrading effect on the force field of blades, especially in the downwind part of rotation.

As the downstream wake becomes stronger, this leads to lower streamwise velocity values. This is shown in Figure 5.16 which presents the instantaneous streamwise velocity contours in the VAWT

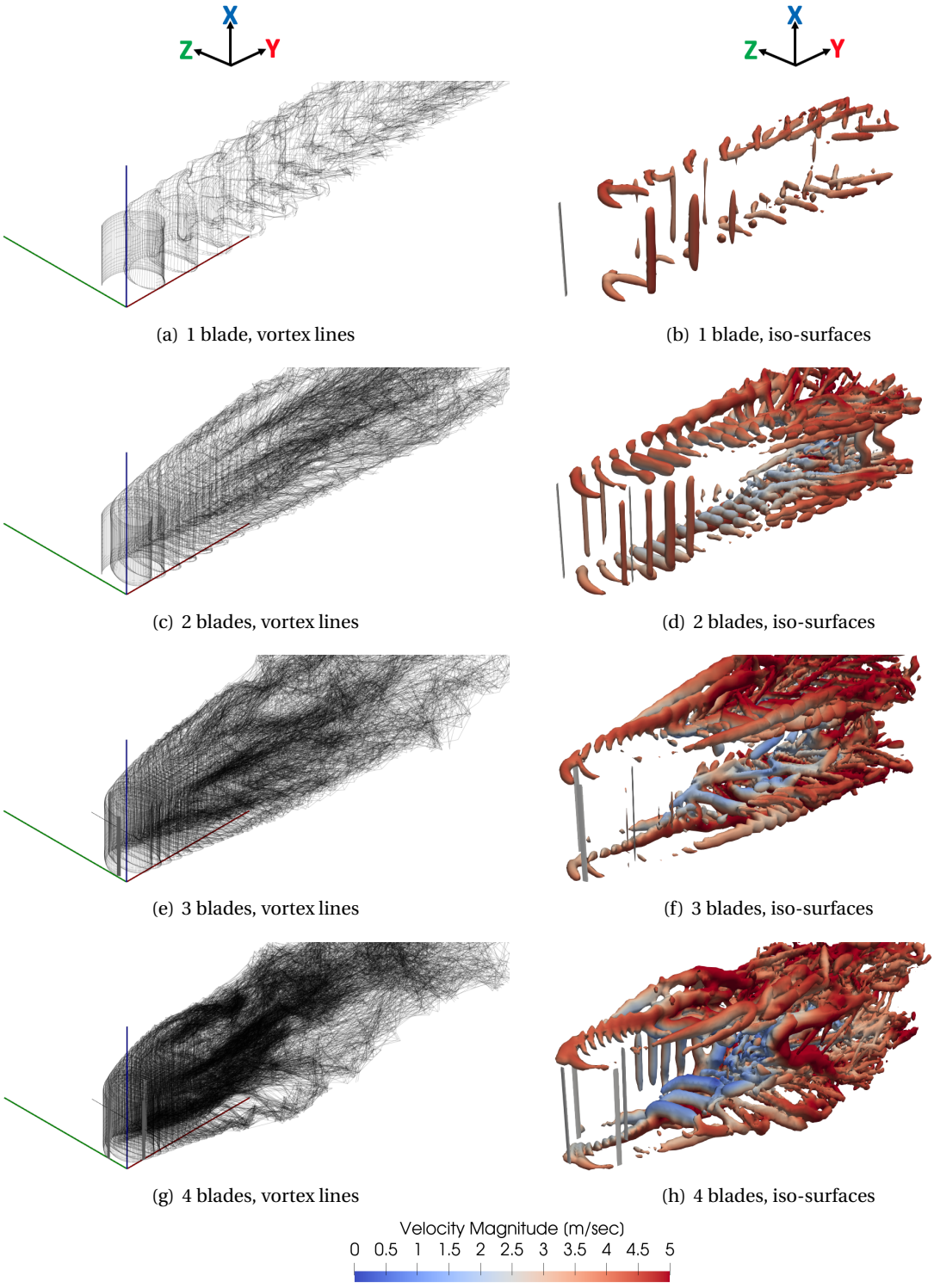

(a) 1 blade, vortex lines

(b) 1 blade, iso-surfaces

(c) 2 blades, vortex lines

(d) 2 blades, iso-surfaces

(e) 3 blades, vortex lines

(f) 3 blades, iso-surfaces

(g) 4 blades, vortex lines

(h) 4 blades, iso-surfaces

Figure 5.14: Visualization of vortex lines shed from the VAWT blades and instantaneous 3D flowfield using iso-surfaces of the Q-criterion ($Q = 6\ 1/\text{sec}^2$) for vortices visualisation, using mid-fidelity LLFVW at TSR of 3.3

wake on a 2D plane located at the blade mid-span location, using both LBM and LLFVW methods for TSR = 3.3. More blades provide more blockage to the flow, reducing the velocity induced at the upstream blades, which decreases even further at the downstream blades. This reduces the aerodynamic performance of the latter when compared to the former, as seen in previous results of thrust,

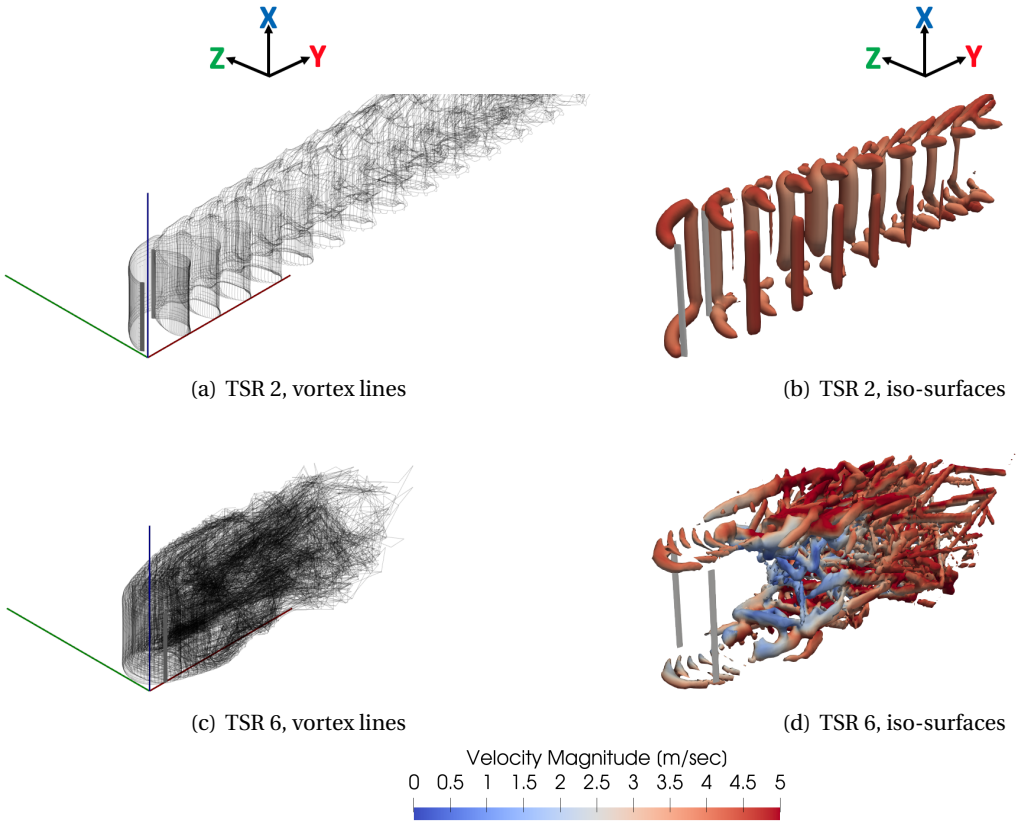

(a) TSR 2, vortex lines

(b) TSR 2, iso-surfaces

(c) TSR 6, vortex lines

(d) TSR 6, iso-surfaces

Figure 5.15: Visualization of vortex lines shed from the VAWT blades and instantaneous 3D flowfield using iso-surfaces of the Q criterion ($Q = 6$ 1/sec^2) for vortices visualisation, using mid-fidelity LLFVW method for 2-bladed VAWT

torque and blade normal forces in Figures 5.10, 5.11 and 5.12. The reduction in streamwise velocities with increasing blade numbers is captured well by both methods, although LLFVW predicts lower values compared to LBM, and this is found for all VAWT configurations simulated.

A stronger force distribution on an airfoil or a blade is also followed by a stronger downstream wake. The increase in strength of the downstream wake proportional to the number of blades, therefore, agrees with the increase in overall rotor thrust shown in Figure 5.10. Similarly, the prediction of lower rotor thrust values by LLFVW compared to LBM in Figure 5.10 and 5.11 also results in the lower prediction of streamwise velocities in the wake, as shown in Figure 5.16. Furthermore, it is noteworthy that the 2D vortex structures, as depicted in Figure 5.16 for LBM, are prominent compared to LLFVW results. Such structures are indicative of shed vortices, as shown in a 3D view in Figure 5.13, and the dissimilarity in vortex modelling approaches implies that the LBM more effectively captures the blade vortex interaction.

The current investigation into the wake of a VAWT revealed that the width of the velocity deficit region at any downstream location in the near-wake increases with an increase in the number of blades. This conclusion is consistent across all simulations conducted using both the LBM and LLFVW methods. The results are presented graphically in Figure 5.17, which shows the streamwise velocity values averaged over a rotation. The values are plotted along lines situated at distances of $0D$ and $1D$ downstream from the VAWT centre at the blade-mid-span 2D plane and are illustrated in Figure 5.16 as black dotted lines. A similar conclusion is made by Tavernier [92] using the Actuator Cylinder Theory when the ratio of loading in the upwind to downwind half of rotation increases, which is what happens when the number of blades increases.

The LLFVW method predicts lower streamwise velocities as compared to LBM, particularly at the centre of the wake. Furthermore, it is interesting to note the asymmetrical nature of the VAWT

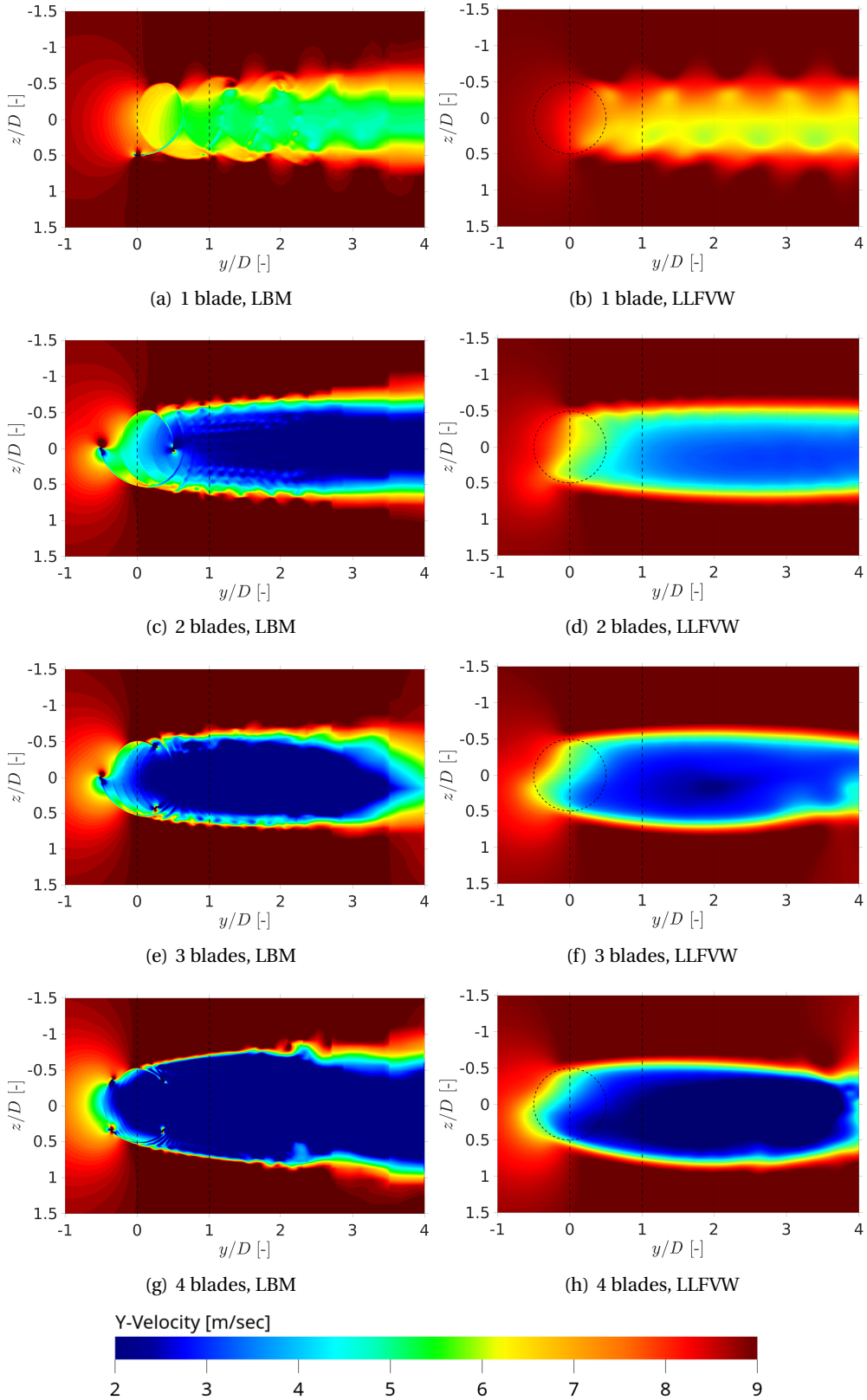

(a) 1 blade, LBM

(b) 1 blade, LLFVW

(c) 2 blades, LBM

(d) 2 blades, LLFVW

(e) 3 blades, LBM

(f) 3 blades, LLFVW

(g) 4 blades, LBM

(h) 4 blades, LLFVW

Figure 5.16: Instantaneous streamwise velocity contours in the VAWT wake on a 2D plane located at the blade mid-span location, using both LBM and LLFVW methods, at TSR = 3.3

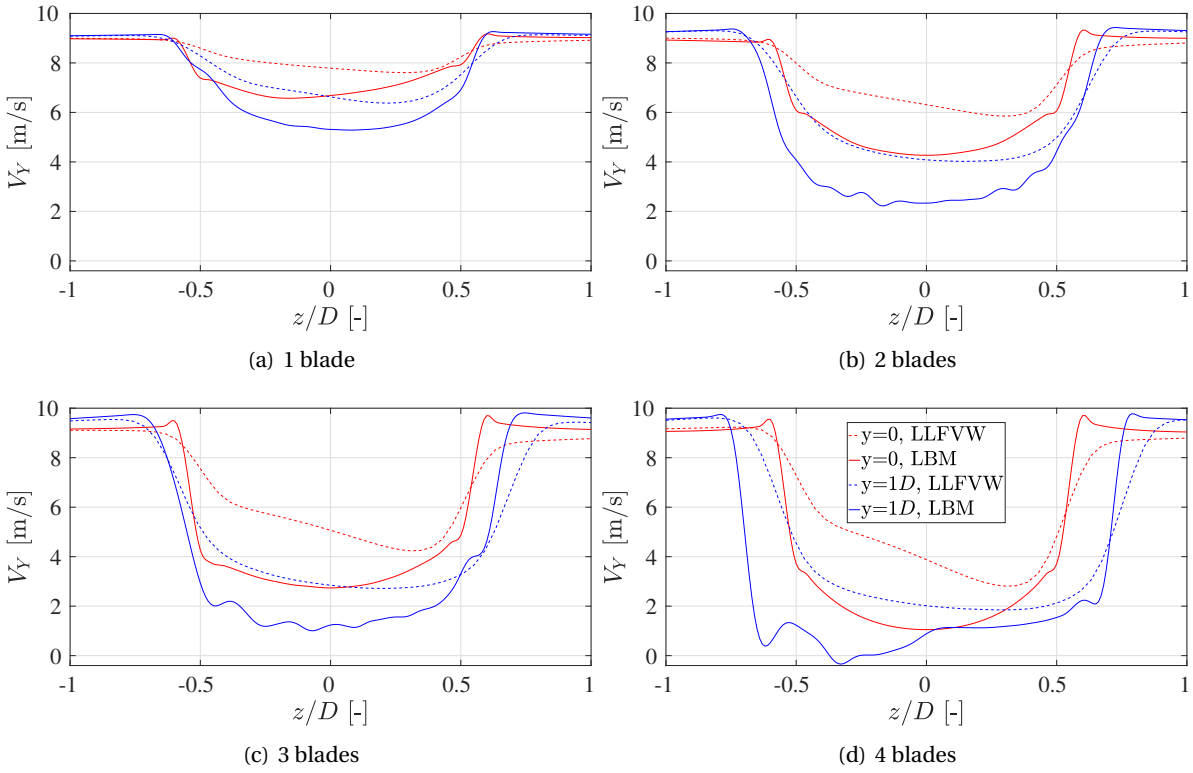

(a) 1 blade (b) 2 blades

(c) 3 blades (d) 4 blades

Figure 5.17: Comparison of streamwise velocities, averaged over a rotation, in the downstream VAWT flowfield using high-fidelity LBM and mid-fidelity LLFVW at two different locations, at TSR = 3.3

flow field, which is demonstrated across all configurations and shown by both methods used. Instantaneous streamwise velocities experienced by the VAWT blade at the most upstream (90°) and most downstream location (270°) are visualised in Figure 5.18. The results of this visualisation are compared for the 1-bladed and 3-bladed VAWT configurations using the high-fidelity LBM. An increase in the number of blades resulted in a decrease in induced velocity experienced by the upstream blade, which in turn led to a reduction in blade angle of attack (AoA) and aerodynamic performance. The induced velocity decreased further for the downstream blades, leading to an even lower AoA. These variations in streamwise velocities were consistent with the results presented in Figure 5.16 on a larger scale of the overall rotor wake.

The unsteady pressure data obtained from the VAWT at two different locations, one at the rotor plane ([0,0,7D]) and one out of the rotor plane ([4D,0,7D]), over a single rotor rotation is reported in Figure 5.19. It is observed that with an increase in the number of blades, the amplitude of pressure fluctuations decreases, as depicted at both locations in Figure 5.19 (a) and (b). This decrease is attributed to the reduction in the unsteady fluctuations in overall rotor loading or thrust values as previously shown in Figure 5.10. Additionally, the high-frequency pressure fluctuations are more prominent at the in-plane location than at the out-of-plane location.

The pressure fluctuations from a single blade increase proportionately with the individual blade loading, and Figure 5.19 (c) demonstrates this trend, with the highest fluctuations obtained for the case of a 1-bladed rotor. Furthermore, Figure 5.19 (d) shows the individual contribution from both blades of a 2-bladed rotor, shifted by a phase angle of 180°, and the level of constructive and/or destructive interference in the pressure fluctuations. For the case of 3-bladed and 4-bladed rotors, a similar phase shift of 120° and 90° will be obtained, respectively.

Next, the noise spectra of a VAWT are investigated and analysed. Figure 5.20 reports the Power Spectral Density (PSD) values in dB/Hz for the frequency range of 20-2000 Hz at the two observer

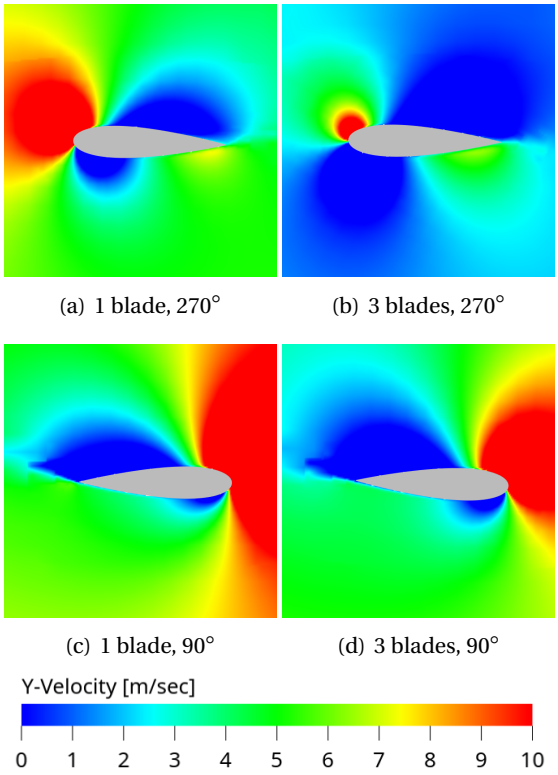

(a) 1 blade, 270° (b) 3 blades, 270°

(c) 1 blade, 90° (d) 3 blades, 90°

Figure 5.18: Comparison of instantaneous velocities experienced by a VAWT blade at the most upstream (90°) and the most downstream location (270°) for the 1-bladed and 3-bladed configurations, using the high-fidelity LBM, at TSR = 3.3

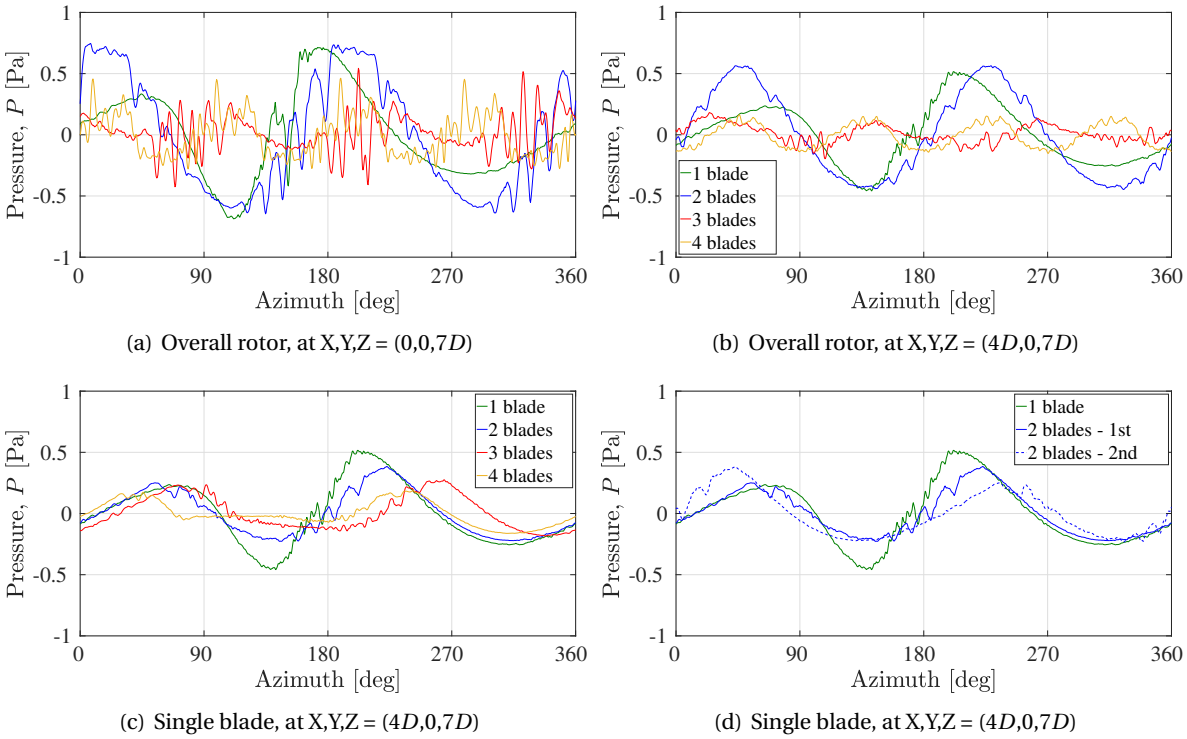

(a) Overall rotor, at X,Y,Z = (0,0,7D)

(b) Overall rotor, at X,Y,Z = (4D,0,7D)

(c) Single blade, at X,Y,Z = (4D,0,7D)

(d) Single blade, at X,Y,Z = (4D,0,7D)

Figure 5.19: Raw unsteady pressure data for different VAWT configurations using the high-fidelity LBM at TSR = 3.3

locations considered in this study, plotted with a frequency resolution (Δf) of 15 Hz. The noise spectra are not plotted below the human hearing range (20 Hz). The figures show that the PSD values for the 1-bladed and 2-bladed configurations are higher at the low-frequency range (20-40 Hz) than the other configurations. This is due to the contribution of tonal blade passage frequency (BPF) noise and is a result of the larger amplitude of azimuthal rotor loading for the 1-bladed and 2-bladed VAWTs as shown in Figure 5.10. On the other hand, at the mid and high-frequency ranges, 3-bladed and 4-bladed configurations produce more noise. This observation is supported by the pressure fluctuations data shown in Figure 5.19 (a) and (b), where high-frequency pressure fluctuations are significantly higher in the 3-bladed and 4-bladed configurations than the other configurations. It is worth noting that the noise is generally higher at the in-plane location than at the out-of-plane location.

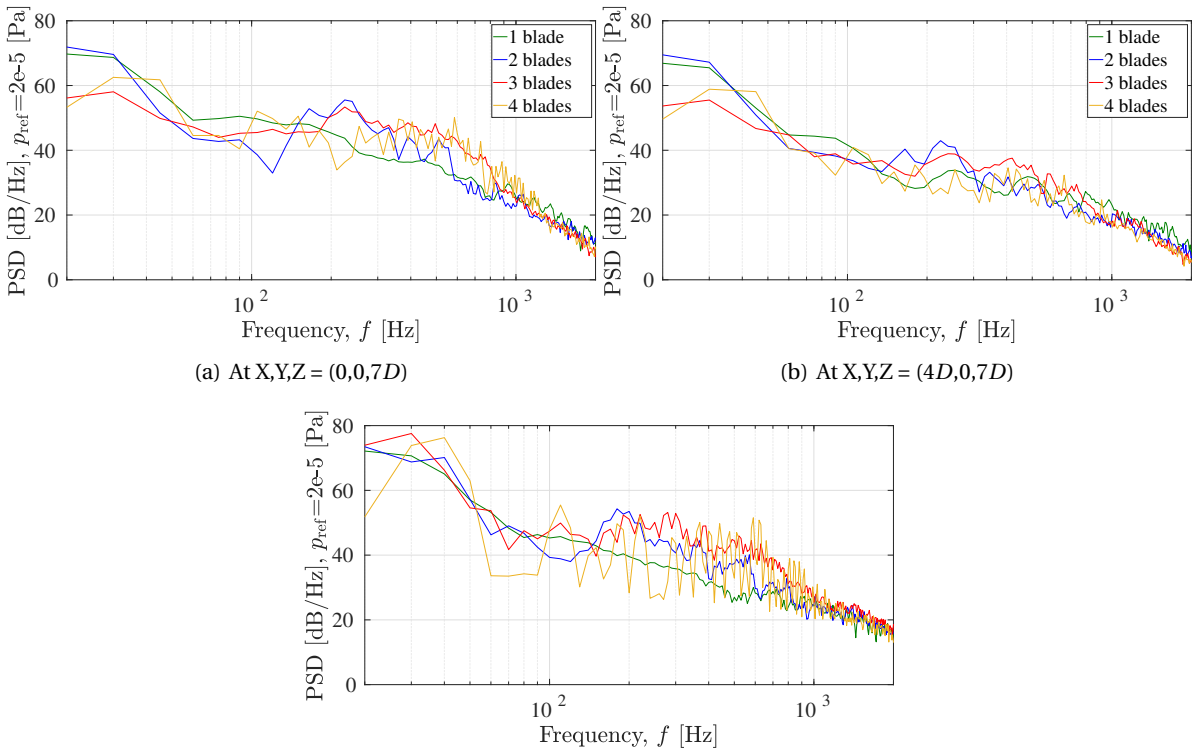

(a) At X,Y,Z = (0,0,7D)

(b) At X,Y,Z = (4D,0,7D)

(c) At X,Y,Z = (0,0,-7D)

Figure 5.20: Power Spectral Density (PSD) spectra using the high-fidelity LBM at two different locations, at TSR = 3.3

Figure 5.21 presents the directivity plot of the overall sound pressure level (OSPL) comparing VAWTs with varying number of blades at TSR of 3.3. The OSPL values are obtained using high-fidelity LBM and are calculated within the frequency range of 20-2000 Hz. For both the YZ and XY planes, noise levels exhibit an increasing trend with an increase in the number of blades until the 3-bladed rotor, after which it decreases for the 4-bladed rotor. This observation can be linked to the overall rotor thrust values depicted in Figure 5.9, where the VAWT thrust decreases for the 4-bladed rotor following a monotonic increase up to the 3-bladed rotor. It should be noted that this study focuses on VAWTs operating in a low Reynolds number regime, where blade loading noise is the predominant noise source [127].

On the YZ plane, both the 3-bladed and 4-bladed VAWTs exhibit an increase in noise levels at 180° azimuth, while a decrease is observed at 0° azimuth. In contrast, the 1-bladed and 2-bladed VAWTs demonstrate relatively constant noise levels throughout the entire 360° azimuth range. There are various noise sources in a VAWT [43–45, 261] and the observed discrepancy indicates that some

noise sources are more dominant in the former configurations compared to the latter configurations. Further investigation utilizing low-fidelity aeroacoustic prediction models can provide valuable insights into the specific contributions of different noise sources for different number of blades.

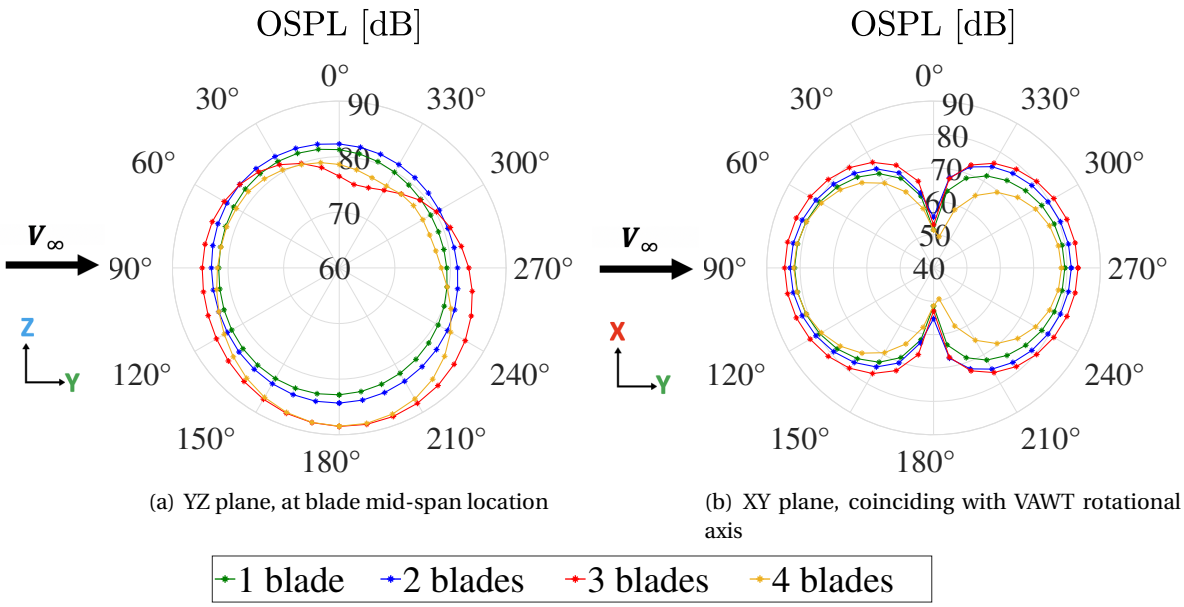

(a) YZ plane, at blade mid-span location

(b) XY plane, coinciding with VAWT rotational axis

Figure 5.21: Directivity plot of overall sound pressure level (OSPL) comparing VAWTs with different number of blades at TSR = 3.3, along a circular array of 36 points situated at a distance of $7D$ from the origin of VAWT ([0,0,0])

5.4. Conclusions and Discussions

The chapter presents a detailed flow physics investigation into the effect of the number of blades on the aerodynamic and aeroacoustic characteristics of vertical axis wind turbines (VAWTs). The objective of the study is twofold: firstly, support the development of a multi-fidelity simulation framework for optimising the aerodynamic and aeroacoustic performance of VAWTs and secondly, study the effect of one of the design parameters - the number of blades. High-fidelity 3D aerodynamic simulations are conducted using the Lattice Boltzmann Method (LBM) and subsequent aeroacoustic post-processing using the Ffowcs Williams and Hawkings (FW-H) methodology to calculate the far-field noise. In addition, mid-fidelity aerodynamic simulations are performed using the Lifting Line Free Vortex Wake (LLFVW) method. The investigation focuses on the effects of blade number on thrust and power performance, and far-field noise, while also comparing the 3D force-field and flow-field results obtained using the mid-fidelity and high-fidelity methods and identifying the differences in modelling fluid dynamic interactions which can be responsible for any observed discrepancies in the results.

A straight-bladed Darrieus VAWT with geometrical parameters replicated from the study by Balduzzi et al. [22] has been employed. Four different VAWT configurations have been simulated, namely the 1-bladed, 2-bladed, 3-bladed, and 4-bladed rotors. The solidity is set at 0.08 for the 1-bladed rotor and increases proportionally to the number of blades. The rotor aspect ratio for all configurations is 1.46. LLFVW method is used to simulate a range of TSRs while LBM is used to simulate only a TSR of 3.3, for all four geometries. The statistical temporal convergence is achieved much earlier for the 1-bladed rotor than for the 3-bladed rotor, for both methods and confirmed by the low uncertainty u values. The grid convergence results showed that the thrust values exhibited better grid convergence than the torque values. The finest of the four grids simulated exhibited the most favourable grid convergence and was subsequently chosen for further flow physics analysis.

For validation purposes, power coefficient (C_P) values of a 1-bladed VAWT obtained using LBM and LLFVW methods were compared with reference data reported by Balduzzi et al. [22] and the results showed excellent agreement.

The study showed that having more blades in a VAWT generates more power at lower TSRs, while the opposite trend is observed at higher TSRs. At low TSR, increasing solidity negligibly increases blade-wake/blade-vortex interaction, which helps in increasing the total blade tangential loading and power produced. However, increasing solidity worsens the tangential loading on each blade and overall rotor power at higher TSR. Consequently, higher solidity leads to a sharper gradient in C_P values than lower solidity cases, over the whole range of TSR. The number of blades in a VAWT affects the optimal TSR, and C_P values show that the optimal TSR decreases as the number of blades increases. The thrust coefficient (C_T) initially increases with increasing TSR and the number of blades and starts decreasing slightly at high TSR and for the 4-bladed rotor. The study further reveals that as the number of blades increases, the amplitude of variation in thrust and torque values decreases, resulting in smoother overall rotor loading variation.

Both the mid-fidelity LLFVW and high-fidelity LBM capture the above-mentioned physical trends very well. However, the LLFVW method predicts lower values of the peak C_T and C_Q values in the upwind and downwind parts of the rotation as compared to LBM, except for the 2-bladed rotor where there is a good agreement. This discrepancy was found to be true also when comparing individual blade normal forces and streamwise velocities in the downstream near-wake region. This shows that the LLFVW method may not be capturing the complex 3D effects in a VAWT flow and force field as strongly as LBM, especially when the number of blades increases. This resulted in the former predicting higher values of the thrust and power values of the overall rotor compared to the latter. Empirical modifications in the airfoil lift and drag polar values are suggested, for the LLFVW method.

The study also compared the aeroacoustic characteristics of all four VAWT configurations. Low-frequency BPF noise was found to be higher in VAWTs with fewer blades, due to the higher rotor loading or thrust values obtained. High-frequency noise was found to be higher in VAWTs with more blades, due to a higher intensity of BVI between the downstream blades and previously shed blade vortices. OSPL directivity plot revealed that overall noise increased with an increase in the number of blades except for the 4-bladed VAWT for which the noise decreased.

This study focuses on a single design parameter, the number of blades. Due to the large 3D design space of VAWTs, there is a need for further investigation into the impact of other geometric parameters, such as the effect of the central tower and supporting struts, aspect ratio, blade design, etc., as well as flow parameters, such as non-uniform inflow, on both aerodynamic performance and noise generation. The forthcoming chapters will focus on the investigation of these parameters.

6

Stand-alone VAWT III: supporting struts and central tower

Summary

This chapter focuses on studying the effects of struts and central tower on aerodynamics and aeroacoustics of small-scale Darrieus VAWTs operating at chord-based Reynolds numbers below 1×10^5. Three VAWT configurations are investigated: the first configuration consists of two blades, the second configuration includes additional struts and a central tower, and the third configuration features struts and a larger tower diameter. The investigations are conducted using the high-fidelity Lattice Boltzmann Method (LBM) and mid-fidelity Lifting Line Free Vortex Wake (LLFVW) method. The objective is to investigate the effect of struts and central tower on the 3D force and flow field of the VAWT. A statistical temporal and grid convergence study is carried out for thrust and torque coefficients. Results show no significant difference in temporal convergence behaviour when struts and tower are added. Power performance analysis showed a decrease in power and thrust values of the rotor due to the presence of struts and tower. Increasing the tower diameter further reduced these performance values. The blade-wake/blade-vortex interactions (BWI/BVI) increase when struts and tower are added, which leads to a decreased amplitude of rotor loading variation in a single rotation. Struts are found to degrade the spanwise distribution of blade loading while tower affects the azimuthal variation in blade loading at the most downstream location. Both the mid-fidelity LLFVW and high-fidelity LBM capture these physical trends well. However, LLFVW is found to predict higher C_T and C_Q values in a single rotation and lower streamwise velocities in the wake, as compared to LBM. This discrepancy increases as the struts and tower are added. In terms of noise, low-frequency noise (50-200 Hz) was observed to decrease while high-frequency noise (> 300 Hz) was observed to increase when struts and tower were added. The reduction in integral blade loading values contributed to the former while an increase in BWI/BVI contributed to the latter.

6.1. Introduction

The increasing demand for renewable energy sources has led to a surge in research focused on improving the efficiency of wind turbines. Vertical axis wind turbines (VAWTs) have garnered significant attention due to their potential for low maintenance, lower noise emissions, and the ability to capture wind from any direction. In VAWT design, the presence of a central tower and supporting struts has a significant impact on the overall aerodynamic and aeroacoustic performance. The objective of this chapter is to provide significant insights into the effect of the central tower and supporting struts on the performance of a VAWT using numerical simulations with mid-fidelity and high-fidelity CFD methods. Such studies are crucial in designing efficient and low-noise VAWTs, which can play a vital role in sustainable energy production.

6.1.1. Literature Review

The strut, commonly referred to as support structures or arms, and central tower are of significant importance as fundamental components of a vertical axis wind turbine (VAWT). In the context of VAWTs with helical and straight blades, struts and tower serves multiple purposes, including providing structural support to withstand aerodynamic, gravitational and inertial forces acting upon the blade. Additionally, they play a crucial role in transmitting torque to the shaft for power generation and exert a substantial influence on the natural frequency of the rotor [5, 153]. In the case of the ϕ-type wind turbine, it was observed that the initial 34 m VAWT developed by Sandia Labs achieved stabilisation of the curved blade through tension, eliminating the need for struts. However, it was emphasised that the increasing weight of the larger VAWT blades requires the use of struts for structural reinforcement [326]. Therefore, regardless of their specific types, all three VAWTs invariably rely on struts to ensure the structural connection and support required, particularly for larger-scale VAWTs.

The presence of struts in a VAWT gives rise to two forms of drag during turbine rotation: direct profile drag resulting from the cross-sectional shape of the struts, and induced drag arising from interference at the interface between the struts and the blades [135, 326]. Various numerical and experimental studies have provided evidence that both types of drag have a substantial negative impact on VAWT aerodynamic performance, which is exaggerated by the presence of a central tower. Experimental tests conducted by SANDIA indicated that the inclusion of struts resulted in a 26% reduction in the maximum power output of the VAWT [363]. Maeda et al. [207] conducted an experiment that revealed a disparity between the power output of a VAWT equipped with struts, as determined by a torque meter and a six-component balance, and the power measured using pressure taps positioned on the blade surface.

Howell et al. [148] conducted wind tunnel experiments for a 2- and 3-bladed VAWT and compared the results with 2D and 3D CFD simulation. Significant differences were observed between the power coefficients (C_P) obtained by 2D and 3D CFD simulations, which were attributed to the presence of blade tip vortices, flow divergence, additional struts and a central tower. Similar differences in 2D and 3D CFD results were obtained by various authors [80, 174, 189, 371] and a decrease in VAWT performance was observed due to the drag loss caused by struts and tower. Simultaneously, struts must possess sufficient strength and stiffness to prevent excessive deflections and support the weight of both the blades and themselves. Consequently, the design of struts necessitates a balance between aerodynamic demands and structural considerations [154].

Elkhoury et al. [112] carried out LES simulations along with wind tunnel experiments for a VAWT with variable-pitch straight blades. The author mentioned that the effect of connecting rods in a VAWT can only be neglected at low TSRs since their effect on C_P values increases with TSR. Miao et al. [228] conducted CFD simulations using various strut profiles and found out that the profile and induced drag of struts reduce the VAWT efficiency. The author also reported a linear increase in strut drag with an increase in profile thickness and a reduction in strut drag with an increase in

chord length. Siddiqui et al. [308] also conducted CFD simulations and reported a decrease in VAWT efficiency and power production, additional profile drag, and generation of strong 3D vortices due to the addition of struts and a central hub.

Struts can also be modelled with mid-fidelity methods such as the 3D nonlinear lifting line method [201] in which the effect of struts can be included as lifting bodies. Mendoza et al. [222] performed simulations using the 3D actuator line method and showed that the VAWT wake structure was not significantly affected by either removing struts or the central tower and therefore had a limited impact on overall performance. De Marco et al. [89] conducted RANS simulations and showed that a balance is required in the number of VAWT arms elements to achieve optimal aerodynamic performance, the finding of which is very similar to the effect of the number of blades [106, 303]. Scheurich et al. [294] performed simulations using the vorticity transport formulation of the Navier–Stokes equations for a VAWT that consists of three curved rotor blades that are twisted helically around the rotational axis of the rotor. A comparison with experimental results showed that the effect of struts is prominent at high TSRs and the inclusion of estimated drag generated by the struts in the numerical model produced better agreement with the experimental results.

Aihara et al. [7] investigated the accuracy of three numerical models in reproducing the effects of struts on turbine aerodynamics. Using a 12 kW H-rotor VAWT at various tip speed ratios, the RANS model, the actuator line method (ALM), and the vortex model show minimal differences in total forces caused by the presence of struts at low TSRs. At high TSRs, the RANS model predicts a 24% decrease in power coefficient, whereas the other models show reductions of less than 14%. Aihara et al. [8] employed the 3D RANS method to investigate the impact of struts and towers on the distribution of blade force and VAWT rotor performance. The results indicate that while the presence of struts significantly affects the blade force distribution and power coefficient, the tower effect does not produce remarkable differences. The findings suggest the need for further research to explore optimal strut designs with minimal influence on performance.

De Marco et al. [89] examined a wind turbine with unconventional arms geometry using the 3D RANS method. The presence of inclined/profiled arms enhances the turbine's average performance coefficient per revolution by increasing wake effects and improving the performance of positive-pitched blades in the downwind zone. However, when the number of turbine elements is increased to three, the significant blockage effect on the incoming wind flow negatively impacts turbine performance. Marsh et al. [214] simulated 3 straight-bladed VAWT configurations using the k-ϵ SST turbulence model. The investigation highlighted the significant impact of the strut section and the design of the blade-strut joint on power output, with low-drag struts and streamlined blade-strut joints yielding over 50% higher power output as compared to high-drag struts with blade-strut connection tabs. The struts positioned at the blade tips resulted in a 12% increase in maximum power output compared to those located at the quarter span.

Various authors have focussed specifically on strut profiles and their effect on VAWT aerodynamics. In the early development of VAWTs, cylindrical strut profiles were commonly employed, primarily for their structural support function [112]. However, it was discovered that the drag effect associated with cylindrical struts was highly significant. To investigate this, Peter et al. [16] conducted a comparative study using a hydraulic tow tank, where they measured the drag characteristics of a NACA 0021 airfoil and a cylinder strut. The findings revealed that the high drag exhibited by the cylinder strut severely impeded power generation, whereas the NACA airfoil strut experienced comparatively lower power losses. This indicates that the streamlined cross-sectional shape of the NACA airfoil effectively reduces the profile drag of the strut itself. Consequently, to address this issue, Islam et al. [152, 153] proposed a specially designed strut profile called MI-Struct1, which they demonstrated through their in-house code to possess a lower profile drag than the E862 airfoil. Other authors have also suggested airfoil-shaped struts for better aerodynamic performance [5, 137].

The spanwise and chordwise positions of struts also affect the aerodynamic efficiency of VAWTs. Based on intuitive reasoning, it may be expected that the middle span positioning of a single strut on each blade of a VAWT, would exhibit the least drag [352]. However, the findings of Marsh et al. [214] and Villeneuve et al. [352] contradict this intuition, demonstrating that VAWTs with struts installed at the end span exhibit higher aerodynamic efficiency. This is attributed to the fact that struts placed at the middle or quarter span of the blades disrupt the high-performance region of the blade surface. In contrast, end span installed struts do not interfere with the blades and additionally contribute to reducing blade tip losses by acting as endplates [352]. In the fabrication of VAWTs, it is a common practice to connect the struts at the mid-chord position (0.5c) of the blade [101]. However, Bianchini et al. [38] conducted a study indicating that the positioning of the struts at 0.5c can result in a change in the actual force acting on the blade, as the aerodynamic center of most subsonic airfoils is located at 0.25c. This displacement causes a slight increase in the blade radius and an additional pitch angle, subsequently generating a pitching moment due to the normal component force of the blade. This phenomenon is more prominent in smaller wind turbines characterised by higher solidity. As a result, a chordwise connecting position of 0.25c for the struts was recommended based on the findings.

The type of connection between the strut and the blade gives rise to aerodynamic interference, which is commonly referred to as induced drag. In their experimental investigation, Marsh et al. [214] examined the impact of two strut-to-blade connection types, namely the bolted flat strut and the fused NACA 0012 profiles strut, on the power efficiency of a vertical axis tidal turbine. Their findings revealed a significant decrease of 50% in efficiency for the turbine employing flat struts. However, the experiment was unable to conclusively isolate whether the profile or induced drag had a stronger influence, though their combined effect on turbine performance remained substantial. Hara et al. [137] compared the effect of three different strut profiles (NACA 0018 airfoil, rectangular, and circular) with identical thickness on the resistance torque (direct drag) and tangential torque (induced drag). They decomposed these torque components into differential pressure and frictional drags, concluding that the impact of struts on blade frictional drag was minimal. Additionally, their investigation revealed an intriguing finding that the profile drag outweighed the induced drag for rectangular and circular struts, while the opposite was observed for NACA airfoil profiles.

6.1.2. Research objectives

With the aforementioned studies in mind, the primary objective of this investigation is to initiate the development of a multi-fidelity simulation framework aimed at understanding the effect of supporting struts and central tower on the aerodynamic and aeroacoustic performance of vertical axis wind turbines. To accomplish this objective, the study employs high-fidelity 3D aerodynamic simulations based on the Lattice Boltzmann Method (LBM) for VAWTs with straight blades. Additionally, aeroacoustic post-processing is conducted using the Ffowcs Williams and Hawkings (FW-H) methodology to calculate far-field noise. Moreover, mid-fidelity aerodynamic simulations are executed utilizing the unsteady Lifting Line Free Vortex Wake (LLFVW) model.

The investigation aims to yield valuable insights into the significance of distinct fluid dynamic interactions associated with struts and central tower, as captured by mid-fidelity and high-fidelity aerodynamic methods. The employment of high-fidelity simulations facilitates precise resolution of the flow surrounding the VAWT blades and within the wake, enabling the examination of three-dimensional effects on force and flow fields in the context of the presence of struts and tower. These effects encompass non-uniform blade loading and wake, dynamic stall, blade-vortex interaction, and wake recovery. Conversely, the adoption of mid-fidelity simulations involves simplified modelling of the flow field using vortex lifting lines, contributing to a fundamental understanding of the three-dimensional effects when struts and a tower are present in a VAWT.

Conducting a comparative analysis between the two aforementioned methods is crucial for

evaluating the viability of the mid-fidelity approach as a potential alternative to the high-fidelity method, leading to significant time and computational resource savings. Assessing the reliability and accuracy of the mid-fidelity solver holds paramount importance for specific applications where a comprehensive examination of the VAWT flow and force field is not required. Furthermore, this research aims to address a literature gap by investigating the effect of supporting struts and central tower and their optimal design, considering both aerodynamic and aeroacoustic performance. For this chapter, the following research questions are formulated:

Research Questions

- How does the presence of struts and central tower affect VAWT performance parameters such as thrust, power, and far-field noise?
- How do the results for the effect of struts and central tower obtained using the mid-fidelity and high-fidelity methods compare? What are the fluid dynamic interactions responsible for any differences observed?
- How do 3D effects of blade loading on thrust and power values, trailing and shed vortices, and wake dynamics vary when struts and central tower are present?
- What are the key noise sources contributing to the aeroacoustic performance of VAWTs when struts and central tower are present?

The chapter is structured as follows. Section 6.2 presents the computational setup of both mid-fidelity LLFVW and high-fidelity LBM, including VAWT geometrical properties, flow and grid settings. Section 6.3 reports the results obtained for the grid convergence study, detailed force and flow field analysis and aeroacoustic performance of the VAWT to investigate the effect of struts and central tower. The last section 6.4 presents important conclusions of the study and a discussion on the understanding of the highly unsteady and turbulent VAWT blade-strut and blade-tower interactions.

6.2. Computational setup

A detailed account of the numerical and geometrical aspects of the simulation, including the description of the flow conditions and the generation of the computational grids has been provided. This will help in establishing the reliability and accuracy of the numerical simulation, and it enables the reader to assess the validity of the results presented in the subsequent sections.

6.2.1. Geometry

In this chapter, a straight-bladed VAWT design with 2 blades is employed and a total of three different configurations are simulated. The first configuration consists of only the two blades, without the inclusion of any struts or central tower. The second configuration consists of four supporting struts, a central tower (named Tower A), and the associated blades. The geometry employed for this configuration is replicated from a previous study by Brandetti et al. [47]. To validate the results obtained for the second configuration, numerical data from Brandetti et al. [47] and experimental data from LeBlanc et al. [181, 182] are utilised. An important point to note is that both the reference studies use boundary layer (BL) trips at 15% chord location, while no BL trips have been used in this study.

Finally, in the third configuration, the diameter of the central tower is increased to twice the diameter in the second configuration and the tower is named Tower B. The geometric models for all three configurations are shown in Figure 6.1, while Table 6.1 presents the geometric values for

all configurations and Table 6.2 presents the geometric values for the struts and central tower. The VAWT solidity is set at 0.1 and the rotor aspect ratio is 1 for all configurations. The inclusion of additional struts and central tower is expected to result in stronger 3D effects and increased blade-vortex interaction. These fluid dynamic interactions may lead to differences in the unsteadiness of VAWT blade loading, which, in turn, affects wake dynamics and aeroacoustic behaviour.

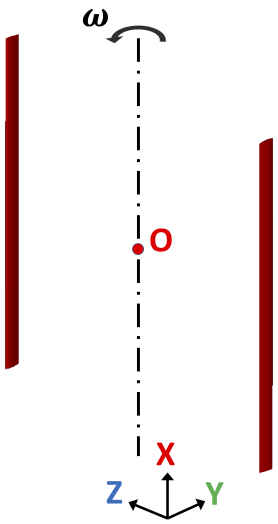

(a) First configuration - only the blades

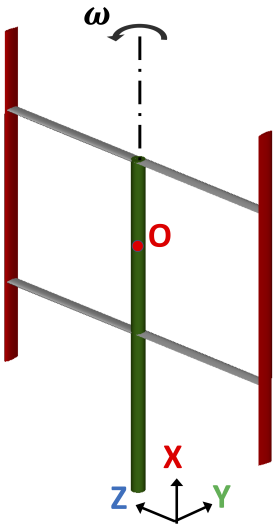

(b) Second configuration - with struts and central tower A

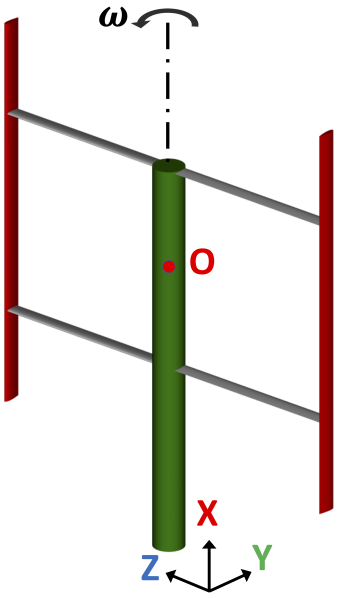

(c) Third configuration - with struts and central tower B

Figure 6.1: VAWT configurations used in this chapter; O represents origin of the coordinate system

The current investigation employs high-fidelity LBM to simulate all VAWT configurations. Additionally, each configuration is simulated using the mid-fidelity LLFVW method. Accurate and reliable airfoil data play a crucial role in generating precise results through both low and mid-fidelity methods. To achieve this objective, a virtual geometry is derived based on the NACA 0021 profile, accounting for the virtual camber effect in a manner similar to Chapter 5. The transformed airfoil

Table 6.1: VAWT geometrical parameters for all three configurations

Blade length (L)	**Rotor diameter (D)**	**Blade chord (c)**	**Blade airfoil**
1.5 m	1.5 m	0.075 m	NACA 0021

Table 6.2: VAWT geometrical parameters for the second and third configurations with struts and central towers A and B, respectively

Strut length (L_s)	**Strut chord (c_s)**	**Strut airfoil**	**Strut location**	**Tower diameter (D_t)**	**Tower length (L_t)**
0.75 m	0.06 m	NACA 0018	0.36 m from blade tips	0.06 m (Tower A) & 0.12 m (Tower B)	1.5 m

is depicted in Figure 5.2 (c). Lift and drag polars are obtained for Reynolds numbers ranging from 5×10^4 to 1×10^6 using XFoil [104]. The XFoil analysis employs an *NCrit* value of nine and incorporates forced transition at the leading edge of both the pressure and suction side. To ensure a smooth extrapolation in the post-stall regime, the airfoil static polar data is extended to a 360° angle of attack (AoA) using the Montgomerie method [241]. Balduzzi et al. [22] provide an example of the extrapolated 360° polars.

6.2.2. Numerical setup

Both for high-fidelity and mid-fidelity simulations, the setups used are similar to what is used in Chapter 5. For high-fidelity LBM, a simulation volume is implemented, which is a cube with each side measuring $100D$, with the Darrieus geometry positioned at the centre of the volume. The boundary conditions are presented in Figure 5.2 (a) in Chap 5. The velocity inlet is set to the freestream velocity V_∞ in the direction of the Y-axis. An ambient pressure of 101.325 kPa is applied at the pressure outlet. The blade surface is subjected to a no-slip boundary condition. PowerFLOW generates a Cartesian volume grid around the individual solid components in the domain by beginning with the minimum hexahedral cell (voxel) size and a specified number of variable resolution (VR) levels. To optimise computational efficiency, the present study utilises 17 VR regions, with higher resolutions near the blade and strut surfaces with an offset, and coarser regions located farther from the blade and struts. This methodology permits the allocation of computational effort primarily to areas of interest and where high-flow gradients are anticipated. Figure 5.2 (b) from Chapter 5 shows this grid refinement when approaching the centre of the domain where the VAWT is located. The VR levels are arranged in a range from fine to coarse, with a voxel size change factor of 2 between adjacent VRs which creates distinct VR regions. The software automatically intersects the Cartesian mesh with the solid parts to produce a collection of polygons, or surfels, that represent the true surface of the body.

Similar to chapter 5, only the FW-H solid formulation is used for far-field noise calculation in which the blade surfaces of the VAWT are considered as the FW-H solid surfaces. The reason is the difficulty in eliminating spurious noise sources from FW-H permeable data when only three spherical surfaces are utilised within the context of a VAWT. Similar to Chapters 4 and 5, analyzing the noise spectra up to 4000 Hz is sufficient for VAWT aeroacoustics while using a sampling time of 8 steady rotor rotations. Therefore, pressure data are sampled at a frequency of 8000 Hz, in accordance with the Nyquist criterion. To ensure the accurate capture of acoustic waves, a criterion of a minimum of 15 points per wavelength is adopted. Subsequently, noise spectra are computed using a Hanning window with a 50% overlap and a frequency resolution (Δf) of 15 Hz, using the *pwelch* function in MATLAB. It should be noted that future studies will address a separate investigation to explore the implementation of the FW-H permeable formulation for VAWT aeroacoustics in a more

efficient manner.

For the mid-fidelity LLFVW simulation, Table 6.3 outlines the values of the simulation parameters utilised which are adopted from previous studies [22, 306].

Table 6.3: Simulation parameters used for the LLFVW method

	LLFVW
Density	1.225 kg/m^3
Kinematic viscosity	1.65 e-5 m^2/s
Blade discretisation	21 (cosine)
Azimuthal discretisation	3 deg
Full wake length	12
Vortex time offset	1 e-4 sec
Turbulent vortex viscosity	20

6.2.3. Flow conditions and grid settings

For the current study, the operational settings of the VAWT are presented in Table 6.4. The tip speed ratio (TSR) is employed as a measure of the system's operational condition, defined as the ratio of the blade rotational speed to the freestream velocity, i.e., $\omega R/V_\infty$, where ω, R, and V_∞ represent the rotational speed in radians per second, the wind turbine radius, and the freestream velocity, respectively. The freestream velocity is maintained at a constant value of 4 m/s, in accordance with the reference value [47], while ω is adjusted to vary the TSR value. The chord-based Reynolds number (Re_c) is calculated as 8.12×10^4, based on the average velocity experienced by a blade during a single rotation.

The approach of adjusting the rotational speed based on wind speed measurements to maintain the TSR close to its optimal value emulates real-life situations. Additionally, the freestream Mach number (M) is 0.12, while the values of freestream turbulence intensity (I_t) and turbulence length scale (L_t) are set to 0.1% and 1 mm, respectively. It is anticipated, based on a prior study [63], that these parameters will have minimal impact on the evolution of the unsteady flow field. In the present study, the high-fidelity method (LBM) is exclusively utilised for TSR = 4, while the mid-fidelity method (LLFVW) is employed to simulate a range of TSR values spanning from 1 to 7. Notably, all operational conditions considered in this study exhibit chord-based Reynolds numbers (Re_c) below 4×10^5.

Table 6.4: VAWT operational settings for the mid-fidelity (LLFVW) and high-fidelity method (LBM)

Parameter	**Value**
Tip speed ratio (TSR)	4
Rotations per minute (RPM)	203.718
Freestream velocity V_∞	4 m/s
Chord-based Reynolds number (Re_c)	8.12×10^4

In the context of the grid convergence study, the high-fidelity LBM is employed to simulate the VAWT with only the blades, using three different grid resolutions. Variable resolution (VR) regions are implemented near the blade surface with varying voxel densities per chord for Grid 1, Grid 2, and Grid 3 resolutions. The minimum and maximum voxel densities are allocated to the Grid 1 and Grid 3 resolutions, respectively, while the resolutions of other VR regions are adjusted proportionally. The y^+ values and voxels per chord for all grid resolutions are presented in Table 6.5. The y^+ value is a dimensionless parameter that signifies the distance of the first cell centre from the computational domain's wall in the wall-normal direction. It is calculated using the average velocity

value experienced by the blade at the mid-span location over a single rotation. The voxels per chord represent the number of grid cells along the blade chord direction. Figure 6.2 shows the finest mesh around the blade with 4 different VRs for the setup with Grid 3.

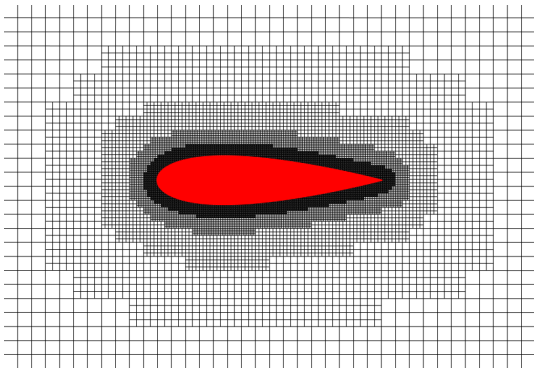

Figure 6.2: Cross-sectional view of the finest mesh around the blade

Figure 6.3 shows the cross-sectional view of the mesh in the domain for Grid 3, both near the VAWT blades and further away from it. The minimum voxel sizes for Grid 1 and Grid 3 grid resolutions are reported as 0.826 mm and 0.413 mm, respectively. For the 2-bladed VAWT, the fine equivalent voxels in the computational domain amount to 7.06 million and 24.6 million for Grid 1 and Grid 3 resolutions, respectively. These fine equivalent voxels are derived by multiplying the number of voxels with the time stepping rate, which is directly linked to the mesh resolution level. The computational effort, represented by the CPU hours required for simulating 12 rotor rotations (1.31 s), is evaluated for the Grid 1 and Grid 3 configurations of the 2-bladed VAWT. The simulation using Grid 1 necessitates 3261 CPU hours, while Grid 3 demands 46380 CPU hours. These simulations are conducted on a Linux workstation equipped with an AMD Ryzen Threadripper 3990X Gen3 processor having 64 cores and 128GB DDR4 3GHz platform. It is pertinent to mention that both the fine equivalent voxels and CPU hours have similar values for all three VAWT configurations, with only a slight increase for the configurations with struts and tower. Furthermore, the physical time step for Grid 1 and Grid 3 resolutions corresponds to a Courant-Friedrichs-Lewy (CFL) number of 1 in the finest VR level and is measured at 7.51×10^{-6} s and 3.76×10^{-6} s, respectively.

Table 6.5: VAWT grid settings for the high-fidelity LBM simulation

		Grid 1	**Grid 2**	**Grid 3**
First configuration - only blades	y^+	50	33.3	25
	Voxels per chord	9.1×10^1	1.36×10^2	1.81×10^2

The integral and time-varying behaviour of the VAWT thrust coefficient (C_T) and torque coefficient (C_Q) are reported. These coefficients are defined as:

$$C_T = \frac{T}{0.5\rho A V_\infty^2}, \tag{6.1}$$

$$C_Q = \frac{Q}{0.5\rho A V_\infty^2 R}, \tag{6.2}$$

where, T and Q are VAWT thrust and torque respectively, ρ is the air density, A is swept area ($D \times L$) where is D is rotor diameter and L is blade length, R is rotor radius and V is freestream velocity. Using high-fidelity LBM, unsteady pressure data, Power Spectral Density (PSD) spectra and Overall Sound Pressure Level (OSPL) values obtained using FW-H solid formulation are also reported and analysed.

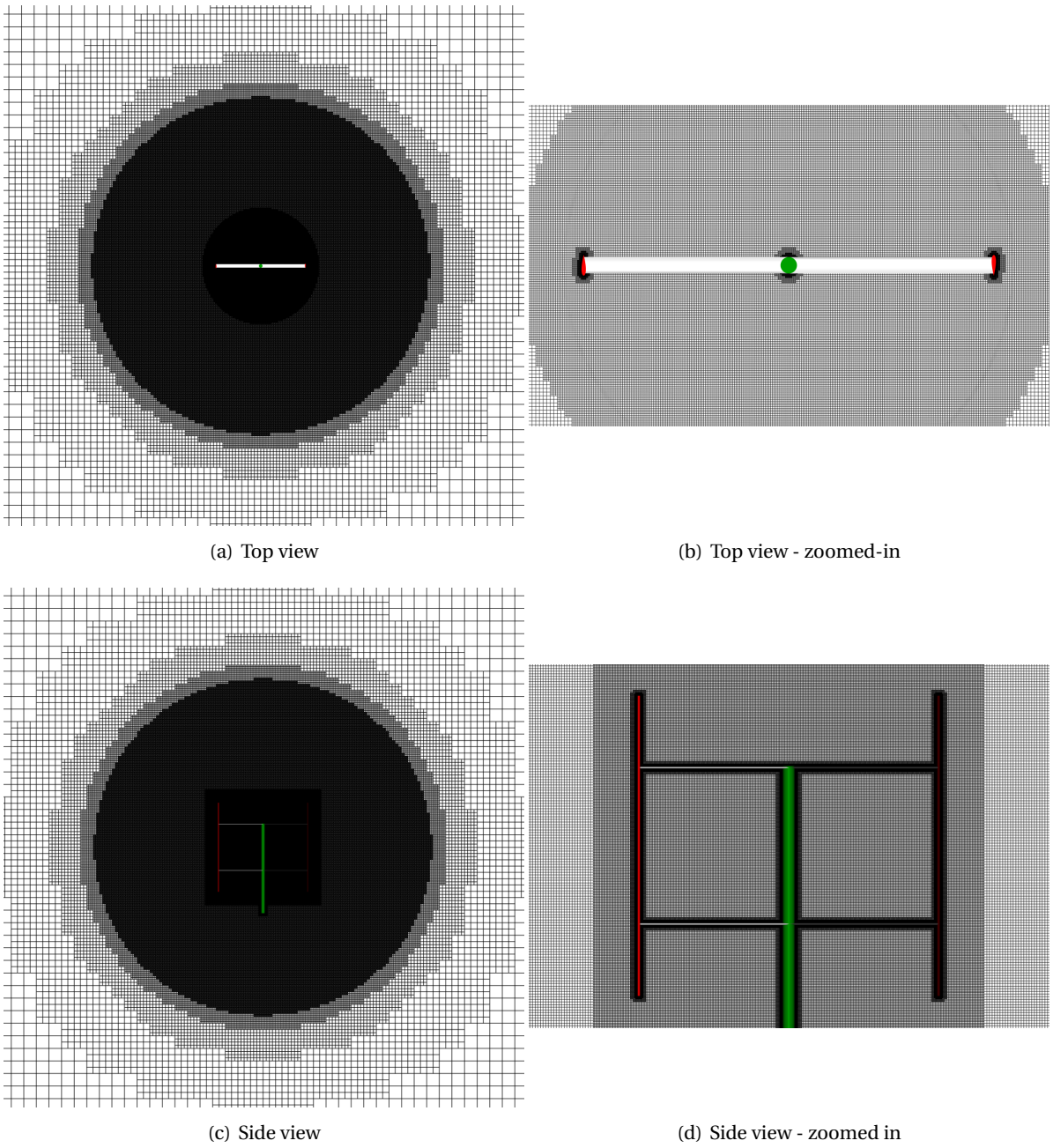

(a) Top view

(b) Top view - zoomed-in

(c) Side view

(d) Side view - zoomed in

Figure 6.3: Cross-sectional view of the mesh for the high-fidelity LBM simulation

6.3. Results

6.3.1. Temporal and grid convergence study

Figure 6.4 presents a subset of the results, illustrating the temporal convergence characteristics of the thrust coefficient (C_T) and torque coefficient (C_Q) for two VAWT configurations: first configuration without any struts and tower and second configuration with struts and tower A. These results are obtained using both the high-fidelity Lattice Boltzmann Method (LBM) and the mid-fidelity Lifting Line Free Vortex Wake (LLFVW) method. The reported values in these figures represent the overall rotor, encompassing all the blades and struts/tower, if applicable, within a configuration.

The uncertainty values (u) presented in each figure are determined as a percentage of the stan-

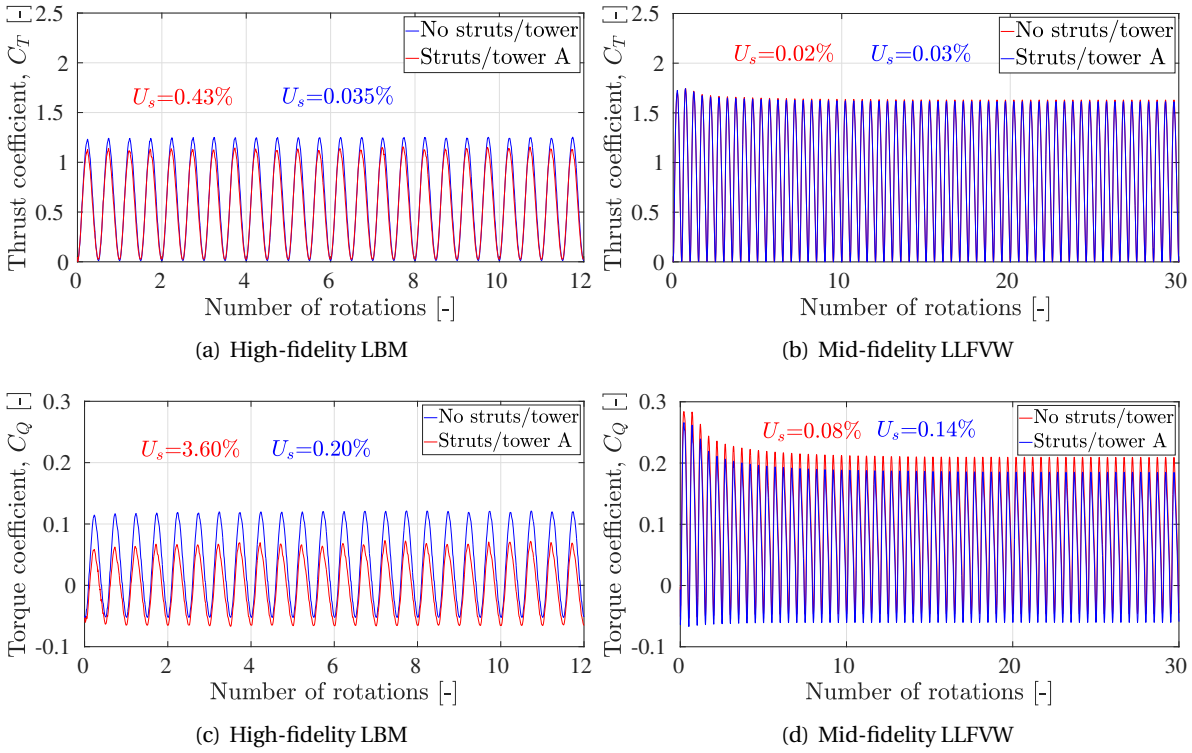

(a) High-fidelity LBM (b) Mid-fidelity LLFVW

(c) High-fidelity LBM (d) Mid-fidelity LLFVW

Figure 6.4: Statistical temporal convergence study for VAWT thrust coefficient C_T and torque coefficient C_Q using the high-fidelity LBM and mid-fidelity LLFVW for the finest Grid 3; the values are representative of the overall rotor

dard deviation of the thrust and torque coefficients, which are averaged over a complete rotation of the VAWT. These uncertainty values serve to indicate the degree of variability or uncertainty in the calculated thrust and torque coefficients over time, resulting from the inherent unsteadiness and stochastic nature of the fluid dynamic interactions. Lower values of u are indicative of a higher level of confidence in the simulation results, suggesting that the simulations have achieved temporal convergence. All u values depicted in the figures are calculated after the 10th rotor rotation for the high-fidelity LBM and the 20th rotor rotation for the mid-fidelity LLFVW method. These specific time points are chosen to ensure a sufficient number of rotations for the simulation to reach a state of temporal stability and reliability, allowing for meaningful uncertainty assessment [146].

On the whole, the statistical temporal convergence behaviour is observed to be similar for the two configurations reported, suggesting there is no significant effect on unsteady blade loading due to the increased fluid dynamic interactions caused by struts and tower. The figures reveal a notable distinction in the statistical temporal convergence between thrust and torque values when employing both numerical methods. Specifically, it is observed that thrust values exhibit superior convergence, as evident from the lower values of uncertainty (u), compared to torque values. This trend aligns with findings from a prior investigation on VAWTs operating at low Reynolds numbers [304], further corroborating the present study's outcomes. In the case of C_T values, convergence is achieved after approximately 3 rotor rotations for LBM simulations and 5 rotor rotations for LLFVW simulations. On the other hand, for C_Q values, the temporal convergence requires around 5 rotor rotations for LBM and 10 rotor rotations for LLFVW simulations. These results highlight the robust ability of the mid-fidelity LLFVW method to accurately capture the unsteady phenomenon in the VAWT force field, as demonstrated by the convergence outcomes.

Interestingly, these findings diverge from those reported by Rezaeiha [274], where more than 20 rotor rotations were necessary to attain temporal convergence in high-fidelity CFD simulations

utilizing the incompressible Unsteady Reynolds-Averaged Navier-Stokes (URANS) method. Such variations in convergence behaviour can be attributed to the different computational methods employed, as well as variations in grid resolution and turbulence models. It is essential to acknowledge that in the present study, the LBM simulations for the finer grid are initialised using the results from the coarser grid. This pragmatic seeding approach aligns with best practices for simulations of this nature, where a coarser resolution is initially simulated for a minimum of 10 rotor rotations. Subsequently, the final frame of this coarser simulation is utilised to seed the finer resolution simulation, which is executed with an initial settling time of a few blade-passage periods [63]. Such an approach likely contributes to the reduced transient period observed in the convergence process.

Figure 6.5 showcases the temporal convergence of unsteady pressure data for the VAWT configuration without struts and the central tower. The high-fidelity LBM is employed, and the finest grid utilised in this study is considered for data collection. The pressure data is recorded at two distinct locations, both positioned along a line parallel to the VAWT rotational axis and situated at a lateral distance of 2.6 times the blade diameter (D). The specific locations of interest are (0,0,2.6D) and (0.87D,0,2.6D). To conserve computational resources, the pressure data is recorded starting from the 6th rotor rotation. The investigation reveals that the temporal convergence of the unsteady pressure data is achieved after the 6th rotor rotation for both locations of interest. This observation underscores the stability and accuracy of the LBM simulations in the case of complex aerodynamic interactions and unsteady flow behaviours, further affirming the reliability of the computational methodology. To follow a prudent approach in the present chapter, all subsequent results are reported based on data obtained after the 10th rotor rotation for the high-fidelity LBM and the 20th rotor rotation for the mid-fidelity LLFVW method.

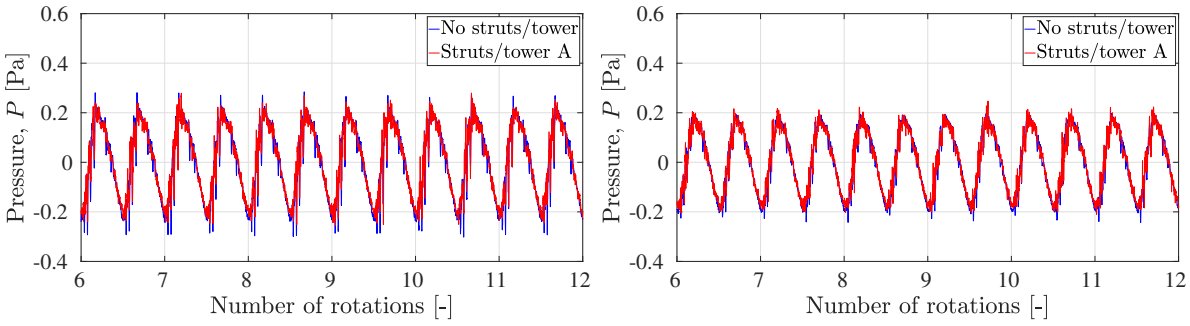

(a) At location (X,Y,Z)=(0,0,2.6D)

(b) At location (X,Y,Z)=(0.87D,0,2.6D)

Figure 6.5: Statistical temporal convergence study for unsteady pressure data for the first configuration without struts and tower at TSR = 4, at two different locations using the high-fidelity LBM for the finest Grid 3

The outcome of the grid convergence study for the first VAWT configuration, excluding the struts and central tower, is depicted in Figure 6.6. This figure presents the variation of the normal force coefficient (C_{Fn}) over a single rotation, for a single blade across three different numerical grids utilised in the high-fidelity LBM simulations. Such an investigation is essential to validate the independence of the obtained results from the numerical grid employed, ensuring the robustness and accuracy of the simulations. The results reveal that the normal forces converge favourably when employing the finest Grid 3, encompassing both the upwind and downwind portions of the rotor rotation.

Grid convergence for integral C_T and C_Q values are also investigated for the first VAWT configuration, presented in Figure 6.7. The reported values represent the overall rotor, encompassing both blades in the VAWT. The resolution is characterised by the grid spacing (h), normalised with respect to the blade chord (c). Specifically, h corresponds to the smallest grid (voxel) size within the numerical domain. Moreover, the figure includes values obtained through the Richardson extrapolation method [304], which enables the determination of C_T and C_Q as $h/c \rightarrow 0$. This extrapolation

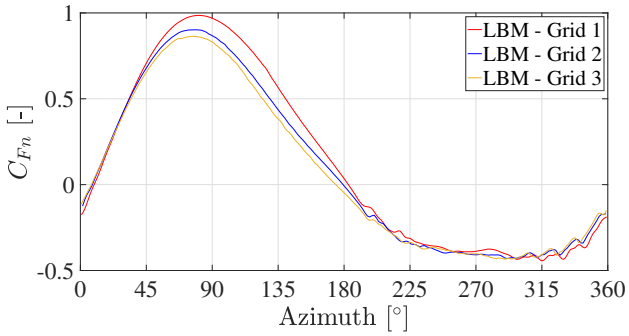

Figure 6.6: Grid convergence study for VAWT normal force coefficient C_{Fn} of a single blade, using the high-fidelity LBM for TSR = 4

physically signifies the approach towards the continuum limit, wherein an infinite number of cells is utilised in the Cartesian grid. The figure also presents the Grid Convergence Index (GCI) for each scenario, which is based on the difference between two adjacent grid resolutions [220, 304] and is an essential metric for estimating the error in the solution.

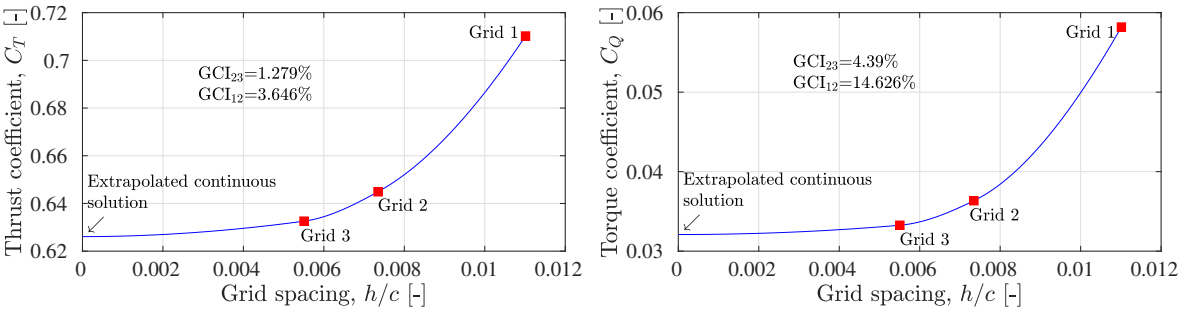

(a) Thrust values (b) Torque values

Figure 6.7: Grid convergence study for VAWT thrust coefficient C_T and torque coefficient C_Q for the first configuration without struts and tower, using the high-fidelity LBM at TSR = 4

The results demonstrate that the thrust values exhibit superior grid convergence compared to the torque values. GCI represents the grid convergence index between any two different grids and gives an idea of the quantitative measure of the discretization error in CFD simulations, indicating the level of numerical accuracy achieved as the computational grid is refined. GCI$_{12}$ represents this value between Grid 1 and Grid 2, and GCI$_{23}$ represents this value between Grid 2 and Grid 3. C_T exhibits more favourable GCI values than C_Q indicating that a coarser grid resolution is adequate to capture converged blade loading values. Conversely, a finer grid resolution is required to attain converged blade torque (or power) values. This discrepancy arises from the substantial impact of skin friction and drag values, which depend significantly on the variation in y^+ values. The accurate prediction of airfoil drag for both low and high Reynolds number flows still remains an area of active research [347]. For the present VAWT setup, GCI$_{23}$ is consistently lower than GCI$_{12}$ for both C_T and C_Q, which was also found in Chapter 5 when the number of blades was varied. This implies that increasing the grid resolution can lead to more precise and reliable results since the differences related to the numerical grid diminish, enhancing the accuracy of the simulations. However, it is essential to recognise that the relative GCI values may vary in VAWT simulations, depending on factors such as the simulated tip speed ratio and rotor scale [304].

Additionally, the findings from Chapter 4 revealed that the grid convergence of the OSPL is comparable to that of thrust values and superior to torque values. This aligns with the fact that, in the

context of VAWTs operating at low Reynolds numbers, loading noise has the most significant contribution to the overall noise [127]. Consequently, given the favourable convergence observed for Grid 3, it is judicious to select this grid resolution for all subsequent numerical simulations. It is deemed sufficient to enable an accurate and insightful physical analysis of the fluid dynamic interactions and noise sources in the VAWT.

6.3.2. Numerical validation

Figure 6.8 shows normal force coefficient C_{Fn} variation for a single blade for the full rotation, comparing the results of the Grid 3 of the current high-fidelity setup, mid-fidelity setup, reference high-fidelity simulation [47] and experiments [181, 182]. 'Experiment - clean' is for the result without any boundary layer (BL) trip and 'Experiment - trip' is with the BL trip at 15% chord, on both the pressure and suction side of the airfoil, to force flow transition. The reference high-fidelity simulation also used a BL trip at the same location while there is no BL trip used in the current study.

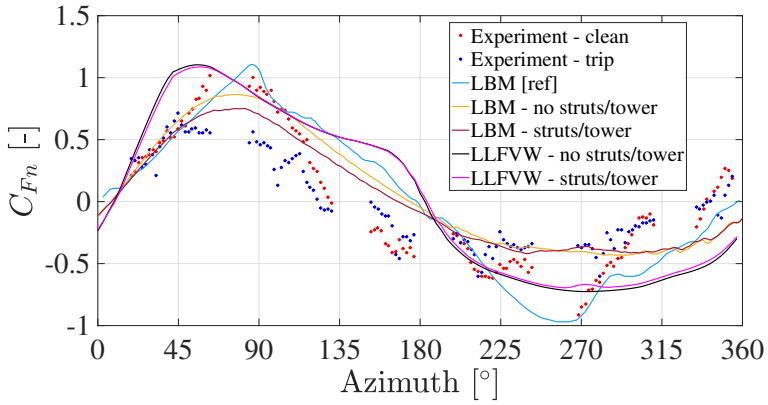

Figure 6.8: Normal force coefficient C_{Fn} of a single blade using high-fidelity LBM and mid-fidelity LLFVW in the current study, compared with experimental and reference high-fidelity LBM results, at TSR = 4; [ref] - reference

The obtained results exhibit a favourable agreement between the LBM simulations of the current study (without struts/tower), the reference LBM simulation, and the experiment without the boundary layer trip, particularly in the upwind region of the rotor rotation. However, in the downwind portion, there exists a discrepancy around the most downstream position (270°) between the two aforementioned LBM results. The boundary layer trip is expected to induce a significant increase in blade loading in the reference LBM simulation, particularly evident in the downwind region. Both the mid-fidelity LLFVW results demonstrate favourable agreement in the upwind portion of the rotation, yet a mismatch is observed in the downwind region. Overall, the validation of both the mid-fidelity and high-fidelity setups utilised in this study is deemed satisfactory. These validated setups can be effectively employed to delve further into the investigation of VAWT fluid dynamic interactions and wake dynamics, offering valuable insights into the intricacies of VAWT performance.

In both the upwind and downwind halves of rotation, absolute values of C_{Fn} predicted by LBM are lower compared to those obtained through LLFVW (both with and without struts/tower). This disparity indicates that the latter method fails to capture the blade-wake interaction as prominently as the former. Additionally, in the case of LBM, the presence of struts and a central tower leads to a reduction in blade loading in the upwind part of rotation, with a relatively consistent loading in the downwind region, except for a slight decrease around the azimuth of 270°, precisely downstream of the central tower. This downstream effect is also well-captured by the LLFVW results, although the differences in the upwind region due to the presence of struts and tower remain minimal.

Figure 6.9 shows instantaneous streamwise velocities experienced by the cross-sectional airfoil at different azimuth locations, as obtained using high-fidelity LBM. These results can be compared

with the results of Brandetti et al. [47] shown in Figure 6.10. The results show that at all azimuth locations, the BL trip induces more prominent flow separation in the latter, as compared to the present study. This results in differences in blade loading, both in the upwind and downwind parts of rotation, as evident in Figure 6.8. It is crucial to note that the ratio of BL trip height to chord length (t/c) used both in the reference LBM simulation and experiment is 0.0067 (corresponding to $t = 0.5$ mm) which exceeds the typical values employed for VAWTs or other types of rotors (0.0027 by Pearson [261] using $t = 0.15$ mm and 0.003 by Weber et al. [357] using $t = 0.15$ mm). The increased BL trip height might have resulted in its functioning as a step in the flow over the NACA 0021 airfoil, rather than serving its intended purpose of enforcing flow transition from laminar to turbulent regimes. These observations highlight the sensitivity of VAWT aerodynamics to BL trip configurations and the need for future studies to explore their optimised design and chordwise location on the VAWT blades.

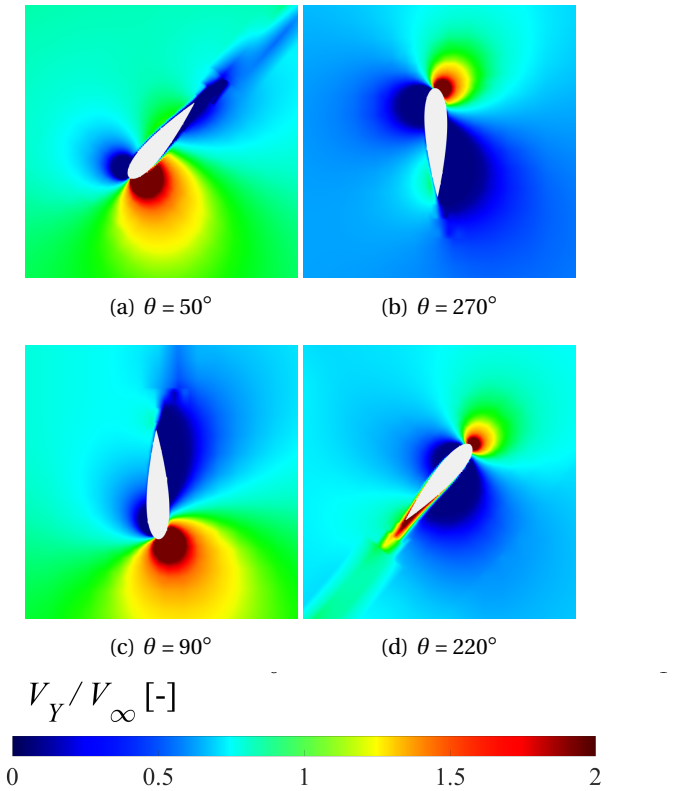

Figure 6.9: Instantaneous streamwise velocities experienced by a VAWT blade at different azimuth locations for the VAWT configuration without struts and tower, using the high-fidelity LBM at TSR = 4

6.3.3. Effect of struts and a central tower

Figure 6.11 displays the computed values of C_P and C_T for the three distinct VAWT configurations used in this chapter. While the mid-fidelity LLFVW method is employed to simulate the full range of TSRs, the high-fidelity LBM simulations are specifically conducted for a TSR of 4. The utilisation of multiple fidelity levels in this study facilitates a pragmatic balance between computational cost and accuracy, allowing for the exploration of a wide range of operating conditions. Furthermore, the combination of high-fidelity simulations only at TSR 4, together with mid-fidelity simulations encompassing a range of TSR values, is anticipated to provide comprehensive insights into the VAWT fluid dynamic interactions arising from the presence of struts and tower.

The mid-fidelity results reveal some trends with regard to the impact of struts and tower on VAWT performance. At all TSRs, the inclusion of struts and tower (both for towers A and B) exerts

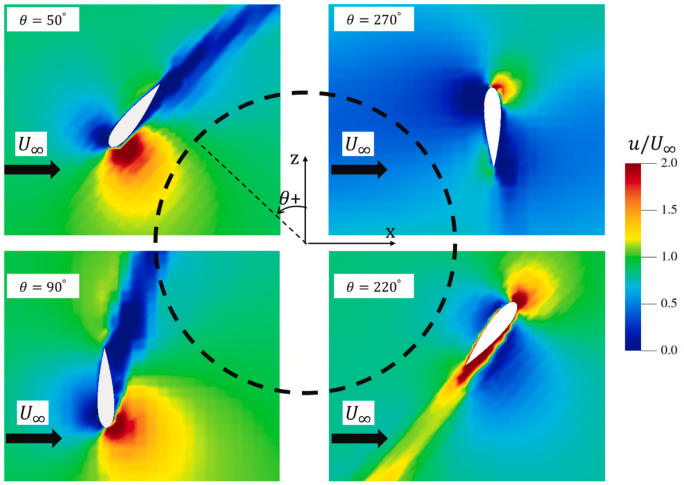

Figure 6.10: Instantaneous streamwise velocities experienced by a VAWT blade at different azimuth locations as obtained by Brandetti et al. [47]; u: streamwise velocity, U_∞: freestream velocity (reprinted after written permission)

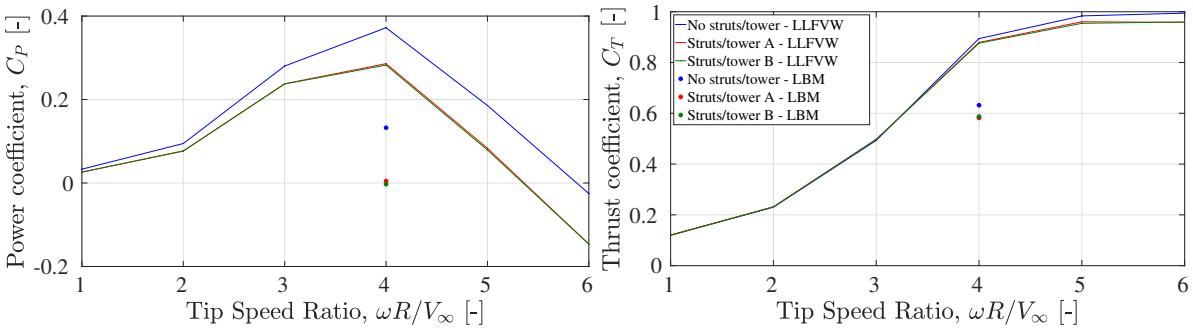

(a) (b)

Figure 6.11: Power and thrust curve obtained for the three VAWT configurations using the mid-fidelity LLFVW and high-fidelity LBM; line represents mid-fidelity and dot represents high-fidelity results

a negative effect on both the C_P and C_T values. This effect is particularly pronounced as TSR increases. This is expected since at lower TSRs, the blades operate more independently and there is minimal increase in blade-wake/blade-vortex interaction due to the addition of these support structures. Consequently, the decrease in C_P and C_T values is less significant at these TSRs. However, as TSR increases, so does the induction factor and the significance of blade-wake/blade-vortex interaction. The presence of the support structures further exacerbates these interactions, resulting in worsened loading on each blade and, subsequently, reduced overall rotor power and thrust. For the same reason, higher TSR exhibits a sharper gradient in C_P values than lower TSR. Interestingly, the addition of struts and tower exert minimal impact on the VAWT self-starting capability(C_P at very low TSR). However, a severe effect is observed at the optimal TSR value (TSR = 4 in this case). Notably, the optimal TSR value remains unchanged when struts and tower are added, unlike the observed trend in Chapter 5, where the optimal TSR decreases with an increase in the number of blades. It is recommended that future studies investigate the behaviour of the optimal TSR when even more support structures are employed while maintaining the same VAWT blade design and solidity.

The thrust coefficient (C_T) exhibits an asymptotic trend with an increase in TSR for all three VAWT configurations used. The inclusion of struts and tower has a less severe impact on the C_T values, with the differences becoming visible only after the TSR reaches 3.5. In contrast, the de-

crease in C_P is evident even at lower TSRs. This observation suggests that the tangential loading of the blades is more sensitive to the influence of these support structures compared to the normal loading. Moreover, the increase in the diameter of tower B, relative to tower A, results in reductions in both C_P and C_T values. However, the magnitude of this reduction is found to be relatively insignificant.

A comparison between the mid-fidelity LLFVW and high-fidelity LBM results at a TSR of 4 reveals differences in both the C_P and C_T values. Notably, these differences become more pronounced with the addition of struts and a central tower to the VAWT configurations. For the VAWT without struts and tower, the difference in C_P between the mid-fidelity and high-fidelity simulations is only 0.24. However, this difference increases to 0.281 and 0.285 for the second and third VAWT configurations, respectively, when struts and tower are introduced. Remarkably, the power generation even turns negative for the third configuration with tower B. A similar trend is observed for the C_T values, wherein the difference between the LBM and LLFVW simulations increases with the addition of struts and tower.

These observations suggest that the mid-fidelity method may not be capturing the complex 3D effects in the VAWT flow and force field as effectively as the high-fidelity method, particularly in the near-wake region where blade-wake/blade-vortex interactions are most significant. This discrepancy in results is not unexpected, given the inherent differences in fluid modelling between the two methods. The mid-fidelity approach relies on simplifications and assumptions to reduce computational costs, which may lead to limitations in accurately capturing certain flow features. Conversely, the high-fidelity LBM method provides a more detailed and accurate representation of the fluid dynamics, enabling a more comprehensive analysis of the VAWT behaviour. However, it is noteworthy that the trends in C_P and C_T observed by the mid-fidelity LLFVW method agree with the LBM results at TSR = 4, wherein the addition of struts and tower results in a degradation of power and thrust values.

Figure 6.12 depicts the temporal variation of the C_T and C_Q plotted for the overall rotor over a complete 360° azimuth. The data is obtained using the high-fidelity LBM and mid-fidelity LLFVW methods at a TSR of 4. Additionally, the figure presents the average values over the rotation, corresponding to the values shown in Figure 6.11. The analysis reveals that the presence of struts and tower leads to a reduction in both thrust and torque values, particularly at the most upstream and downstream locations, compared to the VAWT without struts and tower. Additionally, the increase in tower diameter exacerbates this reduction, leading to further decreases in these values.

Both the mid-fidelity LLFVW and high-fidelity methods demonstrate an accurate representation of this physical behavior. However, a notable difference arises when comparing the peak C_T and C_Q values in the upwind and downwind parts of the rotation. Specifically, LLFVW tends to predict higher values for both C_T and C_Q compared to LBM, across all three VAWT configurations. This behavior is consistent with the statistical time convergence results presented in Figure 6.4. Interestingly, this observation contrasts with the findings in Chapter 5, where LLFVW predicted lower blade loading values in the upwind part and higher values in the downwind part of the rotation, compared to LBM. The reason for this discrepancy can be attributed to the utilisation of XFOIL polar values (C_l and C_d vs angle of attack α) in the analytical formulation of LLFVW, which influence the blade angle of attack and induced velocity. It is suggested to modify these polars accordingly by introducing empirical corrections in future investigations. An alternative approach involves using airfoil polar values for 360° angle of attack obtained through wind tunnel experiments [300].

Figure 6.13 presents the variation of C_T and C_Q for a single blade throughout a complete 360° azimuth, using both high-fidelity and mid-fidelity methods at TSR = 4. The figure also displays the corresponding average values over the rotation. The results exhibit a decrease in both C_T and C_Q values due to the presence of struts and tower, observed across both the upwind and downwind parts of the rotation. This decline can be attributed to the increased blade-wake/blade-vortex inter-

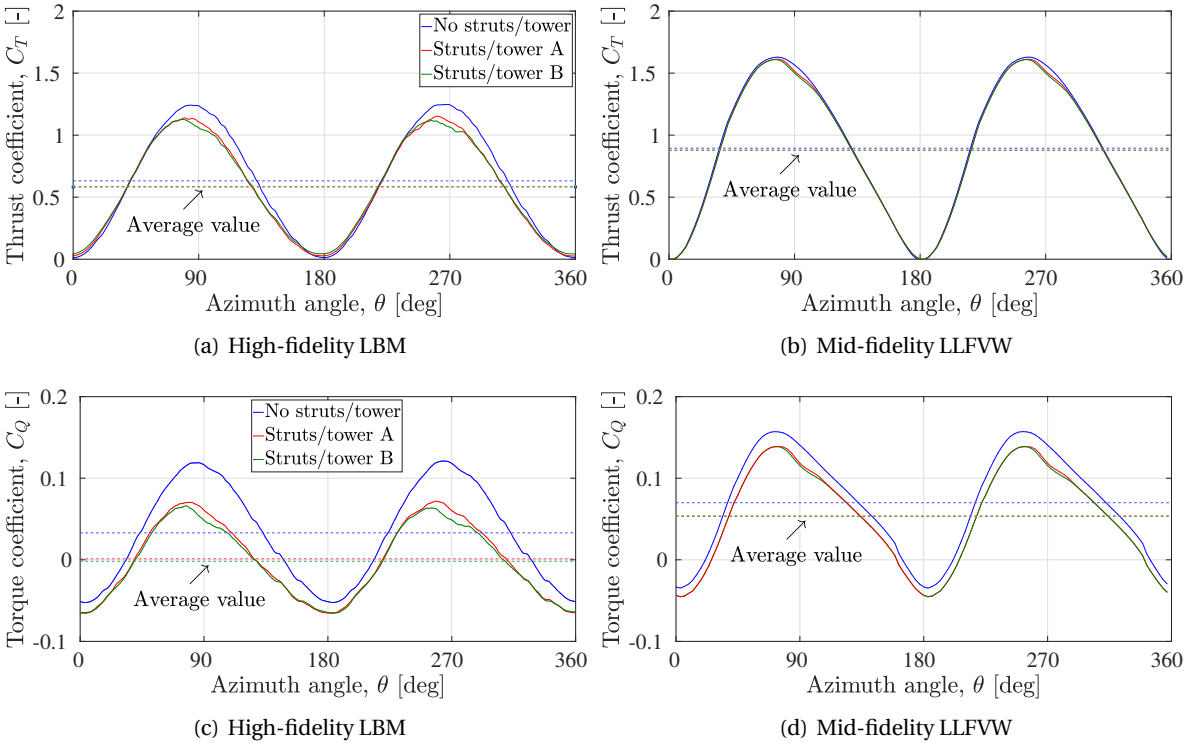

(a) High-fidelity LBM

(b) Mid-fidelity LLFVW

(c) High-fidelity LBM

(d) Mid-fidelity LLFVW

Figure 6.12: Variation of thrust coefficient C_T and torque coefficient C_Q for the overall rotor over a complete rotation, using the high-fidelity LBM and mid-fidelity LLFVW at TSR = 4

actions arising from the introduction of these support structures, leading to a reduced aerodynamic efficiency of the individual blade. Moreover, downstream blades produce lower thrust and torque values compared to their upstream counterparts, with a prominent reduction observed at around 270° azimuth, which is precisely downstream of the central tower. This reduction in performance further increases with an increase in tower diameter, contributing to a reduction in the average rotor thrust and torque values, as evident in Figures 6.11 and 6.12.

The results also reveal negative torque production during a significant portion of the rotation when struts and tower are present, indicating the extent of blade-wake interaction induced by the additional structures in VAWTs. Both the mid-fidelity LLFVW and high-fidelity LBM simulations effectively capture these physical characteristics. However, when comparing the C_T and C_Q values between the two methods, it is observed that LLFVW predicts higher values than LBM for the entire rotation. Additionally, the investigation demonstrates that LBM results exhibit a more pronounced degradation in blade performance than LLFVW, with negligible differences observed in the upwind part of the rotation for the latter. A similar trend can be observed in Figure 6.12 and this discrepancy between the two methods highlights a potential drawback of vortex-based methods in accurately modeling unsteady aerodynamic interactions and wake dynamics, especially in the presence of complex support structures such as struts and tower.

The above-mentioned unsteady force field characteristics can also be visualised from Figure 6.14 which presents the variation in blade normal forces (F_n) for a single blade over the equivalent 3D cylindrical surface traced by the VAWT blades at TSR = 4. The comparison of values over both azimuthal and spanwise directions is conducted for all three VAWT configurations between LBM and LLFVW. The analysis reveals several noteworthy observations. Firstly, normal blade forces exhibit degradation in the downwind part of the rotation as compared to the upwind part, and this behavior is accurately captured by both numerical methods for all VAWT configurations. This variation in

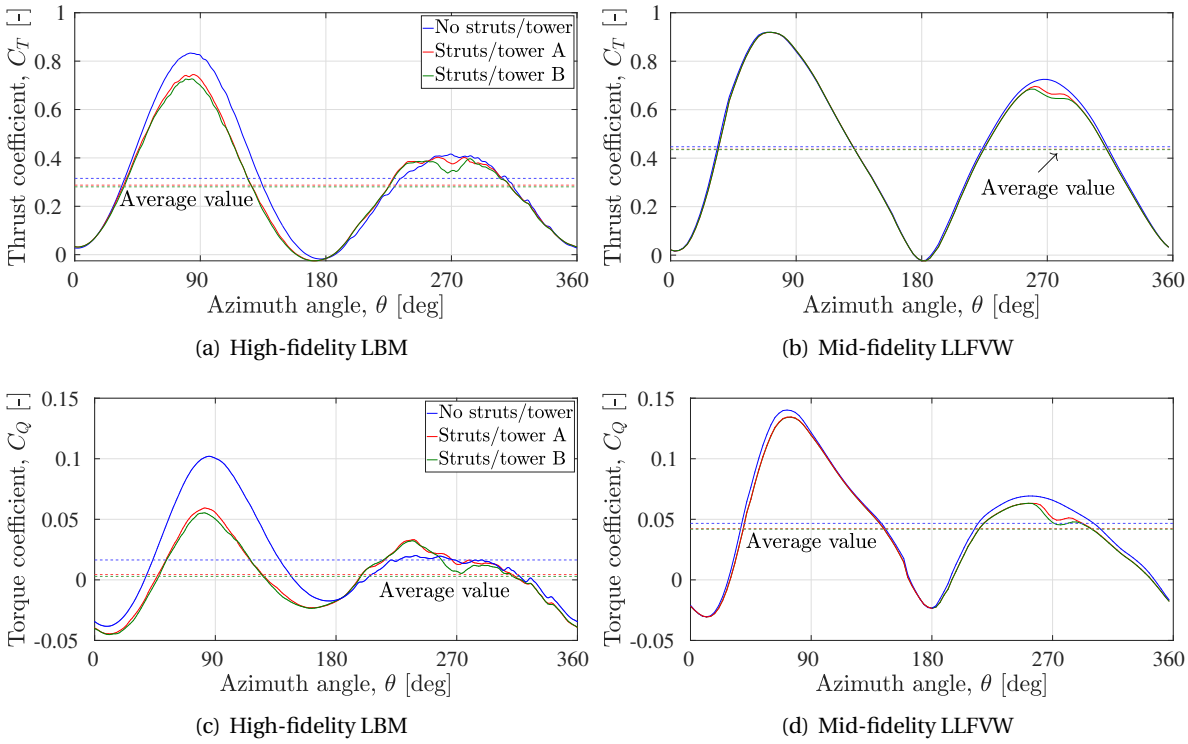

(a) High-fidelity LBM (b) Mid-fidelity LLFVW

(c) High-fidelity LBM (d) Mid-fidelity LLFVW

Figure 6.13: Variation of thrust coefficient C_T and torque coefficient C_Q for a single blade over a complete rotation, using the high-fidelity LBM and mid-fidelity LLFVW at TSR = 4

loading is inherent to VAWTs and is a consequence of the complex blade-wake/blade-vortex interactions. Moreover, the presence of the two struts located at h/H of 0.26 and -0.26 has a noticeable effect on the spanwise distribution of blade loading. The struts induce a deficit in blade loading, particularly prominent in the upwind part of the rotation, resulting in reduced overall blade loading as observed in Figure 6.13. In the downwind part, where the blade loading is inherently reduced and highly unsteady, the impact of the struts becomes less apparent. Interestingly, this effect of the struts is not adequately captured by the mid-fidelity simulation, both in the upwind and downwind parts of rotation. This discrepancy can be attributed to the use of a symmetrical airfoil for the struts at a zero angle of attack, leading to no shedding of vortex lines from the lifting line of the strut blades. This results in the lack of a visible effect on the spanwise blade loading in the mid-fidelity simulation.

The influence of the central tower is evident in both the mid-fidelity and high-fidelity results, particularly in the downwind part of the rotation. The presence of the tower induces a deficit in blade loading, prominently observed around the most downstream location at 270° azimuth. As the tower diameter increases, the deficit becomes more pronounced, leading to the observed dip in thrust and torque values in Figure 6.13. Moreover, LLFVW consistently predicts higher values of blade loading over the entire rotation, as compared to LBM. This discrepancy is reflected in the thrust and torque values of a single blade and the overall rotor, as demonstrated earlier in Figures 6.13 and 6.12, respectively. Additionally, the 3D effects of tip vortices on the force field are more pronounced with LBM than with LLFVW, as can be seen around h/H of -0.5 and 0.5 in Figure 6.14. This observation further supports the conclusion that mid-fidelity vortex methods may not fully capture the intricacies of 3D fluid dynamic interactions, although the general trends align with those observed in the high-fidelity LBM method.

Figure 6.15 provides insights into the instantaneous vortices in the downstream region of the VAWT flow field, using iso-surfaces of the λ_2 criterion (λ_2 = -500 1/sec^2).

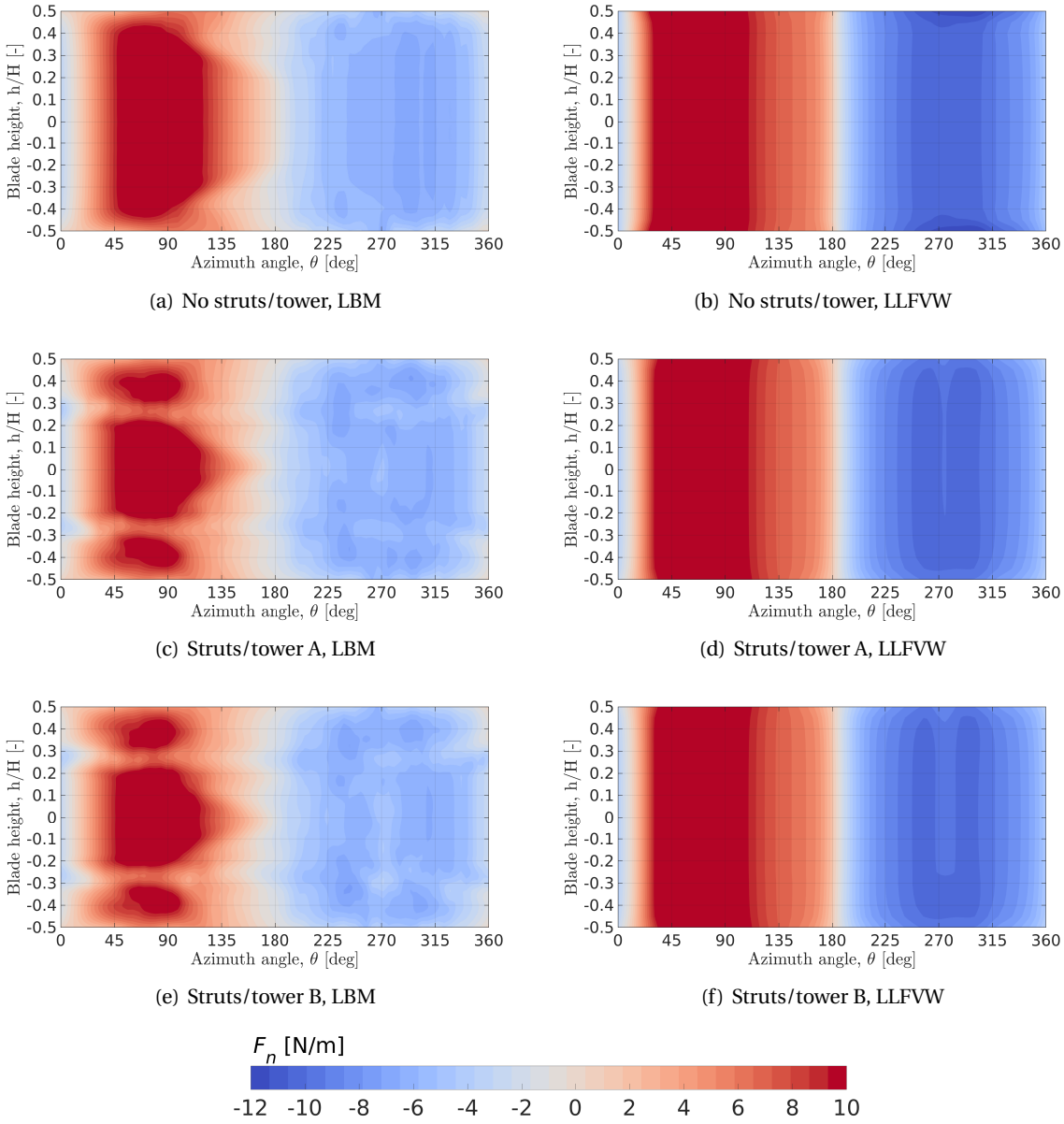

Figure 6.14: Normal force contour for a single blade over azimuthal and spanwise directions, using the high-fidelity LBM and mid-fidelity LLFVW, at TSR = 4

The 3D flow field visualisation helps to gain a deeper understanding of the influence of blade-wake/blade-vortex interactions (BWI/BVI) on the overall VAWT performance. The coherent tip vortices, which are shed from the tips of each blade, propagate downstream, giving rise to a distinctive spiral flow pattern known as a "vortex ring" that encircles the axis of the turbine. This convective motion of the large vortex structures is accompanied by the expansion of the wake and the gradual breakdown into smaller-scale structures due to flow instabilities and spatial modulation. These smaller structures eventually dissipate and intermingle with the surrounding fluid [12, 196]. An important observation is that the density of smaller, incoherent vortex structures increases with the addition of struts and a central tower. Consequently, BWI/BVI increases, which disrupts the ideal pressure and loading distribution along both the chordwise and spanwise directions. This disruption leads to a reduction in blade loading when struts and a central tower are added. This obser-

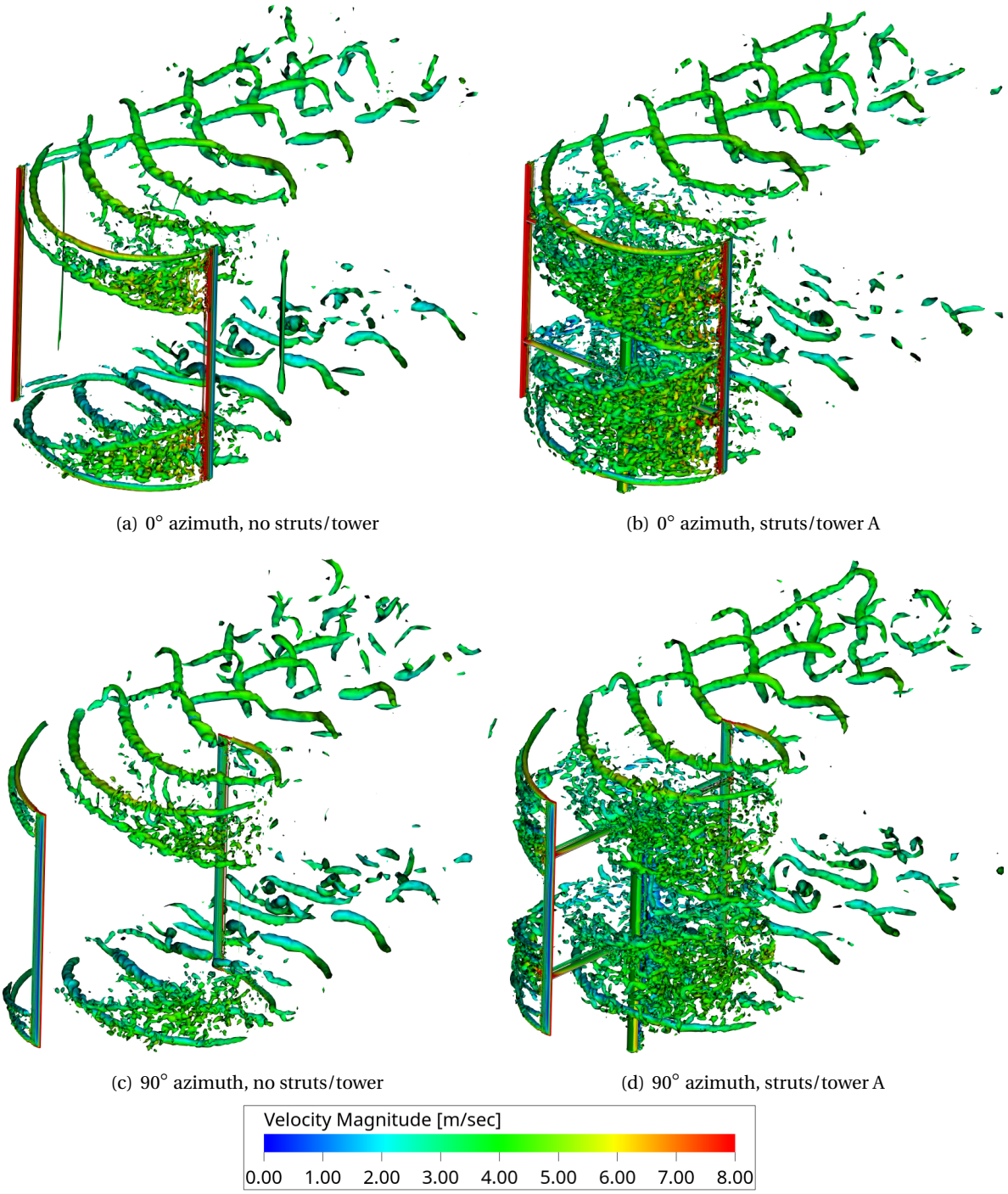

(a) 0° azimuth, no struts/tower

(b) 0° azimuth, struts/tower A

(c) 90° azimuth, no struts/tower

(d) 90° azimuth, struts/tower A

Figure 6.15: Instantaneous 3D flowfield using iso-surfaces of the λ_2 criterion (λ_2 = -500 1/sec^2) for vortices visualisation, using high-fidelity LBM at TSR = 4

vation aligns well with the results reported in the preceding figures (Figure 6.12, 6.13, and 6.14), confirming the significant influence of struts and tower on VAWT performance.

Figure 6.16 presents a set of visualizations for the wake structures of VAWTs for all three configurations, simulated using the mid-fidelity LLFVW method at a TSR of 4. The left column depicts the vortex lines shed from the VAWT blades, while the right column illustrates the instantaneous 3D flow field using iso-surfaces of the Q-criterion (Q = 6 1/sec^2).

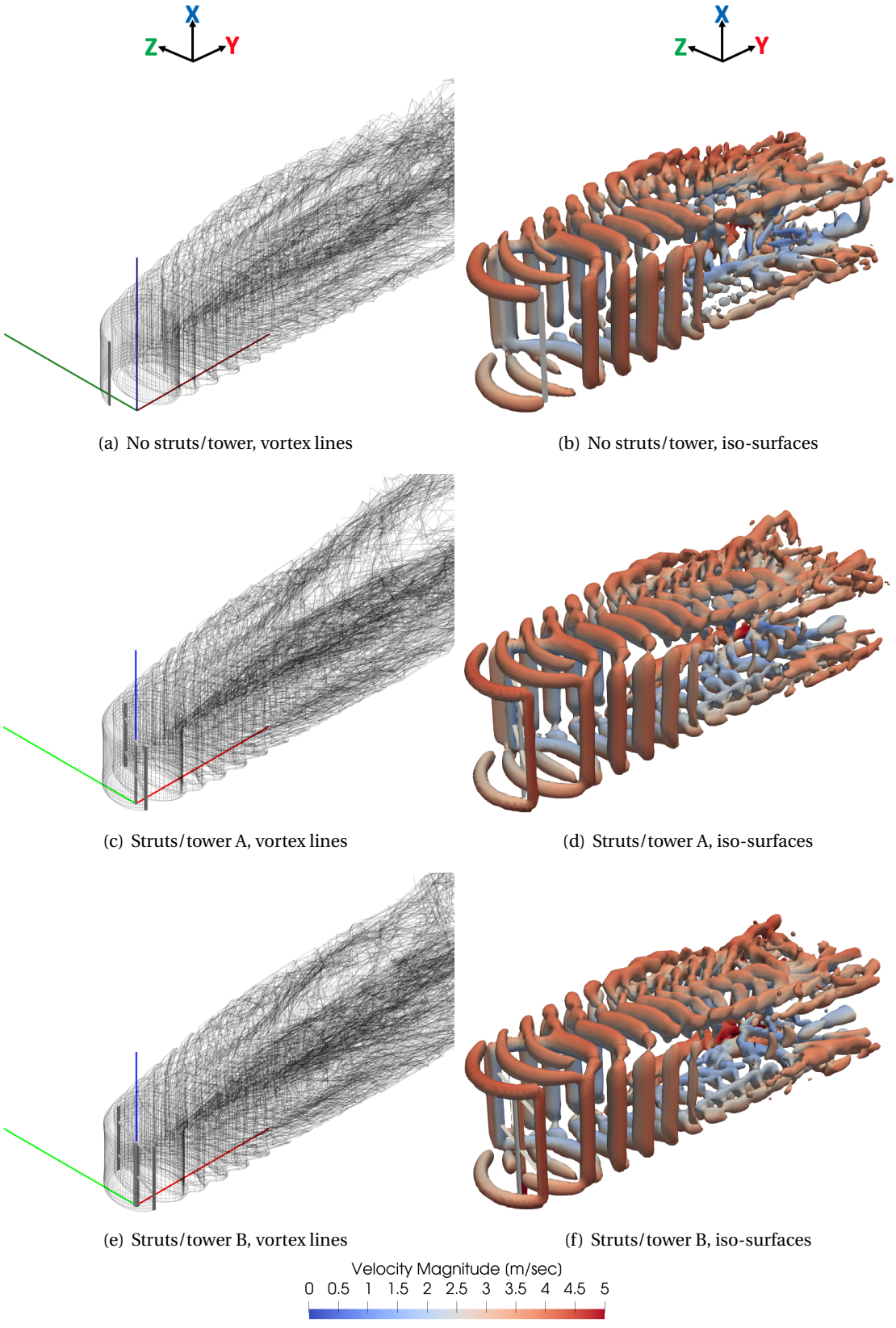

(a) No struts/tower, vortex lines

(b) No struts/tower, iso-surfaces

(c) Struts/tower A, vortex lines

(d) Struts/tower A, iso-surfaces

(e) Struts/tower B, vortex lines

(f) Struts/tower B, iso-surfaces

Figure 6.16: Visualization of vortex lines shed from the VAWT blades and instantaneous 3D flowfield using iso-surfaces of the Q-criterion ($Q = 6\ 1/\text{sec}^2$) for vortices visualisation, using mid-fidelity LLFVW at TSR = 4

The figures show no significant change in vortex density and wake strength as the struts and central tower are added, unlike the high-fidelity results (in Figure 6.15). The high-fidelity method provides higher resolution and captures finer details of the vortex structures, including the breakup of primary vortices into secondary vortices, as compared to the mid-fidelity method. This allows for a more accurate representation of small-scale vortices and intricate flow features which are shed from the struts and central tower. The mid-fidelity method, while capturing the overall wake structure and major vortex interactions, lacks the resolution to depict smaller vortices from such support structures.

The increase in strength of the VAWT wake resulting from the presence of struts and tower is also evident in Figure 6.17. This figure illustrates the instantaneous streamwise velocity contours in the VAWT wake on a 2D plane situated at the blade mid-span location. The results are compared for both LBM and LLFVW simulations at TSR = 4.

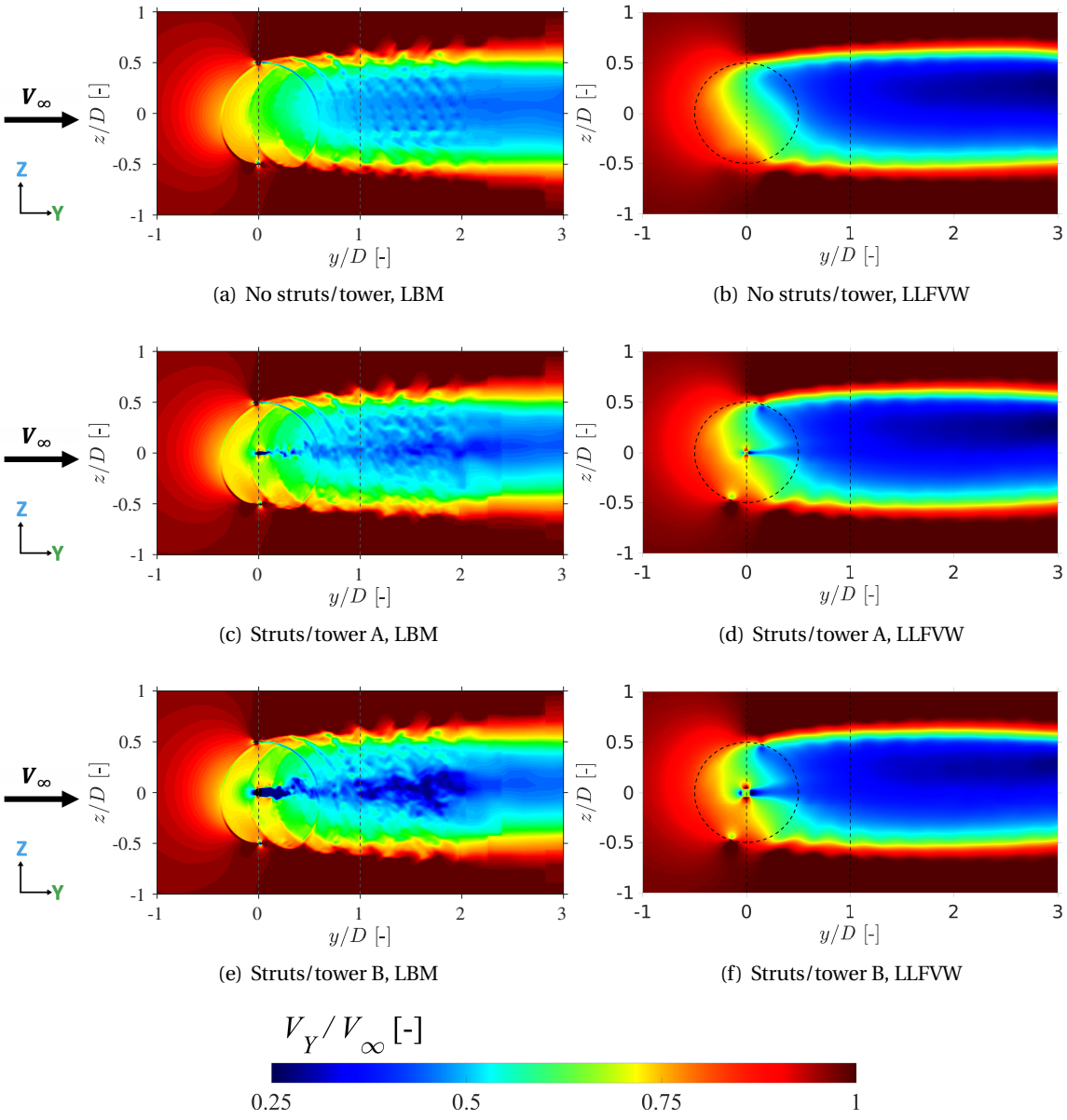

(a) No struts/tower, LBM

(b) No struts/tower, LLFVW

(c) Struts/tower A, LBM

(d) Struts/tower A, LLFVW

(e) Struts/tower B, LBM

(f) Struts/tower B, LLFVW

Figure 6.17: Instantaneous streamwise velocity contours in the VAWT wake on a 2D plane located at the blade mid-span location, using both LBM and LLFVW methods, at TSR = 4

The central tower introduces an additional velocity deficit in the downstream wake, leading to a decrease in streamwise velocity. This reduction in velocity corresponds to the observed decline in blade loading values around 270° azimuth, as depicted in Figures 6.13 and 6.14. Moreover, the velocity deficit increases as the tower diameter increases and the severity of BWI/BVI is expected to increase due to the vortices shed from the tower, contributing to further modifications in the wake dynamics. The impact of the central tower is effectively captured by both numerical methods. However, it is noteworthy that LLFVW predicts lower wake velocities (i.e., a stronger wake) compared to LBM, consistently observed across all VAWT configurations simulated.

The presence of a stronger force distribution on an airfoil or blade corresponds to a more pronounced downstream wake, characterised by enhanced velocity deficits and vortical structures. This observation is consistent with the higher rotor thrust values predicted by LLFVW compared to LBM, as depicted in Figures 6.12 and 6.13. Notably, the 2D vortex structures depicted in Figure 6.17 for LBM simulations are more prominent than those observed in LLFVW results. These structures are indicative of shed vortices, as observed in the 3D view in Figure 6.15 and similar to those shown in Chapter 5 (Figure 5.13). The presence of such vortical structures highlights the dissimilarity in vortex modelling approaches between the two methods, with high-fidelity LBM demonstrating a more accurate capture of blade vortex interactions compared to the mid-fidelity LLFVW method.

The differences in wake velocities between the two numerical methods are further examined in a more quantitative manner through Figure 6.18, which presents the streamwise velocity values averaged over a complete rotation for all three VAWT configurations.

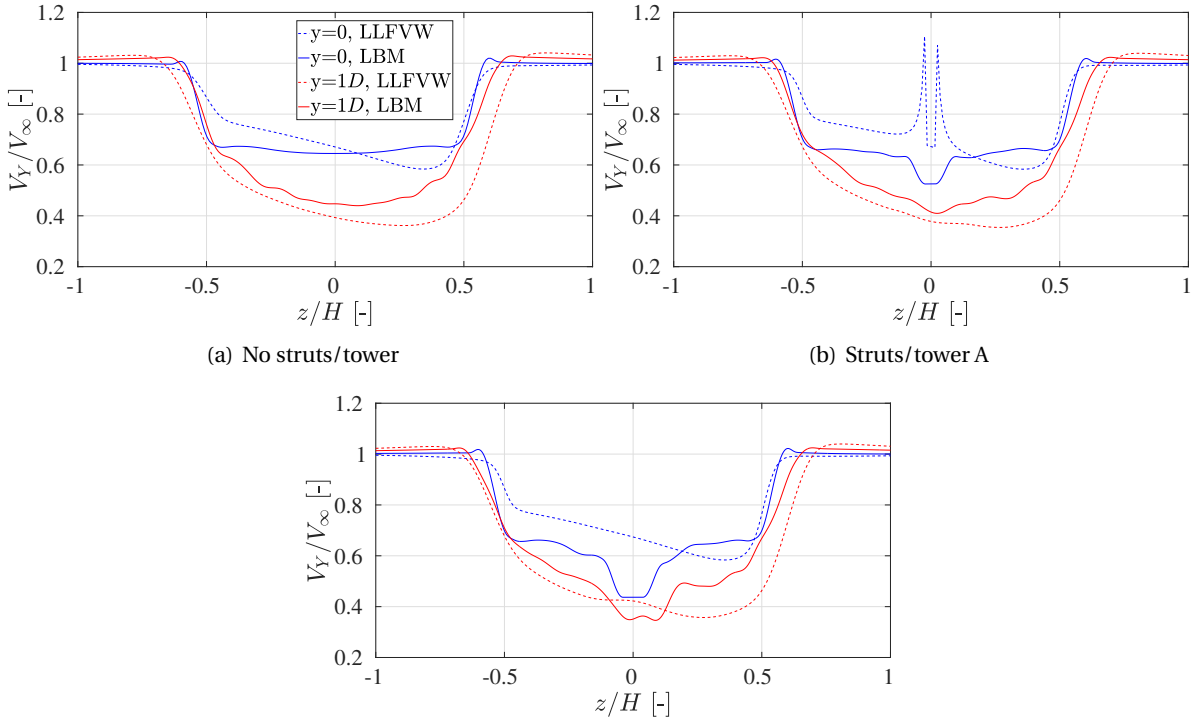

(a) No struts/tower

(b) Struts/tower A

(c) Struts/tower B

Figure 6.18: Comparison of streamwise velocities, averaged over a rotation, in the downstream VAWT flowfield using high-fidelity LBM and mid-fidelity LLFVW at two different downstream locations, at TSR = 4

The velocity values are plotted along lines positioned at distances of $0D$ and $1D$ downstream from the VAWT center at the blade-mid-span 2D plane, as illustrated in Figure 6.17 by black dotted lines. Along the centreline of the VAWT ($y = 0D$), the mid-fidelity LLFVW method predicts higher streamwise velocities compared to the high-fidelity LBM. Conversely, at a downstream location ($y =$

1D), the LLFVW method predicts lower streamwise velocities compared to LBM. Notably, the VAWT flow field exhibits an asymmetrical nature across all three configurations, particularly evident with the mid-fidelity LLFVW method.

Instantaneous streamwise velocities experienced by the VAWT blade at the mid-span location are visualised in Figure 6.19. The results are compared for all three VAWT configurations using the high-fidelity LBM, at the most upstream (90°) and most downstream location (270°). The addition of struts and tower does not significantly affect the induced velocity experienced at the 90° azimuth. However, at 270° azimuth, the presence of the tower upstream leads to a decrease in induced velocity, resulting in a reduction in the blade angle of attack (AoA), blade loading, and overall aerodynamic performance. This decrease in induced velocity and AoA becomes even more pronounced as the tower diameter increases. The impact on blade loading can be observed in Figures 6.13 and 6.14. These variations in streamwise velocities align with the findings presented in Figure 6.17 on a larger scale of the overall rotor wake.

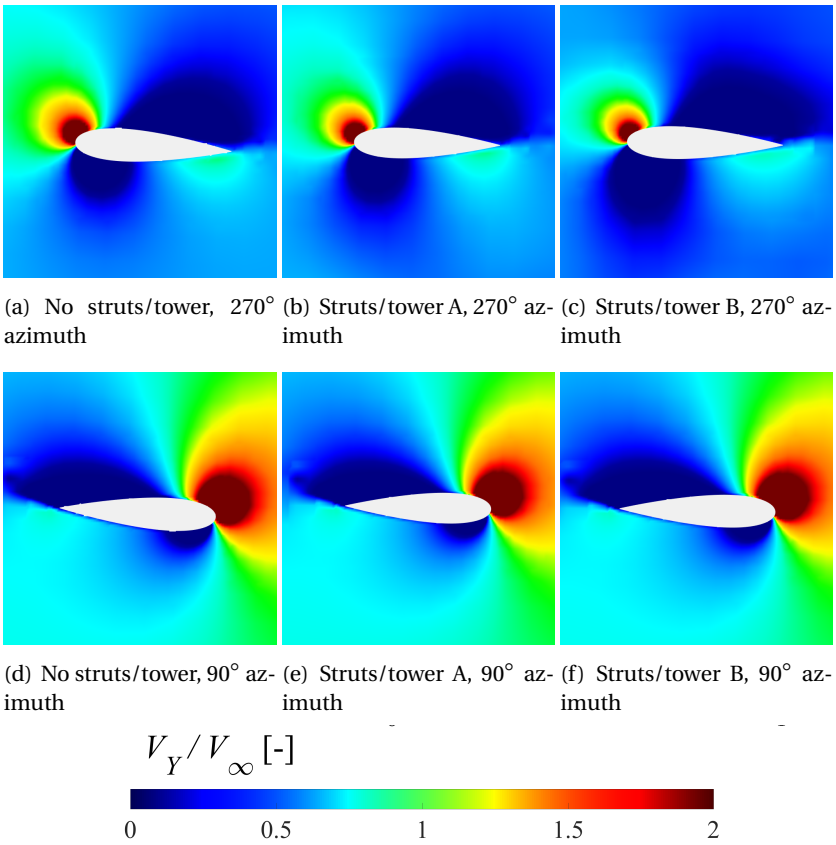

(a) No struts/tower, 270° azimuth (b) Struts/tower A, 270° azimuth (c) Struts/tower B, 270° azimuth

(d) No struts/tower, 90° azimuth (e) Struts/tower A, 90° azimuth (f) Struts/tower B, 90° azimuth

Figure 6.19: Comparison of instantaneous velocities experienced by a VAWT blade at the most upstream (90°) and the most downstream location (270°) for all three configurations, using the high-fidelity LBM at TSR = 4

The unsteady pressure data acquired at two distinct locations, namely the rotor plane (0,0,2.6D) and a position outside the rotor plane (0.87D,0,2.6D), over a single rotor rotation is depicted in Figure 6.20. The dataset includes contributions from both the blades and the struts/tower, if applicable to a particular configuration. Firstly, a comparison between the two locations reveals that the high-frequency pressure fluctuations are lower at the out-of-plane location as compared to the in-plane location. This observation is consistent with the findings reported in previous chapters (Chapter 4 at different TSRs and Chapter 5 with different numbers of blades). Secondly, the addition of struts and the central tower does not lead to a significant increase in unsteady pressure fluctuations, with only minor differences observed for the in-plane location. This result aligns with the

findings presented in Figure 6.4 where minimal effect of struts and tower is found on the temporal convergence behaviour. Across all three configurations, sharp drops in pressure values are evident at approximately 30°, 45°, and 60° azimuth locations. These pressure variations can be attributed to the interaction of downstream blades with the vortices shed by the upstream blades in the wake.

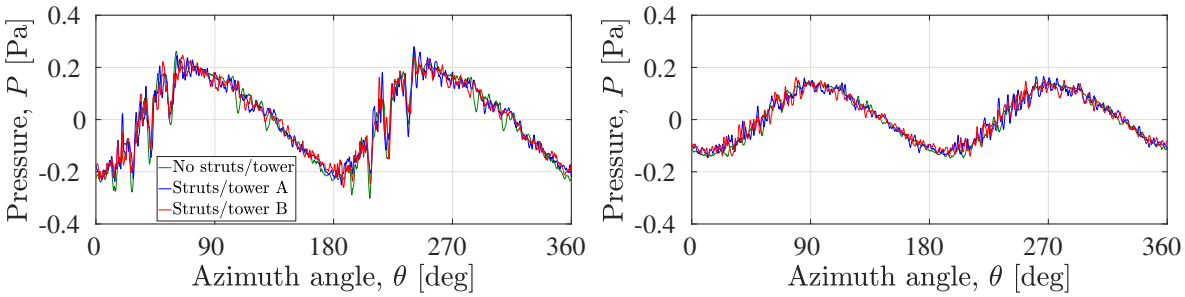

(a) At X,Y,Z = (0,0,2.6D) (b) At X,Y,Z = (0.87D,0,2.6D)

Figure 6.20: Raw unsteady pressure data using the high-fidelity LBM at two different locations, at TSR = 4

To gain deeper insights into the effect of struts and tower on noise generation, the noise spectra of all three VAWT configurations are analysed. Figure 6.21 reports the PSD values in dB/Hz for the frequency range of 20-2000 Hz at the two observer locations considered in this study, plotted with a frequency resolution (Δf) of 15 Hz. The noise spectra are not plotted below the human hearing range (20 Hz) where some blade passage frequency (BPF) peaks are observed. The results demonstrate that the inclusion of struts and tower leads to higher PSD values for frequencies exceeding ≈300 Hz. This trend is evident for both observer locations. This increase in PSD values is attributed to the increased BWI/BVI present in the flow field when struts and tower are introduced. This can be observed using the visualisation of instantaneous 3D vortices in Figure 6.15. Conversely, in the low-frequency range (50-200 Hz), PSD values are lower when struts and tower are present. This phenomenon can be associated with the decrease in integral blade loading due to the presence of struts and a tower, as observed in Figure 6.12 and 6.13. The reduction in the tonal component for blade loading noise results in lower PSD values at lower frequencies. It is important to note that the aforementioned effect is more pronounced for the in-plane location, as the influence of blade loading on the tonal component is most significant in the plane of rotation. Furthermore, as expected from Figure 6.20, noise levels are higher for the in-plane location compared to the out-of-plane location across the entire frequency range.

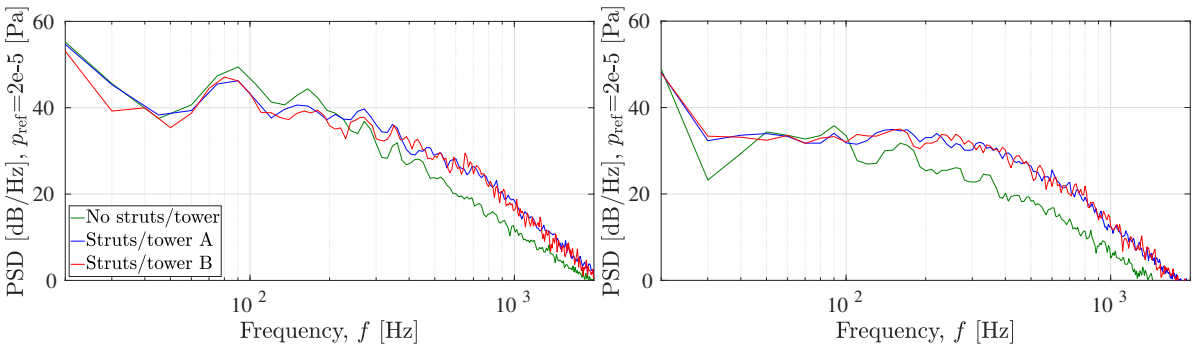

(a) At X,Y,Z = (0,0,2.6D) (b) At X,Y,Z = (0.87D,0,2.6D)

Figure 6.21: Power Spectral Density (PSD) spectra using the high-fidelity LBM at two different locations, at TSR = 4

Figure 6.22 presents the directivity plot of the overall sound pressure level (OSPL) showing the

effect of struts and central tower on VAWT aeroacoustics. The OSPL values are obtained using high-fidelity LBM and are calculated within the frequency range of 10-2000 Hz. For both the YZ and XY planes, noise levels decrease when struts and central tower are added. This is especially seen around the windward (0°) and leeward (180°) parts of the rotation. This observation can be linked to the overall rotor thrust values depicted in Figure 6.11, where the VAWT thrust decreases due to the addition of the support structures at the TSR of 4. With the larger diameter tower B, thrust decreases even further which also shows in the OSPL values.

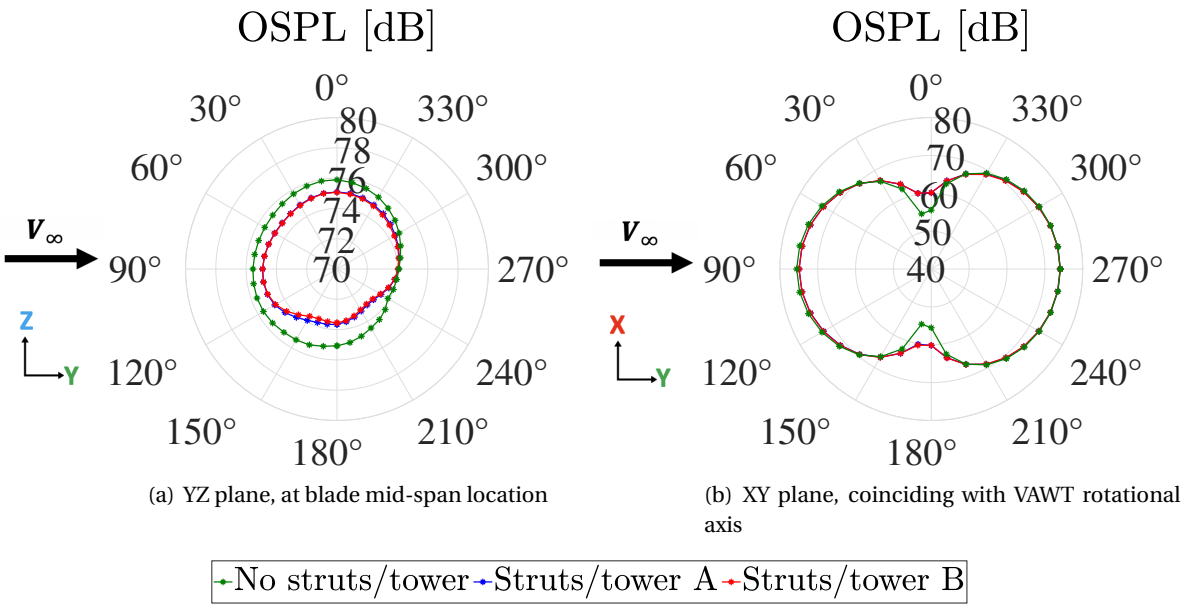

(a) YZ plane, at blade mid-span location

(b) XY plane, coinciding with VAWT rotational axis

Figure 6.22: Directivity plot of overall sound pressure level (OSPL) comparing different VAWT configurations at TSR = 4, along a circular array of 36 points situated at a distance of $7D$ from the origin of VAWT ([0,0,0])

On the YZ plane, VAWTs with struts and central tower exhibit a relatively larger reduction around the leeward side (180°), which shows that some noise sources in a VAWT [43–45, 261] are less dominant in these configurations (around that azimuth angle) as compared to the configuration without struts and central tower. On the XY plane, noise increases exactly at the topmost (0°) and bottom-most (180°) locations for the former, due to the presence of these support structures which are not present in the latter configuration. The behaviour of the XY directivity plot (around 0° and 180°) is even found in all configurations in Chapters 5 and 4 where struts and central tower are not present. Further investigation utilizing low-fidelity aeroacoustic prediction models can provide valuable insights into the specific contributions of different noise sources due to the presence of struts and central tower.

6.4. Conclusions and Discussions

The chapter presents a detailed flow physics investigation into the effect of supporting struts and central tower on the aerodynamic and aeroacoustic characteristics of vertical axis wind turbines (VAWTs). The objective of the study is twofold: firstly, support the development of a multi-fidelity simulation framework for optimising the aerodynamic and aeroacoustic performance of VAWTs and secondly, study the effect of one of the VAWT design components - struts and central tower. High-fidelity 3D aerodynamic simulations are conducted using the Lattice Boltzmann Method (LBM) and subsequent aeroacoustic post-processing using the Ffowcs Williams and Hawkings (FW-H) methodology to calculate the far-field noise. In addition, mid-fidelity aerodynamic simulations are performed using the Lifting Line Free Vortex Wake (LLFVW) method. The investigation focuses

on the effects of struts and tower on thrust and power performance, and far-field noise, while also comparing the 3D force-field and flow-field results obtained using the mid-fidelity and high-fidelity methods and identifying the differences in modelling fluid dynamic interactions which can be responsible for any observed discrepancies in the results.

A straight-bladed Darrieus VAWT with geometrical parameters replicated from the study by Brandetti et al. [47] and LeBlanc et al. [181, 182] is employed. Three different VAWT configurations have been simulated. The first configuration consists of only the two blades, without the inclusion of any struts or central tower. The second configuration consists of four supporting struts, a central tower, and the associated blades. In the third configuration, the diameter of the central tower is increased to twice the diameter in the second configuration. The VAWT solidity is set at 0.1 and the rotor aspect ratio is 1 for all configurations. LLFVW method is used to simulate a range of TSRs while LBM is used to simulate only a TSR of 4, for all three configurations. ,

The statistical temporal convergence behaviour is observed to be similar for the first two configurations, suggesting no significant effect on unsteady blade loading due to the increased fluid dynamic interactions caused by struts and tower. Thrust values exhibit superior convergence and has lower values of uncertainty than the torque values. Similarly, the grid convergence results showed that the thrust values exhibit better grid convergence than the torque values. The finest of the three grids simulated exhibited the most favourable grid convergence and was subsequently chosen for further flow physics analysis. For validation purposes, normal force coefficient C_{Fn} variation for a single blade for the full rotation is compared for the current high-fidelity and mid-fidelity setup with the reference high-fidelity simulation [47] and experiments [181, 182] and the analysis showed acceptable agreement.

The study showed a decrease in integral power and thrust values at all TSRs due to the presence of struts and tower, although the effect on thrust is minimal. The inclusion of struts and tower worsens the tangential and normal loading on each blade and overall rotor performance; the presence of struts especially degrades the spanwise distribution of forces. The severity of this phenomenon increases with an increase in TSR. Azimuthal blade loading decreases due to the presence of struts and tower for both the upwind and downwind parts of the rotation. This is attributed to the increased blade-wake/blade-vortex interactions arising from these support structures. There is a notable reduction in blade loading values around 270° azimuth which is precisely downstream of the central tower. This is due to tower wake, the thickness of which increases with an increase in tower diameter and the blade loading reduces further. The inclusion of struts and tower does not affect the self-starting capability and optimal TSR value, even though the optimal power decreases.

Both the mid-fidelity LLFVW and high-fidelity LBM capture the above-mentioned physical trends very well. However, the LLFVW method predicts higher values of thrust and torque in the upwind and downwind parts of the rotation as compared to LBM. This discrepancy was found to be true also when comparing individual blade normal forces and torque values and is consistent for all three VAWT configurations. This shows that the LLFVW method may not capture the complex 3D effects in a VAWT flow and force field as strongly as LBM, especially when struts and tower are present in the geometry. This resulted in the former predicting higher values of the integral thrust and power values of the overall rotor as compared to the latter. Empirical modifications in the airfoil lift and drag polar values are suggested, for the LLFVW method. Due to increased blade loading, streamwise wake velocities predicted were lower by the LLFVW method, contributing to a stronger wake, as compared to LBM. These findings underscore the importance of considering the appropriate fidelity level in wind turbine simulations, especially when complex 3D interactions are involved. Further research efforts should be directed towards refining the airfoil polar data used in the LLFVW method to better represent the blade-wake/blade-vortex interactions and to ensure consistency with the experimental data. The study also compared the aeroacoustic characteristics of all three VAWT configurations. Low-frequency noise was observed to be decrease when struts

and tower are added, due to the lower integral blade loading or thrust values obtained. Conversely, high-frequency noise was observed to increase, due to higher intensity of blade-wake/blade-vortex interactions between the downstream blades and vortices shed from all the upstream structures.

This study focuses on two important Darrieus VAWT supporting structures. Due to the large 3D design space of VAWTs, there is a need for further investigation into the impact of other geometric parameters, such as the effect of the airfoil shape, aspect ratio, blade design, blade pitch etc., as well as flow parameters, such as non-uniform inflow, on both aerodynamic performance and noise generation. The forthcoming chapters will focus on the investigation of these parameters.

7

Stand-alone VAWT IV: skewed inflow

Summary

This chapter investigates the effect of skewed inflow of aerodynamics and aeroacoustics of small-scale Darrieus VAWTs operating at chord-based Reynolds numbers below 1×10^5. Three inflow conditions are investigated using a 2-bladed Darrieus VAWT: skew angle of 0°, 20° and 40°. Both the high-fidelity Lattice Boltzmann Method (LBM) and mid-fidelity Lifting Line Free Vortex Wake (LLFVW) methods are utilised. In the temporal convergence analysis, results show faster convergence of thrust coefficient (C_T) and torque coefficient (C_Q) for the skew angle of 40° than 20°. The performance assessment indicates an initial increase in rotor power and thrust till 20° skew angle followed by a decline. This is attributed to a reduction in blade-wake/blade-vortex interactions (BWI/BVI) in the downwind part of rotation, due to skewed downstream wake. In the upwind part of rotation, blade loading decreases as the skew angle increases due to subsequent reduction in the horizontal component of freestream velocity. Both the mid-fidelity LLFVW and high-fidelity LBM methods are effective in capturing these physical phenomena. However, the LLFVW predicts higher C_T and C_Q, both integral and azimuthal values, along with lower streamwise velocities in the wake when compared with LBM. The difference between the results of LLFVW and LBM increases as skew angle increases. Regarding noise, the skewed inflow conditions lead to a decrease in low-frequency noise (50-200 Hz) and an increase in high-frequency noise (> 200 Hz). The reduction in integral blade loading accounts for the former, while the latter is influenced by an increase in flow separation on blades contributing to Separation-Stall (SS) noise. The flow separation occurs due to an additional spanwise velocity component on the blades.

7.1. Introduction

The chapter delves into an important and often understudied aspect of vertical axis wind turbine (VAWT) performance - the effect of skewed inflow conditions. While the general consensus in wind energy research has traditionally focused on the optimal performance conditions, namely, uniform, unidirectional wind flow, the real-world wind energy scenario is far from this ideal. A significant portion of wind energy resources exists in regions with complex terrain and built environments that naturally result in skewed inflow conditions. This departure from ideal conditions can substantially affect the performance, efficiency, and durability of vertical axis wind turbines. Therefore, a thorough investigation of these effects is crucial not only for predicting the aerodynamic performance more accurately but also for enhancing the operational strategies of VAWTs to withstand skewed inflow conditions and design a low-noise configuration.

7.1.1. Literature Review

A significant focus in the present study is on roof-mounted VAWTs where they operate in the wake of bluff bodies (eg. buildings) larger than the rotor scale. This makes the blades frequently experience inflow conditions which are skewed in the positive vertical direction; the position vertical direction is shown in Figure 7.1 and this reference will be used in the current chapter. According to Jones [159], if β is the skew angle, only the component $V_\infty cos\beta$ will influence the VAWT performance (perpendicular to VAWT axis) and not $V_\infty sin\beta$ (parallel to VAWT axis). Therefore, the effective tip speed ratio (TSR) increases to $\lambda/cos\beta$, where λ is the TSR when the flow direction is normal. Over the years, several studies have been undertaken on this subject, albeit with varying degrees of depth and focus. The results show the inherently complex nature of skewed inflow conditions - an issue that makes the analysis more nuanced, with both the positive and negative effects on power performance and noise generation of VAWTs.

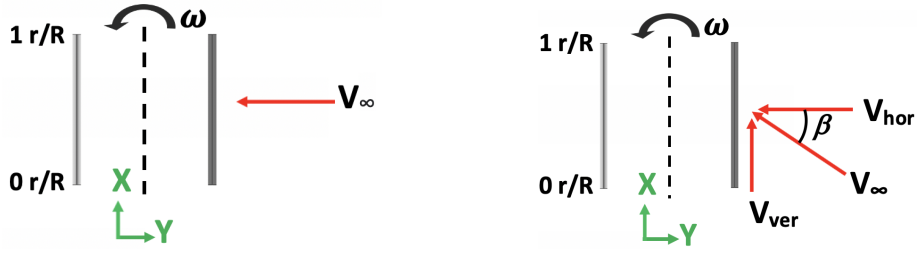

(a) Horizontal inflow (b) Skewed inflow

Figure 7.1: Reference used for skewed inflow condition; positive angle β is referred to as positive vertical direction for the airflow

A good review of the effect of skewed inflow conditions for vertical axis wind turbines is given by Fazlizan et al. [118, 119]. Various experimental and numerical investigations into VAWTs have revealed an increased power output under skewed flow conditions, depending on the rotor's geometric ratios. In skewed inflow conditions, the interaction between the blades and the oncoming flow changes. Since the VAWT blades trace a cylindrical volume, contrasting with the planar surface generated by a HAWT, this phenomenon effectively increased the total swept area of the vertical rotor, potentially enhancing power generation. Furthermore, the increased swept area causes expanded airflow in the rotor's downwind region. In the case of a sufficiently small aspect ratio of VAWT, the skewed convection of the wake leads to a larger interaction surface between the skewed airflow and the rotor blades which induces greater lift, generating higher torque and subsequently augmenting power output. This demonstrates the suitability of the Darrieus VAWTs for built environments where skewed wind flows occur frequently.

One of the earliest studies on skewed inflow conditions is conducted by Bussel et al. [344]. Wind tunnel experiments were conducted from 10° to 60° and power curves were analysed. The data revealed a significant increase in power output at skew angles between 25 to 30 degrees, with a peak power coefficient (C_P) of 0.175 at a tip speed ratio of 3.25. This translates to a substantial performance improvement of nearly 35% and can be attributed to an increase in "projected area". The C_P for a straight-bladed VAWT is associated with the projected swept area ($2R \times H$), where R denotes the rotor radius and H is its height. In the context of skewed airflow, the projected swept area (on a plane perpendicular to the incoming flow) apparently increases, thus enhancing the capacity for power extraction. At a skew angle of 25°, the increase in projected area is given by the Eq. 7.1, showing a 40% increase in swept area compared to a zero-skew-angle scenario, for the wind tunnel model.

$$A_{\text{skew}} = 2RH\cos 25^\circ + \pi R^2 \sin 25^\circ \approx 1.81RH + 1.33R^2 \ . \tag{7.1}$$

Mertens et al. [226, 227] developed a theoretical model for skewed inflow operation by modifying the multiple streamtube theory and highlighting the utilisation of a low-fidelity model for such complex flow conditions. The flow was divided into two parts: the single rotor part area where there is a single interaction between the flow and rotor blades and the double rotor part area where this interaction is two times. It was shown that C_P of an H-Darrieus in skewed inflow can exceed that in non-skewed conditions when based on the projected frontal rotor area at zero skew angle. This effect, which has been both observed and modelled, arises from the 3D geometry of the H-Darrieus. Such a geometry effectively enlarges the energy extraction area in skewed flow. An H-Darrieus with a higher rotor aspect ratio exhibits a smaller increase in the maximum C_P in skewed inflow compared to a lower rotor aspect ratio. This is because the relative increase in rotor area experiencing clean freestream flow is less in the former. Furthermore, TSR at maximum C_P is higher in skewed inflow conditions and this should be an essential factor while designing a VAWT since centrifugal force scales with the square of the TSR.

Another analytical method was presented by Ferreira et al. [120] which is computationally cheaper than the previous method discussed. The method avoids the cost to compute flow behaviour and the absolute value of C_P at different skew angles but only required the ratio between C_P at a non-zero skew angle and zero skew angle. The numerical predictions were close to experimental results and validate the accuracy of the proposed method for forecasting the thrust, torque, angular velocity, and power generation variations of an H-Darrieus VAWT under skewed inflow conditions. This approach also enables predictions of optimal rotor aspect ratios for the VAWT, although its validity may be affected by the turbine loading, blade-vortex interactions, and viscous effects. The comparison of this method with experimental results [226, 288] underscores the significance of aerodynamic interference due to tip vortices and struts linking the blade to the rotor axis under skewed inflow conditions.

Ferreira et al. [311] performed experiments and flow visualisation using smoke visualisation for the tip vortex expansion, hotwire measurements of the flow upwind and downwind of the rotor and VAWT thrust force measurements to determine its variation with skew angles. The VAWT demonstrates an increase in thrust values with a skew angle until the 30°-40° range, followed by a decrease, which aligns with the findings of the fore-mentioned studies. Flow visualisation showed that the interaction of the tip vortex created at the most upwind blade position has substantial implications on the downwind blade, possibly explaining differences between theoretical and experimental thrust outcomes. Hotwire measurements showed that the power gain in skewed inflow is generated by the part of the blade that in the downwind part of rotation does not interact with the wake of the upstream blades.

As an extension of the above work, Ferreira et al. [310] performed wind tunnel experiments using Particle Image Velocimetry (PIV) and modelled the rotor and wake with the 3D unsteady panel

method. The study reported that the skew angle causes wake asymmetry in the direction parallel to rotor axis, affecting its position, the intensity of shed and trailing vortices, and the expansion of the wake in the lateral direction. The experiments quantified the effects of skew angle on the strength of the tip vortex and its convection, and the 3D unsteady free wake panel code was found capable of replicating these effects. The study also revealed that the extra power obtained in skewed inflow arises from an increasingly exposed area of the downwind blade passage, operating outside the upwind-generated wake. However, this gain is counterbalanced by a non-uniform decrease in the flow component normal to the blade's lifting line, an effect linked to the asymmetrical spanwise induction of the wake.

Scheurich et al. [293] used Vorticity Transport Model (VTM) to model VAWT aerodynamics and wake dynamics in skewed inflow conditions. The author reported that VAWT can achieve a higher C_P in skewed inflow compared to normal flow, provided its height-to-radius ratio (rotor aspect ratio) is adequately small. This aligns with the findings of previous studies and this effect becomes more pronounced at higher TSRs, as the vortex structures in the turbine wake are swept away more efficiently from the rotational trajectory of the blades. The azimuthal variation of C_P in a single rotation reduces when the flow is skewed, as compared to when the flow is normal. Notably, VAWTs with helically twisted blades demonstrate a relatively constant C_P over the entire azimuth, regardless of whether the flow is normal or oblique. This underscores the importance of both operational conditions (eg. TSR) and geometric properties (eg. helical) when analyzing VAWT performance under various conditions.

The previous chapter 6 highlighted the importance of struts when predicting VAWT performance. Islam et al.[154] showed that airfoil-shaped struts help to increase the performance in skewed inflows. It helps to reduce parasitic drag and creates additional torque from the lift forces. Balduzzi et al. [20] experimented with hybrid Darrieus-Savonius VAWT on a rooftop and reported the power production for different horizontal and vertical wind speeds separately. The study reported a decrease in power production as vertical wind speed increases, for a fixed value of horizontal wind speed. This result is in contradiction to other studies [226, 293, 311, 344] where an increase in power production was observed for non-zero vertical wind speeds (with non-zero skew angles). Interestingly, the author also reported that 90% of the peak power is produced when skew angle is 45°, which supports the conclusion of other researchers [120, 226, 310].

A similar result is shown by Orlandi et al. [252] who utilised the unsteady 3D URANS method to predict VAWT performance in skewed inflow conditions and validated the results with experiments. The C_P value increases in skewed inflow conditions and this is attributed to the downwind portion of the rotor being minimally affected by the wake generated by the upwind blades. Through open-air experiments on a rooftop, Lee et al. [185] demonstrated that skewed inflow was experienced by the VAWT on the rooftop in 99% of all measured instances. More than 90% of power output occurs when the vertical wind speed to horizontal wind speed ratio is less than or equal to 1.0, or the skew angle is $\leq 45°$. The power output is notably more influenced by vertical wind speed when horizontal wind speed is higher. The research concludes that for a VAWT installed on a rooftop, the key contributors to efficiency are horizontal wind speeds greater than 8 m/s, vertical angles less than 45°, and lower turbulence intensity.

Bianchini et al. [36] performed a theoretical investigation of VAWTs in skewed inflow by modifying the momentum models [210, 248, 317, 331], both Multiple Streamtubes [248, 317] and Double Multiple Streamtubes with variable interference factors [141, 254, 256]. The cross-flow principle was employed for lift and drag assessments of the airfoils in skewed flow, alongside a precise evaluation of the turbine's projected swept area. This consideration also integrated contributions from parts of the downwind half of the machine. Furthermore, the analysis examined the torque output across different zones of the turbine, taking into account scenarios of both double and single flow-rotor interactions. Validation with experimental data revealed an impressive match with the simulated

outcomes.

7.1.2. Research objectives

In light of the preceding research, the primary goal of the present investigation is to support the development of a multi-fidelity simulation framework, to study the impact of skewed inflow on the aerodynamic and aeroacoustic performance of VAWTs. The investigation utilises high-fidelity 3D aerodynamic simulations using the Lattice Boltzmann Method (LBM), focusing particularly on straight-bladed VAWTs. A future study is planned by using helical and troposkien blade shapes. Aeroacoustic post-processing is performed employing the Ffowcs Williams and Hawkings (FW-H) methodology, thereby enabling the calculation of far-field noise. Furthermore, mid-fidelity aerodynamic simulations are performed by using the unsteady Lifting Line Free Vortex Wake (LLFVW) model.

This investigation focuses on analyzing distinct fluid dynamic interactions with VAWTs under skewed inflow conditions. High-fidelity simulations are employed to achieve precise resolution of the flow around VAWT blades and within the wake. This method enables a detailed examination of 3D effects on force and flow fields during skewed flow. Specific effects analysed include non-uniform blade loading, wake behaviour, dynamic stall, blade-vortex interaction, and wake recovery. Conversely, mid-fidelity simulations involve simpler modelling of the flow field with vortex lifting lines. This approach contributes to a basic understanding of the unsteady 3D effects connected with skewed inflow conditions, without delving into the complexities observed in high-fidelity simulations.

This chapter conducts a comparative analysis between mid-fidelity and high-fidelity simulation results. This analysis is vital to evaluate the mid-fidelity approach as a potential time- and resource-saving alternative to the high-fidelity method. The assessment focuses on the reliability and accuracy of the mid-fidelity solver, especially in cases where a detailed examination of the VAWT flow and force field is unnecessary. Additionally, this study addresses a gap in the literature by investigating the effects of non-uniform inflow conditions, such as skewed inflow, on both the aerodynamic and aeroacoustic performance of VAWTs. For this chapter, the following research questions are formulated:

Research Questions

- How do skewed inflow conditions affect VAWT performance parameters such as thrust, power, and far-field noise?
- How do the results for the effect of skewed inflow conditions obtained using the mid-fidelity and high-fidelity methods compare? What are the fluid dynamic interactions responsible for any differences observed?
- How do 3D effects of blade loading on thrust and power values, trailing and shed vortices, and wake dynamics vary when the inflow conditions are vertically skewed?
- What are the key noise sources contributing to the aeroacoustic performance of VAWTs when skewed inflow conditions are experienced?

The chapter is structured as follows. Section 6.2 presents the computational setup of both mid-fidelity LLFVW and high-fidelity LBM, including VAWT geometrical properties, flow and grid settings. Section 6.3 reports the results obtained for the temporal convergence study, detailed force and flow field analysis and aeroacoustic performance of the VAWT to investigate the effect of skewed inflow conditions. The last section 6.4 presents important conclusions of the study and a discussion on the understanding of the highly unsteady and turbulent VAWT fluid dynamic interactions in skewed inflow conditions.

7.2. Computational setup

The simulation's numerical and geometrical aspects, along with a description of the flow conditions, have been detailed. This information establishes the reliability and accuracy of the numerical simulation. It also enables readers to assess the validity of the results presented in subsequent sections. The overall computational setup used in this chapter is the same as Chapter 6 when no supporting struts and a central tower are used. The difference is only in the direction of freestream velocity, skewed in the positive vertical direction (Figure 7.1). The description of the setup is repeated below, in brief, for the convenience of the readers.

7.2.1. Geometry

A straight-bladed VAWT design with 2 blades is utilised in this chapter. The blade geometry is replicated from a study by Brandetti et al. [47] and by LeBlanc et al. [181, 182]. There are no supporting struts, central tower or boundary layer (BL) trips present in the geometry. The geometric model for the VAWT configuration is shown in Figure 7.2, while Table 7.1 presents the geometric values for the configuration. The VAWT solidity is set at 0.1 and the rotor aspect ratio is 1. Since there is no variation in the geometry in this chapter, the sole variations in 3D effects and blade-vortex interaction will stem from differences in flow around the blades, influencing unsteadiness in blade loading, wake dynamics, and aeroacoustic behaviour.

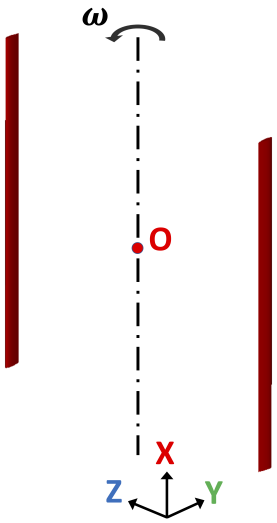

Figure 7.2: VAWT configuration used in this chapter; 'O' denotes the coordinate origin

Table 7.1: VAWT geometrical parameters for all three configurations

Blade length (L)	**Rotor diameter** (D)	**Blade chord** (c)	**Blade airfoil**
1.5 m	1.5 m	0.075 m	NACA 0021

This study utilises both the high-fidelity Lattice Boltzmann Method (LBM) and mid-fidelity Lifting Line Free Vortex Wake (LLFVW) methods to simulate the VAWT configuration. To ensure accurate and reliable airfoil polar data for the mid-fidelity LLFVW method, a NACA 0021 profile is employed to derive a virtual geometry, reflecting the virtual camber effect in a manner similar to Chapter 5, as depicted in Figure 5.2 (c). Lift and drag polars are derived using XFoil [104], with Reynolds numbers between 5×10^4 and 1×10^6, an *NCrit* value of nine, and forced transition at the leading edge of both the pressure and suction side. Smooth extrapolation in the post-stall regime is

ensured by extending the airfoil static polar data to 360° AoA, using the Montgomerie method [241]. Balduzzi et al. [22] provide an example of the extrapolated 360° polars.

7.2.2. Numerical setup

The high-fidelity LBM simulation setup employs a cubic volume of $100D$ on each side, with the Darrieus geometry at the centre. The boundary conditions, depicted in Figure 5.2 (a) in Chap 5, include a velocity inlet (freestream velocity V_∞) aligned with the Y-axis and an ambient pressure of 101.325 kPa at the outlet. A no-slip condition is applied to the blade surface. The grid generation begins with PowerFLOW creating a Cartesian volume grid around solid components using the minimum hexahedral cell size and 17 variable resolution (VR) levels. Higher resolutions are applied near blade and strut surfaces, with coarser regions farther away. This optimises computational efficiency by focusing effort where high-flow gradients are expected. Figure 5.2 (b) from Chapter 5 shows this grid refinement when approaching the centre of the domain where the VAWT is located. VR levels vary in size, with a voxel size change factor of 2 from fine to coarse levels, thus forming distinct VR regions. Finally, the software intersects the mesh with solid parts, generating polygons, or surfels, that accurately represent the surface of the body.

Similar to chapter 4, 5 and 6, only the FW-H solid formulation is used for far-field noise calculation in which the VAWT blade surfaces are considered as the FW-H solid surfaces. Furthermore, analyzing the noise spectra up to 4000 Hz is sufficient for VAWT aeroacoustics while using a sampling time of 8 steady rotor rotations. Therefore, pressure data are sampled at a frequency of 8000 Hz, in accordance with the Nyquist criterion. To ensure accurate capture of acoustic waves, a criterion of a minimum of 15 points per wavelength is adopted. Subsequently, noise spectra are computed using a Hanning window with a 50% overlap and a frequency resolution (Δf) of 15 Hz, using the *pwelch* function in MATLAB.

For the mid-fidelity LLFVW simulation, Table 7.2 outlines the values of the simulation parameters utilised which is adopted from previous studies [22, 306].

Table 7.2: Simulation parameters used for the LLFVW method

	LLFVW
Density	1.225 kg/m^3
Kinematic viscosity	1.65 e-5 m^2/s
Blade discretisation	21 (cosine)
Azimuthal discretisation	3 deg
Full wake length	12
Vortex time offset	1 e-4 sec
Turbulent vortex viscosity	20

7.2.3. Flow conditions and grid settings

For the current chapter, the operational settings of the VAWT for the baseline case (0° skew angle) are presented in Table 7.3. The tip speed ratio (TSR) is employed as a measure of the system's operational condition, defined as the ratio of the blade rotational speed (ω) to the freestream velocity (V_∞), i.e., $\omega R/V_\infty$, where ω, R, and V_∞ represent the rotational speed in radians per second, the wind turbine radius, and the freestream velocity, respectively. The freestream velocity is maintained at a constant value of 4 m/s, in accordance with the reference value [47], while ω is adjusted to vary the TSR value. The chord-based Reynolds number (Re_c) is calculated as 8.12×10^4, based on the average velocity experienced by a blade during a single rotation.

In this chapter, skew angles of 20° and 40° are examined. The freestream velocity, V_∞, remains consistent with the 0° skew angle case, with only the direction being varied as shown in Figure 7.1.

Table 7.3: VAWT operational settings for the mid-fidelity (LLFVW) and high-fidelity method (LBM) for all the inflow conditions studied in this chapter

Parameter	Value
Tip speed ratio (TSR)	4
Rotations per minute (RPM)	203.718
Freestream velocity V_∞	4 m/s
Chord-based Reynolds number (Re_c)	8.12×10^4

For instance, at a 20° skew angle, the blades experience horizontal and vertical velocities of 3.76 and 1.37 m/s, respectively. The freestream Mach number is 0.12, and the turbulence intensity (I_t) and turbulence length scale (L_t) are set to 0.1% and 1 mm, respectively. According to a prior study [63], these parameters are expected to minimally influence the unsteady flow field evolution. The high-fidelity method (LBM) in this research is applied solely for a Tip Speed Ratio (TSR) of 4. Conversely, the mid-fidelity method (LLFVW) is used to simulate TSR values ranging from 1 to 7. Importantly, all operational conditions in this investigation maintain chord-based Reynolds numbers (Re_c) below 4 $\times 10^5$.

In this chapter, Grid 3 from Chapter 6 is utilised, having previously established temporal and grid convergence. Figure 6.2 shows the finest mesh around the blade with 4 different VRs with Grid 3 and Figure 6.3 shows the cross-sectional view of the mesh in the domain, both near the VAWT blades and further away from it. The grid's y^+ value is 25, and there are 1.81×10^2 voxels per blade chord length. Grid 3 has a minimum voxel size of 0.413 mm, with 24.6 million fine equivalent voxels in the computational domain for the 2-bladed VAWT. These fine equivalent voxels are derived by multiplying the number of voxels with the time stepping rate, which is directly linked to the mesh resolution level. Simulating 12 rotor rotations (1.31 s) requires 46380 CPU hours, utilizing a Linux workstation with an AMD Ryzen Threadripper 3990X Gen3 processor, featuring 64 cores and 128GB DDR4 3GHz platform. It is noteworthy that the fine equivalent voxels and CPU hours are consistent across all three inflow conditions simulated in this chapter. Furthermore, the physical time step for Grid 3 resolution corresponds to a Courant-Friedrichs-Lewy (CFL) number of 1 in the finest VR level and is measured at 3.76×10^{-6} s.

The integral and time-varying behaviour of the VAWT thrust coefficient (C_T) and torque coefficient (C_Q) are reported. These coefficients are defined as:

$$C_T = \frac{T}{0.5\rho A V_\infty^2}, \tag{7.2}$$

$$C_Q = \frac{Q}{0.5\rho A V_\infty^2 R}, \tag{7.3}$$

where, T and Q are VAWT thrust and torque respectively, ρ is the air density, A is swept area ($D \times L$) where is D is rotor diameter and L is blade length, R is rotor radius and V is freestream velocity. Using high-fidelity LBM, unsteady pressure data, Power Spectral Density (PSD) spectra and Overall Sound Pressure Level (OSPL) values obtained using FW-H solid formulation are also reported and analysed.

7.3. Results

7.3.1. Temporal and grid convergence study

Figure 6.4 presents a subset of the results, representing the temporal convergence characteristics for the thrust coefficient (C_T) and torque coefficient (C_Q) for the two skew angles subject to investigation. These results are obtained using both the high-fidelity Lattice Boltzmann Method (LBM)

and the mid-fidelity Lifting Line Free Vortex Wake (LLFVW) method. Notably, the values reported in these figures are representative of the overall rotor, comprising all the blades within the VAWT configuration.

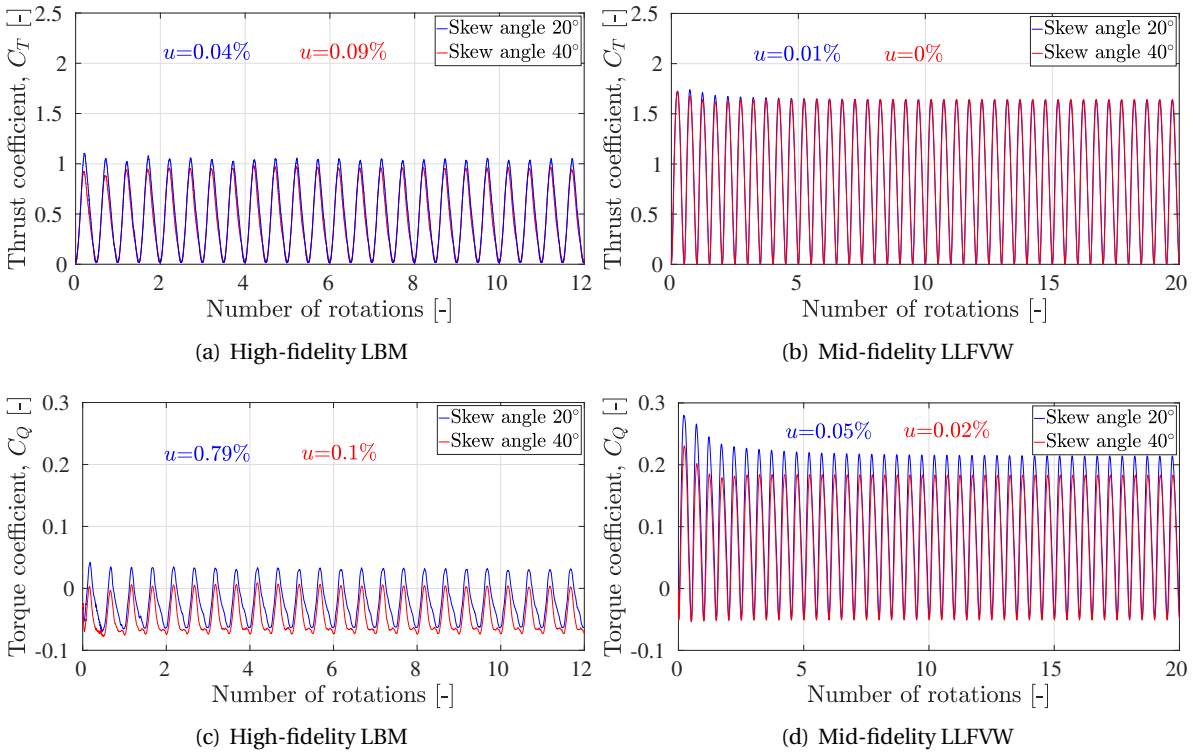

(a) High-fidelity LBM (b) Mid-fidelity LLFVW

(c) High-fidelity LBM (d) Mid-fidelity LLFVW

Figure 7.3: Statistical temporal convergence study for VAWT thrust coefficient C_T and torque coefficient C_Q using the high-fidelity LBM and mid-fidelity LLFVW; the values are representative of the overall rotor

In the figures, the uncertainty values (u) are defined as a percentage of the standard deviation of the integral thrust and torque coefficients averaged over a full rotation of the VAWT. Simply put, these uncertainty values help to show the amount of change or uncertainty in the computed thrust and torque coefficients as time progresses, resulting from the natural instability and random behaviour of the fluid dynamic interactions. Lower u values mean that there is a greater level of trust in the simulation outcomes, implying that the simulations have reached simulations have achieved temporal convergence. All the uncertainty values shown in the figures are calculated after the 10th rotor rotation for the high-fidelity LBM and after the 20th rotor rotation for the mid-fidelity LLFVW method. These specific time points are chosen to ensure a sufficient number of rotations for the simulation to reach a state of temporal stability and reliability, allowing for meaningful uncertainty assessment [146].

Overall, the statistical temporal convergence for 40° skew angle is better than the 20° skew angle. This can be observed in the faster convergence of torque values for the former, both for LBM and LLFVW results. Specifically, in the case of LLFVW, the C_Q convergence is achieved after only the 7th rotor rotation for a 20° angle, while for a 40° angle, it occurs even earlier, after the 4th rotation. The lower value of u for the 40° angle also supports this observation. It implies that the 40° skew angle has reduced unsteady fluid dynamic interactions with the blades, which decreases the unsteadiness in blade loading. Similar to the trend found in all previous chapters and an earlier study focusing on VAWTs working at low Reynolds numbers [304, 306], the statistical temporal convergence for thrust values is observed to be better than torque values, as indicated by the smaller u value for the former. In more concrete terms, for the 20° skew angle, convergence for thrust coefficient (C_T)

is reached after about 2 rotor rotations for LBM and 4 rotor rotations for LLFVW. Conversely, for torque coefficient (C_Q) at the same skew angle, achieving temporal convergence requires around 3 rotor rotations for LBM and 7 for LLFVW.

The investigation underlines the robust capability of the mid-fidelity LLFVW method to accurately represent the unsteady phenomena within the VAWT force field when dealing with non-uniform inflow conditions. In adopting a logical approach for this chapter, all subsequent results are reported after the 10th rotor rotation for the LBM and the 20th rotor rotation for the LLFVW method. Furthermore, given the favourable grid convergence and numerical validation seen in Chapter 6, it seems wise to continue with the same grid resolution and numerical setup for all numerical simulations in this chapter. This setup is considered sufficient to enable an accurate and insightful physical analysis of the fluid dynamic interactions and noise sources in the VAWT, in case of skewed inflow conditions.

7.3.2. Effect of skewed inflow

Figure 7.4 illustrates the calculated values of the power coefficient (C_P) and thrust coefficient (C_T) across various skew angles, considering three different tip speed ratios (TSRs). The mid-fidelity LLFVW method is utilised to examine the entire range of skew angles from 0° to 70°, whereas the high-fidelity LBM simulations are specifically carried out for a TSR of 4, focusing on three distinct skew angles. The adoption of multiple fidelity levels offers a practical trade-off between the computational cost and accuracy of the results and permits the exploration of a broad array of VAWT operating conditions. Moreover, the combination of high-fidelity simulations at TSR 4, complemented by mid-fidelity simulations spanning different TSRs and skew angles, is expected to provide comprehensive insights into the VAWT fluid dynamic interactions arising from non-uniform inflow conditions. This combination ensures that the study is both cost-effective and capable of delivering insightful observations.

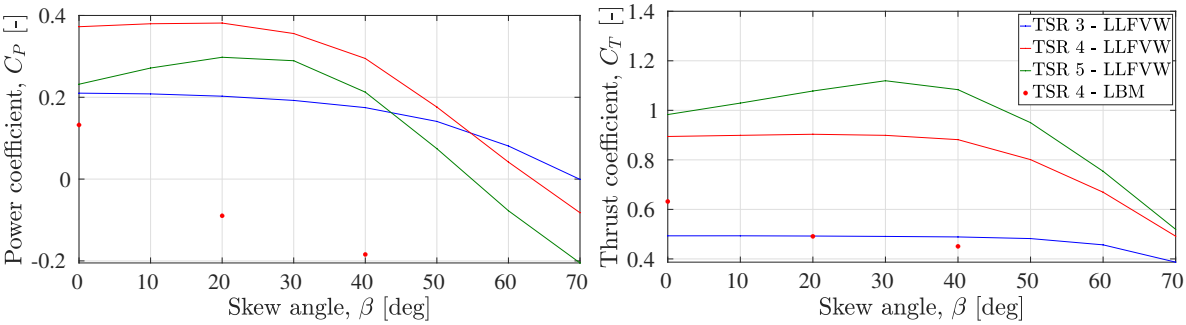

Figure 7.4: Power and thrust curve obtained for different skew angles using the mid-fidelity LLFVW and high-fidelity LBM

The mid-fidelity results shed light on specific trends concerning the effect of skew angles on VAWT performance. At a TSR of 3, an increase in skew angle leads to a reduction in both C_P and C_T, with C_P decreasing at a quicker rate. This indicates a greater sensitivity of blade tangential loading and skin friction to the flow conditions, as opposed to blade normal loading. When examining TSR 4, a slight rise in both C_P and C_T is observed up to a 20° skew angle, followed by a decline. At TSR 5, this initial increase in C_P and C_T is more pronounced, again rising until a 20° skew angle, before subsequently falling. This observed increase in performance with skew angle is consistent with prior studies [226, 293, 311, 344], and has been attributed to a reduction in blade vortex interaction in the downwind part of rotation.

The rates of change in C_P and C_T values are more pronounced at higher TSRs as compared to lower TSRs. When operating at lower TSRs, the blades function more independently, and the blade-

wake/blade-vortex interaction (BWI/BVI) is minimal. As a result, any reduction in BWI/BVI caused by skewed inflow has a smaller effect at these TSRs. On the other hand, as TSR increases, both the induction factor and the importance of BWI/BVI interaction grow. Consequently, the decrease in BWI/BVI resulting from skewed inflow becomes more substantial at higher TSRs. This leads to improved loading on individual blades, and in turn, enhances overall rotor power and thrust. For the same reason, the rise in C_P and C_T values at smaller skew angles is more noticeable at higher TSRs than at lower ones. This trend highlights a strong correlation between non-zero skew angles and BWI/BVI in determining the VAWT performance.

A direct comparison of the mid-fidelity LLFVW with the high-fidelity LBM results at a TSR of 4 illustrates the differences in both C_P and C_T values. As the skew angle increases, the difference between the values predicted by the two methods also increases. Specifically, the discrepancies in C_P for skew angles of 0°, 20°, and 40° are 0.24, 0.47, and 0.48, respectively. These findings indicate that LBM shows a more pronounced decline in VAWT performance with skew angles compared to LLFVW. Notably, at skew angles of 20° and 40°, the power generation is even predicted to turn negative. A similar pattern is observed for the C_T values, where the difference between the LBM and LLFVW results increases with an increase in the skew angle.

These observations indicate that the mid-fidelity method may not be representing the complex 3D effects in the VAWT flow and force field as effectively as the high-fidelity method, especially in the near-wake region where BWI/BVI is most significant. This difference in results aligns with expectations due to the fundamental variations in fluid modelling between the two approaches. The mid-fidelity method uses simplifications and assumptions to lower computational costs, leading to limitations in accurately capturing certain unsteady flow characteristics. In contrast, the high-fidelity method offers a more detailed and accurate representation of fluid dynamics, allowing an in-depth analysis of the VAWT aerodynamic behaviour. Despite these differences, it's worth noting that the trends in C_P and C_T calculated by the mid-fidelity LLFVW method align with the high-fidelity LBM results at TSR = 4. Here, an increase in skew angle results in a decline in power and thrust values, with the reduction in thrust being less marked compared to torque values, a trend noticed with both LBM and LLFVW results.

Figure 7.5 illustrates the temporal variation of C_T and C_Q values for the overall rotor across a full 360° azimuth. This data is obtained from the high-fidelity LBM and mid-fidelity LLFVW method at a TSR of 4. The figure also shows the average values for these coefficients over one complete rotation, corresponding to the values presented in Figure 6.11. The LBM results indicate that an increase in skew angles causes a decline in both thrust and torque values, especially at the highest azimuthal values of C_T and C_Q. A noteworthy observation is the change in the azimuthal position where these peak values are reached, with the azimuth angle for this position decreasing as the skew angle increases. On the other hand, the LLFVW method shows a slight increase in torque and thrust values for the 20° skew angle, with a corresponding increase in the peak azimuthal values, followed by a reduction for the 40° skew angle.

Both the mid-fidelity LLFVW and the high-fidelity LBM demonstrate a fairly accurate representation of the physical behaviour of VAWT in skewed inflow conditions. Nevertheless, a notable difference arises in the comparison of the peak values for C_T and C_Q during the upwind and downwind parts of rotation. Specifically, LLFVW tends to predict higher values for both C_T and C_Q relative to LBM across all three skew angles simulated. This trend aligns with the statistical time convergence results shown in Figure 7.3. Interestingly, this observation contradicts with the conclusions drawn in Chapter 5, where LLFVW estimated lower blade loading in the upwind part and higher values in the downwind part of rotation compared to LBM. The cause of this inconsistency can be traced back to the usage of XFOIL polar values (C_l and C_d versus angle of attack α) in the analytical formulation of LLFVW. These values affect the blade angle of attack and induced velocity. Future investigations should consider modifying these polars through the application of empirical corrections. Another

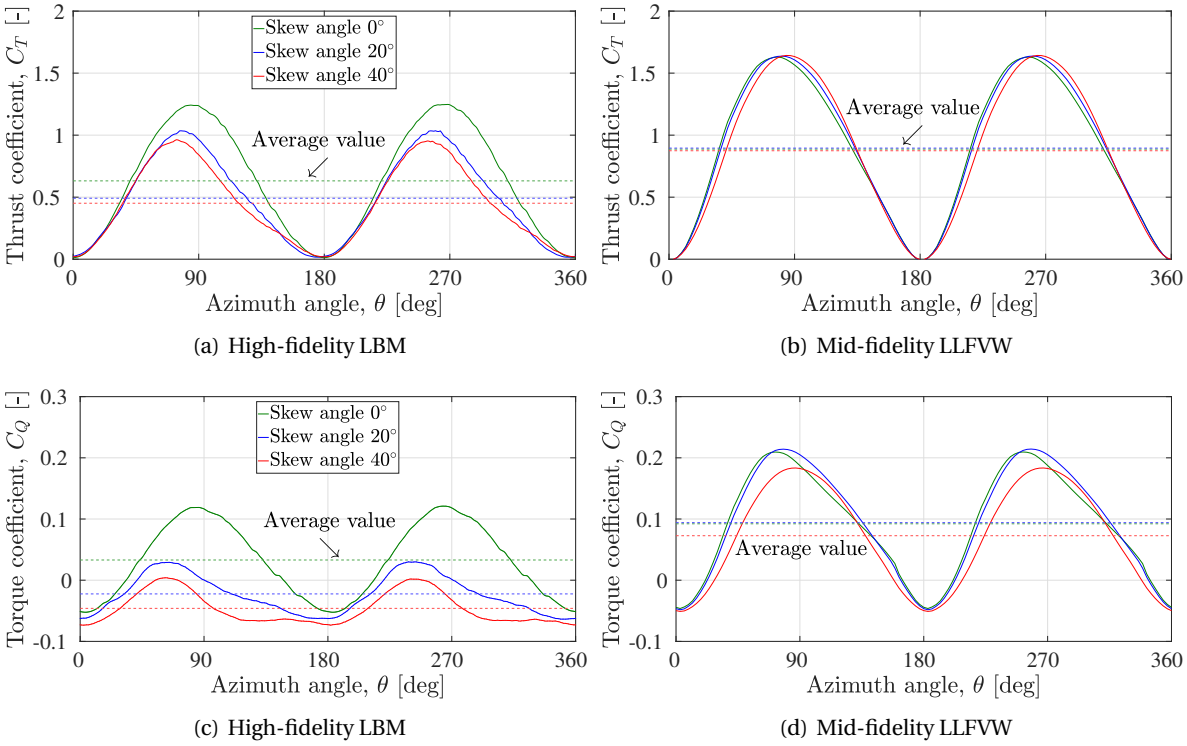

(a) High-fidelity LBM (b) Mid-fidelity LLFVW

(c) High-fidelity LBM (d) Mid-fidelity LLFVW

Figure 7.5: Variation of thrust coefficient C_T and torque coefficient C_Q for the overall rotor over a complete rotation, using the high-fidelity LBM and mid-fidelity LLFVW at TSR = 4

strategy could involve using airfoil polar values for a 360° angle of attack as derived from wind tunnel experiments [300].

Figure 7.6 presents the azimuthal variation in C_T and C_Q for a single blade over a full 360° azimuth. This data is obtained using both the high-fidelity and mid-fidelity methods at a TSR of 4. The figure also includes the corresponding average values over a single rotation, providing clearer insight into the individual blade's performance. The upwind part of rotation exhibits a decline in both C_T and C_Q values with an increase in skew angle. This is observed using both LBM and LLFVW, although the decrease in thrust using LLFVW is minimal. The reduction in C_T and C_Q is attributed to the reduced horizontal component of velocity ($V_\infty \cos\beta$) that the blades experience as the skew angle increases. Contrarily, in the downwind rotation phase, the peak values of C_T and C_Q either increase with an increase in skew angle or remain consistent across all skew angles. This is observed using both LBM and LLFVW methods. The increase in the downwind part is ascribed to the reduced blade-wake/blade-vortex interactions (BWI/BVI) that result from skewed inflow conditions, thereby enhancing the aerodynamic efficiency of each blade. Overall, the contrasting effects in the upwind and downwind parts of rotation collectively influence rotor performance. This effect is evident in Figures 7.4 and 7.5, characterizing the compounded impact on the rotor system.

The LBM results reveal negative torque production for a significant part of rotation at a skew angle of 40°. This underscores the substantial influence of the horizontal component of velocity ($V_\infty \cos\beta$) on blade tangential loading. Both mid-fidelity LLFVW and high-fidelity LBM simulations effectively capture these VAWT physical characteristics under skewed inflow conditions. However, a comparison of the C_T and C_Q values between LLFVW and LBM shows that LLFVW predicts higher values throughout the rotation. Furthermore, the LBM results predict a higher decline in blade performance relative to LLFVW, a pattern consistent with previous chapters. This trend is also apparent in Figure 7.5 and this inconsistency between the two methods sheds light on a potential limitation

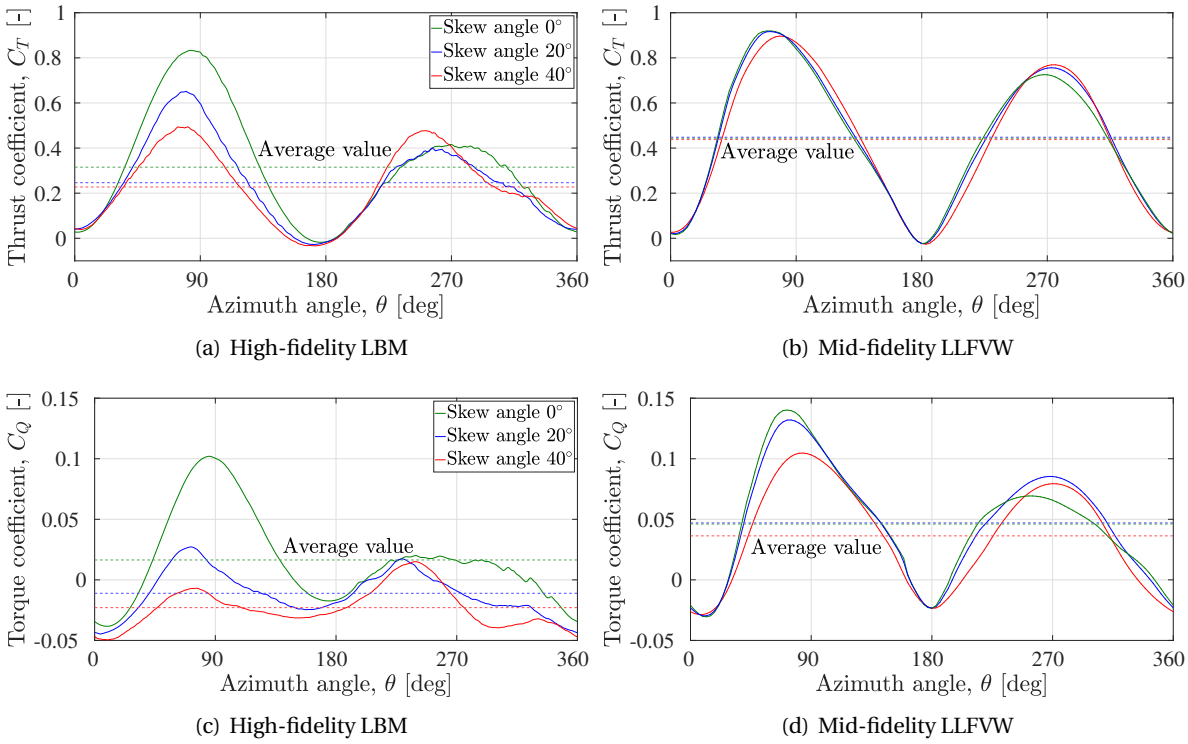

(a) High-fidelity LBM

(b) Mid-fidelity LLFVW

(c) High-fidelity LBM

(d) Mid-fidelity LLFVW

Figure 7.6: Variation of thrust coefficient C_T and torque coefficient C_Q for a single blade over a complete rotation, using the high-fidelity LBM and mid-fidelity LLFVW at TSR = 4

of vortex-based methods in accurately modelling unsteady aerodynamic interactions and wake dynamics, particularly in non-uniform inflow conditions.

Figure 7.7 displays the aforementioned unsteady force field characteristics across the equivalent 3D cylindrical surface traced by the VAWT blades at a TSR of 4, depicting the variation in blade normal forces (F_n) for a single blade. The study includes a comparative analysis in both azimuthal and spanwise directions at all three skew angles, between both the LBM and LLFVW methods. The investigation reveals several interesting findings. Firstly, there is a clear degradation in blade normal forces in both upwind and downwind phases of rotation as the skew angle increases. This degradation is more pronounced in LBM results than in LLFVW, reinforcing the earlier conclusion that LBM predicts a stronger reduction in blade performance under skewed inflow conditions. Furthermore, blade normal forces show an increase in the downwind part of rotation, leading to increased downwind blade loading as shown in Figure 7.6. Both LBM and LLFVW results reflect this increase in the 2D contour plot, with the effect being more obvious in the latter.

In the comparison between LBM and LLFVW regarding the predicted F_n values, LLFVW consistently predicts higher values throughout the entire rotation relative to LBM. This difference is evident in the thrust and torque values of both a single blade and the complete rotor, as previously illustrated in Figures 7.6 and 7.5, respectively. Furthermore, the 3D effects of tip vortices on the force field appear more significant in the LBM results than in LLFVW. This is observable around h/H of -0.5 and 0.5 in Figure 7.7. Such an observation further supports the assertion that mid-fidelity vortex methods may lack accuracy in capturing the complexities of 3D fluid dynamic interactions. Nonetheless, the general trends in these mid-fidelity LLFVW simulations are found to be in agreement with those observed using the high-fidelity LBM approach.

Figure 7.8 provides insights into the instantaneous vortices in the downstream region of the VAWT flow field by utilizing iso-surfaces of the λ_2 criterion (λ_2 = -1500 1/sec^2). This 3D visualisation of the flow field aids in an in-depth understanding of the effect of skew angle on blade-wake/blade-

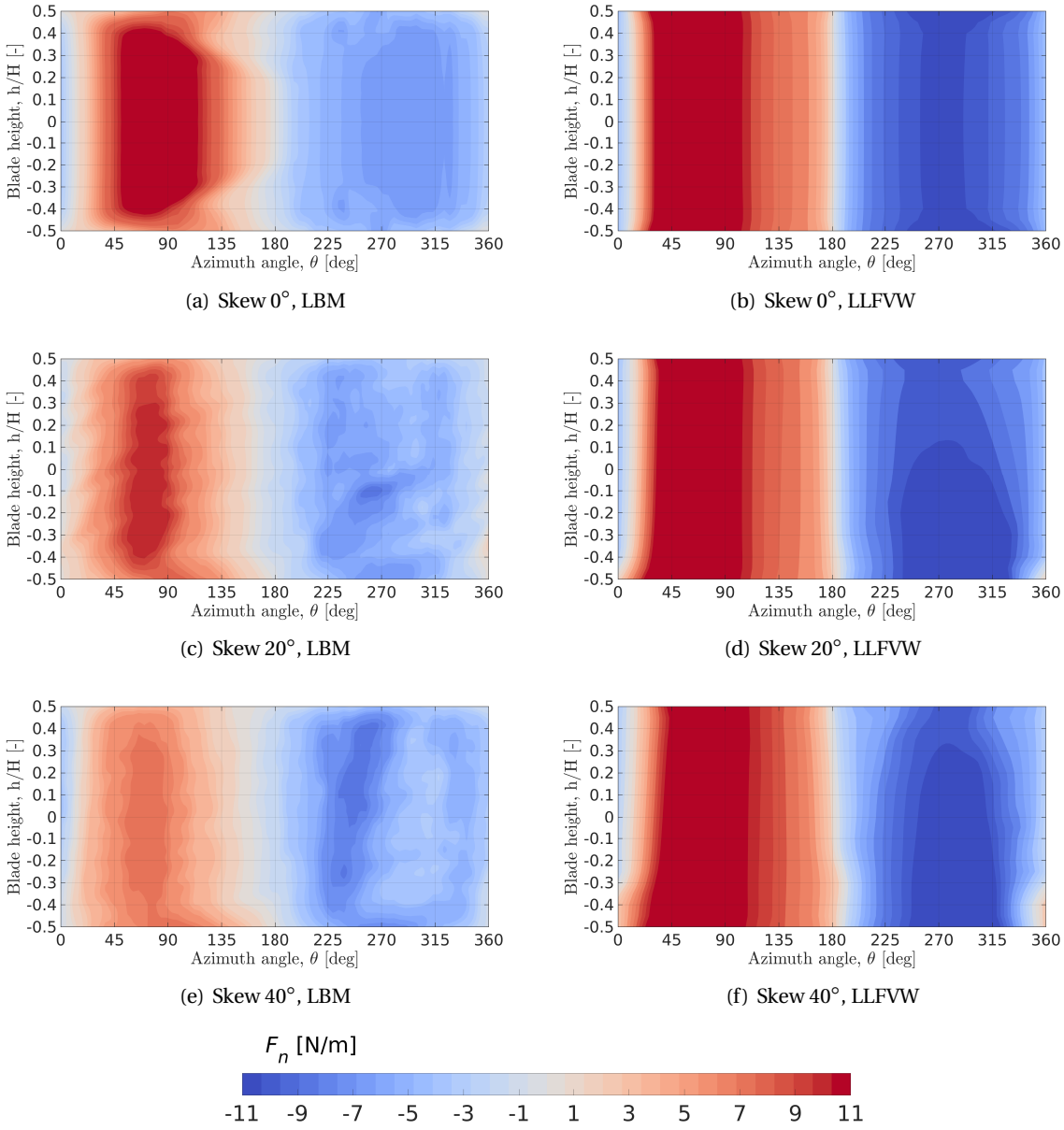

Figure 7.7: Normal force contour for a single blade over azimuthal and spanwise directions, using the high-fidelity LBM and mid-fidelity LLFVW, at TSR = 4

vortex interactions (BWI/BVI), and consequently on the overall VAWT performance. The coherent tip vortices, shed from the tip of each blade, convect downstream in the direction of the skewed inflow, as expected. This propagation gives rise to a unique spiral flow pattern, often referred to as a "vortex ring," encircling the turbine's rotational axis. Accompanying the convective motion of this large vortex structure is the wake expansion and its eventual fragmentation into smaller-scale structures. This breakdown is a result of flow instabilities and spatial modulation, leading to dissipation in the smaller structures as they blend with the surrounding fluid [12, 196].

An important observation is that the density of smaller incoherent vortex structures remains relatively constant as the skew angle increases. As a result, the variation in blade performance in the downwind part of rotation can be solely attributed to a reduction in BWI/BVI resulting from the

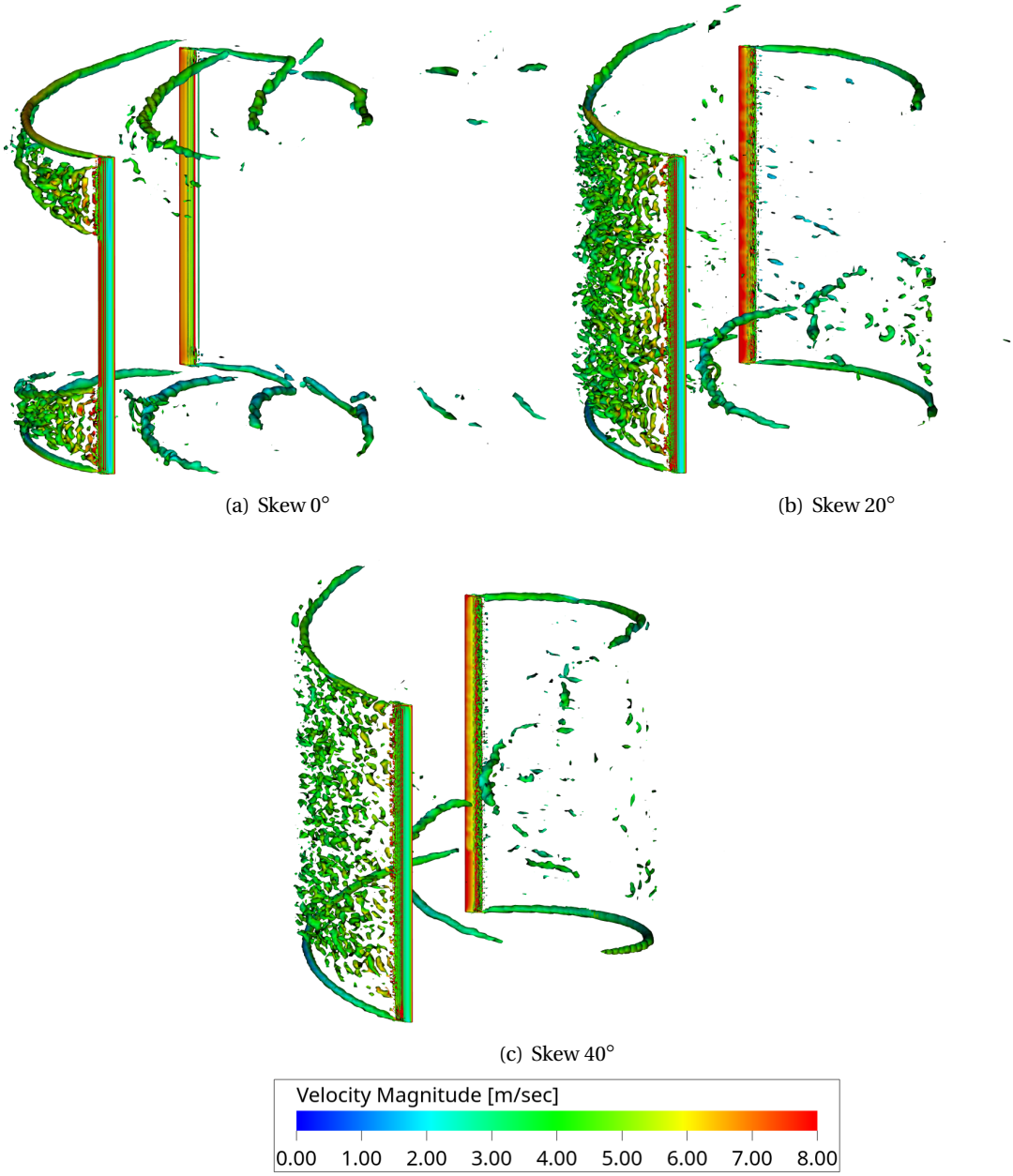

(a) Skew 0° (b) Skew 20°

(c) Skew 40°

Figure 7.8: Instantaneous 3D flowfield using iso-surfaces of the λ_2 criterion (λ_2 = -1500 1/sec^2) for vortices visualisation, using high-fidelity LBM at TSR = 4

skew angle of the oncoming flow. This helps to preserve the optimal pressure and loading distribution across both the chordwise and spanwise directions of that segment of the blade, resulting in increased blade loading in the downwind part. This observation aligns with the findings reported in earlier figures (Figures 7.5, 7.6, and 7.7) further confirming the significant influence of the skew angle on the overall performance of VAWTs.

Figure 7.9 presents a set of visualizations for the wake structures of VAWTs at different skew angles, simulated using the mid-fidelity LLFVW method at a TSR of 4. The figures depict the vortex lines shed from the VAWT blades and convecting downstream in the direction of the skew angle, away from the rotational plane (at non-zero skew angles). The wake structure becomes more organised and periodic at higher skew angles, characterized by well-defined vortex lines. This signals

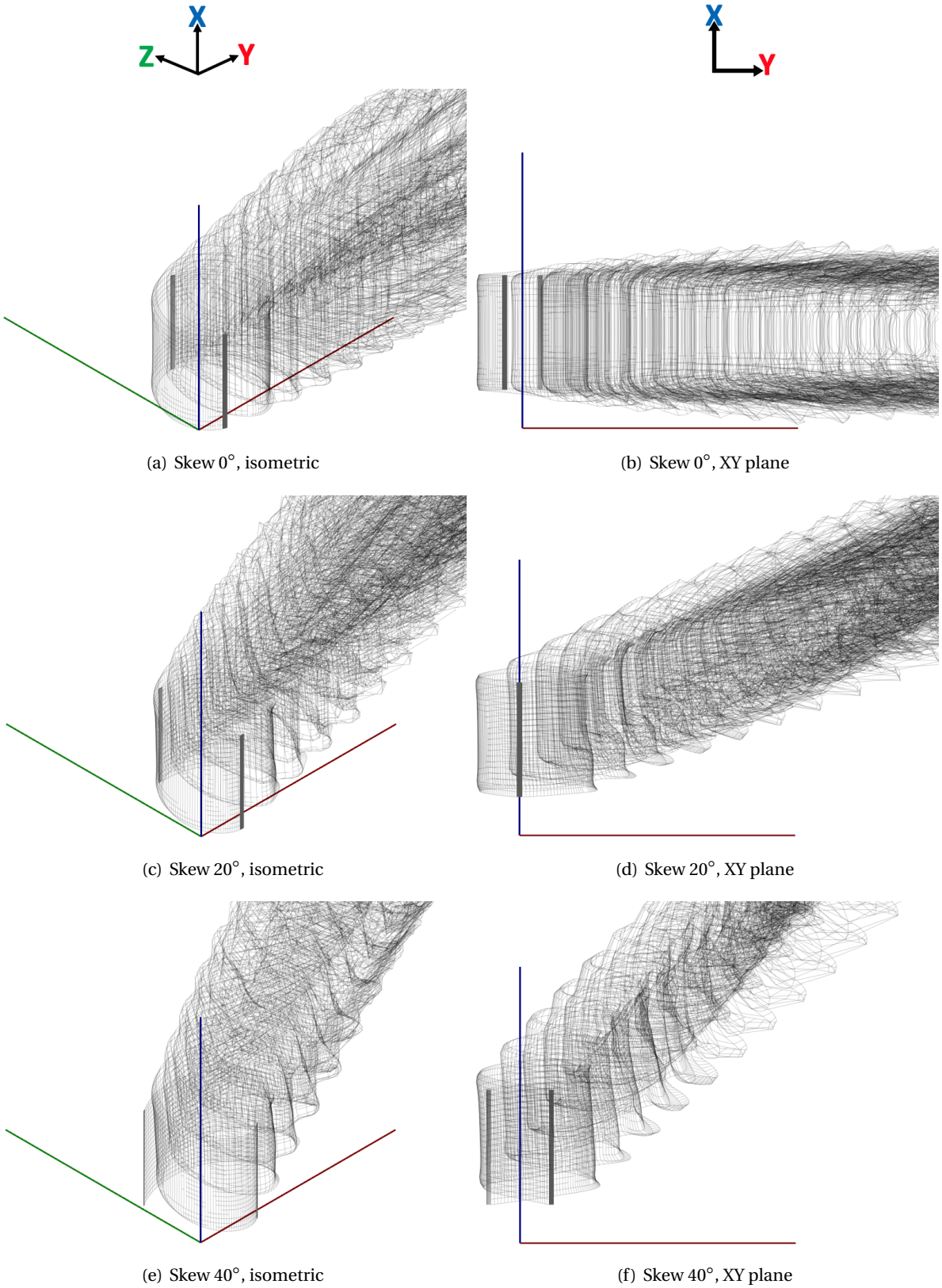

(a) Skew 0°, isometric

(b) Skew 0°, XY plane

(c) Skew 20°, isometric

(d) Skew 20°, XY plane

(e) Skew 40°, isometric

(f) Skew 40°, XY plane

Figure 7.9: Visualization of vortex lines shed from the VAWT blades in the downstream wake, using mid-fidelity LLFVW method at TSR of 4

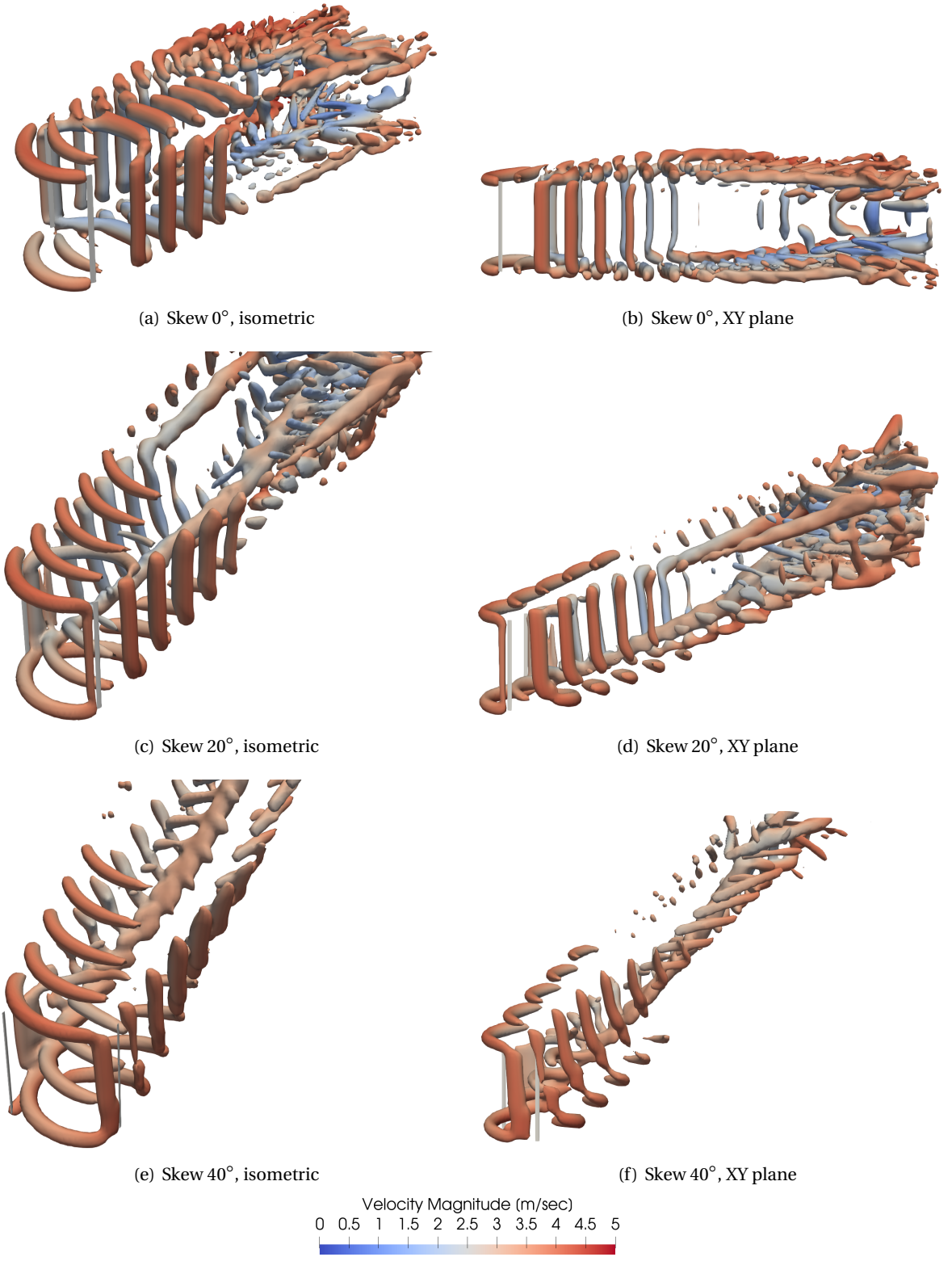

(a) Skew 0°, isometric

(b) Skew 0°, XY plane

(c) Skew 20°, isometric

(d) Skew 20°, XY plane

(e) Skew 40°, isometric

(f) Skew 40°, XY plane

Figure 7.10: Instantaneous 3D flowfield using iso-surfaces of the Q-criterion ($Q = 6\ 1/\text{sec}^2$) for vortices visualisation, using mid-fidelity LLFVW at TSR of 4

the fact that BWI/BVI decreases with an increase in skew angle, as discussed in Figure 7.8. Figure 7.10 illustrates the instantaneous 3D flow field using iso-surfaces of the Q-criterion (Q = 6 1/sec^2) using the mid-fidelity LLFVW method at TSR of 4. The coherent shed and trailing vortices can be seen convecting in the downstream direction, with reduced vortex structures as the skew angle increases. The comparison between the mid-fidelity LLFVW and high-fidelity LBM results reveals that the latter provides higher resolution and captures finer details of the vortex structures compared to the former, which is also seen in Chapters 5 and 6. Although the mid-fidelity method lacks the resolution to depict small-scale vortices and detailed flow dynamics, it shows the overall behaviour of the wake when the skew angle is non-zero. This involves less intensity of vortex breakup and fragmentation when the skew angle increases.

Figure 7.11 depicts the variation in VAWT flowfield as TSR is varied, for a fixed skew angle of 40°. The results are similar to the effect of the number of blades in Chapter 5 and the effect of TSR in Chapter 4 since flow blockage and BWI/BVI are affected both by the number of blades and TSR.

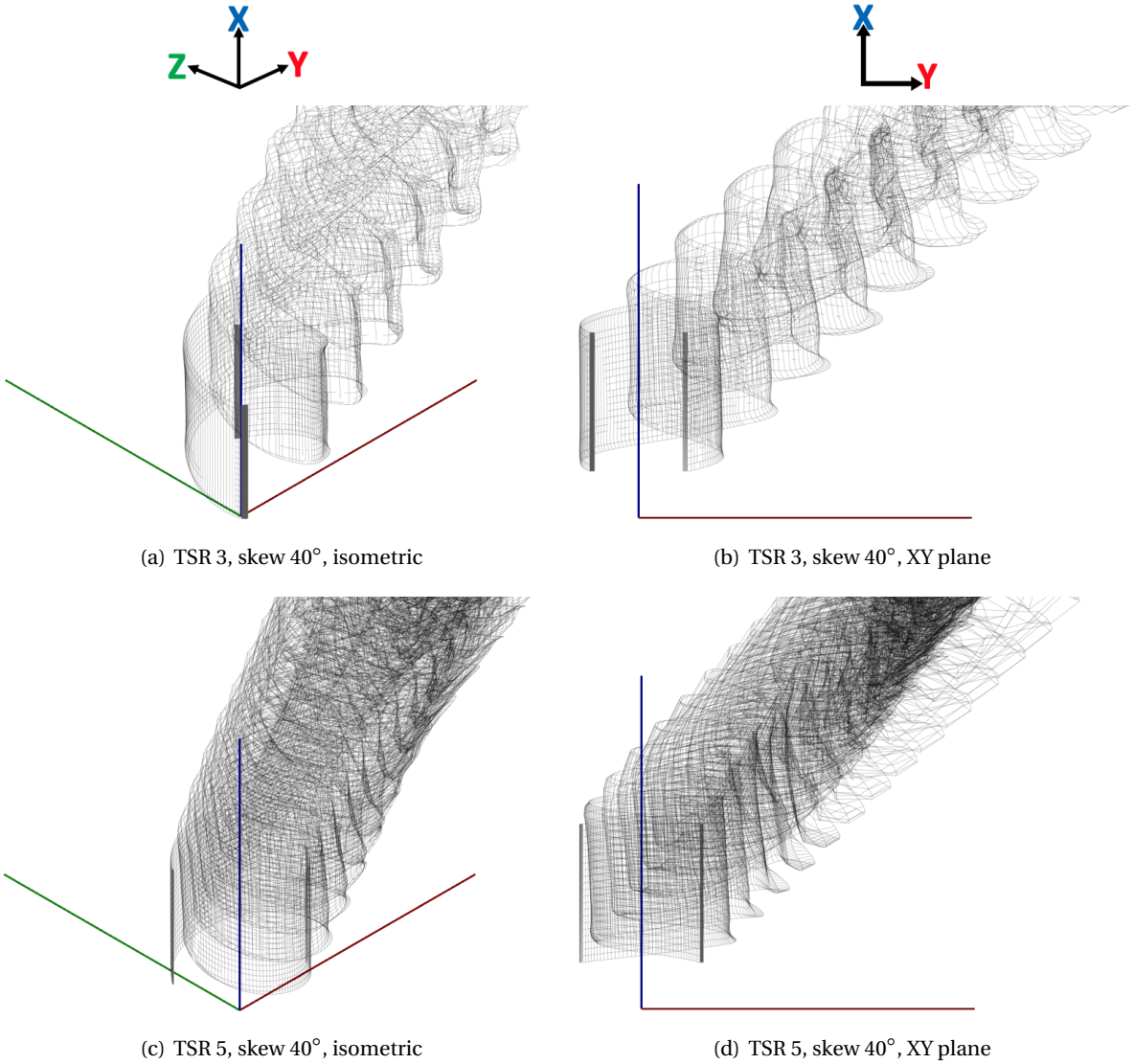

(a) TSR 3, skew 40°, isometric

(b) TSR 3, skew 40°, XY plane

(c) TSR 5, skew 40°, isometric

(d) TSR 5, skew 40°, XY plane

Figure 7.11: Visualization of vortex lines shed from the VAWT blades in the downstream wake, using mid-fidelity LLFVW method at TSRs 3 and 5

As TSR increases, the density of vortex lines increases which depicts a complex and turbulent wake with a higher degree of wake inter-mixing and complex interactions. Similarly, Figure 7.12

shows the effect of TSR using iso-surfaces of the Q-criterion ($Q = 6\ 1/\text{sec}^2$). The density of coherent trailing and tip vortices increases as the TSR increases, which increases BWI/BVI. Since a non-zero skew angle decreases the fluid dynamic interactions, the effect of this decrease will be greater at higher TSRs, where BWI/BVI is already large and will help increase the VAWT performance more. This is seen in Figure 7.4 where TSR 5 showed an increase in C_P and C_T at skew angles of 20°-30°, which is more than what is seen at TSR 4 (TSR 3 doesn't show any increase).

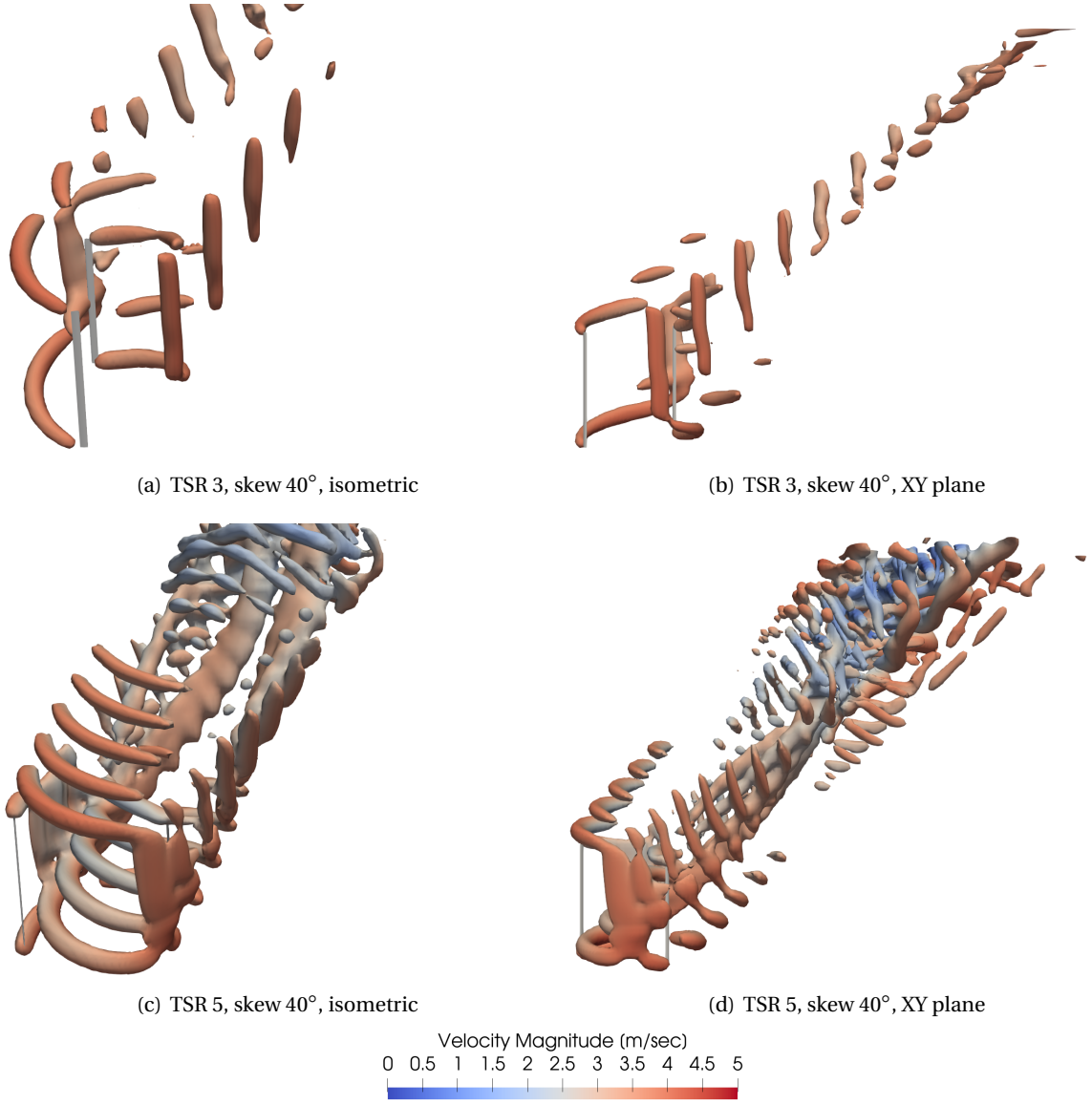

(a) TSR 3, skew 40°, isometric

(b) TSR 3, skew 40°, XY plane

(c) TSR 5, skew 40°, isometric

(d) TSR 5, skew 40°, XY plane

Figure 7.12: Instantaneous 3D flowfield using iso-surfaces of the Q-criterion ($Q = 6\ 1/\text{sec}^2$) for vortices visualisation, using mid-fidelity LLFVW at TSRs 3 and 5

Figure 7.13 highlights the behaviour of the VAWT wake in skewed inflow conditions, depicting the instantaneous streamwise velocity contours on a 2D plane aligned with the rotational axis. The results are assessed for both LBM and LLFVW simulations at a TSR of 4. As observed previously, the wake is convected in the direction of the skew angle, and its strength reduces as the skew angle increases. This phenomenon can be interpreted using the blade loading characteristics observed in Figures 7.5 and 7.6. Here, increased blade loading correlates with a stronger wake, marked by increased velocity deficits and vortical structures. Additionally, the velocity contours make it clearly

evident that blades in the downwind part of rotation encounter reduced BWI/BVI with the vortices shed from the upwind blades, as the skew angle increases. Consequently, downwind blade loading increases. Both numerical methods employed effectively capture these physical phenomena, affirming their utility in modelling these complex aerodynamic interactions.

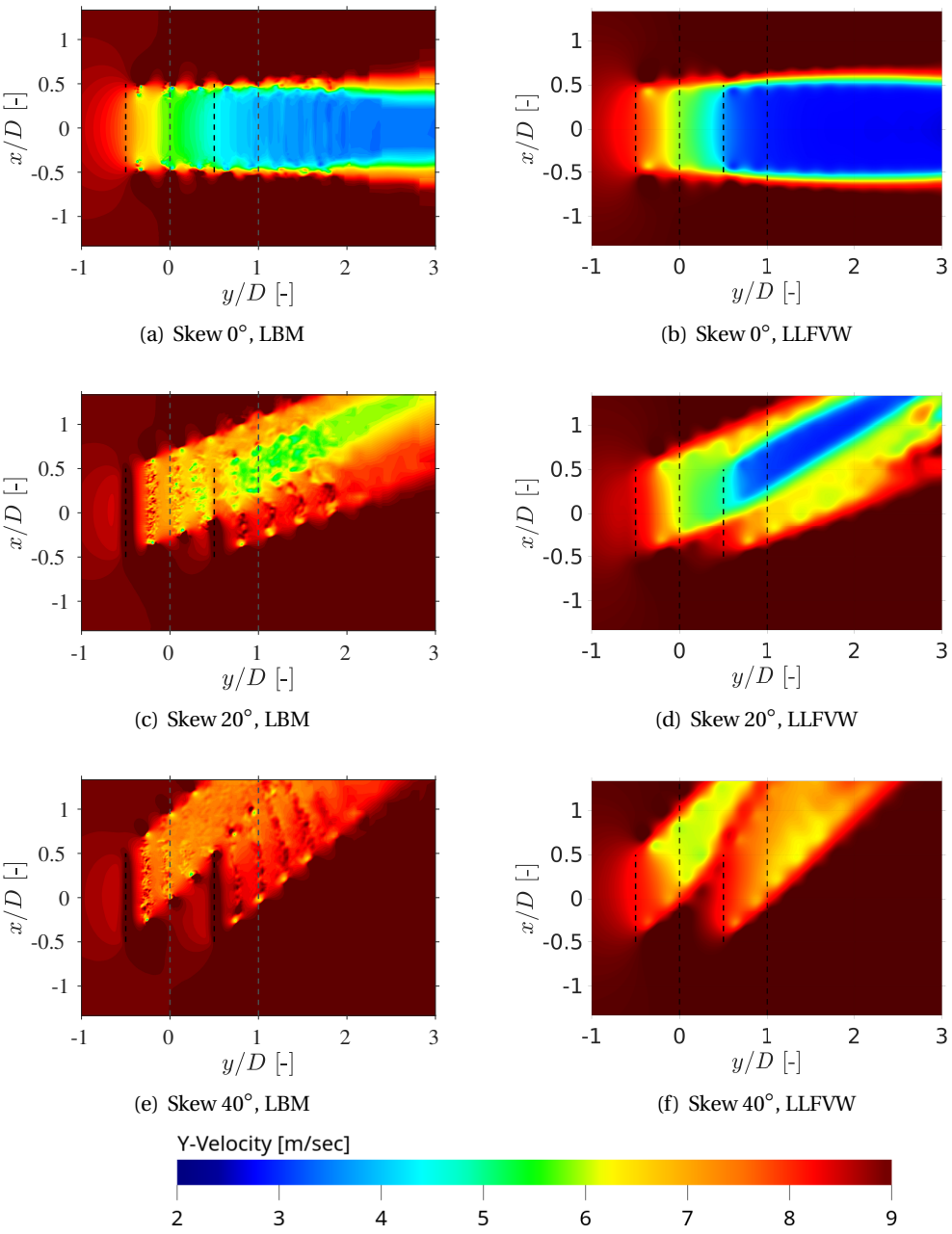

(a) Skew 0°, LBM (b) Skew 0°, LLFVW

(c) Skew 20°, LBM (d) Skew 20°, LLFVW

(e) Skew 40°, LBM (f) Skew 40°, LLFVW

Figure 7.13: Instantaneous streamwise velocity contours in the VAWT wake on a 2D plane located along the VAWT rotational axis, using both LBM and LLFVW methods, at TSR = 4

Figure 7.14 depicts the instantaneous streamwise velocity contours in the VAWT wake on a 2D plane positioned at the blade mid-span location. Both LBM and LLFVW simulations are compared at a TSR of 4 and build up on the prior observation of a reduction in BWI/BVI for the downwind blades with an increase in the skew angle. The convection of the VAWT wake notably reduces in the horizontal direction (Y-axis), reflecting the $V_\infty \cos\beta$ component of the freestream velocity. Again,

these phenomena are effectively captured by both numerical methods employed.

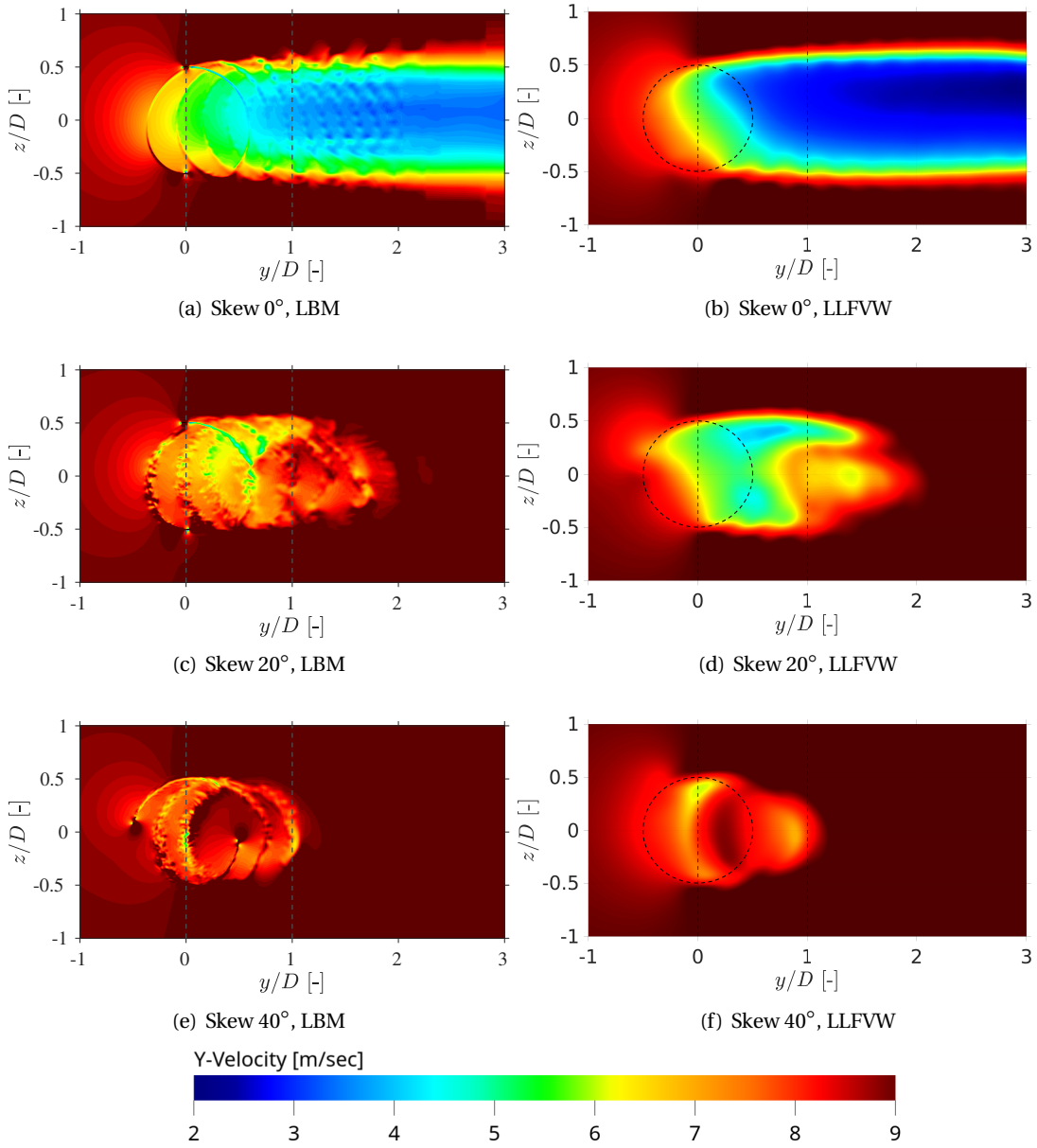

(a) Skew 0°, LBM (b) Skew 0°, LLFVW

(c) Skew 20°, LBM (d) Skew 20°, LLFVW

(e) Skew 40°, LBM (f) Skew 40°, LLFVW

Figure 7.14: Instantaneous streamwise velocity contours in the VAWT wake on a 2D plane located at the blade mid-span location, using both LBM and LLFVW methods, at TSR = 4

However, it is noteworthy that the LLFVW method predicts lower wake velocities, or equivalently a stronger wake, in comparison to the LBM results. This finding is consistently observed across all simulated skewed inflow conditions, as evidenced in both Figures 7.13 and 7.14. Such an observation aligns with the higher blade loading values predicted by LLFVW as compared to LBM, as represented in Figures 7.5 and 7.6. Furthermore, the 2D vortex structures portrayed in the LBM velocity contours are more distinguishable than those seen in LLFVW results. These particular structures are indicative of the vortex formations visible in the 3D depiction in Figure 7.8, and similar to those reported in Chapter 5 (Figure 5.13) and Chapter 6 (Figure 6.15). The presence of these vortex structures underscores the differences in vortex modelling approaches between the two methods. Here, it is safe to assume that high-fidelity LBM exhibits a more precise representation of blade vor-

tex interactions as opposed to the mid-fidelity LLFVW approach, even though the latter predicts a stronger VAWT downstream wake. Consequently, LBM shows a more pronounced decline in VAWT performance with an increase in skew angle when compared with LLFVW, a trend observed by Figure 7.4.

The effect of skew angles on wake velocities is investigated quantitatively in Figures 7.15 and 7.16. These figures display the streamwise velocity values, averaged over an entire rotation, for three different skew angles. The velocities are plotted on lines positioned at distances of $0D$ and $1D$ downstream from the VAWT centre at the blade mid-span 2D plane. This is depicted by black dotted lines in Figures 7.13 and 7.14. At both $y = 0D$ and $y = 1D$ locations, the mid-fidelity LLFVW method predicts lower streamwise velocities in comparison to the high-fidelity LBM. Notably, the VAWT flow field exhibits asymmetrical characteristics across all the skewed inflow conditions studied, a feature that is adequately captured by both numerical methods employed.

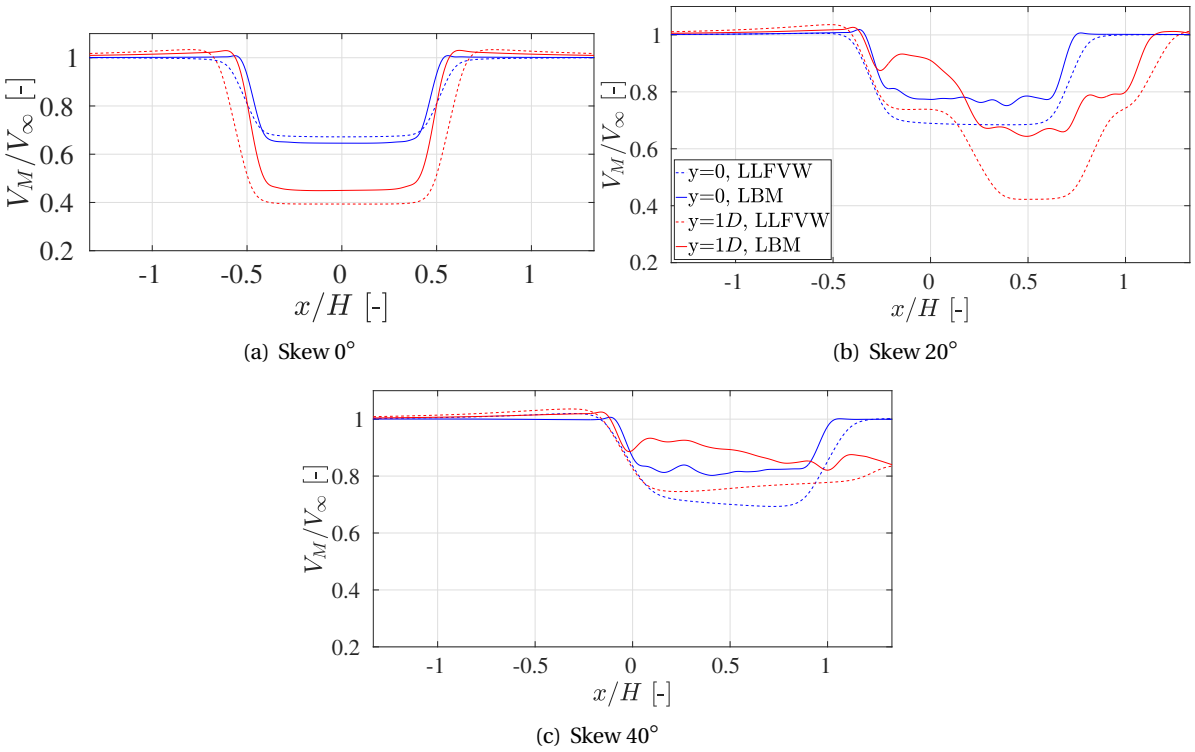

(a) Skew 0° (b) Skew 20°

(c) Skew 40°

Figure 7.15: Comparison of streamwise velocities, averaged over a rotation, in the downstream VAWT flowfield using high-fidelity LBM and mid-fidelity LLFVW at two different locations, at TSR = 4

In summation, the strength of the VAWT wake diminishes with an increase in skew angle, evidenced by a rise in streamwise velocities. This observation is justified by Figures 7.15 and 7.16 and is consistent with the streamwise velocity contours in Figures 7.13 and 7.14. For a skew angle of 0°, the strength of the VAWT wake increases in the downstream direction, as evident from the decrease in streamwise velocities from $y = 0D$ to $y = 1D$. Conversely, when the skew angle reaches 20°, the streamwise velocity at $y = 1D$ exceeds that at $y = 0D$, a pattern that persists at the 40° skew angle. This indicates a decrease in BWI/BVI in the downwind part of the rotation, allowing the blade to encounter a relatively undisturbed flow. Figure 7.15 illustrates the increased skewness of the wake with a rise in skew angle, as the velocity deficit location shifts laterally along the rotational axis.

The instantaneous streamwise velocities encountered by the VAWT blade at the mid-span location are visualised in Figure 7.17. These results are evaluated for all three skewed inflow conditions using the high-fidelity LBM method, both at the most upstream position (90°) and the most down-

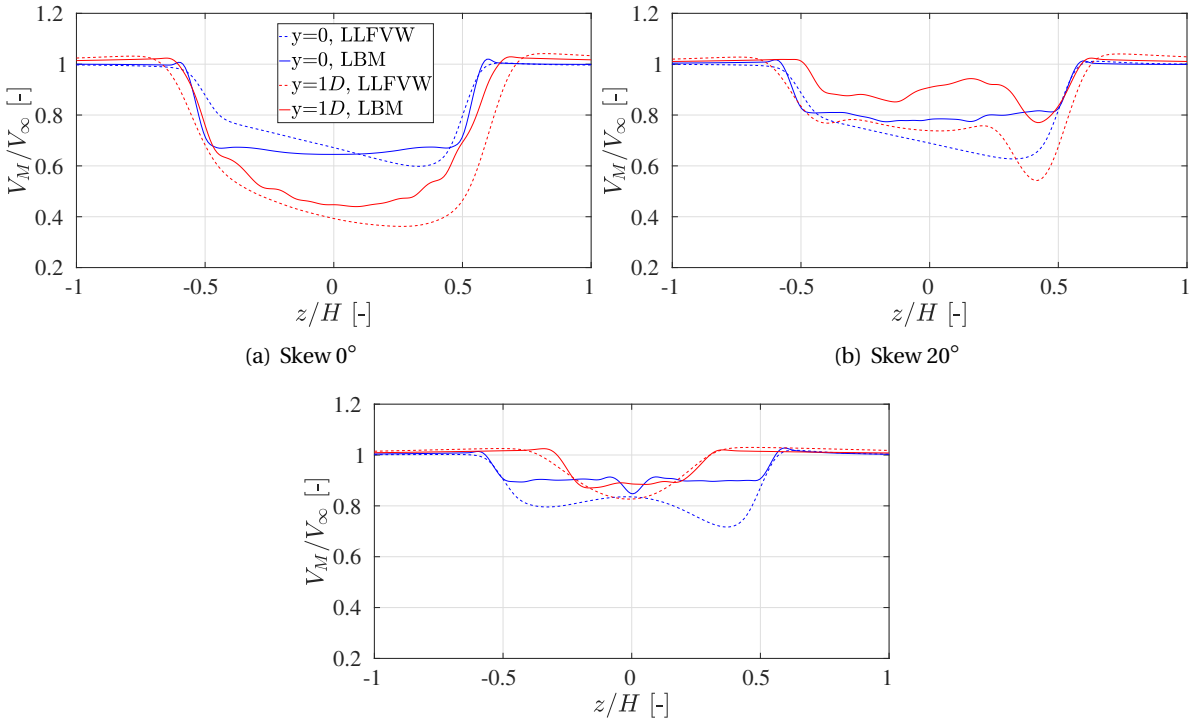

(a) Skew 0°

(b) Skew 20°

(c) Skew 40°

Figure 7.16: Comparison of streamwise velocities, averaged over a rotation, in the downstream VAWT flowfield using high-fidelity LBM and mid-fidelity LLFVW at two different locations, at TSR = 4

stream position (270°).

With an increase in skew angle, the blade encounters a reduced horizontal component of velocity ($V_\infty \cos\beta$) in the upwind part of rotation, leading to a reduced blade angle of attack (AoA) and blade loading. Conversely, in the downwind part, the velocity increases (corresponding to a reduction in wake strength) with the increase in skew angle, a trend that is in line with the earlier results in this chapter. This increase in induced velocity in the downwind part of rotation translates to an increase in both blade AoA and blade loading. The effect on blade loading can be observed in Figures 7.6 and 7.7. Such variations in the streamwise velocities are in agreement with the observations made in Figures 7.13 and 7.14, reflecting the larger scale of the overall rotor wake.

The unsteady pressure data, gathered at two distinct locations (the rotor plane at (0,0,2.6D) and a position outside the rotor plane at (0.87D,0,2.6D)), over a single rotor rotation, is presented in Figure 7.18, and includes contributions from both blades. First, the comparison between the two locations shows that high-frequency pressure fluctuations are lower at the out-of-plane location relative to the in-plane location. This observation aligns with findings from previous chapters, specifically Chapter 4 (varied TSRs), Chapter 5 (different numbers of blades), and Chapter 6 (involving struts and tower). Second, an increase in skew angle results in a rise in high-frequency unsteady pressure fluctuations at both observation points. This phenomenon can be understood from Figure 7.17, depicting that skewed inflow causes flow separation on the airfoil much earlier (along the chordwise direction) compared to when the skew angle is 0°. This can be attributed to the spanwise component of velocity ($V_\infty \sin\beta$) experienced by the blades in the former case, and absent in the latter. The resulting separated flow leads to a significant increase in Separation-Stall noise [127], observed as increased unsteady pressure fluctuations. Another contributing factor could be the interaction of the mid-span region of downstream blades (where blade loading peaks in the spanwise direction) with the tip vortices shed by upstream blades in the wake when inflow is skewed. This interaction

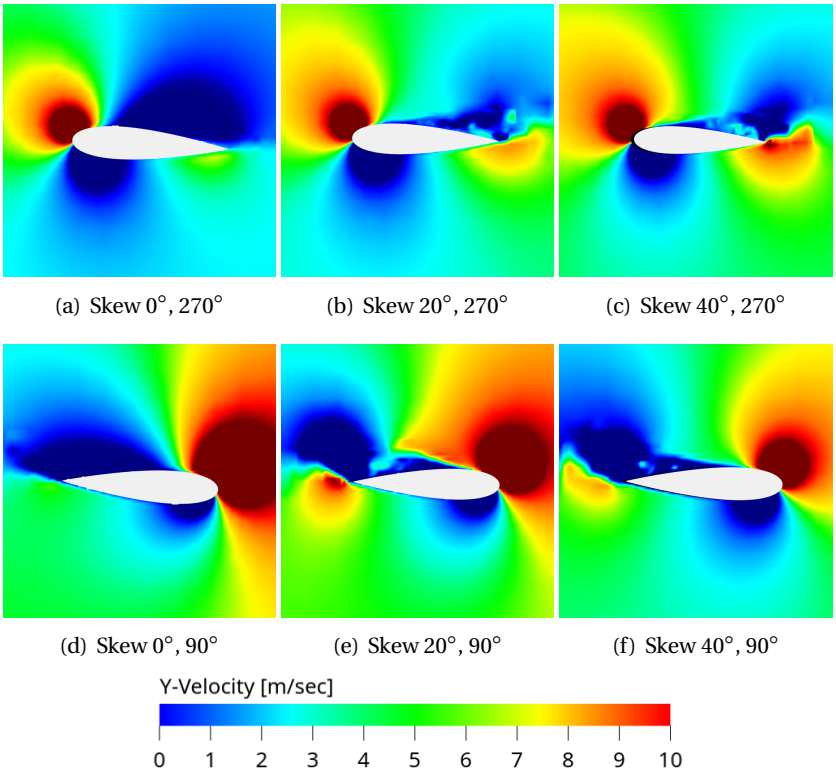

(a) Skew 0°, 270° (b) Skew 20°, 270° (c) Skew 40°, 270°

(d) Skew 0°, 90° (e) Skew 20°, 90° (f) Skew 40°, 90°

Figure 7.17: Comparison of instantaneous velocities experienced by a VAWT blade at the most upstream (90°) and the most downstream location (270°) for the three skewed inflow conditions, using the high-fidelity LBM, at TSR = 4

can be observed in Figures 7.8 and 7.13.

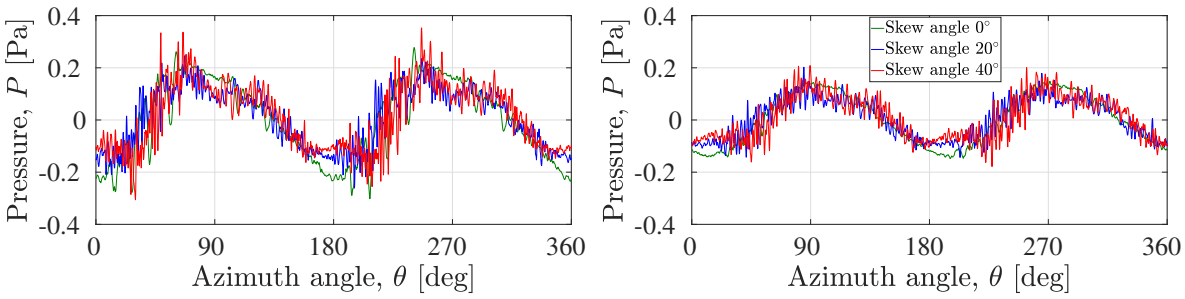

(a) At X,Y,Z = (0,0,2.6D) (b) At X,Y,Z = (0.87D,0,2.6D)

Figure 7.18: Raw unsteady pressure data using the high-fidelity LBM at two different locations, at TSR = 4

The effect of skewed inflow on noise generation is investigated through the noise spectra under all three skewed inflow conditions. Figure 7.19 reports the Power Spectral Density (PSD) values in dB/Hz within the frequency range of 20-2000 Hz at the two observer locations selected for this study, plotted with a frequency resolution (Δf) of 15 Hz. The noise spectra are not plotted below the human hearing range (20 Hz) where some blade passage frequency (BPF) peaks are observed. The skewed inflow conditions results in increased PSD values for frequencies above ≈200 Hz, a pattern apparent at both observer locations. This trend corresponds to the increased high-frequency pressure fluctuations illustrated in Figure 7.18. On the contrary, in the low-frequency range (50-200 Hz), an increase in skew angle results in reduced PSD values. This observation can be linked to the reduction in integral blade loading resulting from skewed inflow, as reported in Figures 7.5

and 7.6. The corresponding decrease in the tonal component of blade loading noise results in these lower PSD values in the low-frequency range. It is important to note that the aforementioned effect is more pronounced at the in-plane location, since the influence of blade loading on the tonal component is most significant in the plane of rotation [127] than in the out-of-plane location. Additionally, as expected from Figure 7.18, the in-plane location exhibits greater noise levels compared to the out-of-plane location, particularly in the low-frequency range.

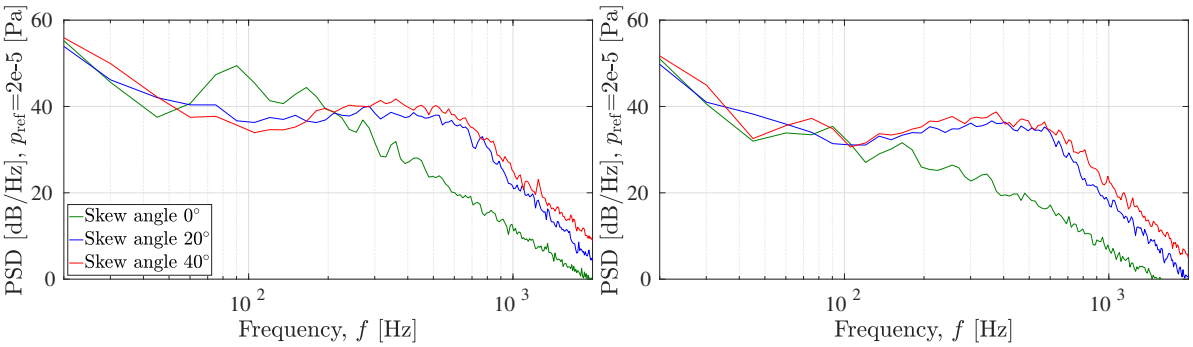

(a) At X,Y,Z = (0,0,2.6D) (b) At X,Y,Z = (0.87D,0,2.6D)

Figure 7.19: Power Spectral Density (PSD) spectra using the high-fidelity LBM at two different locations, at TSR = 4

Figure 7.20 presents the directivity plot of the overall sound pressure level (OSPL) comparing VAWTs at different skew angles. The OSPL values are obtained using high-fidelity LBM and are calculated within the frequency range of 10-2000 Hz. For both YZ and XY planes, zero skew angle exhibits the highest overall noise, except around the most downstream location 270°. In the windward side (0°), skew angle 20° has the lowest noise whereas, in the upwind (90°) and leeward part (180°) of rotation, skew angle 40° exhibits the lowest noise. This observation can be linked to the overall rotor thrust values depicted in Figure 7.4, where the VAWT thrust decreases as the skew angle increases, at the TSR of 4.

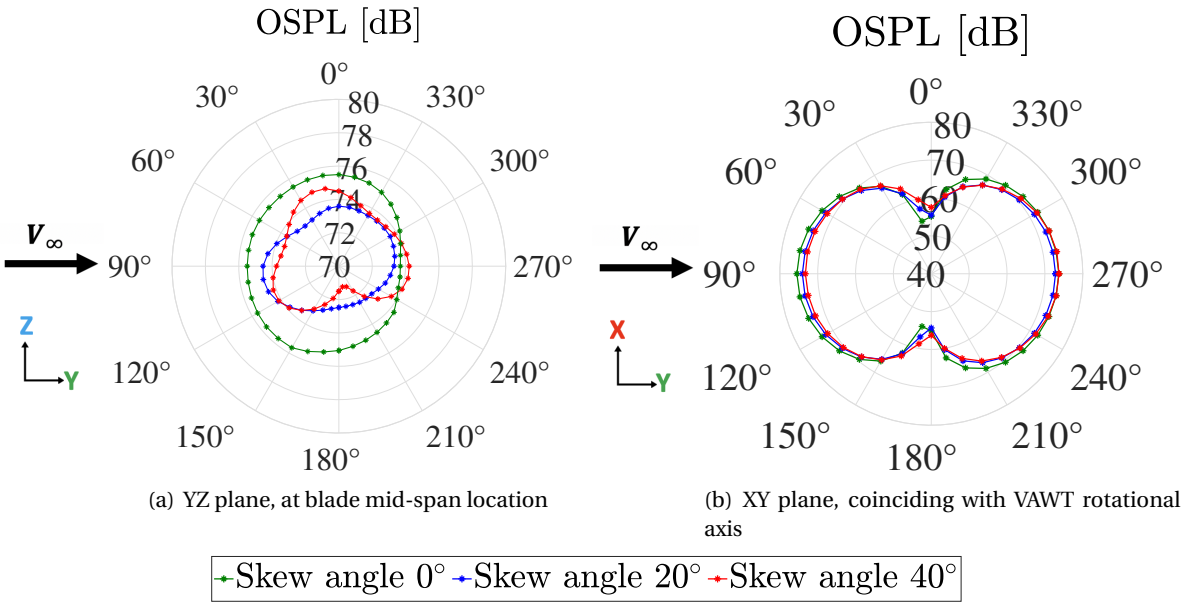

(a) YZ plane, at blade mid-span location (b) XY plane, coinciding with VAWT rotational axis

Figure 7.20: Directivity plot of overall sound pressure level (OSPL) comparing different VAWT configurations at TSR = 4, along a circular array of 36 points situated at a distance of 7D from the origin of VAWT ([0,0,0])

On the YZ plane, non-zero skew angles demonstrate a large range of variation in noise levels in

a single rotation. The noise levels are higher in the upwind and downwind locations but decrease around the windward and leeward side of rotations, except for the windward side with skew angle 40° (where noise increases). VAWT with skew angle 0° shows relatively constant noise levels throughout the entire 360° azimuth range. There are various noise sources in a VAWT [43–45, 261] and the observed discrepancy indicates that some noise sources are more dominant in the zero skew angle configurations compared to the non-zero skew angle configuration, such as the Separation-Stall noise [127]. Further investigation utilizing low-fidelity aeroacoustic prediction models can provide valuable insights into the specific contributions of different noise sources for different skew angles.

7.4. Conclusions and Discussions

The chapter investigates detailed flow physics into the effect of skewed inflow conditions on the aerodynamics and aeroacoustics of vertical axis wind turbines (VAWTs). The purpose of this research is twofold. First, it aims to assist the development of a multi-fidelity simulation framework to enhance the aerodynamic and aeroacoustic efficiency of VAWTs. Second, it investigates the effects of skewed inflow, a specific type of non-uniform inflow condition encountered by a VAWT. The study employs the Lattice Boltzmann Method (LBM) for high-fidelity 3D aerodynamic simulations and the Ffowcs Williams and Hawkings (FW-H) methodology for subsequent aeroacoustic post-processing to determine the far-field noise. Mid-fidelity aerodynamic simulations are also conducted using the Lifting Line Free Vortex Wake (LLFVW) method. The focus of the investigation is the influence of skewed inflow on thrust and power performance and far-field noise. A comparative analysis of the 3D force-field and flow-field results obtained through both mid-fidelity and high-fidelity methods is also performed. The goal is to identify differences in the modelling of fluid dynamic interactions, which may account for any observed inconsistencies in the findings.

A straight-bladed Darrieus VAWT with geometrical parameters replicated from the study by Brandetti et al. [47] and LeBlanc et al. [181, 182] is employed. The VAWT solidity is set at 0.1 and the rotor aspect ratio is 1 for all the investigations conducted. Three different skew angles have been simulated - 0°, 20° and 40°. LLFVW method is used to simulate tip speed ratios (TSRs) of 3, 4 and 5 and a range of skew angles from 0° to 70°, while LBM is used to simulate only 0°, 20° and 40° skew angles for a TSR of 4. The 40° skew angle demonstrates superior statistical temporal convergence compared to the 20° skew angle. This is especially evident for torque values in both LBM and LLFVW results. A reduced value of uncertainty (u) for the 40° skew angle supports this finding, suggesting reduced fluid dynamic interactions for this case that lessen unsteadiness in blade loading. Consistent with previous chapters, the temporal convergence is better for thrust values, shown again by lower uncertainty (u), compared to torque values. The grid convergence and numerical validation for the current setup are shown in the previous Chapter 6.

At a TSR of 3, an increase in skew angle leads to a decline in C_P and C_T values, with C_P demonstrating a more rapid degradation. At TSR 4, an initial increase in C_P and C_T values occurs up to a 20° skew angle, followed by a decrease, with this pattern of increase being more pronounced at TSR 5. As the skew angle increases, a consistent decrease in C_T and C_Q values for a single blade is detected in the upwind part of rotation. This is attributed to the decrease in the horizontal component of velocity ($V_\infty cos\beta$) as the skew angle increases. In the downwind part, an increase in C_T and C_Q values is observed as the skew angle increases. Such a performance boost is attributed to a reduction in blade wake/blade vortex interaction (BWI/BVI) in the downwind portion of rotation due to skewed inflow. This is observed as an increase in wake velocities experienced by the downwind blades, as the skew angle increases. Streamwise velocity 2D contours and 3D vortices visualisation also show that downwind blades experience more clean flow as the skew angle increases. The combination of the two opposing factors in the upwind and downwind parts of rotation dictates the overall ro-

tor performance. The results also indicate a robust correlation between non-zero skew angles and BWI/BVI in a VAWT.

Both the mid-fidelity LLFVW and high-fidelity LBM methods capture the physical trends of the effect of skew angle very well, although some inherent differences are observed. First and foremost, the LLFVW method predicts higher integral thrust and power values for the overall rotor in comparison to LBM. This difference progressively increases with the increase in skew angle. Despite this divergence, there is an agreement between the trends observed in C_P and C_T values as the skew angle increases predicted by both LBM and LLFVW methods. The LLFVW method also predicts higher values of azimuthal thrust and torque, in both upwind and downwind phases of rotation, as compared to LBM. This discrepancy is also observed to be true when individual blade normal forces are evaluated and are consistent for all three skewed inflow conditions studied. This shows that the LLFVW method may not be capturing the complex 3D effects in a VAWT flow and force field as strongly as LBM, particularly when blades encounter skewed inflow. Empirical modifications in the airfoil lift and drag polar values are suggested, for the LLFVW method framework. Furthermore, the streamwise wake velocities predicted by the LLFVW method are lower, attributable to increased blade loading, which led to a stronger wake as compared with LBM predictions. These findings emphasise the need for consideration of the appropriate fidelity level in wind turbine simulations, especially when complex 3D fluid dynamic interactions are involved. Further research efforts should be directed towards refining the airfoil polar data in the LLFVW method to accurately represent the blade-wake and blade-vortex interactions and to ensure consistency with the experimental data.

The study also compared aeroacoustic characteristics across three skewed inflow conditions studied. A decrease in low-frequency noise is observed with an increase in the skew angle, a phenomenon that can be attributed to the lower integral blade loading or thrust values obtained. Conversely, an increase in high-frequency noise is observed with an increase in the skew angle. This can be ascribed to increased flow separation on the blades within the downwind phase of rotation, because of an additional spanwise velocity component, thereby contributing to an increased Separation-Stall (SS) noise. Another factor can be the increased interaction of the mid-span region of downstream blades (where blade loading is highest in the spanwise direction) with the tip vortices shed by the upstream blades within the wake region.

The present study focuses on a common non-uniform inflow condition within Vertical Axis Wind Turbines: the skewed inflow condition. Recognizing the inherent challenges and differences between mid-fidelity and high-fidelity methods in the aerodynamic modelling of the blades, the research underscores the necessity to address these disparities to increase the fidelity of the simulations. Such refinements and enhancements will pave the way for more reliable and robust predictions, contributing to a deeper understanding of the fluid dynamic interactions within VAWTs, and will equip engineers and researchers with the analytical tools necessary for informed design and optimisation strategies. Furthermore, due to the large 3D design space of VAWTs, there is a compelling need for further investigation of various geometric parameters on both aerodynamic performance and noise generation. These parameters include but are not confined to, the effect of airfoil shape, aspect ratio, blade design, blade pitch, and the dynamics of VAWT clusters. The forthcoming chapters will systematically explore these configurations.

8

VAWT cluster

Summary

This chapter investigates the effect of VAWT separation and direction of rotor rotation on the aerodynamics and aeroacoustics of Darrieus VAWT clusters, consisting of two VAWTs and operating at chord-based Reynolds numbers below 4×10^5. Three cluster configurations are investigated: parallel VAWTs in a co-rotating configuration, parallel VAWTs in a contra-rotating configuration and tandem VAWTs in a co-rotating configuration using the high-fidelity Lattice Boltzmann Method (LBM). As the VAWT separation decreases, the fluid dynamic interactions between the VAWTs increase. This leads to an increase in power production for the parallel VAWT configuration, by 3.68% to 6.21% for a separation of 3m and 1.5m, respectively, as compared to the standalone VAWT. A similar trend is followed by the low-frequency noise below 40 Hz. For the second cluster configuration, there is minimal difference in the power output, with the co-rotating setup exhibiting more power than the contra-rotating setup only by 0.09%. At low frequencies (< 50 Hz), the former generates more noise than the latter and at high frequencies (> 1000 Hz), the latter generates more noise than the former. In the tandem configuration, for all VAWT separations, the downstream VAWT exhibited negative power values attributed to intense blade-wake/blade-vortex interactions (BWI/BVI) due to the wake shed from the upstream VAWT. At a separation of 2m and 4m, the power production of the VAWT cluster is 60.1% and 45.7% less than the standalone VAWT, respectively. In terms of noise, downstream VAWT generates less low-frequency noise (< 40 Hz) and more mid-frequency noise (40-400 Hz) than the upstream VAWT. The former is attributed to the mean blade loading and the latter is attributed to the BWI/BVI in the downstream wake.

8.1. Introduction

The present chapter is dedicated to the VAWT clusters, wherein multiple VAWTs are situated in proximity to each other leading to mutual aerodynamic interaction. Certain configurations of such clusters yield positive interaction amongst the blades of different VAWTs, thereby enhancing the power efficiency of each individual turbine [14]. This feature is often overlooked in the context of VAWTs, particularly when intended for urban applications where horizontal space is a significant constraint. This mutual interaction also significantly influences the aeroacoustic properties of both individual VAWTs and the entire cluster. Accurately capturing the flow physics of VAWT clusters poses a challenge, due to the increased computational demand (owing to an increased number of blades) and the requirement for high-fidelity CFD methodologies due to the dominance of blade-vortex interaction. Consequently, an in-depth investigation into the effects of diverse VAWT cluster configurations is essential for devising effective applications in an urban locality, optimizing the utilisation of limited available space and amplifying power generation in confined areas.

8.1.1. Literature Review

The presence of additional VAWTs in the vicinity affects the flow experienced by individual VAWTs. This affects the starting torque of the turbine, power generated at operating TSR and the downstream wake (which in turn affects any downstream VAWT present). A number of investigations have explored the flow physics of VAWT clusters using low and mid-fidelity aerodynamic methods (since they are much cheaper to run) and experiments. Azadani [14] gave a review of various studies on VAWT cluster configurations and concluded that power improvement is indeed possible when VAWTs are placed close to each other. Various parameters were analysed which affect the power performance of such cluster configurations such as spacing between the wind turbines, co-rotating and contra-rotating configurations, number of wind turbines in a cluster, blade pitch angle for deflection of downstream wake, solidity, aspect ratio and operational TSR of a VAWT.

In a tandem arrangement of HAWTs, the power output of the downstream turbine diminishes from 66% of the power of the upstream turbine at a spacing of $7D$, to 35% at a spacing of $3D$ [82], where D represents the HAWT diameter. Due to the need for this extensive spacing, HAWT wind farms typically exhibit low power density. Thomas [337] showed that two VAWTs in proximity can produce more power than a standalone VAWT. Subsequently, Dabiri [87] demonstrated via field experiments that VAWT wind farms can achieve a higher power density in comparison to their horizontal counterparts. While HAWT wind farms can possess a power density ranging from 2–3 W/m^2 [203], the power density of VAWT wind farms can span between 6–30 W/m^2 [87].

For a pair of VAWTs, there exist three potential configurations determined by each turbine's rotation direction [14]. The turbines can rotate in the same direction (co-rotating) or in the opposite direction (contra-rotating), where there can be two different configurations for the latter. One situation in which the direction of rotation of blades in the gap between two wind turbines is the same as the wind direction (contra-rotating down) and another in which it is opposite to the wind direction (contra-rotating up). Thomas [337] showed that the contra-rotating down configuration yields higher power output due to increased vortex interactions between the turbines. In the context of two parallel straight-bladed Darrieus VAWTs, studies have indicated the superior efficiency of the contra-rotating down configuration over the contra-rotating up configuration [23, 87, 126, 138, 158, 297, 318, 370]. Additionally, the co-rotating configuration has been observed to produce more power than the contra-rotating configuration [6, 297]. Similar findings were reported by Sun et al. [322] for Savonius hydro turbines. It is also noteworthy that the power coefficient for all configurations diminishes as the spacing between turbines increases [297] and each turbine approaches the performance of a standalone VAWT.

The influence of rotational direction is also dependent upon various parameters, including the tip speed ratio (TSR) [87], wind velocity [6, 307], turbine spacing, and prevailing wind direction. At

low wind velocities, the co-rotating configuration exhibits superior efficiency. Conversely, at high wind velocities, the contra-rotating down configuration demonstrates enhanced performance [6]. The effect of rotational direction becomes more pronounced at closer proximities between turbines. With increased separation, the mean power coefficient for each configuration converges to that of an isolated turbine. Broadly, the power performance of two parallel VAWTs decreases in this order: contra-rotating down, co-rotating, and then contra-rotating up. Given that the induced flow in the contra-rotating down configuration aligns with the wind direction, the shear layer in the fluid remains minimal. This results in reduced turbulence and energy dissipation, resulting in increased power output relative to the co-rotating and contra-rotating up configurations [87]. The wake deflection direction downstream of a turbine is determined by its rotational direction. Therefore, in staggered arrangements (when one VAWT is located downstream of the other VAWT), it is essential that the downstream wind turbine is positioned away from the upstream turbine wind wake to ensure optimal power performance of the former.

There is considerable influence of wind direction on the overall performance of the VAWT cluster. The angle α, between the wind flow and the line joining the rotational axes of two turbines, can vary from -90° to +90°. In the case of 0°, downstream VAWT is fully inside the wake of the upstream VAWT (tandem arrangement) and in the case of -90° or +90°, the two VAWTs are in a parallel arrangement. Schatzle et al. [291], using two curved-bladed Darrieus VAWT at a constant distance between them, showed a significant reduction in the power coefficient of the downstream turbine at lower α values compared to a standalone turbine. Rajagopalan et al. [271] analysed the effect of angle α on the power production of two straight-bladed Darrieus VAWT. Their observations suggested that with increased α values, the average power coefficient of the tandem turbines surpassed that of a standalone turbine, which agrees with the findings when different directions of VAWT rotations were studied. In studies involving two contra-rotating straight-bladed Darrieus VAWTs [370] and two co-rotating Savonius VAWTs [298], the parallel configuration exhibited higher power efficiency relative to staggered setups with reduced α values (between 0° and 90°). Sahebzadeh et al. [285] determined that for two co-rotating straight-bladed Darrieus VAWTs, the optimal α value stands at 75°.

When the downstream VAWT is positioned outside the wake of the upstream VAWT, its power production exceeds that of the upstream turbine [54, 271, 370]. Further, Brownstein et al. [55] demonstrated that in a staggered arrangement (α between 0° and 90°), both turbines can experience increased power generation. The effect of wind direction on the power yield of two straight-bladed Darrieus VAWTs becomes pronounced at higher solidities and TSRs [90] as well as at higher wind velocities [193].

The spacing between the VAWTs also affects the power performance of a VAWT cluster. The mean power coefficient of VAWTs increases as this spacing between two VAWTs increases but subsequently decreases with further spacing augmentation [285, 298]. This shows that an optimal wind turbine spacing exists at which the mean power coefficient of the VAWT cluster reaches its peak. At extremely narrow spacings, airflow is obstructed, preventing passage between the VAWTs. Consequently, the VAWT pair operates similarly to a single bluff body, characterised by an increased drag coefficient and diminished power yield [137]. The ideal turbine spacing is influenced by factors such as wind direction and VAWT rotational direction. For two co-rotating straight-blades Darrieus VAWTs, the optimal spacing decreases with an increase in angle α [285]. For tandem configurations, the mean power coefficient increases with an increase in spacing. The optimal spacing for $\alpha = 30°$ is $2.25D$, while for $\alpha = 45°$, it stands at $1.75D$. In contrast, for parallel VAWTs, the power performance decreases with an increase in spacing, suggesting an optimal spacing of less than $1.25D$. A similar decline in the mean power coefficient of two parallel straight-bladed Darrieus VAWTs with respect to spacing has been reported in other studies [90, 93, 126, 155].

Another parameter affecting the power performance of the VAWT cluster is the angular separa-

tion between the azimuth angles of the corresponding blades of two VAWTs (β). The azimuth angle shift profoundly influences the power production of two Savonius wind turbines [322]. Conversely, for straight-bladed Darrieus VAWTs, this shift exerts a minimal effect on power output [78, 155, 286]. The effect of azimuth angle shift is less for co-rotating wind turbines, and more significant for contra-rotating wind turbines. Moreover, for the latter, the effect of the azimuth angle shift is dependent upon the wind orientation [286]. For two parallel Darrieus VAWTs, the peak power coefficient is achieved at an azimuth angle shift of 60°, marking only a 1.19% enhancement compared to a shift of 0° [155].

The airfoil profile significantly influences the power production of an individual VAWT and, by extension, VAWT clusters. Peng et al. [262] examined the effects of four distinct NACA airfoil profiles — 0015, 0018, 0021, and 0024 — on the power yield of a two-turbine cluster, considering various layout and design parameters. The findings indicated the NACA 0018 as the optimal airfoil profile. Similarly, solidity markedly affects the power output of an array of VAWT clusters. Increased solidities amplify the Venturi effect's role in boosting VAWT performance [25]. Thus, the positive aerodynamic interaction between two nearby VAWTs becomes more pronounced at increased solidities [90, 93]. In the context of aspect ratio, the enhancement in the mean power coefficient for two VAWTs relative to a single one is more substantial at higher aspect ratios [13]. Chen et al. [79] studied the influence of pitch angle on two co-rotating staggered turbines with $\alpha = 30°$ (wind direction). They observed that adjusting the downstream VAWT pitch angle from -6° to 0° increases the upstream VAWT power output. Furthermore, increasing the upstream VAWT pitch angle increases the downstream VAWT power production, attributable to the change in the wake path trailing the upstream VAWT.

The intensity of aerodynamic interaction between two VAWTs is dependent significantly upon TSR. Schatzle et al. [291] investigated the effect of TSR on the mean power coefficient of two curved-bladed Darrieus VAWTs in a tandem arrangement. Their findings indicated that as the upstream VAWT TSR increases, the downstream VAWT power performance reduces. This phenomenon primarily stems from the increased strength of the wake and vortices shed by the upstream VAWT, resulting in a reduced angle of attack on the downstream VAWT blades and, subsequently, diminished power production. Increasing the TSR for two parallel straight-bladed Darrieus VAWTs reduces their wind permeability, leading to a decline in wind flow through the wind turbines and an increase in flow around them. The accelerated flow within the space between the VAWTs enhances power output [370]. Therefore, the increase in power performance for contra-rotating up and down configurations, with respect to a standalone VAWT, is more at higher TSRs. Additionally, the maximum value of the power coefficient for a VAWT cluster shifts towards higher TSRs, as compared to a standalone VAWT [134, 318, 351, 370].

The power performance of a three-turbine VAWT cluster, similar to paired turbines, depends on various factors such as VAWT rotational direction, wind direction, and spacing, among other factors. At reduced spacings, the flow that is induced between the VAWTs and their interaction with the prevailing wind predominantly governs the VAWT cluster power performance. Conversely, at large spacings, the wake deflection direction from the upstream VAWTs becomes essential. Shaaban et al. [296] examined the effect of the rotational direction of each VAWT on the power yield of the cluster, in the case when one VAWT is upstream and two VAWTs are downstream and parallel. The observations indicated that, at narrow spacings, clusters with contra-rotating downstream turbines exhibit superior performance. However, at broader spacings, clusters with co-rotating turbines produce greater power. When downstream VAWTs are positioned in the wake of the upstream VAWTs, the mean power coefficient is reduced. Whereas, when all three VAWTs are parallel to each other (the line connecting the centre of VAWTs perpendicular to the flow), this coefficient reaches its maximum [309].

In clusters comprising more than three wind turbines, both layout and design parameters crit-

ically influence the VAWT cluster power performance. Whittlesey et al. [360] conceptualised layouts for 4 × 4, 16 × 16, and 32 × 32 VAWT clusters, drawing inspiration from the vortex patterns in the wakes of fish schools. These configurations demonstrated a marked power increase relative to standalone VAWTs. Duraisamy et al. [109] analysed a column of seven co-rotating straight-bladed Darrieus VAWTs, spaced 2.5D apart laterally. Their findings indicated that this column's power yield ranged between 50% and 100% more than a standalone VAWT. Subsequently, Bremseth et al. [48] incorporated four additional columns, assessing the power output across five VAWT columns at varying TSRs and stream-wise separation between the VAWTs. Notably, under optimal conditions, downstream VAWT columns had higher performance than their upstream counterparts.

Optimal performance for clusters of 2, 4, 8, and 16 Savonius VAWTs is achieved when all wind turbines align parallel to the wind flow. Furthermore, tighter turbine spacing combined with a larger turbine count enhances power performance. An increment in turbine count from 2 to 16 increases power performance by 19% (Mereu et al. [225]). Hezaveh et al. [143] compared the efficiency of four distinct VAWT cluster configurations: aligned, staggered, staggered triangular clusters when there are two upstream VAWTs (in parallel) and one downstream VAWT, and staggered triangular clusters when there is one upstream VAWT and two downstream VAWTs (in parallel). The study reported that VAWT wind farms adopting the former configuration of the staggered triangular clusters exhibited superior efficiency, attributed to the mutual aerodynamic interactions within each cluster enhancing power performance.

Wake interaction is also an essential phenomenon, determining the power increase or decrease in a VAWT cluster with increased proximity, relative to a standalone VAWT. Troldborg et al. [341] investigated the wake interaction of two straight-bladed Darrieus VAWTs, considering different wind directions, VAWT separations, and turbulence intensities. The observations highlighted that increased flow turbulence leads to faster wake recovery for the upstream VAWT, subsequently enhancing the downstream VAWT power performance.

For two co-rotating turbines, the wake exhibits asymmetry relative to the VAWT central axis. In contrast, the wakes of contra-rotating VAWTs, including both contra-rotating down and contra-rotating up configurations, have symmetry [175, 264]. The lateral wake displacement for co-rotating turbines increases with rising TSR [264]. The width of the wake deficit for the contra-rotating up arrangement is smaller than its contra-rotating down counterpart. Moreover, the downstream wake is much longer in the contra-rotating up configuration, with a slow flow velocity recovery [158, 243, 350, 351]. Conversely, the contra-rotating down configuration wake exhibits faster velocity recovery, achieving full recovery post 5D distance [243]. Contrary to the aforementioned investigations, Lam [175] reported increased aerodynamic interaction within the wake for the contra-rotating up configuration, and with a reduced length of the downstream wake. Adding to this observation, an optimal layout was proposed for a cluster of three VAWTs: a triangular arrangement when there are two upstream VAWTs (in parallel) and one downstream VAWT, where the upstream VAWTs adopt the contra-rotating down configuration. The disparities between Lam's [175] conclusions and other studies might originate from the high-solidity VAWTs employed by the former.

Despite the existing body of literature on the various VAWT cluster configurations and their power performance, there is still a lack of detailed flow physics studies utilizing full 3D high-fidelity numerical simulations studying unsteady blade loads and downstream turbulent near-wake, since most of the previous studies are conducted using low-to-mid fidelity CFD methods. Furthermore, based on the observations in all the previous chapters, high-fidelity simulations are essential to capture intricate flow features in a VAWT flow field to better quantify blade-vortex/blade-wake interactions (BVI/BWI). Based on this motivation, the current chapter uses only the high-fidelity method for simulating a cluster of VAWTs, since the significance of BVI/BWI is even higher than a standalone VAWT. In the field of aeroacoustics, there is a significant research gap in determining the effect of different parameters such as spacing between VAWTs, the direction of rotation, wind direction, cluster

orientation, etc. on the overall aeroacoustic performance of the VAWT cluster, as well as identifying the various noise sources that affect the overall noise signature. Hence, this chapter aims to address these gaps in flow physics investigation and contribute to the development of low-noise and high-performance VAWT cluster configurations.

8.1.2. Research Objectives

Given the above-mentioned motivation, the current investigation's objective is to take a major step towards creating a high-fidelity simulation framework for studying the aerodynamic and aeroacoustic performance of VAWT clusters, using different configurations. To achieve this, high-fidelity 3D aerodynamic simulations based on the Lattice Boltzmann Method (LBM) are conducted for straight-bladed VAWT clusters consisting of two VAWTs separated by a specified distance. Subsequently, aeroacoustic post-processing is performed using the Ffowcs Williams and Hawkings (FW-H) methodology to calculate the far-field noise.

The study will draw important conclusions regarding the significance of different fluid dynamic interactions for a group of VAWTs, that can be captured by the high-fidelity aerodynamic method employed. The high-fidelity simulation campaign enables accurate resolution of the flow around the VAWT blades and in the wake, thus enabling the study of 3D effects on the force and flow field for different blade numbers. These effects include non-uniform blade loading and non-uniform wake, dynamic stall, blade-vortex interaction, and wake recovery of the cluster as a whole. This study also aims to increase the scientific knowledge of the aerodynamic noise generated by the cluster as compared to a standalone VAWT. The following research questions are formulated for this chapter:

Research Questions

- What are the significant fluid dynamic interactions for a VAWT cluster that can be captured using a high-fidelity aerodynamic method?
- How does the VAWT spacing affect performance parameters such as thrust, power, and far-field noise of a cluster?
- How does the direction of rotation of a VAWT affect performance parameters such as thrust, power, and far-field noise of a cluster?
- How do 3D effects of blade loading on thrust and power values, trailing and shed vortices, and wake dynamics vary for different VAWT cluster configurations?
- What are the key noise sources contributing to the aeroacoustic performance of the VAWT cluster in different configurations?

The chapter is structured as follows. Section 8.2 presents the computational setup of the high-fidelity LBM, including VAWT geometrical properties, flow and grid settings. Section 8.3 reports the results obtained for the grid convergence study, detailed force and flow field analysis and aeroacoustic performance of the VAWT for the different number of blades. The last section 8.4 presents important conclusions of the study and a discussion on the understanding of the highly unsteady and turbulent VAWT fluid dynamic interactions.

8.2. Computational setup

The simulation's numerical and geometrical aspects, along with a description of the flow conditions, have been detailed. This will enable the readers to assess the validity and reliability of the results presented in subsequent sections. The VAWT geometry used in this chapter is the same as Chapter 5, where the 2-bladed VAWT is adopted for the cluster. The computational setup is also the same, in

general, except a cluster of VAWTs replaces the geometry of a single VAWT.

8.2.1. Geometry

This chapter employs a 2-bladed straight-shaped VAWT design in a 2-turbine cluster configuration, where the two turbines are named VAWT1 and VAWT2 in each cluster. VAWT1 is located on the leeward side and VAWT2 is located on the windward side of the cluster. The blade geometrical parameters have been replicated from the study by Balduzzi et al. [22] for which the results have already been validated in Chap 5. To investigate the flow physics, three different cases of cluster configurations are investigated. The first configuration (Case 1) consists of two VAWTs in parallel and rotating in the same direction (co-rotating), with different spacing between the VAWTs. The second configuration (Case 2) is the same as the first configuration, with one co-rotating and one contra-rotating down case. The contra-rotating down situation is in which the direction of rotation of blades in the gap between two wind turbines is the same as the wind direction. The third configuration (Case 3) consists of two VAWTs in tandem (downstream VAWT inside the wake of upstream VAWT) and rotating in the same direction (co-rotating), with different spacing between the VAWTs.

Figure 8.1 depicts the geometric model for the first and third configurations, while Table 8.1 presents the geometric values of a single VAWT and the blade used and freestream velocity experienced by the cluster. Table 8.2 lists all different cluster configurations used in this study. The 2-bladed VAWT solidity and rotor aspect ratio are 0.16 and 1.46, respectively. The presence of dual VAWTs in proximity to each other potentially gives rise to stronger 3D effects and increased blade-vortex interaction. The variations in these fluid dynamic interactions for different cluster configurations are expected to result in differences in the unsteadiness of VAWT blade loading, which, in turn, affects wake dynamics and aeroacoustic behaviour.

Table 8.1: A single VAWT geometry and operational settings

Blade length (L)	**Rotor diameter (D)**	**Chord length (c)**	**Freestream velocity (V_∞)**	**Airfoil**	**Tip Speed Ratio**
1.5 m	1.03 m	0.086 m	9 m/s	NACA 0021	3.3

Table 8.2: Different VAWT cluster configurations and their naming convention used in this chapter; each cluster involved two VAWTs

			Spacing [m]
Case 1	**Parallel co-rotating**	C1.5	1.5
		C2	2
		C2.5	2.5
		C3	3
Case 2	**Parallel: co-rotating vs contra-rotating down**	C2	2
		CC2	2
Case 3	**Tandem co-rotating**	CW2	2
		CW3	3
		CW4	4

8.2.2. Numerical setup

The current chapter involves only the high-fidelity Lattice Boltzmann Method (LBM) to simulate all the VAWT cluster configurations. A simulation volume is implemented, which comprises a cube with dimensions of $100D$ on each side. The cluster geometry is situated at the centre of this volume. The boundary conditions for the domain are shown in Figure 5.2 (b) in Chap 5. At the velocity inlet,

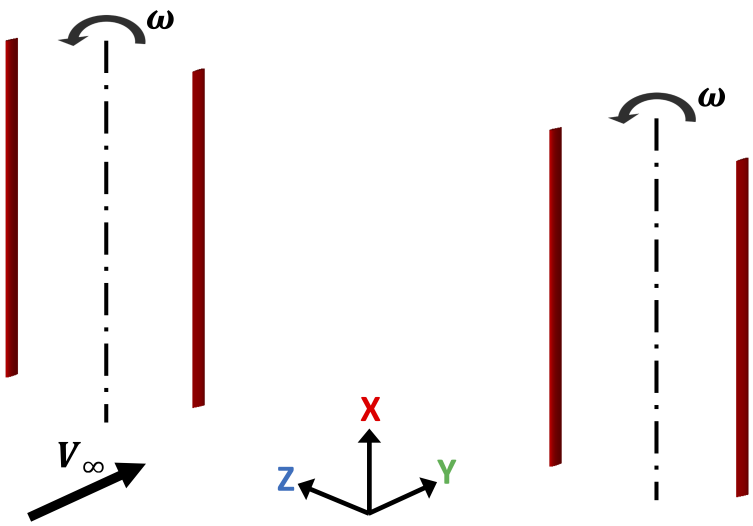

(a) Case 1 - Co-rotating parallel VAWTs with a separation of 3m

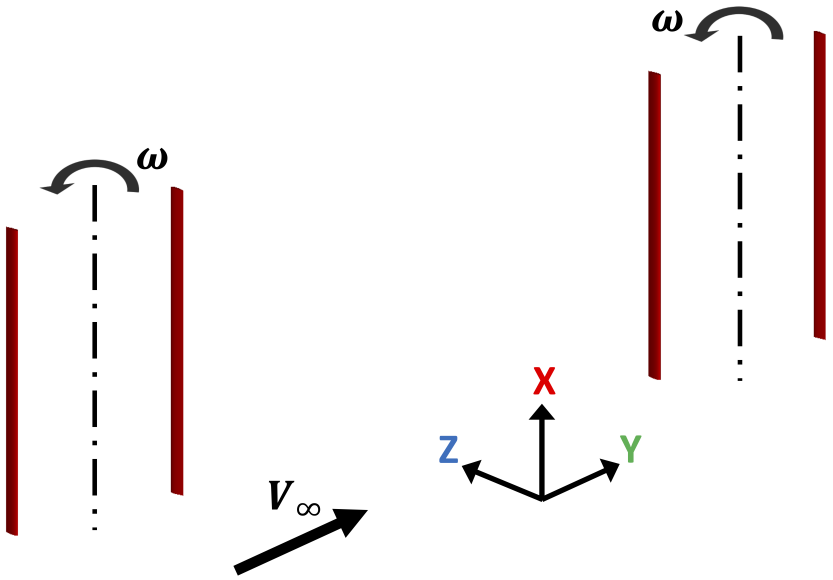

(b) Case 3 - Co-rotating tandem VAWTs with a separation of 4m

Figure 8.1: Schematic of the VAWT configurations used in this chapter, where VAWT1 and VAWT2 are on the right- and left-hand side, respectively; Case 2 is with additional contra-rotating down configuration

the velocity is set to the freestream velocity V_∞ in the direction of the Y-axis. An ambient pressure of 101.325 kPa is imposed at the pressure outlet. A no-slip boundary condition is applied to the blade surface. The PowerFLOW Cartesian volume grid is generated the same way as all the previous chapters. To optimise computational efficiency, the present study employs 17 VR regions, with the highest resolutions near the blade surface of each VAWT in the cluster, with an offset, and coarser regions located farther from the blade and cluster. This approach enables computational effort to be allocated primarily to regions of interest and where high flow gradients are expected.

To calculate the far-field noise, only the FW-H solid formulations are employed where the blade surfaces of the VAWT are used for sampling the pressure fluctuations, similar to all previous chapters. The reason is the difficulty in eliminating spurious noise sources from FW-H permeable data when only three spherical permeable surfaces (Figure 5.2 (a)) are utilised within the context of a VAWT. Similar to all previous chapters, analyzing the noise spectra up to 4000 Hz is sufficient for

understanding the aeroacoustics of VAWT clusters while using a sampling time of 8 steady rotor rotations. Therefore, pressure data are sampled at a frequency of 8000 Hz, in accordance with the Nyquist criterion. To ensure accurate acoustic wave capture, a criterion of a minimum of 15 points per wavelength is selected. Subsequently, noise spectra are calculated utilizing a Hanning window with 50% overlap and a frequency resolution (Δf) of 15 Hz, using the *pwelch* function in MATLAB.

8.2.3. Flow conditions and grid settings

For the present investigation, Table 8.3 illustrates the operational settings of each VAWT in different cluster configurations. Tip speed ratio (TSR), defined as the ratio of the blade rotational speed and the freestream velocity, i.e. $\omega r/V_\infty$, where ω denotes the rotational speed in radians per second, r signifies the wind turbine radius and V_∞ represents the freestream velocity, is used as a measure of the system's operational condition. To change the TSR, V_∞ is maintained at a constant value of 9 m/s in order to keep it same as the validated setup in Chap 5, while ω is varied to adjust the TSR value. The freestream velocity corresponds to the freestream Mach number of 0.026 and chord-based Reynolds number (Re_c) is calculated as 1.73×10^5, based on the average velocity experienced by a blade during a single rotation. The high-fidelity method (LBM) is employed for the simulation of TSR = 3.3. The freestream turbulence intensity (I_t) and turbulence length scale (L_t) are assigned values of 0.1% and 1 mm, respectively.

Table 8.3: VAWT operational settings for each VAWT in a cluster

Parameter	Value
Tip speed ratio (TSR)	3.3
Rotations per minute (RPM)	550.71
Chord-based Reynolds number (Re_c)	1.73×10^5

In this chapter, Grid 3 from the validated setup of Chapter 5 is utilised. The grid's y^+ value is 50, and there are 1.78×10^2 voxels per blade chord length. Grid 3 has a minimum voxel size of 0.32 mm, with 40.07 million fine equivalent voxels in the computational domain for the 2-turbine VAWT cluster. These fine equivalent voxels are derived by multiplying the number of voxels with the time stepping rate, which is directly linked to the mesh resolution level.Figure 8.2 shows the finest mesh around the blade with 4 different VRs for the setup with Grid 3.

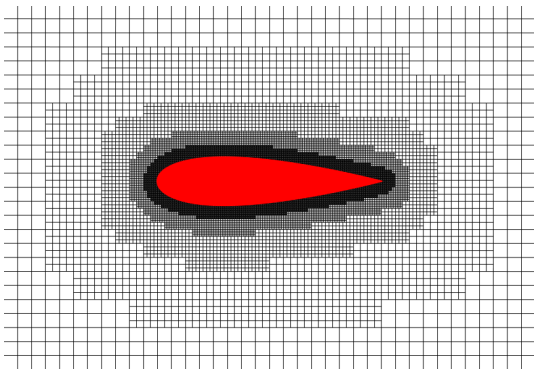

Figure 8.2: Cross-sectional view of the finest mesh around the blade

Figure 8.3 shows the cross-sectional view of the mesh in the domain for Grid 3, both near the VAWT blades and further away from it. Simulating 18 rotor rotations (1.96 s) requires 3.22×10^6 CPU hours, utilizing a Linux workstation with an AMD Ryzen Threadripper 3990X Gen3 processor, featuring 64 cores and 128GB DDR4 3GHz platform. It is noteworthy that the fine equivalent voxels and CPU hours are consistent across all the VAWT cluster configurations simulated in this chapter.

Furthermore, the physical time step for Grid 3 resolution corresponds to a Courant-Friedrichs-Lewy (CFL) number of 1 in the finest VR level and is measured at 2.26×10^{-6} s.

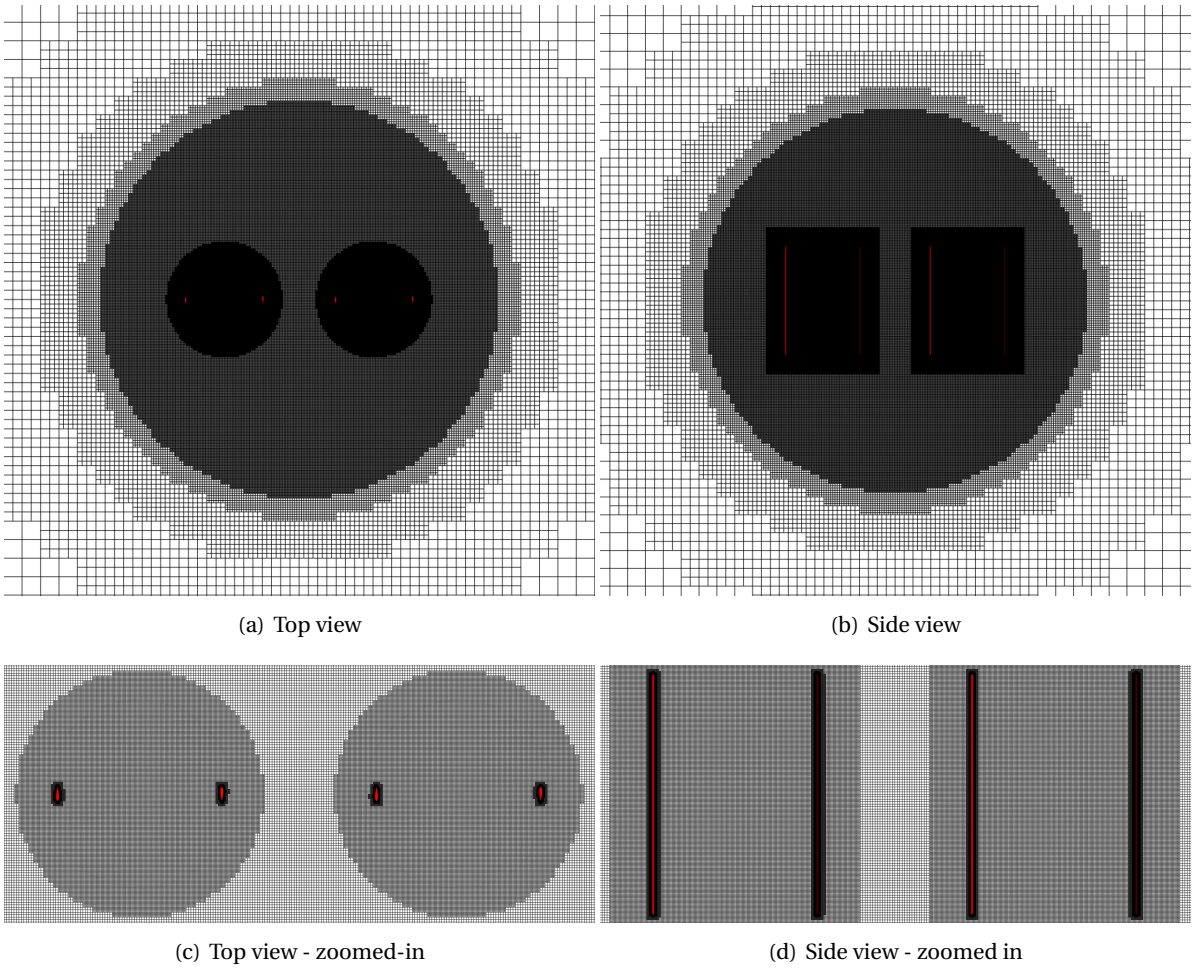

(a) Top view (b) Side view

(c) Top view - zoomed-in (d) Side view - zoomed in

Figure 8.3: Cross-sectional view of the mesh for the high-fidelity LBM simulation

The integral and time-varying behaviour of the thrust coefficient (C_T) and torque coefficient (C_Q) of each VAWT and the cluster as a whole, are reported. These coefficients are defined as:

$$C_T = \frac{T}{0.5\rho A V_\infty^2}, \tag{8.1}$$

$$C_Q = \frac{Q}{0.5\rho A V_\infty^2 R}, \tag{8.2}$$

where, T and Q are VAWT thrust and torque respectively, ρ is the air density, A is swept area ($D \times L$) where is D is rotor diameter and L is blade length, R is rotor radius and V is freestream velocity. The unsteady pressure data, Power Spectral Density (PSD) spectra and Overall Sound Pressure Level (OSPL) values obtained using FW-H solid formulation are also reported and analysed.

8.3. Results

8.3.1. Temporal and grid convergence study

Figure 8.4 reports a subset of the results to depict the temporal convergence characteristics of thrust coefficient (C_T) and torque coefficient (C_Q) for two distinct configurations in Case 1, namely C1.5

and C3. The values reported in these figures are representative of one of the rotors in the cluster, namely VAWT1, comprising all blades in that rotor.

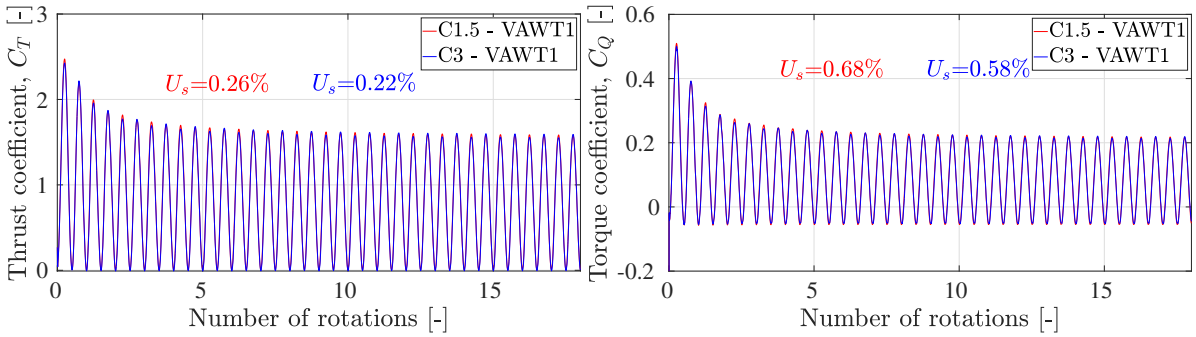

(a) (b)

Figure 8.4: Statistical temporal convergence study for thrust coefficient C_T and torque coefficient C_Q for Case 1 VAWT clusters; the values are representative of one of the rotors VAWT1

The uncertainty values (u) presented in each figure are calculated as a percentage of the standard deviation of thrust and torque values averaged over a complete rotation. These uncertainty values represent the level of uncertainty in the calculated coefficients over time and in turn the unsteadiness and randomness in the fluid dynamic interactions in the cluster. Lower values of u indicate a higher level of confidence in the simulation results, suggesting that the simulation has achieved temporal convergence. All u values shown are calculated after the 12th rotor rotation for the cluster.

The figures indicate that the statistical temporal convergence for all the cases shown is achieved after 12 rotor rotations and there is minimal difference between the convergence characteristics of different cases. This is confirmed by low uncertainty values (u) for both configurations. This behaviour is also found for Case 2 and Case 3 clusters, although the results are not shown to avoid repetition. Notably, the temporal convergence in the case of VAWT clusters is delayed as compared to standalone VAWTs in all the previous chapters, where the convergence was achieved after just 4-6 rotations for a 2-bladed VAWT. This shows that high-fidelity LBM captures the increased unsteady phenomenon and fluid dynamic interactions in the VAWT cluster, as compared to standalone VAWTs. Subsequently, all results in this chapter are reported based on data obtained after the 12th rotor rotation.

8.3.2. Parallel VAWT cluster: effect of VAWT separation

Figure 8.5 (a) and (b) shows the effect of VAWT separation on the thrust coefficient C_T and torque coefficient C_Q of the overall cluster. The values show a linear increase in both C_T and C_Q as separation decreases. This shows the advantage of using a cluster with closely spaced turbines for power performance gains. For both C_T and C_Q, a linear curve and the corresponding equation are shown which represents the best linear fit for the reported values. Figures (c) and (d) show the comparison between a single VAWT of a cluster (VAWT1) and a standalone VAWT (which is similar to a 2-bladed VAWT from Chap 5). The C_T of the standalone VAWT is 0.8002. Therefore, substituting twice this value as y in the linear equation of Figure 8.5 (a) gives the value of x as 4.2205 m, which is the predicted VAWT separation needed to achieve negligible fluid dynamic interactions between the two VAWTs. This brings C_T of a cluster twice that of a standalone VAWT.

On the other hand, C_Q of a standalone VAWT is 0.0795. Performing similar steps using the equation shown in Figure 8.5 (b) gives the value of x as 5.19 m. This shows that torque gets affected more strongly than thrust, from the resulting mutual fluid dynamic interactions between the two VAWTs in proximity, and therefore needs larger VAWT separation to reduce these interactions to negligible

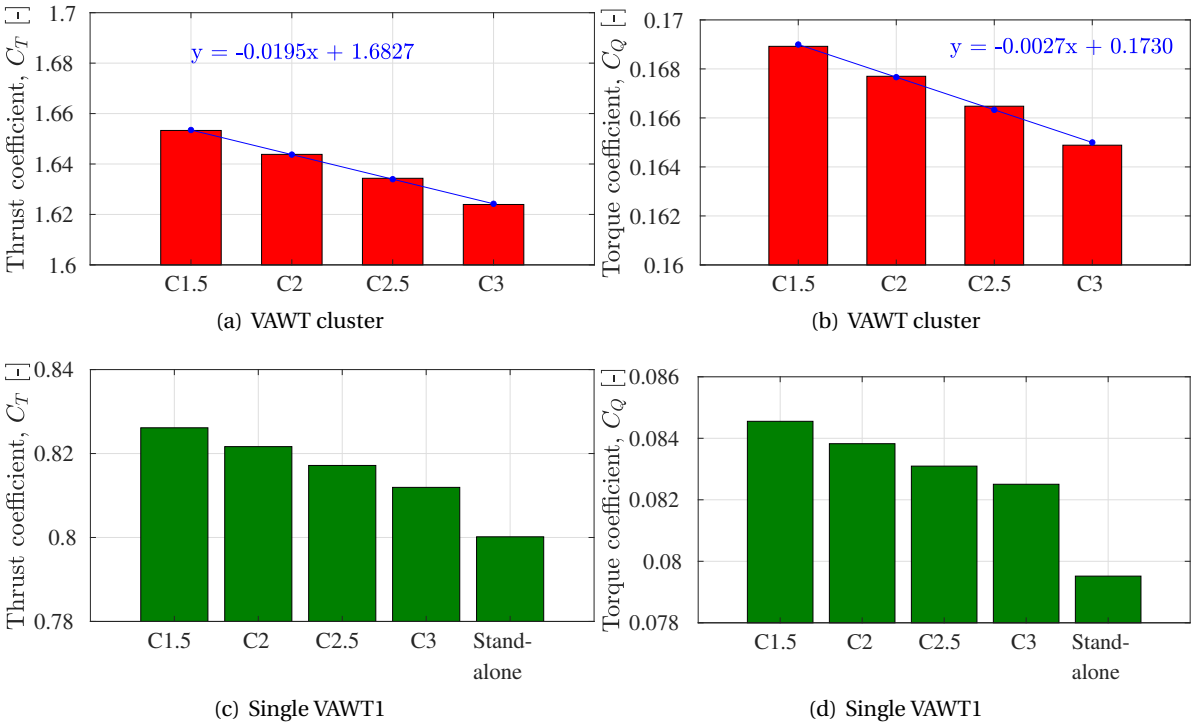

(a) VAWT cluster (b) VAWT cluster

(c) Single VAWT1 (d) Single VAWT1

Figure 8.5: Effect of VAWT separation on thrust coefficient C_T and torque coefficient C_Q for Case 1 VAWT clusters

values. However, it is likely that both C_T and C_Q will approach the standalone VAWT values asymptotically rather than linearly when the separation is increased even further than what is shown in the figures. In that case, the actual x value is likely to be higher than the predicted value. Table 8.4 lists the values of power density for different VAWT separations in the cluster. The area for the cluster is taken as twice the area of a single VAWT, where, for a single VAWT, the area is calculated as the square with diameter D as one side. As expected from the previous result, power density increases as VAWT separation reduces, which is in agreement with all previous studies on the aerodynamics of VAWT clusters.

Table 8.4: Variation of power density with different VAWT separation and comparison with the standalone VAWT; Area is calculated for a square with diameter D as one side

	Power produced (W)	**Area** (m^2)	**Power density** (W/m^2)
Standalone	181.03	1.06	170.64
C1.5	384.56	2.12	181.24
C2	381.77	2.12	179.93
C2.5	378.99	2.12	178.62
C3	375.37	2.12	176.91

Figure 8.6 shows the effect of VAWT separation on the C_T and C_Q of individual turbines in the cluster. For both C1.5 and C2, individual VAWTs do not exhibit the same value of C_T and C_Q; VAWT2 (windward side of the cluster) has higher values than VAWT1 (leeward side of the cluster). This shows the asymmetrical behaviour of a VAWT cluster, which is also exhibited by a standalone VAWT [92, 334]. As a means to verify the flow physics, the same co-rotating VAWT cluster setup was also simulated with the rotation direction reversed for the blades. In that case, the results for VAWT1 and VAWT2 also reversed.

Figure 8.7 illustrates the variation in C_T and C_Q plotted for a single blade for a complete 360°

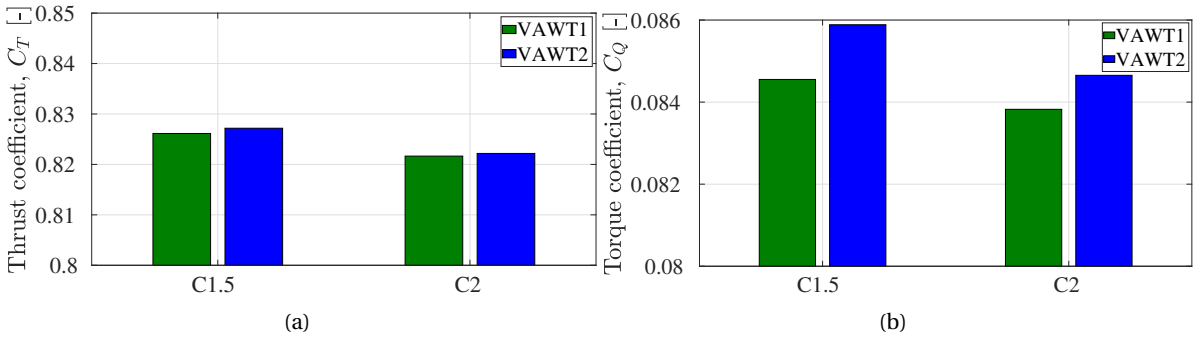

Figure 8.6: Effect of VAWT separation on thrust coefficient C_T and torque coefficient C_Q of each VAWT in the VAWT cluster: VAWT1 (leeward side) and VAWT2 (windward side), and compared to a standalone VAWT

azimuth, for VAWT1. The figure also shows the average value over the rotation and all the results are compared to the standalone VAWT. Although the blade loading values are very similar for all three cases, in both the upwind and downwind parts of rotation, both C_T and C_Q values decrease as the distance between the two VAWTs increases and finally approaches the standalone VAWT. This was also reflected in all previous figures. This is attributed to increased blade-wake and blade-vortex interactions between the two turbines, leading to increased power performance. It is expected that if TSR is increased for all VAWTs (currently it is 3.3), the difference in C_T and C_Q between the three cases shown will be more prominent. Similar to Figure 5.12 in Chap 5, the blade normal forces across the entire span of blades are expected to show differences in blade loading between the single blade of a VAWT cluster and that of a standalone VAWT. The blade normal forces will decrease as VAWT separation increases with the lowest normal forces shown by the standalone VAWT case.

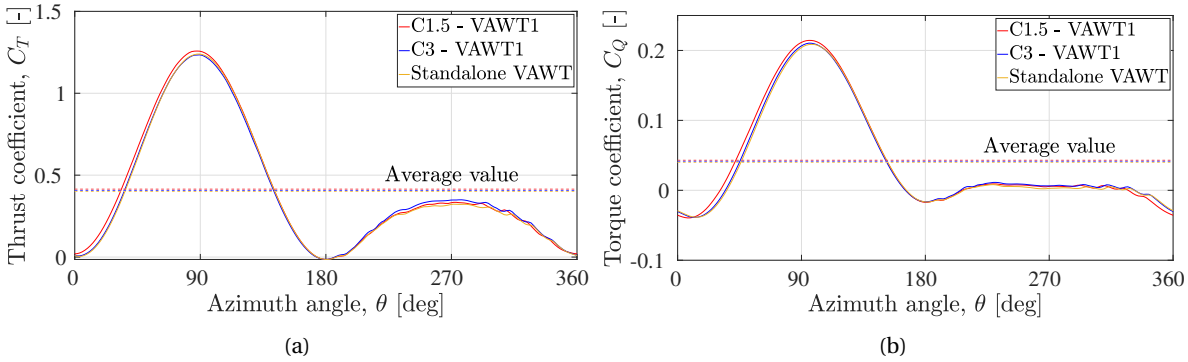

Figure 8.7: Variation of thrust coefficient C_T and torque coefficient C_Q for a single blade of VAWT1 over a complete rotation

To better understand the blade-wake and blade-vortex interactions (BWI/BVI) and their effect on the overall cluster performance, visualizing the 3D VAWT flowfield is crucial. Figure 8.8 provides insight into instantaneous vortices in the downstream part of the VAWT cluster flowfield using iso-surfaces of the λ_2 criterion (λ_2 = -2000 1/sec^2). The visualisation is done for two values of VAWT separation - 1.5m and 3m, and the standalone VAWT. As the separation decreases, there is an increase in BWI/BVI, which can be seen from the close proximity of the large vortex structures, consisting of the coherent shed and trailing (tip) vortices, and smaller incoherent vortex structures in the flowfield. The tip vortices in the VAWT cluster create a similar spiral flow pattern as the standalone VAWT, known as the "vortex ring", that wraps around the axis of the turbine.

As the large vortex structures convect downstream, they experience wake expansion and gradually breakdown into smaller-scale structures due to flow instabilities and spatial modulation, which

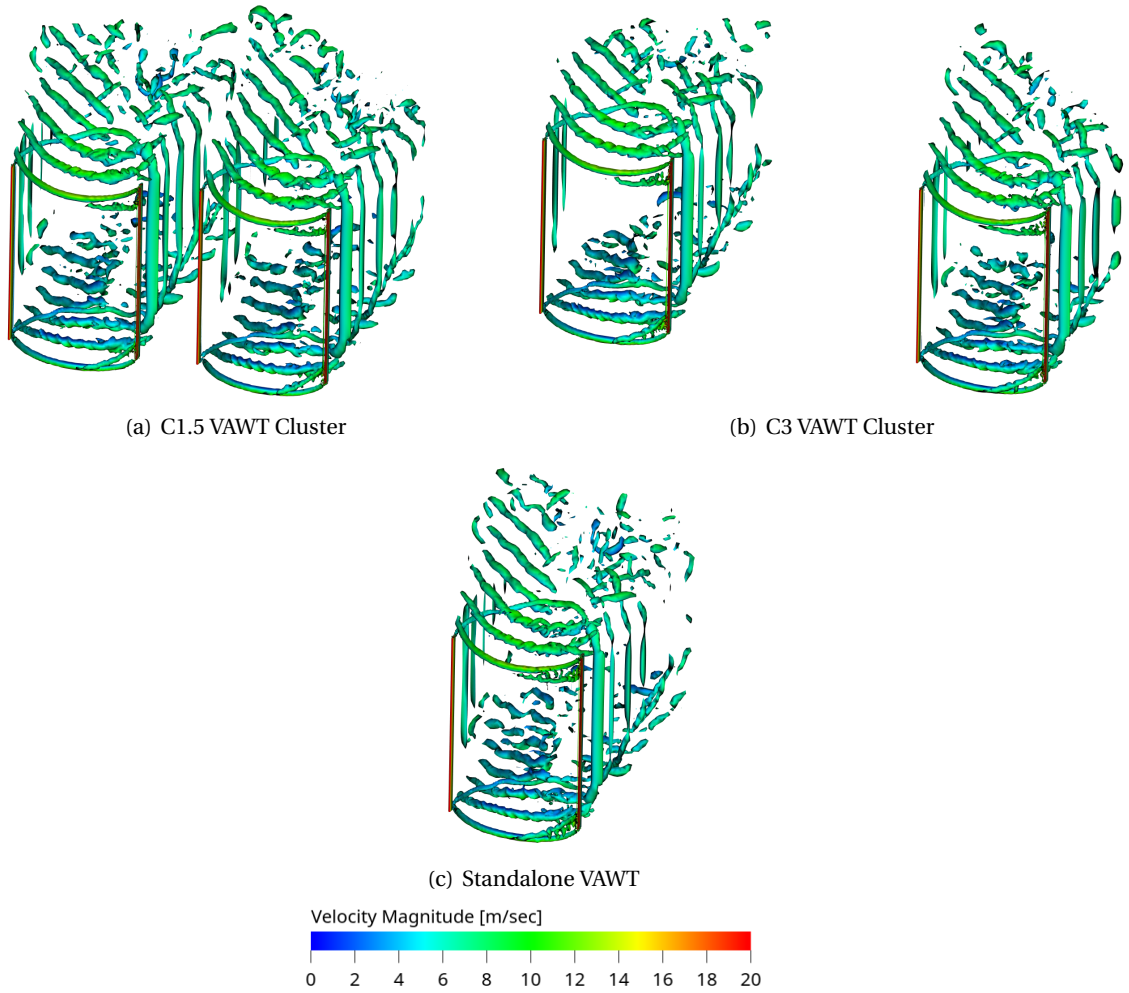

(a) C1.5 VAWT Cluster

(b) C3 VAWT Cluster

(c) Standalone VAWT

Figure 8.8: Instantaneous 3D flowfield using iso-surfaces of the λ_2 criterion (λ_2 = -2000 1/sec^2) for vortices visualisation of two different VAWT clusters and comparison with the standalone VAWT

eventually dissipate and are mixed into the surrounding fluid [12, 196]. As the VAWT separation decreases, the increase in BWI/BVI leads to a faster breakdown and dissipation of such vortex structures. This observation is similar when the number of blades was increased in Chap 5 or struts/central tower was added in Chap 6, where the ideal pressure and loading distribution along the chordwise and spanwise directions of the blades gets disturbed due to this phenomenon.

The increase in BWI/BVI also has an effect on the streamwise velocity values. This is shown in Figure 8.9 which presents the instantaneous streamwise velocity contours in the wake of the VAWT cluster on a 2D plane located at the blade mid-span location. The decrease in VAWT separation increases the streamwise velocity in the space between the two VAWTs. Furthermore, stronger interaction between the wakes can be seen at the downstream location, for the configuration with reduced VAWT separation.

The above-mentioned flow-field results are presented quantitatively in Figure 8.10, which shows the streamwise velocity values averaged over a rotation. The values are plotted along lines situated at distances of $0D$ and $1D$ downstream from the VAWT centre at the blade-mid-span 2D plane and are illustrated in Figure 8.9 as black dotted lines. The results for standalone VAWT are superimposed on each VAWT in the cluster, by shifting the z value on the x-axis for the former by $+d/2$ (for windward side VAWT) and $-d/2$ (for leeward side VAWT), where d is the VAWT separation distance. The results show that decreasing VAWT separation increases the velocity experienced by each VAWT

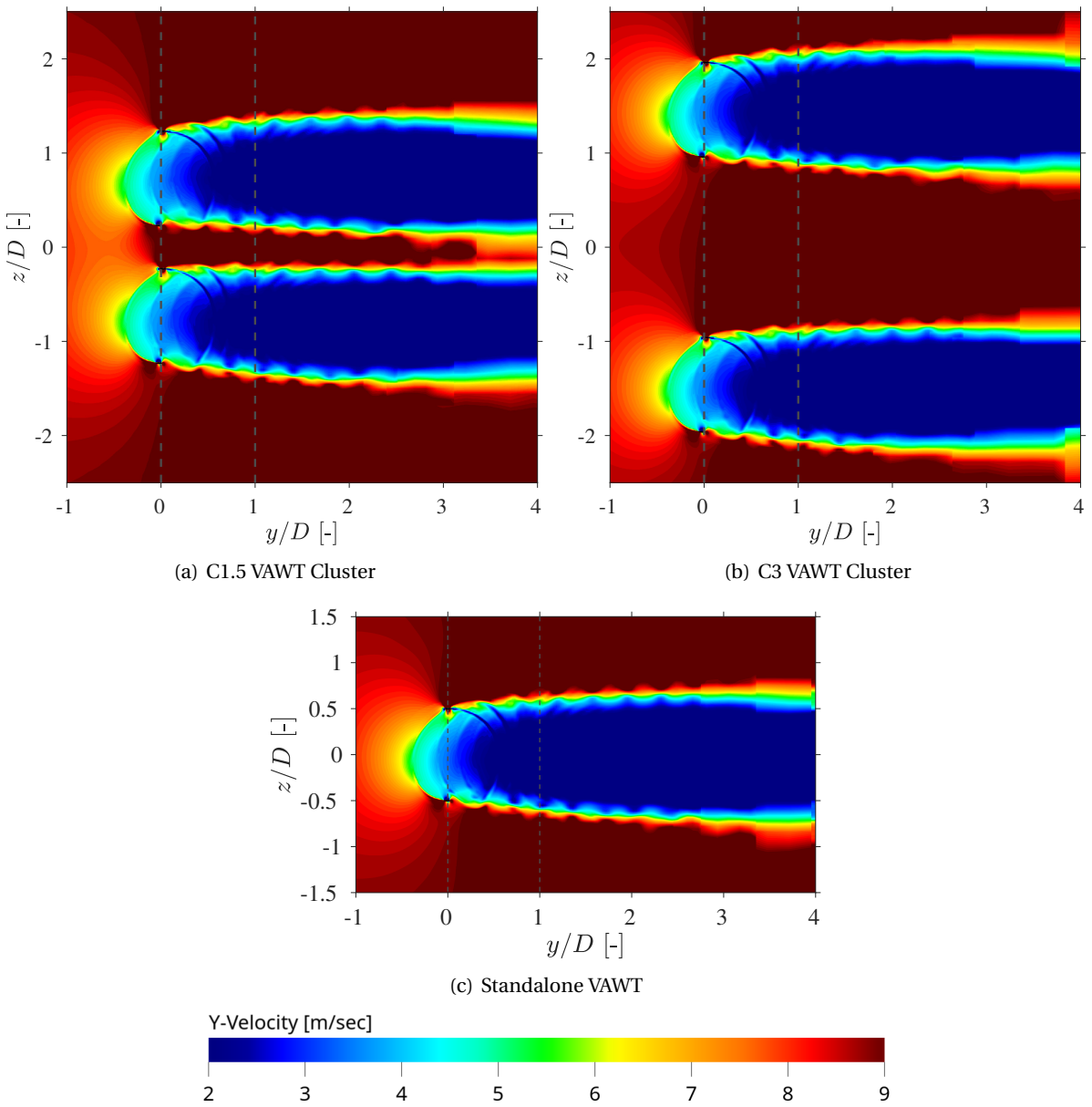

(a) C1.5 VAWT Cluster

(b) C3 VAWT Cluster

(c) Standalone VAWT

Figure 8.9: Instantaneous streamwise velocity contours in the downstream wake on a 2D plane located at the blade mid-span location

in the cluster, as compared to the standalone VAWT. This increases the aerodynamic performance of the cluster as a whole, due to an increase in blade loading, as seen in previous results of thrust, torque and power density in Figures 8.5, 8.6 and 8.7, and Table 8.4. Furthermore, the increase in velocity between the VAWTs reduces the width of the VAWT wake in both C1.5 and C3 clusters, as compared to the standalone VAWT. For the same reason, C1.5 exhibits a wake width smaller than the C3 case. This is particularly visible for the values plotted at $y = 1D$ and depicts the effect of mutual induction between two VAWTs at close proximities.

The unsteady pressure data, gathered at two distinct locations (the rotor plane at (0,0,7D) and a position outside the rotor plane at (4D,0,7D)), over a single rotor rotation, is presented in Figure 8.11 (a) and (b), and includes contributions from both the VAWTs in the cluster. First, the comparison between the two locations shows that high-frequency pressure fluctuations and the overall amplitude of those fluctuations are lower at the out-of-plane location relative to the in-plane lo-

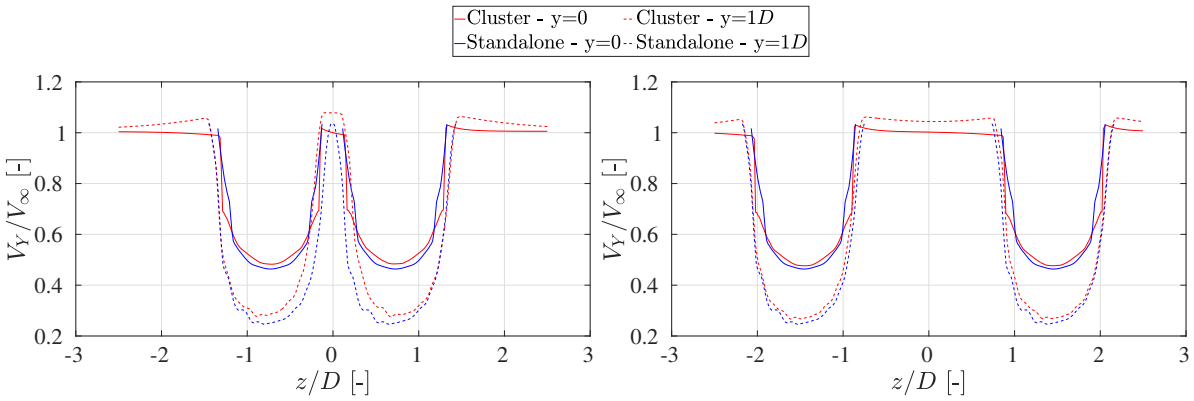

(a) C1.5 VAWT Cluster (b) C3 VAWT Cluster

Figure 8.10: Comparison of streamwise velocities, averaged over a rotation, in the downstream VAWT flowfield of the cluster and compared with the standalone VAWT

cation. This observation aligns with findings from all the previous chapters for standalone VAWTs. Second, an increase in VAWT separation (1.5m to 3m in the figure shown) results in a decrease in the amplitude of pressure fluctuations at both observation points. This decrease is attributed to the reduction in overall rotor loading or thrust values when VAWT separation increases, as previously shown in Figure 8.7.

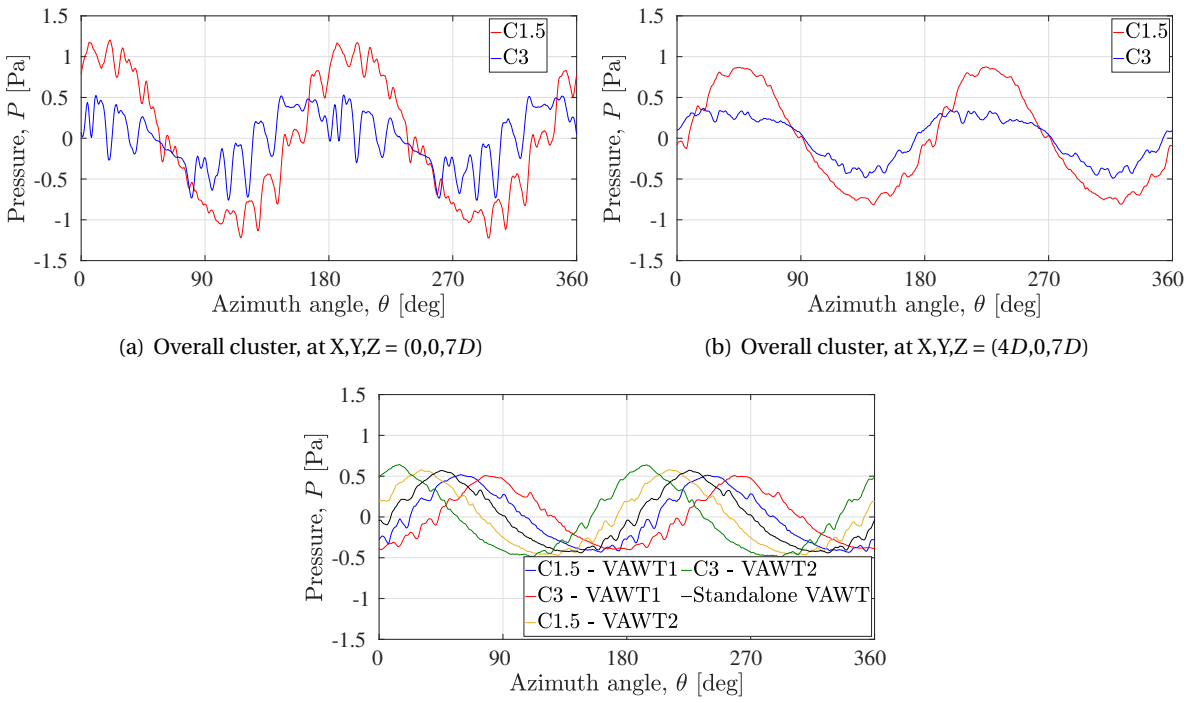

(a) Overall cluster, at X,Y,Z = (0,0,7D) (b) Overall cluster, at X,Y,Z = (4D,0,7D)

(c) Individual VAWTs, at X,Y,Z = (4D,0,7D)

Figure 8.11: Raw unsteady pressure data for two different VAWT separations for Case 1 VAWT clusters

The resulting noise spectra at the two above-mentioned observer locations are shown in Figure 8.12 (a) and (b). The figure reports the Power Spectral Density (PSD) values in dB/Hz within the frequency range of 20-2000 Hz, plotted with a frequency resolution (Δf) of 15 Hz. The noise spectra are not plotted below the human hearing range (20 Hz). At both locations, for the low-frequency

range, an increase in VAWT separation results in a decrease in decibel values, which corresponds to the pressure fluctuation data shown before. For mid and high-frequency ranges, the decibel values remain mostly similar. This depicts that the effect of VAWT separation on overall noise from the cluster happens majorly due to changes in integral loading on individual VAWT blades and a corresponding change in the tonal component of blade loading noise. There is minimal change in high-frequency loading fluctuations from BWI/BVI due to changes in VAWT separation.

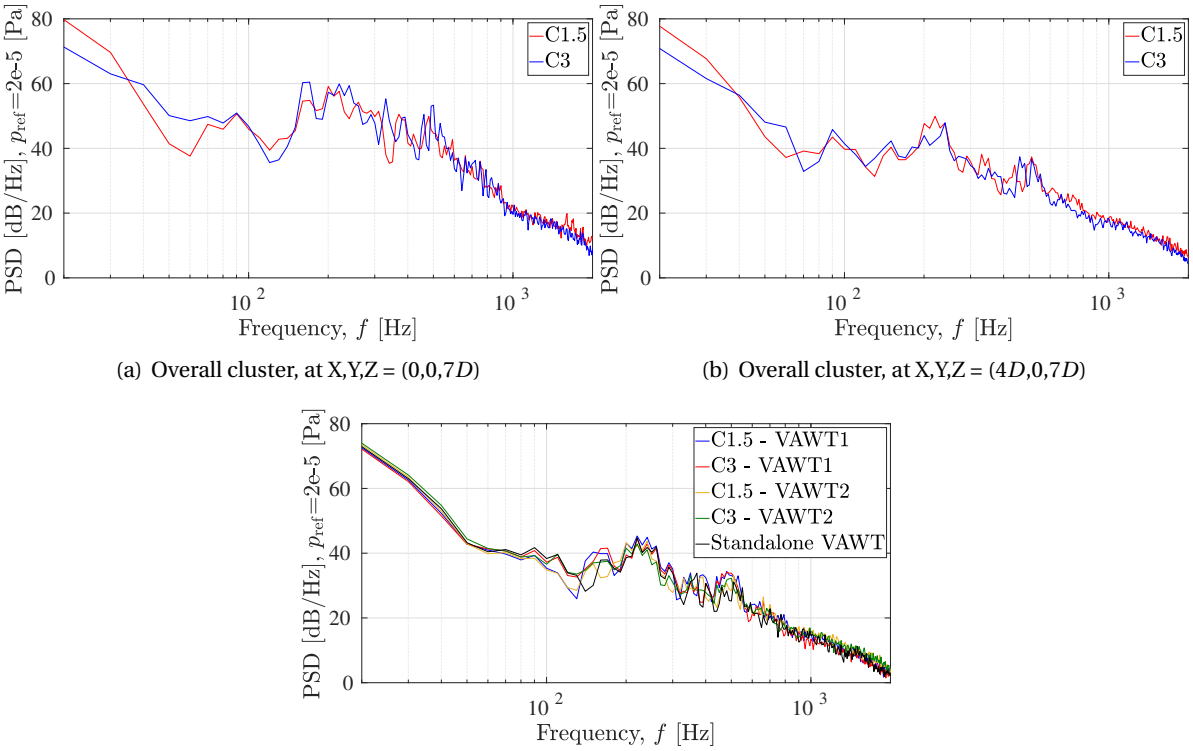

(a) Overall cluster, at X,Y,Z = (0,0,7D)

(b) Overall cluster, at X,Y,Z = (4D,0,7D)

(c) Individual VAWTs, at X,Y,Z = (4D,0,7D)

Figure 8.12: Power Spectral Density (PSD) spectra for two different VAWT separations for Case 1 VAWT clusters

Figure 8.11 (c) shows the pressure fluctuation contributions from individual VAWTs for both C1.5 and C3 clusters along with the standalone VAWT, at the out-of-plane observer location. Due to increased VAWT spacing, both VAWTs of C3 exhibit a larger difference in phase angle than for C1.5. This causes a destructive interference between the pressure fluctuations from individual VAWTs of C3, whereas, C1.5 exhibit a more constructive interference. Furthermore, VAWT2 of both clusters have a higher amplitude of pressure fluctuations than VAWT1, which corresponds to the increased VAWT loading of the former reported in Figure 8.6. The corresponding noise spectra of individual VAWTs are shown in Figure 8.12 (c) and report higher decibel values for VAWT2 than VAWT1, for both the clusters, at the low-frequency range.

Figure 8.13 presents the directivity plot of the overall sound pressure level (OSPL) comparing C1.5 and C3 VAWT clusters. The OSPL values are calculated within the frequency range of 20-2000 Hz. On the whole, for both the YZ and XY planes, noise levels exhibit an increasing trend with a decrease in the VAWT spacing of the cluster. This is more apparent in the former plane and can be linked to the overall VAWT cluster thrust values depicted in Figure 8.5, where the C_T value increases following a decrease in the VAWT spacing. All VAWTs in this study operate in a low Reynolds number regime, where blade loading noise is the predominant noise source [127].

Between 150° and 180° on the YZ plane, the trend reverses and noise produced by the C3 cluster is higher. The C1.5 cluster demonstrates relatively constant noise levels throughout the entire 360°

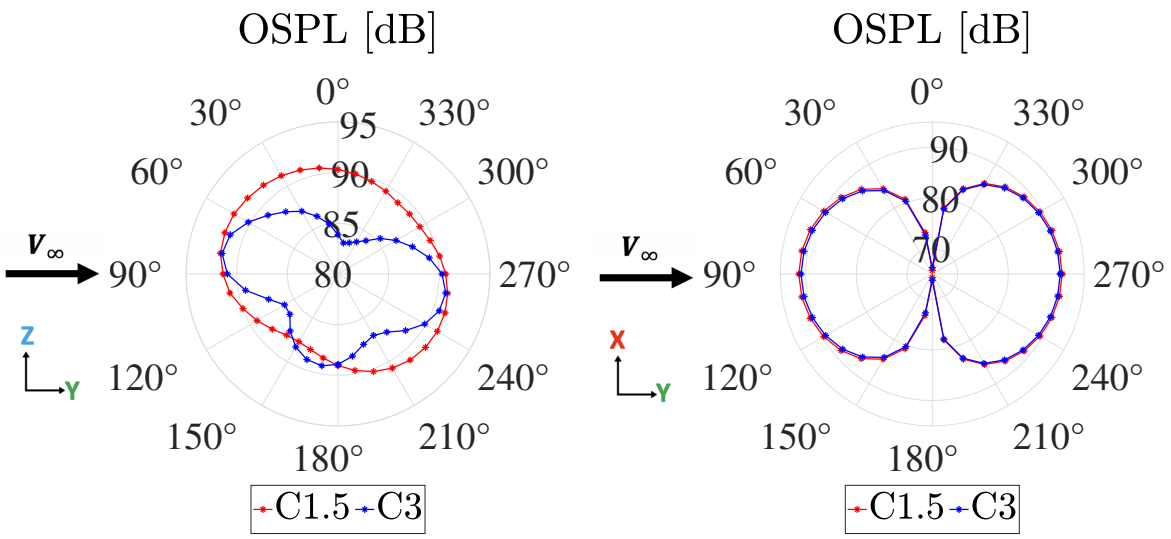

(a) YZ plane, at blade mid-span location

(b) XY plane, coinciding with centre of VAWT cluster

Figure 8.13: Directivity plot of overall sound pressure level (OSPL) comparing two different VAWT separations for Case 1 VAWT clusters, along a circular array of 36 points situated at a distance of 7D from the origin of VAWT cluster ([0,0,0])

azimuth range, as compared to the C3 cluster, which observes a sharp drop in noise around 0°, 120° and 210° azimuth. There are various noise sources in a VAWT [43–45, 261] and the observed directivity behaviour indicates that some noise sources are more dominant at particular azimuth values than others. In the XY plane, the directivity behaviour is similar to that of a standalone VAWT, as observed in Chap 5.

8.3.3. Parallel VAWT cluster: co-rotating vs contra-rotating

Figure 8.14 shows the effect of direction of rotation on the C_T and C_Q of the overall VAWT cluster. The VAWT separation is a constant value of 2m for both the configuration: co-rotating (C2) and contra-rotating down (CC2). The former shows higher C_T and C_Q values than the latter, which shows VAWTs rotating in the same direction exhibit preferable fluid dynamic interactions. Figures (c) and (d) show the comparison between a single VAWT of both the clusters (VAWT1) and the 2-bladed standalone VAWT. The C_T and C_Q values of both the cluster configurations are higher than the standalone VAWT. From a previous study [14], even a contra-rotating up configuration of the cluster will exhibit higher power performance than the standalone VAWT.

Table 8.5 lists the values of power density for different VAWT cluster configurations for Case 2, and compared with the standalone VAWT. As expected from the previous result, power density is highest for the co-rotating configuration (C2) amongst all the three cases reported and lowest for the standalone VAWT.

Table 8.5: Variation of power density with different direction of rotation for the Case 2 VAWT cluster and comparison with the standalone VAWT; Area is calculated for a square with diameter D as one side

	Power produced (W)	**Area** (m^2)	**Power density** (W/m^2)
Standalone	181.03	1.06	170.64
C2	381.77	2.12	179.93
CC2	381.41	2.12	179.91

Figure 8.15 illustrates the variation in C_T and C_Q plotted for a single blade for a complete 360° azimuth, for VAWT1 of Case 2 clusters. The figure also shows the average value over the rotation and

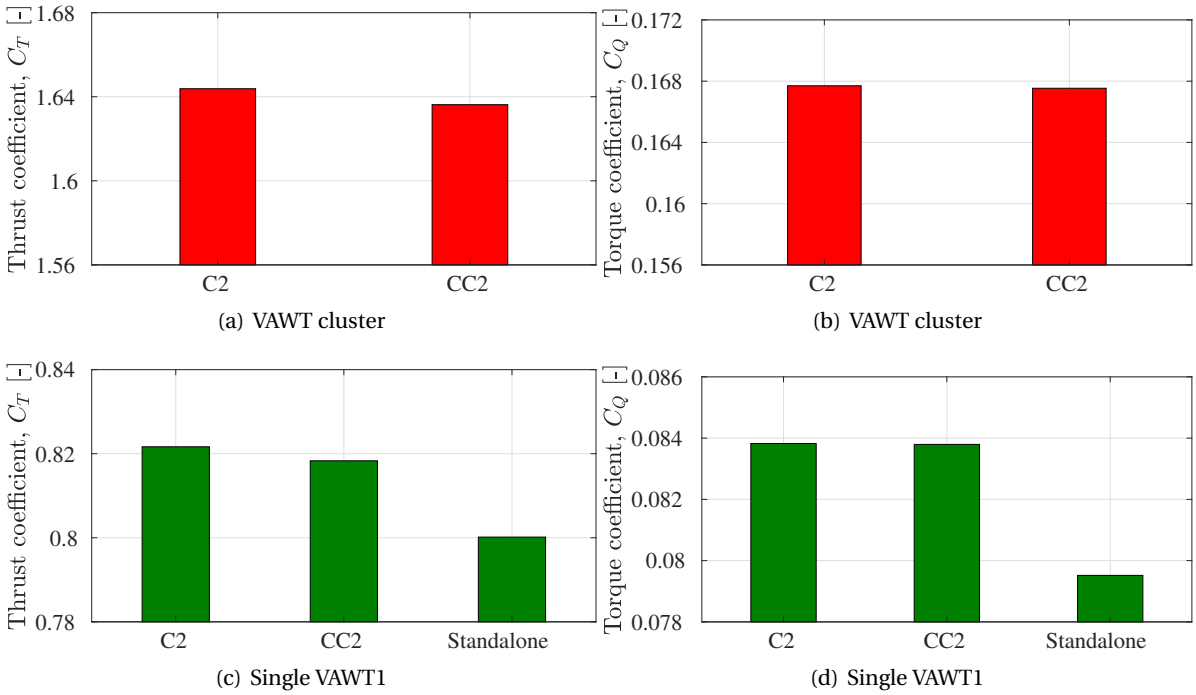

(a) VAWT cluster (b) VAWT cluster

(c) Single VAWT1 (d) Single VAWT1

Figure 8.14: Effect of rotation direction on thrust coefficient C_T and torque coefficient C_Q for Case 2 VAWT clusters; C2 - co-rotating, CC2 - contra-rotating down

all the results are compared to the standalone VAWT. In both the upwind and downwind parts of rotation, the co-rotating configuration produces higher C_T and C_Q values than both contra-rotating down and standalone VAWT configurations. Only for a small part of the rotation (between 90° and 180°), the contra-rotating down configuration performs better than both configurations. This results in the average value of the full rotation being the same as what was observed in Figure 8.14. Again, it is expected that if TSR is increased for all VAWTs (currently it is 3.3), the difference in C_T and C_Q between the three cases shown will be more prominent.

This is attributed to increased blade-wake and blade-vortex interactions between the two turbines, leading to increased power performance.

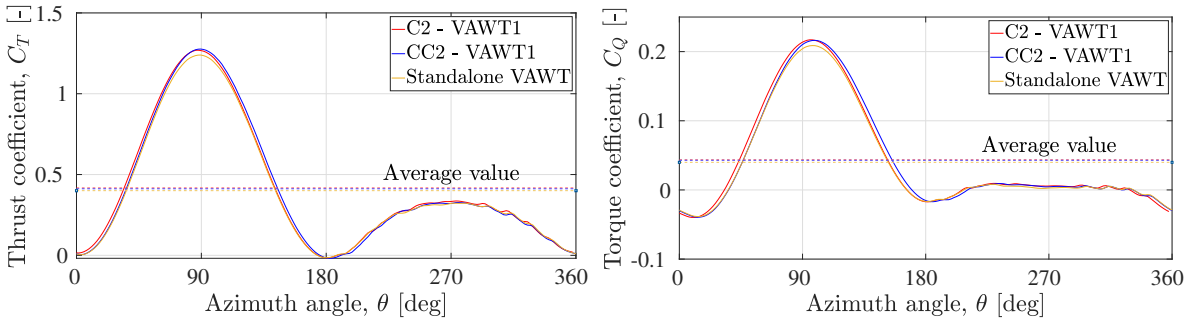

(a) (b)

Figure 8.15: Variation of thrust coefficient C_T and torque coefficient C_Q for a single blade of VAWT1 over a complete rotation and comparison with the standalone VAWT

To understand the effect of the direction of rotation on BWI/BVI, Figure 8.16 provides insight into instantaneous vortices in the downstream part of the VAWT cluster flowfield using iso-surfaces of the λ_2 criterion (λ_2 = -2000 1/sec^2). The visualisation is done for the two VAWT cluster configura-

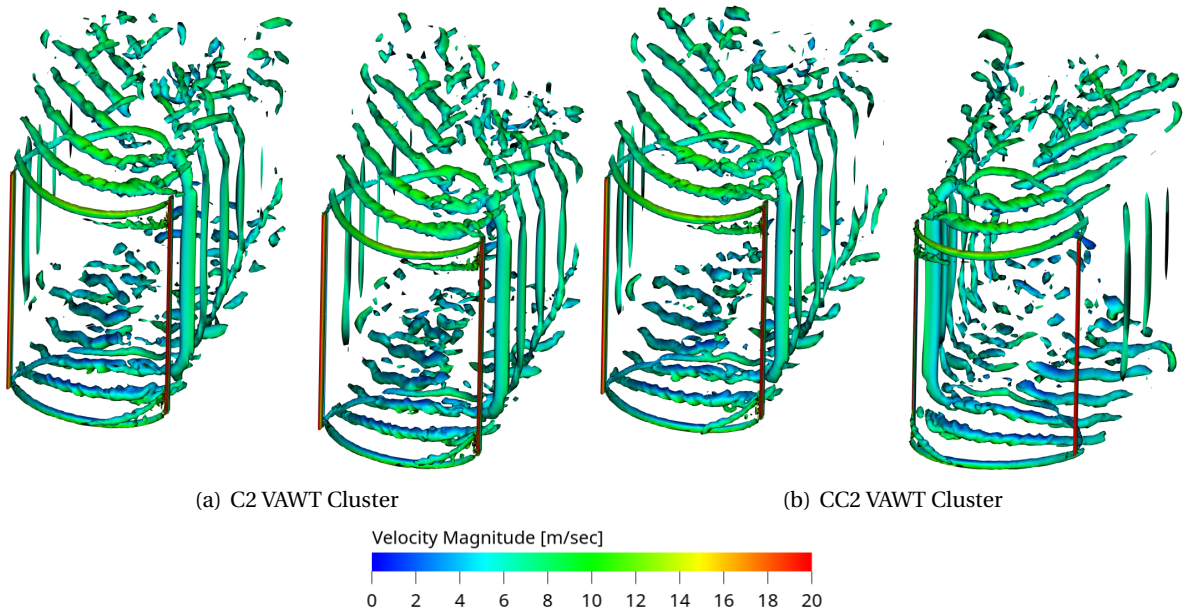

(a) C2 VAWT Cluster (b) CC2 VAWT Cluster

Figure 8.16: Instantaneous 3D flowfield using iso-surfaces of the λ_2 criterion (λ_2 = -2000 1/sec^2) for vortices visualisation of two different VAWT clusters of Case 2

tions with two different directions of rotation. The figure shows no significant qualitative difference between the two cases, in the context of fluid dynamic interactions between the blades and the vortices, even though the co-rotating configuration has better performance than its contra-rotating counterpart.

Figure 8.17 presents the instantaneous streamwise velocity contours in the wake of the VAWT cluster on a 2D plane located at the blade mid-span location. Again, there are no significant qualitative differences observed between the two configurations. Both cases highlight the contraction of wake as flow convects downstream and the increase in flow velocity in the space between the two VAWTs.

To understand the flow-field results in a quantitative manner, Figure 8.18 shows the streamwise velocity values averaged over a rotation. The values are plotted along lines situated at distances of $0D$ and $1D$ in the same manner as the previous Figure 8.10. The results show that the C2 co-rotating configuration exhibits higher streamwise velocities than the CC2 contra-rotating down configuration, while the lowest velocity values are shown by the standalone VAWT. This increases the aerodynamic performance of the C2 configuration as a whole, due to an increase in blade loading, as seen in previous results of thrust, torque and power density in Figures 8.14 and 8.15, and Table 8.5. Furthermore, the width of the VAWT wake remains similar for both the clusters shown, whereas the standalone VAWT shows a slightly wider wake than the individual turbines of the clusters. This is particularly visible for the values plotted at $y = 1D$. This depicts the effect of mutual induction between two closely-spaced VAWTs, with either direction of rotation.

The unsteady pressure data, gathered at two distinct locations (the rotor plane at (0,0,7D) and a position outside the rotor plane at (4D,0,7D)), over a single rotor rotation, is presented in Figure 8.19 (a) and (b), and includes contributions from both the VAWTs in the cluster. The contra-rotating configuration CC2 exhibits a higher amplitude of pressure fluctuations than the co-rotating configuration C2. This increase is attributed to the higher overall rotor loading or thrust values for the former than the latter, as previously shown in Figure 8.15.

In Figure 8.19 (c), the pressure fluctuations of individual VAWTs are compared for 360° azimuth angle. VAWT1 of both clusters show less amplitude of pressure fluctuations than the standalone

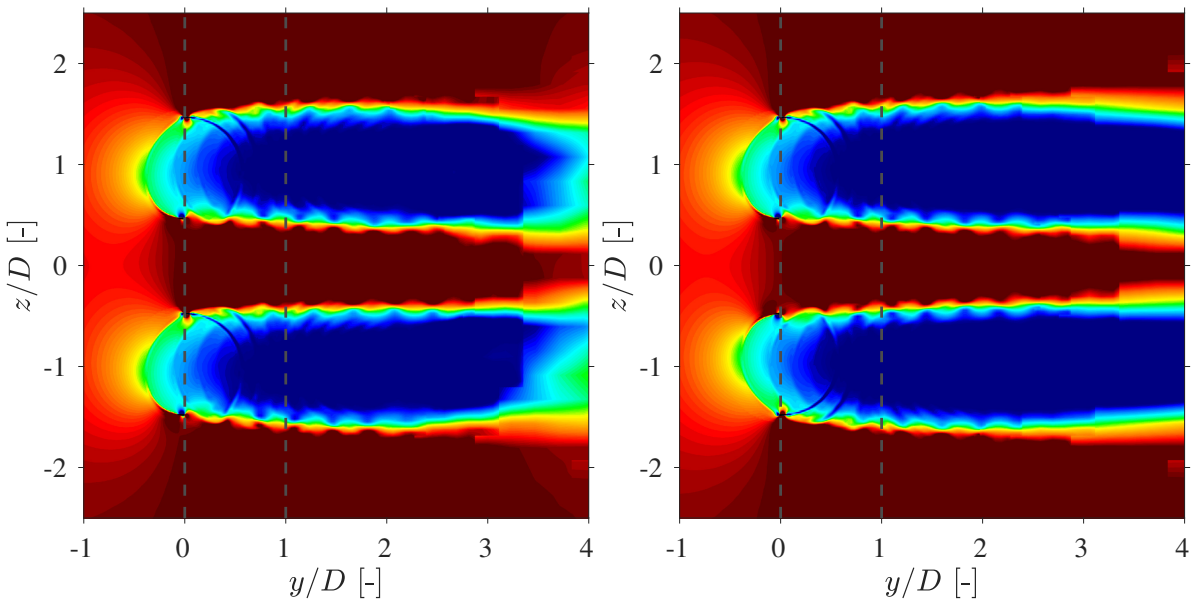

(a) C2 VAWT cluster (b) CC2 VAWT cluster

Figure 8.17: Instantaneous streamwise velocity contours in the downstream wake on a 2D plane located at the blade mid-span location, for Case 2 VAWT clusters

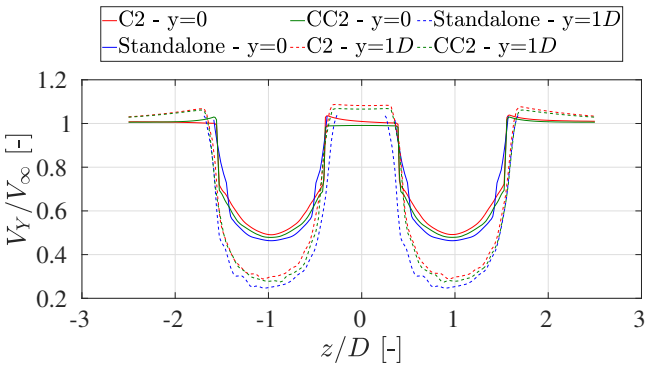

Figure 8.18: Comparison of streamwise velocities, averaged over a rotation, in the downstream VAWT flowfield of the cluster C2 and CC2 of Case 2 and compared with the standalone VAWT

VAWT and VAWT2 of both clusters.

The resulting noise spectra at the two above-mentioned observer locations are shown in Figure 8.20 (a) and (b) within the frequency range of 20-2000 Hz, plotted with a frequency resolution (Δf) of 15 Hz. The noise spectra are not plotted below the human hearing range (20 Hz). At both locations, for the low-frequency range, the co-rotating configuration has lower decibel values compared to the contra-rotating configuration. For mid and high-frequency ranges, the decibel values remain fairly similar, except above 1000 Hz where contra-rotating configuration exhibits higher values. This shows that there is minimal change in blade-wake/blade-vortex interaction when the direction of rotation is changed for the VAWT which affects the high-frequency loading fluctuations on the blades. The variation in overall noise arises majorly due to changes in mean blade loading as seen in Figure 8.14.

Similarly, Figure 8.20 (c) shows the noise for individual VAWTs in the clusters and compares them with the standalone VAWT. The noise spectra remain fairly similar for all VAWTs except for VAWT1 of the contra-rotating configuration which changed the direction of rotation. At the high-

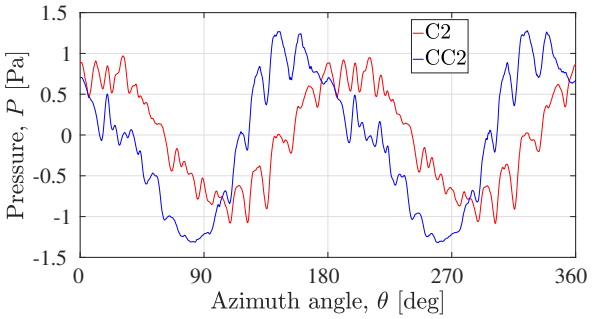

(a) Overall cluster, at X,Y,Z = (0,0,7D)

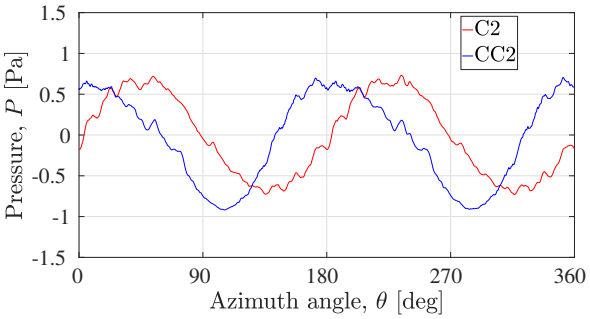

(b) Overall cluster, at X,Y,Z = (4D,0,7D)

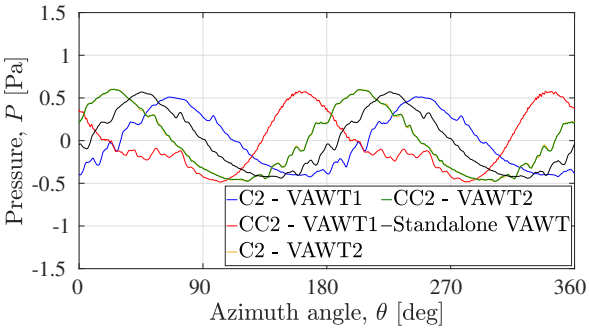

(c) Individual VAWTs, at X,Y,Z = (4D,0,7D)

Figure 8.19: Raw unsteady pressure data for co-rotating and contra-rotating configuration of Case 2 VAWT clusters

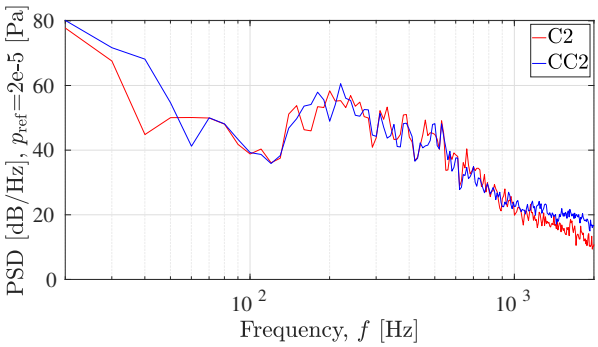

(a) Overall cluster, at X,Y,Z = (0,0,7D)

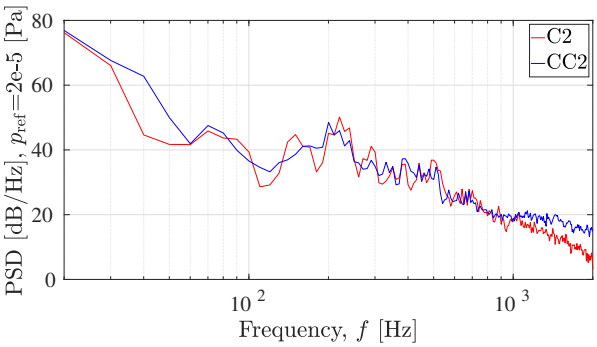

(b) Overall cluster, at X,Y,Z = (4D,0,7D)

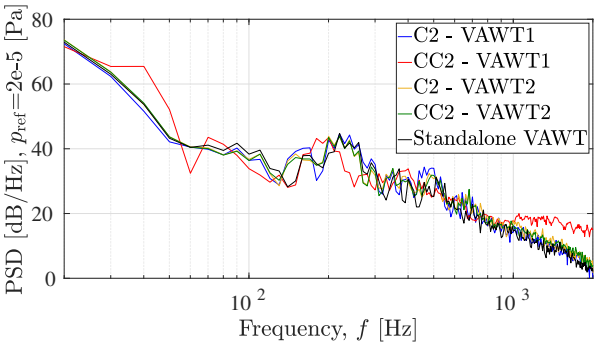

(c) Individual VAWTs, at X,Y,Z = (4D,0,7D)

Figure 8.20: Power Spectral Density (PSD) spectra using the high-fidelity LBM at two different locations

frequency range (> 1000 Hz), the decibel values are higher for the latter which shows an increase in high-frequency loading fluctuations due to the change in direction of rotation.

Figure 8.21 presents the directivity plot of the overall sound pressure level (OSPL) (calculated within the frequency range of 20-2000 Hz) comparing C2 and CC2 VAWT clusters. For the YZ plane, the CC2 configuration produces more noise between 150° and 15° (mostly downwind part) whereas the C2 configuration produces more noise between 15° and 150° (mostly upwind part). For the CC2 configuration, the noise is relatively higher in the downwind part of the rotation as compared to the upwind part, whereas, for the C2 configuration, the values remain fairly similar in both parts of the rotation. In the XY plane, the directivity behaviour is similar to that of a standalone VAWT, as observed in Chap 5 and CC2 configurations exhibit higher noise values than the C2 configuration.

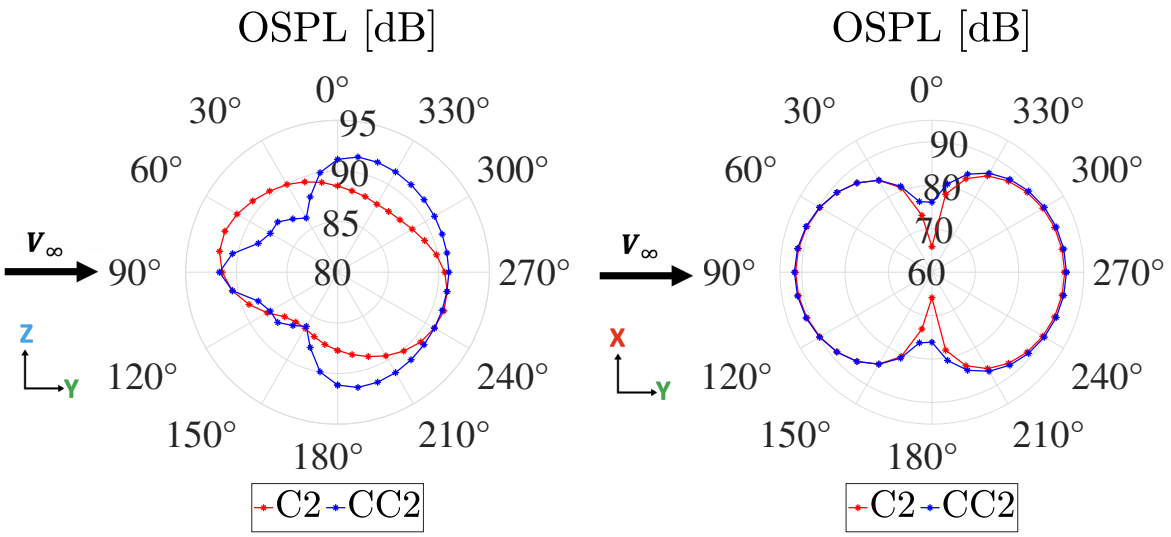

(a) Overall cluster, at X,Y,Z = (0,0,7D)

(b) Overall cluster, at X,Y,Z = (4D,0,7D)

Figure 8.21: Directivity plot of overall sound pressure level (OSPL) comparing two different VAWT configurations for Case 2 VAWT clusters, along a circular array of 36 points situated at a distance of 7D from the origin of VAWT cluster ([0,0,0])

8.3.4. Tandem VAWT cluster: effect of VAWT separation

Figure 8.5 (a) and (b) shows the effect of VAWT separation on the C_T and C_Q of the overall cluster. The values show an increase in both C_T and C_Q as separation increases, an opposite trend when the VAWTs are in parallel. This shows the degrading nature of BVI/BWI for VAWTs when placed in tandem positions and in close proximity. Also, the percentage change in thrust values is less than the torque values, from the increased VAWT separation. This was also seen in parallel VAWT cluster cases (Case 1 and Case 2) where the thrust values were less affected than torque values by the proximity in VAWTs and the BVI/BWI resulting because of that.

Figures 8.5 (c) and (d) show the comparison between the individual VAWTs of a cluster (VAWT1 and VAWT2) and the standalone VAWT (2-bladed) to depict the effect of tandem cluster arrangement in a much better way. For the upstream VAWT (VAWT1), the C_T and C_Q values increase as the separation is increased and ultimately approaches equal to the standalone VAWT value. For the downstream VAWT, the C_T and C_Q values also increase as the separation is increased although these values are significantly less than their upstream counterparts. This shows the negative impact of upstream VAWT wake on the performance of the downstream VAWT. The impact decreases as the VAWT separation increases due to a decrease in BVI/BWI and the performance of the downstream VAWT will approach the values of the standalone VAWT at large spacings. For C_Q, negative values can be observed for the downstream VAWTs showing the extent of the negative impact of BVI/BWI

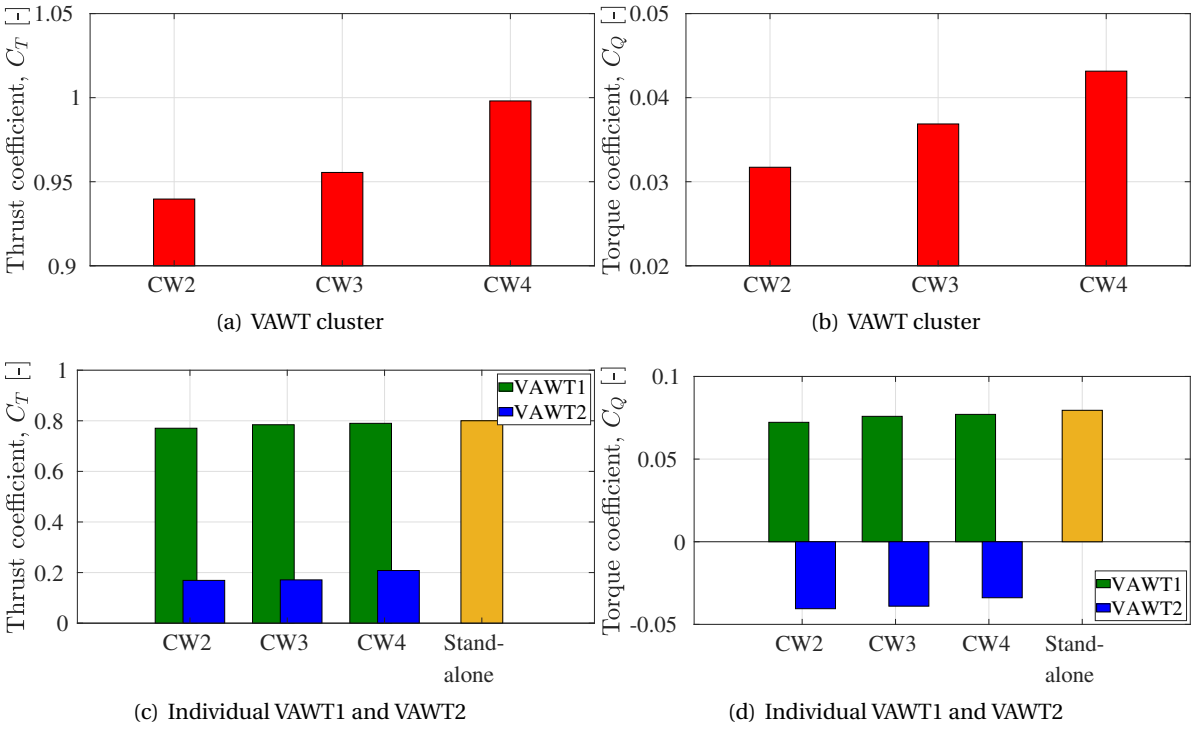

(a) VAWT cluster (b) VAWT cluster

(c) Individual VAWT1 and VAWT2 (d) Individual VAWT1 and VAWT2

Figure 8.22: Effect of VAWT separation on thrust coefficient C_T and torque coefficient C_Q for Case 3 tandem VAWT clusters; numbering represents VAWT separation in metres

for closely spaced VAWTs. Negative power means the power has to be input to the rotor to keep it running at a particular TSR, therefore, acting as a propeller instead. Furthermore, there will be a particular VAWT spacing for which the torque/power production will be 0 for the downstream VAWT. This means removing the downstream VAWT from the overall cluster (or adding another VAWT downstream to a standalone VAWT at that particular spacing) will not affect the performance of the overall cluster.

Table 8.6 lists the values of power density for different VAWT separations in the cluster and is calculated in a similar way as the previous sections. There is a significant decrease in power density exhibited by the tandem VAWT clusters, as compared to their standalone counterpart and the major role in this phenomenon is played by the downstream VAWT, as can be seen from the aforementioned C_Q values.

Table 8.6: Variation of power density with different VAWT separation and comparison with the standalone VAWT for Case 3 tandem VAWT clusters; Area is calculated for a square with diameter D as one side

	Power produced (W)	**Area** (m^2)	**Power density** (W/m^2)
Standalone	181.03	1.06	170.64
CW2	72.21	2.12	34.06
CW3	83.94	2.12	39.59
CW4	98.24	2.12	46.34

Figure 8.23 illustrates the variation in C_T and C_Q plotted for a single blade for a complete 360° azimuth, for both the individual VAWTs of the cluster. In the upwind part of the rotation, upstream VAWT1 of both the clusters have the same performance values as the standalone VAWT, whereas, in the case of the downwind part, performance decreases as the VAWT separation decreases. For the downwind VAWT2, in both the upwind and downwind parts of the rotation, performance decreases

as the VAWT separation decreases, although the difference is more visible for the downwind part. This gets reflected in the average C_T and C_Q values in a single rotation which is also shown in the previous Figure 8.22 (for the overall cluster) and in Table 8.6 (power production density of the cluster). The investigation shows that due to the presence of another VAWT in the proximity, the effect due to the mutual interaction between the VAWTs is more visible in the downwind part of the rotation. This effect can be termed as an upstream influence for the upstream VAWT1 and vice-versa for the downstream VAWT2.

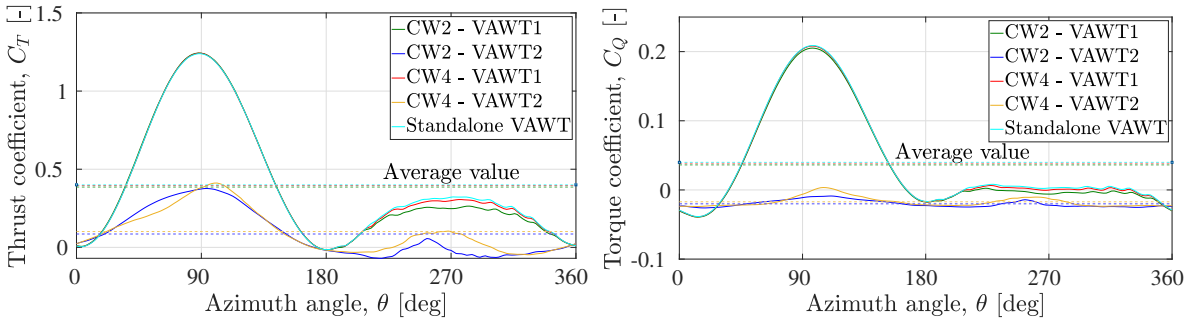

(a) (b)

Figure 8.23: Variation of thrust coefficient C_T and torque coefficient C_Q over a complete rotation, for a single blade of VAWT1 and VAWT2 of Case 3 tandem cluster configurations and comparison with the standalone VAWT

Figure 8.24 provides insight into instantaneous vortices in the wake of the VAWT cluster using iso-surfaces of the λ_2 criterion (λ_2 = -2000 1/sec^2). The visualisation is done for two values of VAWT separation - 2m (CW2) and 4m (CW4).

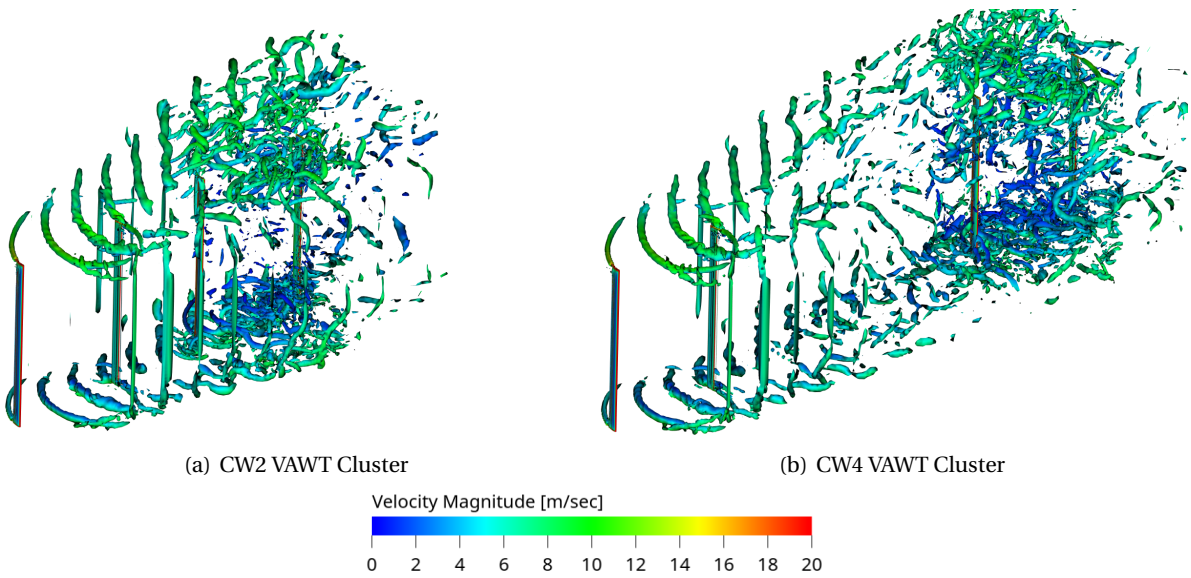

(a) CW2 VAWT Cluster (b) CW4 VAWT Cluster

Figure 8.24: Isometric view of the instantaneous 3D flowfield using iso-surfaces of the λ_2 criterion (λ_2 = -2000 1/sec^2) for vortices visualisation of two different VAWT clusters of Case 3

As opposed to the parallel VAWT clusters, tandem VAWT clusters exhibit strong BWI/BVI due to the interaction of the wake vortices generated from the upstream VAWT with the downstream VAWT. The spiral flow pattern of the tip vortices (vortex ring) of the upstream VAWT is broken down by the interaction with the downstream VAWT. In the case of CW2, there is closer proximity of the downstream VAWT to the large vortex structures, consisting of the coherent shed and trailing (tip)

vortices, which causes higher degradation in the performance of the downstream VAWT. As the separation increases, there is a decrease in BWI/BVI and the performance of the downstream VAWT increases.

The interaction of the tip and shed vortices with the downstream VAWT is more apparent from Figure 8.25, which shows a side view of the instantaneous vortices in the downstream wake. In the case of increased spacing, the large vortex structures break down primarily due to vortex stretching and contraction [173], inherent instabilities in the flow [57, 111] and viscous effects [250, 313], before it interacts with the downstream VAWT. In the case of decreased spacing, those large structures break down primarily due to the interaction with the blades of the downstream VAWT [114, 131, 343, 372]. The vortex structures shedding the downstream VAWT are smaller and more chaotic in nature as compared to the upstream VAWT or the standalone VAWT in Figure 8.8 (c). Additionally, as the spacing between the VAWTs decreases, the upstream VAWT wake expands more in the axial direction, suggesting a much stronger development of the wake which interacts with the downstream VAWT.

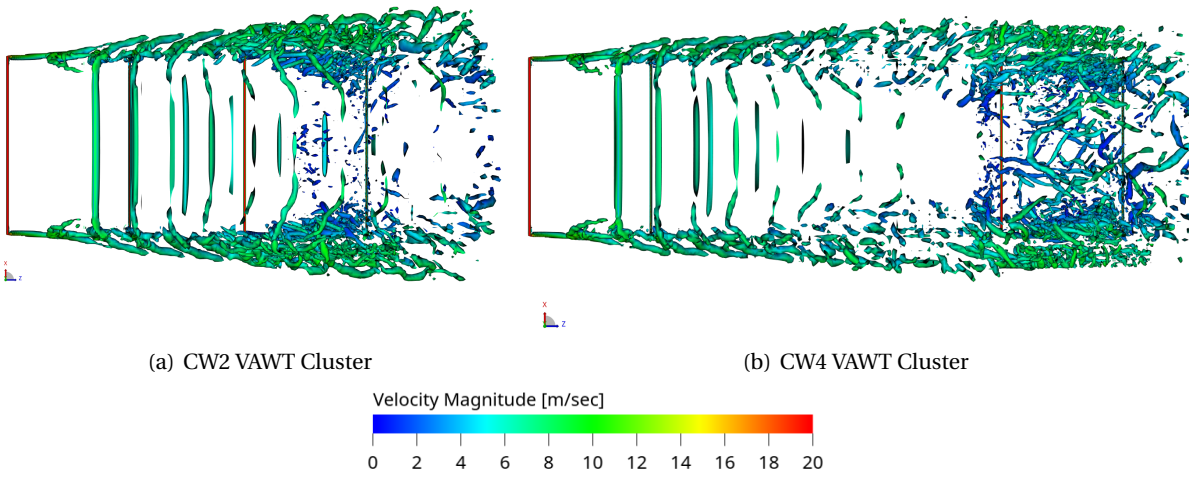

(a) CW2 VAWT Cluster (b) CW4 VAWT Cluster

Figure 8.25: Side view of the instantaneous 3D flowfield using iso-surfaces of the λ_2 criterion (λ_2 = -2000 1/sec^2) for vortices visualisation of two different VAWT clusters of Case 3

The above argument on BWI/BVI can also be visualised using the instantaneous streamwise velocity contours shown in a 2D plane in Figure 8.26. When the spacing decreases, the downstream VAWT experiences a much stronger wake (decreased flow velocity) shed from the upstream VAWT, which decreases the performance of the former and as a result, of the overall cluster.

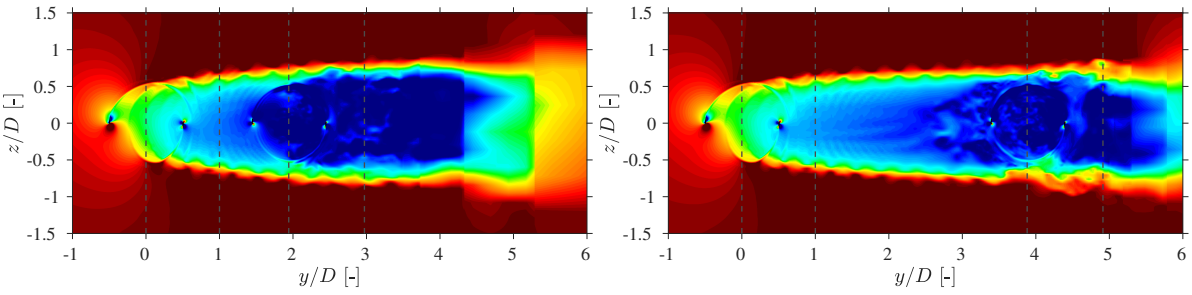

(a) CW2 VAWT Cluster (b) CW4 VAWT Cluster

Figure 8.26: Instantaneous streamwise velocity contours in the downstream wake on a 2D plane located at the blade mid-span location, for Case 3 VAWT clusters

The variation in flow velocities can also be understood from Figure 8.27 which represents the streamwise wake velocities averaged over a single rotation. The values are plotted along lines situated at distances of 0D and 1D downstream from the centre of both the individual VAWTs and are illustrated in Figure 8.26 as black dotted lines.

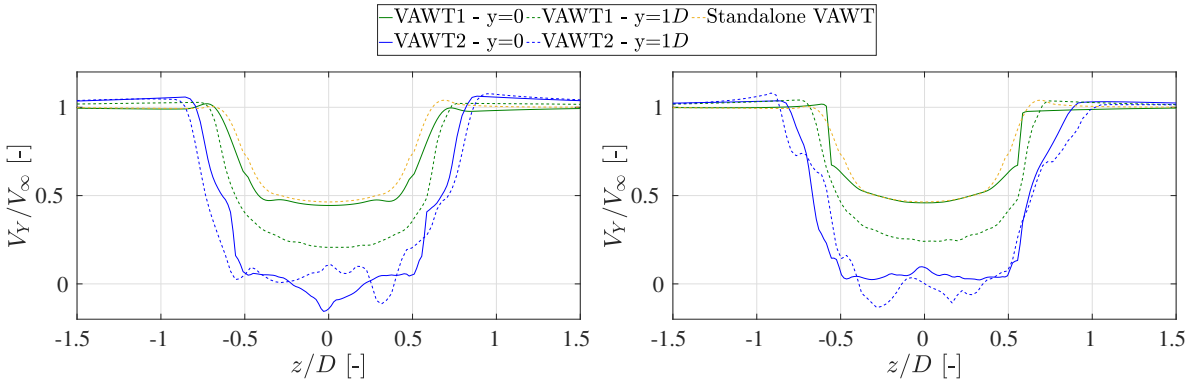

(a) CW2 VAWT Cluster (b) CW4 VAWT Cluster

Figure 8.27: Comparison of streamwise velocities, averaged over a rotation, in the downstream VAWT flowfield of the Case 3 VAWT clusters and compared with the standalone VAWT

The results are compared with the standalone VAWT at $y = 0$ location (centre of the VAWT). It can be observed that increased proximity between the two VAWTs leads to a decrease in streamwise velocities, for both the VAWTs, but is prominent for the downstream VAWT2. The increase in inflow turbulence for the downstream VAWT (for both CW2 and CW4) can also be seen from the chaotic and unsteady nature of the flow velocities at both $y = 0$ and $y = 1D$ locations. Furthermore, when the wake of VAWT1 at $y = 1D$ location is compared between the two clusters, the CW2 cluster exhibits a wider wake than the CW4 cluster; this is also true for VAWT2 at $y = 1D$ location. This can also be visualised from Figure 8.24, 8.25 and 8.26. The closer proximity of the rotors in the CW2 cluster tends to provide more flow blockage which causes the expansion of the downstream wake in the lateral direction.

The unsteady pressure data, gathered at the two spatial coordinates (the rotor plane at (0,0,7D) and a position outside the rotor plane at (4D,0,7D)), over a single rotor rotation, is presented in Figure 8.28. The first two figures include contributions from both the VAWTs in the cluster, while the third figure presents the data separately for the two VAWTs in addition to the standalone VAWT. In all figures, in addition to the highest peak observed, there are multiple smaller peaks in pressure data which symbolises the unsteady blade loading arising due to blade vortex interaction (BVI) in the cluster. This is a contribution of both VAWT1 and VAWT2, as can be seen from Figure 8.28 (c), which also shows that VAWT2 produces smaller pressure fluctuations than the VAWT1. The closeness of the lines for all clusters (CW2, CW3 and CW4) indicate that the pressure fluctuations exhibit only slight variations with different separations between the VAWTs within the cluster. In that, the highest pressure fluctuations are exhibited by CW2 and the least by CW4, at both locations sampled. This is because both the VAWTs of CW4 are in a more destructive interference position, as compared to the case of CW2. Furthermore, between 90° and 150° azimuth angles, pressure fluctuation is higher in VAWT1 of both clusters than the standalone VAWT, which highlights the increase in BVI in the former due to the proximity of two rotors.

The resulting noise spectra for the three clusters at the two above-mentioned locations are shown in Figure 8.29. The figure reports the Power Spectral Density (PSD) values in dB/Hz within the frequency range of 20-2000 Hz, plotted with a frequency resolution (Δf) of 15 Hz. The noise spectra are not plotted below the human hearing range (20 Hz). At both locations, for the low-frequency range (20-40 Hz), an increase in VAWT separation results in a decrease in decibel values, which

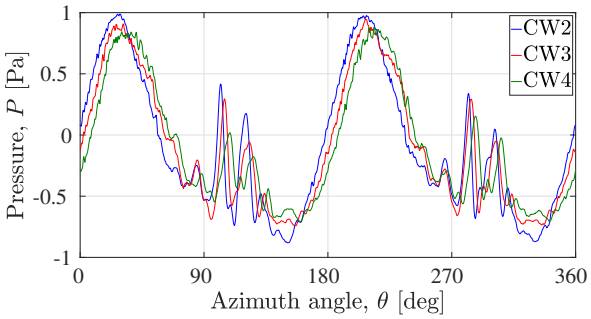

(a) Overall cluster, at X,Y,Z = (0,0,7D)

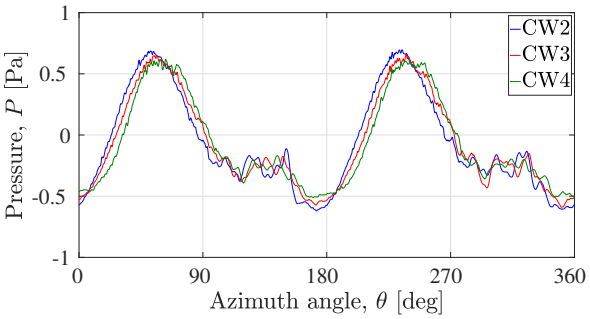

(b) Overall cluster, at X,Y,Z = (4D,0,7D)

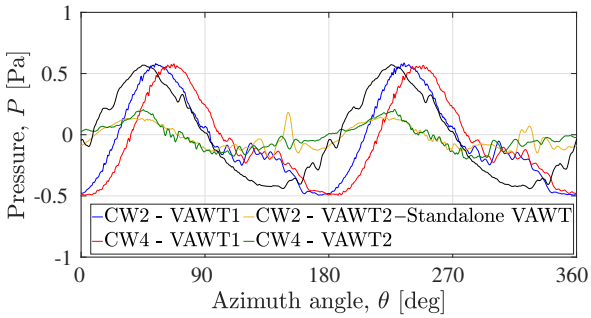

(c) Individual VAWTs, at X,Y,Z = (4D,0,7D)

Figure 8.28: Raw unsteady pressure data using the high-fidelity LBM at two different locations

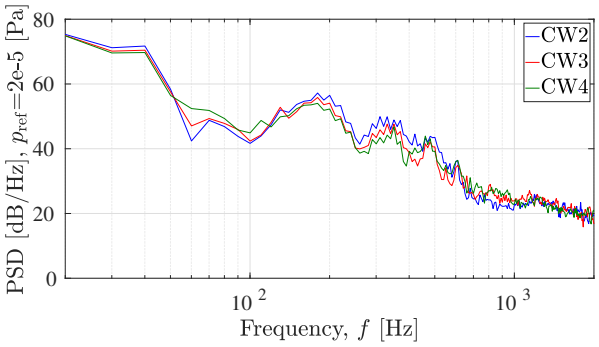

(a) Overall cluster, at X,Y,Z = (0,0,7D)

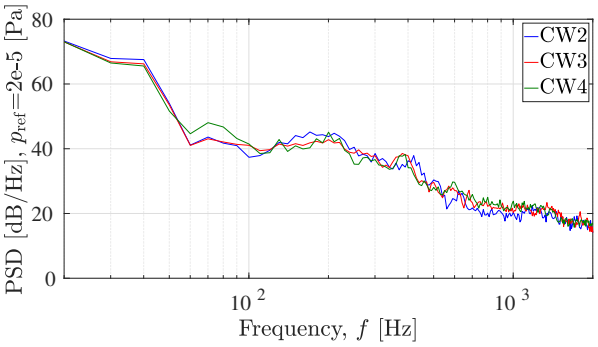

(b) Overall cluster, at X,Y,Z = (4D,0,7D)

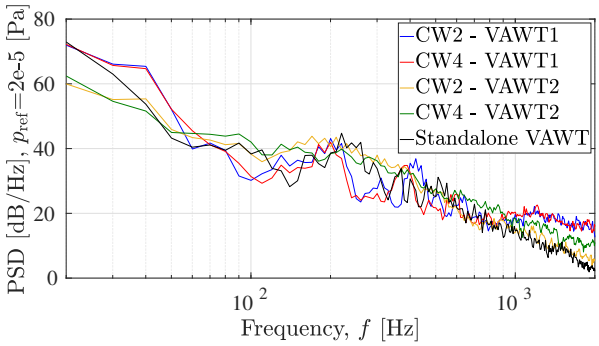

(c) Individual VAWTs, at X,Y,Z = (4D,0,7D)

Figure 8.29: Power Spectral Density (PSD) spectra using the high-fidelity LBM at two different locations

corresponds to the pressure fluctuation data shown before. For the mid-frequency range (100-500 Hz), CW2 has the highest decibel values which suggest a higher blade wake interaction causing an increase in unsteady blade loading; this is observed before in Figure 8.28 as multiple peaks in the pressure data. This is a result of increased proximity of both the VAWTs as discussed in the aerodynamic results. For the high-frequency range (> 500 Hz), no conclusive results are observed since the results are close to each other.

Figure 8.29 (c) shows that at the low-frequency range (20-40 Hz), VAWT1 of both clusters and the standalone VAWT produce higher noise than VAWT2 and this results from higher blade loading of the former as observed in Figure 8.23. Around the mid-frequency range (100-800 Hz), VAWT2 has higher decibel values than VAWT1 and this can interpreted again from the increased unsteady blade loading for the former due to higher blade wake interaction, than the latter.

Figure 8.13 presents the directivity plot of the overall sound pressure level (OSPL) comparing the three VAWT clusters. The OSPL values are calculated within the frequency range of 20-2000 Hz. On the whole, for both the YZ and XY planes, noise levels exhibit an increasing trend with a decrease in the VAWT spacing of the cluster. This is similar to the results of configuration when VAWTs when placed parallel to each other. This can be linked to the overall VAWT cluster thrust values depicted in Figure 8.22, where the C_T value increases following a decrease in the VAWT spacing.

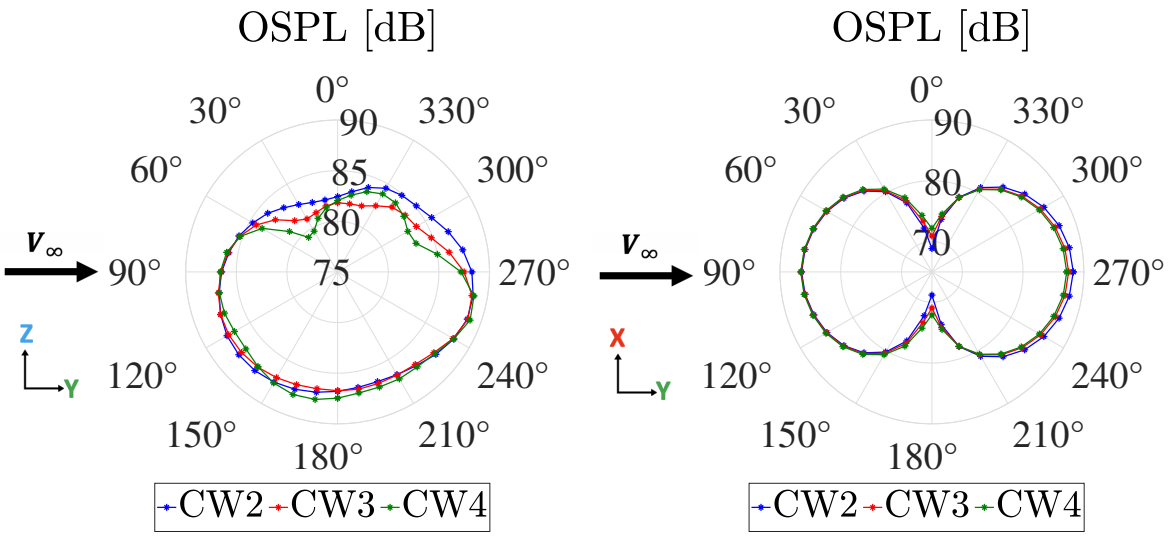

(a) Overall cluster, at X,Y,Z = (0,0,7D)

(b) Overall cluster, at X,Y,Z = (4D,0,7D)

Figure 8.30: Directivity plot of overall sound pressure level (OSPL) comparing three different VAWT separations for Case 3 VAWT clusters, along a circular array of 36 points situated at a distance of 7D from the origin of VAWT cluster ([0,0,0])

Between 150° and 220° on the YZ plane, the trend reverses and noise produced by the CW4 cluster is the highest. The OSPL values of all clusters demonstrate strong dependency on the azimuth values, where the values are higher in the -Z direction than the +Z direction. Similarly, OSPL values are higher in the +Y direction than the -Y direction. CW4 cluster observes a sudden drop in OSPL values around 30° and 300°, and this drop smoothens out in CW3 and CW2 clusters. In the XY plane, the directivity behaviour is similar to that of a standalone VAWT, as observed in Chap 5.

8.4. Conclusions and Discussions

The chapter presents a comprehensive flow physics investigation into the aerodynamics and aeroacoustics of VAWT clusters. The objective of the study is to understand the effect of different parameters which are specific to VAWT clusters such as rotor spacing and direction of rotor rotation. The

study uses only the high-fidelity Lattice Boltzmann Method (LBM) since the previous chapters have shown its efficacy over the mid-fidelity Lifting Line Free Vortex Wake (LLFVW) method. Furthermore, aeroacoustic post-processing using the Ffowcs Williams and Hawkings (FW-H) methodology is used to calculate the far-field noise. The investigation reports the thrust and power performance of the clusters, in addition to the far-field noise, while also comparing the 3D force-field and flow-field results.

Darrieus VAWT clusters consisting of two 2-bladed VAWTs are used in this study. The geometrical design of each VAWT is similar to the 2-bladed VAWT used in Chapter 5 in which the design parameters have been replicated from the study by Balduzzi et al. [22]. Three different cluster configurations have been investigated: the first configuration with parallel VAWTs in a co-rotating configuration, the second configuration with parallel VAWTs in a contra-rotating configuration and the third configuration with tandem VAWTs in a co-rotating configuration. In a parallel setup, the line connecting the VAWTs is perpendicular to the freestream velocity, while in the tandem setup, that line is parallel to the freestream velocity (one VAWT in the wake of the other VAWT). In the first and third configurations, the effect of separation between the VAWTs has been studied. In the second configuration, the effect of the direction of rotation has been studied. The VAWT solidity is set at 0.1, the aspect ratio is 1 and the results are reported for a TSR of 3.3, for all three configurations.

For all VAWT clusters, the statistical temporal convergence is achieved only after 12 rotor rotations which is significantly more than 6 rotations required for a standalone VAWT. This shows the increased fluid dynamic interactions in the former which leads to higher unsteady blade loading, as compared to the latter. In the first cluster configuration, the power generation of each VAWT increased as the separation between them decreased. An increased interaction between the VAWTs was observed due to them being in the vicinity of each other which caused an increase in the induced velocity experienced by the blades and a subsequent increase in blade loading and power generation. At a separation of 1.5m and 3m, the power generated is 6.21% and 3.68% more than the standalone VAWT, respectively. It is estimated that with a separation of more than 5.19m, each VAWT of the cluster will approach the thrust and power values of the standalone VAWT, thus, minimal VAWT interaction in the cluster. In the context of noise generation, at low frequencies (< 40 Hz), noise decreases with an increase in VAWT separation and at frequencies higher than 100 Hz, noise generation is similar for all VAWT separations.

In the second cluster configuration, the co-rotating configuration exhibits higher power generation than the contra-rotating configuration by 0.09%. Subsequently, the blade loading and streamwise velocity experienced by the blades are higher in the former than in the latter. At low frequencies (< 50 Hz), the former generates more noise than the latter and at high frequencies (> 1000 Hz), the latter generates more noise than the former. In the third cluster configuration, the downstream VAWT shows increased blade-wake interaction due to the wake shed from the upstream VAWT and as a consequence, shows lower blade loading and negative power generation as compared to the upstream VAWT. As the VAWT separation increases, the power production of both the VAWTs increases and approaches the value of the standalone VAWT, with the rate of increase being higher for the downstream VAWT. At a separation of 2m and 4m, the power production of the cluster as a whole is 60.1% and 45.7% less than the standalone VAWT, respectively.

This study proves the benefits of parallel cluster configuration in increasing the power generation capacity of individual VAWTs in a cluster. This is essential for the urban built environment where horizontal space is limited and closely spaced VAWTs will be important to efficiently utilise that available space. There is a need for further investigation into the design of the VAWT cluster to maximise the amount of power generation, especially when more than two VAWTs are present. Instead of having a common TSR for all VAWTs, different TSRs for each VAWT should also be explored, depending on the streamwise velocity experienced by each VAWT. VAWT clusters can help increase the adoption of wind turbines, both urban and floating offshore wind turbines, due to their

immense potential to enhance power generation.

9

Conclusions and Discussions

Summary

This chapter synthesises the major findings from a study focused on the aerodynamics and aeroacoustics of VAWTs. The primary objective was to understand the complexities of the flow physics and acoustics associated with VAWTs. Employing a multi-fidelity methodology, the study compared mid-fidelity and high-fidelity aerodynamic methods to assess their predictive capabilities in modelling VAWT force-field and flow-field. The chapter reflects on the studies conducted by varying the design and operational parameters for standalone VAWTs, and the potential benefits of VAWT clusters on aerodynamic and aeroacoustic characteristics. It also delves into practical insights for VAWT designers and city planners. Finally, the chapter proposes future studies aimed at advancing the understanding of VAWT design and operation and ends with final comments highlighting the need for continued research and development to fully realise their potential in the global clean energy landscape.

9.1. Major findings in this study

Nevertheless, both mid-fidelity and high-fidelity methods can be effective tools for understanding the complex aerodynamics of a VAWT, especially at different design stages.

The primary objective of this study was to thoroughly examine the flow physics associated with vertical axis wind turbines (VAWTs) and their impact on both aerodynamic and aeroacoustic characteristics. VAWTs, through their airfoil-shaped blades, produce an unsteady force field which interacts with the incoming freestream flow and results in an unsteady flow field in the downstream wake. The unsteady force field also causes pressure fluctuations in the near-field and far-field, which is perceived as aerodynamic noise by humans. Additionally, this research aimed to employ a multi-fidelity methodology to better understand the mutual interaction between the force field and the flow field. To achieve this, two distinct aerodynamic analysis methods were utilised: a mid-fidelity approach and a high-fidelity approach. For the mid-fidelity method, the lifting line free vortex wake (LLFVW) method was utilised which offers a balanced approach between computational cost and accuracy. For the high-fidelity method, the Lattice Boltzmann/Very Large Eddy Simulation (LB-VLES) approach was chosen.

The overall objective of this study, as mentioned at the beginning of this thesis, is mentioned below:

Thesis Objectives

- Understand and compare the capabilities of the mid-fidelity and high-fidelity methods in predicting the 3D force-field, flow-field and overall performance of a VAWT
- Investigate the effect of different operational and design parameters on how the unsteady blade loading influences the downstream wake development and energy extraction from the flow
- Develop a first-hand understanding of the VAWT aeroacoustic behaviour and the effect of different operational and design parameters
- Investigate the aerodynamic and aeroacoustic performance of a VAWT cluster and how the force-field and flow-field of VAWTs interact with each other in close proximity

9.1.1. On temporal and grid convergence (Chapter 4)

- Using high-fidelity LBM, thrust coefficients (C_T) take less number of rotations to converge than the torque coefficients (C_Q); the former takes around 4-6 rotations whereas the latter takes around 6-8 rotations.

- Similarly, thrust, cross-streamwise/lateral force coefficients (C_{Fz}) and overall sound pressure level (OSPL) show much better grid convergence than torque coefficients. Between the finest and second finest grid, the Grid Convergence Index (GCI) ranges from 0.0% - 1.2% for the former coefficients and from 9.02% - 10.6% for the torque coefficient which can also go as high as 36.4% for lower tip speed ratios.

- This means a coarser grid is enough to model blade loading and noise values, but a finer grid is required to model torque (or power) values. This phenomenon is because the drag values and skin friction coefficients are more sensitive to grid sizes and therefore require much finer grids for accurate predictions. These aforementioned observations have been obtained for all three different designs of VAWTs (Chapter 4, 5 and 6) which have been simulated in this thesis.

- Grid convergence behaviour also varies with tip speed ratio. TSR = 2.23 reported GCI in the range of 0.0% - 9.02% including all physical parameters observed, whereas for both TSR = 1.12 and 2.97, GCI was in the range of 0.104% - 10.6%. This implies that VAWTs experiencing different flow phenomena (such as dynamic stall at low TSR or parasitic drag and blade vortex interaction (BVI) at high TSR) require different levels of grid refinement for accurate prediction of thrust, torque or noise values.

- The mid-fidelity LLFVW results also show the same observations on the grid convergence characteristics, as the high-fidelity LBM results. The GCI values for C_T range from 0.9% - 1.1% and for C_Q range from 2.6% - 4.0%. And, GCI values for TSR = 3.3 range from 0.9% - 2.6% and for TSR = 5 (at which, VAWT experiences more parasitic drag and BVI than TSR = 3.3) range from 1.1% - 4%. This indicates that the mid-fidelity approach yields comparable trends in predicting the performance and fluid dynamic interactions of VAWTs, similar to the high-fidelity method.

- Using the high-fidelity method, grid convergence for noise spectra shows that variation in mid-to-high-frequency noise with different grids is higher than that of low-frequency noise. Lower-frequency noise is generated due to mean blade loading and larger-scale vortices interacting with the blades and is more easily captured even with coarser grids because their wavelengths are longer. On the other hand, higher-frequency noise is caused due to high-frequency unsteady blade loading and smaller-scale BVI. These higher-frequency noises have shorter wavelengths, so a finer grid is necessary to accurately capture and resolve these details. The variation in grid sizes, therefore, leads to greater variation in noise measurement at these frequencies.

9.1.2. On tip speed ratio (Chapter 4)

- Using the high-fidelity LBM method, it was shown that for both C_T and C_Q, the upwind part of rotation performed better than the downwind part and the difference between the values obtained in the two parts increases with TSR. The ratio of C_T obtained in the upwind to downwind part increases from 1.3 at TSR = 0.37 to 17.6 at TSR = 2.97. The upwind C_T increases monotonically with TSR whereas the downwind C_T increases till TSR = 1.12 and then decreases due to an increase in blade-wake interaction (BWI) between the downwind blades and wake shed from the upwind blades.

- The C_Q for the upwind part increases till TSR = 2.23 and then decreases. Whereas for the downwind part, C_Q monotonically decreases with an increase in TSR and becomes negative for TSR = 1.12 and higher. This again highlights the increase in BWI with an increase in TSR during the downwind part of rotor rotation which significantly reduces C_Q more than C_T.

- The 3D vortices and 2D streamwise velocities visualisation show much stronger wake and BVI/BWI for the case of higher TSR as compared to lower TSR. As TSR increases, the blade loading is higher and stronger vortices and wake are shed from the blades which causes lower streamwise velocities in the downstream wake.

- Higher TSR also contributes to higher noise values. This increase happens due to an increase in mean blade loading as TSR increases, contributing towards low-frequency noise and an increase in BWI/BVI as TSR increases, contributing towards high-frequency noise. This can also be seen in the directivity plot where noise increases at all points around the VAWT as TSR increases.

9.1.3. On number of blades (Chapter 5)

- Utilizing the mid-fidelity LLFVW method, it was demonstrated that in VAWTs, a higher number of blades results in an enhanced power coefficient (C_P) at TSRs. Conversely, at higher TSRs, this trend is reversed. At low TSRs, an increase in solidity negligibly increases BWI/BVI, which helps enhance blade loading and power output. However, at higher TSRs, greater solidity adversely affects blade loading and overall rotor power. Consequently, higher solidity leads to a sharper gradient in C_P than lower solidity cases, over the whole range of TSR.

- The number of blades in a VAWT affects the optimal TSR, and C_P values show that the optimal TSR decreases as the number of blades increases. More blades increase BWI/BVI which means that the VAWT reaches its optimal power generation capacity at a lower TSR.

- The C_T initially increases with increasing TSR and the number of blades and starts decreasing slightly at high TSRs, specifically for the 4-bladed rotor. The study further reveals that as the number of blades increases, the amplitude of variation in C_T and C_Q values decreases, resulting in smoother overall blade loading variation.

- When comparing the mid-fidelity LLFVW and high-fidelity LBM results, the former predicts higher values of mean C_T and C_Q in a single rotation, as compared to the latter. In terms of azimuthal values, in the upwind part of the rotation, the former predicts higher values as compared to the latter, whereas, the opposite trend is true in the case of the downwind part. However, the trends predicted by both methods are the same when number of blades is varied.

- The discrepancy is also found to be true when comparing streamwise velocities in the wake. The mid-fidelity method predicts lower streamwise velocities as compared to the high-fidelity method. The lower values of blade loading in the former in the upwind part of the rotation contribute to less strong wake, as compared to the latter.

- Low-frequency noise was found to be higher in VAWTs with fewer blades, due to the higher mean blade loading values observed. High-frequency noise was found to be higher in VAWTs with more blades, due to a higher intensity of BVI between the downstream blades and previously shed blade vortices.

- OSPL directivity plot showed that overall noise increased with an increase in the number of blades except for the 4-bladed VAWT for which the noise is lowest amongst all the VAWTs.

9.1.4. On supporting struts and central tower (Chapter 6)

- The study showed a reduction in overall C_P across all TSRs attributable to the presence of struts and a tower, with a negligible reduction in C_T. The addition of struts and a tower detrimentally affects tangential and normal blade loading, as well as overall rotor efficiency. Notably, struts significantly affect the spanwise force distribution on the blade, which intensifies as the TSR increases.

- The presence of struts and a tower leads to a decrease in azimuthal blade loading during the upwind and downwind rotation phases. This effect is primarily due to enhanced BWI/BVI caused by these supporting structures. A significant reduction in blade loading is observed around the 270° azimuth, directly downstream of the central tower, attributable to the wake generated by the tower. The thickness of this wake, and consequently the reduction in blade loading, escalates with an increase in the tower diameter.

- The inclusion of struts and a tower does not affect the self-starting capability and optimal TSR value, even though the optimal power decreases.

- The mid-fidelity results predicted higher values of mean C_P and C_T, azimuthal C_T and C_Q and blade normal forces, as compared to the high-fidelity results, even though the trends predicted are the same by both methods when struts and a central tower is added. This resulted in lower streamwise velocities predicted by the former as compared to the latter.

- Low-frequency noise was observed to decrease when struts and a tower were added, due to the lower mean blade loading values obtained. Conversely, high-frequency noise was observed to increase, due to higher intensity of BWI/BVI between the downstream blades and vortices shed from all the upstream structures.

9.1.5. On skewed inflow (Chapter 7)

- For a non-uniform inflow such as skewed inflow, at a TSR of 3, an increase in skew angle results in reduced values of both mean C_P and C_T in a single rotation, with C_P experiencing a more pronounced decline. At a TSR of 4, both C_P and C_T initially increase, peaking at approximately 20° skew angle, before subsequently decreasing. This trend of initial increase becomes more marked at a TSR of 5.

- With an increasing skew angle, there is a consistent decline in the C_T and C_Q values for a single blade during the upwind rotation phase. This is linked to the reduced horizontal component of velocity ($V_\infty cos\beta$) as the skew angle increases. Conversely, in the downwind phase, there is an observed increase in both C_T and C_Q values with increasing skew angle. This is attributed to the reduced BWI/BVI in the downwind rotation, resulting from the skewed inflow.

- The 2D streamwise velocity contours and 3D vortices visualisation reveal an increase in clean airflow experienced by downwind blades as the skew angle increases. The contrasting effects observed in the upwind and downwind rotation phases dictate the overall VAWT performance.

- The mid-fidelity method predicts higher mean C_P and C_T, azimuthal blade loading values and lower streamwise wake velocities when compared with the high-fidelity results. Despite this, the trends observed in C_P and C_T are the same in both methods, when the skew angle is varied. Also, the difference between the predictions of both methods increases with an increase in skew angle.

- There is a notable reduction in low-frequency noise with an increase in skew angle, attributable to the decreased mean blade loading. In contrast, high-frequency noise increases with the skew angle. This rise is linked to higher flow separation on the blades during the downwind rotation phase due to an additional spanwise velocity component on the blades, leading to elevated Separation-Stall (SS) noise. Additionally, the increased interaction of the mid-span region of downstream blades, where spanwise blade loading is at its peak, with the tip vortices shed by upstream blades contributes to this phenomenon.

9.1.6. On VAWT clusters (Chapter 8)

- In a parallel cluster configuration of VAWTs, it is observed that C_P for each VAWT increases as their separation diminishes. This increase is attributed to the enhanced fluid dynamic interaction between the VAWTs owing to their proximity, which leads to an increase in the induced velocity on the blades, subsequently increasing mean blade loading.

- At separations of 1.5m and 3m, the C_P is enhanced by 6.21% and 3.68% respectively, compared to a solitary VAWT. It is projected that with separations exceeding 5.19 meters, the C_P and C_T of each VAWT in the cluster will approximate those of a standalone VAWT, indicating minimal interaction among the VAWTs in the cluster.

- In the context of noise generation, at low frequencies (< 40 Hz), noise decreases with an increase in VAWT separation and at frequencies higher than 100 Hz, noise generation is similar for all VAWT separations.

- When comparing a co-rotating and a contra-rotating configuration, the former exhibits higher C_P than the latter by 0.09%. Subsequently, the blade loading and induced velocity experienced by the blades are higher in the former than in the latter.

- At low frequencies (< 50 Hz), the former generates more noise than the latter and at high frequencies (> 1000 Hz), the latter generates more noise than the former.

- When one of the VAWTs is placed in the wake of another VAWT in a tandem configuration, the downstream VAWT shows increased BWI due to the wake shed from the upstream VAWT and as a consequence, shows lower blade loading and negative C_P as compared to the upstream VAWT. As the VAWT separation increases, the C_P of both VAWTs increase and approach the value of the standalone VAWT, with the rate of increase being higher for the downstream VAWT. At a separation of 2m and 4m, the power production of the 2-VAWT cluster as a whole is 60.1% and 45.7% less than the standalone VAWT, respectively.

- In the low-frequency spectrum (20-40 Hz), greater separation between VAWTs corresponds to reduced noise levels. In the mid-frequency spectrum (100-500 Hz), the VAWT having the smallest separation exhibits the highest noise levels, indicative of intensified BWI and resultant unsteady blade loading, as evidenced by multiple peaks in the raw pressure data. For the high-frequency spectrum (above 500 Hz), the results are inconclusive, with observed values for all separations closely aligned.

9.1.7. Implications for designers

This study, though primarily computational and theoretical, provides valuable practical insights for designers and planners working with VAWTs. These insights can be relevant in both computational modelling, practical design and policy and planning perspectives.

- A key takeaway is the capability of *mid-fidelity* methods in VAWT performance calculations. Despite their lower accuracy compared to high-fidelity methods, they reliably predict correct trends. Integration of *low-fidelity* methods within the same multi-fidelity framework is suggested for performance calculation and optimisation.

- For VAWTs with a control system capable of maintaining a constant TSR reliably under variable inflow conditions, opting for a *three-bladed design* (higher solidity) is advantageous. This distributes blade loading more evenly across a single rotor rotation, potentially reducing vibrations in the tower structure and aerodynamic noise generated.

- The exploration of *new blade designs* in VAWTs is recommended. Although not covered in this thesis, simulations using both mid-fidelity and high-fidelity methods were conducted [336] and indicated advantages in specific designs: *helical* blades for lower noise generation and smoother blade loading characteristics in a single rotation, and *troposkein* shapes for smoother C_P versus TSR curves. The potential of hybrid designs amalgamating these characteristics should be explored.

- *VAWT clusters* demonstrate higher power density compared to standalone units, as shown in this study. Thus, installing two smaller VAWTs in proximity could be more advantageous than one larger VAWT, due to their higher combined power potential.

- Collaboration with *local authorities* is crucial for implementing necessary rules and regulations for VAWTs, particularly in urban settings. Even though no experiments were conducted in this thesis, we tried installing a helical-shaped VAWT on a university campus and our experiences highlighted the necessity of adapting and reforming local city regulations to accommodate VAWTs near buildings and human settlements.
- The installation of *rooftop VAWTs* on residential buildings (such as detached, semi-detached or terraced houses) poses structural challenges due to the weak roof structure. *"Community VAWTs"*, larger than typical rooftop units and configured in clusters, can be a more viable solution when installed on the ground. While commercial and multi-story buildings have stronger roofs, the installation of VAWTs on such structures remains complex.

9.2. Contributions to knowledge

This section discusses the pivotal contributions to the understanding of flow physics of VAWTs, derived from the studies conducted in this thesis and its findings:

- The thesis underscores the necessity of *high-fidelity methods* for simulating fluid dynamics in VAWTs. These methods are crucial for accurately capturing the detailed force-field and flow-field of a VAWT. Fine resolution is required, particularly over the blades and in the downwind part of rotor rotation, where unsteady fluid dynamic interactions are most pronounced. Such intricate details are inadequately resolved by mid-fidelity vortex methods.
- While *mid-fidelity methods* may not fully resolve the detailed flow physics of VAWTs, they reliably predict trends in C_P and C_T values, as evidenced across various VAWT designs simulated in this thesis. This establishes the utility of mid-fidelity methods for performance analysis and potential design optimisation, offering a balance between accuracy and computational efficiency.
- The results observed in this thesis enhance the understanding of the *physics of VAWT force-field and flow-field*. Comprehensive investigations have been conducted on the effect of variables such as tip speed ratios, number of blades, supporting struts and a central tower, skewed inflow, for a standalone VAWT, and various VAWT cluster configurations. These insights are instrumental in guiding the design process for VAWTs, whether for urban or deep offshore applications.
- The thesis places particular emphasis on the *aeroacoustics of VAWTs*. It reveals a correlation between low-frequency noise and mean blade loading and between high-frequency noise and the high-frequency fluctuations in blade loading caused by intense BWI/BVI. This knowledge is vital in identifying potential noise sources in VAWTs and devising strategies to mitigate them during the design phase.
- The results obtained for *VAWT clusters* underscore the importance of cluster configurations for achieving higher aerodynamic performance and power density in a constrained horizontal space, especially in urban areas. High-fidelity investigations show the increased fluid dynamic interactions between VAWTs when placed in proximity and also the potential for noise reduction through destructive interference of corresponding blades in adjacent turbines.

9.3. Recommendations for future studies

There remain several unexplored areas critical for deepening the understanding of the interaction between the force field and flow field in Vertical-axis Wind Turbines (VAWTs), which is essential

for their efficient design. For that purpose, this section proposes a series of prospective studies. These suggestions encompass not only short-term extensions to the current studies but also leverage the insights obtained in this thesis to fulfil long-term objectives for the VAWT research community. These proposals aim to facilitate future studies that can further investigate the complexities of VAWT dynamics and contribute to the advancement of this field.

1. **Research Question: How do mid-fidelity and high-fidelity methods differ in predicting the aerodynamic performance of VAWTs with different design parameters like blade shape, airfoil shape, and aspect ratio?** This study would involve systematic simulations of VAWTs using both mid-fidelity and high-fidelity methods across a range of design parameters. The objective would be to assess the accuracy of mid-fidelity methods in various design and operational scenarios, determining their viability as substitutes for high-fidelity methods. This study would also enhance the understanding of flow physics in VAWTs and inform the selection of simulation methods based on specific design considerations.

2. **Research Question: What are the aerodynamic, aeroacoustic and aeroelastic benefits and drawbacks of different VAWT blade shapes, including hybrid designs?** The investigation would entail an aerodynamic analysis of various blade shapes, including troposkein, helical, straight, and hybrid designs by combining them. Computational simulations and possibly experimental wind tunnel tests should be used to evaluate each design's efficiency, structural stability, and suitability for different operational conditions in urban and deep offshore locations.

3. **Research Question: Can other vortex methods outperform the Lifting Line Free Vortex Wake method (LLFVW) in predicting VAWT performance parameters?** This study will compare the efficacy of various vortex methods like the Vortex Panel Method (VPM), Vortex Lattice Method (VLM), and Vortex Particle Method (VPM) against the LLFVW method used in the thesis. The study would involve simulations to determine which method provides the most accurate predictions of VAWT performance and under what operational and design conditions.

4. **Research Question: Do Leading Edge and Trailing Edge blade serrations improve VAWT performance and reduce noise?** The study would involve CFD simulations and aeroacoustic post-processing to analyse the effect of serrated leading and trailing edges on blades. The focus would be on understanding changes in aerodynamic performance and noise characteristics, contributing to the design of more efficient and quieter VAWTs.

5. **Research Question: How can dynamic stall be more accurately captured in mid-fidelity and high-fidelity simulations to enhance VAWT performance at low TSRs?** Dynamic stall is an inherent VAWT phenomenon at low TSRs affecting the power and noise performance significantly. Investigating the dynamic stall phenomenon in a VAWT requires high-fidelity simulations with a much finer mesh and potentially quasi-2D setups to manage computational costs. The study would focus on understanding the implications of dynamic stall on self-starting capabilities under diverse operational conditions and force-field and flow-field characterstics at low TSRs. In numerous mid-fidelity aerodynamic models, the dynamic stall is not intrinsically represented, necessitating the incorporation of engineering models like the Beddoes-Leishmann method. The study should use and refine these dynamic stall models and integrate them into VAWT analytical aerodynamic codes. Moreover, since dynamic stall models can be validated with or without the use of vortex generators (VGs), the impact of VGs on dynamic stall phenomena and overall VAWT operation can also be comprehensively assessed [92].

6. **Research Question: Can analytical aeroacoustic methods accurately predict noise in VAWTs, and how do they compare with the noise levels predicted by high-fidelity methods?** This study would employ analytical aeroacoustic methods such as the semi-empirical Brooks-Pope-Marcolini (BPM) and iTNO model for the airfoil self-noise and Paterson and Amiet model for the turbulence-interaction noise, comparing results with those from high-fidelity simulations using the FW-H acoustic analogy. The goal would be to identify the most accurate and efficient method for noise prediction and understand various noise sources in VAWTs.

7. **Research Question: How does variable pitch in a single VAWT rotation influence power performance and aeroacoustics, and how does it perform wake steering? Can a VAWT re-energise the wind farm?** Investigating the impact of variable pitch on VAWT performance and aeroacoustics would involve computational simulations using both mid-fidelity and high-fidelity aerodynamic methods. The study would also explore how variable pitch affects the wake dynamics, such as wake steering which will affect the performance of any downstream VAWT present in a cluster. The results should be compared with HAWT wind farms and it should be studied whether a VAWT allows wake steering and re-energising wind farms more efficiently than a HAWT.

8. **Research Question: Can flow control devices improve VAWT performance and aeroacoustics and how does it affect the overall force field?** The utilisation of flow control devices, such as vortex generators (VGs), should be investigated for their ability to manipulate the VAWT force-field. VGs can be used especially when the increase in lift coefficient outweighs the drag penalty, a scenario often seen in cases of early transition. Such integration not only enhances C_P but may also allow for chord reduction, benefiting the blade's structural aspects. Similar to HAWTs, the study should focus on how to mitigate the risks associated with dynamic stall using VGs in a VAWT design and if it is possible to reduce noise generation simultaneously. The airfoil optimisation process could be expanded to include VGs, replacing traditional tools like Xfoil with modified versions like XfoilVG for calculating lift and drag polars. Additionally, active flow control devices, such as plasma actuators or suction/blowing systems, can offer an economically viable and low-maintenance alternative to individual blade pitching, potentially altering the VAWT force field through controlled circulation and should be explored using a multi-fidelity approach.

9. **Research Question: In a tandem configuration of a VAWT cluster, how does having a different design of each VAWT affect overall power production and wake interaction?** This study would involve CFD simulations of tandem VAWT configurations with different designs for each VAWT. The focus would be on understanding how these design variations influence individual and collective power output, as well as the wake interactions between the turbines. The inflow conditions experienced by each VAWT are different, and therefore, having different designs for them can potentially increase the power performance.

10. **Research Question: How does clustering more than two VAWTs affect power production density, and what is the optimal configuration for maximum efficiency?** The study would analyse power production in clusters with more than two VAWTs using CFD simulations. The aim should be to optimise cluster configurations for maximal power generation while minimizing adverse wake effects on downstream turbines and noise production using a multi-objective optimisation framework. Ideas for an efficient cluster design can also be taken from nature, such as how schools of fish swim or flocks of birds fly together to reduce the hydrodynamic or aerodynamic resistance to a minimum, respectively.

11. **Research Question: How can uncertainty analysis and uncertainty optimisation improve VAWT design efficiency in variable inflow conditions?** This study would involve CFD simu-

lations and aeroacoustic post-processing using a multi-fidelity approach combined with uncertainty analysis to design efficient VAWTs in uncertain inflow conditions either in urban or deep offshore floating platforms. The uncertainty in design can also arise from the manufacturing of the blades which can incorporate various types of uncertainties (e.g., Gaussian, Binomial, Poisson or Bernoulli distributions). This will help to understand how the uncertainty is propagated towards VAWT performance and acoustic parameters, leading to designing more reliable and robust VAWTs.

12. **Research Question: Can the usage of experimentally generated airfoil lift and drag polars improve lifting line method predictions and how do different techniques compare?** Experimentally, airfoil lift and drag properties can be determined using various methods, including airfoil pressure distribution, wall pressure distribution, or a balance system. Notably, the wall pressure method necessitates significant numerical data manipulation, raising concerns about its accuracy [92]. A comparative benchmark study should be done comparing the polars derived from these various methods by using identical models and operational conditions to ensure a fair assessment. Previous research by Olsen et al. [251] suggests discrepancies in maximum lift coefficients obtained via different methodologies. Another fundamental assumption in wind tunnel testing of airfoils is the two-dimensionality of the flow, an assumption that does not hold in the stall region due to the formation of stall cells. Consequently, an experimental campaign should be conducted to explore the behaviour of these stall cells and their impact on lift and drag, under both steady and unsteady conditions and the study can be complemented with CFD simulations of the wind tunnel test section.

9.4. Final comments

VAWTs have recently garnered increased attention among designers, researchers, and urban planners, particularly for their suitability in urban environments and floating deep offshore locations. This interest contrasts with the longer-established design and understanding of HAWTs, highlighting a relative infancy in VAWT development. A common misconception has been the inefficiency of VAWTs in power generation, a notion this thesis has sought to rectify. Through exploring the 3D design space of VAWTs, this work has validated the effectiveness of both open-source and commercial tools in modelling the aerodynamics and aeroacoustics of VAWTs. The primary goal has been to demonstrate that VAWTs can be beneficial for various applications and that the 3D design space can be easily exploited to increase power performance while reducing noise generation. Additionally, the deployment of smaller VAWTs in cluster formations has been proposed as a means to utilise the space available in the most efficient way possible.

Looking ahead, advancements in computational resources and modelling capabilities are expected to significantly impact VAWT research and development positively. This progression will enable a more holistic approach to VAWT design, encompassing not only aerodynamics and aeroacoustics but also extending to structural design, life-cycle assessment, fatigue life, wind farm layout, drivetrain efficiency, environmental impact, cost-benefit analysis, and the design of platforms and mooring systems for floating VAWTs. There is substantial scope for further enhancing VAWT performance, as discussed in this and preceding chapters. VAWTs possess the potential to either outperform HAWTs or complement them within a broader strategy to reduce the impact of climate change. Achieving this will aid in increasing public acceptance and adoption of VAWTs among various stakeholders, including the general public, real estate developers, and urban planners. This shift towards VAWTs can significantly accelerate the global clean energy strategy.

A

List of publications

A.1. First author journal papers

1. Shubham, S., Naik, K., Sachar, S. and Ianakiev, A., 2023. Performance analysis of low Reynolds number vertical axis wind turbines using low-fidelity and mid-fidelity methods and wind conditions in the city of Nottingham. Energy, 279, p.127904. https://doi.org/10.1016/j.energy.2023.127904

2. Shubham, S., Wright, N. and Ianakiev, A. Richardson extrapolation method applied to aerodynamic and aeroacoustic characteristics of VAWT using Lattice Boltzmann Method. (*Submitted and under review*)

3. Shubham, S., Wright, N. and Ianakiev, A. Aerodynamics and aeroacoustics of vertical axis wind turbines and effect of tip speed ratio using Lattice Boltzmann Method. (*Submitted and under review*)

4. Shubham, S., Wright, N., Avallone, F. and Ianakiev, A. Aerodynamics and aeroacoustics of vertical axis wind turbines with different number of blades using a multi-fidelity approach. (*In progress*)

5. Shubham, S., Avallone, F., Brandetti, L., Wright, N. and Ianakiev, A. Effect of struts and central tower on aerodynamics and aeroacoustics of vertical axis wind turbines using a multi-fidelity approach. (*In progress*)

6. Shubham, S., Avallone, F., Brandetti, L., Wright, N. and Ianakiev, A. Effect of skewed inflow on aerodynamics and aeroacoustics of vertical axis wind turbines using a multi-fidelity approach. (*In progress*)

7. Shubham, S., Wright, N. and Ianakiev, A. Aerodynamic and aeroacoustic investigation of vertical axis wind turbine clusters in parallel configuration using Lattice Boltzmann Method. (*In progress*)

8. Shubham, S., Wright, N. and Ianakiev, A. Aerodynamic and aeroacoustic investigation of vertical axis wind turbine clusters in tandem configuration using Lattice Boltzmann Method. (*In progress*)

A.2. First author conference papers

1. Shubham, S., Ianakiev, A. and Wright, N., 2021, November. Review of standalone small-scale Darrieus wind turbines-a Nottingham case study. In 17th EAWE PhD Seminar on wind energy. https://doi.org/10.5281/zenodo.11163484

2. Shubham, S., Wright, N. and Ianakiev, A., 2022. Application of Richardson extrapolation method to aerodynamic and aeroacoustic characteristics of low Reynolds number vertical axis wind turbines. In 28th AIAA/CEAS aeroacoustics 2022 conference (p. 3022). https://doi.org/10.2514/6.2022-3022

3. Shubham, S., Wright, N., Avallone, F. and Ianakiev, A., 2023. Aerodynamic and aeroacoustic investigation of vertical axis wind turbines with different number of blades using mid-fidelity and high-fidelity methods. In AIAA AVIATION 2023 Forum (p. 3642). https://doi.org/10.2514/6.2023-3642

4. Shubham, S., Avallone, F., Brandetti, L., Wright, N. and Ianakiev, A., 2024. Effect of struts and central tower on aerodynamics and aeroacoustics of vertical axis wind turbines using mid-fidelity and high-fidelity methods. In AIAA SCITECH 2024 Forum (p. 1485). https://doi.org/10.2514/6.2024-1485

A.3. Co-author journal papers

1. Sachar, S., Shubham, S., Flaszynski, P., Doerffer, P. and Ianakiev, A., 2024. Wind Speed Probabilistic Forecast Based Wind Turbine Selection and Siting for Urban Environment. (Accepted in IET Renewable Power Generation)

2. Naik, K., Ianakiev, A., Galadanci, A.S., Cucca, G., Shubham, S. and Sun, M., 2024. Evaluating the potential of wind and solar energy in achieving zero energy ratings in residential homes: A Nottingham case study. Smart Energy, 13, p.100129. https://doi.org/10.1016/j.segy.2023.100129

A.4. Co-author conference papers

1. Thambidurai Arasi, T.R., Shubham, S. and Ianakiev, A., 2024. Effect of Blade Shape on Aerodynamic and Aeroacoustic characteristics of Vertical Axis Wind Turbines using mid-fidelity and high-fidelity methods. In AIAA SCITECH 2024 Forum (p. 1488). https://doi.org/10.2514/6.2024-1488

B

Curriculum Vitae

Shubham

Goldington Road, Bedford, MK40 3FD, United Kingdom • shubham.phdaero@gmail.com
+44-7884-986457 • LinkedIn • ResearchGate

Personal Statement

Passionate engineer and consultant with 5+ years of experience in **aeroacoustics**, **aerodynamics**, **mechanical design**, **data analysis** and **computational data engineering**. Skilled in programming languages like MATLAB, Python, C/C++, Julia and computational tools for numerical modelling, CFD, CAA, CAE, aeroelasticity, structures, multi-body dynamics, data processing and visualization, data analysis, ML/AI methods and multi-disciplinary design optimisation.

Work Experience

May 2023-Present (Full time, >1 year)

Research Fellow (Team of 10)
Cranfield University, UK
- **Uncertainty analysis** and ML/AI methods for modelling of future aircraft design architecture
- Development of multi-disciplinary multi-fidelity analysis and multi-objective **optimisation** methodologies for a **propeller** system integrated with the wing
- **Simulations** for aircraft **aeroacoustic** performance and aeroelastic flutter and fatigue

May 2023-Jan 2024 (Freelance, 9 months)

AeroEngine CFD Consultant, Dovetail Electric Aviation (Team of 4)
- Meredith effect on the **propeller's** performance in hydrogen-powered fuel cell aircrafts
- Collaborating with **cross-functional teams** to develop custom simulation models to design the overall engine hub assembly along with propeller pitch
- Provided expert **consulting** services in **ANSYS** for CFD design and trade-off studies

Mar 2021-Feb 2023 (Freelance, 2 years)

Propeller Aeroacoustic Consultant, The Eplane Company (Team of 4)
- High-fidelity aerodynamic and **aeroacoustic** and mid-fidelity vortex methods for flow-field analysis of tilt-rotor propeller and mutual interaction between rotor, hub and wing for an **eVTOL**
- **Trained** other colleagues in using multi-fidelity methods for **CFD/CAA** investigations
- Gained real-life technical **project management** skills in a DeepTech **fast-paced** startup

May 2020-Apr 2023 (Full time, 3 years)

Marie Curie Early Stage Researcher
Nottingham Trent University, UK
- Experimental **Aerodynamic** and **Aeroacoustic** Investigation of Vertical Axis Wind Turbines
- **Power performance** analysis, aero-structural and **experimental** campaign design
- **Collaboration** with *Global Partnerships Ltd* company for their QR6 wind turbine design

Nov 2018-Apr 2019 (Full time, 6 months)

CFD and Experimental Data Engineer, Engine Systems Team (Team of 3)
General Electric (GE) Aviation, Munich, Germany
- CFD, **Big data analysis** and thermal analysis of icing conditions on Aero Engines
- Validation & verification of **experimental flight** dataset with finite volume results on *ANSYS*
- **Optimization** and **multi-disciplinary** design solutions for meeting customer requirements

Education

Doctorate of Philosophy in Rotor Aerodynamics and Aeroacoustics (Passed)
Nottingham Trent University, UK

Master of Science in Aerospace Engineering (8.0/10)
Delft University of Technology, the Netherlands
- *Specialization* : **Aerodynamics** and **Aeroacoustics**
- *Master Thesis* : Aeroacoustics of Co-rotating rotors for **Urban Air Mobility**
- *Relevant courses* : CFD, Internal Flows, Aircraft Aerodynamics, Aeroacoustics

Bachelor of Technology in Mechanical Engineering (8.72/10)
Indian Institute of Technology (IIT) BHU, India
- *Relevant courses* : Fluid Mechanics, Turbomachinery, Industrial Management

Project Experience

Aug 2018-Oct 2018 (Full time, 3 months)

Trainee, Department of Helicopters, Institute of Aerodynamics (Team of 2)
German Aerospace Center (DLR), Germany

- **Validation** of in-house Unsteady Panel Method CFD code and Boundary Layer module
- Modeling of rotor wake using combination of *Lifting Line* model and *Unsteady Aerodynamics*
- Validation with **numerical tools** - *VSAERO*, *XFOIL* and experiments of airfoil and rotor test cases

Feb 2018-Jul 2018 (Part time, 6 months)

Aerodynamics Project
Faculty of Aerospace Engineering, TU Delft, the Netherlands

- **Aerodynamic** analysis of a feathered propeller during cruise conditions at varying pitch angles
- Used *CATIA* (CAD), *ANSYS Fluent* (RANS, LES) along with wind tunnel results for **CFD** validation
- Preliminary feasibility study for using **propeller** in regenerative (wind turbine) mode during aircraft landing and its **aeroacoustic** signature

Voluntary Work

Jan-Mar 2017 (14 hours/week)

Student Incharge, Institute Day, IIT BHU, India

- **Organized** the 3rd Institute Day comprising all the 16 faculties of the institute
- Successful **participation** of over 500 undergraduate, graduate and doctoral students
- Learnt the importance of **time management** and developed **conflict resolution** skills while working with a large team of 22

Extra-Curricular

Jan-Apr 2015 (4 hours/week)

Team QUADROTON (Team of 5)
AeroModelling Club, IIT BHU, India

- **Optimized** a Quadcopter performance by reducing its weight and vibrations
- Manufactured and used **Carbon Fiber** and **Glass Fiber**, instead of Aluminium
- Developed effective **decision making** skills and becoming a **team player**

Skills

Software:	CATIA ●●●●○	ANSYS ●●●●○	3DS PowerFLOW ●●●●○
	Star-CCM+ ●●●○○	COMSOL ●●○○○	SolidWorks ●●○○○
	ParaView ●●●●○	XROTOR/XFOIL ●●●●●	OpenVSP ●●●○○
Code:	C/C++ ●●●○○	MATLAB ●●●●○	Python ●●●○○
	FORTRAN ●●●●○	Julia ●●●○○	HPC ●●●○○

Languages

ENGLISH: Fluent | DUTCH & GERMAN: Beginner | HINDI: Mother Tongue

Hobbies and Interests

RC Plane, Quadcopter, Rocketry - Developed scratch-built remote controlled models
Bike sports (twice a month), *Badminton* & *Table Tennis* (1-2 days a week), *Countryside trips* (Weekends)
Reading Biography, Aerospace and history-related blogs, Music (EDM & Classical)

Bibliography

[1] Gebreel Abdalrahman, William Melek, and Fue-Sang Lien. Pitch angle control for a small-scale darrieus vertical axis wind turbine with straight blades (h-type vawt). *Renewable energy*, 114:1353–1362, 2017.

[2] Nima Aboufazeli, Pooyan Hashemi Tari, Roghayeh Gavagsaz-ghoachani, and Majid Zandi. The strategy for the use of wind power in urban areas by hybrid vertical axis wind turbines. *Journal of Renewable and New Energy*, 7(1):65–73, 2020.

[3] Little Ice Age and Medieval Climate Anomaly. Global signatures and dynamical origins of the. *J. Clim*, 21:2283, 2008.

[4] Amit Agrawal, Hari Mohan Kushwaha, Ravi Sudam Jadhav, Amit Agrawal, Hari Mohan Kushwaha, and Ravi Sudam Jadhav. Burnett equations: derivation and analysis. *Microscale Flow and Heat Transfer: Mathematical Modelling and Flow Physics*, pages 125–188, 2020.

[5] Mojtaba Ahmadi-Baloutaki, Rupp Carriveau, and David SK Ting. Straight-bladed vertical axis wind turbine rotor design guide based on aerodynamic performance and loading analysis. *Proceedings of the Institution of Mechanical Engineers, Part A: Journal of Power and Energy*, 228(7):742–759, 2014.

[6] Mojtaba Ahmadi-Baloutaki, Rupp Carriveau, and David SK Ting. A wind tunnel study on the aerodynamic interaction of vertical axis wind turbines in array configurations. *Renewable energy*, 96:904–913, 2016.

[7] Aya Aihara, Victor Mendoza, Anders Goude, and Hans Bernhoff. Comparison of three-dimensional numerical methods for modeling of strut effect on the performance of a vertical axis wind turbine. *Energies*, 15(7):2361, 2022.

[8] Aya Aihara, Victor Mendoza, Anders Goude, and Hans Bernhoff. A numerical study of strut and tower influence on the performance of vertical axis wind turbines using computational fluid dynamics simulation. *Wind Energy*, 25(5):897–913, 2022.

[9] Charles G Alexander, Hudong Chen, Satheesh Kandasamy, Richard A Shock, and Suresh R Govindappa. Simulations of engineering thermal turbulent flows using a lattice boltzmann based algorithm. *ASME-PUBLICATIONS-PVP*, 424:115–126, 2001.

[10] KM Almohammadi, DB Ingham, L Ma, and M Pourkashan. Computational fluid dynamics (cfd) mesh independency techniques for a straight blade vertical axis wind turbine. *Energy*, 58:483–493, 2013.

[11] Shawn Armstrong, Andrzej Fiedler, and Stephen Tullis. Flow separation on a high reynolds number, high solidity vertical axis wind turbine with straight and canted blades and canted blades with fences. *Renewable energy*, 41:13–22, 2012.

[12] Francesco Avallone, Daniele Ragni, and Damiano Casalino. On the effect of the tip-clearance ratio on the aeroacoustics of a diffuser-augmented wind turbine. *Renewable Energy*, 152: 1317–1327, 2020.

[13] Leila N Azadani and Mojtaba Saleh. Effect of blade aspect ratio on the performance of a pair of vertical axis wind turbines. *Ocean Engineering*, 265:112627, 2022.

[14] LN Azadani. Vertical axis wind turbines in cluster configurations. *Ocean Engineering*, 272: 113855, 2023.

[15] P Bachant, A Goude, and M Wosnik. Turbinesfoam/turbinesfoam: v0. 0.8, zenodo, 2018.

[16] Peter Bachant, Martin Wosnik, Budi Gunawan, and Vincent S Neary. Experimental study of a reference model vertical-axis cross-flow turbine. *PloS one*, 11(9):e0163799, 2016.

[17] Christophe Bailly and Daniel Juve. Numerical solution of acoustic propagation problems using linearized euler equations. *AIAA journal*, 38(1):22–29, 2000.

[18] JR Baker. Features to aid or enable self starting of fixed pitch low solidity vertical axis wind turbines. *Journal of Wind Engineering and Industrial Aerodynamics*, 15(1-3):369–380, 1983.

[19] Roel H Bakker, Eja Pedersen, Godefridus Petrus van den Berg, Roy E Stewart, W Lok, and J Bouma. Impact of wind turbine sound on annoyance, self-reported sleep disturbance and psychological distress. *Science of the total environment*, 425:42–51, 2012.

[20] Francesco Balduzzi, Alessandro Bianchini, Ennio Antonio Carnevale, Lorenzo Ferrari, and Sandro Magnani. Feasibility analysis of a darrieus vertical-axis wind turbine installation in the rooftop of a building. *Applied energy*, 97:921–929, 2012.

[21] Francesco Balduzzi, Alessandro Bianchini, Giovanni Ferrara, and Lorenzo Ferrari. Dimensionless numbers for the assessment of mesh and timestep requirements in cfd simulations of darrieus wind turbines. *Energy*, 97:246–261, 2016.

[22] Francesco Balduzzi, David Marten, Alessandro Bianchini, Jernej Drofelnik, Lorenzo Ferrari, Michele Sergio Campobasso, Georgios Pechlivanoglou, Christian Navid Nayeri, Giovanni Ferrara, and Christian Oliver Paschereit. Three-dimensional aerodynamic analysis of a darrieus wind turbine blade using computational fluid dynamics and lifting line theory. *Journal of Engineering for Gas Turbines and Power*, 140(2), 2018.

[23] Galih Bangga, Thorsten Lutz, and Ewald Krämer. Energy assessment of two vertical axis wind turbines in side-by-side arrangement. *Journal of Renewable and Sustainable Energy*, 10(3), 2018.

[24] Galih Bangga, Amgad Dessoky, Zhenlong Wu, Krzysztof Rogowski, and Martin OL Hansen. Accuracy and consistency of cfd and engineering models for simulating vertical axis wind turbine loads. *Energy*, 206:118087, 2020.

[25] Andrew Barnes and Ben Hughes. Determining the impact of vawt farm configurations on power output. *Renewable energy*, 143:1111–1120, 2019.

[26] Andrew Barnes, Daniel Marshall-Cross, and Ben Richard Hughes. Validation and comparison of turbulence models for predicting wakes of vertical axis wind turbines. *Journal of Ocean Engineering and Marine Energy*, 7(4):339–362, 2021.

[27] Srikanth Bashetty and Selahattin Ozcelik. Review on dynamics of offshore floating wind turbine platforms. *Energies*, 14(19):6026, 2021.

[28] L Battisti, L Zanne, S Dell'Anna, Vincenzo Dossena, G Persico, and Berardo Paradiso. Aerodynamic measurements on a vertical axis wind turbine in a large scale wind tunnel. *Journal of energy resources technology*, 133(3), 2011.

[29] L Battisti, G Persico, V Dossena, B Paradiso, M Raciti Castelli, A Brighenti, and E Benini. Experimental benchmark data for h-shaped and troposkien vawt architectures. *Renewable energy*, 125:425–444, 2018.

[30] Leonardo Bergami and Mac Gaunaa. Ateflap aerodynamic model, a dynamic stall model including the effects of trailing edge flap deflection. 2012.

[31] Saman Beyhaghi and Ryoichi S Amano. Analysis of turbulent flow around horizontal axis wind turbines using algebraic stress model. In *ASME International Mechanical Engineering Congress and Exposition*, volume 57502, page V08BT10A018. American Society of Mechanical Engineers, 2015.

[32] Mahendra J Bhagwat and J Gordon Leishman. Stability, consistency and convergence of time-marching free-vortex rotor wake algorithms. *Journal of the American Helicopter Society*, 46(1): 59–71, 2001.

[33] MMSRS Bhargav, Velamati Ratna Kishore, and Vaitla Laxman. Influence of fluctuating wind conditions on vertical axis wind turbine using a three dimensional cfd model. *Journal of Wind Engineering and Industrial Aerodynamics*, 158:98–108, 2016.

[34] Prabhu Lal Bhatnagar, Eugene P Gross, and Max Krook. A model for collision processes in gases. i. small amplitude processes in charged and neutral one-component systems. *Physical review*, 94(3):511, 1954.

[35] Muhammad Mahmood Aslam Bhutta, Nasir Hayat, Ahmed Uzair Farooq, Zain Ali, Sh Rehan Jamil, and Zahid Hussain. Vertical axis wind turbine–a review of various configurations and design techniques. *Renewable and Sustainable Energy Reviews*, 16(4):1926–1939, 2012.

[36] Alessandro Bianchini, Giovanni Ferrara, Lorenzo Ferrari, and Sandro Magnani. An improved model for the performance estimation of an h-darrieus wind turbine in skewed flow. *Wind Engineering*, 36(6):667–686, 2012.

[37] Alessandro Bianchini, Francesco Balduzzi, John M Rainbird, Joaquim Peiro, J Michael R Graham, Giovanni Ferrara, and Lorenzo Ferrari. An experimental and numerical assessment of airfoil polars for use in darrieus wind turbines: Part 1—flow curvature effects. In *Turbo Expo: Power for Land, Sea, and Air*, volume 56802, page V009T46A006. American Society of Mechanical Engineers, 2015.

[38] Alessandro Bianchini, Francesco Balduzzi, Giovanni Ferrara, and Lorenzo Ferrari. Influence of the blade-spoke connection point on the aerodynamic performance of darrieus wind turbines. In *Turbo Expo: Power for Land, Sea, and Air*, volume 49873, page V009T46A012. American Society of Mechanical Engineers, 2016.

[39] Alessandro Bianchini, Francesco Balduzzi, Peter Bachant, Giovanni Ferrara, and Lorenzo Ferrari. Effectiveness of two-dimensional cfd simulations for darrieus vawts: a combined numerical and experimental assessment. *Energy Conversion and Management*, 136:318–328, 2017.

[40] Ben F Blackwell, Robert E Sheldahl, and Louis V Feltz. Wind tunnel performance data for the darrieus wind turbine with naca 0012 blades. Technical report, Sandia Labs., Albuquerque, N. Mex.(USA), 1976.

[41] Jasmin Blanchette and Mark Summerfield. *C++ GUI programming with Qt 4*. Prentice Hall Professional, 2006.

[42] Jay P Boris, Fernando F Grinstein, Elaine S Oran, and Ronald L Kolbe. New insights into large eddy simulation. *Fluid dynamics research*, 10(4-6):199, 1992.

[43] J Botha, A Rasam, D Catháin, H Rice, and A Shahrokhi. Some noise predictions for small wind turbines. In *Proceedings of ISMA*, pages 4019–4032, 2016.

[44] Jason DM Botha. *Predictions of Rotor Broadband Noise*. PhD thesis, Trinity College Dublin, 2018.

[45] JDM Botha, A Shahroki, and H Rice. An implementation of an aeroacoustic prediction model for broadband noise from a vertical axis wind turbine using a cfd informed methodology. *Journal of Sound and Vibration*, 410:389–415, 2017.

[46] Livia Brandetti, Francesco Avallone, Carlos Simao Ferreira, and Damiano Casalino. Aerodynamics and aeroacoustics of a vertical axis wind turbine. In *15th EAWE PhD Seminar on Wind Energy*, 10 2019.

[47] Livia Brandetti, Francesco Avallone, Delphine De Tavernier, Bruce LeBlanc, Carlos Simão Ferreira, and Damiano Casalino. Assessment through high-fidelity simulations of a low-fidelity noise prediction tool for a vertical-axis wind turbine. *Journal of Sound and Vibration*, 547: 117486, 2023.

[48] J Bremseth and K Duraisamy. Computational analysis of vertical axis wind turbine arrays. *Theoretical and Computational Fluid Dynamics*, 30:387–401, 2016.

[49] Kenneth S Brentner and Feri Farassat. Analytical comparison of the acoustic analogy and kirchhoff formulation for moving surfaces. *AIAA journal*, 36(8):1379–1386, 1998.

[50] Kenneth S Brentner and Feridoun Farassat. Modeling aerodynamically generated sound of helicopter rotors. *Progress in aerospace sciences*, 39(2-3):83–120, 2003.

[51] GA Brès, Kenneth Steven Brentner, G Perez, and HE Jones. Maneuvering rotorcraft noise prediction. *Journal of Sound and Vibration*, 275(3-5):719–738, 2004.

[52] Guillaume Brès, Franck Pérot, and David Freed. Properties of the lattice boltzmann method for acoustics. In *15th AIAA/CEAS Aeroacoustics Conference (30th AIAA Aeroacoustics Conference)*, page 3395, 2009.

[53] Thomas F Brooks, D Stuart Pope, and Michael A Marcolini. Airfoil self-noise and prediction. Technical report, 1989.

[54] Ian D Brownstein, Matthias Kinzel, and John O Dabiri. Performance enhancement of downstream vertical-axis wind turbines. *Journal of Renewable and Sustainable Energy*, 8(5), 2016.

[55] Ian D Brownstein, Nathaniel J Wei, and John O Dabiri. Aerodynamically interacting vertical-axis wind turbines: Performance enhancement and three-dimensional flow. *Energies*, 12(14): 2724, 2019.

[56] S Brusca, R Lanzafame, and M Messina. Design of a vertical-axis wind turbine: how the aspect ratio affects the turbine's performance. *International Journal of Energy and Environmental Engineering*, 5(4):333–340, 2014.

[57] Dhawal Buaria, Eberhard Bodenschatz, and Alain Pumir. Vortex stretching and enstrophy production in high reynolds number turbulence. *Physical Review Fluids*, 5(10):104602, 2020.

[58] M Sergio Campobasso and Mohammad H Baba-Ahmadi. Analysis of unsteady flows past horizontal axis wind turbine airfoils based on harmonic balance compressible navier-stokes equations with low-speed preconditioning. In *Turbo Expo: Power for Land, Sea, and Air*, volume 54617, pages 729–745, 2011.

[59] M Sergio Campobasso, Fabio Gigante, and Jernej Drofelnik. Turbulent unsteady flow analysis of horizontal axis wind turbine airfoil aerodynamics based on the harmonic balance reynolds-averaged navier-stokes equations. In *Turbo Expo: Power for Land, Sea, and Air*, volume 45660, page V03BT46A009. American Society of Mechanical Engineers, 2014.

[60] D Casalino. An advanced time approach for acoustic analogy predictions. *Journal of Sound and Vibration*, 261(4):583–612, 2003.

[61] Damiano Casalino, André FP Ribeiro, and Ehab Fares. Facing rim cavities fluctuation modes. *Journal of Sound and Vibration*, 333(13):2812–2830, 2014.

[62] Damiano Casalino, André FP Ribeiro, Ehab Fares, and Swen Nölting. Lattice–boltzmann aeroacoustic analysis of the lagoon landing-gear configuration. *AIAA journal*, 52(6):1232–1248, 2014.

[63] Damiano Casalino, Andreas Hazir, and Adrien Mann. Turbofan broadband noise prediction using the lattice boltzmann method. *AIAA Journal*, 56(2):609–628, 2018.

[64] Damiano Casalino, Wouter C van der Velden, and Gianluca Romani. Community noise of urban air transportation vehicles. In *AIAA Scitech 2019 Forum*, page 1834, 2019.

[65] Marco Raciti Castelli, Stefano De Betta, and Ernesto Benini. Effect of blade number on a straight-bladed vertical-axis darreius wind turbine. *International Journal of Aerospace and Mechanical Engineering*, 6(1):68–74, 2012.

[66] Ishmail B Celik, Urmila Ghia, Patrick J Roache, and Christopher J Freitas. Procedure for estimation and reporting of uncertainty due to discretization in cfd applications. *Journal of fluids Engineering-Transactions of the ASME*, 130(7), 2008.

[67] Ismail B Celik and Jun Li. Assessment of numerical uncertainty for the calculations of turbulent flow over a backward-facing step. *International Journal for Numerical Methods in Fluids*, 49(9):1015–1031, 2005.

[68] IPCC Climate Change et al. Mitigation of climate change. *Contribution of working group III to the fifth assessment report of the intergovernmental panel on climate change*, 1454:147, 2014.

[69] Sydney Chapman and Thomas George Cowling. *The mathematical theory of non-uniform gases: an account of the kinetic theory of viscosity, thermal conduction and diffusion in gases*. Cambridge university press, 1990.

[70] Philippe Chatelain, Matthieu Duponcheel, Denis-Gabriel Caprace, Yves Marichal, and Grégoire Winckelmans. Vortex particle-mesh simulations of vertical axis wind turbine flows: from the airfoil performance to the very far wake. *Wind Energy Science*, 2(1):317–328, 2017.

[71] Hudong Chen, Shiyi Chen, and William H Matthaeus. Recovery of the navier-stokes equations using a lattice-gas boltzmann method. *Physical review A*, 45(8):R5339, 1992.

[72] Hudong Chen, Chris Teixeira, and Kim Molvig. Realization of fluid boundary conditions via discrete boltzmann dynamics. *International Journal of Modern Physics C*, 9(08):1281–1292, 1998.

[73] Hudong Chen, Satheesh Kandasamy, Steven Orszag, Rick Shock, Sauro Succi, and Victor Yakhot. Extended boltzmann kinetic equation for turbulent flows. *Science*, 301(5633):633–636, 2003.

[74] Hudong Chen, Steven A Orszag, Ilya Staroselsky, and Sauro Succi. Expanded analogy between boltzmann kinetic theory of fluids and turbulence. *Journal of Fluid Mechanics*, 519:301–314, 2004.

[75] Hudong Chen, Olga Filippova, James Hoch, Kim Molvig, Rick Shock, Chris Teixeira, and Raoyang Zhang. Grid refinement in lattice boltzmann methods based on volumetric formulation. *Physica A: Statistical Mechanics and its Applications*, 362(1):158–167, 2006.

[76] Hudong Chen, Isaac Goldhirsch, and Steven A Orszag. Discrete rotational symmetry, moment isotropy, and higher order lattice boltzmann models. *Journal of Scientific Computing*, 34:87–112, 2008.

[77] Hudong Chen, Pradeep Gopalakrishnan, and Raoyang Zhang. Recovery of galilean invariance in thermal lattice boltzmann models for arbitrary prandtl number. *International Journal of Modern Physics C*, 25(10):1450046, 2014.

[78] Wei-Hsin Chen, Ching-Ying Chen, Chun-Yen Huang, and Chii-Jong Hwang. Power output analysis and optimization of two straight-bladed vertical-axis wind turbines. *Applied energy*, 185:223–232, 2017.

[79] Yaoran Chen, Limin Kuang, Jie Su, Dai Zhou, Yong Cao, Hao Chen, Zhaolong Han, Yongsheng Zhao, and Shixiao Fu. Investigation of pitch angles on the aerodynamics of twin-vawt under staggered arrangement. *Ocean Engineering*, 254:111385, 2022.

[80] Qian Cheng, Xiaolan Liu, Ho Seong Ji, Kyung Chun Kim, and Bo Yang. Aerodynamic analysis of a helical vertical axis wind turbine. *Energies*, 10(4):575, 2017.

[81] Zhengshun Cheng, Kai Wang, Zhen Gao, and Torgeir Moan. A comparative study on dynamic responses of spar-type floating horizontal and vertical axis wind turbines. *Wind Energy*, 20 (2):305–323, 2017.

[82] Nak Joon Choi, Sang Hyun Nam, Jong Hyun Jeong, and Kyung Chun Kim. Numerical study on the horizontal axis turbines arrangement in a wind farm: Effect of separation distance on the turbine aerodynamic power output. *Journal of Wind Engineering and Industrial Aerodynamics*, 117:11–17, 2013.

[83] FN Coton, RA McD Galbraith, and D Jiang. The influence of detailed blade design on the aerodynamic performance of straight-bladed vertical axis wind turbines. *Proceedings of the Institution of Mechanical Engineers, Part A: Journal of Power and Energy*, 210(1):65–74, 1996.

[84] GWEC – Global Wind Energy Council. Global wind report 2023. *Available online at: https://gwec.net/globalwindreport2023/*, 2023.

[85] Curious.Earth. 30 of the most impactful climate change quotes. *Available online at: https://curious.earth/blog/climate-change-quotes/*.

[86] N Curle. The influence of solid boundaries upon aerodynamic sound. *Proceedings of the Royal Society of London. Series A. Mathematical and Physical Sciences*, 231(1187):505–514, 1955.

[87] John O Dabiri. Potential order-of-magnitude enhancement of wind farm power density via counter-rotating vertical-axis wind turbine arrays. *Journal of renewable and sustainable energy*, 3(4):043104, 2011.

[88] Javier Damota, MI Lamas, Antonio Couce-Casanova, and JuanDeDios Rodriguez-Garcia. Vertical axis wind turbines: Current technologies and future trends. In *International conference on renewable energies and power quality (ICREPQ'15)*, volume 1, pages 530–535, 2015.

[89] Agostino De Marco, Domenico P Coiro, Domenico Cucco, Fabrizio Nicolosi, et al. A numerical study on a vertical-axis wind turbine with inclined arms. *International Journal of Aerospace Engineering*, 2014, 2014.

[90] D De Tavernier, Carlos Ferreira, Ang Li, US Paulsen, and HA Madsen. Towards the understanding of vertical-axis wind turbines in double-rotor configuration. In *Journal of Physics: Conference Series*, volume 1037, page 022015. IOP Publishing, 2018.

[91] D De Tavernier, Carlos Ferreira, U Paulsen, and H Madsen. The 3d effects of a vertical-axis wind turbine: rotor and wake induction. In *Journal of Physics: Conference Series*, volume 1618, page 052040. IOP Publishing, 2020.

[92] DAM De Tavernier. Aerodynamic advances in vertical-axis wind turbines. 2021.

[93] Delphine De Tavernier, Carlos Simao Ferreira, Ang Li, Uwe S Paulsen, and Helge A Madsen. Vawt in double-rotor configuration: the effect on airfoil design. In *2018 Wind Energy Symposium*, page 0992, 2018.

[94] Pierre-Luc Delafin, Takafumi Nishino, Lin Wang, and Athanasios Kolios. Effect of the number of blades and solidity on the performance of a vertical axis wind turbine. In *Journal of Physics: Conference Series*, volume 753, page 022033. IOP Publishing, 2016.

[95] Jan W Delfs, Marcus Bauer, Roland Ewert, Herwig A Grogger, Markus Lummer, and Thomas GW Lauke. Numerical simulation of aerodynamic noise with dlr's aeroacoustic code piano. 2008.

[96] Energy & Industrial Strategy Department for Business. Offshore wind energy revolution to provide a third of all uk electricity by 2030. *2020-02-24. https://www.gov.uk/government/news/offshore-wind-energy-revolution-to-provide-a-third-of-all-uk-electricity-by-2030.*

[97] Amgad Dessoky, Galih Bangga, Thorsten Lutz, and Ewald Krämer. Aerodynamic and aeroacoustic performance assessment of h-rotor darrieus vawt equipped with wind-lens technology. *Energy*, 175:76–97, 2019.

[98] Patrick Devine-Wright. Beyond nimbyism: towards an integrated framework for understanding public perceptions of wind energy. *Wind Energy: An International Journal for Progress and Applications in Wind Power Conversion Technology*, 8(2):125–139, 2005.

[99] Dominique d'Humieres. Generalized lattice-boltzmann equations. *Rarefied gas dynamics*, 1992.

[100] P Di Francescantonio. A new boundary integral formulation for the prediction of sound radiation. *Journal of Sound and Vibration*, 202(4):491–509, 1997.

[101] John Keithley Difuntorum and Louis Angelo M Danao. Improving vawt performance through parametric studies of rotor design configurations using computational fluid dynamics. *Proceedings of the Institution of Mechanical Engineers, Part A: Journal of Power and Energy*, 233 (4):489–509, 2019.

[102] R Dominy, P Lunt, A Bickerdyke, and J Dominy. Self-starting capability of a darrieus turbine. *Proceedings of the Institution of Mechanical Engineers, Part A: Journal of Power and Energy*, 221(1):111–120, 2007.

[103] Sally Dray. Climate change targets: the road to net zero? *UK Parliment, May*, 24, 2021.

[104] Mark Drela. Xfoil: An analysis and design system for low reynolds number airfoils. In *Low Reynolds number aerodynamics*, pages 1–12. Springer, 1989.

[105] Longhuan Du, Grant Ingram, and Robert G Dominy. Experimental study of the effects of turbine solidity, blade profile, pitch angle, surface roughness, and aspect ratio on the h-darrieus wind turbine self-starting and overall performance. *Energy Science & Engineering*, 7(6):2421–2436, 2019.

[106] Longhuan Du, Grant Ingram, and Robert G Dominy. A review of h-darrieus wind turbine aerodynamic research. *Proceedings of the Institution of Mechanical Engineers, Part C: Journal of Mechanical Engineering Science*, 233(23-24):7590–7616, 2019.

[107] Horia Dumitrescu, Vladimir Cardos, Alexandru Dumitrache, and Florin Frunzulica. Low-frequency noise prediction of vertical axis wind turbines. *Proceedings of the Romanian Academy*, 11(1):47–54, 2010.

[108] Elise Dupont, Rembrandt Koppelaar, and Hervé Jeanmart. Global available wind energy with physical and energy return on investment constraints. *Applied Energy*, 209:322–338, 2018.

[109] Thirumalai Duraisamy, Daniel NT Hay, Louis Messerle, and Abdessadek Lachgar. Octahedral hexatantalum halide clusters. *Inorganic Syntheses: Volume 36*, pages 1–7, 2014.

[110] Okeoghene Eboibi, Louis Angelo M Danao, and Robert J Howell. Experimental investigation of the influence of solidity on the performance and flow field aerodynamics of vertical axis wind turbines at low reynolds numbers. *Renewable Energy*, 92:474–483, 2016.

[111] Rami Ahmad El-Nabulsi and Waranont Anukool. Fractal dimensions in fluid dynamics and their effects on the rayleigh problem, the burger's vortex and the kelvin–helmholtz instability. *Acta Mechanica*, 233(1):363–381, 2022.

[112] M Elkhoury, T Kiwata, and E Aoun. Experimental and numerical investigation of a three-dimensional vertical-axis wind turbine with variable-pitch. *Journal of wind engineering and Industrial aerodynamics*, 139:111–123, 2015.

[113] M Dolores Esteban, J Javier Diez, Jose S López, and Vicente Negro. Why offshore wind energy? *Renewable energy*, 36(2):444–450, 2011.

[114] Jordi Estevadeordal, Steven E Gorrell, and William W Copenhaver. Piv study of wake-rotor interactions in a transonic compressor at various operating conditions. *Journal of propulsion and power*, 23(1):235–242, 2007.

[115] Aidan Cronin (ETIPWind). The way forward for offshore wind possible scenarios. *Available online at: https://www.sintef.no/globalassets/project/eera-deepwind-2019/presentations/closing$_c$ronin.pdf*, 2019.

[116] F Farassat and George P Succi. The prediction of helicopter rotor discrete frequency noise. *In: American Helicopter Society*, pages 497–507, 1982.

[117] Ehab Fares, Damiano Casalino, and Mehdi R Khorrami. Evaluation of airframe noise reduction concepts via simulations using a lattice boltzmann approach. In *21st AIAA/CEAS Aeroacoustics Conference*, page 2988, 2015.

[118] Ahmad Fazlizan, Mohd Azimin Elias, Mohd Fadhli, Wan Khairul Muzammil, and Mohd Azlan Ismail. Skewed wind flows and the performance of wind energy devices on rooftops: A review.

[119] Ahmad Fazlizan, Wan Khairul Muzammil, Mohd Azlan Ismail, Mohd Fadhli Ramlee, and Adnan Ibrahim. Skewed wind flows energy exploitation in built environment. *Alam Cipta*, 12: 53–60, 2019.

[120] C Ferreira, G Van Bussel, and G Van Kuik. An analytical method to predict the variation in performance of a h-darrieus in skewed flow and its experimental validation. In *Proceedings of the European Wind Energy Conference 2006*. Athens, 2006.

[121] C Simao Ferreira, H Aagaard Madsen, Matthew Barone, Björn Roscher, Paul Deglaire, and Igor Arduin. Comparison of aerodynamic models for vertical axis wind turbines. In *Journal of Physics: Conference Series*, volume 524, page 012125. IOP Publishing, 2014.

[122] Kevin James Ferrigno. *Challenges and strategies for increasing adoption of small wind turbines in urban areas*. PhD thesis, Massachusetts Institute of Technology, 2010.

[123] Andrzej J Fiedler and Stephen Tullis. Blade offset and pitch effects on a high solidity vertical axis wind turbine. *Wind engineering*, 33(3):237–246, 2009.

[124] Masoud Ghasemian and Amir Nejat. Aero-acoustics prediction of a vertical axis wind turbine using large eddy simulation and acoustic analogy. *Energy*, 88:711–717, 2015.

[125] Tarek A Ghonim, AM Nebiewa, and WA El-Askary. Effect of aspect ratio on self-starting capability of darrieus rotor.

[126] Simone Giorgetti, Giulio Pellegrini, and Stefania Zanforlin. Cfd investigation on the aerodynamic interferences between medium-solidity darrieus vertical axis wind turbines. *Energy Procedia*, 81:227–239, 2015.

[127] Stewart Glegg and William Devenport. *Aeroacoustics of low Mach number flows: fundamentals, analysis, and measurement*. Academic Press, 2017.

[128] Tuhfe Göçmen and Barış Özerdem. Airfoil optimization for noise emission problem and aerodynamic performance criterion on small scale wind turbines. *Energy*, 46(1):62–71, 2012.

[129] Benjamin Goldman and Kenneth Brentner. New algorithms for reduced memory and real-time noise prediction. In *18th AIAA/CEAS Aeroacoustics Conference (33rd AIAA Aeroacoustics Conference)*, page 2237, 2012.

[130] Ignacio Gonzalez-Martino and Damiano Casalino. Fan tonal and broadband noise simulations at transonic operating conditions using lattice-boltzmann methods. In *2018 AIAA/CEAS aeroacoustics conference*, page 3919, 2018.

[131] Emil Göttlich, Jakob Woisetschläger, Paul Pieringer, Bernd Hampel, and Franz Heitmeir. Investigation of vortex shedding and wake-wake interaction in a transonic turbine stage using laser-doppler-velocimetry and particle-image-velocimetry. 2006.

[132] Harold Grad. Note on n-dimensional hermite polynomials. *Communications on Pure and Applied Mathematics*, 2(4):325–330, 1949.

[133] The Guardian. Wind turbines in the southern lake district in the uk. *Available online at: https://www.theguardian.com/environment/2023/feb/28/fears-grow-government-will-renege-on-lifting-onshore-windfarm-ban-in-england*.

[134] M Guilbot, S Barre, G Balarac, C Bonamy, and N Guillaud. A numerical study of vertical axis wind turbine performances in twin-rotor configurations. In *Journal of Physics: Conference Series*, volume 1618, page 052012. IOP Publishing, 2020.

[135] Brian Hand and Andrew Cashman. Aerodynamic modeling methods for a large-scale vertical axis wind turbine: A comparative study. *Renewable Energy*, 129:12–31, 2018.

[136] Morten Hartvig Hansen, Mac Gaunaa, and Helge Aagaard Madsen. *A Beddoes-Leishman type dynamic stall model in state-space and indicial formulations*. 2004.

[137] Yutaka Hara, Naoki Horita, Shigeo Yoshida, Hiromichi Akimoto, and Takahiro Sumi. Numerical analysis of effects of arms with different cross-sections on straight-bladed vertical axis wind turbine. *Energies*, 12(11):2106, 2019.

[138] Yutaka Hara, Yoshifumi Jodai, Tomoyuki Okinaga, and Masaru Furukawa. Numerical analysis of the dynamic interaction between two closely spaced vertical-axis wind turbines. *Energies*, 14(8):2286, 2021.

[139] SM Rakibul Hassan, Mohammad Ali, and Md Quamrul Islam. The effect of solidity on the performance of h-rotor darrieus turbine. In *AIP Conference Proceedings*, volume 1754, page 040012. AIP Publishing LLC, 2016.

[140] Xiaoyi He and Li-Shi Luo. Lattice boltzmann model for the incompressible navier–stokes equation. *Journal of statistical Physics*, 88:927–944, 1997.

[141] JV Healey. Tandem-disk theory-with particular reference to vertical axis wind turbines. *Journal of Energy*, 5(4):251–254, 1981.

[142] JV Healy. The influence of blade thickness on the output of vertical axis wind turbines. *Wind Engineering*, pages 1–9, 1978.

[143] Seyed Hossein Hezaveh, Elie Bou-Zeid, John Dabiri, Matthias Kinzel, Gerard Cortina, and Luigi Martinelli. Increasing the power production of vertical-axis wind-turbine farms using synergistic clustering. *Boundary-layer meteorology*, 169:275–296, 2018.

[144] David Hilbert. Begründung der kinetischen gastheorie. *Mathematische Annalen*, 72(4):562–577, 1912.

[145] N Hill, R Dominy, G Ingram, and J Dominy. Darrieus turbines: the physics of self-starting. *Proceedings of the Institution of Mechanical Engineers, Part A: Journal of Power and Energy*, 223(1):21–29, 2009.

[146] Kevin R Holst, Ryan S Glasby, and Ryan B Bond. On the effect of temporal error in high-order simulations of unsteady flows. *Journal of Computational Physics*, 402:108989, 2020.

[147] T Hommes, J Bosschers, and HWM Hoeijmakers. Evaluation of the radial pressure distribution of vortex models and comparison with experimental data. In *Journal of Physics: Conference Series*, volume 656, page 012182. IOP Publishing, 2015.

[148] Robert Howell, Ning Qin, Jonathan Edwards, and Naveed Durrani. Wind tunnel and numerical study of a small vertical axis wind turbine. *Renewable energy*, 35(2):412–422, 2010.

[149] Ahmed Khalid Ibrahim and Ramiz Ibraheem Saeed. A comprehensive review of vertical axis wind turbines for urban usage. 2022.

[150] Tomoaki Ikeda, Shunji Enomoto, Kazuomi Yamamoto, and Kazuhisa Amemiya. Quadrupole corrections for the permeable-surface ffowcs williams–hawkings equation. *AIAA Journal*, 55 (7):2307–2320, 2017.

[151] World Resources Institute. Country greenhouse gas emissions data (1990-2016). *Available online at: http://cait.wri.org*, 2019.

[152] Mazharul Islam, M Amin, David Ting, and Amir Fartaj. A new airfoil for the supporting struts of smaller-capacity straight-bladed vawt. In *12th AIAA/ISSMO Multidisciplinary Analysis and Optimization Conference*, page 5874, 2008.

[153] Mazharul Islam, M Amin, David Ting, and Amir Fartaj. Performance analysis of a smaller-capacity straight-bladed vawt with prospective airfoils. In *46th AIAA aerospace sciences meeting and exhibit*, page 1333, 2008.

[154] Mazharul Islam, Amir Fartaj, and Rupp Carriveau. Analysis of the design parameters related to a fixed-pitch straight-bladed vertical axis wind turbine. *Wind engineering*, 32(5):491–507, 2008.

[155] Guoqing Jin, Zhi Zong, Yichen Jiang, and Li Zou. Aerodynamic analysis of side-by-side placed twin vertical-axis wind turbines. *Ocean Engineering*, 209:107296, 2020.

[156] Xin Jin, Gaoyuan Zhao, KeJun Gao, and Wenbin Ju. Darrieus vertical axis wind turbine: Basic research methods. *Renewable and Sustainable Energy Reviews*, 42:212–225, 2015.

[157] Xin Jin, Yaming Wang, Wenbin Ju, Jiao He, and Shuangyi Xie. Investigation into parameter influence of upstream deflector on vertical axis wind turbines output power via three-dimensional cfd simulation. *Renewable Energy*, 115:41–53, 2018.

[158] Yoshifumi Jodai and Yutaka Hara. Wind tunnel experiments on interaction between two closely spaced vertical-axis wind turbines in side-by-side arrangement. *Energies*, 14(23):7874, 2021.

[159] Robert Thomas Jones. *Wing theory*, volume 1052. Princeton University Press, 2014.

[160] Franklyn Kanyako and Isam Janajreh. Vertical axis wind turbine performance prediction for low wind speed environment. In *2014 IEEE Innovations in Technology Conference*, pages 1–10. IEEE, 2014.

[161] Vishal Kaushik and R Naren Shankar. Review of experimental approaches for the analysis of aerodynamic performance of vertical axis wind turbines. In *Innovative Design, Analysis and Development Practices in Aerospace and Automotive Engineering*, pages 473–480. Springer, 2021.

[162] Mehdi R Khorrami, Ehab Fares, and Damiano Casalino. Towards full aircraft airframe noise prediction: lattice boltzmann simulations. In *20th AIAA/CEAS aeroacoustics conference*, page 2481, 2014.

[163] Daegyoum Kim and Morteza Gharib. Efficiency improvement of straight-bladed vertical-axis wind turbines with an upstream deflector. *Journal of Wind Engineering and Industrial Aerodynamics*, 115:48–52, 2013.

[164] Brian K Kirke and Benoit Paillard. Predicted and measured performance of a vertical axis wind turbine with passive variable pitch compared to fixed pitch. *Wind Engineering*, 41(1):74–90, 2017.

[165] Brian Kinloch Kirke. *Evaluation of self-starting vertical axis wind turbines for stand-alone applications*. PhD thesis, Griffith University Australia, 1998.

[166] Jon Kjellin, Fredrik Bülow, Sandra Eriksson, Paul Deglaire, Mats Leijon, and Hans Bernhoff. Power coefficient measurement on a 12 kw straight bladed vertical axis wind turbine. *Renewable energy*, 36(11):3050–3053, 2011.

[167] Ronny Klæboe and Hanne Beate Sundfør. Windmill noise annoyance, visual aesthetics, and attitudes towards renewable energy sources. *International journal of environmental research and public health*, 13(8):746, 2016.

[168] Annette Claudia Klein, Sirko Bartholomay, David Marten, Thorsten Lutz, George Pechlivanoglou, Christian Navid Nayeri, Christian Oliver Paschereit, and Ewald Krämer. About the suitability of different numerical methods to reproduce model wind turbine measurements in a wind tunnel with a high blockage ratio. *Wind Energy Science*, 3(1):439–460, 2018.

[169] Paul C Klimas and Mark H Worstell. Effects of blade preset pitch/offset on curved-blade darrieus vertical axis wind turbine performance. 1981.

[170] Rupesh B Kotapati, Richard Shock, and Hudong Chen. Lattice-boltzmann simulations of flows over backward-facing inclined steps. *International Journal of Modern Physics C*, 25(01): 1340021, 2014.

[171] Timm Krüger, Halim Kusumaatmaja, Alexandr Kuzmin, Orest Shardt, Goncalo Silva, and Erlend Magnus Viggen. The lattice boltzmann method. *Springer International Publishing*, 10 (978-3):4–15, 2017.

[172] Rakesh Kumar, Kaamran Raahemifar, and Alan S Fung. A critical review of vertical axis wind turbines for urban applications. *Renewable and Sustainable Energy Reviews*, 89:281–291, 2018.

[173] HC Kuo, LY Lin, CP Chang, and RT Williams. The formation of concentric vorticity structures in typhoons. *Journal of the atmospheric sciences*, 61(22):2722–2734, 2004.

[174] HF Lam and HY Peng. Study of wake characteristics of a vertical axis wind turbine by two- and three-dimensional computational fluid dynamics simulations. *Renewable Energy*, 90: 386–398, 2016.

[175] HF Lam and HY Peng. Measurements of the wake characteristics of co-and counter-rotating twin h-rotor vertical axis wind turbines. *Energy*, 131:13–26, 2017.

[176] HF Lam, YM Liu, HY Peng, CF Lee, and HJ Liu. Assessment of solidity effect on the power performance of h-rotor vertical axis wind turbines in turbulent flows. *Journal of Renewable and Sustainable Energy*, 10(2):023304, 2018.

[177] Yejun Lao, Mario A Rotea, Justin P Koeln, Mohammad S Sakib, and D Todd Griffith. Economic nonlinear model predictive control of offshore vertical-axis wind turbines. In *2022 American Control Conference (ACC)*, pages 3518–3525. IEEE, 2022.

[178] Brian Edward Launder and Dudley Brian Spalding. The numerical computation of turbulent flows. In *Numerical prediction of flow, heat transfer, turbulence and combustion*, pages 96–116. Elsevier, 1983.

[179] Bruce Leblanc and Carlos Ferreira. Experimental demonstration of thrust vectoring with a vertical axis wind turbine using normal load measurements. In *Journal of Physics: Conference Series*, volume 1618, page 052030. IOP Publishing, 2020.

[180] Bruce LeBlanc and Carlos Ferreira. Estimation of blade loads for a variable pitch vertical axis wind turbine from particle image velocimetry. *Wind Energy*, 2021.

[181] Bruce LeBlanc and Carlos Ferreira. Estimation of blade loads for a variable pitch vertical axis wind turbine from particle image velocimetry. *Wind Energy*, 25(2):313–332, 2022.

[182] Bruce LeBlanc and Carlos Simao Ferreira. Overview and design of pitchvawt: Vertical axis wind turbine with active variable pitch for experimental and numerical comparison. In *2018 Wind Energy Symposium*, page 1243, 2018.

[183] Bruce P LeBlanc and Carlos Simao Ferreira. Experimental determination of thrust loading of a 2-bladed vertical axis wind turbine. In *Journal of Physics: Conference Series*, volume 1037, page 022043. IOP Publishing, 2018.

[184] Choong Hee Lee, Seung Yong Min, Cheon Jin Park, and Seung Jo Kim. Optimal design and verification tests of cycloidal vertical axis wind turbine. *Journal of Renewable and Sustainable Energy*, 7(6):063116, 2015.

[185] Kung-Yen Lee, Shao-Hua Tsao, Chieh-Wen Tzeng, and Huei-Jeng Lin. Influence of the vertical wind and wind direction on the power output of a small vertical-axis wind turbine installed on the rooftop of a building. *Applied Energy*, 209:383–391, 2018.

[186] Hang Lei, Dai Zhou, Jiabao Lu, Caiyong Chen, Zhaolong Han, and Yan Bao. The impact of pitch motion of a platform on the aerodynamic performance of a floating vertical axis wind turbine. *Energy*, 119:369–383, 2017.

[187] Gordon J Leishman. *Principles of helicopter aerodynamics with CD extra*. Cambridge university press, 2006.

[188] Sanjiva K Lele and Joseph W Nichols. A second golden age of aeroacoustics? *Philosophical Transactions of the Royal Society A: Mathematical, Physical and Engineering Sciences*, 372 (2022):20130321, 2014.

[189] Chao Li, Songye Zhu, You-lin Xu, and Yiqing Xiao. 2.5 d large eddy simulation of vertical axis wind turbine in consideration of high angle of attack flow. *Renewable energy*, 51:317–330, 2013.

[190] Chao Li, Yiqing Xiao, You-lin Xu, Yi-xin Peng, Gang Hu, and Songye Zhu. Optimization of blade pitch in h-rotor vertical axis wind turbines through computational fluid dynamics simulations. *Applied Energy*, 212:1107–1125, 2018.

[191] Q Li, T Maeda, Y Kamada, J Murata, T Kawabata, K Furukawa, and T Kogaki. Effect of blade number on flow around straight-bladed vertical axis wind turbine. *Transactions of the JSME (in Japanese)*, 80(816), 2014.

[192] Shengmao Li and Yan Li. Numerical study on the performance effect of solidity on the straight-bladed vertical axis wind turbine. In *2010 Asia-Pacific power and energy engineering conference*, pages 1–4. IEEE, 2010.

[193] Shoutu Li, Ye Li, Congxin Yang, Qiang Wang, Bin Zhao, Deshun Li, Ruiwen Zhao, Tongxin Ren, Xiaobo Zheng, Zhiteng Gao, et al. Experimental investigation of solidity and other characteristics on dual vertical axis wind turbines in an urban environment. *Energy Conversion and Management*, 229:113689, 2021.

[194] Yan Li, Kotaro Tagawa, and Wei Liu. Performance effects of attachment on blade on a straight-bladed vertical axis wind turbine. *Current Applied Physics*, 10(2):S335–S338, 2010.

[195] Michael James Lighthill. On sound generated aerodynamically i. general theory. *Proceedings of the Royal Society of London. Series A. Mathematical and Physical Sciences*, 211(1107):564–587, 1952.

[196] LEM Lignarolo, D Ragni, F Scarano, CJ Simão Ferreira, and GJW Van Bussel. Tip-vortex instability and turbulent mixing in wind-turbine wakes. *Journal of Fluid Mechanics*, 781:467–493, 2015.

[197] San-Yih Lin, Yang-You Lin, Chi-Jeng Bai, and Wei-Cheng Wang. Performance analysis of vertical-axis-wind-turbine blade with modified trailing edge through computational fluid dynamics. *Renewable Energy*, 99:654–662, 2016.

[198] David Lockard and Jay Casper. Permeable surface corrections for ffowcs williams and hawkings integrals. In *11th AIAA/CEAS Aeroacoustics Conference*, page 2995, 2005.

[199] David P Lockard. Reprint of: In search of grid converged solutions. *Procedia IUTAM*, 1:224–233, 2010.

[200] Leonard V Lopes, David D Boyd Jr, Douglas M Nark, and Karl E Wiedemann. Identification of spurious signals from permeable ffowcs williams and hawkings surfaces. In *American Helicopter Society (AHS) International Annual Forum and Technology Display*, number NF1676L-25336, 2017.

[201] Willie Lu. Aerodynamic modelling of vertical axis wind turbine struts: Using the lifting line method cactus. 2020.

[202] Anastasios S Lyrintzis. Surface integral methods in computational aeroacoustics—from the (cfd) near-field to the (acoustic) far-field. *International journal of aeroacoustics*, 2(2):95–128, 2003.

[203] David JC MacKay. *Sustainable Energy-without the hot air*. Bloomsbury Publishing, 2016.

[204] Helge Aagaard Madsen. The actuator cylinder: A flow model for vertical axis wind turbines. Technical report, Institute of Industrial Constructions and Energy Technology, Aalborg University Centre, Denmark, 1982.

[205] Helge Aagaard Madsen. *On the ideal and real energy conversion in a straight bladed vertical axis wind turbine*. Institute of Industrial Constructions and Energy Technology, Aalborg ..., 1983.

[206] Takao Maeda, Yasunari Kamada, Junsuke Murata, Kazuma Furukawa, Masayuki Yamamoto, et al. Effect of number of blades on aerodynamic forces on a straight-bladed vertical axis wind turbine. *Energy*, 90:784–795, 2015.

[207] Takao Maeda, Yasunari Kamada, Junsuke Murata, Kento Shimizu, Tatsuhiko Ogasawara, Alisa Nakai, Takuji Kasuya, et al. Effect of solidity on aerodynamic forces around straight-bladed vertical axis wind turbine by wind tunnel experiments (depending on number of blades). *Renewable energy*, 96:928–939, 2016.

[208] Takao Maeda, Yasunari Kamada, Kento Shimizu, Tatsuhiko Ogasawara, Alisa Nakai, Takuji Kasuya, et al. Effect of rotor aspect ratio and solidity on a straight-bladed vertical axis wind turbine in three-dimensional analysis by the panel method. *Energy*, 121:1–9, 2017.

[209] Michel Make and Guilherme Vaz. Analyzing scaling effects on offshore wind turbines using cfd. *Renewable Energy*, 83:1326–1340, 2015.

[210] James F Manwell, Jon G McGowan, and Anthony L Rogers. *Wind energy explained: theory, design and application*. John Wiley & Sons, 2010.

[211] Carlos Henrique Marchi, Márcio André Martins, Leandro Alberto Novak, Luciano Kiyoshi Araki, Márcio Augusto Villela Pinto, Simone de Fátima Tomazzoni Gonçalves, Diego Fernando Moro, and Inajara da Silva Freitas. Polynomial interpolation with repeated richardson extrapolation to reduce discretization error in cfd. *Applied Mathematical Modelling*, 40(21-22): 8872–8885, 2016.

[212] Darrieus Georges Jean Marie. Turbine having its rotating shaft transverse to the flow of the current, December 8 1931. US Patent 1,835,018.

[213] Simon Marié, Denis Ricot, and Pierre Sagaut. Comparison between lattice boltzmann method and navier–stokes high order schemes for computational aeroacoustics. *Journal of Computational Physics*, 228(4):1056–1070, 2009.

[214] Philip Marsh, Dev Ranmuthugala, Irene Penesis, and Giles Thomas. Three-dimensional numerical simulations of straight-bladed vertical axis tidal turbines investigating power output, torque ripple and mounting forces. *Renewable Energy*, 83:67–77, 2015.

[215] David Marten. Qblade: a modern tool for the aeroelastic simulation of wind turbines. 2020.

[216] David Marten and Juliane Wendler. Qblade guidelines. *Ver. 0.6, Technical University of (TU Berlin), Berlin, Germany*, 2013.

[217] David Marten, Georgios Pechlivanoglou, Christian Navid Nayeri, and Christian Oliver Paschereit. Nonlinear lifting line theory applied to vertical axis wind turbines: Development of a practical design tool. *Journal of Fluids Engineering*, 140(2), 2018.

[218] Marco Mauri, I Bayati, and M Belloli. Design and realisation of a high-performance active pitch-controlled h-darrieus vawt for urban installations. In *3rd Renewable power generation conference (RPG 2014)*, pages 1–6. IET, 2014.

[219] Simon Charles McIntosh. *Wind energy for the built environment*. PhD thesis, University of Cambridge, 2009.

[220] Andrés Meana-Fernández, Jesus Manuel Fernandez Oro, Katia María Argüelles Díaz, Mónica Galdo-Vega, and Sandra Velarde-Suárez. Application of richardson extrapolation method to the cfd simulation of vertical-axis wind turbines and analysis of the flow field. *Engineering Applications of Computational Fluid Mechanics*, 13(1):359–376, 2019.

[221] S Mendez, M Shoeybi, SK Lele, and P Moin. On the use of the ffowcs williams-hawkings equation to predict far-field jet noise from large-eddy simulations. *International Journal of Aeroacoustics*, 12(1-2):1–20, 2013.

[222] Victor Mendoza, Peter Bachant, Carlos Ferreira, and Anders Goude. Near-wake flow simulation of a vertical axis turbine using an actuator line model. *Wind Energy*, 22(2):171–188, 2019.

[223] J-L Menet. A double-step savonius rotor for local production of electricity: a design study. *Renewable energy*, 29(11):1843–1862, 2004.

[224] Long Meng, Yan-ping He, Jun Wu, Yong-sheng Zhao, and Zi-wei Guo. Simulation of tower shadow effect for offshore wind turbine by cfd method. In *The 26th International Ocean and Polar Engineering Conference*. OnePetro, 2016.

[225] Riccardo Mereu, D Federici, G Ferrari, Paolo Schito, and Fabio Inzoli. Parametric numerical study of savonius wind turbine interaction in a linear array. *Renewable Energy*, 113:1320–1332, 2017.

[226] Sander Mertens, Gijs van Kuik, and Gerard van Bussel. Performance of an h-darrieus in the skewed flow on a roof. *J. Sol. Energy Eng.*, 125(4):433–440, 2003.

[227] Sander Mertens, Gijs van Kuik, and Gerard van Bussel. Performance of a high tip speed ratio h-darrieus in the skewed flow on a roof. In *Wind Energy Symposium*, volume 75944, pages 136–145, 2003.

[228] Weipao Miao, Qingsong Liu, Qiang Zhang, Zifei Xu, Chun Li, Minnan Yue, Wanfu Zhang, and Zhou Ye. Recommendation for strut designs of vertical axis wind turbines: Effects of strut profiles and connecting configurations on the aerodynamic performance. *Energy Conversion and Management*, 276:116436, 2023.

[229] Daniel Micallef and Abdolrahim Rezaeiha. Floating offshore wind turbine aerodynamics: Trends and future challenges. *Renewable and Sustainable Energy Reviews*, 152:111696, 2021.

[230] Daniel Micallef and Gerard Van Bussel. A review of urban wind energy research: aerodynamics and other challenges. *Energies*, 11(9):2204, 2018.

[231] Luc Mieussens and Henning Struchtrup. Numerical comparison of bhatnagar–gross–krook models with proper prandtl number. *Physics of Fluids*, 16(8):2797–2813, 2004.

[232] PG Migliore, WP Wolfe, and JB Fanucci. Flow curvature effects on darrieus turbine blade aerodynamics. *Journal of Energy*, 4(2):49–55, 1980.

[233] Charles Mockett, Werner Haase, and Dieter Schwamborn. Go4hybrid: Grey area mitigation for hybrid rans-les methods, 2018.

[234] MH Mohamed. Performance investigation of h-rotor darrieus turbine with new airfoil shapes. *Energy*, 47(1):522–530, 2012.

[235] MH Mohamed. Impacts of solidity and hybrid system in small wind turbines performance. *Energy*, 57:495–504, 2013.

[236] MH Mohamed. Aero-acoustics noise evaluation of h-rotor darrieus wind turbines. *Energy*, 65:596–604, 2014.

[237] MH Mohamed. Reduction of the generated aero-acoustics noise of a vertical axis wind turbine using cfd (computational fluid dynamics) techniques. *Energy*, 96:531–544, 2016.

[238] MH Mohamed. Criticism study of j-shaped darrieus wind turbine: Performance evaluation and noise generation assessment. *Energy*, 177:367–385, 2019.

[239] Erik Möllerström, Sebastian Larsson, Fredric Ottermo, Jonny Hylander, and Lars Bååth. Noise propagation from a vertical axis wind turbine. In *inter. noise 2014, 43rd International Congress on Noise Control Engineering, Melbourne, Australia, November 16-19, 2014*. Australian Acoustical Society, 2014.

[240] Erik Möllerström, Fredric Ottermo, Jonny Hylander, and Hans Bernhoff. Noise emission of a 200 kw vertical axis wind turbine. *Energies*, 9(1):19, 2016.

[241] Björn Montgomerie. Methods for root effects, tip effects and extending the angle of attack range to±180, with application to aerodynamics for blades on wind turbines and propellers. *FOI, Swedish Defence Research Agency, Stockholm, Sweden, Report No. FOI*, 2004.

[242] Patrick J Moriarty and A Craig Hansen. Aerodyn theory manual. Technical report, National Renewable Energy Lab., Golden, CO (US), 2005.

[243] Stephanie Müller, Valentine Muhawenimana, Catherine AME Wilson, and Pablo Ouro. Experimental investigation of the wake characteristics behind twin vertical axis turbines. *Energy Conversion and Management*, 247:114768, 2021.

[244] Jonathan Murray and Matthew Barone. The development of cactus, a wind and marine turbine performance simulation code. In *49th AIAA Aerospace Sciences Meeting including the New Horizons Forum and Aerospace Exposition*, page 147, 2011.

[245] PJ Musgrove. Energy from wind in rural and urban communities. *Passive and Low Energy Ecotechniques*, pages 290–309, 1985.

[246] PJ Musgrove. Wind energy conversion: recent progress and future prospects. *Solar & wind technology*, 4(1):37–49, 1987.

[247] NASA. Global climate change: vital signs of the planet. *Available online at: https://climate.nasa.gov/*.

[248] BG Newman. Actuator-disc theory for vertical-axis wind turbines. *Journal of Wind Engineering and Industrial Aerodynamics*, 15(1-3):347–355, 1983.

[249] P. Tans (NOAA/GML) and R. Keeling (Scripps Institution of Oceanography). Trends in atmospheric carbon dioxide. *Available online at: https://gml.noaa.gov/ccgg/trends/ and https://scrippsco2.ucsd.edu/*.

[250] C Olendraru and Antoine Sellier. Viscous effects in the absolute–convective instability of the batchelor vortex. *Journal of Fluid Mechanics*, 459:371–396, 2002.

[251] AS Olsen, NN Sørensen, C Bak, M Gaunaa, R Mikkelsen, A Fischer, J Beckerlee, and S Ildvedsen. Why is the measured maximum lift in wind tunnels dependent on the measurement method? In *Journal of Physics: Conference Series*, volume 1618, page 032040. IOP Publishing, 2020.

[252] A Orlandi, M Collu, Stefania Zanforlin, and A Shires. 3d urans analysis of a vertical axis wind turbine in skewed flows. *Journal of Wind Engineering and Industrial Aerodynamics*, 147:77–84, 2015.

[253] Pablo Ouro. Seatwirl's wind farm layouts analysis. *Available online at: https://seatwirl.com/content/uploads/SeaTwirl-wind-farm-layout-design-v5-FINAL.pdf*.

[254] Ion Paraschivoiu. Double-multiple streamtube model for darrieus in turbines. 1981.

[255] Ion Paraschivoiu. Double-multiple streamtube model for studying vertical-axis wind turbines. *Journal of propulsion and power*, 4(4):370–377, 1988.

[256] Ion Paraschivoiu. *Wind turbine design: with emphasis on Darrieus concept*. Presses inter Polytechnique, 2002.

[257] UK Parliament. Commons library analysis: Energy: The renewables obligation. *Available online at: https://commonslibrary.parliament.uk/research-briefings/sn05870/*, 2016.

[258] UK Parliament. Government policy on reaching net zero by 2050. *Available online at: https://commonslibrary.parliament.uk/research-briefings/cdp-2023-0124/*, 2023.

[259] RW Paterson and RK Amiet. Noise of a model helicopter rotor due to ingestion of isotropic turbulence. *Journal of Sound and Vibration*, 85(4):551–577, 1982.

[260] Uwe S Paulsen, Michael Borg, Helge Aa Madsen, Troels Friis Pedersen, Jesper Hattel, Ewen Ritchie, Carlos S Ferreira, Harald Svendsen, Petter A Berthelsen, and Charles Smadja. Outcomes of the deepwind conceptual design. *Energy Procedia*, 80:329–341, 2015.

[261] Charlie Pearson. *Vertical axis wind turbine acoustics*. PhD thesis, University of Cambridge, 2014.

[262] HY Peng, ZD Han, HJ Liu, K Lin, and HF Lam. Assessment and optimization of the power performance of twin vertical axis wind turbines via numerical simulations. *Renewable Energy*, 147:43–54, 2020.

[263] HY Peng, HJ Liu, and JH Yang. A review on the wake aerodynamics of h-rotor vertical axis wind turbines. *energy*, 232:121003, 2021.

[264] Antonio Posa. Wake characterization of coupled configurations of vertical axis wind turbines using large eddy simulation. *International Journal of Heat and Fluid Flow*, 75:27–43, 2019.

[265] VWT Power. Quiet revolution 6 vawt. *Available online at: https://vwtpower.com/bespoke-and-branded-versions-of-the-qr6/*.

[266] Sayyad Basim Qamar and Isam Janajreh. A comprehensive analysis of solidity for cambered darrieus vawts. *International Journal of Hydrogen Energy*, 42(30):19420–19431, 2017.

[267] J Qu, MW Xu, and Y Li. Effects of blade number on self-starting performance of vertical axis wind turbine with self-adapting wind speed under low wind speed. *Transactions of the Chinese Society for Agricultural Machinery*, 5:173–178, 2014.

[268] Quiet-Revolution. Quiet revolution vawt. *Available online at: https://www.quietrevolution.com/products/*.

[269] G Rahier, M Huet, and J Prieur. Additional terms for the use of ffowcs williams and hawkings surface integrals in turbulent flows. *Computers & Fluids*, 120:158–172, 2015.

[270] John M Rainbird, Alessandro Bianchini, Francesco Balduzzi, Joaquim Peiró, J Michael R Graham, Giovanni Ferrara, and Lorenzo Ferrari. On the influence of virtual camber effect on airfoil polars for use in simulations of darrieus wind turbines. *Energy Conversion and Management*, 106:373–384, 2015.

[271] R Ganesh Rajagopalan, Ted L Rickerl, and Paul C Klimas. Aerodynamic interference of vertical axis wind turbines. *Journal of Propulsion and Power*, 6(5):645–653, 1990.

[272] Sepehr Rasekh and Saeed Karimian. Effect of solidity on aeroacoustic performance of a vertical axis wind turbine using improved delayed detached eddy simulation. *International Journal of Aeroacoustics*, 20(3-4):390–413, 2021.

[273] Pierre-Elouan Réthoré, Paul van der Laan, Niels Troldborg, Frederik Zahle, and Niels N Sørensen. Verification and validation of an actuator disc model. *Wind Energy*, 17(6):919–937, 2014.

[274] Abdolrahim Rezaeiha, Ivo Kalkman, and Bert Blocken. Cfd simulation of a vertical axis wind turbine operating at a moderate tip speed ratio: Guidelines for minimum domain size and azimuthal increment. *Renewable energy*, 107:373–385, 2017.

[275] Abdolrahim Rezaeiha, Ivo Kalkman, Hamid Montazeri, and Bert Blocken. Effect of the shaft on the aerodynamic performance of urban vertical axis wind turbines. *Energy conversion and management*, 149:616–630, 2017.

[276] Abdolrahim Rezaeiha, Hamid Montazeri, and Bert Blocken. Towards optimal aerodynamic design of vertical axis wind turbines: Impact of solidity and number of blades. *Energy*, 165: 1129–1148, 2018.

[277] Lewis Fry Richardson and J Arthur Gaunt. Viii. the deferred approach to the limit. *Philosophical Transactions of the Royal Society of London. Series A, containing papers of a mathematical or physical character*, 226(636-646):299–361, 1927.

[278] Patrick J Roache. Quantification of uncertainty in computational fluid dynamics. *Annual review of fluid Mechanics*, 29(1):123–160, 1997.

[279] Patrick J Roache. *Verification and validation in computational science and engineering*, volume 895. Hermosa Albuquerque, NM, 1998.

[280] Sung-Cheoul Roh and Seung-Hee Kang. Effects of a blade profile, the reynolds number, and the solidity on the performance of a straight bladed vertical axis wind turbine. *Journal of Mechanical Science and Technology*, 27(11):3299–3307, 2013.

[281] G Romani. Computational aeroacoustics of rotor noise in novel aircraft configurations: A lattice-boltzmann method-based study. 2022.

[282] Thomas D Rossing and Thomas D Rossing. *Springer handbook of acoustics*, volume 1. Springer, 2007.

[283] Royall-Products. Windspire turbine. *Available online at: https://www.windspireenergy.com/*.

[284] A Sagharichi, M Zamani, and Am Ghasemi. Effect of solidity on the performance of variable-pitch vertical axis wind turbine. *Energy*, 161:753–775, 2018.

[285] Sadra Sahebzadeh, Abdolrahim Rezaeiha, and Hamid Montazeri. Towards optimal layout design of vertical-axis wind-turbine farms: Double rotor arrangements. *Energy Conversion and Management*, 226:113527, 2020.

[286] Sadra Sahebzadeh, Abdolrahim Rezaeiha, and Hamid Montazeri. Vertical-axis wind-turbine farm design: Impact of rotor setting and relative arrangement on aerodynamic performance of double rotor arrays. *Energy Reports*, 8:5793–5819, 2022.

[287] Tonio Sant. Improving bem-based aerodynamic models in wind turbine design codes. 2007.

[288] JA Sardo. Theory and measurements on h-darrieus turbines in skewed flow. *Master project at the Delft University of technology, report WE-03193, Delft, The Netherlands*, 9, 2003.

[289] Joseph Saverin, David Marten, David Holst, George Pechlivanoglou, Christian Oliver Paschereit, Giacomo Persico, and Vincenzo Dossena. Comparison of experimental and numerically predicted three-dimensional wake behaviour of a vertical axis wind turbine. In *Turbo Expo: Power for Land, Sea, and Air*, volume 50961, page V009T49A009. American Society of Mechanical Engineers, 2017.

[290] Sigard J Savonius. The s-rotor and its applications. *Mechanical engineering*, 53(5):333–338, 1931.

[291] PR Schatzle, Paul C Klimas, and HR Spahr. Aerodynamic interference between two darrieus wind turbines. *Journal of Energy*, 5(2):84–88, 1981.

[292] Frank Scheurich. *Modelling the aerodynamics of vertical-axis wind turbines*. PhD thesis, University of Glasgow, 2011.

[293] Frank Scheurich and Richard Brown. Vertical-axis wind turbines in oblique flow: sensitivity to rotor geometry. *EWEA Annual event (formerly known as EWEC)*, 2011.

[294] Frank Scheurich and Richard E Brown. Effect of dynamic stall on the aerodynamics of vertical-axis wind turbines. *AIAA journal*, 49(11):2511–2521, 2011.

[295] Hidetaka Senga, Hiroki Umemoto, and Hiromichi Akimoto. Verification of tilt effect on the performance and wake of a vertical axis wind turbine by lifting line theory simulation. *Energies*, 15(19):6939, 2022.

[296] S Shaaban, A Albatal, and MH Mohamed. Optimization of h-rotor darrieus turbines' mutual interaction in staggered arrangements. *Renewable Energy*, 125:87–99, 2018.

[297] Mohammed Shaheen and Shaaban Abdallah. Efficient clusters and patterned farms for darrieus wind turbines. *Sustainable Energy Technologies and Assessments*, 19:125–135, 2017.

[298] Mohammed Shaheen, Mohamed El-Sayed, and Shaaban Abdallah. Numerical study of two-bucket savonius wind turbine cluster. *Journal of Wind Engineering and Industrial Aerodynamics*, 137:78–89, 2015.

[299] Xiaowen Shan, Xue-Feng Yuan, and Hudong Chen. Kinetic theory representation of hydrodynamics: a way beyond the navier–stokes equation. *Journal of Fluid Mechanics*, 550:413–441, 2006.

[300] Robert E Sheldahl and Paul C Klimas. Aerodynamic characteristics of seven symmetrical airfoil sections through 180-degree angle of attack for use in aerodynamic analysis of vertical axis wind turbines. Technical report, Sandia National Labs., Albuquerque, NM (USA), 1981.

[301] S Shubham, A Ianakiev, and N Wright. Review of standalone small-scale darrieus wind turbines-a nottingham case study. In *17th EAWE PhD Seminar on wind energy*, 11 2021.

[302] Shubham Shubham. Computational aeroacoustic investigation of co-rotating rotors for urban air mobility. 2020.

[303] Shubham Shubham, Anton Ianakiev, and Nigel Wright. Review of standalone small-scale darrieus wind turbines - a nottingham case study. In *17th EAWE PhD Seminar on Wind Energy*, 11 2021.

[304] Shubham Shubham, Nigel Wright, and Anton Ianakiev. Application of richardson extrapolation method to aerodynamic and aeroacoustic characteristics of low reynolds number vertical axis wind turbines. In *28th AIAA/CEAS Aeroacoustics 2022 Conference*, page 3022, 2022.

[305] Shubham Shubham, Kevin Naik, Shivangi Sachar, and Anton Ianakiev. Performance analysis of low reynolds number vertical axis wind turbines using low-fidelity and mid-fidelity methods and wind conditions in the city of nottingham. *Energy*, 279:127904, 2023.

[306] Shubham Shubham, Nigel Wright, Francesco Avallone, and Anton Ianakiev. Aerodynamic and aeroacoustic investigation of vertical axis wind turbines with different number of blades using mid-fidelity and high-fidelity methods. In *2023 AIAA Aviation and Aeronautics Forum and Exposition (AIAA AVIATION Forum)*, 2023.

[307] Lih Shyng Shyu. A pilot study of vertical-axis turbine wind farm layout planning. *Advanced Materials Research*, 953:395–399, 2014.

[308] M Salman Siddiqui, Naveed Durrani, and Imran Akhtar. Numerical study to quantify the effects of struts and central hub on the performance of a three dimensional vertical axis wind turbine using sliding mesh. In *ASME Power Conference*, volume 56062, page V002T09A020. American Society of Mechanical Engineers, 2013.

[309] Jeffrey E Silva and Louis Angelo M Danao. Varying vawt cluster configuration and the effect on individual rotor and overall cluster performance. *Energies*, 14(6):1567, 2021.

[310] Carlos Simao Ferreira, Kristian Dixon, Claudia Hofemann, Gijs van Kuik, and Gerard van Bussel. Vawt in skew: Stereo-piv and vortex modeling. In *47th AIAA aerospace sciences meeting including the new horizons forum and aerospace exposition*, page 1219, 2009.

[311] Carlos J Simão Ferreira, Gerard JW Van Bussel, and Gijs AM Van Kuik. Wind tunnel hotwire measurements, flow visualization and thrust measurement of a vawt in skew. 2006.

[312] CJ Simao Ferreira. *The near wake of the vawt - 2d and 3d views of the vawt aerodynamics*. PhD thesis, Delft University of Technology, 2009.

[313] S Singh, A Karchani, and RS Myong. Non-equilibrium effects of diatomic and polyatomic gases on the shock-vortex interaction based on the second-order constitutive model of the boltzmann-curtiss equation. *Physics of Fluids*, 30(1), 2018.

[314] H Snel, R Houwink, and WJ Piers. Sectional prediction of 3 d effects for separated flow on rotating blades. 1992.

[315] Philippe R Spalart, Kirill V Belyaev, Mikhail L Shur, Mikhail Kh Strelets, and Andrey K Travin. On the differences in noise predictions based on solid and permeable surface ffowcs williams–hawkings integral solutions. *International Journal of Aeroacoustics*, 18(6-7):621–646, 2019.

[316] John E Stone, David Gohara, and Guochun Shi. Opencl: A parallel programming standard for heterogeneous computing systems. *Computing in science & engineering*, 12(3):66, 2010.

[317] James H Strickland. Darrieus turbine: a performance prediction model using multiple streamtubes. Technical report, Sandia Labs., Albuquerque, N. Mex.(USA), 1975.

[318] Hao Su, Haoran Meng, Timing Qu, and Liping Lei. Wind tunnel experiment on the influence of array configuration on the power performance of vertical axis wind turbines. *Energy Conversion and Management*, 241:114299, 2021.

[319] Jie Su, Hang Lei, Dai Zhou, Zhaolong Han, Yan Bao, Hongbo Zhu, and Lei Zhou. Aerodynamic noise assessment for a vertical axis wind turbine using improved delayed detached eddy simulation. *Renewable energy*, 141:559–569, 2019.

[320] Abhishek Subramanian, S Arun Yogesh, Hrishikesh Sivanandan, Abhijit Giri, Madhavan Vasudevan, Vivek Mugundhan, and Ratna Kishore Velamati. Effect of airfoil and solidity on performance of small scale vertical axis wind turbine using three dimensional cfd model. *Energy*, 133:179–190, 2017.

[321] Sauro Succi. *The lattice Boltzmann equation: for fluid dynamics and beyond*. Oxford university press, 2001.

[322] Xiaojing Sun, Daihai Luo, Diangui Huang, and Guoqing Wu. Numerical study on coupling effects among multiple savonius turbines. *Journal of Renewable and Sustainable Energy*, 4(5), 2012.

[323] Xiaojing Sun, Yajun Chen, Yang Cao, Guoqing Wu, Zhongquan Zheng, and Diangui Huang. Research on the aerodynamic characteristics of a lift drag hybrid vertical axis wind turbine. *Advances in Mechanical Engineering*, 8(1):1687814016629349, 2016.

[324] Xuejing Sun, Jianyang Zhu, Zongjin Li, and Guoxing Sun. Rotation improvement of vertical axis wind turbine by offsetting pitching angles and changing blade numbers. *Energy*, 215: 119177, 2021.

[325] Agus Sunyoto, Frederikus Wenehenubun, and Hadi Sutanto. The effect of number of blades on the performance of h-darrieus type wind turbine. In *2013 International Conference on QiR*, pages 192–196. IEEE, 2013.

[326] Herbert J Sutherland, Dale E Berg, and Thomas D Ashwill. A retrospective of vawt technology. *Sandia National Laboratories*, pages 1–64, 2012.

[327] Christopher KW Tam. Computational aeroacoustics-issues and methods. *AIAA journal*, 33 (10):1788–1796, 1995.

[328] Christopher KW Tam. Computational aeroacoustics: An overview of computational challenges and applications. *International Journal of Computational Fluid Dynamics*, 18(6):547–567, 2004.

[329] J Tangler. The evolution of rotor and blade design. Technical report, National Renewable Energy Lab.(NREL), Golden, CO (United States), 2000.

[330] Christopher M Teixeira. Incorporating turbulence models into the lattice-boltzmann method. *International Journal of Modern Physics C*, 9(08):1159–1175, 1998.

[331] RJ Templin. Aerodynamic performance theory for the nrc vertical-axis wind turbine. Technical report, National Aeronautical Establishment, Ottawa, Ontario (Canada), 1974.

[332] Erik Tengs, Pål-Tore Storli, and Martin Holst. Optimization procedure for variable speed turbine design. *Engineering Applications of Computational Fluid Mechanics*, 12(1):652–661, 2018.

[333] C Teruna. Aerodynamic noise reduction with porous materials: Aeroacoustics investigations and applications. 2022.

[334] G Tescione, D Ragni, C He, CJ Simão Ferreira, and GJW Van Bussel. Near wake flow analysis of a vertical axis wind turbine by stereoscopic particle image velocimetry. *Renewable Energy*, 70:47–61, 2014.

[335] C Testa, F Porcacchia, S Zaghi, and M Gennaretti. Study of a fwh-based permeable-surface formulation for propeller hydroacoustics. *Ocean Engineering*, 240:109828, 2021.

[336] Tarun Ramprakash Thambidurai Arasi, Shubham Shubham, and Anton Ianakiev. Effect of blade shape on aerodynamic and aeroacoustic characteristics of vertical axis wind turbines using mid-fidelity and high-fidelity methods. In *AIAA SCITECH 2024 Forum*, page 1488, 2024.

[337] Robert Nason Thomas. Coupled vortex vertical axis wind turbine, August 31 2004. US Patent 6,784,566.

[338] Wenlong Tian, Zhaoyong Mao, Xinyu An, Baoshou Zhang, and Haibing Wen. Numerical study of energy recovery from the wakes of moving vehicles on highways by using a vertical axis wind turbine. *Energy*, 141:715–728, 2017.

[339] Eric B Tingey and Andrew Ning. Parameterized vertical-axis wind turbine wake model using cfd vorticity data. In *34th Wind Energy Symposium*, page 1730, 2016.

[340] Willy Tjiu, Tjukup Marnoto, Sohif Mat, Mohd Hafidz Ruslan, and Kamaruzzaman Sopian. Darrieus vertical axis wind turbine for power generation i: Assessment of darrieus vawt configurations. *Renewable energy*, 75:50–67, 2015.

[341] Niels Troldborg, Gunner C Larsen, Helge A Madsen, Kurt S Hansen, Jens N Sørensen, and Robert Mikkelsen. Numerical simulations of wake interaction between two wind turbines at various inflow conditions. *Wind Energy*, 14(7):859–876, 2011.

[342] UNFCCC. The paris agreement. *Available online at: https://unfccc.int/process-and-meetings/the-paris-agreement/the-paris-agreement*, 2015.

[343] TV Valkov and CS Tan. Effect of upstream rotor vortical disturbances on the time-averaged performance of axial compressor stators: Part 2—rotor tip vortex/streamwise vortex–stator blade interactions. 1999.

[344] GJW Van Bussel, S Mertens, H Polinder, and HFA Sidler. Turby®: concept and realisation of a small vawt for the built environment. In *Proceedings of the EAWE/EWEA Special Topic conference" The Science of making Torque from Wind", Delft, The Netherlands*, 2004.

[345] WCP van der Velden, Damiano Casalino, P Gopalakrishnan, A Jammalamadaka, Y Li, R Zhang, and H Chen. Validation of jet noise simulations and resulting insights of acoustic near field. *AIAA Journal*, 57(12):5156–5167, 2019.

[346] A Van Garrel. Development of a wind turbine aerodynamics simulation module. 2003.

[347] J Vassberg. Challenges and accomplishments of the aiaa cfd drag prediction workshop series. In *AVT-246 Specialists' Meeting on Progress and Challenges in Validation Testing for Computational Fluid Dynamics, Avila, Spain, Sept*, pages 26–28, 2016.

[348] John C Vassberg and Antony Jameson. In pursuit of grid convergence for two-dimensional euler solutions. *Journal of Aircraft*, 47(4):1152–1166, 2010.

[349] Kartik Venkatraman, Julien Christophe, Christophe F Schram, and Stephane Moreau. Numerical investigation of the effect of inflow non-uniformity on the noise radiated by a vertical axis wind turbine. In *AIAA AVIATION 2021 FORUM*, page 2216, 2021.

[350] Antoine Vergaerde, Tim De Troyer, Sara Muggiasca, Ilmas Bayati, Marco Belloli, and Mark C Runacres. Influence of the direction of rotation on the wake characteristics of closely spaced counter-rotating vertical-axis wind turbines. In *Journal of Physics: Conference Series*, volume 1618, page 062017. IOP Publishing, 2020.

[351] Antoine Vergaerde, Tim De Troyer, Lieven Standaert, Joanna Kluczewska-Bordier, Denis Pitance, Alexandre Immas, Frédéric Silvert, and Mark C Runacres. Experimental validation of the power enhancement of a pair of vertical-axis wind turbines. *Renewable Energy*, 146:181–187, 2020.

[352] Thierry Villeneuve, Grégoire Winckelmans, and Guy Dumas. Increasing the efficiency of vertical-axis turbines through improved blade support structures. *Renewable Energy*, 169: 1386–1401, 2021.

[353] Claus Wagner, Thomas Hüttl, and Pierre Sagaut. *Large-eddy simulation for acoustics*, volume 20. Cambridge University Press, 2007.

[354] Biao Wang, LD Cot, Luc Adolphe, and Sandrine Geoffroy. Estimation of wind energy of a building with canopy roof. *Sustainable Cities and Society*, 35:402–416, 2017.

[355] Zhijian J Wang, Krzysztof Fidkowski, Rémi Abgrall, Francesco Bassi, Doru Caraeni, Andrew Cary, Herman Deconinck, Ralf Hartmann, Koen Hillewaert, Hung T Huynh, et al. High-order cfd methods: current status and perspective. *International Journal for Numerical Methods in Fluids*, 72(8):811–845, 2013.

[356] Johannes Weber, Stefan Becker, Christoph Scheit, Jens Grabinger, and Manfred Kaltenbacher. Aeroacoustics of darrieus wind turbine. *International Journal of Aeroacoustics*, 14(5-6):883–902, 2015.

[357] Johannes Weber, Sebastian Riedel, Julian Praß, Andreas Renz, Stefan Becker, and Jörg Franke. Effect of boundary layer tripping on the aeroacoustics of small vertical axis wind turbines. In *Advanced Engineering Forum*, volume 19, pages 3–9. Trans Tech Publ, 2016.

[358] David Wafula Wekesa, Cong Wang, Yingjie Wei, and Weidong Zhu. Experimental and numerical study of turbulence effect on aerodynamic performance of a small-scale vertical axis wind turbine. *Journal of Wind Engineering and Industrial Aerodynamics*, 157:1–14, 2016.

[359] Juliane Wendler, David Marten, George Pechlivanoglou, Christian Navid Nayeri, and Christian Oliver Paschereit. An unsteady aerodynamics model for lifting line free vortex wake simulations of hawt and vawt in qblade. In *Turbo Expo: Power for Land, Sea, and Air*, volume 49873, page V009T46A011. American Society of Mechanical Engineers, 2016.

[360] Robert W Whittlesey, Sebastian Liska, and John O Dabiri. Fish schooling as a basis for vertical axis wind turbine farm design. *Bioinspiration & biomimetics*, 5(3):035005, 2010.

[361] JE Ffowcs Williams and David L Hawkings. Sound generation by turbulence and surfaces in arbitrary motion. *Philosophical Transactions for the Royal Society of London. Series A, Mathematical and Physical Sciences*, pages 321–342, 1969.

[362] Maarten Wolsink. Wind power implementation: the nature of public attitudes: equity and fairness instead of 'backyard motives'. *Renewable and sustainable energy reviews*, 11(6):1188–1207, 2007.

[363] Mark H Worstell. Aerodynamic performance of the doe/sandia 17-m-diameter vertical-axis wind turbine. *Journal of Energy*, 5(1):39–42, 1981.

[364] Carlos M Xisto, José C Páscoa, and Michele Trancossi. Geometrical parameters influencing the aerodynamic efficiency of a small-scale self-pitch high-solidity vawt. *Journal of Solar Energy Engineering*, 138(3):031006, 2016.

[365] Hui Xu and Pierre Sagaut. Optimal low-dispersion low-dissipation lbm schemes for computational aeroacoustics. *Journal of Computational Physics*, 230(13):5353–5382, 2011.

[366] Victor Yakhot and Steven A Orszag. Renormalization group analysis of turbulence. i. basic theory. *Journal of scientific computing*, 1(1):3–51, 1986.

[367] VSASTBCG Yakhot, SA Orszag, Siva Thangam, TB Gatski, and CG1167781 Speziale. Development of turbulence models for shear flows by a double expansion technique. *Physics of Fluids A: Fluid Dynamics*, 4(7):1510–1520, 1992.

[368] Yanzhao Yang, Zhiping Guo, Yanfeng Zhang, Ho Jinyama, and Qingan Li. Numerical investigation of the tip vortex of a straight-bladed vertical axis wind turbine with double-blades. *Energies*, 10(11):1721, 2017.

[369] Saman Naghib Zadeh, Matin Komeili, and Marius Paraschivoiu. Mesh convergence study for 2-d straight-blade vertical axis wind turbine simulations and estimation for 3-d simulations. *Transactions of the Canadian Society for Mechanical Engineering*, 38(4):487–504, 2014.

[370] Stefania Zanforlin and Takafumi Nishino. Fluid dynamic mechanisms of enhanced power generation by closely spaced vertical axis wind turbines. *Renewable Energy*, 99:1213–1226, 2016.

[371] LX Zhang, YB Liang, XH Liu, QF Jiao, and Jianhua Guo. Aerodynamic performance prediction of straight-bladed vertical axis wind turbine based on cfd. *Advances in Mechanical Engineering*, 5:905379, 2013.

[372] Ning Zhang, Minguan Yang, Bo Gao, Zhong Li, and Dan Ni. Investigation of rotor-stator interaction and flow unsteadiness in a low specific speed centrifugal pump. *Strojniški vestnik-Journal of Mechanical Engineering*, 62(1):21–31, 2016.

[373] Raoyang Zhang, Chenghai Sun, Yanbing Li, Rajani Satti, Richard Shock, James Hoch, and Hudong Chen. Lattice boltzmann approach for local reference frames. *Communications in Computational Physics*, 9(5):1193–1205, 2011.